Pro-apoptotic and radiosensitizing potential of four candidate microtubule regulators in breast cancer cells

Elsie Nolte

▶ **To cite this version:**

Elsie Nolte. Pro-apoptotic and radiosensitizing potential of four candidate microtubule regulators in breast cancer cells. Cellular Biology. Université Grenoble Alpes; University of Pretoria, 2019. English. NNT : 2019GREAV002 . tel-02918664

HAL Id: tel-02918664
https://theses.hal.science/tel-02918664

Submitted on 21 Aug 2020

HAL is a multi-disciplinary open access archive for the deposit and dissemination of scientific research documents, whether they are published or not. The documents may come from teaching and research institutions in France or abroad, or from public or private research centers.

L'archive ouverte pluridisciplinaire **HAL**, est destinée au dépôt et à la diffusion de documents scientifiques de niveau recherche, publiés ou non, émanant des établissements d'enseignement et de recherche français ou étrangers, des laboratoires publics ou privés.

UNIVERSITEIT VAN PRETORIA
UNIVERSITY OF PRETORIA
YUNIBESITHI YA PRETORIA

Communauté
UNIVERSITÉ Grenoble Alpes

THÈSE

Pour obtenir le grade de

DOCTEUR DE LA COMMUNAUTE UNIVERSITE GRENOBLE ALPES

préparée dans le cadre d'une cotutelle *entre la Communauté Université Grenoble Alpes* et *l'Université de Pretoria (Afrique du Sud)*

Spécialité : **Biologie Cellulaire**

Arrêté ministériel : le 6 janvier 2005 – 25 mai 2016

Présentée par

Elsie NOLTE »

Thèse dirigée par **Anne MERCIER** et **Laurence LAFANECHERE**

préparée au sein de l'Équipe Régulation et Pharmacologie du Cytosquelette de L'Institut pour l'Avancée de Biosciences, Grenoble, France and the Department of Physiology, Cancer Cell Physiology Laboratory, University of Pretoria, Pretoria, South Africa

dans **les Écoles Doctorales de Chimie et Sciences du Vivant et de School of Medicine, Department of Physiology, University of Pretoria**

Étude du potentiel pro-apoptotique et radiosensibilisateur de quatre candidats-médicaments régulateurs des microtubules, sur les cellules de cancer du sein

Thèse soutenue publiquement le **20 Février 2019**
devant le jury composé de :

Monsieur Jean-Luc COLL
Directeur de Recherche, Institut pour l'Avancée des Biosciences, Président
Monsieur Siamak HAGHDOOST
Professeur, Université de Stockholm, Suède, Rapporteur
Madame Megan Jean BESTER
Professeur, Université de Pretoria, Afrique du Sud, Rapporteur
Madame Anne Mercier
MCU-PH, Université de Pretoria, Afrique du Sud, Directrice de Thèse
Madame Laurence LAFANECHERE
Directeur de Recherche, Institut pour l'Avancée des Biosciences, Directrice de thèse

UNIVERSITEIT VAN PRETORIA
UNIVERSITY OF PRETORIA
YUNIBESITHI YA PRETORIA

Communauté
UNIVERSITÉ Grenoble Alpes

Thesis submitted in fulfilment of the requirements for the degree
Philosophiæ Doctor (Ph.D) in Human Physiology

Title:

Pro-apoptotic and radiosensitizing potential of four candidate microtubule regulators in breast cancer cells

by

Elsie Magdalena Nolte
(UP:10005022; UGA:61600881)

Department of Physiology
School of Medicine, Faculty of Health Sciences
University of Pretoria

February 2019

Project supervisors

Supervisor: Dr. AE Mercier

Department of Physiology, University of Pretoria,

Pretoria, South Africa

Prof. L Lafanechère

Institute for Advanced Biosciences, INSERM U1209/ UMR

CNRS 5309, Université Grenoble Alpes, Grenoble, France

Co-supervisor: Prof. AM Joubert

Department of Physiology

University of Pretoria, Pretoria, South Africa

Prof. R Lakier

Department of Radiation Oncology

Steve Biko Academic Hospital

University of Pretoria, Pretoria, South Africa

“I am just a child who has never grown up. I still keep asking these 'how' and 'why' questions. Occasionally, I find an answer.”

- Stephen Hawking -

“Tog, ondanks ons stukkende vlerke, leer ons vlieg. Hoër en verder as wat ons ooit kon droom”

- Annelie Botes -

"En as ek die dag my hand in joune sit, sal ek my padkaarte bêre met die wete: my reise opsoek na jou is nou verby!" - Antjie Krog.

Zander Coetzee, dankie dat jy jou lewe (en Whispers) met my deel!

Summary

Microtubule targeting agents are effective anti-cancer drugs. Their use as part of a combined treatment modality with ionising radiation is also a promising strategy. However, the emergence of chemical and radiation resistance requires searching for alternative treatments. Our laboratories have recently described several drugs that directly or indirectly target the cellular microtubules. 2-Ethyl-3-*O*-sulphamoyl-estra-1,3,5(10)16-tetraene (ESE-16), an analogue of 2-methoxyestradiol, is a microtubule targeting agent that binds to microtubules causing the formation of abnormal mitotic spindles. 9-Benzoyloxy-5,11-dimethyl-2H,6H-pyrido[4,3-b]carbazol-1-one (LimPyr1) is a novel inhibitor of LIM kinases that indirectly induces microtubule stabilization. As microtubule-targeting drugs, both agents, ESE-16 and LimPyr1, induce mitotic defects. We thus hypothesized that they could sensitize cells to radiation as the G_2/M phase is the most radiosensitive phase of the cell cycle. The aim of this PhD project was to test that hypothesis and, more specifically, to investigate whether low-doses of ESE-16 and LimPyr1 could increase apoptosis and delay nuclear repair induced by radiation in breast cancer cells *in vitro*.

Breast cancer cell lines namely MCF-7-, MDA-MB-231- and BT-20 cells, were exposed to ESE-16 and LimPyr1 for 24-hours prior to 8 Gy radiation. The effects of these combination therapies were compared to those obtained from cells exposed to the compounds alone or only to radiation. The activation of the survival and intrinsic apoptotic pathways were investigated. Results revealed altered survival and death signaling in cells exposed to the individual treatments. The combination treatments decreased cell survival while apoptotic signaling was increased, resulting in increased cell death. Furthermore, the combination treatments significantly increased the presence of micronuclei in BT-20 cells, indicating an increase in deoxyribonucleic acid (DNA) damage. MCF-7- and MDA-MB-231 cells displayed similar micronuclei formation when exposed to the combination treatments or radiation only. Phosphorylation of H2AX (γH2AX) (normally increased upon DNA damage) and Ku70 expression (required for DNA repair) were decreased in pre-treated breast cancer cells 2

hours after irradiation compared to cells exposed to radiation only. The expression of γH2AX and Ku70, however, were significantly increased 24 hours after irradiation in the pre-treated cells. LimPyr1 decreased radiation resistance development from dose fractionation by increasing the permeability of the mitochondrial membrane. An increase in the generation of reactive oxygen species (ROS) was not observed in ESE-16 pre-treated cells exposed to fractionated radiotherapy. We also observed pro-apoptotic signaling between cells exposed to radiation and non-exposed cells via the radiation-induced bystander effect.

In conclusion, the anti-mitotic effect of ESE-16 and LimPyr1 renders the chromosomes more exposed to radiation damage as assessed by the increased occurrence of micronuclei. Moreover, both compounds decreased the signaling and trafficking of DNA damage and repair proteins. Additionally, LimPyr1 prevented the development of radiation resistance in cells exposed to fractionated radiation doses. Future studies will aim to elucidate the molecular mechanisms responsible for ESE-16 and LimPyr1 radiosensitization, as well as validate the safety and efficacy of this approach *in vivo*.

Key words: Cancer, radiation therapy, 2-methoxyestradiol, LIM kinase, ESE-16, LimPyr1, radiosensitization, Akt, FoxO1/3a, reactive oxygen species, Bax, mitochondria, caspase, DNA damage and repair, γH2AX, Ku70, apoptosis, radiation-induced bystander effect, radiation resistance

Research outputs

1. Internationally peer-reviewed accredited scientific publications

1. **Nolte EM**, Joubert AM, Lakier R, Van Rensburg A, Mercier AE. Exposure of breast and lung cancer cells to a novel estrone analog prior to radiation enhances Bcl-2-mediated cell death. Int J Mol Sci. 2018;19(10):2887.
2. Sadoul K, Joubert C, Michallet S, **Nolte E**, Peronne L, Ramirez-Rios S, Ribba AS, Lafanechère L. Déchiffrage du code tubuline-Le voile se lève sur le rôle de l'acétylation et de la détyrosination. Med Sci. 2018;34(12):1047-1055.
3. Helena JM, Joubert AM, Grobbelaar S, **Nolte EM**, Nel M, Pepper MS, Coetzee M, Mercier AE. Deoxyribonucleic acid damage and repair: Capitalizing on our understanding of the mechanisms of maintaining genomic integrity for therapeutic purposes. Int J Mol Sci. 2018;19(4):1148.
4. Verwey M, **Nolte EM**, Joubert AM, Theron AE. Autophagy induced by a sulphamoylated estrone analogue contributes to its cytotoxic effect on breast cancer cells. Cancer Cell Int. 2016;16(1):91.
5. Klionsky DJ, *et al*. Guidelines for the use and interpretation of assays for monitoring autophagy. Autophagy. 2016;12(1):1-222.
6. Theron A, **Nolte E**, Lafanechere L, Joubert A. Molecular crosstalk between apoptosis and autophagy induced by a novel 2-methoxyestradiol analogue in cervical adenocarcinoma cells. Cancer Cell Int. 2013; 13(1):87.
7. AE Theron, R Prudent, **E Nolte**, I van den Bout, R Punchoo, S Marais, P Du Toit, Y Hlope, D van Papendorp, L Lafanechère and A Joubert. Novel *in silico*-designed estradiol analogues are cytotoxic to a multidrug-resistant cell line at nanomolar concentrations. Cancer Chemother. Pharmacol. 2015;75(2):431-437.

2. Published conference proceedings and conference presentations

1. **Nolte EM**, Joubert AM, Lakier R, Sebopa L, Prudent R, Lafanechère L, Mercier AE. Intra- and intercellular signaling pathways driving the radiosensitizating effect of a Lim kinase inhibitor *in vitro*. Oral presentation at the 56th annual South African Association of Physicists in Medicine and Biology congress (SAAPMB) (22-26 October 2018).
2. Helena JM, Joubert AM, Mabeta P, Coetzee M, Lakier R, **Nolte EM**, Nel M, Sebopa L, Rathidili M, Mercier AE. Radiosensitization of *in vitro* metastasis models by a spindle disruptor potentially involves increased DNA damage, proapoptotic signaling and inhibiting neovascularization. Oral presentation at the 56th annual South African Association of Physicists in Medicine and Biology congress (SAAPMB) (22-26 October 2018).
3. **Nolte EM**, Joubert AM, Lakier R, Etsebeth M, Sebopa L, Prudent R, Lafanechère, Mercier AE. Disruption of both actin- and microtubule dynamics sensitizes triple negative breast cancer cells to radiation. Oral presentation at the 45th Conference of the Physiology Society of Southern Africa (27-31 August 2017).
4. **Nolte EM**, Joubert AM, Lakier R, Etsebeth M, Sebopa L, Lafanechère L & Mercier AE. A novel estradiol analogue delays deoxyribonucleic acid repair in triple negative breast cancer cells exposed to radiation *in vitro.* Physica Medica. 2017;41:S11.
5. **Nolte EM**, Joubert AM, Lakier R, Etsebeth M, Sebopa L, Prudent R, Lafanechère L & Mercier AE. Targeting actin dynamics with a novel LIM kinase inhibitor results in radiosensitization of triple negative breast cancer cells and radiation-induced pro-apoptotic bystander effects. Physica Medica. 2017;41:S14-15.
6. Helena JM, Joubert AM, Mabeta P, Coetzee M, Lakier R, **Nolte E**, Verwey M, Etsebeth M, Moosa S, Sebopa L, Mercier AE. Radiosensitization capacities of a novel microtubule disruptor assessed on a deconstructed bone metastasis model. Physica Medica. 2017;41:S6.
7. **Nolte EM**, Joubert AM, Hargrave SD, Helena JM, Lakier R, Etsebeth M, Verwey M, Theron AE. O41. Novel microtubule disruptors radiosensitize cancer cells *in vitro*. Physica Medica. 2016;32:154.

8. Verwey M, Joubert AM, Meijer W, **Nolte EM**, Lakier R, Etsebeth M, Helena J, Theron AE. P10. Radiosensitization of breast adenocarcinoma cells by a novel estrone analogue is dependent on reactive oxygen species signaling. Physica Medica. 2016;32:164.
9. **Nolte EM**, Lakier R, Etsebeth M, Helena JM, Verwey M, Joubert A.M, Lafanechère L & Theron AE. Cellular mechanisms involved in the radiosensitization of breast- and lung cancer cells by novel agents targeting microtubule dynamics. Oral presentation at the 18th International Conference on Integrative Biology and Physiology (3-4 November 2016).
10. **Nolte EM**, Lakier R, Van Rensburg A, Helena JM, Verwey M, Matlala P, Punchoo R, du Toit P, Joubert AM and Theron AE. Potential radiosensitization of breast cancer cells by a novel anti-mitotic estrone analogue. Poster at the 17th National Congress of South African Society of Medical Oncology (SASMO) and South African Society of Clinical & Radiation Oncology (SASCRO) (7-9 Augusts 2015)
11. **EM Nolte**, R. Lakier, A Van Rensburg, JM Helena, M Verwey, AM. Joubert, and AE Theron. P.11-Potential radiosensitisation of breast-and lung cancer cells by a novel anti-mitotic oestrone analogue. Physica Medica. 2015;31: S17-S18.
12. Helena JM, Lakier R, van Rensburg A, **Nolte EM**, Verwey M, Matlala P, Mlambo R, Joubert AM and AE Theron. Radiosensitization of cancer cells with a novel estradiol analogue affects nuclear repair mechanisms. Poster at the Microscopy Association of Southern Africa Annual Congress (29 November - 4 December 2015).
13. **Nolte, E.M**., Joubert, A.M. & Theron, A.E. Early and late cell death characteristic induced by novel anticancer estradiol analogue *in vitro*. Poster presentation at the Annual Congress of The South African Academy for Science and Arts: Division Biological Sciences (16 October 2013).

3. Postgraduate supervision

1. Mr Scott Hargrave: Co-supervisor BSc Hons [Human physiology] (2016)

4. Academic awards

1. 68th Lindau Nobel Laureate Meeting Participant, 24-29 June 2018, Lindau, Germany

- The 68th Lindau Nobel Laureate Meeting was dedicated to physiology and medicine. A total of 43 Nobel Laureates met 600 of the most qualified undergraduate students, PhD candidates and post-doctoral fellows. The one week scientific program consisted of lectures, master classes and panel discussions where Nobel Laureates and young scientist had the opportunity to exchange ideas, knowledge and experiences.

2. Third place for oral presentation at the annual University of Pretoria, Department of Health Sciences' Faculty day for basic sciences (2016)

- **Nolte EM**, Lakier R, Etsebeth M, Helena JM, Verwey M, Joubert A.M, Lafanechère L & Theron AE. Cellular mechanisms involved in the radiosensitization of breast- and lung cancer cells by novel agents targeting microtubule dynamics.

3. Runner-up for best non-clinical research paper in the Faculty of Health Sciences, UP (2014)

- Theron A, **Nolte E**, Lafanechere L, Joubert A. Molecular crosstalk between apoptosis and autophagy induced by a novel 2-methoxyestradiol analogue in cervical adenocarcinoma cells. Cancer Cell Int. 2013;13(87):13-87.

Acknowledgements

With sincere gratitude to:

- Dr Joji Mercier, my supervisor - Thank you for your support and encouragement over the past three years. Thank you for making me a better scientist and human being. Thank you for challenging me to rise higher than I ever thought I could.

- Prof Laurence Lafanechère, my French supervisor - Il n'y a pas assez de mots pour vous remercier pour m'avoir donné l'incroyable opportunité de réaliser ma thèse en co-tutelle avec vous dans votre laboratoire. Vous m'avez accueillie à bras ouverts et m'avez fourni les conseils et le soutien indispensables tout au long de mon année en France. Vous étiez mon superviseur, mon interprète et ma 'mère française'. Avec un cœur généreux, vous m'avez soutenu financièrement pour assister à la réunion des lauréats du prix Nobel Lindau: une opportunité que je chérirai pour toujours. Ce fut un privilège de travailler avec vous.

- Prof Annie Joubert, my co-supervisor - Ek sal ewig dankbaar wees vir al die ondersteuning wat Prof aan my gebied het deur hierdie avontuur. Prof het altyd 'n helpende hand uitgereik, 'n ondersteunende oor gebied en kosbare ure spandeer om seker te maak ek voltooi hierdie graad suksesvol. Die ondersteuning wat Prof gebied het die laaste week voor die senutergende 'defence' is van onskatbare waarde en ek sal dit vir ewig in my hart koester. Prof is nie net my 'co-supervisor' nie, prof is werklik my rolmodel!

- Prof Roy Lakier, my co-supervisor - Thank you for welcoming me into your department and allowing me to use your equipment. Thank you for all your assistance and support, it is much appreciated.

- Leanor Sebopa and Prof Laurence Chaperot, my radiation partners - Thank you for assisting me in radiating hundreds of samples. Without you this project wouldn't have been possible.

- Lauralie, Sacnicte, Karin, Anne-Sophie, Clotilde and Sophie, my French friends - À mes amies françaises Lauralie, Sacnicte, Karin, Anne-Sophie, Clotilde et Sophie - Merci pour toute votre patience et votre aide. Vous avez fait de mon année en France une année toute particulière et je continuerai de garder dans mon coeur tous nos merveilleux souvenirs.

- Marcel, my best friend - Vir 'n beter 'partner in crime' kon ek nie vra nie. Jy het saam met my liters koffie gedrink, jy het geluister na my gekerm en kla, jy het saam met my op die kantoormat gelê as alles net te veel geraak het. Jy was altyd net daar. Jy het elke oorwinning saam met my gevier en elke terugslag reg 'gedokter' met 'n cocktail. Jou vriendskap beteken oneindig baie vir my. Dankie!

- Ria and Fritz Nolte, my parents - Jare se gebed, liefde, geduld, ondersteuning, en onbaatsugtige en onbenoemde opofferings het gelei tot hierdie sukses. Nooit het julle ophou glo in my vermoë om suksesvol te wees nie. Die trane in jull oë as julle met my 'spog' maak alles die moeite werd. Dankie dat julle my ten volle voorberei het vir die 'grootmens' wêreld. My sukses is bloot 'n refleksie van julle opvoeding.

- André, my big baby brother - Dankie dat jy my gereeld herinner dat die lewe geleef moet word. Dat die klein oorwinnings net soveel waarde dra soos die grotes. Jy was nog altyd trots daarop dat ek jou sussie is, maar soveel meer is ek dankbaar dat jy my broer is. Jy sal my altyd bly inspireer.

- Zander, my husband - Hoe sê mens dankie vir jare se opofferings, bystand, aanmoediging en ondersteuning? Woorde is nie genoeg nie. Jy het elke treë van hierdie pad saam met my gestap. Elke opdraende en afdraende, jy was daar. Jy het my met 'n hartseer maar trotse hart op 'n vliegtuig laat klim sodat ek my droom kon

najaag om in Frankryk navorsing te doen. Jy het opoffering na opoffering gemaak en nooit enige iets terugverwag nie. Ek is ‘n besonderse gelukkige vrou om met ‘n man soos jy die res van my lewe te spandeer. Ek het jou lief!

- My heavenly Father - ICKE JAG UTAN GUD I MIG

Table of contents

Summary v
Research outputs vii
1. Internationally peer-reviewed accredited scientific publications vii
2. Published conference proceedings and conference presentations viii
3. Postgraduate supervision ix
4. Academic awards x
Acknowledgements xi
List of figures xx
List of tables xxvii
List of abbreviations xxxi
1. Introduction and literature study 1
1.1 Breast cancer 1
1.1.1 Classification of breast cancer 3
1.1.2 Treatment options for breast cancer 4
1.2 The cell cycle 5
1.2.1 The G_1 phase 7
1.2.2 The S phase 8
1.2.3 The G_2 phase 8
1.2.4 The M phase 9
1.2.5 Cell cycle checkpoints 10
1.2.5.1 DNA structure checkpoints 10
1.2.5.2 Spindle assembly checkpoint 11
1.3 Cell death 13
1.3.1 Necrosis 13
1.3.2 Apoptosis 14
1.3.2.1 Regulation of apoptosis 15
1.3.2.2 Involvement of reactive oxygen species in apoptosis 18

1.4 Radiotherapy as an effective anti-cancer treatment modality 19
1.4.1 DNA damage signaling and repair 22
1.4.2 Cell death induced by radiation 24
1.4.3 Radiation resistance 26
1.4.4 Radiation-induced bystander effect 28
1.5 Intracellular microtubule dynamics 30
1.6 2-Methoxyestradiol 33
1.6.1 2-Methoxyestradiol analogues 37
1.7 Lin-11, Isl-1 and Mec-3 (LIM) kinase: A regulator of the cytoskeleton 39
1.7.1 The role of the actin skeleton in cell migration 42
1.7.2 LIM kinase involvement in the cell cycle progression 42
1.7.3 LIM kinase inhibitors 43
1.8 Paclitaxel 44
1.8.1 Paclitaxel resistance 45
1.8.2 Paclitaxel based combination chemotherapy 48
1.8.2.1 Paclitaxel-doxorubicin combination therapy 48
1.8.2.2 Paclitaxel-cisplatin combination therapy 49
1.8.2.3 Paclitaxel-cyclophosphamide combination therapy 50
1.8.2.4 Paclitaxel-vinorelbine combination therapy 50
1.8.3 Compound T4 sensitizes cells to non-lethal doses of paclitaxel *in vitro* 51
1.9 Radiosensitization by agents targeting the cytoskeleton 51
2. Aims and objectives 53
3. Materials and methods 57
3.1 Cell lines 57
3.2 General cell culture maintenance 57
3.2.1 Cell culture maintenance reagents 58
3.2.2 Maintenance 58
3.3 General method for experiments 59
3.3.1 Compounds and positive controls 60
3.3.2 General experimental method 60
3.3.3 Radiation exposure 62

3.4 Experimental setup 62
3.5 Drug properties and relative cytotoxicity 64
3.5.1 Tubulin competitive binding assay: Tritiated [^{3}H] colchicine binding 64
3.5.2 Time-lapse imaging: ESE-16's anti-mitotic effect 65
3.5.3 IncuCyte® Cytotoxicity assay 66
3.5.4 Scratch wound cell migration assay 67
3.5.5 Cytotoxicity studies: Spectrophotometric quantification of 3-(4,5-dimethylthiazol-2-yl)-2,5-diphenyltetrazolium bromide (MTT) 68
3.5.6 Visualization of the cytoskeleton: Fluorescent microscopy 70
3.6 Radiation dose-reponse curve 71
3.6.1 Apoptosis induction in cells exposed to radiation doses: Annexin V quantification via flow cytometry 71
3.6.2 Cell cycle analysis of cells exposed to radiation doses: Flow cytometry employing propidium iodide 72
3.7 Compound dose-response curve 74
3.7.1 Apoptosis induction in cells exposed to compound doses: Flow cytometric quantification of Annexin V 74
3.7.2 Cell cycle analysis of cells exposed to compound doses: Flow cytometry employing propidium iodide 74
3.8 Radiosensitization studies 74
3.8.1 Flow cytometric quantification of Annexin V-FITC 74
3.8.2 Cell cycle analysis 75
3.8.3 Intracellular signaling pathways induced by pre-exposing breast cancer cells to the novel compounds prior to radiation 75
3.8.3.1 Reactive oxygen species production: Flow cytometric quantification of superoxide employing hydroethidine 76
3.8.3.2 Mitochondrial transmembrane potential: Flow cytometric quantification of Mitocapture™ 76
3.8.3.3 Western blots 77
3.8.4 Morphological studies: Polarization-optical transmitted light differential interference contrast microscopy 82
3.8.5 Cell survival assay: Long term cellular proliferation quantified via a crystal violet stain…… 83

3.8.6 DNA damage and repair 84
3.8.6.1 Quantification of phosphorylated H2AX via flow cytometry 84
3.8.6.2 Micronuclei quantification 85
3.8.6.3 Quantification of the DNA repair response via Western blot analysis of Ku70 expression 86
3.9 Evaluation of the bystander effect induced by irradiated cells 87
3.10 Evaluation of radiation-induced resistance due to dose fractionation in cells exposed to the combination treatment 88
3.11 Statistical analysis 88
3.12 Logistics and funding 90
3.13 Ethics approval 90
4. Results 91
4.1 Drug properties and relative cytotoxicity 91
4.1.1 Tubulin competitive binding assay: Tritiated [^{3}H] colchicine binding 91
4.1.2 Time-lapse imaging: ESE-16's anti-mitotic effect 93
4.1.3 IncuCyte® Cytotoxicity assay 94
4.1.4 Scratch wound cell migration assay 96
4.1.5 Cytotoxicity studies: Spectrophotometric quantification of 3-(4,5-dimethylthiazol-2-yl)-2,5-diphenyltetrazolium bromide 98
4.1.6 Visualization of the cytoskeleton: Fluorescent microscopy 100
4.2 Radiosensitization studies 105
4.2.1 Flow cytometric quantification of annexin V-FITC 105
4.2.2 Cell cycle analysis 117
4.2.3 Intracellular signaling pathways induced by pre-exposing breast cancer cells to the novel compounds prior to radiation 130
4.2.3.1 Reactive oxygen species production: Flow cytometric quantification of superoxide employing hydroethidine 130
4.2.3.2 Mitochondrial transmembrane potential: Flow cytometric quantification of Mitocapture™ 143
4.2.3.3 Western blot 148
4.2.4 Morphological studies: Polarization-optical transmitted light differential interference contrast microscopy 167
4.2.5 Long term cellular proliferation quantified via a crystal violet stain 171

4.2.6 DNA damage and repair 175
4.2.6.1 Quantification of phosphorylated H2AX via flow cytometry 175
4.2.6.2 Micronuclei quantification 187
4.2.6.3 Quantification of the DNA repair response via Western blot analysis of Ku70 expression. 196
4.3 Evaluation of the bystander effect induced by irradiated cells 207
4.3.1 Reactive oxygen species production: Flow cytometric quantification of superoxide employing hydroethidine 207
4.3.2 Mitochondrial transmembrane potential: Flow cytometric quantification of Mitocapture™ 211
4.3.3 Long term cellular proliferation quantified by crystal violet staining. 215
4.3.4 DNA damage and repair: Quantification of γH2AX and Ku70 proteins via a western blot 219
4.4 Evaluation of radiation-induced resistance due to dose fractionation in irradiated cells 222
4.4.1 Reactive oxygen species production: Flow cytometric quantification of superoxide employing hydroethidine 222
4.4.2 Mitochondrial transmembrane potential: Flow cytometric quantification of MitoCapture™ 227
5. Discussion 233
5.1 Drug properties and cytotoxicity 243
5.2 Regulation of the cell cycle 251
5.3 Cellular survival and apoptotic cell death 255
5.4 DNA damage and repair 266
5.5 Radiation-induced resistance due to dose fractionation and radiation-induced bystander effect 273
6. Conclusion 277
7. Acknowledgement of funding 280
8. References 281
9. Additional file 1 354
9.1 Radiation dose response curve: Flow cytometric quantification of apoptosis induction 354

9.2 Radiation dose response curve: Flow cytometric analysis of cell cycle progression. 358
10. Additional file 2 364
10.1 Compound dose response curve: Flow cytometric quantification of apoptosis induction 364
10.2 Compound dose response curve: Flow cytometric analysis of cell cycle progression 373
11. Appendix A: Data analysis of Incucyte® experiments 384
12. Appendix B: Distribution of micronuclei in breast cancer cells exposed to various treatment conditions 387
13. Video's 389
14. Ethics approval 389
15. Declaration 390

List of figures

Figure 1.1: The phases of the cell cycle 6
Figure 1.2: The spindle assembly checkpoint 12
Figure 1.3: The intrinsic and extrinsic apoptotic pathways 16
Figure 1.4: Cellular response to radiation-induced DNA double strand breaks 21
Figure 1.5: Factors contributing to the development of radiation resistance 27
Figure 1.6: Microtubule dynamics 31
Figure 1.7: Hepatic metabolism of estradiol 34
Figure 1.8: *In silico*-designed sulphamoylated 2-methoxyestradiol analogues 39
Figure 1.9: LIM kinase protein structure 39
Figure 1.10: Regulation of the cytoskeleton by LIM kinase 41
Figure 1.11: Chemical structure of 9-benzoyloxy-5,11-dimethyl-2H,6H-pyrido[4,3-b]carbazol-1-one (Pyr1). 44
Figure 1.12: Cellular mechanisms involved in Paclitaxel resistance 46
Figure 3.1: Experimental setup 63
Figure 4.1: Binding of tritiated colchicine to tubulin in the presence of various anti-mitotic compounds 92
Figure 4.2: Time-lapsed imaging of HeLa Kyoto cells exposed to the anti-mitotic agent, ESE-16 93
Figure 4.3: Real time IncuCyte® Cytotox Green fluorescence in HeLa cells exposed to two anti-mitotic compounds indicating the number of dead HeLa cells 95
Figure 4.4: Graphical representation of IncuCyte® Cytotox Green fluorescence in HeLa cells exposed to ESE-15-one and ESE-16 96
Figure 4.5: Wound closure in HeLa cells exposed to ESE-15-one and ESE-16 indicating the effect on cell migration 97
Figure 4.6: Graphical representation of wound closure in HeLa cells exposed to ESE-15-one and ESE-16 98

Figure 4.7: Dose response curves of breast cancer cells exposed to various microtubule regulators and T4, a compound that sensitizes cells to non-lethal doses of paclitaxel 99
Figure 4.8: Response of the cytoskeleton of BT-20 cells exposed to various microtubule regulating agents for 24 hours..... 102
Figure 4.9: Response of the cytoskeleton of MCF-7 cells exposed to ESE-16 and LimPyr1 103
Figure 4.10: Response of the cytoskeleton of MDA-MB-231 cells exposed to ESE-16 and LimPyr1 for 24 hours..... 104
Figure 4.11: Representative flow cytometric dot plots of annexin V-FITC indicating apoptosis in BT-20 cells exposed to various treatment modalities 107
Figure 4.12: Graphical representation of annexin V-FITC quantification in BT-20 cells exposed to various treatment conditions 109
Figure 4.13: Representative flow cytometric dot plots of annexin V-FITC indicating apoptosis in MCF-7 cells exposed to various treatment modalities 111
Figure 4.14: Graphical representation of annexin V-FITC quantification in MCF-7 cells exposed to various treatment conditions..... 113
Figure 4.15: Representative flow cytometric dot plots of annexin V-FITC indicating apoptosis in MDA-MB-231 cells exposed to various treatment modalities..... 114
Figure 4.16: Graphical representation of annexin V-FITC quantification in MDA-MB-231 cells exposed to various treatment conditions..... 116
Figure 4.17: Histograms representing the cell cycle distributions of BT-20 cells exposed to various treatment conditions..... 119
Figure 4.18: Graphical representation of cell cycle analysis in BT-20 cells exposed to various treatment conditions 122
Figure 4.19: Histograms representing the cell cycle distributions of MCF-7 cells exposed to various treatment conditions..... 124
Figure 4.20: Graphical representation of cell cycle analysis in MCF-7 cells exposed to various treatment conditions 126
Figure 4.21: Histograms representing the cell cycle distributions of MDA-MB-231 cells exposed to various treatment conditions..... 127

Figure 4.22: Graphical representation of the cell cycle analysis of MDA-MB-231 cells exposed to various treatment conditions 129
Figure 4.23: Representative overlay histograms of superoxide detection in MCF-7 cells 132
Figure 4.24: Graphical representation of superoxide quantification in MCF-7 cells after exposure to different treatment conditions 134
Figure 4.25: Representative overlay histograms of superoxide detection in MDA-MB-231 cells 136
Figure 4.26: Graphical representation of superoxide quantification in MDA-MB-231 cells after exposure to the different treatment conditions 138
Figure 4.27: Representative overlay histograms of superoxide detection in BT-20 cells 140
Figure 4.28: Graphical representation of superoxide quantification in BT-20 cells after exposure to different treatment conditions 142
Figure 4.29: Representative overlay histograms of Mitocapture™ detection in MCF-7-, MDA-MB-231- and BT-20 cells exposed to appropriate controls and various treatment conditions 145
Figure 4.30: Graphical representation of Mitocapture™ quantification in MCF-7-, MDA-MB-231- and BT-20 cells after exposure to different treatment conditions 147
Figure 4.31: Western blots visualizing Bax and cleaved caspase 3 protein expressions in MCF-7-, MDA-MB-231- and BT-20 cells exposed to various treatment conditions 150
Figure 4.32: Graphical representation of Bax expression in MCF-7 cells exposed to different treatment conditions 153
Figure 4.33: Graphical representation of Bax and cleaved caspase 3 proteins in MDA-MB-231 cells exposed to different treatment conditions 154
Figure 4.34: Graphical representation of Bax and cleaved caspase 3 proteins in BT-20 cells exposed to different treatment conditions 155
Figure 4.35: Western blots visualizing phosphorylated Akt and FoxO1/3a protein levels in MCF-7-, MDA-MB-231- and BT-20 cells exposed to various treatment conditions 158

Figure 4.36: Graphical representation of Akt and FoxO1/3a phosphorylation in MCF-7 cells exposed to different treatment conditions 161
Figure 4.37: Graphical representation of Akt and FoxO1/3a phosphorylation in MDA-MB-231 cells exposed to different treatment conditions 162
Figure 4.38: Graphical representation of Akt and FoxO1/3a phosphorylation in BT-20 cells exposed to different treatment conditions 163
Figure 4.39: Cyclin B1 quantification in MCF-7-, MDA-MB-231- and BT-20 cells exposed to various treatment conditions..... 165
Figure 4.40: PlasDIC micrographs of MCF-7 cells exposed to various treatment conditions .. 168
Figure 4.41: PlasDIC micrographs of MDA-MB-231 cells exposed to various treatment conditions..... 169
Figure 4.42: PlasDIC micrographs of BT-20 cells exposed various treatment conditions 170
Figure 4.43: Cellular proliferation 14 days after radiation in MCF-7-, MDA-MB-231- and BT-20 cells exposed to various treatment conditions 172
Figure 4.44: Graphical representation of long term cellular proliferation 14 days after radiation in MCF-7-, MDA-MB-231- and BT-20 cells exposed to various treatment conditions 174
Figure 4.45: Representative overlay histograms of γH2AX detection in MCF-7 cells 178
Figure 4.46: Graphical representation of γH2AX quantification in MCF-7 cells exposed to different treatment conditions 180
Figure 4.47: Representative overlay histograms of γH2AX detection in MDA-MB-231 cells... 181
Figure 4.48: Graphical representation of γH2AX quantification in MDA-MB-231 cells exposed to different treatment conditions..... 183
Figure 4.49: Representative overlay histograms of γH2AX detection in BT-20 cells..... 184
Figure 4.50: Graphical representation of γH2AX quantification in BT-20 cells exposed to different treatment conditions 186
Figure 4.51: Graphical representation of micronuclei quantification in MCF-7 cells exposed to various treatment conditions 191
Figure 4.52: Graphical representation of micronuclei quantification in MDA-MB-231 cells exposed to various treatment conditions..... 193

Figure 4.53: Graphical representation of micronuclei quantification in BT-20 cells exposed to various treatment conditions 195
Figure 4.54: Distribution of micronuclei in MCF-7-, MDA-MB-231- and BT-20 cells exposed to various treatment condition 197
Figure 4.55: Western blots illustrating Ku70 protein expression in MCF-7-, MDA-MB-231- and BT-20 cells 2 and 24 hours after radiation 200
Figure 4.56: Graphical representation of Ku70 protein expression in MCF-7 cells 2 and 24 hours after irradiation 202
Figure 4.57: Graphical representation of Ku70 protein expression in MDA-MB-231 cells 2 and 24 hours after irradiation 204
Figure 4.58: Graphical representation of Ku70 protein expression in BT-20 cells 2 and 24 hours after irradiation 206
Figure 4.59: Representative overlay histograms of superoxide detection in untreated BT-20 cells propagated in conditioned media obtained from cells exposed to appropriate controls and different treatment conditions for 48 hours 208
Figure 4.60: Graphical representation of superoxide quantification in untreated BT-20 cells propagated in conditioned media obtained from cells exposed to various treatment conditions for 48 hours 210
Figure 4.61: Representative overlay histograms of Mitocapture™ detection in untreated BT-20 cells exposed to conditioned media obtained from cells exposed to appropriate controls and different treatment conditions 212
Figure 4.62: Graphical representation of Mitocapture™ detection in untreated BT-20 cells following a 48 hour exposure to conditioned media obtained from cells exposed to various treatment modalities 214
Figure 4.63: Cell proliferation in untreated BT-20 cells propagated in conditioned media for 14 days obtained from cells exposed to various controls and treatment conditions 216
Figure 4.64: Graphical representation of cell survival in untreated BT-20 cells propagated for 14 days in conditioned media obtained from treated cells 218

Figure 4.65: Western blots visualizing γH2AX and Ku70 protein expressions in untreated BT-20 cells propagated in conditioned media obtained from cells exposed to various treatment conditions for 2 hours 220
Figure 4.66: Graphical representation of γH2AX and Ku70 expression in untreated BT-20 cells exposed for 2 hours to conditioned media transferred from cells exposed to various treatment conditions 221
Figure 4.67: Representative overlay histograms of superoxide detection measured by flow cytometry in BT-20 cells exposed to ESE-16 or LimPyr1, single dose and fractionated radiotherapy 224
Figure 4.68: Graphical representation of superoxide quantification in BT-20 cells exposed to single dose or fractionated radiotherapy 226
Figure 4.69: Representative overlay histograms of MitoCapture™ in BT-20 cells exposed to microtubule regulating agents, single dose and fractionated radiotherapy 230
Figure 4.70: Graphical representation of MitoCapture™ quantification in BT-20 cells exposed to microtubule regulating agents, single dose or fractionated radiotherapy 231
Figure 6.1: Summary of proposed signaling pathways induced by ESE-16 and LimPyr1 to increase the sensitivity of breast cancer cells to radiation 279

Additional file 1

Figure 1A: Representative flow cytometric dot plots of annexin V-FITC of breast cancer cells exposed to a radiation dose range 355
Figure 1B: Graphical representation of annexin V-FITC analysis of MCF-7-, MDA-MB-231- and BT-20 breast cancer cells exposed to a radiation dose range. 357
Figure 1C: Histograms representing the cell cycle distributions of MCF-7-, MDA-MB-231- and BT-20 cells exposed to a radiation dose-response curve 360
Figure 1D: Graphical representation of the cell cycle analysis of MCF-7-, MDA-MB-231- and BT-20 cells exposed to a radiation dose range 362

Additional file 2

Figure 2A: Apoptotic cell death in BT-20 cells exposed to compound dose-response curves as illustrated by flow cytometric dot plots of annexin V-FITC 366
Figure 2B: Graphical representation of annexin V-FITC quantification in BT-20 cells exposed to compound dose-response curves 368
Figure 2C: Apoptotic cell death in MCF-7- and MDA-MB-231 cells exposed to compound dose-response curves as illustrated by flow cytometric dot plots of annexin V-FITC 370
Figure 2D: Graphical representation of annexin V-FITC quantification in MCF-7- and MDA-MB-231 cells exposed to compound dose-response curves 372
Figure 2E: Histograms representing the cell cycle distributions of BT-20 cells exposed to compound dose-response curves 376
Figure 2F: Graphical representation of the cell cycle analysis of BT-20 cells exposed to compound dose-response curves 379
Figure 2G: Histograms representing the cell cycle distributions of MCF-7- and MDA-MB-231 cells exposed to compound dose-response curves 380
Figure 2H: Graphical representation of the cell cycle analysis of MCF-7- and MDA-MB-231 cells exposed to compound dose-response curves 382

List of tables

Table 3.1: Densities seeded for cytotoxicity and radiosensitizing experiments on MCF-7-, MDA-MB-231- and BT-20 cells 61
Table 3.2: Dilution series of ESE-15-one, ESE-16, LimPyr1 and T4 that were used during cytotoxicity studies 69
Table 3.3: Reagents required to hand-cast 10% running and 4 % stacking SDS-polyacrylamide (SDS-PAGE) gels 78
Table 4.1: Binding of tritiated colchicine to purified bovine tubulin in competition with colchicine, vinblastine and ESE-16. 92
Table 4.2: Time HeLa Kyoto cells spent in metaphase following exposure to DMSO and an anti-mitotic compound, ESE-16 94
Table 4.3: Half maximum growth inhibitory concentrations (GI50) for ESE-15-one, ESE-16, LimPyr1 and T4 after exposure to BT-20-, MCF-7- and MDA-MB-231 breast cancer cells for 48 hours 100
Table 4.4: Apoptotic induction measured by annexin V-FITC quantification in BT-20 cells exposed to various treatment conditions 108
Table 4.5: Apoptotic induction measured by annexin V-FITC quantification in MCF-7 cells exposed to various treatment conditions 112
Table 4.6: Apoptotic induction measured by annexin V-FITC quantification in MDA-MB-231 cells exposed to various treatment conditions 115
Table 4.7: Cell cycle analysis of BT-20 cells exposed to various treatment conditions 121
Table 4.8: Cell cycle analysis of MCF-7 cells exposed to various treatment conditions 125
Table 4.9: Cell cycle analysis of MDA-MB-231 cells exposed to the various treatment conditions 128
Table 4.10: Superoxide detection in MCF-7 cells exposed to various treatment conditions 133
Table 4.11: Superoxide detection in MDA-MB-231 cells exposed to various treatment conditions 137
Table 4.12: Superoxide detection in BT-20 cells exposed to various treatment conditions 141

Table 4.13: Mitocapture™ quantification in breast cancer cells exposed to various treatment conditions 146
Table 4.14: Bax expression in MCF-7-, MDA-MB-231- and BT-20 cells exposed to various treatment conditions 151
Table 4.15: Cleaved caspase 3 expression in MDA-MB-231 and BT-20 cells exposed to various treatment conditions 152
Table 4.16: Akt phosphorylation in MCF-7-, MDA-MB-231- and BT-20 cells exposed to various treatment conditions 159
Table 4.17: FoxO1/3a phosphorylation in MCF-7-, MDA-MB-231- and BT-20 cells exposed to various treatment conditions 160
Table 4.18: Cyclin B1 quantification in MCF-7-, MDA-MB-231- and BT-20 cells exposed to various treatment conditions 166
Table 4.19: Cellular proliferation measure 14 days after radiation in MCF-7-, MDA-MB-231- and BT-20 cells following exposure to various treatment conditions 173
Table 4.20: Quantification of γH2AX in MCF-7 cells exposed to various treatment conditions 179
Table 4.21: Quantification of γH2AX in MDA-MB-231 cells exposed to various treatment conditions 182
Table 4.22: Quantification of γH2AX in BT-20 cells exposed to various treatment conditions 185
Table 4.23: Micronuclei quantification in MCF-7 cells 2 and 24 hours after radiation 190
Table 4.24: Micronuclei quantification in MDA-MB-231 cells 2 and 24 hours after radiation 192
Table 4.25: Micronuclei quantification in BT-20 cells 2 and 24 hours after radiation 194
Table 4.26: Ku70 expression in MCF-7 cells 2 and 24 hours after irradiation 201
Table 4.27: Ku70 expression in MDA-MB-231 cells 2 and 24 hours after irradiation 203
Table 4.28: Ku70 expression in BT-20 cells 2 and 24 hours after irradiation 205
Table 4.29: Superoxide detection in untreated breast cancer cells exposed to conditioned media obtained from treated cells for 48 hours 209
Table 4.30: Mitocapture™ detection in untreated breast cancer cells following a 48 hour exposure to conditioned media obtained from treated cells 213

Table 4.31: Cellular survival in untreated BT-20 cells exposed to conditioned media obtained from BT-20 cells exposed to various controls and treatment conditions 217
Table 4.32: Expression of DNA damage (γH2AX) and DNA repair (Ku70) proteins in untreated BT-20 via the bystander effect 2 hours post transfer 220
Table 4.33: Superoxide detection by means of flow cytometry employing hydroethidine in BT-20 cells exposed to single dose and fractionated radiotherapy 225
Table 4.34: MitoCapture™ quantification in breast cancer cells exposed to single dose and fractionated radiotherapy 229

Additional file 1

Table 1A: Annexin V-FITC analysis of MCF-7-, MDA-MB-231- and BT-20 breast cancer cells following exposure to a radiation dose range 356
Table 1B: Cell cycle analysis of three breast cancer cell lines after exposure to a radiation dose-response curve 361

Additional file 2

Table 2A: Compound dose-response curve concentrations exposed to BT-20-, MCF-7- and MDA-MB-231 cells 364
Table 2B: Annexin V-FITC quantification in BT-20 cells exposed to compound dose-response curves 367
Table 2C: Annexin V-FITC quantification in MCF-7- and MDA-MB-231 cells exposed to compound dose-response curves 371
Table 2D: Flow cytometric analysis of BT-20 cells exposed to compound dose-response curves 378
Table 2E: Flow cytometric analysis of MCF-7- and MDA-MB-231 cells exposed to compound dose-response curves 381

Appendix A

Table A1: IncuCyte® Cytotox Green fluorescence in HeLa cells exposed to ESE-15-one and ESE-16, indicating cell death..... 384
Table A2: Wound healing in HeLa cells exposed to ESE-15-one and ESE-16, indicating cell migration. 386

Appendix B

Table B1: Micronuclei quantification in breast cancer cells pre-treated with ESE-16. 387
Table B2: Micronuclei quantification in breast cancer cells pre-treated with LimPyr1. 388

List of abbreviations

+TIP	Plus-end tracking proteins
[^{3}H] colchicine	Tritiated colchicine
°C	Degrees Celsius
µg	Microgram
µL	Microliter
µm	Micrometer
µM	Micromolar
17β-HSD	17β-hydroxysteriod dehydrogenase
2-ME	2-Methoxyestradiol
53BP1	p53-binding protein 1
ABC	ATP-binding cassette
ADF	Actin-depolymerizing factor
ADP	Adenosine diphosphate
AIF	Apoptosis inducing factor
Akt	v-Akt murine thymoma viral oncogene also known as protein kinase B
AMP	Adenosine monophosphate
AMPK	5’ AMP-activated protein kinase
ANOVA	Analysis of variance
Apaf	Apoptotic protease activating factor
APC/C	Anaphase promoting complex/cyclosome
APS	Ammonium persulfate
ATCC	American Type Culture Collection
ATM	Ataxia–telangiectasia-mutated
ATP	Adenosine triphosphate
ATR	Ataxia telangiectasia and Rad3-related
Bad	Bcl-2-associated death promoter
Bak	Bcl-2 homologous antagonist-killer
Bax	Bcl-2 associated X protein
BC	Before Christ
Bcl	B-cell lymphoma
Bcl-XL	Bcl-extra large
BH	Bcl-2 homology domain
Bid	BH3 interacting-domain death agonist
Bim	Bcl-2-like protein 11
BMPRII	Bone morphogenetic protein receptor II
BRCA	Breast cancer gene
BSA	Bovine serum albumin
Bub	Budding uninhibited by benzimidazoles
CA	California

CAII	Carbonic anhydrase II
CAIX	Carbonic anhydrase XI
CAK	Cyclin activating kinase
CANSA	Cancer Association of South Africa
CARD	Caspase recruitment domain
Cdc	Cell division cycle
CDK	Cyclin dependent kinases
CDKI	Cyclin-dependent kinase inhibitor
CDT1	Chromatin licensing and DNA replication factor 1
CE	Common Era
cGy	Centigray
CIN	Chronophin
Cip/Kip	CDK interacting protein/Kinase inhibitory protein
Ckh	Checkpoint kinase
CLIP-170	Cytoplasmic linker protein
cm	Centimeter
CNRS	Le Centre National de la Recherche Scientifique
CO_2	Carbon dioxide
COMT	Catechol-O-methyltransferase
COX	Cyclooxygenase
CYP	Cytochrome P450 family
Da	Dalton
DAPI	4’,6-Diamidino-2-phenylindole
dATP	Deoxyadenosine triphosphate
ddH_2O	Double-distilled water
DDR	DNA damage response
DEAE	Diethylaminoethyl
DED	Death effector domain
DISC	Death-inducing signalling complex
DMEM	Dulbecco's Modified Eagle's medium
DMSO	Dimethyl sulfoxide
DNA	Deoxyribonucleic acid
DNA-PK	DNA dependent protein kinase
DNA-PKcs	DNA-dependent protein kinase catalytic subunit
DR	Death receptor
DSB	DNA double strand breaks
E2F	Elongation factor 2
EB3	Microtubule-associated protein RP/EB family member 3
ECL	Enhanced chemiluminescence
EDTA	Ethylenediaminetetraacetic acid
EGF	Epidermal growth factor
EGFR	Epidermal growth factor receptor
EGTA	Ethylene glycol-bis(β-aminoethyl ether)-N,N,N',N'-tetraacetic acid
EMCCD	Electron multiplying charge coupled device

EMT	Epithelial–mesenchymal transition
EndoR	Endoplasmic reticulum
eNOS	Endothelial nitric oxide synthase
ER	Estrogen receptor
ERK	Extracellular signal-regulated kinases
ESE-15-one	2-ethyl-3-*O*-sulphamoyl-estra-1,3,5(10),15-tetraen-17-one
ESE-16	2-ethyl-3-*O*-sulphamoyl-estra-1,3,5(10)16-tetraene
F-actin	Filamentous actin
FADD	Fas-associated protein with death domain
FasL	Fas ligand
FC	Fold change
FCS	Fetal calf serum
FEI	Field Electron and Ion Company
FITC	Fluorescein isothiocyanate
FKBP	FK506-binding protein
FL	Florida
FoxO	Forkhead box proteins
FRAP	FKBP-rapamycin-associated protein
g	Gram
G_0 phase	Quiescent phase
G_1 phase	Gap 1 phase
G_2 phase	Gap 2 phase
GADD	DNA damage inducible gene
GCP	γ-Tubulin complex protein
GDP	Guanosine diphosphate
GFP	Green fluorescent protein
GI_{50}	Half maximum growth inhibitory concentration
GJIC	Gap junctional intercellular communication
GSH	Glutathione
GSK3β	Synthase kinase-3β
GSSG	Glutathione disulphide
GTP	Guanosine triphosphate
Gy	Gray
H_2O_2	Hydrogen peroxide
HCl	Hydrochloric acid
Her2	Human epidermal growth factor receptor 2
HIF	Hypoxia-inducible factor
HR	Homologous recombination
HRP	Horseradish peroxidase
IAB	Institute for Advanced Biosciences
IgG	Immunoglobulin G
IL	Interleukin
INK4	Inhibitors of the cyclin-dependent kinase 4
INSERM	Institut national de la santé et de la recherche médicale

JNK	c-Jun N-terminal kinases
KCl	Potassium chloride
kDa	Kilodalton
keV	Kiloelectronvolts
kg	Kilogram
KH_2PO_4	Potassium dihydrogen phosphate
Ki	Inhibitor constant
Kif	Kinesin heavy chain member
Ku	Ku70-Ku80 heteromere
L	Liter
LET	Linear energy transfer
Lig4	DNA ligase IV
LIM	Lin-11, Isl-1 and Mec-3
LIMK1	LIM kinase 1
LIMK2	LIM kinase 2
LTC4	Glutathione conjugate of leukotriene C4
M phase	Mitotic phase
M%	Averaged percentage
MA	Massachusetts
Mad	Mitotic arrest deficiency protein
MAPK	Mitogen-activated protein kinases
MAPs	Microtubule-associated proteins
MCAK	Mitotic centromere-associated kinesin
MCC	Mitotic checkpoint complex
MCM complex	Minichromosome maintenance protein complex
MDH	Malate dehydrogenase
Mdm2	Mouse double minute 2 homolog
MDR	Multiple drug resistance
MDRP	Multidrug resistant protein
mETC	Mitochondrial electron transport chain
mg	Milligram
$MgCl_2$	Magnesium chloride
MGMT	O^6-MeG-DNA methyltransferase
miRNAs	micro-ribonucleic acids
mL	Milliliter
MLH1	MutL homolog 1
mm	Millimeter
mM	Milimolar
MO	Missouri
MPF	Mitosis promoting factor
MRN	Mre11-Rad50-Nbs1 complex
mROS	Mitochondrial ROS
MTOC	Microtubule organizing centres
mTOR	Mammalian target of rapamycin

MTT	3-(4,5-dimethylthiazol-2-yl)-2,5-diphenyltetrazolium bromide
MU	Monitor unit
MutS	Mutator S
Na_2HPO_4	Disodium hydrogen phosphate
NaCl	Sodium chloride
NADH	Nicotinamide adenine dinucleotide
NADPH	Nicotinamide adenine dinucleotide phosphate
NF-κB	Nuclear factor kappa-light-chain-enhancer of activated B cells
NHEJ	Non-homologous end joining
nm	Nanometer
NMSC	Non-melanoma skin cancer
NO	Nitric oxide
NPC	Nasopharyngeal carcinoma
NRF	National Research Foundation
O^6-MeG	O^6-Methylguanine
OH^-	Hydroxide ion
OH	Ohio
OR	Oregon
ORC	Origin recognition complex
P%	Percentage viable cells
PA	Pennsylvania
PAK	p21 activated kinases
PARP	Poly-ADP-ribose polymerase
PBS	Phosphate buffered saline
PDT	Population doubling time
PDZ	Post-synaptic density protein 95 drosophila disc large tumour suppressor zona occludens 1
PerCP	Peridinin chlorophyll protein complex
PgP	P-glyco-protein pumps
PhD	Doctor of Philosophy
PI	Propidium iodide
PI3K	Phosphatidylinositol 3-kinase
PIPES	Piperazine-N,N'-bis(2-ethanesulfonic acid)
PlasDIC	Polarization-optical transmitted light differential interference contrast microscopy
PLK-1	Polo-like kinase-1
PME	PIPES-$MgCl_2$-EGTA
PMS2	PMS1 homolog 2, mismatch repair system component
PR	progesterone receptor
pRB	Retinoblastoma protein
pre-RC	Pre-replication complex
PRKDC	Protein kinase DNA-activated catalytic polypeptide
PS	Phosphatidylserine
psi	Pounds per square inch
PUMA	p53 upregulated modulator of apoptosis
PVDF	Polyvinylidene difluoride

Pyr1	9-Benzoyloxy-5,11-dimethyl-2H,6H-pyrido[4,3-b]carbazol-1-one
qPCR	Quantitative real-time polymerase chain reaction
R point	Restriction point
Rac1	Ras-related C3 botulinum toxin substrate 1
RBBP8	Retinoblastoma binding protein 8
RESCOM	Research Committee (School of Medicine) of the University of Pretoria
RFP	Red fluorescent protein
RIPA	Radioimmunoprecipitation assay
RNA	Ribonucleic acid
RNS	Reactive nitrogen species
ROCK	Rho-associated protein kinase
ROS	Reactive oxygen species
RPMI	Roswell Park Memorial Institute
S phase	Synthesis phase
SAC	Spindle assembly checkpoint
Sc	Absolute absorption of compound-exposed cells
SD	Standard deviations
SDS	Sodium dodecyl sulfate
SDS-PAGE	Sodium dodecyl sulfate polyacrylamide gel electrophoresis
SEM	Standard error of the mean
Ser	Serine
SERMs	Selective estrogen receptor modulators
SHBG	Sex hormone-binding globulin
siRNA	Small interfering ribonucleic acids
Smac	Second mitochondria-derived activator of caspases
SMTT DMSO	Absolute absorption of the DMSO control
SMTT SDS	Absolute absorption of the SDS control
SOD	Superoxide dismutase
SSH	Slingshot family
SSH-IL	Slingshot phosphatases
STDV	Standard deviation
tBid	Truncated form of Bid
TBS	Tris-buffered saline
TEM	Transmission electron microscopy
TEMED	N,N,N',N'-tetramethylethylenediamine
TGF	Transforming growth factor
Thr	Threonine
TNF	Tumour necrosis factor receptor
TP53	Tumor protein p53
TPPP	Tubulin polymerization–promoting protein
TRAIL	TNF-related apoptosis-inducing ligand
Tris	Trisaminomethane
TSC	Tuberous sclerosis complex
TUNEL	Terminal deoxynucleotidyl transferase deoxyuridine triphosphate nick end labeling
Tyr	Tyrosine

U/mL	Units per milliliter
UGA	Université Grenoble Alpes
UK	United Kingdom
uPA	Urokinase type plasminogen activator
uPAR	Urokinase receptor
USA	United States of America
UVB	Ultraviolet B
V	Volt
v/v	Volume/volume
VA	Virginia
VEGF	Vascular endothelial growth factor
VT	Vermont
VTN	Vitronectin
WA	Washington
x *g*	Times gravity
XFL	XRCC4-like factor
XKCM1	*Xenopus* kinesin catastrophe modulator-1
XRCC	X-ray repair cross-complementing protein
α	Alpha
β	Beta
γ	Gamma
γH2AX	Phosphorylated H2AX
γ-TuRC	γ-Tubulin ring complex

1. Introduction and literature study

"Nothing in life is to be feared. It is only to be understood. Now is the time to understand more, so that we may fear less."

-Marie Curie-

1.1 Breast cancer

"If thou examinst a man having bulging tumors on his breast, and if thou puttst thy hand upon his breast upon these tumors, and thou finds them very cool, there being no fever at all when thy hand touches him, they have no granulation, they form no fluid, they do not generate secretions of fluid, and they are bulging to thy hand. Thou should say concerning him: One having bulging tumors. An ailment with which I will not contend". This is one of the earliest references to a breast tumor as translated from the Edwin Smith Surgical Papyrus dated from 1600 Before Christ (BC) (1). In this piece of ancient Egyptian literature eight cases of breast tumors were described (2). These tumors were treated by cauterisation (3), a futile method as stated by the author: "There is no treatment."

For centuries breast cancer has been diagnosed and treated according to Galenic principles based on the theory by Hippocrates (460 BC) and Galen (200 Common Era (CE)) that ascribed breast cancer to the accumulation of black bile produced by the liver (4). The tumors were described to have a 'crab-like' appearance due to dark veins surrounding them (5) and were often treated with castor oil, sulphuric acid and opium (6). Hippocrates strongly advised against surgery as the procedure was more life threating than receiving no treatment (5). The Catholic Church discouraged the surgical removal of tumors during the Middle Ages, thus surgery was only introduced in the 18th century as a form of breast cancer treatment (6). As the depth of our understanding regarding the cellular nature of cancer

increased novel treatment regimens were developed for the treatment and management of breast cancer. Chemotherapy, radiotherapy, targeted and hormonal therapies are successfully used to increase patient life expectancy and quality, or even induce remission (7). However, the development of chemo and radiation resistance as well as the treatment of triple receptor-negative breast cancers poses yet unsolved challenges.

Breast cancer is increasing as a cause of morbidity and mortality among men and women. Globally, breast cancer was ranked second for cancer incidence (2.09 million cases) and fifth for cancer deaths (627 000 deaths) in 2018 according to the World Health Organization (8). Africa carries a large percentage of the breast cancer burden due to the socioeconomical constraints of the continent. Thus a more time and cost-effective treatment regime with fewer side effects is imperative and remains a priority on the research agenda.

Breast cancer is the development of a malignant tumor resulting from the uncontrolled growth of breast tissue cells. Gradually these cancer cells invade healthy breast tissue, infiltrate the lymph nodes and can metastasize to other parts of the body. Breast cancer is caused by genetic mutations. However, only 5-10% of patients diagnosed with breast cancer inherit the breast cancer gene 1 (BRCA1) or -2 (BRCA2) mutation (9). A BRCA1 mutation increases the probability of developing breast cancer with 55-65%, whereas a 45% increase in probability is observed with a BRCA2 mutation (10). The proteins encoded by BRCA1 and BRCA2 are tumor suppressor proteins and contribute to deoxyribonucleic acid (DNA) repair. A mutation in these genes decreases the production of the tumor suppressor proteins, resulting in increased genetic aberrations and cancer development (10). Genetic mutations can also be acquired as a result of the aging process. A total of 85-90% of breast cancer patients do not inherit the genetic mutations, but acquire them as a result of every day ‘wear and tear’ (9). Additionally being of Caucasian race, increased age, obese or from high socioeconomic status also increased the risk for breast cancer development (11), as does a mutation in the tumor suppressor protein p53 (12). It has also been reported that some

environmental factors and lifestyle choices such as caffeine consumption, cigarette smoke and radiation exposure contribute to cancer development (13).

1.1.1 Classification of breast cancer

Breast cancer is classified and treated based on the breast cancer type, grade and stage, as well as gene expression. Breast cancer types are categorized based on the location and aggressiveness of the neoplasm. Cancer that develops in the connective tissue of the breast is referred to as breast sarcoma (14), while a carcinoma refers to cancer located in the breast ducts and lobules (15). Further classification is based on whether the cancer is invasive or *in situ* (not invasive). Histologically breast cancer can further be classified based on the tumor grade. The latter refers to the biological appearance of the neoplastic cells. A grade 1 tumor refers to neoplastic cells that are well differentiated and have a morphology similar to that of healthy breast cells (16). The morphology of grade 2 breast cancers is moderately differentiated, whereas a grade 3 classification refers to fast growing poorly differentiated cells (16). Breast cancer is classified into five stages. Breast cancer is classified as stage 0 when neoplastic cells are non-invasive (17). Stage 1 is reserved for locally invasive breast cancers that are less than 2 centimeters (cm) in size and have not spread to the lymph nodes (1A) or has formed isolated small clusters of cancerous cells (2 millimeters (mm)) in the lymph nodes (1B). Once the cancer has spread to the auxiliary lymph nodes the patient is diagnosed with stage 2 breast cancer (17). Stage 3 is termed 'locally advanced breast cancer' and has spread to numerous lymph nodes as well as tissue surrounding the breast such as muscle and skin. Once the cancer has spread to distant sites, such as the lung, liver or bones, the patient has stage 4 disease (17). Lastly, breast cancer can be divided into four groups based on gene expression. Using a 50-gene quantitative real-time polymerase chain reaction (qPCR) assay (PAM50 test), breast cancer can be classified as: Luminal A (estrogen receptor (ER) and/or progesterone receptor (PR) positive; human epidermal growth factor receptor 2 (Her2) negative), luminal B (ER positive and/or PR positive, Her2 positive), triple receptor-negative (ER negative, PR negative, Her2 negative), and Her-2 enriched or negative (18).

1.1.2 Treatment options for breast cancer

Various treatment options are available to combat breast cancer. Treatment may include surgery, radiotherapy (radiation therapy) and/or chemotherapy. Treatment regimens are based on the type and stage of the cancer; whether the cancerous cells express certain receptors making them sensitive to hormone therapy; and the health status of the patient. Surgical removal of the cancerous mass may be included in the primary treatment strategy. Various surgical procedures are available. A lumpectomy is the surgical removal of the breast cancer, sparing the breast tissue, whereas the entire breast is removed during a mastectomy (7). A mastectomy may be coupled with an axillary lymph node dissection where lymph nodes that drain from the breast are removed. Lastly, a less invasive option includes a sentinel node biopsy where a controlled number of lymph nodes are identified, removed and examined for the presence of cancer cells (7). This form of treatment is successful in removing tumors of early staged breast cancer, however surgical treatment of invasive tumors remains inadequate. Additionally, several surgical and postsurgical risks such as stroke, infection, pulmonary complications and cardiac arrhythmias are associated with breast cancer surgery (19).

Breast cancer surgery is generally used in combination with radiotherapy and/or chemotherapy. Radiation therapy is used for localized tumors and uses ionizing radiation to induce DNA damage in genes associated with cell growth and division, resulting in cell death (20). Unfortunately, radiotherapy is associated with long-term side effect such as anatomical aberrations, surrounding organ and tissue dysfunction and myelosupression, limiting the radiation dose (20). Chemotherapy is commonly used in a combination with surgery for the treatment of localized and metastasized tumors. Various anti-cancer agents such as cytotoxic drugs, hormones and targeted antibodies are used as chemotherapeutic agents to induce apoptosis in rapidly dividing cells such as cancer cells (7). However, rapidly dividing non-cancerous cells such as hair cells and mucosal cells lining the digestive tract are also negatively affected. To potentially decrease these side effects (amongst others) chemotherapeutics can be prescribed in lower doses as part of a combination approach (7).

Neoadjuvant chemotherapy is used to simplify the surgical procedure by shrinking the tumor prior to surgery, whereas adjuvant systemic chemotherapy decreases the recurrence possibility by targeting micro-metastasis (7).

Breast cancer cells that express estrogen or progesterone receptors can be treated with hormone therapy. Selective estrogen receptor modulators (SERMs), such as Tamoxifen, prevent hormone attachment to the cancer cells, resulting in a decreased growth rate and increased cancer cell death (7). Additionally, hormone-dependent breast cancer can also be treated with aromatase inhibitors. Formestrone and anastrozole are examples of aromatase inhibitors and are used to prevent the conversion of androsterone to estrogen (21,22). This decreases the available systemic estrogen levels. Due to the lack of hormonal receptors on triple receptor-negative breast cancers, these hormonal therapies are ineffective. Thus novel innovative approaches for treating these patients are imperative.

1.2 The cell cycle

The pathological deregulation of cancer can only be comprehended once the intrinsic mechanisms of normal cell growth and death are understood. The cell cycle is a tightly regulated complex process through which genetic material is accurately duplicated into identical chromosomal copies and segregated into two daughter cells (23,24). The cell cycle is divided into two stages: interphase, which is comprised of the G_1 (gap 1) phase, the synthesis or S phase and the G_2 (gap 2) phase; and the mitotic or M phase (Figure 1.1) (25). Transition through these different cell cycle phases is regulated by different cellular proteins. Cyclin dependent kinases (CDK) are a family of serine/threonine kinases and associate with regulatory proteins called cyclins in order to initiate cell cycle progression (23). CDK 1, -2, -4 and -5 are involved in the regulation of the cell cycle and are the catalytic subunits of the cyclin-CDK complex (26,27). Activation of CDK during different cell cycle stages depends upon their activation by cyclin A, -B, -D or -E (Figure 1.1) (28).

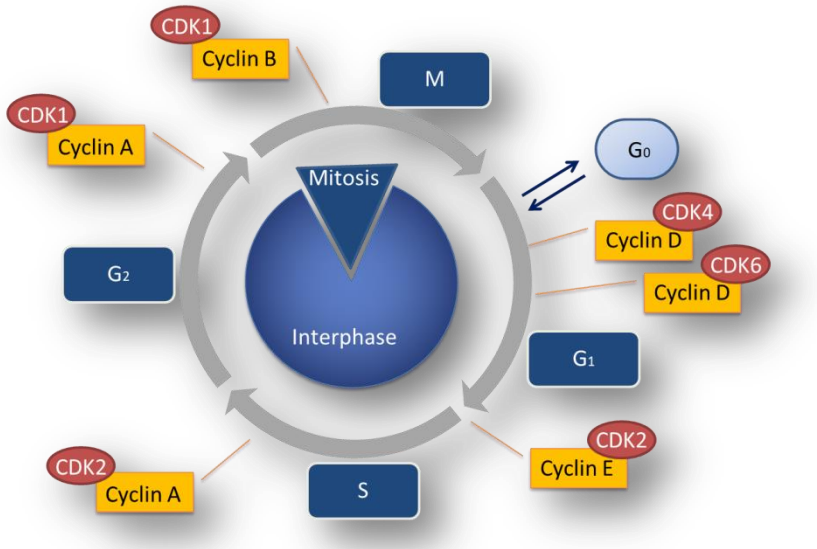

Figure 1.1: The phases of the cell cycle. The cell cycle consists of 2 phases: Interphase and mitosis. Interphase is divided into the gap 1 (G_1) phase, the synthesis (S) phase and the gap 2 (G_2) phase. During interphase genetic material is prepared (G_1 phase) and duplicated (S phase). Mitotic preparation is conducted in the G_2 phase prior to the onset of mitosis. The mitotic (M) phase is reserved for cell division and produces two identical daughter cells. Cyclin dependent kinases (CDK)-cyclin complexes are sequentially formed throughout the cell cycle and are responsible for phase progression. Adapted from Vermeulen *et al.* (2003) (29), using Microsoft PowerPoint 2010.

DNA replication is initiated by the phosphorylation of histones by aurora kinases during the S phase (30). The S phase is preceded by the G_1 phase during which cells prepare for DNA replication by synthesizing cellular components and relevant proteins required for the subsequent phase (24,31). The S phase is followed by the G_2 phase where cells prepare to enter mitosis by increasing protein synthesis and growth of intracellular organelles (24,32). The M phase is reserved for chromosomal segregation and cytosolic division, achieved by orchestrated events divided into prophase, metaphase, anaphase and telophase. Mitosis is completed by cytokinesis, resulting in two identical daughter cells (23,24). The newly formed daughter cells can immediately enter the G_1 preparatory phase or exit the cell cycle

and enter the G_0 phase (33) (Figure 1.1). Cells present in the G_0 phase are in a quiescent stage and are not actively preparing for cell division due to factors such as high cell numbers and mitogen deprivation (29,32). These cells enter G_0 temporarily pending external stimuli activation.

1.2.1 The G_1 phase

The G_1 phase is often referred to as the growth phase of the cell cycle. During this phase cells receive positive and negative cues from networks signaling growth, influencing cell division and development. Based on the interpretation of these inputs, a decision is made to enter the S phase, temporarily stop replication or exit the cell cycle and enter quiescence (24). The decision to progress to the S phase and replicate the DNA is made at the restriction (R) point, located in the mid to late G_1 phase, and is irreversible (34). The transition from the G_1 phase to the S phase is tightly regulated by the tumor suppressor retinoblastoma protein (pRB) family members (pRB, p107 and p130) (35,36). Transcription of genes required for DNA synthesis and cell cycle progression is mediated by the elongation factor 2 (E2F) family (37). In its phosphorylated state pRB acts as a transcriptional suppressor by binding to and inhibiting the E2F transcription of S phase genes. Progression to the S phase is facilitated by the dissociation of E2F from pRB which is mediated by the phosphorylation of pRB (38-40). Additionally, growth factor activation of phosphatidylinositol 3-kinase (PI3K) and receptor mediated Ras intracellular signaling cascade initiates the association of cyclin D and CDK4 and -6, contributing to the inactivation of pRB and triggering G_1 progression (41). The cyclin E-CDK2 complex also plays an important role in the G_1-S transition by maintaining the hyperphosphorylated state of pRB (42). The phosphorylation status of CDK4/6 and CDK2 is tightly regulated by CDK inhibitors. Two groups of CDK inhibitors have been identified: the inhibitors of the cyclin-dependent kinase 4 (INK4) ($p16^{INK4a}$, $p15^{INK4b}$, $p18^{INK4c}$, $p19^{INK4d}$) (29,38) and the CDK interacting protein/Kinase inhibitory protein (Cip/Kip) ($p21^{cip1/waf1}$, $p27^{kip1}$, $p57^{kip2}$) (29,43). The INK4 family members bind to CDK4/6, preventing the association of these kinases with cyclin D during the G_1 phase (29,38,39,43). Cip/Kip proteins can induce a G_1 phase arrest by binding

to the CDKs which prevents them from phosphorylating pRB, however Cip/Kip proteins operate in all phases of the cell cycle (29,38).

1.2.2 The S phase

The S phase is reserved for DNA replication, a process during which an exact copy of the genome of the cell is made (30). The onset of DNA replication takes place at the origin recognition complex (ORC) located at different sites on the chromosome (44). The pre-replication complex (pre-RC) is a multi-protein complex and consists of cell division cycle (Cdc) 6, chromatin licensing and DNA replication factor 1 (CDT1) proteins and the minichromosome maintenance protein complex (MCM complex) (45). This multi-protein assembles on the ORC during the initial step of DNA replication. The MCM complex unwinds the DNA ahead of each replication fork, limiting DNA replication to once per cell cycle (46). The assembly of the pre-RC is completed once the MCM complex binds to the chromatin. This is followed by the phosphorylation of the DNA replication machinery facilitated by the cyclin A-CDK2 complex, thus activating the pre-RC (39). Subsequently, the ORC at each replication origin changes to a post-replication state and DNA replication is initiated (44).

1.2.3 The G_2 phase

Preparation for mitotic entry is completed in the G_2 phase, where DNA and cytoplasmic replication is checked. Progression from the G_2 to M phase is initiated by the association of cyclin B with CDK1 (47). This forms the mitosis promoting factor (MPF) and is regulated by CDK1 activity which is controlled by reversible phosphorylation and protein-protein interactions (48). The activity of CDK1 is inhibited by phosphorylation of its threonine (Thr)14 and tyrosine (Tyr)15 amino acid residues by Wee-1 and Myt-1 kinases. The up-regulation and phosphorylation of Wee-1 and Myt-1 kinases are facilitated by checkpoint kinase 1 and 2 (Chk1, Chk2) (49). These two kinases are involved in the DNA structure

checkpoint and prevent CDK1 entry into the nucleus. Activation of CDK1 initiates the association with cyclin B at the end of the G_2 phase and cells enter mitosis (40,43). CDK1 is activated and translocates to the nucleus via phosphorylation of its Thr161 amino acid residue by cyclin activating kinase (CAK) and dephosphorylation of Thr14 and Tyr15 by dual specificity phosphatase Cdc25B and Cdc25C (49). The polo-like kinase-1 (Plk-1)-dependent phosphorylation of Cdc25C at serine (Ser)214 and Thr130 activates the phosphatase, generating a positive feedback loop between Cdc25C and CDK1 (50). Chk1 and Chk2 inhibit the activity of Cdc25C via phosphorylation at Ser216 throughout interphase. Once Cdc25C activity is inhibited, Cdc25C is associated with 14-3-3σ in the cytoplasm, resulting in Cdc25C sequestering (51). Plk-1 activity is regulated by the DNA damage status, signaled via ataxia-telangiectasia-mutated (ATM) and ataxia telangiectasia and Rad3-related protein (ATR), in addition of Chk1 and Chk2 regulation (52).

1.2.4 The M phase

Mitosis is initiated by chromosome condensation during prophase (30). Metaphase is entered into as the chromosomes align on the metaphase plate. Chromosomes attach to the mitotic spindles via specialized protein complexes known as kinetochores (53). Kinetochores assemble at the centromeres of chromosomes, which are responsible for the equatorial alignment. Segregation of sister chromatids to opposite poles of the cell occurs during anaphase, a process that depends on microtubule motor proteins and microtubule dynamics (54). The kinetochore/centromere complex contains the growing end of the microtubules (53). The kinetochore microtubules initiate the division of the centromere allowing segregation of the sister chromatids. Cell division in completed during telophase. Telophase is characterized by spindle disintegration, chromosome unraveling, nuclear membrane reassembling and cytokinesis (24,30).

1.2.5 Cell cycle checkpoints

Successful cellular replication is monitored by cell cycle checkpoints. These checkpoints inspect each phase of the cell cycle to ensure that the genetic material is correctly replicated (DNA replication checkpoint), that no DNA damage has occurred (DNA damage checkpoint), and that the replicated DNA is correctly divided among the two daughter cells (spindle and mitotic checkpoints) (55). Should critical errors be detected, the checkpoints will induce cell cycle arrest followed by the recruitment and activation of repair machinery (56). Once the errors are mended the checkpoint will allow the cell to re-enter the cell cycle and proceed to the subsequent phase. Cellular damage that is irreparable will result in permanent cell cycle arrest. The latter is followed by the induction of cell death (56).

Entry of quiescent cells into the cell cycle is monitored by the G_1/S checkpoint, while the G_2/M checkpoint regulates mitotic entry. Correct spindle attachment and chromatid segregation is crucial for mitotic exit and is regulated by the spindle checkpoint.

1.2.5.1 DNA structure checkpoints

The DNA damage checkpoints are located at the G_1/S and G_2/M transition point (57). DNA damage will thus prevent entry into the S and M phases, respectively. Cell cycle arrest at the G_1/S checkpoint is p53 dependent (58,59). Activation of p53 requires its phosphorylation by ATM and ATR upon DNA damage and induces transcription of the p53 negative regulator mouse double minute 2 homolog (Mdm2), multiple anti-cancer proteins including p21 (CDK inhibitor) and the apoptotic promoting gene B-cell lymphoma (Bcl)-2 associated X protein (Bax) (58,59).

DNA damage detected during the G_2/M transition activates the checkpoint via p38 mitogen-activated protein kinases (MAPK) activity (57). Mitotic arrest will be induced in an attempt

to repair the damaged DNA or induce apoptosis prior to mitotic completion if the damage is too severe (60). Cell cycle arrest at the G_2/M checkpoint can occur irrespective of the p53 status (29). Mitotic entry is prevented by maintaining the inactivity of CDK1. Upregulation of p53 activates several genes including DNA damage inducible gene (Gadd)45, p21 and 14-3-3σ (61). Gadd45 and p21 keep CDK1 in its inactive form by dissociating the cyclin B-CDK1 complex and inducing cyclin B degradation, respectively (61,62). This prevents the activation of the MPF, facilitating the metaphase arrest. Entry into mitosis is also delayed due the association of 14-3-3σ to cyclin B which inhibits the activation of the cyclin B-CDK1 complex, thus preventing MPF activation (63). In addition to the p53-dependent CDK1 inactivation, CDK1's activity can also be inhibited in a p53 independent manner. Chk1 and Chk2 are ATM dependent kinases which are activated upon DNA damage (64). These checkpoint kinases phosphorylate and inhibit the tyrosine phosphatase, Cdc25 (64). Cdc25 is responsible for the dephosphorylation and activation of cyclin B-CDK1 (65). However, in its phosphorylated state Cdc25 is unable to activate CDK1, preventing mitotic progression.

1.2.5.2 Spindle assembly checkpoint

Accurate segregation of mitotic chromosomes is ensured by the spindle assembly checkpoint (SAC) (66). This is achieved by inhibiting the commencement of anaphase until each kinetochore is properly attached to their mitotic spindle (48). Chromosomal segregation is mediated by the Cdc20 activated anaphase promoting complex/cyclosome (APC/C) (67) which targets cyclin B and securin for degradation once proper mitotic spindle-chromosome attachment is achieved (68) (Figure 1.2). Degradation of the cyclin results in the inactivation of the CDK1, inducing a metaphase block (68). The APC/C is a target of the SAC (66). Improperly attached kinetochores will result in the inhibition of the APC/C by the SAC, preventing the transition from metaphase to anaphase. The latter is achieved by the formation of the mitotic checkpoint complex (MCC) (69) which consists of budding uninhibited by benzimidazoles (Bub)R1 and Bud3, Cdc20 and mitotic arrest deficiency protein (Mad)2 (70,71) (Figure 1.2). SAC detection of improper kinetochore attachment activates the MCC via checkpoint protein signaling. These proteins include the Mad1, Mad2

and Mad2/BubR1 and the Bub1 and Bub3 proteins and inhibit the Cdc20-APC/C complex ubiquitin ligase activity of the mitotic cyclins and the protein securin (72) (Figure 1.2). Securin regulates the activity of separase, a protein responsible for cleaving the cohesion complex between two sister chromatids (71). Thus, by halting the APC/C, securin is not able to initiate chromatid separation, preventing the onset of anaphase. Once all the kinetochores are correctly attached to the mitotic spindles, the SAC becomes inactive. The checkpoint proteins' activity is inhibited and they dissociate from Cdc20. Cdc20 activates the APC/C which initiates the degradation of cyclin B, initiating the progression to anaphase (71) (Figure 1.2).

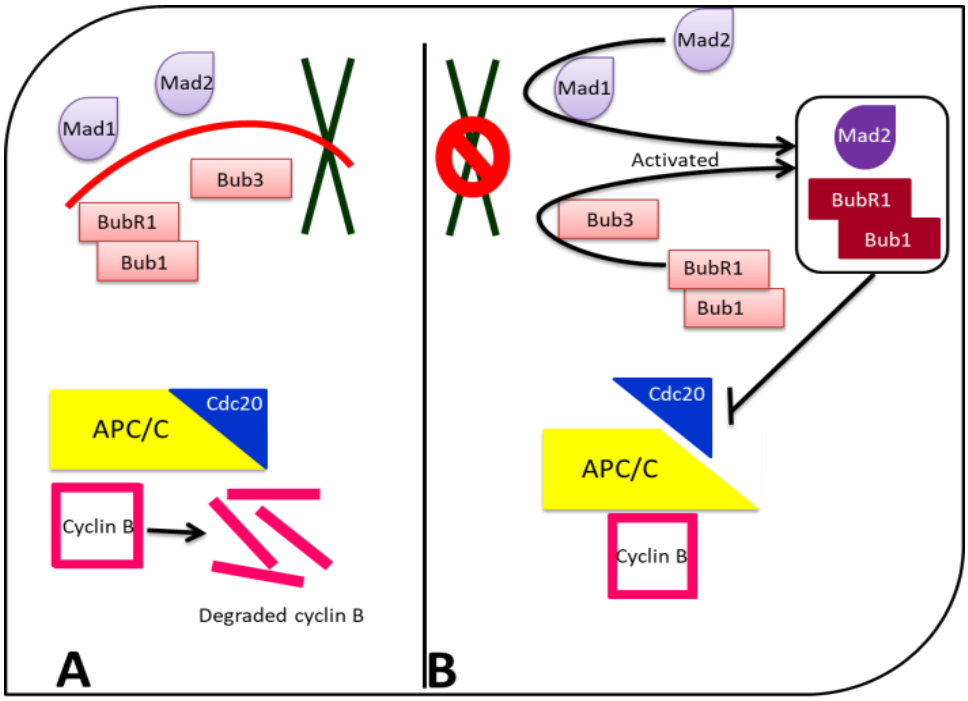

Figure 1.2: The spindle assembly checkpoint. The anaphase promoting complex or cyclone (APC/C) inhibits the degradation of cyclin B following improper chromosome attachment. This process is regulated by the spindle assembly checkpoint (SAC) and will delay the progression from metaphase to anaphase pending proper chromosome attachment. **A.** Proper attachment of the chromosomes to the microtubules prevents the activation of the checkpoint proteins budding uninhibited by benzimidazoles (Bud)R1, Bud1 and mitotic arrest deficiency protein (Mad)2. This is followed by the activation of the APC/C by cell

division cycle (Cdc)20. The APC/C initiates cyclin B degradation and the mitotic block is dismissed (73). **B.** Detection of improper chromosome attachment activates the aforementioned checkpoint proteins. This prevents APC/C activation by Cdc20 resulting in the accumulation of cyclin B and a mitotic block is induced by the checkpoint (73). Adapted from Matson and Stukenberg (2011) (73), using Microsoft PowerPoint 2010.

1.3 Cell death

Cell death can be classified as apoptotic or necrotic based on morphological changes during the process. Apoptosis is controlled by programmed cellular cascades, whereas certain types of necrosis are described as an unprogrammed 'accidental' death (74). Apoptosis is described as a 'clean' form of cell death as all the cellular content remains within cell membrane envelopes during degradation. This limits the immune response. In contrast, during necrosis cellular content are expelled into the extracellular space, triggering an immune response. Lastly, cell death can be categorized according to enzymological criteria based on the involvement of nucleases or proteases (74).

1.3.1 Necrosis

Necrotic cell death does not require energy and is characterized by cell and membrane swelling. This is followed by cell membrane rupture during the early stages of necrosis and results in spillage of intracellular material into the extracellular space, triggering an inflammatory response (75,76). Due to compromised membranes, proteolytic enzymes are release from lysosomes and enter the cytosol (77-79). The death sequence commences via lysosomal breakdown of the cell, which result in metabolic failure with subsequent adenosine triphosphate (ATP) depletion (80,81).

The onset of necrosis is mediated by poly-adenosine diphosphate (ADP)-ribose polymerase (PARP), the formation of reactive oxygen species (ROS), cathepsins, calcium-activated nonlysosomal proteases and the influx of calcium ions through the plasma membrane (82,83). The intracellular ATP stores are rapidly depleted by the catalyzation of DNA strand break repair mechanisms, a process facilitated by the DNA repair enzyme, PARP (82,83). The rapid depletion of ATP renders the cells necrotic. Additionally, PARP also plays a role in apoptosis, however, the aforementioned necrotic response is muted during the early stages of apoptosis (84,85). The latter is achieved by rapid cleavage and degradation of the PARP enzyme, preserving ATP. This is necessary for successful apoptotic induction as several apoptotic effector processes are energy dependent. Apoptotic cell death may be shifted to necrotic cell death, if the ATP stores become depleted (84,85). The effect of calcium on the induction of cell death is origin-dependent. The release of calcium from the endoplasmic reticulum (EndoR) induces apoptotic cell death, whereas necrosis is a result of the rapid influx of calcium ion across the cell membrane (79).

Necrotic cell death can be distinguished from other forms of cell death by using small ionized molecules which are unable to cross intact cell membrane (86). The propidium iodide staining method is often used to distinguish between dead and viable cells where propidium iodide can only cross the plasma membrane of necrotic cells (due to the loss of membrane integrity) and binds to DNA with a corresponding increase in fluorescence (87).

1.3.2 Apoptosis

Morphological changes observed in apoptotic cells (type I programmed cell death) contrast those seen during necrosis. Apoptotic cells maintain their membrane integrity until late stages (79,87) and are characterized by cell shrinkage caused by aspartame-specific protease cleavage of the subcellular infrastructure, pseudopodia retraction, and plasma membrane blebbing (74). Additionally, chromatin condensation and fragmentation of the nucleus, termed pyknosis and karyorrhexis, respectively, are also observed during apoptotic

cell death (74). Plasma membrane blebbing results in the formation of apoptotic bodies. Contained within these apoptotic bodies are nuclear and cytoplasmic fragments, as well as tightly packed organelles (88). These cellular fragments are engulfed by macrophages, parenchymal cells and neoplasmic cells followed by lysosomal degradation (88). The aforementioned engulfed fragments do not produce and release cytokines, thus apoptotic cell death does not trigger an immune response (89,90). Unlike necrosis, apoptotic cell death is a highly energy dependent process (79). Membrane asymmetry facilitates the externalization of the negatively charged membrane phospholipid, phosphatidylserine (PS) (79). The plasma membrane consists of a phospholipid bilayer. On the outer cell membrane sphingomyelin and phosphatidylcholine are located, whereas PS is located at the inner cytosolic position (91). Externalization of PS is noted as an early apoptotic event and initiates macrophage recognition, followed by phagocytosis. Additionally, PS externalization is used to detect and quantify apoptotic cells. The 35 kilodalton (kDA) phospholipid-binding protein, annexin V, has a high affinity for PS in the presence of calcium, and is incorporated into laboratory techniques for apoptotic cell death detection and quantification (91).

1.3.2.1 Regulation of apoptosis

Caspases are aspartame-specific cytokine proteases and play an essential role in orchestrating the cascade which executes apoptotic cell death mechanisms (92). A pro-apoptotic signal, initiated by DNA damage or oxidative stress for example, activates the initiator caspases (caspase 2, -8, -9, -10 and -11) which associate and subsequently activate effector caspases (caspase 3, -6 and -7) (93). The origin of the pro-apoptotic signal determines the mode of activation of the initiator caspase. Caspase 8 is activated by extrinsic apoptotic signaling and binds to the death effector domain (DED) on the Fas-associated protein with death domain (FADD) co-factor (94,95). Activation of caspase 9 is stimulated by intrinsic apoptotic signals. This caspase binds to the co-factor apoptotic protease activating factor (Apaf)-1 via the caspase recruitment domain (CARD) (96). Activation of the initiator caspase strengthens the apoptotic signal and activates the

effector caspases. The effector caspases cleave specific substrates resulting in cellular disassembly (97).

The extrinsic apoptotic pathway involves transmembrane receptor-mediated interactions, facilitated by the tumor necrosis factor (TNF) receptor family (98), and is thus also referred to as the death receptor pathway (93) (Figure 1.3). The extrinsic apoptotic pathway is activated in response to membrane death receptor ligation. The TNF receptor ligand, Fas ligand (FasL), and TNF-related apoptosis-inducing ligand (TRAIL) complex with their respective death receptors on the cell membrane (98). This results in the formation of a death-inducing signaling complex (DISC) via the recruitment of the intracytoplasmic adaptor protein, FADD, which binds to the receptor-ligand death domain (99). FADD binds to- and dimerizes pro-caspase 8, completing the DISC formation and activating caspase 8. This result in the recruitment of additional initiator caspases (caspase 8 and/or -10) followed by the cleavage of effector caspases such as caspase 3 and/or -6 and/or -7 (Figure 1.3). Additionally, the cleavage and mitochondrial translocation of BH3 interacting-domain death agonist (Bid) may be facilitated by caspase 3, indirectly activating the intrinsic apoptotic pathway (Figure 1.3) (93).

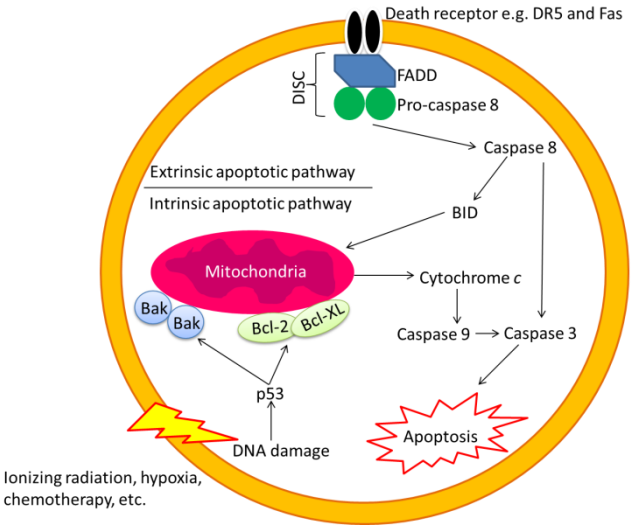

Figure 1.3: The intrinsic and extrinsic apoptotic pathways. The intrinsic apoptotic pathway is activated upon the release of cytochrome *c* from the mitochondria. The cytosolic

cytochrome *c* activates the initiator caspase 9, which in turn activates the executioner caspase 3. Caspase 3 is also activated through the extrinsic apoptotic pathway. The extrinsic apoptotic, or death receptor pathway, is activated by the death-inducing signaling complex (DISC). The DISC is formed by the association of a ligand to the death receptor (eg. Fas and death receptor 5 (DR5)). Fas-associated protein with death domain (FADD) and pro-caspase 8 are recruited to the activated receptor to complete the DISC formation. The extrinsic pathway will proceed by activating caspase 8, resulting in BH3 interacting-domain death agonist (Bid) cleavage. The latter will increase the permeability of the mitochondrial membrane allowing the release of pro-apoptotic proteins. Caspase 8 also activates caspase 3. Activated caspase 3 will initiate a caspase cascade resulting in the induction of apoptosis. Adapted from de Vries *et al.* (2006) (100), using Microsoft PowerPoint 2010.

Intrinsic pro-apoptotic signaling is stimulated by cytokines, radiation-induced DNA damage, hormones, free radicals and hypoxia (88). The intrinsic apoptotic pathway is characterized by the extravasation of mitochondrial proteins such as cytochrome *c* (98) (Figure 1.3). The permeabilization of the mitochondrial membrane is facilitated by a family of Bcl proteins. These proteins are classified as pro-apoptotic BH123 proteins (Bax and Bcl-2 homologous antagonist-killer (Bak)), anti-apoptotic BH1234 proteins (Bcl-2 and Bcl-extra large (Bcl-XL)) and Bcl-2 homology domain (BH)3 only proteins (Bid and Bcl-2-associated death promoter (Bad)). The pro-apoptotic proteins (BH123) and the anti-apoptotic proteins (BH1234) are polar opposites with regards to their function, while the BH3-only proteins regulate their activity (93). Noxious stimulation produced as a result of cell damage or stress will activate the BH3-only proteins. The latter will activate the BH123 pro-apoptotic proteins, while simultaneously neutralizing the BH1234 anti-apoptotic proteins (93). Once the mitochondria are permeabilized by the pro-apoptotic proteins, the next step of the intrinsic apoptotic pathway is entered into. This step involves the formation of an apoptosome in the cellular cytosol. An apoptosome consist of the released cytochrome *c*, apoptotic protease Apaf-1, pro-caspase 9 and deoxyadenosine triphosphate (dATP) (93). Successful association of the apoptosome will result in the activation of caspase 9, followed by effector caspase activation (Figure 1.3).

1.3.2.2 Involvement of reactive oxygen species in apoptosis

Reactive oxygen species (ROS) such as singlet oxygen, superoxide, hydrogen peroxide (H_2O_2), hypochlorous acid, nitric oxide and hydroxyl radicals are generated as a result of incomplete (one-electron) reduction of oxygen (101,102). The latter is facilitated by the electron transport chain, peroxidases, lipoxygenases, cyclooxygenases, hemoproteins, arachidonic acid metabolizing enzymes, cytochrome P450 and nicotinamide adenine dinucleotide phosphate (reduced form) (NADPH) oxidases (101).

Mitochondrial ROS production is tightly regulated for its participation in physiological cell signaling and is one of the major sources of cellular ROS production (103). Superoxide is produced by the mitochondria and can be converted into other ROS forms (104). Under normal physiological conditions, mitochondrial ROS are maintained in equilibrium by antioxidant activity (105). Superoxide dismutases (SOD) are located in the mitochondrial inner membrane space and cytosol (SOD1), as well as the mitochondrial matrix (SOD2) and extracellular matrix (SOD3) (105). The latter removes excess ROS by converting superoxide into H_2O_2. This is followed by the H_2O_2-facilitated oxidation of several enzymes including glutathione peroxidases and peroxiredoxin 2 and -5 which are located within the mitochondria (105). The oxidation process reduces H_2O_2 to water and initiates the reduction of glutathione peroxidases by glutathione activity and peroxiredoxins reduction by thioredoxin, thioredoxin reductase and NADPH (105).

ROS also serves as a type I (apoptosis) or type II (autophagy) cell death stimulus once the physiological ROS threshold has been exceeded (101,106). The intrinsic apoptotic pathway is activated by ROS signaling Bax/Bak oligomerization by the truncated form of Bid (tBid) (107). This results in the insertion of megapores into the mitochondrial membrane with a subsequent decrease in the mitochondrial transmembrane potential. The compromised mitochondrial membrane will release cytochrome *c* into the cytoplasm where it will complex with pro-caspase 9 and Apaf-1 to for the apoptosome (108). The subsequent

activation of caspase 9 will cleave downstream effector caspases such as caspase 3 and -7, inducing apoptosis.

Additionally, ROS activates autophagy as a salvage pathway. The 5' AMP-activated protein kinase (AMPK) is a key energy sensor and maintains energy homeostasis by regulating metabolism (109). Nutrient deficiency and energy depletion are detected by the AMPK. In order to maintain the cellular energy homeostasis, AMPK promotes autophagy by inhibiting mammalian target of rapamycin (mTOR) activity (109). Under normal physiological conditions, phosphorylated v-Akt murine thymoma viral oncogene (Akt) (also known as protein kinase B) regulates mTOR activation, suppressing autophagy. Downstream effectors of activated Akt are, among others, the forkhead box proteins (FoxO). The latter are a family of transcription factors involved in protein degradation and apoptosis. Activated Akt phosphorylates and sequesters the FoxO proteins, translocating them to the cytoplasm (110). Due to the nuclear exclusion, FoxO can no longer facilitate apoptotic signaling. Akt-dependent phosphorylation of FoxO thus contributes to cell survival, proliferation and growth. ROS serve as an autophagy survival pathway stimuli by inhibiting Akt activity with a simultaneous activation of AMPK (110).

1.4 Radiotherapy as an effective anti-cancer treatment modality

Locoregional radiotherapy is a fundamental component in the treatment of various cancers. Radiation therapy is included in at least 50% of all cancer patients' treatment regimes, complementing local and systemic tumor treatments such as chemotherapy and surgery (111,112). Conventional radiotherapy is delivered to tumors using a high energy beam composed of x-rays. Solid tumors receive a total radiation dose of 60-70 gray (Gy) delivered in 30-35 daily fractions over 6-7 weeks (113). However, the therapeutic radiation dose is limited by the adverse reactions of non-cancerous cells surrounding the tumor and those located within the cancerous mass (113). Additionally, the development of radiation

resistance due to the fractionated regime further limits the therapeutic effect of radiotherapy (114,115). Two clinically important strategies have been investigated to improve the therapeutic window between tumor control and normal tissue damage: protecting normal cells from radiation damage and sensitizing tumor cells to radiation utilizing various anti-cancer drugs (116). Radiation is also used in the treatment of breast cancer that metastasized to the spinal cord. Palliative radiotherapy is used as part of a multidisciplinary treatment regime for treating these bone metastases and aim to decrease neurological pain symptoms and spinal cord compression (117). Additionally, palliative radiotherapy assists in recalcifying the bone while minimizing the risk of paraplegia (117).

Exposure of biological material to radiation results in ionization through the removal of electrons from the atoms. Energy is deposited from the high energy rays to the biological material, causing the molecular bonds to break (118). Ionizing radiation is classified according to their linear energy transfer (LET). LET refers to the ionization density of the radiation tracks and is quantified by the average energy deposited per track length (119,120). LET values of 0.2-5 kiloelectronvolts (keV)/micrometer (µm) is considered low-LET radiation, while ionizing radiation types like neutrons and heavier ions produce LET-values of 50-200 keV/µm and are referred to as high-LET (121). The relative biological effectiveness of high-LET radiation is greater compared to the lower LET-radiation due to the increased energy transferred (121). Damage to various cellular components including nucleic acids, lipids and proteins are obtained when exposed to radiation (118). The main target of ionizing radiation is the cell nucleus containing the DNA, which can be ionized directly or indirectly (122,123). Direct ionization of the DNA molecule is mainly induced by high-LET radiation and is achieved by the transient electron or ion itself, while indirect ionization is obtained through ionized water molecules (116,124,125). Water molecules surrounding the DNA molecule become ionized following exposure to radaition, which produce highly reactive hydroxyl radicals ($^{\bullet}$OH). These radicals diffuse to the DNA, react with the molecules and induce DNA damage (124,125). Low-LET irradiation results in direct and indirect ionization in the ratio of 1:3.

Nuclear DNA damage may include, amongst others, single and double strand breaks (122,123). A single strand break is classified as the cleavage of a single strand of the DNA double helix and is rapidly repaired by employing DNA ligase and use of the undamaged strand as a template for base excision repair (122,123). Double strand break repairs are more complex and play a vital role in cell fate (Figure 1.4). Double strand breaks may result in the loss of genetic material due to incompletely- or unrepaired DNA damage (118). The damaged DNA is now incorporated into the chromosomes may induce cell death or result in carcinogenesis (Figure 1.4). DNA damage is detected by transducer-, sensor- and effector cellular proteins. Damage to the cell's genome will launch a signaling cascade for the damage to be repaired. These signaling proteins will induce cell cycle arrest, preventing the damaged DNA to be transferred to the next generation of cells (118). The arrest will be maintained until the damaged DNA has been repaired, or cell death will be induced if the damaged is too severe (Figure 1.4).

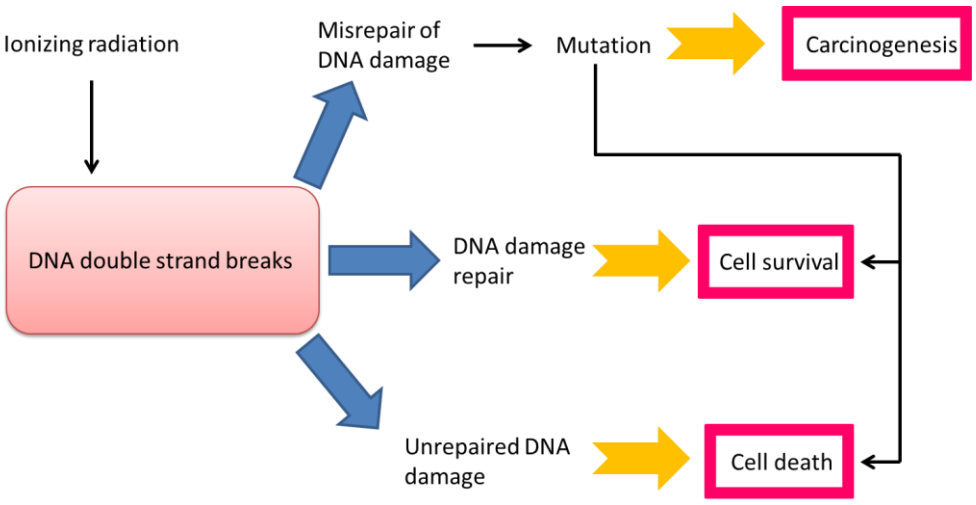

Figure 1.4: Cellular response to radiation-induced DNA double strand breaks. Ionizing radiation can induce DNA double strand breaks. As a response, cell cycle arrest is induced and cellular mechanisms involved in DNA repair are recruited to the site of damage. Successful repair of this damaged DNA allows the surviving cells to re-enter the cell cycle. Cell death is induced when the DNA damage is too severe and cannot be rectified. Misrepair of the DNA damage result in a genetic mutation that is transferred to the next generation of cells. Unless this mutation is detected (cell death) or rectified (cell survival) the mutation

give rise to carcinogenesis. Adapted from Prise and O'Sullivan (2009) (118), using Microsoft PowerPoint 2010.

1.4.1 DNA damage signaling and repair

The DNA damage response (DDR) is initiated upon the induction of DNA damage (126,127). Double strand breaks are detected and regulated by the ATM kinase (128), while the ATR kinase is mostly activated upon single strand breaks and are responsible for stalling the replication fork (129). These kinases phosphorylate and activate downstream proteins involved in the recruitment of DNA repair proteins. The first step in the DDR is the induction of cell cycle arrest at the G_1/S or G_2/M phase transitions (130). A temporary phase arrest facilitates DNA repair by DNA repair proteins that are recruited to the site of damage, and ensures genome stability (130). Cell cycle arrest is achieved by the phosphorylation of cell cycle regulators, Chk1 and Chk2, located downstream of ATM (131). The guardian of the genome, p53, becomes phosphorylated at Ser15 ('arrest'p53) by the active ATM and checkpoint kinases, whereafter, it translocates to the nucleus and determines whether the cell death or survival pathway will be activated (132). Severe and complex DNA damage is often irreparable and result in prolonged p53 activation, activating the 'killer' p53 through phosphorylation at Ser46 (132). Activation of the 'killer' p53 results in the induction of apoptosis (133,134).

Homologous recombination (HR) and non-homologous end joining (NHEJ) are the two main pathways through which double strand breaks can be repaired (135). DNA damage detected during the G_1 phase of the cell cycle is mainly repaired by NHEJ, however, NHEJ functions throughout the cell cycle. NHEJ accurately repairs simple double strand breaks with complementary overhangs and phosphorylated 5' and hydroxylated and 3' ends (135). If any processing of the DNA end is required prior to DNA ligation, NHEJ causes short additions and deletions of DNA sequences (135). The latter may result in the loss of genetic information and inaccurate DNA repair which will result in the formation of micronuclei (136).

Micronuclei result from chromosomal translocation and rearrangement, as well as the formation of dicentric and acentric chromosomes, which subsequently result in aneuploidy (136). Although NHEJ is used for most double strand break repairs, a more 'error free' method is used by HR. Unfortunately, this method can only be used in the late S- and G_2 phase due to the requirement of an undamaged sister chromatid for the recombination (135).

Double strand breaks initiate the recruitment of the Ku70-Ku80 (Ku) heteromere to the site of damage (137). Ku binds to the damaged DNA ends and prevents DNA 5' end resectioning by HR. Both ends of the damaged DNA are kept in close proximity by the Ku heteromere, allowing direct re-joining facilitated by NHEJ (137). Additionally, DNA damaged ends are further protected from HR via the activation of the p53-binding protein 1 (53BP1) by Ku (137). Double strand breaks are highlighted in the nucleosome by the phosphorylation of histone 2A variant X (H2AX) at Ser139 (gamma (γ)-H2AX) (138). This allows the DNA repair machinery, such as artemis and protein kinase DNA-activated catalytic polypeptide (PRKDC), to accumulate at the site of damage by acting as an assembly scaffold (138). DNA ligation by x-ray repair cross-complementing protein (XRCC)4-like factor (XLF), DNA ligase IV (Lig4) and XRCC4 complete the double strand break repair via NHEJ (135). Double strand break repair by HR is initiated by the Mre11-Rad50-Nbs1 (MRN) complex, which transmits the signal to ATM and ATR in order to initiate phosphorylation of downstream factors (139). In combination with retinoblastoma binding protein 8 (RBBP8), the MRN complex facilitates the resectioning of double stranded ends in preparation for DNA end processing. The DNA strand is degraded from the 3' end to the 5' end, allowing the release of Ku from the double strand break ends. Activation of HR then commences by annealing the undamaged sister chromatid to the newly generated single-stranded DNA (135). The choice of which DNA repair pathway is activated is made by BRCA1. During the S and G_2 phases of the cell cycle BRCA1 antagonises 53BPI. The latter activates DNA repair via HR while silencing NHEJ (140,141).

1.4.2 Cell death induced by radiation

Radiation therapy aims to deprive malignant cells of their reproductive potential. This is achieved by inducing severe DNA damage that is irreparable by the cell's DNA repair machinery. The modes of cell death in radiation exposed cell are often mitotic catastrophe (p53 independent), apoptosis (p53 dependent) or senescence (142). The mode of cell death is determined by a number of factors. The cell type is one of the major decision makers in cell death. Apoptotic cell death is predominantly observed in leukemic-, hematopoietic- and lymphoid cells, whereas normal tissues enter senescence following radiation exposure (116). Mitotic catastrophe and apoptosis are usually induced in solid tumors, depending on the dose and quality of the radiation received (116).

One of the most predominant cells death mechanisms induced by radiation is mitotic catastrophe (142). Mitotic catastrophe is a delayed cell death and is entered into due to the DNA damage causing premature mitotic entry (142). The phase checkpoint is not satisfied if the cell enters mitosis prematurely and causes aberrant mitotic processes (143,144). Additionally, mitotic catastrophe is used by hyperamplified centrosomes (144,145). In contrast to the normal function of centrosomes which are responsible for bipolar mitotic spindle formation (146), hyperamplified centrosomes result in multipolar spindle formation (147). The latter results in atypical segregation of the chromosomes, resulting in aberrant nuclear morphology (144,148), micronuclei formation (122) and multinucleated cells (144,149). Micronuclei are whole chromosomes or chromosome fragments that were excluded from the nuclei of the newly formed daughter cells (150). These additional nuclear bodies are similar in morphology compared to the main nucleus with the main difference being the size (smaller compared to the cell nucleus). The micronuclei can be observed during interphase in the cellular cytoplasm in close proximity to the nucleus (151). The cytokinesis-block micronucleus assay is an international standard method for DNA damage quantification. Cells are exposed to cytochalasin B prior to micronuclei quantification. This method prevents cytokinesis and produces binucleated cells in which an accurate quantification of DNA damage can commence (152). Quantification of binucleated cells is

essential as some of the DNA damage may only be observed in the next nuclear division following exposure to radiation.

Ionizing radiation activates a cellular caspase cascade resulting in apoptotic cell death. The activation of the intrinsic apoptotic pathway is facilitated by the inhibition of the anti-apoptotic protein, Bcl-2, with a subsequent activation of pro-apoptotic proteins such as Bax and BH3 only proteins (153-155). These pro-apoptotic proteins are activated by p53 in a rate-limiting fashion (156,157). The BH3 only protein, p53 upregulated modulator of apoptosis (PUMA), plays an important role in radiation-induced apoptosis by promoting the Bax/Bak mitochondrial megapore insertion, increasing mitochondrial permeability (156-158). Additionally the oligemerization of Bax/Bak is facilitated by tBid. Elevated intracellular ROS levels produced upon radiation-exposure act as a stimulus to activate tBid (159). As a result of the increased mitochondrial permeability, cytochrome *c* is released into the cytosol where it participates in the formation of the apoptosome (160). This is followed by the activation of initiator caspase 9 and executioner caspase 3 (161,162), which targets cell cycle regulatory proteins and DNA repair proteins in order to facilitate apoptosis induction (159).

The last mechanism through which radiation prevents cellular proliferation is senescence (163-165). Enlarged flattened cells that present with increased granularity are said to be in a state of senescence (166). Senescent cells have exited the active cell cycle and entered a permanent state of cell cycle arrest (167). Upon radiation exposure cells enter senescence due to a sustained DNA damage response signal. This ensures that cellular proliferation is arrested and that the DNA damage obtained from the radiation is not transferred to the daughter cells (167,168). Radiation-induced senescence should not be confused with 'proliferation limiting senescence'. 'Proliferation limiting senescence' refers to the senescence induced due to telomere shortening obtained by cells during their lifespan (168).

1.4.3 Radiation resistance

Radiotherapy is an effective method for the treatment of tumors, however the development of radiation resistance remains a challenge (169). Radiation resistance refers to the process through which cancer cells adapt to the cellular changes induced by radiotherapy. This process is complex and involves multiple genes and cellular mechanisms (170,171).

One of the main factors involved in the development of radiation resistance is the mechanism through which cells repair their damaged DNA (Figure 1.5). By increasing the rate of the DNA damage response, radioresistant cells increase the onset of signaling pathways responsible for DNA repair (172,173). These pathways include the PI3K and the MAPK pathways which promote DNA repair by maintaining steady homologous recombinant levels and mediating the oxidative stress response, respectively (174,175). Additionally, cells increase DNA repair by inducing prolonged cell cycle arrests (Figure 1.5). It has been reported that the G_2/M phase block induced by the protein 14-3-3σ is closely related to the development of radiation resistance (176). Here the cells can utilize the ATM-Chk2 and ATR-Chk1 axes to increase the DNA damage repair signaling and decrease the induction of cell death (177). Another mechanism through which cells obtain radiation resistance is by altering oncogenes and tumor suppressor proteins (Figure 1.5). The development of radiation resistance in nasopharyngeal carcinoma (NPC) has been assigned to alterations in the oncogene vitronectin (VTN) (178,179). VTN is a cell adhesion molecule and deregulation of its expression contributes to cell migration and invasion. Similar effects have been seen in lung- and breast cancer cells where alterations were made in the expression of tumor suppressor micro-ribonucleic acids (miRNAs), such as miR-29c and miR-22 (180,181).

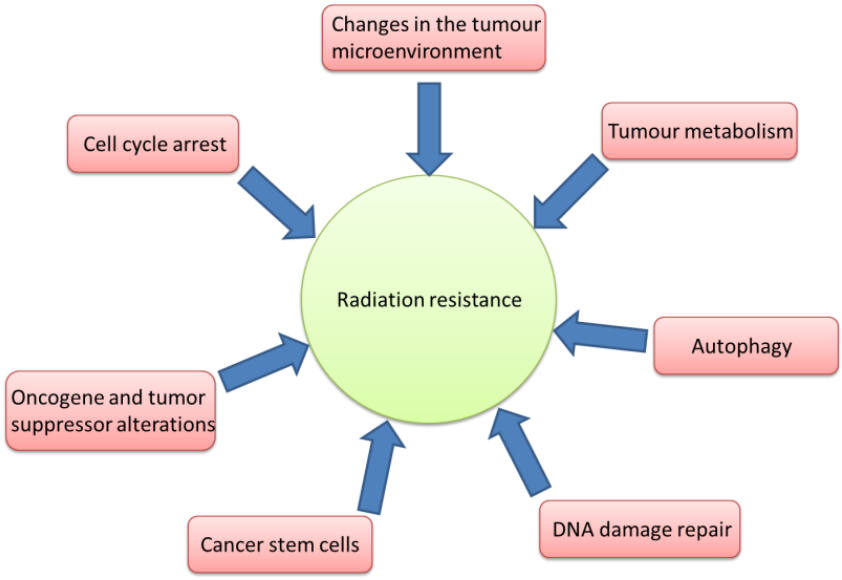

Figure 1.5: Factors contributing to the development of radiation resistance. Constant exposure to radiation results in cellular changes that enable the cells to protect themselves from the radiation damage. As illustrated in the figure, various cellular mechanisms and factors are involved in the development of radiation resistance and contribute to treatment failure in patients. Adapted from Tang *et al*. (2018) (182), using Microsoft PowerPoint 2010.

Immune invasion is a tactic used by tumor cells to maintain their proliferation rate by evading the hosts' immune response (183) (Figure 1.5). The risk of tumor relapse and metastasis is increased by various immunosuppressive processes, thus changes in the tumor microenvironment, such as cytokine levels and epithelial-mesenchymal transition (EMT)-related processes, contribute to the development of radiation resistance (184-187). Cells may also utilize autophagy in order to gain resistance to radiation (188) (Figure 1.5). The initiation of the metabolic-recycling autophagy pathway promotes cell survival and proliferation, whilst decreasing the rate of radiation-induced apoptosis (189,190). Another mechanism extensively studied for its involvement in radiation resistance, is tumor metabolism (191,192) (Figure 1.5). Cellular radioresistance is conferred via altered glycolytic and/or mitochondrial metabolism (193). Cancer stem cells have high oncogenic activity and multi-directional differentiation potential (188) (Figure 1.5). These cells are undifferentiated and have the ability to self-renew, providing a possible mechanism for the development of radiation resistance. Furthermore, cancer stem cells are responsible for tumor cell

heterogeneity, display increased metastatic potential after radiation treatment and rapidly respond to DNA damage (188,194-196).

1.4.4 Radiation-induced bystander effect

'A cell that responds to the fact that its neighbors have been irradiated', is a simple explanation for the complex process known as the radiation-induced bystander effect (197). Unlike the dose-response relationship seen in irradiated cells where the cellular response is directly proportional to the radiation dose, the bystander response is saturated at low radiation doses (198,199). Above this saturation point no additional bystander effects occur, and thus not all the cells exposed to the bystander effects will respond upon contact (200). Although the bystander effects induced by low radiation doses are as effective as the direct response (201), it should be emphasized that the bystander effect is still active at higher radiation doses and play a significant role in the overall effectiveness of radiotherapy (202).

The bystander effect has been studied intensively *in vitro* and *in vivo*. Endothelial cells (203), fibroblast (204), lymphocytes (205) and tumors cells (206) all displayed bystander responses which can either be damaging (genetic mutations (207), DNA damage (208) and cell death (209)) or protective (radioadaptive response (210), terminal differentiation (211) and removal of damaged cells via apoptosis (212)) (213). Two main mechanisms are involved in the radiation-induced bystander effect. The first mechanism describes the relationship between irradiated and non-irradiated cells that are in direct contact. Cells utilized the multimeric protein Gap junctional intercellular communication (GJIC) channels to transmit the bystander signaling molecules (214). These molecule-transmitting structures are individually formed as hemi-channels on the cells. By physically interacting with each other, cells initiate the merging of these structures. Connexion proteins form the gap junctions which typically allow the transport of molecules sized 1000-1500 dalton (Da). These molecules include second messengers such as nucleotides, ions and peptides (215). This bystander signaling mechanisms are more available in non-cancerous cells, due to the GIJC being down-regulated in tumor cells (216). The second mechanism utilized in the radiation-

induced bystander effect involves the release of soluble factors by the irradiated cells (217). These molecules may be regulated by ROS (such as superoxide radicals), are between 1000 and 10000 kDa in size and include cytokines such as TNFα (218), lipid peroxide products (219) and inosine nucleotides (220). The effect of these molecules released by the irradiated cells can be mimicked in an *in vitro* laboratory setting by transferring conditioned media obtained from irradiated cells to non-irradiated cells (209).

Several molecules such as interleukin (IL)6 (221) and IL8 (222), TNFα (223), transforming growth factor (TGF)β-1 (224), ROS (225) and reactive nitrogen species (RNS) (206,226), are involved in cell-cell signaling and the stress response and have been identified as key players in the radiation-induced bystander effect. Additionally, radiation-induced bystander signaling has some similarities to the inflammatory response. Macrophages are phagocytic cells responsible for the elimination of pathogens and apoptotic cells. However, when exposed to radiation under bystander conditions macrophages constantly produce increased levels of oxidative stress molecules (227). The cellular inflammatory response mediator, cyclooxygenase (COX)2, also contributes to radiation-induced bystander signaling. Induction of COX2 synthesis by the activation of the MAPK pathway contributes to transcription factor activation. The downstream signaling includes the activation of NO synthase resulting in an increased production of RNS. Previously published work reported a reduced bystander response in non-exposed cells where the aforementioned pathways were inhibited (223).

The bystander effect is not dependent on signaling from the direct DNA damage obtained by cells exposed to radiation, but rather the energy deposited into the cytoplasm of these cells (228). The deposited energy located in the exposed cytoplasm of the cells increases the production of ROS. This can indirectly induce nuclear damage in exposed and bystander cells (229). Therefore, the mitochondria and other subcellular targets that are able to produce bystander signaling molecules or those participating in the signal transduction have been classified as radiation-induced bystander mediators (230,231). The mitochondria for

example contribute directly to the bystander signaling and response pathway by producing and releasing ROS following radiation exposure. Additionally, radiation exposure results in the loss of mitochondrial transmembrane potential. Cytochrome *c* is released as a result of the increased mitochondrial permeability and induces the production of ROS. In this way the mitochondria also contribute indirectly to the radiation-induced bystander effect.

1.5 Intracellular microtubule dynamics

Microtubules are multifunctional, long filamentous tube-shaped cytoskeletal proteins with an outer diameter of 25 nanometer (nm). These polymers form part of the essential machinery involved in intracellular transport, cell signaling and shape (232). Additionally, microtubules are responsible for spindle formation during mitosis, ensuring accurate attachment and division of chromosomes (232,233).

The microtubule global protein dimer consists of α and β tubulin heteromeres (232). These tubulin heteromeres vary in length and form protofilaments by aligning in a head-to-tail fashion. The subsequently formed protofilaments are arranged in parallel and provide structural polarity which is essential for proper microtubule functioning (232). Centrosomes are the principle microtubule nucleating structures and function as the microtubule organizing centers (MTOC) (234). The centrosome consists of two centrioles, each arranged as nine microtubule triplets bound by peri-centriolar material. The proteins involved in the nucleation of the microtubules, as well as those that assist in microtubule organization, are located within the peri-centriolar material (234). One such protein, γ-tubulin, initiates the formation of the γ-tubulin ring complex (γ-TuRC) by associating with γ-tubulin complex proteins 2 and 3 (GCP2 and GCP3) (235). The minus ends of newly formed microtubules are capped and nucleated by the γ-TuRC which provides stabile binding sites for α and β tubulin dimers (234). By capping and binding the minus end of microtubules, the γ-TuRC ensures a

slow grow rate of these ends (compared to the plus ends) during microtubule assembly (232).

Microtubules are highly dynamic structures and constantly undergo polymerization (growth) and depolymerization (shrinkage). The β tubulin subunits play an important role in microtubule polymerization due to the fact that they are located at the plus ends of the microtubules, while α subunits are located at the minus end (236,237). The β tubulin subunit is equipped with guanosine triphosphate (GTP) (Figure 1.6). During microtubule polymerization, β tubulin facilitates the hydrolysis of GTP to guanosine diphosphate (GDP) which is stored in the tubulin lattice (238). The minimal energy shape of GDP tubulin is bent, however, the microtubule is kept in a straight configuration by being bound to adjacent tubulin polymers (239) (Figure 1.6). This results in the release of GDP and microtubule depolymerization commences (240).

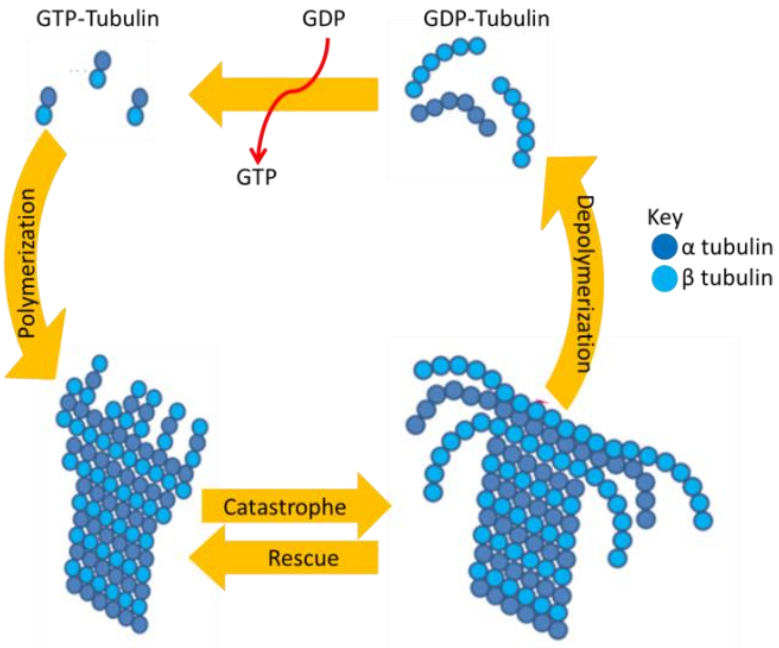

Figure 1.6: Microtubule dynamics. The dynamic microtubules constantly undergo polymerization and depolymerization. Microtubule polymerization is facilitated by the GTP-rich β tubulin. β tubulin hydrolyses guanosine triphosphate (GTP) to guanosine diphosphate (GDP) and microtubule polymerization commences. GDP is released from the straight microtubule, due to its preferred bent configuration, resulting in microtubule

depolymerization. Adapted from Conde and Cáceres 2009 (238), using Microsoft PowerPoint 2010.

In addition to the intrinsic regulation of microtubules by the GTP-cap, microtubules are also extrinsically regulated by microtubule-associated proteins (MAPs) (234). MAPS consist of microtubule stabilizing proteins (MAP2, MAP4 and Tau), as well as microtubule severing proteins (spastin, katanin and fidgetin) (241). Additionally, proteins from the inesisn-13 family, such as kinesin heavy chain member (Kif)2A and mitotic centromere-associated kinesin (MCAK), induce conformational changes to the tubulin structure, resulting in microtubule depolymerization (242-244). The depolymerizing ability of MCAK was first studied in *Xenopus* egg extract, using the homologue *Xenopus* kinesin catastrophe modulator-1 (XKCM1) (245-247). The study revealed a lack of microtubule growth and spindle formation in overexpressed XKCM1 *Xenopus* egg extract, however, XKCM1 depletion resulted in excessive microtubule growth. Microtubule rescue events are coordinated by a group of MAPs called the plus-end tracking proteins (+TIP) (234). The +TIP, cytoplasmic linker protein (CLIP-170), restores microtubule dynamics during the transitions from microtubule shrinkage to microtubule growth (248,249). The aforementioned rescue events are stimulated by the binding of CLIP-170 to the microtubules under the regulation of FK506-binding protein (FKBP)-rapamycin-associated protein (FRAP) (247). Adenosine monophosphate (AMP) kinase inhibits the association of CLIP-170 to the microtubules (250,251), resulting in the +TIPs inactivity and a decrease in rescue events (249).

The intracellular microtubule network is used as a target for anti-cancer drugs. By targeting this dynamic network, the proliferation of rapidly dividing cells can be reduced or halted. The effect of microtubule drugs are more pronounced in rapidly dividing cells. Anti-mitotic drugs can either exhibit microtubule stabilizing or depolymerizing properties (252). The microtubule destabilizing vinca alkaloid, vinblastine, inhibits microtubule polymerization by binding to the tubulin monomers and preventing their association (73,253,254). Paclitaxel is characterized as a microtubule stabilizing agent (255,256). Paclitaxel binds to and stabilizes already formed microtubules by preventing microtubule depolymerization (73,232).

Colchicine is an anti-mitotic agent that permanently induces a curved configuration to tubulin by binding to α and β subunits (252). Colchicine can be classified as a microtubule stabilizing or destabilizing agent as it increase microtubule depolymerization at high concentrations, but inhibits microtubule dynamics at lower concentration (252). These anti-mitotic agents prevent the migration of chromosomes from the spindle poles to the metaphase plate (252). This is accomplished by interfering with the microtubule dynamics and preventing the proper attachment of microtubules to kinetochores (257). The subsequent metaphase block then inhibits cellular proliferation and the cell may be programmed to death (258).

1.6 2-Methoxyestradiol

The hepatic metabolism of estradiol yields a potential anti-cancer agent, 2-methoxyestradiol (2-ME) (259) (Figure 1.7). Estradiol metabolism is initiated by 17β-hydroxysteriod dehydrogenase (17β-HSD) which converts estrone to estradiol (260). Estradiol is further metabolized by the catalytic activity of cytochrome P450 family 1 subfamily B polypeptide 1 (CYP1B1), CYP1A2 and CYP3A. Estradiol is metabolized to 4-hydroxyestradiol by CYP1B1 (261,262), while CYP1A2 and CYP3A convert estradiol into 2-hydroxyestradiol (262-264). Subsequently, these metabolites are methylated by catechol-*O*-methyltransferase (COMT), producing 2-ME and 4-methoxyestradiol (265,266) (Figure 1.7). In circulation, 2-ME binds with low affinity to estrogen and testosterone receptors and was, thus, thought to be inactive (267). However, several *in vitro* and *in vivo* studies highlighted the antitumor and anti-angiogenic properties of 2-ME, rendering it a potential chemotherapeutic agent. 2-ME has been developed as an experimental drug under the trade name Panzem® (268-270).

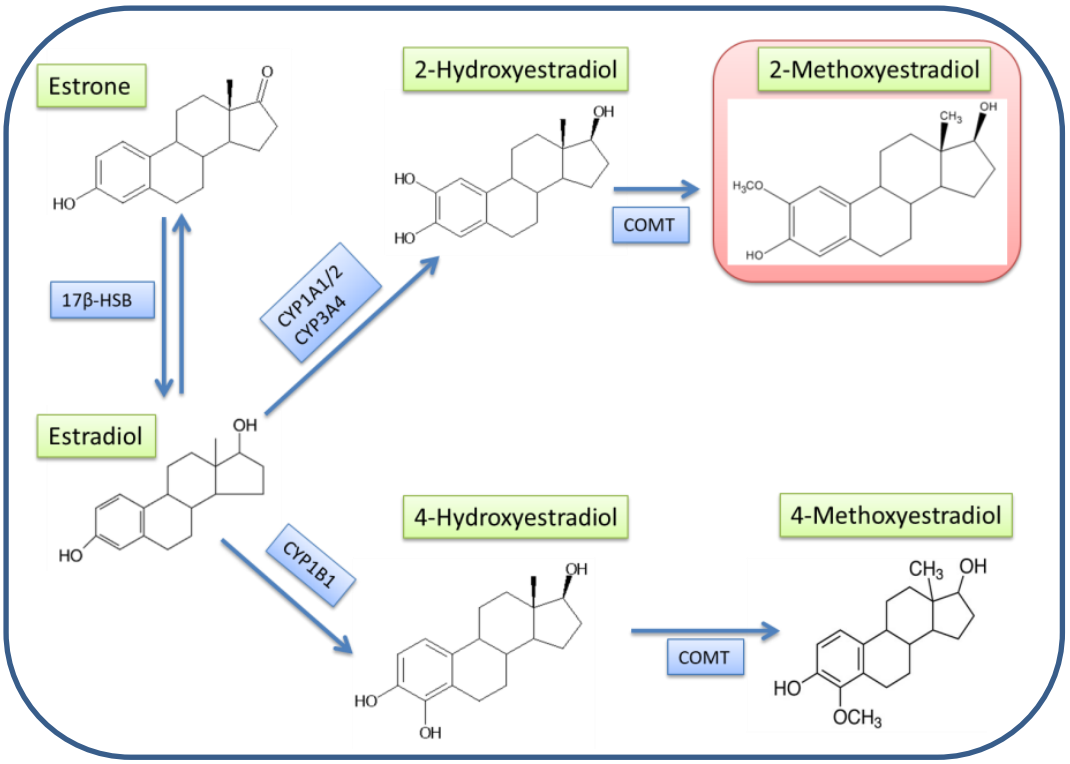

Figure 1.7: Hepatic metabolism of estradiol. Estrone serves as a metabolic intermediate of estradiol. Estradiol is synthesized from estrone, using the 17-β-hydroxysteroid dehydrogenase (17β-HSD) enzyme. Estradiol is further metabolized through the activity of cytochrome P450s (CYPs) to produce 2- and 4-hydroxyestradiol. Catechol-*O*-methyltransferase (COMT) methylates these to produce 2- and 4-methoxyestradiol, respectively. Adapted from Tsuchiya *et al.* (2005) (259), using Microsoft PowerPoint 2010.

2-ME has a higher affinity for sex hormone-binding globulin (SHBG) compared to estrogen (271). The expression of estrogen receptors does not influence 2-ME's antiproliferative and anti-angiogenic activity (272). 2-ME exerts its antiproliferative effect by binding to the colchicine binding sites on microtubules (273,274), resulting in the depolymerization of the latter and induction of a G_2/M phase block (270,273). This prolonged mitotic block prevents cellular proliferation and induces programmed cell death *in vitro* in cervical (275)-, prostate (276,277)- and breast (278-280) cancer cells. By targeting the cellular cytoskeleton, 2-ME's antiprolierative activity is more pronounced in actively dividing cells, such as cancer cells, while quiescent cells are less affected (274). 2-ME's mechanism of action was confirmed during *in vivo* studies, where microtubule depolymerization was observed in orthotopic breast cancer mice models (281). The test subjects were treated daily with 30 or 150

milligram (mg)/kilogram (kg) 2-ME, resulting in tumor morphological changes such as aberrant microtubules and decreased tubulin polymers, which elevated soluble tubulin levels (281).

Substances that prevent the growth of new blood vessels can be categorized as direct or indirect angiogenic inhibitors (282). Angiogenic inhibitors targeting the cells that form the inner cell lining of blood and lymphatic vessels, known as the endothelium, are classified as direct angiogenic inhibitors. Indirect angiogenic inhibitors target the pro-angiogenic growth factors, such as vascular endothelial growth factor (VEGF), which are produced by the cells (283). The angiogenic activities of 2-ME can be classified as both direct and indirect. The ability of 2-ME to prevent proliferation and induce apoptosis in endothelia cells identifies 2-ME as a direct angiogenic inhibitor. However, the ability of 2-ME to inhibit hypoxia-inducible factor (HIF)-1α expression categorizes this microtubule targeting agent as an indirect angiogenic inhibitor (284). HIF-1α interacts with hypoxia response elements which in turn activates pro-angiogenic proteins such as VEGF. HIF-1α exerts its effect in the nucleus (285). 2-ME delays the nuclear translocation of HIF-1α by abrogating the microtubule transport network, decreasing HIF-1α activity (281). 2-ME thus exerts its anti-angiogenic activity in an indirect manner by preventing the activation of pro-angiogenic proteins.

The protein P-glyco-protein pumps (PgP) are primary multidrug transporters located in the plasma membrane (286). Drugs are actively transported out of the cell by binding to the PgP pumps. Active transport is initiated by ATP hydrolysis and the drugs are transported out of the cell against their concentration gradient, decreasing the intracellular drug concentration (287,288). Multidrug resistance may be associated with increased levels of PgP. Increased expression of these efflux pumps in the cell membrane results in constant export of anti-cancer drugs from the cell. This limits the antitumor activity of these compounds, resulting in the development of chemoresistance. This may be observed with the use of classic microtubule targeting agents, such as paclitaxel (73). One major advantage of the use of 2-ME in cancer treatment is the fact that it does not act as a PgP substrate (289). This microtubule targeting agent may thus provide an alternative treatment option for drug-resistant tumors (290). Additionally, compared to clinically used microtubule targeting

agents, 2-ME has a better tolerated side effect profile, with a decrease in neurotoxicity and myelosupression (277,291,292).

Apoptotic cell death induced by 2-ME may occur via the intrinsic as well as the extrinsic pathway. Activation of the extrinsic apoptotic pathway requires the activation of a multiprotein complex called DISC. The DISC is formed by members of the apoptotic-inducing cellular death receptor family (293). Upregulation of death receptor (DR)5 on 2-ME treated cancer cell surfaces was observed in mouse xenograph mouse models *in vivo* (293). This increased the cellular sensitivity to the DR5 ligand, TRAIL (294). Upon ligand binding, initiator caspases, caspase 8 and -9, became active and initiated a caspase cascade (293). The sequential activation of the executioner caspase 3 resulted in 2-ME-induced apoptosis, utilizing the extrinsic pathway. Exposure of cancer cells to 2-ME resulted in the activation of c-Jun N-terminal kinases (JNK). JNK plays a role in the induction of cell death via the intrinsic apoptotic pathway (295). Myeloma cells treated with 2-ME increased the phosphorylated state of JNK, whereafter it has translocated to the mitochondria. At the mitochondrial site, phosphorylated JNK decreased the mitochondrial transmembrane potential by inserting megapores. As a result of the compromised membrane, the pro-apoptotic proteins, cytochrome *c* and second mitochondria-derived activator of caspases (Smac), were released from the mitochondria and the apoptotic caspase cascade was induced (295).

Mitochondrial reactive oxygen species are short-lived highly reactive molecules and play a key role in the ability of 2-ME to induce cell death via the intrinsic apoptotic pathway (296). The mechanism through which 2-ME induces ROS production was identified as the inhibition of SOD1 and copper, and SOD2 (297). These free radical scavenger enzymes play an essential role in preventing cell death by eliminating superoxide radicals. However, these findings were challenged by a report authored by Hagen *et al.* (298). Here, the authors attribute the increased ROS production to the ability of 2-ME to inhibit mitochondrial respiration. This resulted in the inhibition of mitochondrial electron transport chain (mETC) complex 1, which increased ROS production (298). Although the induction of cell death through the mitochondrial pathway is considered to be p53 regulated, previous studies

proved that the ability of 2-ME to induce apoptotic cell death is independent of p53 status (296,299).

The ability of 2-ME to induce cancer cell death has been studied extensively in various *in vitro* cellular models (274,275,277-280,300-304). Ultrastructural changes such as double-membraned vesicles were observed in transmission electron microscopy (TEM) micrographs of cells exposed to 2-ME (305). These vacuolar structures resembled the morphology of structures observe during autophagic cell death called autophagosomes (306,307). The ability of 2-ME to induce two different cell death pathways was confirmed by gene expression microarrays. This technique indicated upregulation of autophagic genes as well as genes involved in apoptosis (305). Additionally, several apoptotic cell death markers such as H_2O_2 and cytochrome *c* were elevated following 2-ME exposure (305). The cells also presented with morphological changes associated with apoptosis, such as hypercondensed chromatin, nuclear fragmentation, cell shrinkage and plasma membrane blebbing (300). The promising results obtained from *in vitro* studies indicated the potential of 2-ME to serve as an anti-cancer drug and gave rise to several *in vivo* studies. The anti-proliferative effect of 2-ME observed in the *in vitro* experimental setup was mirrored in *in vivo* studies. The proliferation of estrogen receptor-negative breast cancer (308) and lung cancer (309) cells was significantly reduced in mouse models following 2-ME treatment. Being able to inhibit the growth of estrogen receptor-negative cancer cells *in vivo* further classified 2-ME as a potential drug for the use in drug resistant tumors.

1.6.1 2-Methoxyestradiol analogues

Structural modification to 2-ME aimed to improve on the anti-mitotic and anti-angiogenic properties of the parent compound. Additionally, 2-ME undergoes rapid 17β-hydroxysteriod dehydrogenase-mediated metabolism (259,310,311), resulting in a short half-life. Thus, improving on the parent compound's bioavailability was of great importance. Stander *et al.* (312) *in silico*-designed several 3' sulphamoylated 2-ME analogues. Modification of the C2' and C17' positions were made to the 2-ME molecule with moieties know to increase the half-life and anti-mitotic effect of the compound. Various combinations of modifications

displaying the optimal colchicine binding site fit were assessed, using The Lamarckian genetic algorithm in AutoDockTools4 with the prepare_ligand4py script. Additionally, the design of these compounds aimed to localize the analogues to tumor cells with preferential binding to carbonic anhydrase IX (CAIX) which is expressed in the acidic tumor micro-milieu (312). The bioavailability of the parent compound was increased by increasing the analogue's binding affinity to carbonic anhydrase II (CAII) in erythrocytes (312). This allows the analogues to bypass the first hepatic metabolism.

Two of these compounds, namely, 2-ethyl-3-*O*-sulphamoyl-estra-1,3,5(10),15-tetraen-17-one (ESE-15-one) and 2-ethyl-3-*O*-sulphamoyl-estra-1,3,5(10)16-tetraene (ESE-16) (Figure 1.8) were synthesized and investigated in a series of *in vitro* experiments for their anti-mitotic and pro-apoptotic abilities. Structurally, ESE-15-one and ESE-16 are very similar, differing only at the C'17 and C'16 positions of the D-ring (312). These compounds are not yet commercially available. Cytotoxicity studies revealed a dose-dependent decrease in proliferation in breast (MDA-MB-231 and MCF-7)-, esophageal (SNO)- and cervical (HeLa) cancer cell lines, when exposed to nanomolar concentrations of both ESE-15-one and ESE-16 (312). Confocal microscopy revealed abnormal microtubule architecture in MDA-MB-231 cells after a 24-hour exposure to ESE-15-one and ESE-16, indicating conservation of the parent compound's anti-mitotic mechanisms (312). These results were mirrored in flow cytometric quantification of the cell cycle in which a significant increase in the G_2/M phase of treated MDA-MB-231 cells was demonstrated. Additionally, a significant increase in the sub-G_1 phase of ESE-15-one and ESE-16 treated MDA-MB-231 cells was observed after a 24-hour exposure, indicating the induction of apoptosis (312). Furthermore, a 48-hour exposure to these compounds revealed a decrease in the G_2/M phase with a concurrent increase in the sub-G_1 phase of the MDA-MB-231 cells. Although the anti-mitotic activity and cytotoxicity of these compounds have been investigated in several cell lines, the potential of ESE-15-one and ESE-16 to radiosensitize breast cancer cells with various receptor statuses has not yet been investigated.

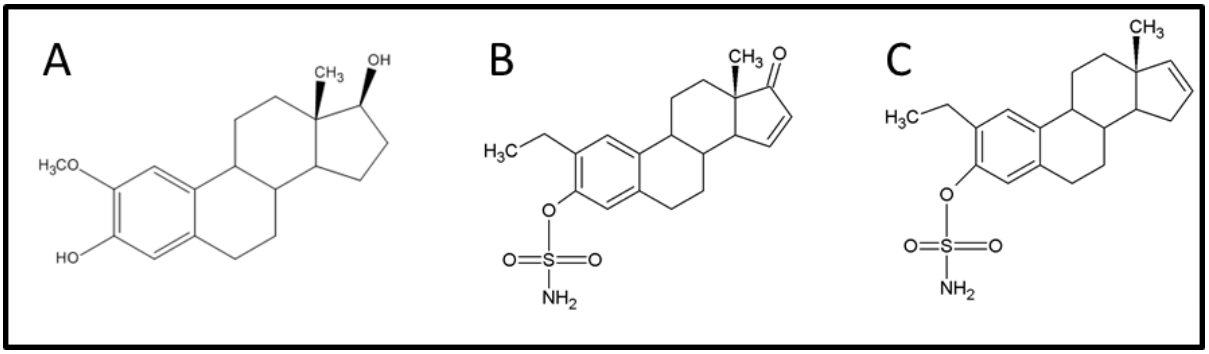

Figure 1.8: *In silico*-designed sulphamoylated 2-methoxyestradiol analogues. 2-Methoxyestradiol (A), 2-ethyl-3-*O*-sulphamoyl-estra-1,3,5(10),15-tetraen-17-one (ESE-15-one) (B) and 2-ethyl-3-*O*-sulphamoyl-estra-1,3,5(10)16-tetraene (ESE-16) (C) (312).

1.7 Lin-11, Isl-1 and Mec-3 (LIM) kinase: A regulator of the cytoskeleton

A key mediator involved in the regulation of the cellular cytoskeleton is LIM kinase. LIM kinase 1 (LIMK1) and LIM kinase 2 (LIMK2) are two members of the LIM motif-containing protein kinase family and play a crucial role in the dynamics of the actin and microtubule cytoskeleton (313). LIMK1 and LIMK2 consist of two LIM double zinc finger domains, a post-synaptic density protein 95 drosophila disc large tumor suppressor zona occludens 1 (PDZ) domain with proline/serine-rich regions and a catalytic protein kinase domain at the C-terminus (Figure 1.9) (314). Although homologous in structure, LIMK1 and LIMK2 are controlled by different upstream pathways, resulting in different biological functions for each kinase in addition to their coinciding cellular functions (315,316). Both LIMK isoforms function as dual-specificity protein kinases and phosphorylate tyrosine and serine/threonine residues (314) under the regulation of Rho GTPase (317).

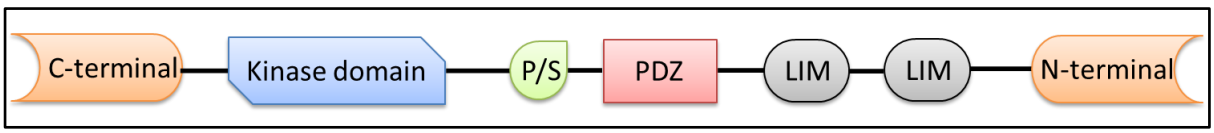

Figure 1.9: LIM kinase protein structure. The LIM kinase protein consist of two LIM domains located at the amino acid N-terminal, a centrally located post-synaptic density protein 95 drosophila disc large tumor suppressor zona occludens 1 (PDZ) domain with proline/serine

(P/S)-rich regions, followed by the kinase domain at the C-terminal. Adapted from Prunier *et al.* (2017) (318), using Microsoft PowerPoint 2010.

LIMK regulates the cyclic phosphorylation and dephosphorylation of the actin severing protein, cofilin (319). LIMK-induced phosphorylation of cofilin results in the inactivation of the protein, preventing the severing of filamentous actin (F-actin) and resulting in the accumulation of actin monomers (Figure 1.10) (320). The subsequent dysregualtion of actin affects several cellular functions, including cell migration and differentiation, stress fiber formation, and extracellular matrix remodeling (315). Additionally, LIMK also contributes to the regulation of microtubule dynamics via a mechanism independent of the actin regulation. Although the mechanism through which LIMK influences microtubule dynamics remains unelucidated, four possible mechanisms have been described in the literature. The first possible target for LIMK-dependent microtubule regulation is the tubulin polymerization-promoting protein, TPPP/p25 (Figure 1.10). TPPP/p25 is a MAP that promotes microtubule stabilization and/or destabilization by directly interacting with the microtubules of the cell (321). Initially, TPPP/p25 was described as a substrate for LIMK, in which LIMK inhibits the ability of TPPP/p25 to assemble microtubules due to phosphorylation of p25 (322). Recent studies revealed that TPPP/p25 is indeed not a substrate for LIMK (323). However, the possibility of an unidentified MAP serving as a LIMK substrate cannot be excluded. A study conducted by Bhardwaj *et al.* (324) suggested that LIMK acts as a MAP itself in its unphosphorylated state, providing the second possible mechanism through which LIMK regulates microtubules. It was observed that unphosphorylated LIMK directly interacts with tubulin (Figure 1.10). This interaction was eliminated upon LIMK phosphorylation, stimulated by the activity of the cytokine CSCL12 (324). The third hypothesis suggested that LIMK1 affects microtubule dynamics via tubulin phosphorylation (Figure 1.10). This was based on the ability of CDK1 to regulate microtubule dynamics during mitosis by phosphorylating β-tubulin (325). The final hypothesis suggests that microtubule dynamics are regulated by LIMK via Aurora A activity (326,327). Aurora A is a key regulator in mitotic progression. Pharmacological inhibition of Aurora A has shown to suppress the dynamic instability of microtubules during interphase by retarding microtubule assembly, shrinkage and catastrophe rescue (328). Thus, LIMK-dependent phosphorylation

of Aurora A resulted in the stabilization of the microtubule network (328,329) (Figure 1.10). Although data suggest that microtubule dynamics can be regulated by LIMK, the underlying mechanisms remain unclear.

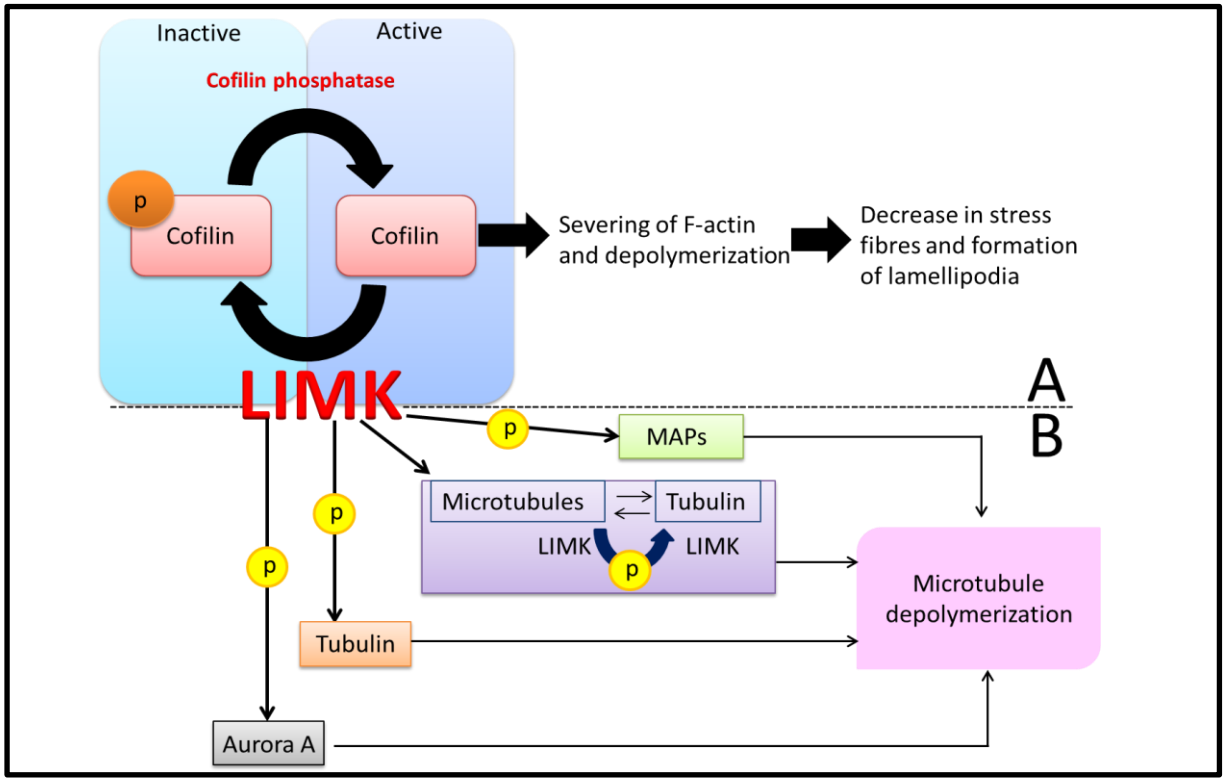

Figure 1.10: Regulation of the cytoskeleton by LIM kinase. (A) LIM kinase (LIMK) phosphorylates cofilin resulting in its inactivation, which reorganizes the actin cytoskeleton. LIM kinase activity increases F-actin severing which results in decreased free barbed ends, reducing cellular protrusions. Additionally, LIM kinase activity increases focal adhesion and stress fiber formation by inhibiting the cofilin driven depolymerization of actin fibers. (B) LIM kinase regulates microtubule dynamics through a still unknown mechanism. Four mechanisms through which LIM kinase activity depolymerize microtubules have been proposed: LIM kinase-dependent phosphorylation of microtubule-associate protein (MAP), tubulin or aurora A kinase, and the direct interaction between tubulin and LIM kinase which acts as a MAP. Adapted from Prunier *et al.* (2017) (318) and Scott and Olsen (2007) (316), using Microsoft PowerPoint 2010.

1.7.1 The role of the actin skeleton in cell migration

By regulating phosphorylation of cofilin, LIM kinase plays a crucial role in cell migration. Chemotaxis is a form of guided cell migration and is functional in wound healing and tumor metastasis (330,331). Cell migration necessitates rearrangement of the cytoskeleton, such as, the polymerization of actin filaments at the leading edge of a cell (332). This allows lamellipodia formation, generally referred to as cellular protrusions (330,331). These protrusions form new contact points on the extracellular matrix (adhesions) and initiate contraction of the cell, whereby the cell body is translocated towards the adhesion. As the cell migrates towards the newly formed adhesion, the rear end of the cell detaches and retracts in order to complete the migration cycle (332).

Formation of cellular protrusions is controlled by cofilin, a key actin dynamic-promoting factor (41,333). By depolymerizing and severing, F-actin cofilin generates free barbed ends. The latter polymerizes actin which is essential for directed lamellipodia formation (334). In addition, cofilin can quickly replenish the dwindling monomeric actin pool. This ensures that the actin filaments continuously extend, creating lamellipodial protrusions (335). Furthermore, *in vitro* studies demonstrated that localized active cofilin has the ability to direct the migration of tumor cells (336,337). Cofilin activity is largely regulated by LIMKs (338-340) (Figure 1.10). LIMK activity is regulated by the Rho-GTPases downstream kinases: Rho-associated protein kinase (ROCK), p21 activated kinases (PAK)1 and PAK4 (341-343). The Rho-GTPase, Rac, signals downstream to PAK, initiating the phosphorylation and activation of LIMK. LIMKs inhibit the binding of cofilin and F-actin via phosphorylation of cofilin at its serine 3 residue (344) (Figure 1.10). Reactivation of cofilin is mediated by dephosphorylation of its serine 3 residue via the activity of two phosphatase families: slingshot family (SSH) and chronophin (CIN) (345-347).

1.7.2 LIM kinase involvement in the cell cycle progression

LIMK1 and LIMK2 have key functions at various stages of cell cycle progression, including mitotic spindle organization, segregation of chromosomes and cytokinesis (348). During the

G_1 phase, LIMK1 maintains extracellular signal-regulated kinases (ERK) activity, which plays a key role in mitosis regulation. LIMK1 activity and a concurrent increase in cofilin phosphorylation are evident in prometaphase and metaphase during mitosis (349). These levels stay elevated until anaphase is reached, whereafter, the phosphorylated cofilin and LIMK activity return to basal levels. Due to the decreased LIMK1 activity during cytokinesis, SSH and CIN are activated with the subsequent dephosphyralation of cofilin. Depending on the mitotic phase, LIMK shows a different localization within the mitotic apparatus. LIMK1 and LIMK2 are directly associated and co-localized with y-tubulin in centrosomes during the early stages of mitosis which enables active LIMK to assist in the assembly of the mitotic spindles (350). Inhibition of LIMK1 activity during mitosis causes disregulation of cofilin phosphorylation, delays the progression from metaphase to anaphase and results in irregular spindle positioning (16).

1.7.3 LIM kinase inhibitors

Metastasis and drug resistance contribute significantly to morbidity and mortality in cancer patients. For many years, microtubules were the target for anti-cancer drugs. Microtubules play a major role in mitosis, rendering it a target for cancer treatment (351,352). Numerous anti-cancer drugs have been identified over the years targeting tubulin, however, tumor resistance to these microtubule targeting drugs is emerging and thus their clinical use is restricted (353). As microtubules are still considered an effective target for anti-cancer drugs, microtubule regulators are considered as an alternative target in order to decrease the development of drug resistance. One such regulator is LIMK. Since LIMK is involved in the regulation of both the actin and microtubule cytoskeletons, it is considered to be a good therapeutic target for decreasing drug resistance development, as well as metastatic spread from the primary tumor (354).

With the use of a cell-based assay that probes the microtubule polymerization status, Prudent *et al.* (353) identified a compound that interacts with microtubule regulators. This compound, 9-benzoyloxy-5,11-dimethyl-2*H*,6*H*-pyrido[4,3-*b*]carbazol-1-one (Pyr1), suppressed microtubule dynamics, causing microtubule stabilization similar to paclitaxel.

Pyr1 is a cell-permeable inhibitor of LIMK1/2 (Figure 1.11) (353). Pyr1 exhibited anti-mitotic and cytotoxic properties in cancer cell lines, including a multidrug resistant uterine sarcoma cell line. Disorganization of astral microtubules, as well as complete dephosphorylation of cofilin was revealed in HeLa cells after Pyr1 treatment *in vitro*. By inhibiting LIMK, rescue of cofilin phosphorylation was demonstrated which resulted in actin severing and depolymerisation of F-actin filaments. However, these results did not correlate with the phenotype observed when LIMK was knocked down by small interfering ribonucleic acids (siRNA) (355). The authors suggested that the differences observed could be in the mechanism of action of siRNA and pharmacologic inhibitors. Pharmacologic inhibitors only inhibited the enzymatic activity of the protein, whereas siRNA reduced the protein levels (353). The ability of Pyr1 to sensitize cancer cells to radiation *in vitro* has not been investigated.

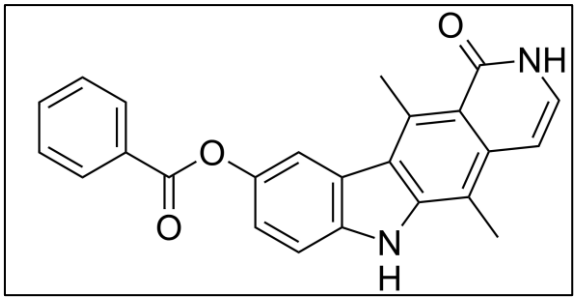

Figure 1.11: Chemical structure of 9-benzoyloxy-5,11-dimethyl-2*H*,6*H*-pyrido[4,3-*b*]carbazol-1-one (Pyr1). Pyr1 is a LIM kinase inhibitor which increases detyrosinated microtubule generation (353).

1.8 Paclitaxel

The hydrophobic molecule, paclitaxel, was isolated from the bark of a *Taxus brevifolia* tree (356), and was first described as a microtubule stabilizing agent in the late 1970s during an *in vitro* microtubule assembly assay (357). This mechanism of action was confirmed a year later in a mouse fibroblast cell model and the investigation of the anti-cancer potential of paclitaxel commenced (358). Paclitaxel induces microtubule stabilization by binding to the

N-terminal region of the β-subunit of tubulin (358,359). The latter prevents depolymerization of these microtubules and induces a G_2/M phase block. The paclitaxel-induced microtubule arrest prevents the dynamic reorganization of the microtubule network, deterring cellular division. Paclitaxel is a hydrophobic mitotic inhibitor, thus, in order to overcome the limited solubility of the molecule, a combination of cremophor/ethanol is used as a vehicle for its delivery to patients (360). Paclitaxel is often prescribed for the treatment of breast- and ovarian cancer, however, paclitaxel related toxic effects such as neutropenia and peripheral neuropathies limits the therapeutic dose (361).

1.8.1 Paclitaxel resistance

The development of drug resistance is one of the major limitations in cancer treatment. Several molecular and cellular mechanisms contribute to the development of drug resistance, such as the overexpression of ATP-binding cassette (ABC) transporters on the cell membrane that increases cellular efflux of the drugs, compartmentalization of the drugs in endocytic vesicles, increased bio-inactivation via metabolism and reduced drug uptake due to down regulation of their associated receptors (362). Additionally, chemoresistance may develop due to increased DNA damage repair, alterations in membrane lipids, inhibition of the Bcl-2 intrinsic apoptotic pathway and changes in cell cycle checkpoint proteins (362). Multiple cellular mechanisms mentioned above are manipulated through paclitaxel to induce drug resistance. Paclitaxel treatment results in the overexpression of the ABC transporters, inhibition of the Bcl-2 and p53 apoptotic pathway, tubulin mutations and changes in β-tubulin binding sites (Figure 1.12) (363,364).

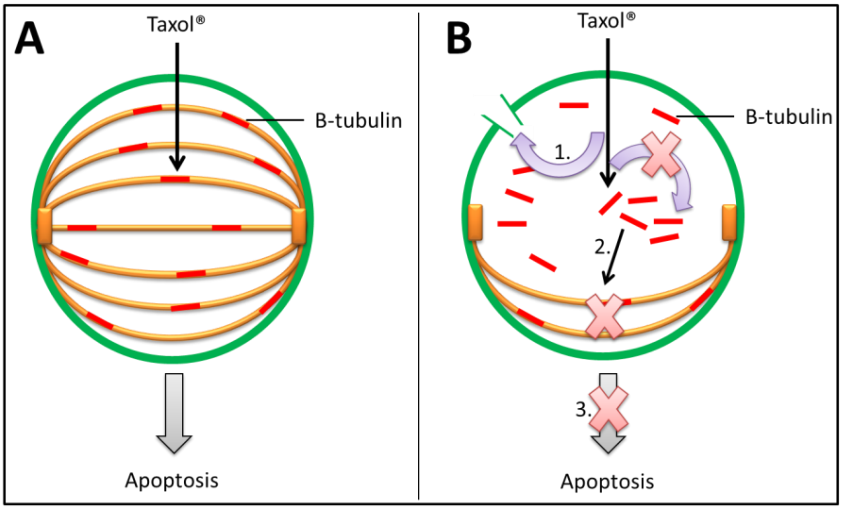

Figure 1.12: Cellular mechanisms involved in Paclitaxel resistance. A. Paclitaxel exerts its effect by binding to intracellular β-tubulin, stabilizing the microtubule network. This results in the induction of a G_2/M phase block, triggering apoptosis. **B.** Resistance to paclitaxel develops due to overexpression of the transmembrane ATP-binding cassette (ABC) efflux transporters, decreasing the intracellular concentration of the drug **(1)**; decreased microtubule stabilization due to a decline in β-tubulin binding as a result of tubulin mutations and unstable microtubule networks **(2)**. The latter hinders the induction of a mitotic block and prevents apoptotic cell death. Additionally, paclitaxel treatment may inhibit the intracellular Bcl-2 and p53 apoptotic pathway, decreasing the induction of apoptosis and contributing to the development of paclitaxel resistance **(3)**. Adapted from Barbuti and Chen (2015) (365), using Microsoft PowerPoint 2010.

One of the most significant mechanisms contributing to paclitaxel resistance is the overexpression of ABC transporters (362) (Figure 1.12). ABC transporters are energy dependent and are present across the cell membrane. ABC transporters hydrolyze ATP in order to facilitate the transport of specific substances across the cell membrane (365). The overexpression of ABC transporter sub-family B, member 1 (ABCB1) and sub-family C, member 10 (ABCC10) plays a significant role in the development of drug resistance associated with paclitaxel therapy. ABCB1, also known as PgP, is encoded by the multiple drug resistance (MDR)1 gene and transports hydrophobic products, including paclitaxel, across the cell membrane (366). By increasing the transport of paclitaxel out of the cell,

ABCB1 decreases the intracellular anti-cancer drug levels, resulting in reduced antitumor activity. The ABCC transporters function as lipophilic anion pumps and regulate ion channels (367-369). ABCC10 is encoded by the ABCC10 gene and is also known as multidrug resistant protein 7 (MRP7) (370). ABCC10 contributes to paclitaxel resistance by transporting two substances involved in cellular detoxification, known as the glutathione conjugate of leukotriene C4 (LTC4) and 17β-estradiol 17-(β-D-glucuronide), across the cell membrane (371). By increasing cellular detoxification in addition to increasing cellular export of paclitaxel, ABCB1 and ABCC10 significantly decrease paclitaxel's cytotoxicity, resulting in chemoresistance.

Disruption of the microtubule dynamics is another important paclitaxel resistance mechanism (363). The α- and β-tubulin heteromers normally combine in a polarized and sequential manner to form 25 nm hollow tubes. During cell division the minus-end of the heterodimer remains embedded in the centrosome, while the plus-end grows towards the plasma membrane (53). The latter provides the transportation for chromosomes during chromosome segregation. Although minor fluctuations in the microtubule dynamics can be tolerated by cells, significant changes can induce a mitotic block and prevent cell division (372). Paclitaxel binds to β-tubulin and stabilizes the polymer (373). This decreases the frequency of microtubule detachment from the centrosome, preventing cellular division. Microtubule alterations, such as α and β-tubulin mutations, changes in paclitaxel-microtubule attachment, alterations in microtubule regulatory proteins or post-translations changes to the microtubule regulatory proteins, limit the response of cells to paclitaxel *in vitro* and *in vivo* (Figure 1.12) (363,374-377). Mutations to the α and β-subunits of tubulin do not affect the binding of paclitaxel to tubulin. Instead, paclitaxel resistance is conferred by the increased frequency of microtubule detachments and spindle disruption during cell division, caused by the aforementioned mutations (373). Additionally, altered microtubule interacting protein-expression also contributes to the development of paclitaxel resistant cells. A family of motor proteins, known as kinesin, utilizes the microtubules to facilitate intracellular transport and mitosis (378). The depolymerization of microtubules is catalyzed by MCAK, a kinesin related motor protein. This protein has been found to be overexpressed in paclitaxel-resistant cancer cells (379,380). The mechanism of action of MCAK counteracts

the paclitaxel-induced microtubule polymerization, decreasing paclitaxel's microtubule stabilization and anti-cancer effect.

1.8.2 Paclitaxel based combination chemotherapy

Clinical trials demonstrated that paclitaxel is effective in breast- and ovarian cancer treatment (381,382). Additionally, paclitaxel has demonstrated clinical success against metastatic breast cancer (383-388). In order to utilize the anti-cancer ability of paclitaxel, while decreasing the development of paclitaxel resistance, lower doses of paclitaxel has been combined with other cytotoxic agents.

1.8.2.1 Paclitaxel-doxorubicin combination therapy

Prior to the discovery of the taxanes the anthracycline, doxorubicin, was used for the treatment of metastatic breast cancer (389). Phase 1 clinical trials for anthracycline and taxane combination therapies were initiated by the Medicine Branch of the National Cancer Institute (United States of America (USA)) and the M. D. Anderson Cancer Center (University of Texas, USA). Based on the administration schedule for paclitaxel single-agent trials, and in order to limit anthracycline-related side effects, the combination therapy was administered via a long duration infusion (390-394). Although these initial trials for anthracycline-taxane combination therapy were effective, several dose-limiting toxicities were reported. Patients presented with diarrhea, mucositis, tiflitis and neutropenic fever. However, no clinically relevant cardiac toxicities were reported, a side effect usually associated with the anthracycline, doxorubicin.

The positive reports of these initial combination trials prompted the design and investigation of new doses and administration methods for this combination. It was hypothesized that the dose of doxorubicin could be increased by shortening the

administration period, however, pharmacokinetic studies revealed a schedule-dependent interaction (395-397). Thus, a combination therapy was designed by investigators based at the Istituto Nazionale Tumori in Italy where a 3-hour long administration of paclitaxel was followed by a bolus administration of doxorubicin. This approach allowed the doses of paclitaxel and doxorubicin to be increased to 100 mg/m^2 and 60 mg/m^2, respectively, without any clinically relevant schedule-dependent interactions. The latter increased the anti-cancer activity of the drugs, with a response rate of above 90% and a complete remission rate grater than 40% (398). Regrettably, patients presented with severe cardiac toxicity. Subsequent clinical trials have been conducted with the major focus on cardiac toxicity (399-401).

1.8.2.2 Paclitaxel-cisplatin combination therapy

Paclitaxel was also combined with other anti-tumor agents in an attempt to increase the anti-cancer activity and decreasing the cardiac toxicity associated with anthracyclines. Cisplatin, clinically known as Platinol, was considered a good candidate for paclitaxel combination therapy due to its pronounced single-agent anti-tumor activity in metastatic breast cancer (402). Compared to other clinically effective agents used in metastatic breast cancer treatment, cisplatin is less myelosuppressive (403). During a phase I/II clinical trial, patients were treated with proper hydration and appropriate premedication prior to 60 mg/m^2 cisplatin treatment. This was followed with 90 mg/m^2 paclitaxel during a 3-hour infusion, and was administered every other week (404). A response was observed in 85% of patients treated with the aforementioned regime, with 11% achieving a complete response. Side effects included nausea, peripheral neuropathy and sever fatigue. No grade VI non-hematologic toxicity was reported, however, neutropenic fever and myelosuppression was observed. Several other successful clinical trials utilized cisplastin in combination with paclitaxel, aiming to establish the optimal dose and administration schedule for this combination therapy (405).

1.8.2.3 Paclitaxel-cyclophosphamide combination therapy

The alkylating agent, cyclophosphamide, is commonly used as part of combination treatment regimens for breast cancer. The mechanism of action of taxanes differs from those of alkylating agents, yielding dissimilar side effects. Additionally, the mechanism of chemoresistance is unrelated, rendering cyclophosphamide a candidate for paclitaxel combination therapy. A dose-escalating study conducted by Tolcher *et al.* (406) reported a 62% response rate in patients treated with a combination of paclitaxel and cyclophosphamide. Myelosuppression is an overlapped toxicity of paclitaxel and cyclophosphamide, thus the administration of hematopoietic growth factors such as granulocyte colony-stimulating factor was necessarily (406). The severe myelosuppression caused by the aforementioned combination therapy rendered this combination less favorable compared to other paclitaxel-based combination therapies.

1.8.2.4 Paclitaxel-vinorelbine combination therapy

Another agent used in metastatic breast cancer treatment is the vinblastine analogue, vinorelbine. This agent is a tubulin-active agent and is well tolerated as a single agent in weekly administered treatment regimens (407,408). Simultaneous intravenous administration of vinorelbine and paclitaxel yielded response rates between 50-65% (409). Dose-limiting toxicities included cumulative neuropathy and neutropenic fever which was decreased with the administration of hematopoietic growth factors (410). The latter allowed higher dose administration, which was limited by the development of neuropathy. Peripheral neuropathy was decreased when vinorelbine and paclitaxel was administered in a sequential treatment schedule (411-413).

1.8.3 Compound T4 sensitizes cells to non-lethal doses of paclitaxel *in vitro*

The research group from Institute for Advanced Biosciences (IAB), Université Grenoble Alpes (UGA)/ Institut national de la santé et de la recherche médicale (INSERM) U1209/ Le Centre National de la Recherche Scientifique (CNRS) 5309 (Grenoble, France) screened 8 000 molecules in order to obtain compounds that sensitize cells to non-lethal doses of paclitaxel. Compound T4 was selected, as it exhibited non-toxic effects when exposed to cells *in vitro* as a single agent. When T4 was combined with low-doses of paclitaxel (also non-toxic when administered as a single agent) a cytotoxic effect is achieved (Unpublished data). *In vitro* studies revealed that T4 exerts its effect by binding directly to tubulin. This induces abnormal mitotic spindles when T4 is combined with non-toxic doses of paclitaxel. Furthermore, it is hypothesized that T4 targets a cell cycle check-point, but has yet to be fully elucidated.

1.9 Radiosensitization by agents targeting the cytoskeleton

Cancer cells progress much faster through the cell cycle compared to their neighboring non-cancerous cells in general. This increased proliferation rate makes them ideal targets for microtubule targeting agents (252). Previous studies revealed that the G_2/M phase of the cell cycle is the most radiosensitive phase due to the exposure of chromosomes to radiation (414-416). Microtubule targeting agents, such as paclitaxel, induce a G_2/M phase block (417). The latter will be more pronounced in cancerous cells due to their rapid proliferation. Thus, by preventing the transition from the G_2 phase to the M phase, microtubule targeting agents can enhance cancer cell radiosensitivity (417). This will allow the administration of lower doses of each modality, while increasing tumor response to the treatment. In theory, the additive effect of combination therapy should improve the therapeutic gain and lessen side-effects commonly associate with traditional chemotherapy and radiotherapy (418).

Several studies have investigated the ability of microtubule targeting agents to radiosensitize cells (418-420). A study utilizing 2-ME successfully illustrated the ability of this microtubule targeting agent to radiosensitize two human glioma cell lines (T98G- and U231MG cells) (419). The experimental protocol entailed a 12-hour pre-exposure of the cancer cells to 2 micromolar (μM) 2-ME, followed by irradiation. The effect of the combination therapy was then evaluated and compared to that of cells exposed to radiation in the absence of 2-ME, using clonogenic studies, apoptosis quantification and the induction of DNA damage, as well as cell cycle alterations. Results obtained from the aforementioned experiments revealed a significant increase in radiation-induced cell death in both glioma cell lines when cell were presensitized with 2-ME (419). Additionally, clonogenic studies showed that the survival fraction of glioma cells exposed to the combination therapy decreased in a dose-dependent manner. The enhanced radiotoxicity observed in pre-treated cells was associated with increased H2AX phosphorylation, indicating increased DNA damage, as well as, phosphorylation of the ATM protein kinase, which resulted in Chk2 activation and a G_2/M phase cell cycle arrest (419). Interesting to note was the inability of estradiol to radiosensitize glioma cells in this experimental setting. This suggested that it was specifically 2-ME that possessed the ability to radiosensitize the glioma cells rather than the general effect of estradiol. Additionally, the authors noted that the radiosensitization and enhanced radio-cytotoxicity were not transferred to normal lymphocytes (419).

The ability of LIMK inhibitors to radiosensitize cancer cells *in vitro* has not been established. A literature study revealed no previous experiments or publications on the radiosensitizing ability of inhibitors targeting LIMK specifically. By evaluating the potential of LIMK inhibitors, such as Pyr1, during the completion of this study, a novel application of LIMK inhibitors as radiosensitizing agents may be established. Additionally, the compound T4 has not been used in radiosensitization studies previously. Results obtained from this *in vitro* study may provide a foundation upon which future studies can build to develop more strategic treatment regimens with the aim of increasing the effectivity of radiation therapy, decrease metastasis and prevent the development of treatment resistance.

2. Aims and objectives

"The most exciting phrase to hear in science, the one that heralds new discoveries, is not 'Eureka!' but 'That's funny...'"

-Isaac Asimov-

The aim of this study was to determine whether ESE-15-one, ESE-16, LimPyr1 and T4 induce cell death in the estrogen receptor-positive (MCF-7)-, estrogen receptor-negative (MDA-MB-231)- and triple receptor-negative (BT-20) breast cancer cell lines and whether these compounds increase the sensitivity of cancer cells to radiation.

The objectives of the study were to describe the cellular effects of ESE-15-one, ESE-16, LimPyr1 and T4 on breast cancer cells and to investigate their potential radiosensitization abilities. Two compounds were selected for radiosensitization studies. Apoptotic signaling, cellular proliferation and survival, and DNA damage and repair mechanisms were assessed. Additionally, these two compounds were investigated to ascertain the effects of the combination therapy on the radiation-induced bystander effect and radiation-induced resistance due to dose fractionation in BT-20 cells.

To this aim the experiments conducted intended to:

i. Determine the ability of ESE-16 to bind to the colchicine binding sites on tubulin using an *in vitro* colchicine binding assay;

ii. Determine the ability of ESE-16 to induce a metaphase block in HeLa Kyoto cells via live video microscopy;

iii. Determine the long term cytotoxic effects of ESE-15-one and ESE-16 via IncuCyte® measurement using HeLa cells;

iv. Investigate the effects of ESE-15-one and ESE-16 on cell migration utilizing the IncuCyte® system using HeLa cells;

v. Determine the half maximum growth inhibitory concentration (GI_{50}) of ESE-15-one, ESE-16, LimPyr1 and T4 after a 48-hour exposure to MCF-7-, MDA-MB-231- and BT-20 breast cancer cell lines via spectrophotometry using 3-(4,5-dimethylthiazol-2-yl)-2,5-diphenyltetrazolium bromide (MTT) staining;

vi. Visualize the effect of ESE-15-one, ESE-16, T4 and LimPyr1 on the microtubule and actin skeletons of MCF-7-, MDA-MB-231- and BT-20 cells with fluorescence microscopy;

vii. Determine the lowest concentrations of the compounds and radiation that significantly induced apoptosis in MCF-7-, MDA-MB-231- and BT-20 cell lines via flow cytometry. These compound concentrations were used to pre-treat cells 24 hours prior to radiation in all sensitization experiments;

viii. Evaluate the effect of the compounds (at low doses) in combination with radiation on cell cycle progression and the induction of apoptosis using flow cytometry in MCF-7-, MDA-MB-231- and BT-20 cells. Based on the results obtained from BT-20 cells the two compounds that showed the most potential to sensitize cells to radiation were selected for further investigation;

ix. Determine the temporal production of reactive oxygen species in MCF-7-, MDA-MB-231- and BT-20 cells pre-treated with ESE-16 and LimPyr1 for 24 hours prior to radiation using flow cytometric quantification of superoxide 4-, 24- and 48 hours after radiation;

x. Detect changes in the mitochondrial transmembrane potential of MCF-7-, MDA-MB-231- and BT-20 cells pre-treated with ESE-16 and LimPyr1 for 24 hours prior to radiation via flow cytometry employing MitoCapture™;

xi. Compare the effects of the ESE-16 and LimPyr1/radiation combination treatments with those of the individual treatments by analyzing the intracellular signaling pathways. Bax, cleaved caspase 3, cyclin B1 and the phosphorylation of Akt and FoxO1/3a were quantified, using Western blot analysis 24 hours after radiation in MCF-7-, MDA-MB-231- and BT-20 cells;

xii. Determine the sequential *in vitro* effects on the morphology of MCF-7-, MDA-MB-231- and BT-20 cells when exposed to ESE-16 and LimPyr1 for 24 hours prior to radiation. Images were taken 6-, 24- and 48 hours after radiation using polarization-optical transmitted light differential interference contrast microscopy;

xiii. Determine the effects of ESE-16 and LimPyr1 in combination with radiation on long term MCF-7-, MDA-MB-231- and BT-20 cell survival by staining cell populations 14 days after radiation;

xiv. Quantify DNA damage induced by the ESE-16 and LimPyr1/radiation combination treatments using flow cytometric quantification of γH2AX 2 and 24 hours after radiation in MCF-7-, MDA-MB-231- and BT-20 cells. Light microscopy was employed to quantify micronuclei stained with Giemsa;

xv. Determine the effects of the ESE-16 and LimPyr1/radiation combination treatments on DNA repair within MCF-7-, MDA-MB-231- and BT-20 breast cancer cells via Western bot analysis of Ku70;

xvi. Evaluate the radiation-induced bystander effect by transferring conditioned medium obtained from treated BT-20 cells onto untreated BT-20 cells. Induction of the intrinsic apoptotic pathway and long term cellular survival was evaluated 48 hours after medium transfer via:

a. Flow cytometry to quantify the reactive oxygen species formation and changes in the mitochondrial transmembrane permeability;
b. Cell populations stained with Giemsa 14 days after transfer.

DNA damage and repair mechanism were quantified 2 hours after transfer via

a. Western blot quantification of γH2AX and Ku70.

xvii. Evaluate radiation-induced resistance due to dose fractionation in BT-20 cells exposed to fractionated radiotherapy (2 Gy for 4 consecutive days) compared to BT-20 cells exposed to a single dose of 8 Gy. Apoptosis induction was evaluated using the techniques set out in objective xvi a.

3. Materials and methods

"An experiment is a question which science poses to Nature and a measurement is the recording of Nature's answer."

-Max Planck-

3.1 Cell lines

The radiosensitizing ability of the microtubule regulators were tested *in vitro* on the estrogen receptor-positive MCF-7 (421)-, estrogen receptor-negative MDA-MB-231 (422)- and triple receptor-negative BT-20 (423) tumorigenic human epithelial breast cancer cell lines. The MCF-7 (population doubling time (PDT) is approximately 38 hours (424))- and MDA-MB-231 (PDT is approximately 38 hours (425)) cells were derived from Caucasian females aged 69 and 51 years, respectively (421,422). These cells were derived from metastatic sites, secondary to a primary breast adenocarcinoma. The BT-20 cell line (PDT is approximately 51 hours (426)) consists of neoplastic epithelial cells derived from a primary breast lesion in a 74 year old Caucasian female (423). The effects of the 2-methoxyestratiol analogues, ESE-15-one and ESE-16, were also investigated on human cervical adenocarcinoma (HeLa) cells (427). All cells were acquired from the American Type Culture Collection (ATCC) (Virginia (VA), USA). HeLa cells expressing red fluorescent protein (RFP)-H2B and green fluorescent protein (GFP)-tubulin (HeLa Kyoto cells) were a kind gift from Dr C Guilluy, Institute of Advanced Biosciences (Grenoble, France).

3.2 General cell culture maintenance

Experiments were performed at the Department of Physiology of the University of Pretoria in Pretoria, South-Africa, and at the Institute of Advanced Biosciences in Grenoble, France.

Consumables were ordered from the same manufacturers to minimize experimental variables. All protocols and procedures used in this study were standardized.

3.2.1 Cell culture maintenance reagents

GIBCO® Dulbecco's Modified Eagle's medium (DMEM), GIBCO® HAM F-12 Nutrient Mixture and GIBCO® Roswell Park Memorial Institute (RPMI) medium were purchased from Thermo Fisher Scientific (Massachusetts (MA), USA). Additionally, GIBCO® fetal calf serum (FCS), fungizone, penicillin, streptomycin and GIBCO® trypsin-ethylenediaminetetraacetic acid (EDTA) were purchased from Thermo Fisher Scientific (MA, USA), as was GIBCO® phosphate buffered saline (PBS). A 1x working PBS stock (pH 7.4) was prepared from a 10x concentrated stock (80 gram (g)/liter (L) sodium chloride (NaCl), 2 g/L potassium chloride (KCl), 2 g/L potassium dihydrogen phosphate (KH_2PO_4) and 11.5 g/L disodium hydrogen phosphate (Na_2HPO_4)) and autoclaved (20 minutes, 120 degrees Celsius (°C), 15 pounds per square inch (psi)) prior to use. Sterile cell culture flasks (25 and 75 cm^2), cell culture plates (6, 24 and 96 well), cell culture tubes (15 and 50 milliliter (mL)), serological pipettes and cell scrapers were purchased from Greiner Bio-One (Frickenhausen, Germany).

3.2.2 Maintenance

MCF-7- and MDA-MB-231 cells were cultured in DMEM, whilst the BT-20 cells were cultured in DMEM/HAM F12 (50:50) nutrient mixture. The compounds, LimPyr1 and T4, are not soluble in DMEM, thus MCF-7-, MDA-MB-231- and BT-20 cells were also cultured in RPMI media when exposed to these compounds. All media were supplemented with 10% heat-inactivated FCS (56°C, 30 minutes), 100 microgram (µg)/mL streptomycin, penicillin G (100 units per milliliter (U/mL)) and 250 µg/L fungizone. Cells were culture and maintained in sterile 75 cm^2 tissue culture flasks in a Forma Scientific water-jacketed incubator (Ohio (OH), USA) (5% carbon dioxide (CO_2), 37°C).

Growth medium of the cultured breast cancer cells was replaced every 3-4 days in order to replenished nutrients and maintain a constant pH. Actively dividing cells were trypsinized

when approximately 80% confluent. Trypsinization was done by discarding the media from the adherent cells and rinsing twice with pre-warmed (37°C) PBS to remove cell debris from the culture. Additionally, the PBS rinse ensures that the serum (which contains trypsin inhibitors) is removed from the cells prior to the addition of trypsin. Cells were incubated with trypsin-EDTA until round and easily detachable. The trypsin-EDTA was neutralized with the addition of complete growth media. Cells were collected by centrifugation (500 times gravity (x *g*) for 5 minutes) and either seeded for experiments, sub-cultured up to passage 40 or frozen to preserve cell stock.

Harvested cells were frozen in complete growth medium supplemented with 5% (volume/volume (v/v)) dimethyl sulfoxide (DMSO) (428). Cells were frozen at a concentration of three million cells/mL in Nalgene™ cryogenic tubes (Thermo Fisher Scientific, MA, USA) at -70°C. The cryotubes were transferred to liquid nitrogen for long term storage. Thawing of cells occurred rapidly by placing the cryotube in a water bath at 37°C. Once thawed, cells were centrifuged in order to remove the cryoprotective agent (DMSO) and transferred to 25 cm^2 cell culture flasks containing pre-warmed complete growth media. Growth media were replaced daily until cells were confluent.

Experiments and cell culture were conducted under sterile conditions, using aseptic techniques. Cell culture was conducted in a laminar flow cabinet (Labculture®, Labotec, Midrand, South Africa or MSC-Advantage, Thermo Fisher Scientific, MA, USA) and all the glassware was autoclaved (20 minutes, 120°C, 15 psi) prior to use.

3.3 General method for experiments

Research was conducted as part of the fulfillment for a dual Doctor of Philosophy (PhD) degree at the University of Pretoria (Pretoria, South Africa) and the Université Grenoble Alpes (Grenoble, France). Experiments were performed at the Department of Physiology's cell culture laboratory at the University of Pretoria under the supervision of Dr AE Mercier

and Prof AM Joubert. Prof L Lafanechère supervised experiments conducted at the Institute of Advanced Biosciences (Université Grenoble Alpes, Grenoble, France).

3.3.1 Compounds and positive controls

The compounds (ESE-15-one, ESE-16, LimPyr1 and T4) are not commercially available. The 2-Methoxyestradiol analogues, ESE-15-one and ESE-16, were synthesized by iThemba (Pty) Ltd. Pharmaceuticals (Modderfontein, Gauteng, South Africa). The LIM kinase inhibitor, LimPyr1, and the paclitaxel sensitizer, T4, were synthesized by Elderis (Lyon, France). A 10x working stock was prepared in DMSO and stored at -20°C. Actinomycin D, vinblastine, doxorubicin, rotenone, etoposide, latrunculin B, colchicine and paclitaxel were used as positive experimental controls and were purchased from Sigma Aldrich (St. Louis, Missouri (MO), USA / St. Quentin-Fallavier, France).

3.3.2 General experimental method

HeLa cells were used for the IncuCyte® cytotoxicity assay and the IncuCyte® scratch wound cell migration assay. HeLa cells were seeded in complete DMEM in 96 well plates at densities of 2 500 and 150 000 cells/well for the cytotoxicity and cell migration assays, respectively. HeLa Kyoto cells were used for the time-lapse video microscopy analysis and were seeded in a 2 well µ-slide (chambered coverslip) (ibidi®, Martinsried, Germany,) at a density of 150 000 cells/well. Cytotoxicity and radiosensitizing experiments were performed on MCF-7-, MDA-MB-231- and BT-20 cells seeded at appropriate densities in the required cell culture vessels according to each experimental procedure (Table 3.1).

Table 3.1: Densities seeded for cytotoxicity and radiosensitizing experiments on MCF-7-, MDA-MB-231- and BT-20 cells.

Experiment	Cell culture vessel	MCF-7	MDA-MB-231	BT-20
		Number of cells/flasks or wells		
Cytotoxicity	96 well	5 000	5 000	7 000
Fluorescent microscopy	24 well	40 000	40 000	60 000
Light microscopy	6 well	300 000	300 000	500 000
Long term cellular proliferation	6 well / 35 mm petri dish	80 000	80 000	100 000
Western blot	25 cm^2	500 000	500 000	1 000 000
Micronuclei	25 cm^2	500 000	500 000	1 000 000
Flow cytometry	25 cm^2	500 000	500 000	1 000 000

Cell densities were calculated by counting trypsinized cells with a 0.1 mm Tiefe Depth Profondeur haemocytometer (Precicolor HBG, Hessen, Germany) (429). Trypsinized cells (20 microliter (µL)) were suspended in 80 µL PBS, providing a diluted cell stock. Non-viable cells were excluded via the addition of 20 µL 0.4% trypan blue (Sigma Aldrich, MO, USA) to 20 µL of the diluted cell stock. Trypan blue only penetrates cells when the cell membrane has been compromised. These cells stain blue when viewed under a microscope and were left uncounted (430).

Viable cells per mL were calculated using the following formula:
Cells/mL= Average count of viable cells in corner squares of haemocytometer x dilution factor

Cells were seeded and incubated for 24 hours (5% CO_2 at 37°C) to allow for attachment. Adherent cells were exposed to the compounds at the appropriate concentrations as per experimental design. Several controls were included in each experiment. A negative control consisted of cells propagated in medium only and a DMSO vehicle control consisting of the same amount of DMSO (v/v%) used to dissolve the compounds. The DMSO content of the final dilutions never exceeded 0.5% (431). Cell cultures exposed to actinomycin D (1 µM), vinblastine (0.2 µM) and doxorubicin (0.5 µM) for 24 hours served as positive apoptotic controls. Rotenone (24-hour exposure at 0.5 µM) was used as a positive control for ROS

production, while etoposide (2-hour exposure at 100 µM) was used as a positive control for DNA damage. For visualization of the cytoskeleton, fluorescent microscopy was employed where 0.2 µM (15-minute exposure) latrunculin B was used as a positive control for actin depolymerization. A 24-hour exposure to colchicine (0.5 µM) served as a positive control for microtubule depolymerization and paclitaxel (1 µM, 24-hour exposure) was used as a microtubule stabilizer. After a 24 hour exposure to the compounds the cells were radiated with the Gy as determined by radiation dose-response curves. Apoptosis experiments were terminated 4, 24 or 48 hours after irradiation, DNA damage and repair were assessed 2 and 24 hours after irradiation, and long term cellular proliferation was quantified 14 days after irradiation according to the protocols set out in this thesis.

3.3.3 Radiation exposure

In South Africa, the breast cancer cells were irradiated at the Department of Radiation Oncology (Steve Biko Academic Hospital, University of Pretoria) under the supervision of Prof R Lakier and Ms L Sebopa. Samples were irradiated on a Siemens Oncor 6 MV linear accelerator (Midrand, South-Africa) with a dose rate of 1 centigray (cGy)/ monitor unit (MU) using a 10x10 field with appropriate bolus to ensure that each sample received the full radiation dose. Irradiation of samples in France was done under the supervision of Prof L Chaperot. Samples were irradiated with a BloodXrad 13-69 (Le-Plessis-Pâté, France) with a dose rate of 7 Gy/min. In order to ensure reproducible results of an experiment, all three biological repeats were irradiated with the same radiation machine.

3.4 Experimental setup

As part of the experimental setup, two microtubule disrupters (ESE-15-one and ESE-16), a LIM kinase inhibitor (LimPyr1) and a compound that sensitizes cells to non-lethal doses of paclitaxel (T4) were tested on BT-20 cells. For each compound the GI_{50} was determined by spectrophotometric quantification of MTT (Sigma Aldrich, MO, USA). BT-20 cells were then

exposed to a dose range of the compounds (GI_{50}, ¾ GI_{50}, ½ GI_{50}, ¼ GI_{50} and ⅛ GI_{50}), as well as a radiation dose-response curve (2, 4, 6, 8, and 10 Gy), respectively. The lowest compound and radiation doses that induced apoptosis significantly (as determined by flow cytometry, using Annexin V (BioLegend, California (CA), USA) was used further in all combination studies (Figure 3.1). This comprised of BT-20 cells exposed to the lowest compound concentration that induced cell death significantly 24 hours prior to radiation. For the rest of the cell lines and experiments, the most effective microtubule disrupter (ESE-15-one or ESE-16) and either LimPyr1 or T4 were selected (Figure 3.1).

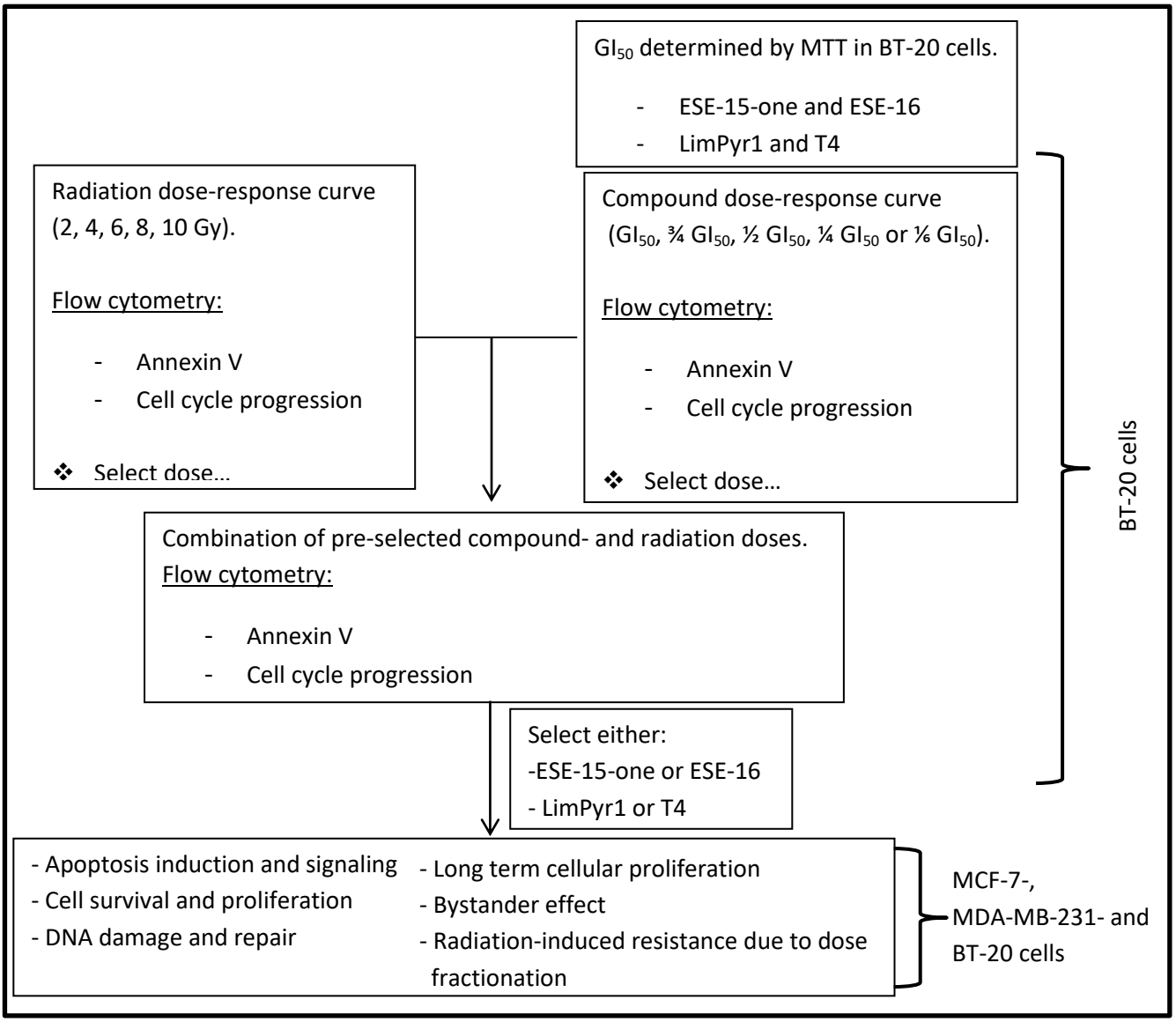

Figure 3.1: Experimental setup. The ability of four compounds to radiosensitize BT-20 cells was investigated by flow cytometry. The two most effective compounds were selected for the full study (bottom box).

3.5 Drug properties and relative cytotoxicity

3.5.1 Tubulin competitive binding assay: Tritiated [^{3}H] colchicine binding

ESE-16 was designed to bind to the colchicine binding sites on microtubules (312). To confirm that the colchicine binding sites on tubulin indeed constitute a target for ESE-16 binding, an *in vitro* tubulin binding assay was performed with tritiated [^{3}H] colchicine in competition with ESE-16. Colchicine is tritiated at the ring C methoxy position with tritium [^{3}H] and it's binding to tubulin can be assessed with radioactivity (432). The experiment was executed by Ms. L Peronne (PhD candidate, Institute of Advanced Biosciences) due to restricted access to the radioactive laboratory.

Materials

The Ultima Gold™ liquid scintillant and [^{3}H] colchicine (82,6 Ci.mmol^{-1}) were purchased from PerkinElmer (MA, USA). Diethylaminoethyl (DEAE) Sephadex A25, piperazine-N,N'-bis(2-ethanesulfonic acid) (PIPES), magnesium chloride ($MgCl_2$), ethylene glycol-bis(β-aminoethyl ether)-N,N,N',N'-tetraacetic acid (EGTA) and pure ethanol were purchased from Sigma-Aldrich (Saint-Quentin Fallavier, France). Pure bovine tubulin was prepared according to the procedure described by Paturle-Lafanechère *et al*., 1991 (433) and was kindly supplied by Ms. L Peronne.

PIPES-$MgCl_2$-EGTA (PME) buffer was prepared as follows: 100 millimolar (mM) PIPES, 1 mM $MgCl_2$, 1 mM EGTA (pH 6.65). DEAE Sephadex A25 was prepared one day prior to use by mixing 1 g DEAE Sephadex A25 in 25 mL PME buffer. The mixture was centrifuged (2400 x *g* for 4 minutes at 4°C) and the supernatant removed. The pellet was rinsed thrice in PME buffer and kept at 4°C overnight. Tubulin and [^{3}H] colchicine were diluted to the desired concentrations in PME buffer prior to use.

Method

The 2-methxyestradiol analogue, ESE-16 (100 μM), and [^{3}H] colchicine (5 μM) were mixed with tubulin (final concentration of 0.3 mg/mL) in PME buffer at 4°C to a final volume of 200 μL. The mixture was vortexed and incubated at 30°C for 30 minutes. The reaction was stopped by placing the samples on ice, followed by the transfer of 50 μL to presedimented DEAE Sephadex A25 in PME buffer. The samples were incubated for 10 minutes on ice with continuous shaking, ensuring quantitative binding of tubulin to the DEAE Sephadex A25 gel. Samples were centrifuged for 4 minutes at 2400 x *g* (4°C) and the supernatant removed. The pellets contained the bound molecule-tubulin complexes and were rinsed four times with 1 mL PME buffer. The tubulin-bound [^{3}H] colchicine was solubilized with the addition of 500 μL ethanol. The samples were incubated for 10 minutes at room temperature. The ethanol solution (400 μL) was transferred to 8 mL of Ultima Gold™ liquid scintillant and [^{3}H] colchicine incorporation was measure using a liquid scintillation counter (Beckman Coulter, LS 6500 spectrometer, CA, USA)*.*

3.5.2 Time-lapse imaging: ESE-16's anti-mitotic effect

Cell behavior can be assessed in real time using time-lapse video microscopy (434). Images are captured at regular time intervals and viewed at an accelerated frame rate, creating a video of the microscopic observations. Data can be acquired continuously throughout the study, an advantage over fixed samples in which data can only be acquired at selected time points. Additionally, this technique allows for the observation of cellular responses to various stimuli and stressors (435). The anti-mitotic effect of ESE-16 was visualized using time-lapse video microscopy.

Materials

The 2 well μ-slide (chambered coverslip) with an intermediate plate was purchased from ibidi® (Martinsried, Germany).

Method

HeLa Kyoto cells were seeded on a 2 well µ-slide (chambered coverslip) with an intermediate plate and incubated for 24 hours prior to a 0.4 µM ESE-16 exposure (concentration selected during a trial run). The microslide was placed on a heated stage (37°C) inside a mini CO_2 incubator (5% CO_2). Images were acquired every 150 seconds by a spinning disk confocal laser microscope (Andromeda iMIC, Munich, Germany) with a focus stabilizer (Field Electron and Ion Company (FEI), Oregon (OR), USA). The microscope was equipped with a Plan-Apochromat 10x/0.45 M27 and iXon electron multiplying charge coupled device (EMCCD) camera (Andor, Belfast, Ireland). Image sequences were acquired using the FEI Live acquisition software v.2.7.0.16 (FEI, OR, USA) and the cellular responses were analyzed manually.

3.5.3 IncuCyte® Cytotoxicity assay

The IncuCyte® Cytotox Green reagent is a cyanine nucleic acid dye that enables real-time evaluation and quantification of cell death (436). The IncuCyte® Cytotox Green reagent is unable to penetrate healthy cells due to intact plasma membranes. However, as the cell membrane integrity diminishes, as a result of cell death, the IncuCyte® Cytotox Green reagent enters the cells, binds the DNA of the apoptotic cells and yields a 100-1000 fold increase in fluorescence that can be analyzed, using the IncuCyte® live-cell analysis system and IncuCyte® integrated analysis software (436).

Materials

The IncuCyte® Cytotox Green reagent was purchased from Sartorius AG (Göttingen, Germany). The IncuCyte® Cytotox Green reagent was diluted to a final concentration of 250 nM prior to addition to seeded cells.

Method

HeLa cells were seeded into a 96 well plates and incubated for 24 hours to allow for attachment. Cells were exposed to ESE-15-one and ESE-16, respectively, and the IncuCyte® Cytotox Green reagent. The plates were placed in the IncuCyte® S3 Live-Cell Analysis System (Essen BioScience, Hertfordshire, United Kingdom (UK)) and two photos per well were taken every two hours over a 72-hour period.

3.5.4 Scratch wound cell migration assay

Cancer metastasis primarily depends on the ability of cancer cells to migrate (437). In addition to cancer metastasis, cell migration is a fundamental component of various biological processes such as angiogenesis and wound healing (438). Microtubules and the actin skeleton play a central role in cell migration. Cell migration is initiated by a stimulus which results in cell polarization and the rapid reorganization of the actin filaments and microtubules (439). As ESE-15-one and ESE-16 exert their effect on the microtubule network, the ability of HeLa cells to migrate was assessed after ESE-15-one and ESE-16 exposure.

Materials

Fribronectin was purchased from Sigma-Aldrich (St. Quentin-Fallavier, France). The IncuCyte® WoundMaker, the ImageLock™ plate and the IncuCyte® S3 Live-Cell Analysis System were provided by Essen BioScience (Hertfordshire, UK) as part of a trial period for the IncuCyte® S3 Live-Cell Analysis System. Plates were coated with 5 µg/mL fibronectin and kept at 4°C overnight. Wells were rinsed thrice with PBS prior to cell seeding.

Method

HeLa cells were seeded in a 96-well ImageLock™ plate pre-coated with fibronectin and incubated for 24 hours to allow for attachment. A scratch was made using the IncuCyte®

WoundMaker (Essen BioScience, Hertfordshire, UK) and the wells were rinsed three times with complete growth medium. Cells were exposed to 0.1 and 0.2 µM ESE-15-one and ESE-16, respectively. Cells were placed in the IncuCyte® S3 Live-Cell Analysis System (Essen BioScience, Hertfordshire, UK) and photos were taken every two hours for 24 hours.

3.5.5 Cytotoxicity studies: Spectrophotometric quantification of 3-(4,5-dimethylthiazol-2-yl)-2,5-diphenyltetrazolium bromide (MTT)

Cytotoxicity studies determined the GI_{50} of ESE-15-one, ESE-16, LimPyr1 and T4 after a 48-hour exposure. Cell survival was indirectly measured via the colorimetric MTT assay, as cellular proliferation can be examined via the reduction of tetrazolium salts such as MTT (440). This water-soluble yellow tetrazolium salt can be reduced intracellular by the action of cellular oxido-reductase enzymes, such as nicotinamide adenine dinucleotide (NADH) and nicotinamide adenine dinucleotide phosphate (NADPH), in metabolically active cells to an insoluble purple formazan (440). The latter can be solubilized and quantified via spectrophotometric means (441).

Materials

MTT (5 mg/mL), RPMI without phenol red, isopropanol, 37% hydrochloric acid (HCl) and Triton® X-100 were purchased from Sigma Aldrich (MO, USA). MTT was diluted in RPMI without phenol red to a working concentration of 0.5 mg/mL. Additionally, PBS and MTT solubilization solution (1800 mL isopropanol, 16 mL 37% HCl and 200 mL Triton® X-100) were used.

Method

Cells were seeded in 96 well plates and incubated for 24 hours to allow for attachment. Cells were then exposed to a dilution series of ESE-15-one, ESE-16, LimPyr1 and T4, as per table 3.2, for 48 hours. Cells exposed to DMSO served as a vehicle control, while cells exposed to 0.1% sodium dodecyl sulfate (SDS) provided a positive control (100% cell death). After

exposure, cells were rinsed with 100 µL warm PBS. Diluted MTT (100 µL) was added to the cells and incubated for 4 hours at 37°C, protected from light. During this incubation, purple formazan crystals formed and were dissolved with the addition of 100 µL MTT solubilization solution. Plates were incubated overnight at room temperature in the dark. The absorbance was read at 570 nanometer (nm), using an ELx800 Universal Microplate Reader (Bio-Tek Instruments Inc., Vermont (VT), USA). Data of three independent biological repeats (n=4) were analyzed, using Microsoft Excel 2010 (Microsoft Corporation, Washington (WA), USA). Cell viability was calculated relative to the DMSO vehicle control and expressed as % cell growth:

P% = 100*[(Sc - SMTT SDS)/ (SMTT DMSO - SMTT SDS)

Where:
P% = percentage viable cells
Sc = absolute absorption of compound-exposed cells
SMTT SDS = absolute absorption of the SDS control (0% viability)
SMTT DMSO = absolute absorption of the DMSO control (100% viability)

Percentage cell growth was plotted graphically, from which the GI_{50} values were extrapolated.

Table 3.2: Dilution series of ESE-15-one, ESE-16, LimPyr1 and T4 that were used during cytotoxicity studies.

Compound	**Dilution series**
ESE-15-one and ESE-16	10 µM, 5 µM, 2.5 µM, 1.25 µM, 0.625 µM, 0.313 µM, 0.156 µM, 0.078 µM, 0.039 µM, 0.02 µM
LimPyr1	25.6 µM, 20.48 µM, 16.384 µM, 13.107 µM, 10.486 µM, 8.389 µM, 6.711 µM, 5.369 µM
T4	45 µM, 41 µM, 36 µM, 33 µM, 30 µM, 27 µM

3.5.6 Visualization of the cytoskeleton: Fluorescent microscopy

The cytoskeleton is composed of microtubules and actin filaments (442). The cytoskeleton is responsible for cellular shape, internal organization, cell motility and cytokinesis (443). To visualize the effect ESE-15-one, ESE-16, LimPyr1 and T4 have on the cytoskeleton, a double-immunofluorescence staining technique was used. The microtubules were stained with a primary tubulin antibody and visualized with Alexa Fluor® 488-conjugated secondary antibody. The actin skeleton was stained red with Phalloidin, a fluorescently-labeled probe with a high affinity for F-actin (444).

Materials

Bovine serum albumin (BSA) and 37% formaldehyde were purchased from Sigma-Aldrich (St. Quentin-Fallavier, France), Triton® X-100 and Tween®-20 were purchased from EUROMEDEX (Mundolsheim, France), ProLong® Diamond Antifade Mountant with 4',6-diamidino-2-phenylindole (DAPI) and Rhodamine Phalloidin were purchased from Invitrogen™ (CA, USA). The primary tubulin antibody, α3A1, is a monocolonal antibody produced by Dr Lafanechère (Grenoble, France) and the secondary polyclonal antibody, Alexa Fluor® 488 Goat Anti-Mouse immunoglobulin G (IgG), was purchased from Jackson ImmunoResearch Laboratories (Pennsylvania (PA), USA).

The primary antibody cocktail was prepared as follows: primary mouse α-tubulin antibody (α3A1) (1:4000) and Rhodamine Phalloidin (1:1000) in 0.1% PBS-Tween®-20 with 2% BSA. The secondary antibody was prepared as follows: Alexa Fluor® 488 Goat Anti-Mouse IgG (1:1000) in 0.1% PBS-Tween®-20 with 2% BSA.

Method

Cells were seeded on 12 mm round sterilized cover slips in 24 well plates and allowed to attach for 48 hours before exposure to the relevant compounds for 24 hours. Termination followed by rinsing the cells with PBS before they were fixed in 3.7% formaldehyde/PBS for

30 minutes at 37°C. Cells were permeabilized with 0.2% Triton® X-100/PBS for 30 minutes at room temperature. Thereafter, cells were rinsed with PBS and incubated with the primary antibody cocktail for 30 minutes at room temperature. Samples were rinsed three times with PBS-Tween®-20 (0.1%) prior to a 30-minute incubation with the secondary antibody at room temperature. Coverslips were mounted on microscope slides with ProLong® Diamond Antifade Mountant with DAPI (Invitrogen™, MA, USA). A Zeiss ApoTome microscope controlled by Axiovision software (Zeiss, Oberkochen, Germany) was used to view the slides (63x oil objective). Images were captured using an AxioCam MRm camera (Zeiss, Oberkochen, Germany).

3.6 Radiation dose-reponse curve

In order to determine the radiation dose (Gy) that decreases cell viability significantly cells were exposed to a range of radiation doses (0, 2, 4, 6, 8 and 10 Gy) 24 hours after seeding. Termination followed 24 hours after radiation via flow cytometry employing Annexin V (apoptosis induction) and propidium iodide (PI) (cell cycle analysis), respectively.

3.6.1 Apoptosis induction in cells exposed to radiation doses: Annexin V quantification via flow cytometry

The internal cell membrane phospholipid, phosphatidylserine, is externalized during early apoptosis (91). The exposed phosphatidylserine can be labeled with the phospholipid binding protein, Annexin V, conjugated to a fluorescein isothiocyanate (FITC) fluorochorme to detect apoptosis via flow cytometry (445). Propidium iodide (PI) is a red fluorescent nuclear stain and was used to differentiate apoptotic cells from necrotic cells due to PI's inability to permeate intact cell membranes (446).

Materials

FITC-labeled Annexin V, PI and Annexin V binding buffer were purchased as part of the FITC Annexin V apoptosis detection kit from BioLegend (CA, USA).

Method

Treated cells were trypsinized and washed with ice-cold PBS. Harvested cells were resuspended in Annexin V binding buffer (0.25-0.1 x 10^7 cells/mL). Each cell suspension (100 µL) was transferred to a 5 mL test tube to which Annexin V-FITC (5 µL) and 10 µL of PI solution were added. Cells were vortexed and incubated for 15 minutes at room temperature, covered with foil to prevent loss of fluorescence. Prior to analysis, 400 µL of Annexin V binding buffer was added to each tube. Cells were analyzed, using a FC500 flow cytometer (Beckman Coulter (CA, USA)). Fluorescence on the FL1 channel (detects emissions at 515-545 nm) was measured for the quantification of FITC, while the FL3 channel (detects emissions at 600 nm) was used for the quantification of PI.

A dot plot was obtained for each sample by plotting FL1 log against FL3 log. Each dot plot was divided into four quadrants, using the Kaluza Analysis version 1.5 software (Florida (FL), USA). The bottom left corner was assigned to viable cells as these cells have minimal FITC and PI staining. Cells undergoing apoptosis (labeled with Annexin V-FITC) were quantified in the top left and right quadrants. Necrotic cells stained positive with PI only were quantified in the bottom right quadrant.

3.6.2 Cell cycle analysis of cells exposed to radiation doses: Flow cytometry employing propidium iodide

Flow cytometry uses hydrodynamic focusing principles to measure the fluorescence of cells or particles with diameters of 0.5-40 µm. The argon laser beam is focused on one cell at a time resulting in scattered light. Cell size is measured by forward scatter (perpendicular to the detectors) and the granularity/complexity of the cell is measured via side scatter (in line

with the detectors) (447). Any fluorochrome with which the cells are labeled releases photons after excitation which is detected by appropriate fluorescent channels (448). PI is a red fluorescent intercalating agent which allows for the identification of different phases of the cell cycle using flow cytometric principles (449). PI binds to the cytosine-guanine nucleotide pair and is thus able to stain both DNA and ribonucleic acid (RNA). In order to eliminate the signaling of RNA-PI binding, the cells are treated with RNAse A prior to PI staining, ensuring that only the DNA content are measured (450,451).

Materials

PI, RNAse A and Triton® X-100 were purchased from Sigma Aldrich (MO, USA) and ethanol (99.9%) was purchased from Merck Co. (Munich, Germany). FCS was purchased from Thermo Fisher Scientific (MA, USA).

Method

Harvested cells were washed in 1 mL of ice-cold PBS prior to centrifugation at 500 x *g* for 2 minutes. Cells were resuspended in 200 µL of ice-cold PBS containing 0.1% FCS to block non-specific binding sites. Fixation of the cells entailed placing the cells on a vortex and adding ice-cold 70% ethanol (4 mL) in a drop-wise manner. Samples were incubated for 24 hours at 4°C. Fixed cells were pelleted by centrifugation (500 x *g* for 5 minutes). The supernatant was discarded and the cells were resuspended in PBS containing PI (40 µg/mL), Triton® X-100 (0.1%) and RNAse A (100 µg/mL). Cells were incubated for 40 minutes at 37°C in the dark.

PI fluorescence was detected on FL3 channel (excitation at 488nm/emission at 535/610 nm) using a FC500 flow cytometer (Beckman Coulter, CA, USA). Kaluza Analysis version 1.5 software (Florida, USA) (Beckman Coulter, CA, USA) was used to analyze the data from at least 10 000 cells per sample. Events from cell debris and clumps of cells were removed from further analysis by gating. Histograms were created for each sample by plotting cell count against PI emission. The phases of the cell cycle were assigned based on the DNA content of the cells.

3.7 Compound dose-response curve

3.7.1 Apoptosis induction in cells exposed to compound doses: Flow cytometric quantification of Annexin V

To determine the lowest doses at which the compounds decreased cell viability significantly flow cytometric quantification of Annexin V was used. Breast cancer cells were exposed to a range of compound doses (GI_{50}, ¾ GI_{50}, ½ GI_{50}, ¼ GI_{50} and ⅛ GI_{50}) for 24 hours and terminated, as per protocol described in section 3.6.1.

3.7.2 Cell cycle analysis of cells exposed to compound doses: Flow cytometry employing propidium iodide

The cell cycle progression of breast cancer cells exposed to a range of compound doses (GI_{50}, ¾ GI_{50}, ½ GI_{50}, ¼ GI_{50} and ⅛ GI_{50}) was assessed 24 hours after exposure, as per protocol set out in section 3.6.2. The lowest compound dose that had a significant effect on the cell cycle was selected for the radiosensitization studies.

3.8 Radiosensitization studies

A series of experiments were conducted on the three breast cancer cell types, in order to determine whether exposure to the novel compounds, prior to radiation, significantly affected the induction of cell death, intracellular signaling pathways and morphological responses of the cells after exposure to low doses of each therapy.

3.8.1 Flow cytometric quantification of Annexin V-FITC

Breast cancer cells were exposed to the lowest dose of the compounds that induced apoptosis significantly after 24 hours (as determined from the dose-response curves in section 3.7). Following the 24-hour exposure, cells were exposed to the radiation dose

which significantly induced apoptosis (as determined from the dose-response curves in section 3.6). Termination followed 24 hours after radiation as per protocol set out in section 3.6.1.

3.8.2 Cell cycle analysis

To determine the effect that drug pre-exposure has on the cell cycle distribution of breast cancer cells exposed to radiation, flow cytometry employing PI was used. Seeded cells were exposed to the compounds for 24 hours followed by radiation at the pre-determined doses. Termination followed 24 hours after radiation as per protocol set out in section 3.6.2.

3.8.3 Intracellular signaling pathways induced by pre-exposing breast cancer cells to the novel compounds prior to radiation

Apoptosis is regulated by a number of signaling pathways. Mitochondrial ROS (mROS) is tightly regulated for its participation in physiological cell signaling. When ROS production is increased beyond a threshold level, the intrinsic apoptotic pathway is activated (101). ROS serves as an apoptotic stimulus which causes the tBid to oligomerizise Bax/Bak (107). The latter inserts megapores into the mitochondrial membrane, decreasing the mitochondria membrane potential (107). Cytochrome *c* translocates from the mitochondria to the cytoplasm and forms the apoptosome with Apaf1 (108). Pro-caspase 9 is then recruited to the apoptosome which in turn cleaves downstream effector caspases 3 and 7 (108). The caspase cascade induces apoptotic cell death. Energy depletion and nutrient deficiency is detected by AMPK (109). The latter results in mTOR inactivation by activating the tuberous sclerosis complex (TSC) resulting in the inhibition of autophagy (109). Class I phosphatidylinositol-4,5-bisphosphate 3-kinase (PI3K)'s downstream effectors, such as Akt, can activate mTOR (452). ROS activates AMPK while inhibiting Akt activity, resulting in mTOR inhibition. Depending on the levels of cellular stress, ROS production leading to autophagy as a salvage pathway, or induction of either programmed cell death type I or II may result (106).

3.8.3.1 Reactive oxygen species production: Flow cytometric quantification of superoxide employing hydroethidine

Hydroethidine is a superoxide indicator that exhibits a blue fluorescence in the cytosol. Superoxide oxidizes hydroethidine to 2-hydroxyethidium which intercalates with the cell's DNA, staining the cell nucleus bright fluorescent red (453).

Materials

Hydroethidine was purchased from Sigma-Aldrich (Missouri, USA) and was diluted in PBS to a working concentration of 10 µM.

Method

Superoxide was measured 4, 24 and 48 hours after irradiation by resuspending trypsinized cells in a 1 mL hydroethidine solution. Incubation followed for 15 minutes at 37°C. 2-Hydroxyethidium (excitation at 488 nm/emission at 535/610 nm) was detected on the FL3 channel, using a FC500 system flow cytometer (Beckman Coulter, CA, USA). Data from at least 10 000 cells were acquired and analyzed, using Kaluza Analysis version 1.5 software (FL, USA).

3.8.3.2 Mitochondrial transmembrane potential: Flow cytometric quantification of Mitocapture™

MitoCapture™ is a cationic dye that exhibits a red fluorescence when accumulated within healthy cell mitochondria. Due to the disrupted mitochondrial membrane in apoptotic cells, MitoCapture™ cannot accumulate in the mitochondria and is limited to the cytoplasm, where it generates a green fluorescence in its monomer form (454).

Materials

The MitoCapture™ Mitochondrial Apoptosis Detection Fluorometric Kit (BioVision, CA, USA) was used to detect changes in mitochondrial transmembrane potential. The MitoCapture™ reagent was diluted at 1:1000 in the provided incubation buffer (pre-warmed to 37°C) prior to use.

Method

Harvested cells (1 x 10^6) were resuspended in 1 mL of diluted MitoCapture™ solution and incubated at 37°C for 20 minutes. Samples were centrifuged (500 x *g* for 5 minutes) and the supernatant discarded. Samples were resuspended in 1 mL of pre-warmed incubation buffer prior to analyses. Fluorescence of the FL1 channel (excitation/emission at 488/530 nm) was measured with a FC500 flow cytometer (Beckman Coulter, CA, USA). Data from at least 10 000 cells were analyzed with Kaluza Analysis version 1.5 software (FL, USA).

3.8.3.3 Western blots

The Western blot technique was used for the evaluation of several proteins in the treated breast cancer cells. The Western blot technique is a multi-step protocol based on the principle of immunochromatography. Proteins are separated according to their molecular weight via a polyacrylamide gel and are transferred to a membrane. The proteins in question are then detected with their specific primary antibody and visualized with a labeled secondary antibody (455).

Materials

NaCl, Trizma® (Tris base), 10% SDS, sodium deoxycholate, EDTA, EGTA, cOmplete™ mini EDTA-free protease inhibitor cocktail tablets, phosphatase inhibitor cocktails 2 and 3, Laemmli buffer, ammonium persulfate (APS), N,N,N',N'-tetramethylethylenediamine (TEMED), glycine and BSA were purchased from Sigma-Aldrich (St. Quentin-Fallavier,

France). Bradford reagent, the Precision Plus protein dual color standards marker, acrylamide/bis-acrylamide (37.5:1), Trans-Blot® Turbo™ Midi-size polyvinylidene difluoride (PVDF) membrane and Clarity™ Western enhanced chemiluminescence (ECL) substrate were purchased from Bio-Rad Laboratories Inc. (CA, USA). Tween®-20, trisaminomethane (Tris)-buffered saline (TBS) and 10x Tris-Glycine-SDS migration buffer were purchased from EUROMEDEX (Mundolsheim, France).

The radioimmunoprecipitation assay (RIPA) buffer was prepared as follows: 150 mM NaCl, 10 mM Tris-HCl (pH 7.4), 0.1% SDS, 0.5% sodium deoxycholate, 1 mM EDTA, 1 mM EGTA, 1x protease inhibitor and 1x phosphatase inhibitor cocktails 2 and 3. A 10x transfer buffer was prepared as follows: Tris-HCl (30 g) and 144 g glycine dissolved in double-distilled water (ddH_2O) to 1 L. Prior to use, 100 mL of the 10x transfer buffer was diluted in 700 mL of 100% ethanol and 200 mL of ddH_2O.

The 10% sodium dodecyl sulfate polyacrylamide gel electrophoresis (SDS-PAGE) gels were prepared as per table 3.3. Glass casting plates (1.5 mm) were clamped in casting frames and set on casting stands (Bio-Rad Laboratories Inc., CA, USA). The running gel was set in the glass casting plates prior to the addition of the stacking gel. A 10 spacer comb was placed in the stacking gel prior to setting to create the loading wells.

Table 3.3: Reagents required to hand-cast 10% running and 4 % stacking SDS-polyacrylamide (SDS-PAGE) gels.

	10% Running (10 mL gel) (mL)	**4 % Stacking (4 mL gel) (mL)**
ddH_2O	4.8	6.3
Trizma® (Tris base)	2.5 (1.5 M pH 8.8)	2.5 (0.5 M pH 6.8)
acrylamide/bis-acrylamide (37.5:1)	2.5	0.41
10% Sodium dodecyl sulphate (SDS)	0.1	0.1
10 % ammonium persulfate (APS)	0.1	0.1
TEMED	0.01	0.01

The following primary antibodies were used:

i. Anti-Bax polyclonal antibody produced in rabbit (BD Pharmingen™, Cat#554104) and anti-caspase 3 monoclonal antibody produced in rabbit (Cell Signaling Technology, Cat#9664)

Apoptosis is inhibited when the pro-apoptotic protein Bax is bound to the phosphorylated anti-apoptotic protein Bcl-2 (456). Once the intrinsic apoptotic pathway is activated, Bax is released from Bcl-2 and translocates to the mitochondria. Bax permeabilizes the outer mitochondrial membrane, resulting in the release of cytochrome *c*. The release of cytochrome *c* from the mitochondria activates the initiator caspase 9, which in turn activates caspase 3, an effector caspase (100). The activation of the caspase cascade results in the induction of programmed cell death type I.

ii. Anti-phospho-Akt (Ser473) monoclonal antibody produced in rabbit (Cell Signaling Technology, Cat#4060) and anti-phospho-FoxO1 (Thr24)/FoxO3a polyclonal antibody produced in rabbit (Thr32) (Cell Signaling Technology, Cat#9464)

The Forkhead family of transcription factors (FoxO1, FoxO4 and FoxO3a) signaling is mediated through a pathway involving Akt (457). Active unphosphorylated FoxO promotes apoptosis and activates $p27^{kip1}$, resulting in cell cycle arrest (458). FoxO's tumor suppressor activity is inactivated upon phosphorylation by phosphorylated Akt. Phosphorylated FoxO is translocated from the nucleus to the cytoplasm and its transcription is inhibited, facilitating cellular survival (459).

iii. Cyclin B1 polyclonal antibody produced in rabbit (Cell Signaling Technology, Cat#4138)

The onset of mitosis is tightly regulated via a serine/threonine protein kinase consisting of CDK1 (catalytic subunit) and cyclin B1 (positive regulatory subunit). The binding of CDK1 to cyclin B1 is essential for the activation of the kinase and forms the mitosis-promoting factor (MPF) (460). The MPF remains inactive until the CDK activating kinase (CAK) phosphorylates CDK1 at Thr161 during the G_2 phase of the cell cycle. The latter activates the MPF and mitosis is triggered (460).

iv. Anti-phospho-histone H2A.X (Ser139) monoclonal antibody produced in mouse (Merck Millipore, Cat#05-636) and anti-Ku70 monoclonal antibody produced in mouse (Santa Cruz Biotechnology, Inc., Cat#sc-56129)

DNA damage is sustained in cells exposed to radiation. Such damage includes DNA double strand breaks (DSB) which can be quantified via the phosphorylation of H2AX (γH2AX) and are repaired by NHEJ (461). NHEJ requires minimal processing of the DNA ends and functions rapidly throughout the cell cycle via the activity of the Ku70-Ku80 complex. The Ku70-Ku80 complex loads onto the free ends of the damaged DNA and recruits DNA repair proteins, such as the DNA damage response (DDR) dependent protein kinase (DNA-PK), Artemis nuclease and ligase IV X-ray repair cross-complementing protein 4 (XRCC4) complex (462).

Method

Western blot samples were prepared by lysing the treated cells with ice-cold RIPA buffer (200 µL). The samples were incubated for 5 minutes on ice. Lysed cells were collected via scraping followed by centrifugation at 21130 × *g* at 4 °C for 30 minutes (Eppendorf® Centrifuge 5424 R, Hamburg, Germany). The supernatant containing the cytosolic content was removed from the pellet (cell debris) and placed on ice.

Protein quantification

The Bradford protein assay was used to determine the protein concentration of each sample. The Bradford protein assay uses Coomassie dye to which protein molecules bind, resulting in a color change from brown to blue. The protein concentration of each sample was demined by adding 2-3 µL of the cytosolic extract to 500 µL ddH_2O in a BioSigma BSA002 Cuvette (Veneto, Italy), followed by the addition of 500 µL Bradford reagent. The absorbance was read at 595 nm, using a BioPhotometer Plus (Eppendorf®, Hamburg, Germany). The protein concentrations of the samples was calculated using a BSA standard curve constructed over a range of concentrations (0, 1, 2, 3, 4, 5 µg/mL).

Gel electrophoresis and membrane transfer of proteins

For each sample, 20 µg of cellular protein were denatured on an Eppendorf® Thermomixer Compact (Eppendorf®, Hamburg, Germany) at 96°C for 5 minutes in Laemmli buffer. Proteins were separated based on their molecular weight and charge via electrophoresis on a 10% SDS-PAGE using a Mini-PROTEAN® Tetra Vertical Electrophoresis Cell (Bio-Rad Laboratories Inc., CA, USA). Gels were run at 80 volt (V) for 3 hours in 1x migration buffer against an appropriate molecular size marker. Separated proteins were transferred to a PVDF membrane activated in 100% ethanol, in transfer buffer. Wet transfer was achieved by applying 100 V to the sandwiched membrane for 90 minutes. Membranes were blocked with 5% BSA in 0.1% TBS-Tween®-20 for 90 minutes and were incubated overnight at 4°C in the primary antibody in 5% BSA in 0.1% TBS-Tween®-20 with agitation (MS Orbital Shaker, MS-NOR-30, Major Science, CA, USA). Membranes were washed 3 times with 0.1% TBS-Tween®-20 prior to a 1 hour incubation with the secondary antibody (donkey anti-rabbit horseradish peroxidase (HRP) conjugated polyclonal antibody (Jackson ImmunoResearch, Cat#711-036-152) or donkey anti-mouse HRP conjugated polyclonal antibody (Jackson ImmunoResearch, Cat#715-035-150) in 2% BSA in 0.1% TBS-Tween®-20 (room temperature). Membranes were washed three times with 0.1% TBS-Tween®-20. Proteins were visualized, using a ChemiDoc MP (Bio-rad, CA, USA) after activating HRP activity with Clarity™ Western ECL Substrate (Bio-Rad Laboratories Inc., CA, USA). Band size was

determined, using Image Lab version 5.2.1 software (Bio-Rad Laboratories Inc., CA, USA). Quantification followed after standardization using bands obtained from actin staining (β-Actin produced in rabbit, Cell Signaling Technology, Cat#4967), using Image Lab version 5.2.1 software (Bio-Rad Laboratories Inc., CA, USA).

3.8.4 Morphological studies: Polarization-optical transmitted light differential interference contrast microscopy

Cell morphology was visualized with polarization-optical transmitted light differential interference contrast microscopy (PlasDIC). Based on the Nomarski-DIC configuration (463), Zeiss combined polarization and interference to develop PlasDIC, which allows the visualization of cells outside the polarization-sensitive area (464). PlasDIC differs from conventional Nomarski-DIC configuration based on the fact that linear polarized light is generated after the object (465), providing high quality images of individual cells and cell clusters due to the DIC effect being invariant to unwanted optical anisotropies stemming from the object, slide, condenser and objective (466). PlasDIC can also be used to visualize apoptotic and necrotic hallmarks (467).

Materials

No additional materials were required.

Method

Breast cancer cells were seeded in 6-well culture plates and incubated for 24 hours at 37°C. Cells were exposed to a vehicle control (DMSO), vinblastine (MCF-7- and MDA-MB-231 cells) or actinomycin D (BT-20 cells) as positive apoptotic controls alongside the compounds (ESE-16 or LimPyr1) for 24 hours. Following the 24 hour pre-treatment with the compounds, cells were exposed to radiation. A Zeiss Axiovert-40 microscope (Gotting, Germany) was used to obtain PlasDIC images (40x magnification) 6, 24 and 48 hours after irradiation.

3.8.5 Cell survival assay: Long term cellular proliferation quantified via a crystal violet stain

Cellular survival and long term proliferation following exposure to the different treatment modalities were assessed, using a crystal violet stain 14 days after radiation exposure. The inability of a cell to proliferate and the loss of reproductive integrity are the two most common mechanisms of cell death described in radiation biology (468). Thus clonogenic studies have been used to successfully evaluate the cellular response to various treatment conditions (469,470). Clonogenic studies evaluate the effectiveness of radiation and/or chemotherapy based on the understanding that clonogenic cells are viable and can proliferate, giving rise to a colony of cells. Nonproliferative cells are unable to multiply due to the inability of these cells to synthesize DNA and proteins, rendering them non-viable (468).

Materials

Crystal violet, 37% formaldehyde and methanol were purchased from Sigma-Aldrich (St. Quentin-Fallavier, France), Triton® X-100 was purchased from EUROMEDEX (Mundolsheim, France). A crystal violet staining solution was prepared in distilled water prior to use: 0.05% crystal violet, 1% formaldehyde, 1x PBS and 1% methanol.

Method

Colonies were stained with crystal violet for 1 hour at room temperature. The staining solution was removed and the plates were rinsed thrice with distilled water. The plates were thoroughly dried. The crystal violet dye was solubilized with the addition of 0.2% Triton® X-100 for 30 minutes at room temperature. The solution was transferred to clean 96-well plates. The absorbance was read at 570 nm, using a FLUOstar OPTIMA Microplate Reader (BMG Labtechnologies, Ortenberg, Germany). Data of three independent biological repeats (n=3) were analyzed for each cell line using Microsoft Excel 2010 (WA, USA).

3.8.6 DNA damage and repair

DNA damage was quantified via H2AX phosphorylation and micronuclei formation. DNA repair was quantified via Ku70 expression, using the Western blot technique. The DNA damage and repair response were measured 2 and 24 hours after irradiation.

3.8.6.1 Quantification of phosphorylated H2AX via flow cytometry

H2AX is a member of the histone H2A family which resides downstream of the DNA damage kinase signaling cascade (471). Upon DNA damage, histone H2AX is phosphorylated at serine 139 and is known as gamma (γ) H2AX. γH2AX accumulates at the sites of DNA damage and recruits response proteins to DNA damage sites (471). In addition to recruiting checkpoint proteins to damaged DNA sites, γH2AX may also play a direct role in DNA repair (472).

Materials

The FlowCellect™ DNA Damage Histone H2A.X Dual Detection Kit was purchased from Merck Millipore (Munich, Germany). The supplied wash buffer (10x) and assay buffer (5x) were diluted in deionized water to a working stock solution (1x) prior to use and stored at 4°C.

Method

Trypsinized cells were washed in 1x wash buffer (500 µL) followed by fixation of cells by adding equal parts fixation buffer to 1x wash buffer (1:1) and incubated on ice for 10 minutes. Cells were centrifuged and the buffer discarded. Cells were resuspended in 1 mL of 1x assay buffer and centrifuged at 300 x *g* for 3 minutes (at 4°C). Permeabilization of the cells followed by adding 1 mL of ice-cold permeabilization buffer and incubated on ice for 20 minutes. Samples were centrifuged and the buffer discarded prior to a rinsing step (200 µL of 1x assay buffer). The latter was followed by the antibody staining step in which cells were

resuspended in 90 µL of assay buffer containing 5 µL of anti-phospho-histone H2A.X-peridinin chlorophyll protein complex (PerCP) (monoclonal antibody). Cells were incubated for 30 minutes in the dark at room temperature. Assay buffer (100 µL) was added to the samples which were centrifuged at 300 x *g* for 5 minutes and the supernatant discarded. A final rinsing step was included (200 µL of 1x assay buffer) prior to analysis. Fluorescence on the FL4 channel (excitation/emission at 477/678 nm) was measured with a FC500 system flow cytometer (Beckman Coulter, CA, USA) and analyzed, using Kaluza Analysis version 1.5 software (FL, USA).

3.8.6.2 Micronuclei quantification

Micronuclei originate either from acentric chromatid and chromosome fragments, or whole chromosomes that fail to be included in a daughter cell nucleus following telophase (136). This is due to the inability of the micronucleus to attach correctly to the spindle apparatus during segregation in anaphase. These fragments are eventually enclosed by a nuclear membrane and display a similar morphological appearance to a nucleus after staining, except the smaller size (136). Micronuclei are visible in cells that have completed nuclear division prior to cellular division. Thus cytochalasin B, a microfilament-assembly inhibitor, is used to prevent cytokinesis (150). The cytokinesis-block-micronucleus assay can provide a measure of chromosome breakage and loss, as well as chromosome rearrangement (150). Therefore, the cytokinesis-block-micronucleus assay is a simple and reliable method to determine DNA damage.

Materials

KCl, NaCl, methanol, acetic acid and giemsa were purchased from Sigma Aldrich (MO, USA). Hypotonic solution (5.2 g KCl / 500 mL distilled water), fixative I (methanol: 0.9% NaCl: acetic acid (v:v:v; 12:13:3)) and fixative II (methanol: acetic acid (v:v; 4:1)) were prepared prior to use.

Method

Micronuclei can be quantified in binucleated cells. MCF-7-, MDA-MB-231- and BT-20 cells were exposed to cytochalasin B 2 and 24 hours after irradiation in order to prevent cytokinesis. The interaction between the microtubule regulating agents and cytochalasin B was prevented by removing the compounds prior to cytochalasin B exposure. Exposure to cytochalasin B lasted for one and a half cell cycles before termination.

Trypsinized cells were centrifuged for 15 minutes at 900 x *g*. The supernatant was discarded and pre-warmed hypotonic solution (5 mL) was slowly added to the cells while being vortexed. Incubation followed at room temperature for 5 minutes. The cells were then centrifuged for 15 minutes at 900 x *g*. The supernatant was removed and 5 mL fixative I was added to the cells and incubated at room temperature for 5 minutes. Samples were centrifuged for 10 minutes at 1000 x *g* and the supernatant discarded. Fixative II was slowly added to the cells (5 mL) and incubated at room temperature for 5 minutes. Cells were centrifuged for 10 minutes at 1000 x *g*. Three drops of each sample were placed on degreased, dry microscope slides. Slides were dried overnight and stained with 10% giemsa the following day. Samples were visualized under a light microscope followed by blind scoring of micronuclei in 500 binucleated cells per repeat.

3.8.6.3 Quantification of the DNA repair response via Western blot analysis of Ku70 expression

The DNA repair response was measured with a standard Western blot technique (as described in section 3.8.3.3) employing anti-Ku70 monoclonal antibody produced in mouse (Santa Cruz Biotechnology, Inc., Cat#sc-56129).

3.9 Evaluation of the bystander effect induced by irradiated cells

The radiation-induced bystander effect demonstrates the relationship between irradiated and non-irradiated cells (473). Traditionally, it was believed that DNA damage only occurs in cells directly exposed to radiation. However, studies have shown that non-irradiated cells neighboring irradiated cells exhibit radiation effects (474). This is due to the transfer of DNA damage signals from irradiated cells (473,474). In this *in vitro* study, the bystander effect was investigated by replacing the medium of non-irradiated cells with conditioned medium collected from irradiated cells. Breast cancer cells were seeded and incubated for 24 hours to allow for attachment. Adherent cells were exposed to the relevant compounds for 24 hours after which the cells were rinsed with PBS and propagated in clean media (compound-free media). This ensured that the compounds were not transferred to non-exposed cells. Treated cells propagated in compound-free media were radiated and the conditioned media were transferred 2 or 24 hours after radiation, depending on the experiment. The following investigations were conducted:

3.9.1 The permeability of the mitochondrial membrane was determined 24 hour after transfer in irradiated cells and was compared to cells propagated in the conditioned medium as per protocol set out in section 3.8.3.2.

3.9.2 ROS generation (section 3.8.3.1) was quantified for both irradiated cells as well as non-irradiated cells propagated in conditioned medium 24 hours after transfer.

3.9.3 The ability of non-irradiated cells propagated in conditioned media to form colonies was assessed 14 days after transfer, as per protocol in section 3.8.5.

3.9.4 DNA damage and repair mechanisms were evaluated 2 hours after medium transfer with a standard Western blot, as per protocol set out in section 3.8.3.3, using an anti-phospho-histone H2A.X (Ser139) monoclonal antibody produced in mouse

(Merck Millipore, Cat#05-636) and an anti-Ku70 monoclonal antibody produced in mouse (Santa Cruz Biotechnology, Inc., Cat#sc-56129).

3.10 Evaluation of radiation-induced resistance due to dose fractionation in cells exposed to the combination treatment

Exposure of cells to repetitive small amounts of DNA stress, such as ionizing radiation, may render the cells resistant to subsequent exposure (475). Hence, the development of radioresistance which decreases the response of the cells to higher radiation doses (476). In order to determine whether pre-treatment of breast cancer cells with agents targeting microtubule regulators reduce this phenomenon, cells were exposed to these compounds 24 hours prior to 8 Gy radiation exposure fractionated over four days (2 Gy per day). These cells were compared to cells exposed to one radiation dose (8 Gy). Termination followed by:

3.10.1 Determining the ROS generation as set out in section 3.8.3.1.

3.10.2 Detecting changes in the mitochondrial membrane potential (section 3.8.3.2).

3.11 Statistical analysis

Variation in results may result from variations within the subjects (biological variation), variations between subjects within a random sample and variation during analytical procedure. Statistical parameters for quantitative- and qualitative studies were determined as described below.

Quantitative studies

Data obtained from three independent biological repeats were presented as either mean percentages or mean fold increases. Variation in the three biological repeats was presented

as the standard deviation. The ANOVA-single factor model followed by a two-tailed Student's *t*-test was used to calculate statistically significant differences. Means were graphically presented in bar charts, with T-bars indicating the standard deviations. A *P*-value <0.05 was regarded as statistically significant and was indicated by an asterisk (*). Three independent repeats were conducted for the colchicine binding and cytotoxicity assays, while two biological repeats were conducted for the IncuCyte® studies. Flow cytometric data of at least 10 000 cells were obtained for annexin V, cell cycle progression, ROS generation, MitoCapture™ and γH2AX analysis. Kaluza Analysis version 1.5 software (FL, USA) was used to analyze all flow cytometric data. The expression of Bax, cleaved caspase 3, cyclin B1, phosphorylated Akt, FoxO1/3a, γH2AX and Ku70 were quantified employing Western blotting. Band size was determined, using Image Lab version 5.2.1 software (Bio-rad, CA, USA). Quantification of band size was determined following standardization, using bands obtained from actin staining as a housekeeping protein. Three biological repeats (n=3) were conducted for the long term cellular proliferation assay. Blind scoring of micronuclei was done in triplicate (500 binucleated cells) for each treatment condition and all relevant controls (in three biological repeats).

Qualitative studies

Morphological studies were conducted by means of light, fluorescent and video microscopy. Two biological repeats were analyzed and captured for each cell line which included all relevant treatment conditions and controls. At least 100 cells were manually analyzed for the time-lapse imaging in order to obtain statistical data, using Image J 1.48v (National Institute of Health, USA). Representative images are displayed in the figures.

Statistical support was granted from Prof P Becker from the research office of the Faculty of Health Sciences of the University of Pretoria, Pretoria, South Africa.

3.12 Logistics and funding

Flow cytometric analyses were performed using the FC500 flow cytometer (Beckman Coulter (CA, USA)) from the Department of Pharmacology, University of Pretoria, Pretoria, South Africa. Fluorescent and video microscopy were completed using equipment provided by the Institute of Advanced Biosciences, Grenoble, France. IncuCyte® cytotoxicity and wound healing assays were performed at the Institute of Advanced Biosciences, using equipment provided by Essen BioScience (Hertfordshire, UK) as part of a trial period for the IncuCyte® S3 Live-Cell Analysis System.

This project was funded by grants awarded to Prof A Joubert by the National Research Foundation (NRF), the Medical Research Council of South Africa, and the Cancer Association of South Africa (CANSA). Dr AE Mercier obtained funding for the project from the NRF and Ms EM Nolte was awarded the PhD student grant from the French Embassy which funded her transport and living costs while in Grenoble. Dr L Lafanechère obtained grants (La Ligue, Fondation Arc) for the experiments conducted in Grenoble, France.

3.13 Ethics approval

Ethical approval for the *in vitro* study entitled: Pro-apoptotic and radiosensitizing potential of four candidate microtubule regulators in breast cancer cells was granted from the University of Pretoria's Ethics Committee in 2017 (ethics approval number: 285/2017).

4. Results

"One thing I have learned in a long life: that all our science, measured against reality, is primitive and childlike -- and yet it is the most precious thing we have."

-Albert Einstein-

4.1 Drug properties and relative cytotoxicity

4.1.1 Tubulin competitive binding assay: Tritiated [^{3}H] colchicine binding

The 2-methoyxestradiol analogue, ESE-16, was *in silico*-designed to bind to the colchicine binding sites on tubulin, preventing microtubule assembly (312). This phenomenon was tested by evaluating ESE-16's ability to prevent colchicine binding to tubulin *in vitro*. Purified bovine tubulin was exposed to ESE-16 in competition with tritiated colchicine ([^{3}H] colchicine). DEAE was used to recover protein bound [^{3}H] colchicine followed by liquid scintillation counting.

Purified bovine tubulin exposed to [^{3}H] colchicine served as a positive control (100% binding). Additionally, 100 µM vinblastine was used as a negative control as vinblastine does not exerts its effect via colchicine binding. No statistically significant difference was observed in [^{3}H] colchicine binding with the addition of vinblastine (99.45±6.85%) (Table 4.1). The binding of [^{3}H] colchicine to tubulin was significantly decreased (9.90±1.49%) with the addition of 100 µM colchicine and served as a positive method control. Similarly, binding of [^{3}H] colchicine was significantly decreased in the presence of 100 µM ESE-16 (23.35±6.25%), confirming that ESE-16 binds to the colchicine binding sites on tubulin (Figure 4.1).

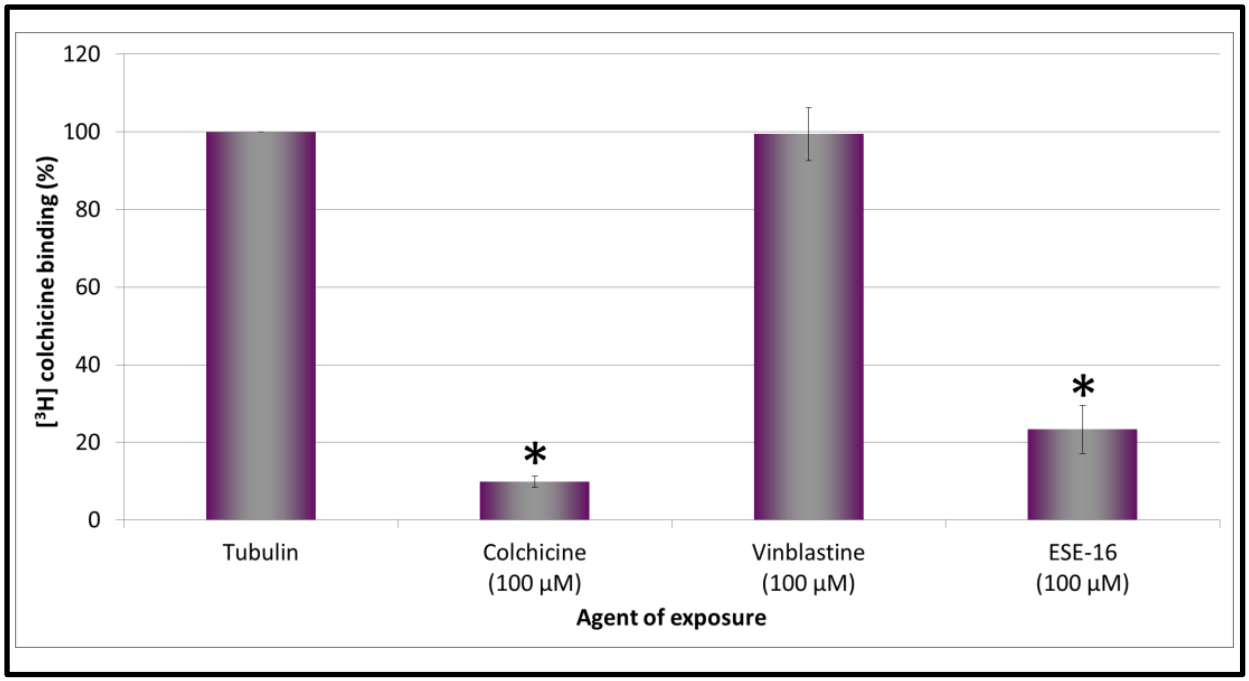

Figure 4.1: Binding of tritiated colchicine to tubulin in the presence of various anti-mitotic compounds. In the presence of colchicine and ESE-16 the binding of tritiated [^{3}H] colchicine to tubulin was significantly decreased compared to the negative control. This illustrates the ability of ESE-16 to bind to the colchicine binding sites on tubulin, preventing microtubule assembly. Vinblastine does not bind to the colchicine binding sites, thus the binding of [^{3}H] colchicine to tubulin was not affected. Bars represent the averaged percentages (n=3) and standard deviations are represented by error bars. Statistical significance (*P*-value <0.05) is indicated by an asterisk (*).

Table 4.1: Binding of tritiated colchicine to purified bovine tubulin in competition with colchicine, vinblastine and ESE-16. The averaged percentages (M%) and standard deviations (SD) of three biological repeats are displayed for all treatment conditions. Statistically significant differences (*P*-value <0.05) were calculated using tritiated [^{3}H] colchicine binding to tubulin as a baseline.

	Tubulin	Colchicine	Vinblastine	ESE-16
M%±SD	100±0.00	9.90±1.49	99.45± 6.85	23.35± 6.25
P-value	-	**5.03E-08**	0.90	**2.91E-05**

4.1.2 Time-lapse imaging: ESE-16's anti-mitotic effect

The colchicine binding assay confirmed that ESE-16 binds to the colchicine binding sites on tubulin. The latter prevents microtubule assembly and induces a metaphase block. The G_2/M phase is the most radiosensitive phase of the cell cycle (414,417), thus microtubule disrupting agents, such as ESE-16, hold promise as radiosensitizing agents. The mitotic progression of autofluorescent HeLa Kyoto cells was monitored via time-lapsed imaging in order to confirm the anti-mitotic ability of ESE-16.

Cells exposed to 0.4 µM of ESE-16 for 24 hours displayed a significant increase in mitotic cells with misaligned chromosomes (Video 4.1). The average duration of metaphase increased in cells exposed to ESE-16 (367.85±19.89 minutes) compared to the DMSO vehicle control (26.3±2.4 minutes) (Table 4.2, Figure 4.2). These results illustrate the ability of ESE-16 to induce a metaphase block, potentially rendering the cells more susceptible to radiation damage.

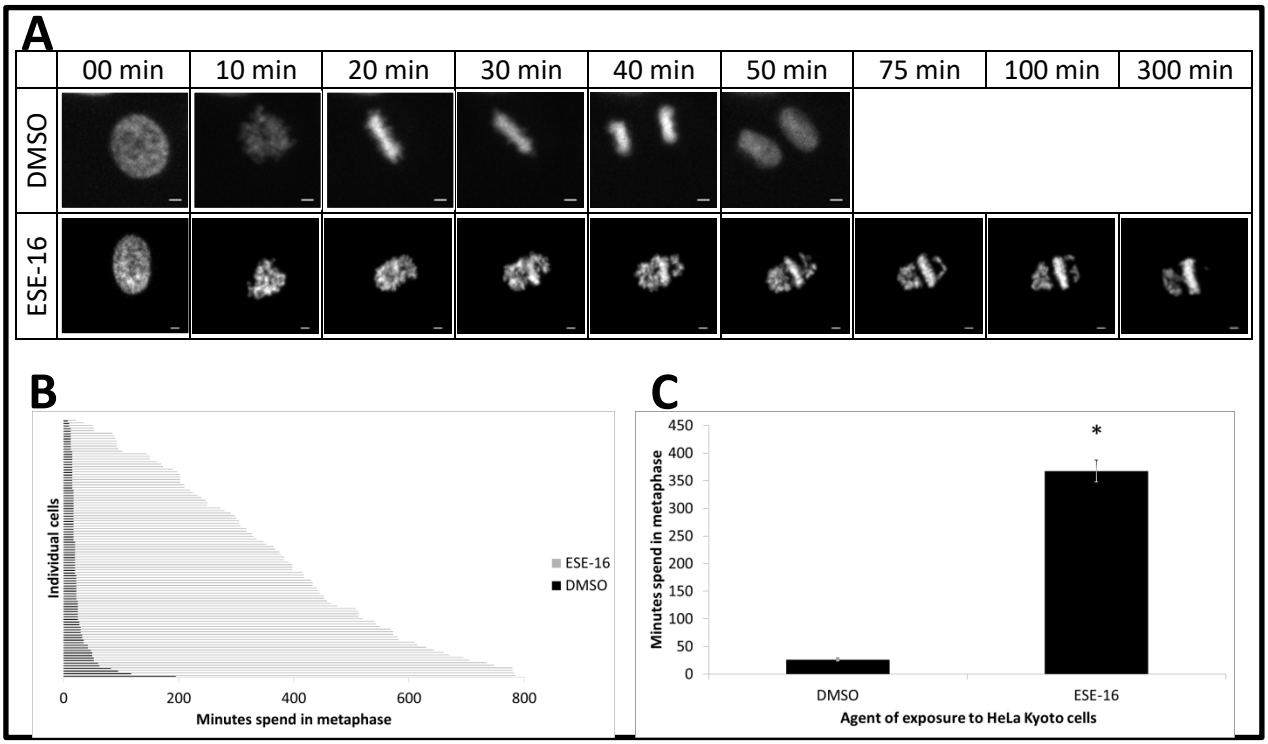

Figure 4.2: Time-lapsed imaging of HeLa Kyoto cells exposed to the anti-mitotic agent, ESE-16. (A) Selected frames from time-lapsed imaging of HeLa Kyoto cells exposed to 0.4 µM ESE-16

illustrating misaligned chromosomes. Scale bars represent 10 µm. (B) ESE-16 caused a marked delay in metaphase progression compared to cells exposed to DMSO as shown in the graphical representation (C). Bars indicate average time spent in metaphase of 100 individual cells, with the standard error of the mean represented by T-bars. Statistical significance (*P*-value <0.001) is indicated by an asterisk (*).

Table 4.2: Time HeLa Kyoto cells spent in metaphase following exposure to DMSO and an anti-mitotic compound, ESE-16. The averaged time in minutes and standard error of the mean (SEM) of two biological repeats are displayed. Statistically significant differences (*P*-value <0.05) were calculated using DMSO (vehicle) as a baseline.

	DMSO	ESE-16
minutes±SEM	26.3± 2.41	367.85± 19.89
P-value	-	**<0.001**

4.1.3 IncuCyte® Cytotoxicity assay

The anti-mitotic properties of the novel 2-methoyestradiol analogues were confirmed during the colchicine binding and time-lapsed imaging assays. The induction of a prolonged metaphase block prevents the progression from metaphase to anaphase and may induce programmed cell death (258). The cytotoxic effect of two 2-methoyestradiol analogues, ESE-15-one and ESE-16, was measured over time in HeLa cells using the fluorescent cell impermeant DNA-binding reagent, IncuCyte® Cytotox Green.

Cell death was measured over 72 hours in HeLa cells exposed to 0.4 µM of ESE-15-one and ESE-16 (Figure 4.3). An increase in rounded cells was observed over the 72 hour time frame. A significant increase in green fluorescence was observed 8 hours (4.13±0.49/mm^2) and 12 hours (4.59±0.35/mm^2) after exposure to ESE-15-one and ESE-16, respectively (Video 4.2), compared to DMSO (2.68±0.40/mm^2 (8 hours) and 3.20±0.42/mm^2 (12 hours), indicating a

significant increase in cell death (Appendix A (Table A1)). The cytotoxic effect of ESE-15-one and ESE-16 was retained over the 72 hour exposure time as indicated by the time-dependent increase in IncuCyte® Cytotox Green fluorescence (Figure 4.4).

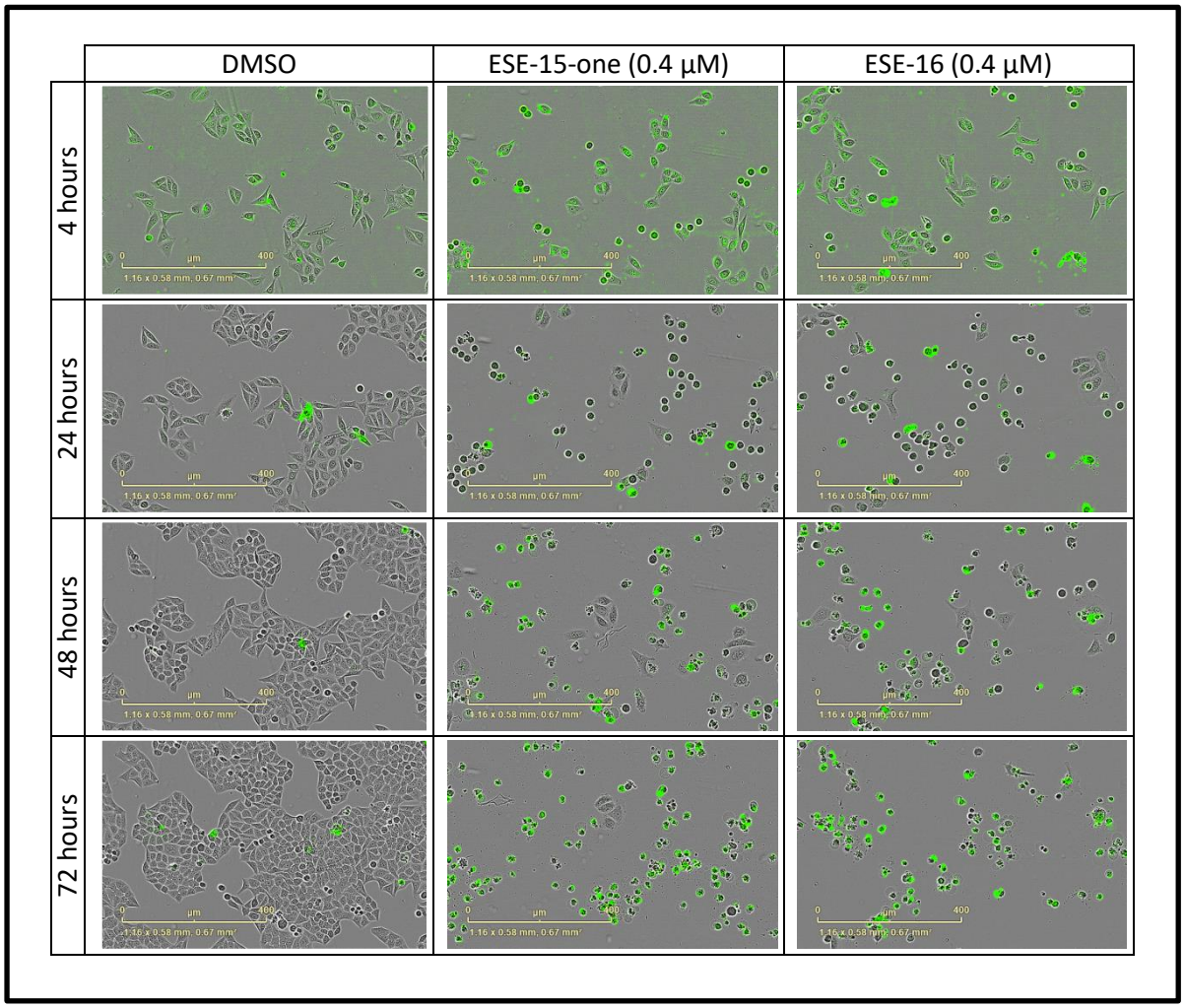

Figure 4.3: Real time IncuCyte® Cytotox Green fluorescence in HeLa cells exposed to two anti-mitotic compounds indicating the number of dead HeLa cells. Selected time frames of HeLa cells exposed to 0.4 µM of ESE-15-one and ESE-16 illustrated an increased number of rounded cells and a time-dependent increase in green fluorescence (cell death). Scale bars represent 400 µm.

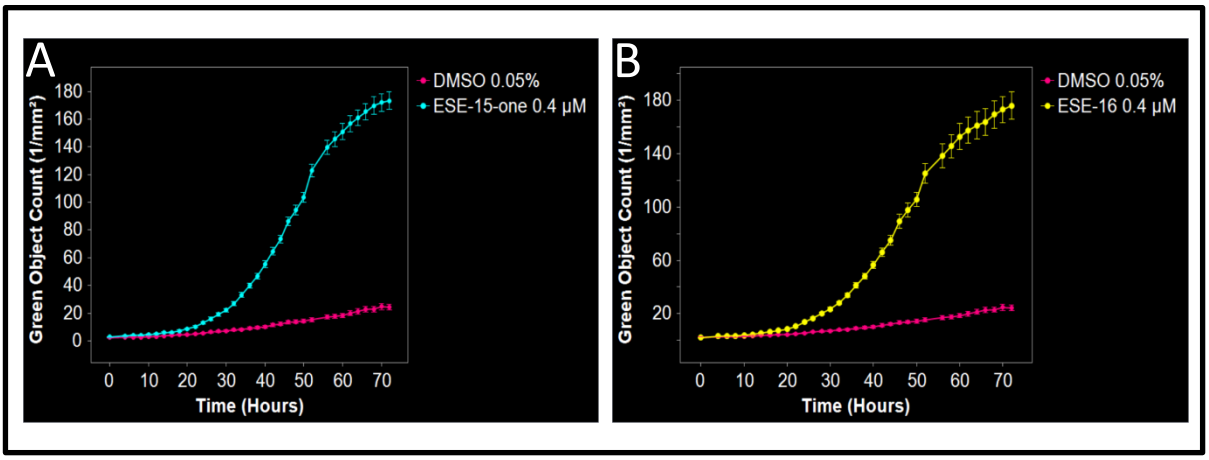

Figure 4.4: Graphical representation of IncuCyte® Cytotox Green fluorescence in HeLa cells exposed to ESE-15-one and ESE-16. Graphs indicate a time-dependent increase in green fluorescence (cell death) being statistically significant at 8 and 12 hours following exposure to ESE-15-one (A) and ESE-16 (B), compared to DMSO.

4.1.4 Scratch wound cell migration assay

Tumor metastasis is instigated by the invasion of neoplastic cells into surrounding tissue and requires chemotactic migration, a process steered by the attachment of the protruding cellular membrane to the extracellular matrix (477). The formation of these pseudopodia requires the rearrangement of the cellular cytoskeleton (439). The 2-methoxyestradiol analogues, ESE-15-one and ESE-16, bind to the colchicine binding sites on tubulin, resulting in the disruption of the microtubule dynamics. The latter may change the mechanical properties of the actin skeleton, decreasing cell motility (478). To investigate whether these two novel compounds have an inhibitory effect on cell migration, scratch assays were performed.

A scratch was made in confluent HeLa cells prior to the addition of 0.2 and 0.4 µM of ESE-15-one and ESE-16, respectively (Figure 4.5). Wound closure was measured every 2 hours for 24 hours. Cell migration was significantly delayed after 8 hours exposure to 0.4 µM ESE-15-one and ESE-16 compared to DMSO (Appendix A (Table A2)) and was maintained for the duration of the study. This significant delay in wound closure was due to the mitotic block induced by the compounds, demonstrated by the increased number of rounded cells (Video 4.3). HeLa cells exposed to 0.2 µM ESE-15-one and ESE-16 also displayed rounded cells, but

to a lesser extend compared to the higher concentration. Cell migration was significantly delayed in 0.2 µM ESE-15-one-exposed HeLa cells 10 hours after exposure. Wound closure was retarded for the duration of the experiment (Figure 4.6). A delay in wound closure was not observed in HeLa cells exposed to the lower concentration of ESE-16.

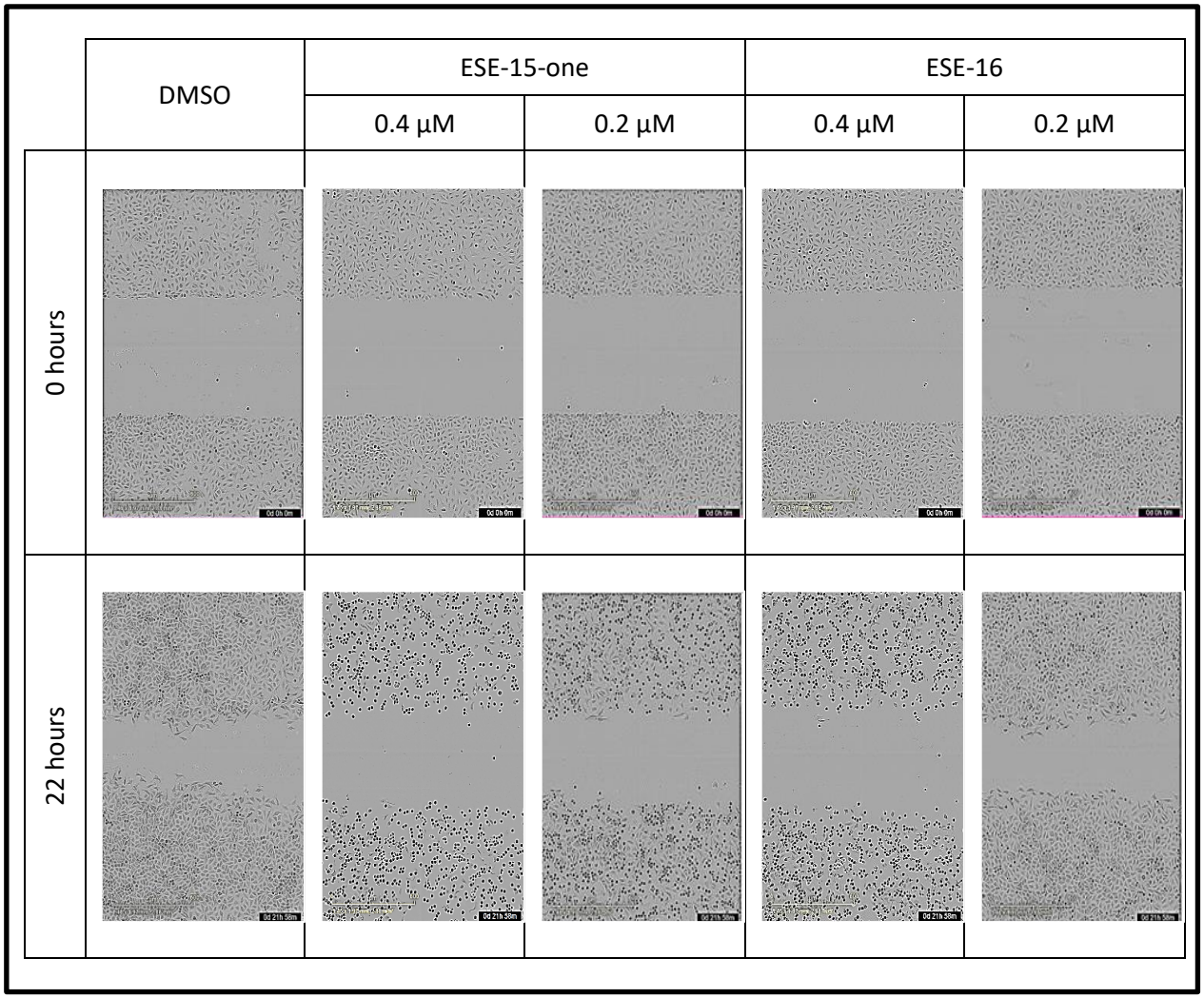

Figure 4.5: Wound closure in HeLa cells exposed to ESE-15-one and ESE-16 indicating the effect on cell migration. Selected time frames of wounds created in confluent HeLa cells illustrating a delay in closure when exposed to ESE-15-one and ESE-16. An increased number of rounded cells were observed in the exposed cells.

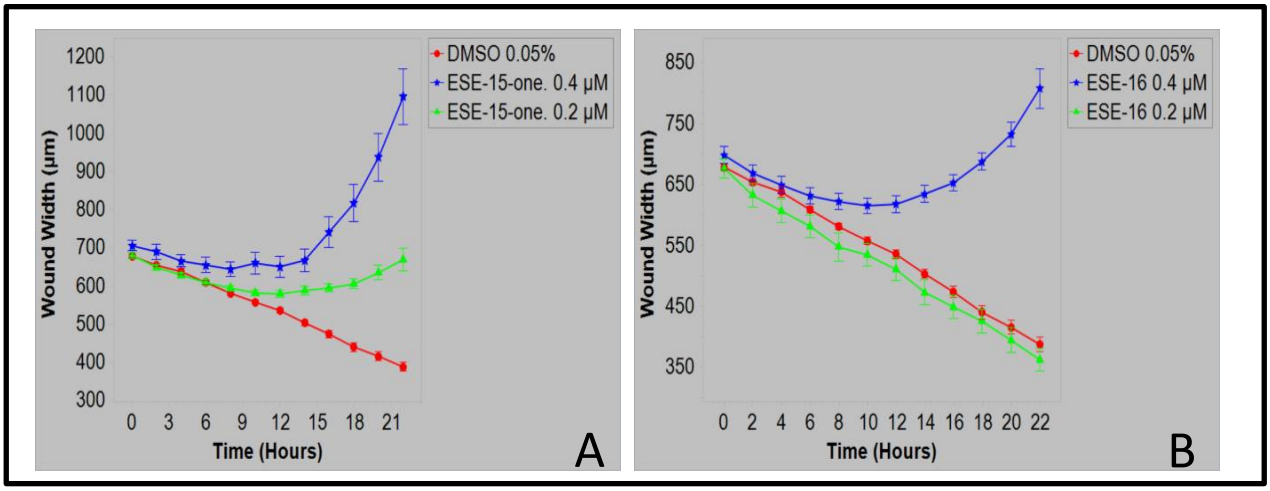

Figure 4.6: Graphical representation of wound closure in HeLa cells exposed to ESE-15-one and ESE-16. Graphs indicate a delay in wound closure becoming statistically significant at 8 hours following exposure to 0.4 µM ESE-15-one (A) and ESE-16 (B), and 10 hours following exposure to 0.2 µM ESE-15-one (A), compared to DMSO. No significant differences were observed in wound closure of cells exposed to 0.2 µM ESE-16 (B).

4.1.5 Cytotoxicity studies: Spectrophotometric quantification of 3-(4,5-dimethylthiazol-2-yl)-2,5-diphenyltetrazolium bromide

Metabolically active cells can reduce a yellow tetrazolium salt, MTT, via dehydrogenase enzyme activity, resulting in the formation of intracellular purple formazan (440). By solubilizing the latter, MTT provides a reliable method for examining cell viability via spectrophotometric means. The GI_{50} of four microtubule regulators were obtained in three breast cancer cell lines. These concentrations were used as a starting point for determining the lowest compound dose that significantly increases apoptosis, which were subsequently used to pre-treat cells prior to radiation exposure.

Breast cancer cells were exposed to ESE-15-one-, ESE-16-, T4- and LimPyr1 doses for 48 hours. Dose response curves revealed a GI_{50} of 0.08±0.02 µM and 0.22±0.04 µM in BT-20 cells which were exposed to ESE-15-one and ESE-16, respectively (Table 4.3). BT-20 cells exposed to T4 and LimPyr1 revealed GI_{50} concentrations of 36.00±1.10 µM and 16.38±0.55 µM, respectively (Figure 4.7 A-D). MCF-7- and MDA-MB-231 cells exposed to ESE-16 displayed GI_{50} concentrations of 0.31±0.62 µM and 0.27±0.06 µM, respectively (Table 4.3).

LimPyr1 displayed a GI_{50} of 19.50±1.41 µM when exposed to MCF-7 cells and 19.50±0.71 µM when exposed to MDA-MB-231 cells (Figure 4.7 E-H).

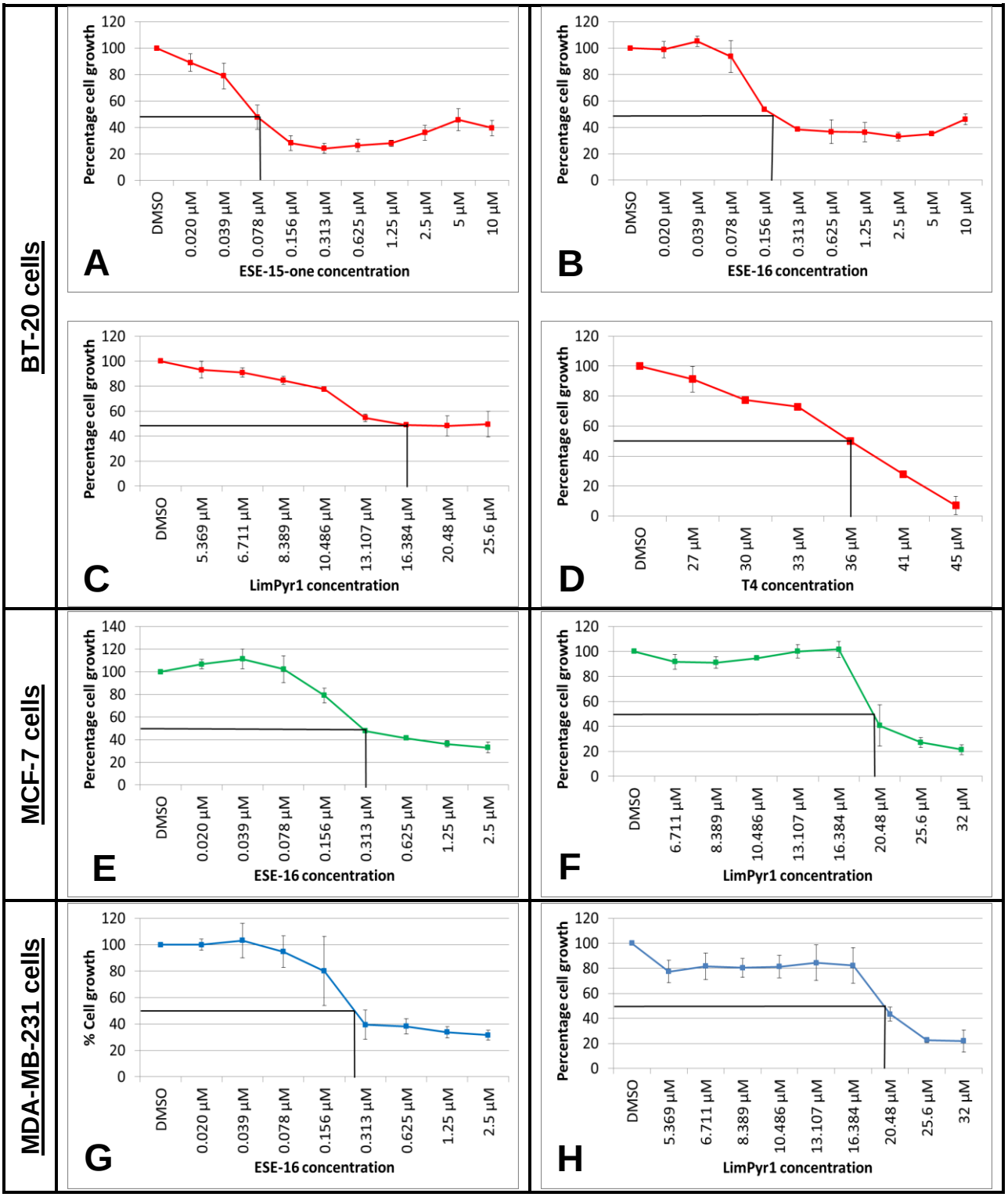

Figure 4.7: Dose response curves of breast cancer cells exposed to various microtubule regulators and T4, a compound that sensitizes cells to non-lethal doses of paclitaxel. BT-20

cells were exposed to ESE-15-one (A), ESE-16 (B), LimPyr1 (C) and T4 (D) doses. MCF-7- (E-F) and MDA-MB-231 cells (G-H) were exposed to ESE-16 and LimPyr1 doses. Cell viability is expressed as % cell growth and was calculated relative to the DMSO vehicle control. Standard deviations are represented by T-bars.

Table 4.3: Half maximum growth inhibitory concentrations (GI_{50}) for ESE-15-one, ESE-16, LimPyr1 and T4 after exposure to BT-20-, MCF-7- and MDA-MB-231 breast cancer cells for 48 hours. The GI_{50} concentration ± standard deviations of three biological repeats are displayed for each cell line exposed to the different compounds.

Compound	GI_{50} (µM)		
	BT-20	**MCF-7**	**MDA-MB-231**
ESE-15-one	0.08±0.02	-	-
ESE-16	0.22±0.04	0.31±0.62	0.27±0.06
LimPyr1	16.38±0.55	19.50±1.41	19.50±0.71
T4	36.00±1.10	-	-

4.1.6 Visualization of the cytoskeleton: Fluorescent microscopy

Cell migration was retarded in the presence of ESE-15-one and ESE-16, as illustrated by the scratch assays. Additionally, LimPyr1 induces morphological changes resulting in decreased wound healing (353). The effect of the paclitaxel sensitizing agent, T4, on cell migration has not been investigated to date. Cell migration is facilitated by the reorganization of the cellular cytoskeleton. Polymerization of the actin skeleton is partially responsible for cell movement and adhesion, and is regulated by leading and trailing edge-regulating proteins trafficked by microtubules (479,480). The effect of the four microtubule regulators (at GI_{50} concentrations) (Table 4.3) on the cytoskeleton of three breast cancer cell lines (24 hour exposure) was visualized with fluorescent microscopy employing an anti-tubulin antibody, Phalloidin (actin staining) and DAPI (nuclear staining).

MCF-7-, MDA-MB-231- and BT-20 cells displayed similar changes in the microtubule network following exposure to the microtubule regulating compounds. Cells propagated in medium only served as a negative control and cells exposed to DMSO as a vehicle control. The cells exposed to the vehicle control displayed intact microtubule networks (green), with most cells present in interphase. Actin staining (red) revealed normal stress fiber formation along the leading edges of the cells, polarizing the cells for movement. The cytoskeleton within cells grown in medium only was identical to that of the DMSO vehicle control, indicating that DMSO had no effect on the cellular cytoskeleton (Figure 4.8-4.10). MCF-7-, MDA-MB-231- and BT-20 cells exposed to paclitaxel served as a positive control for microtubule stabilization, while colchicine exposure provided a positive control for microtubule depolymerization. A 15 min exposure to latrunculin B served as a positive control for actin depolymerization (Figure 4.8-4.10).

BT-20 cells exposed to ESE-15-one and ESE-16 displayed rounded cells with depolymerized microtubules (similar to the colchicine control) and peripheral radial arrangements of actin filaments (Figure 4.8). Cells displayed no stress fiber formation and migration polarity was not evident. Similar disrupted microtubule networks were observed in MCF-7- and MDA-MB-231 cells exposed to ESE-16. However, the actin skeleton of ESE-16 exposed MCF-7- and MDA-MB-231 cells displayed an increase in stress fiber formation and disruption of cell polarity (Figure 4.9 & 4.10). This indicated that ESE-16 stabilized and accumulated F-actin in MCF-7 and MDA-MB-231 cells, potentially preventing migration. BT-20 cells exposed to T4 displayed marginal microtubule stabilization with the formation of a few stress fibers (Figure 4.8). The depolymerizing effect of LimPyr1 on the actin skeleton was evident in all cell lines (Figure 4.8-4.10) and the migration polarity seen in the vehicle control was no longer present. Additionally, LimPyr1 exposed MCF-7-, MDA-MB-231- and BT-20 cells displayed stabilized microtubules (Figure 4.8-4.10).

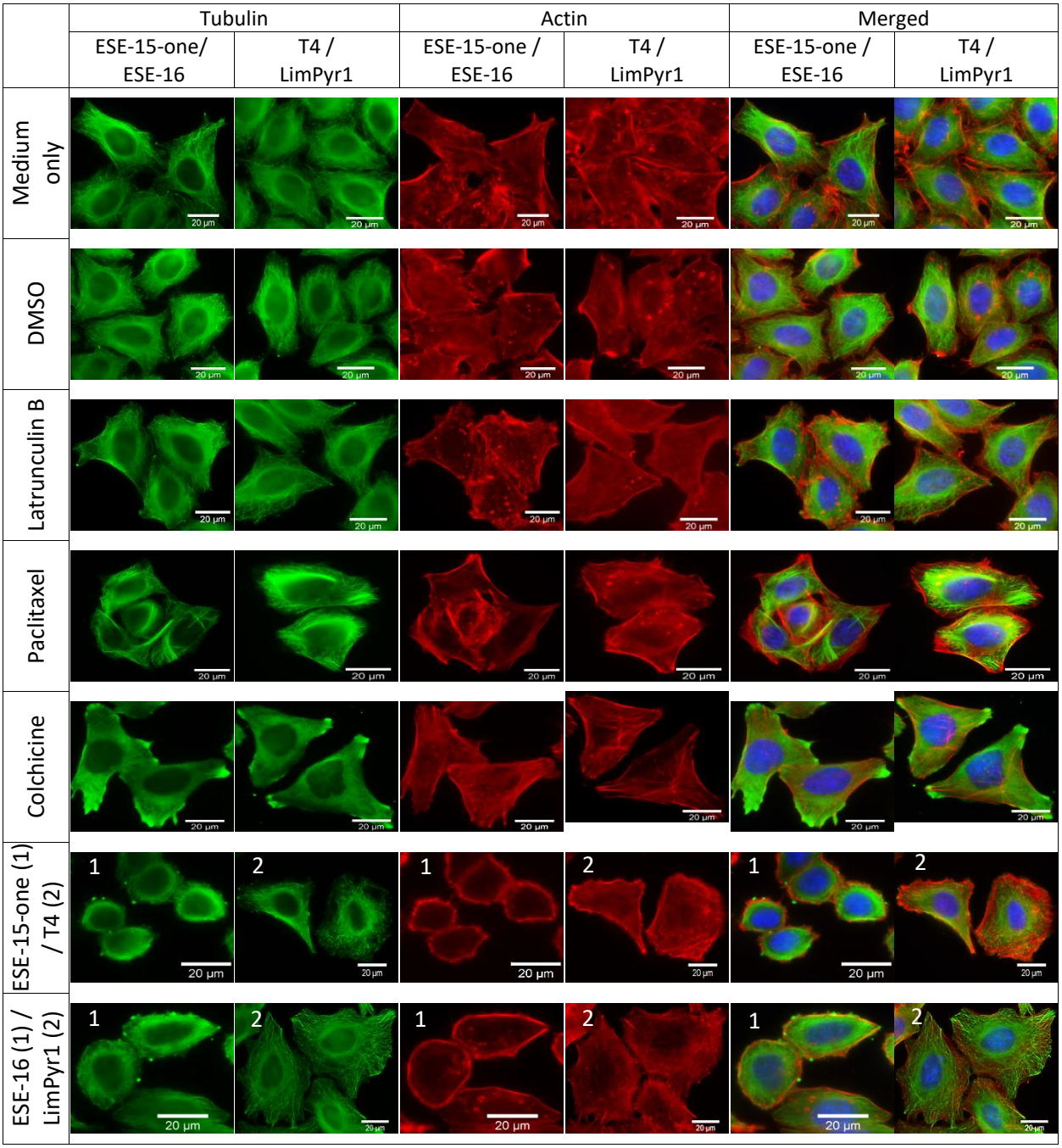

Figure 4.8: Response of the cytoskeleton of BT-20 cells exposed to various microtubule regulating agents for 24 hours. The actin (red) and microtubule (green) cytoskeleton of cells propagated in medium only were identical to cells exposed to DMSO. Latrunculin B exposure provided a positive control for actin depolymerization. Paclitaxel exposure resulted in the stabilization of the microtubules, whereas colchicine exposure resulted in the depolymerization of the microtubule network. BT-20 cells exposed to ESE-15-one and ESE-16 displayed similar microtubule morphology (microtubule depolymerization) to that of the colchicine samples. Cells appeared round with a peripheral radial arrangement of actin filaments. A slight stabilization of the microtubule network was observed in BT-20 cells exposed to T4. Additionally, a few stress fibers were observed after 24 hours. LimPyr1 induced depolymerization of the actin skeleton with a concurrent stabilization of the microtubule network. Scale bars represent 20 µm.

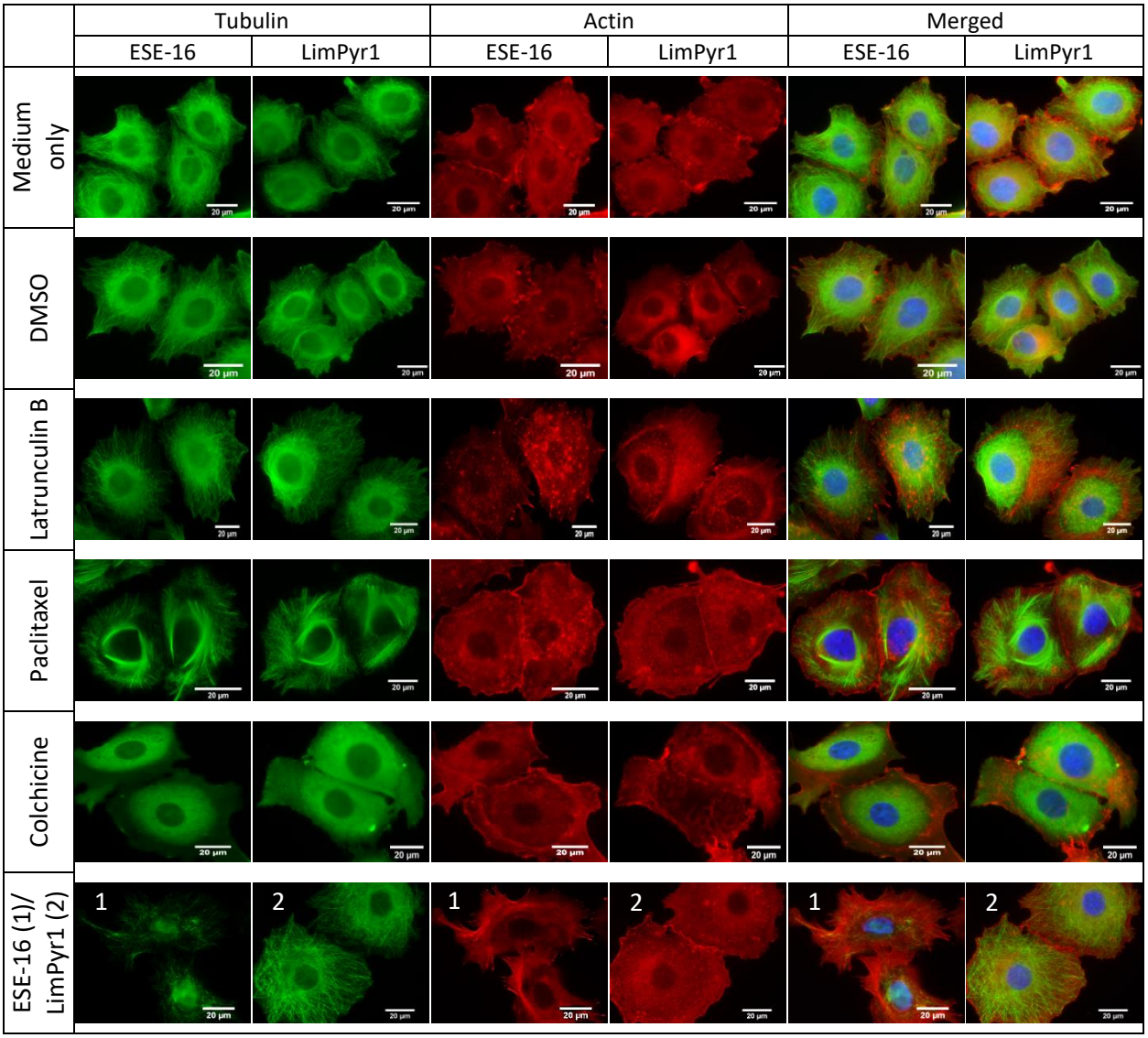

Figure 4.9: Response of the cytoskeleton of MCF-7 cells exposed to ESE-16 and LimPyr1. The negative (cells propagated in medium only) and vehicle (DMSO) controls displayed identical microtubule and actin networks, indicating that the vehicle had no effect on the MCF-7 cellular cytoskeleton. Positive controls were included for microtubule stabilization (paclitaxel), microtubule depolymerization (colchicine) and actin depolymerization (latrunculin B). Similar to the colchicine controls MCF-7 cells exposed to ESE-16 for 24 hours displayed depolymerized microtubules. Stabilization of the actin network was observed after ESE-16 exposure via the increased stress fiber formation. In contrast, LimPyr1 exposure resulted in the depolymerization of the actin skeleton and stabilization of the microtubule network. Scale bars represent 20 µm.

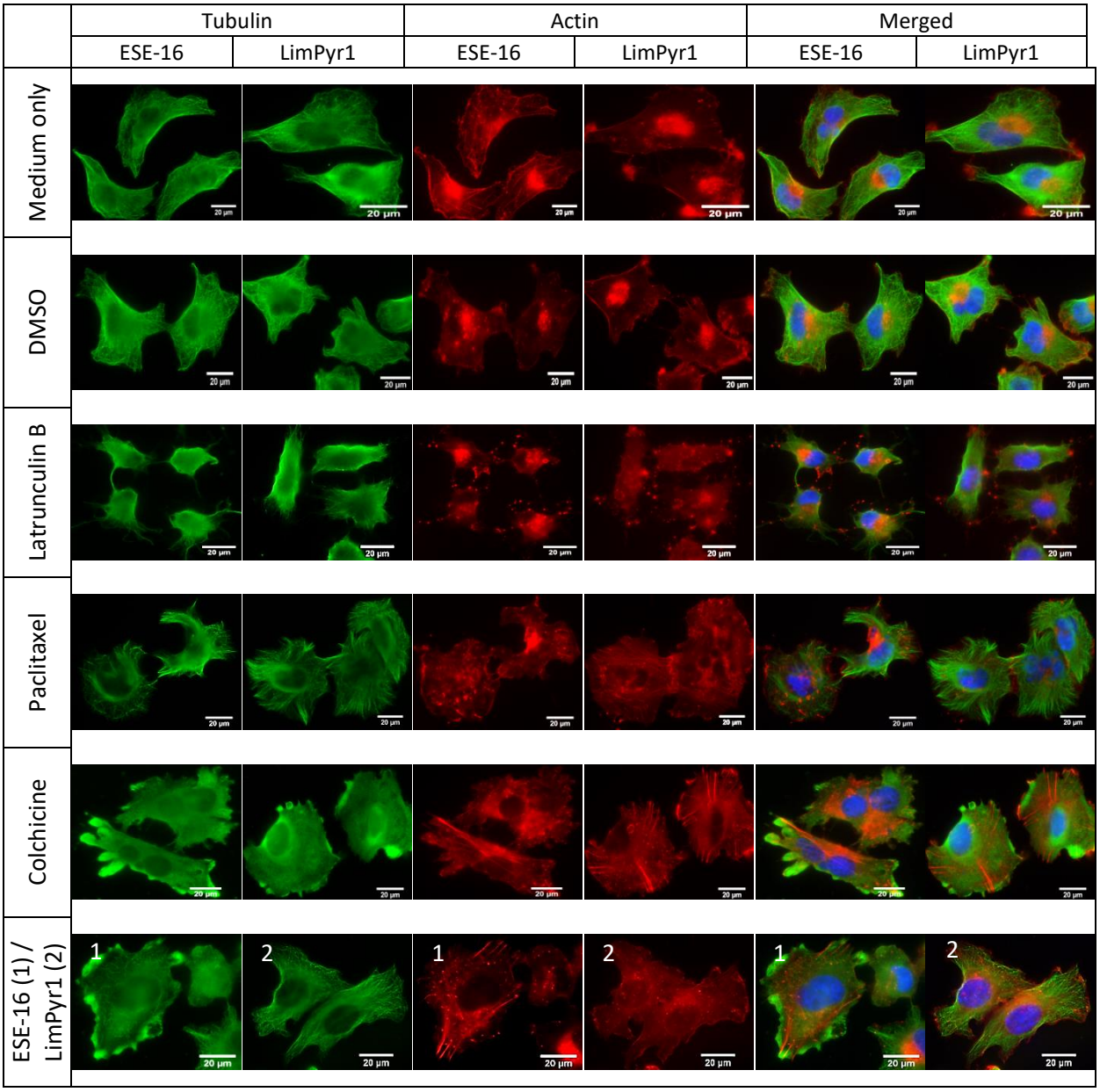

Figure 4.10: Response of the cytoskeleton of MDA-MB-231 cells exposed to ESE-16 and LimPyr1 for 24 hours. The cellular cytoskeleton of DMSO exposed cells did not differ from that of those propagated in media only, confirming that the vehicle had no effect on the cytoskeleton. MDA-MB-231 cells exposed to ESE-16 for 24 hours displayed depolymerized microtubules, similar to the colchicine positive control. An increase in stress fiber formation was observed, indicating accumulation and stabilization of F-actin, potentially decreasing cellular movement. Cells exposed to paclitaxel served as a positive control for microtubule stabilization. MDA-MB-231 cells exposed to LimPyr1 displayed similar morphological changes in the microtubule network, but to a letter extend than that in the paclitaxel positive control. Additionally, migration polarity and stress fiber formation along the leading edges of the cells (as seen in DMSO exposed cells) were decreased in LimPyr1 exposed cells. Scale bars represent 20 µm.

4.2 Radiosensitization studies

MCF-7-, MDA-MB-231- and BT-20 cells were exposed to a range of radiation doses (Additional file 1) in order to determine the lowest radiation dose that significantly decreases cell viability in each cell line. The lowest radiation dose that significantly decreased the viability of all three breast cancer cell lines was determined to be 8 Gy. Additionally, BT-20 cells were exposed to doses of ESE-15-one, ESE-16, T4 and LimPyr1, while MCF-7- and MDA-MB-231 cells were exposed to doses of ESE-16 and LimPyr1 (Additional file 2), in order to determine the lowest dose of each compound that significantly increased apoptosis in each cell line. For further experiments, breast cancer cells were exposed to the compounds for 24 hours prior to 8 Gy radiation. Termination followed 4, 24 and 48 hours after radiation for apoptotic studies, 2 and 24 hours after radiation for DNA damage and repair experiments, respectivey, and 14 days after radiation for cell survival assays.

4.2.1 Flow cytometric quantification of annexin V-FITC

To evaluate whether a 24-hour pre-exposure to low doses ESE-15-one, ESE-16, T4 and LimPyr1 prior to 8 Gy radiation induced apoptosis to a greater extent than the individual treatments, apoptosis induction was quantified via flow cytometry employing annexin V. By labeling the externalization of phosphatidylserine with an annexin V antibody this technique enables the quantification of apoptosis (91). Additionally, propidium iodide was used to measure necrotic cell death.

Breast cancer cells exposed to DMSO served as a vehicle control and showed no statistically significant differences in cell viability or apoptotic induction compared to cells propagated in growth medium only (negative controls). BT-20 cells exposed to actinomycin D, and MCF-7- and MDA-MB-231 cells exposed to vinblastine served as positive controls for apoptosis. Cells exposed to the positive controls revealed a significant decrease in cell viability with a concurrent increase in apoptosis (Figure 4.11, 4.13 and 4.15).

BT-20 cells presented with a decrease in cell viability with a concurrently increase in apoptosis when exposed to ESE-15-one (88.27±3.51% and 10.96±3.37%), ESE-16 (86.41±1.49% and 12.56±1.01%), LimPyr1 (85.21±2.51% and 13.23±1.42 %) and 8 Gy radiation (85.73±1.86% and 13.60±1.53% (DMEM/F-12), 85.90±0.80% and 12.88±1.15% (RPMI)), compared to DMSO (90.68±0.24% and 8.76±0.33% (DMEM/F-12), 90.49±1.02% and 8.73±1.05% (RPMI)), respectively (Table 4.4). BT-20 cells pre-treated with ESE-15-one (12.72±3.03%), ESE-16 (15.83±1.25%), T4 (14.93±4.42%) and LimPyr1 24 hours prior to radiation (19.59±1.11%) displayed a significant increase in apoptosis compared to the vehicle control. Additionally, cells exposed to ESE-15-one-, ESE-16-, T4- or LimPyr1 24 hours prior to radiation displayed a significant decrease in cell viability (86.48±3.22%, 83.35±0.76%, 83.74±4.24% and 78.63±1.44, respectively) compared to DMSO (Figure 4.11). In order to identify the analogues (ESE-15-one or ESE-16 and T4 or LimPyr1) with the greater potential to induce cell death in combination with radiation, the combination treatments were compared to the individual treatment results. BT-20 cells exposed to ESE-15-one or T4 prior to 8 Gy radiation revealed no significant differences in cell viability or apoptosis when compared to the cells exposed to the individual treatment conditions (Figure 4.12). ESE-16 and LimPyr1 pre-treated BT-20 cells displayed an increased number of apoptotic cells with a concurrent decrease in cell viability when compared to cells exposed to the compounds individually. Additionally, decreased cell viability and increased apoptotic cells were observed in LimPyr1 pre-treated cells compared to cells exposed to 8 Gy radiation only. These results suggested that the analogues ESE-16 and LimPyr1 may be more effective in sensitizing the cells to radiation in this experimental setup, and were thus selected as the pre-treatment agents for the remainder of the study (Figure 4.12).

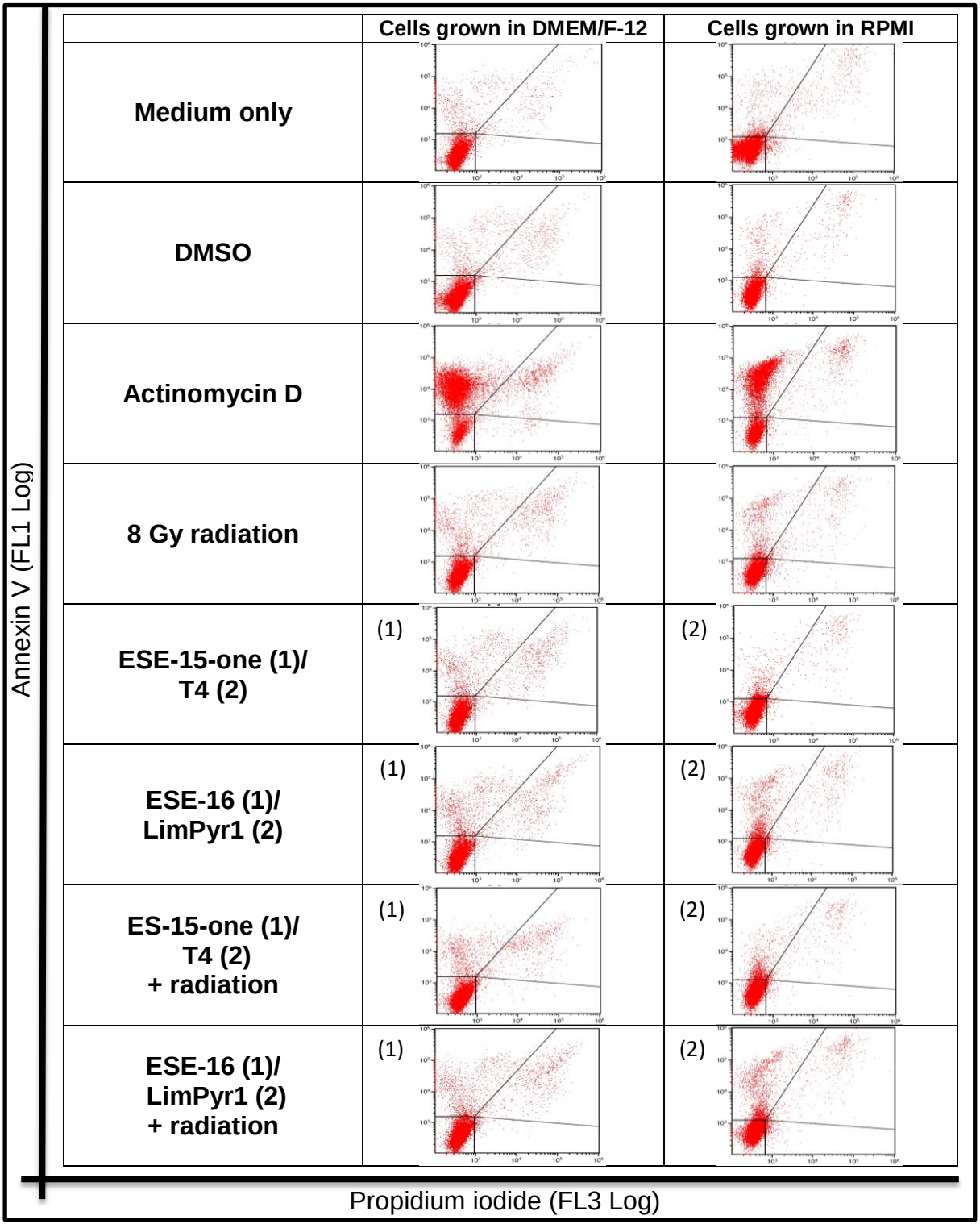

Figure 4.11: Representative flow cytometric dot plots of annexin V-FITC indicating apoptosis in BT-20 cells exposed to various treatment modalities. Annexin V-FITC (FL1 Log) was used to label apoptotic cells and was plotted against permeable cells stained with propidium iodide (FL3 Log). BT-20 cells were propagated in growth media only (negative control), exposed to DMSO and actinomycin D as vehicle and positive apoptotic controls, respectively, and exposed to various treatment modalities. The bottom left corner: viable cells; top left and right quadrants: apoptotic cells; bottom right quadrant: necrotic cells.

Table 4.4: Apoptotic induction measured by annexin V-FITC quantification in BT-20 cells exposed to various treatment conditions. Data were generated, using Kaluza Analysis software version 1.5 (FL, USA), and analyzed using the ANOVA-single factor model. Statistical significance was calculated, using a two-tailed Student's *t*-test. In the table below the averaged percentage (M%) and standard deviations (SD) of three biological repeats are displayed for viable, apoptotic and necrotic BT-20 cells. Cells exposed to DMSO and the individual treatment conditions served as baselines when statistically significant differences (*P*-value <0.05) were calculated.

		Medium only	DMSO	Actinomycin D	ESE-15-one	ESE-16	8 Gy radiation	ESE-15-one + radiation	ESE-16 + radiation
Viable	M%±SD	91.45±1.31	90.68±0.24	16.90±2.24	88.27±3.51	86.41±1.49	85.73±1.86	86.48±3.22	83.35±0.76
	P-value when compared to:								
	DMSO	0.37	-	**5.75E-07**	**3.57E-03**	**8.09E-03**	**1.03E-02**	**0.03**	**8.86E-05**
	ESE-15-one							0.19	
	ESE-16								**0.03**
	Radiation							0.19	0.11
Apoptosis	M%±SD	8.06±1.33	8.76±0.33	82.38±2.29	10.96±3.37	12.56±1.01	13.60±1.53	12.72±3.03	15.83±1.25
	P-value when compared to:								
	DMSO	0.43	-	**6.49E-07**	**2.25E-03**	**3.48E-03**	**5.80E-03**	**1.13E-02**	**6.90E-04**
	ESE-15-one							0.09	
	ESE-16								**0.02**
	Radiation							0.11	0.12
Necrosis	M%±SD	0.48±0.26	0.56±0.32	0.72±0.19	0.78±0.25	1.03±0.82	0.67±0.34	0.79±0.40	0.82±0.49
	P-value when compared to:								
	DMSO	0.76	-	0.50	0.71	0.39	0.41	0.70	0.49
	ESE-15-one							0.80	
	ESE-16								0.73
	Radiation							0.90	0.68
		Medium only	DMSO	Actinomycin D	T4	LimPyr1	8 Gy radiation	T4 + radiation	LimPyr1 + radiation
Viable	M%±SD	90.13±1.27	90.49±1.02	46.28±4.66	86.54±3.48	85.21±2.51	85.90±0.80	83.74±4.24	78.63±1.44
	P-value when compared to:								
	DMSO	0.68	-	**7.55E-06**	0.08	**1.15E-02**	**1.39E-03**	**0.02**	**5.07E-05**
	T4							0.40	
	LimPyr1								**1.71E-02**
	Radiation							0.43	**1.56E-03**
Apoptosis	M%±SD	8.57±0.93	8.73±1.05	52.47±5.18	12.16±3.21	13.23±1.42	12.88±1.15	14.93±4.42	19.59±1.11
	P-value when compared to:								
	DMSO	0.83	-	**1.30E-05**	0.10	**4.65E-03**	**4.22E-03**	**0.03**	**4.37E-05**
	T4							0.40	
	LimPyr1								**3.64E-03**
	Radiation							0.48	**1.90E-03**
Necrosis	M%±SD	1.30±0.69	0.79±0.40	1.26±0.55	1.29±0.43	1.56±1.15	1.22±1.03	1.34±0.93	1.78±1.40
	P-value when compared to:								
	DMSO	0.25	-	0.24	0.17	0.25	0.47	0.32	0.22
	T4							0.95	
	LimPyr1								0.85
	Radiation							0.88	0.61

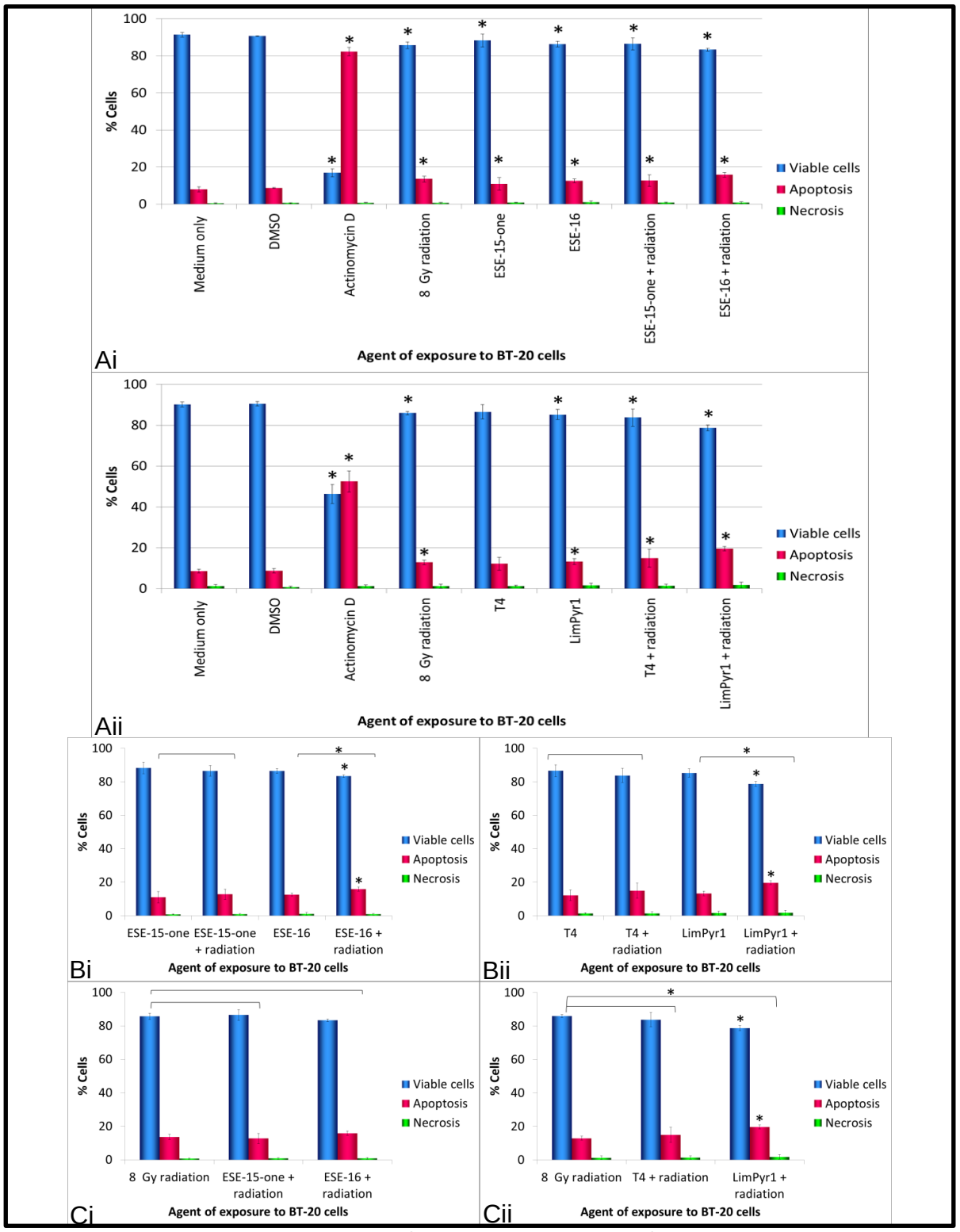

Figure 4.12: Graphical representation of annexin V-FITC quantification in BT-20 cells exposed to various treatment conditions. BT-20 cells exposed to ESE-15-one, ESE-16, LimPyr1 and the combination treatments displayed a statistically significant increase in apoptotic cells (Ai and Aii). BT-20 cells pre-treated with ESE-16 and LimPyr1 displayed a significant increase in apoptosis compared to cells exposed to the compounds only (Bi and Bii). Cell viability was significantly decreased in cells pre-treated with LimPyr1 compared to samples exposed to 8 Gy

radiation only (Cii). Apoptosis was not significantly induced in BT-20 cells pre-treated with ESE-15-one, ESE-16 or T4 compared to cells exposed to 8 Gy radiation only (Ci and Cii). BT-20 cells presensitized with T4 did not show any significant difference in cell viability compared to cells exposed to T4 only (Bii). Three biological repeats were completed for each experiment. The averages of viable, apoptotic and necrotic cells are displayed on the bar graph and the standard deviations are indicated by T-bars. A *P*-value <0.05 was considered statistically significant and are indicated with an asterisk (*).

ESE-16 did not decrease cell viability (90.79±4.99%) or inducing apoptosis (8.79±4.94%) in MCF-7 cells. However, ESE-16 exposed MDA-MB-231 cells displayed a significant decrease in cell viability (89.93±1.81%) and increased apoptosis (9.69±1.89%) compared to DMSO (93.93±1.31% and 4.98±1.39% (MCF-7), 94.98±0.67% and 4.70±0.56% (MDA-MB-231), respectively) (Figures 4.13 & 4.15). MCF-7- and MDA-MB-231 cells exposed to LimPyr1 revealed a significant decrease in cell viability (91.32±0.59% and 87.73±4.50%) with a concurrent increase in apoptotic cells (8.24±0.78% and 11.51±4.28%), compared to the vehicle controls (96.89±0.84% and 2.73±0.69% (MCF-7), 95.81±3.13% and 3.61±2.74% (MDA-MB-231)), respectively (Table 4.5 & 4.6). Radiation exposure statistically significantly decreased cell viability in MCF-7- (84.60±2.75% (DMEM), 85.65±4.80% (RPMI)) and MDA-MB-231 cells (84.81±1.41% (DMEM), 77.82±3.66% (RPMI)). Pre-treatment of MCF-7- and MDA-MB-231 cells with ESE-16 significantly increased apoptosis (25.39±1.84% and 18.76±2.04%) and decreased cell viability (73.68±2.22% and 80.58±2.10%) compared to DMSO, ESE-16-exposed samples and cells exposed to 8 Gy radiation only. Similarly, LimPyr1 pre-treated MCF-7- (30.69±8.36%) and MDA-MB-231 cells (29.55±2.44%) displayed a significant increase in apoptotic induction compared to the vehicle control, LimPyr1-exposed cells and cells exposed to 8 Gy radiation only (Figures 4.14 & 4.16).

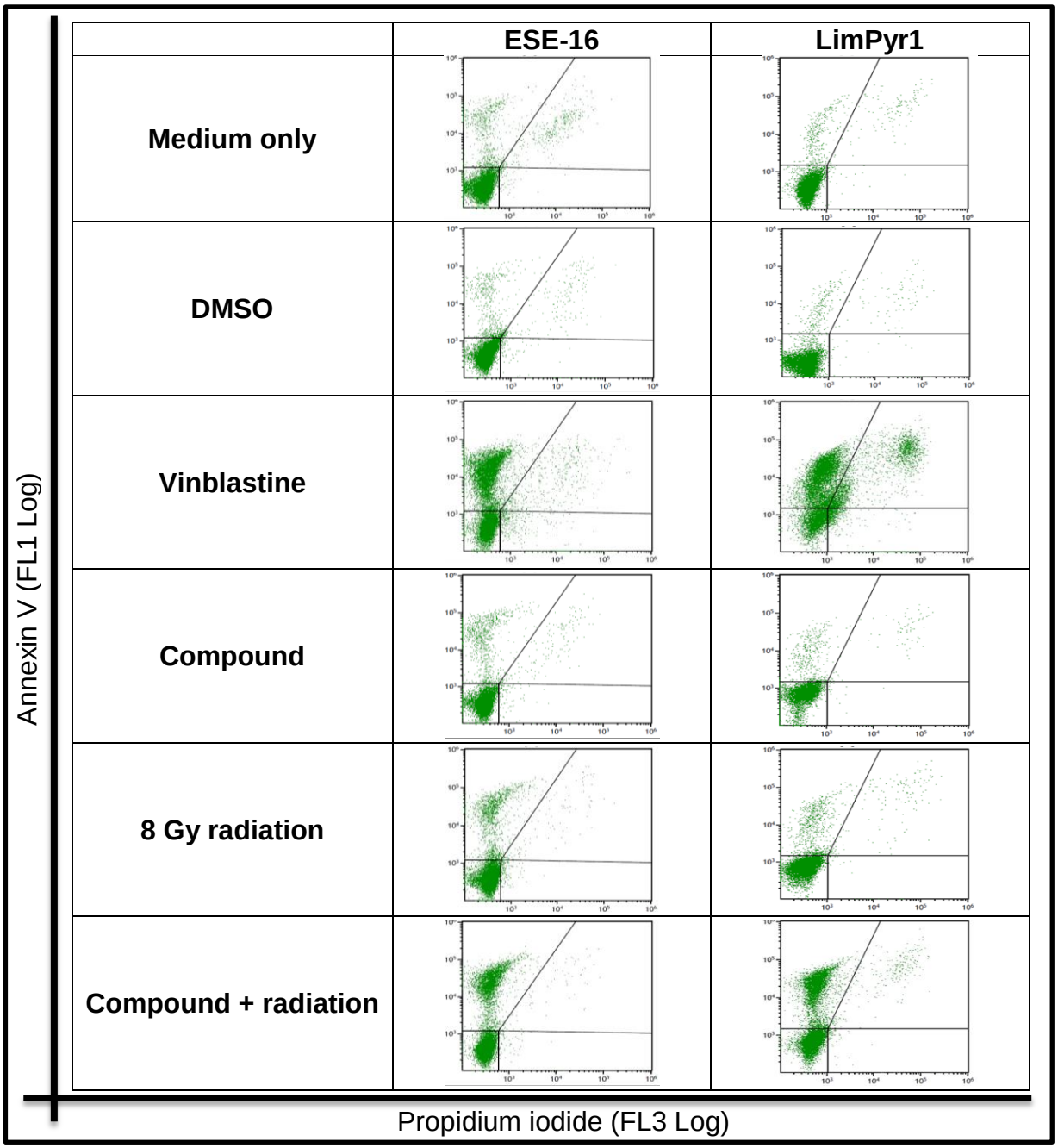

Figure 4.13: Representative flow cytometric dot plots of annexin V-FITC indicating apoptosis in MCF-7 cells exposed to various treatment modalities. Apoptosis was quantified in MCF-7 cells by plotting annexin V-FITC staining (FL1 Log) against propidium iodide which stained permeable cells (FL3 Log). MCF-7 cells were exposed to several controls, individual- or combination treatment conditions. The bottom left corner: viable cells; top left and right quadrants: apoptotic cells; bottom right quadrant: necrotic cells.

Table 4.5: Apoptotic induction measured by annexin V-FITC quantification in MCF-7 cells exposed to various treatment conditions. Kaluza Analysis software version 1.5 (FL, USA) was used to generate data of three biological repeats. The ANOVA-single factor model and a two-tailed Student's *t*-test were used to analyze the data and calculate statistically significant differences, respectively. The table summarizes the averaged percentage (M%) and standard deviations (SD) for viable, apoptotic and necrotic MCF-7 cells. Statistically significant differences (*P*-value <0.05) were calculated using the vehicle (DMSO) and cells exposed to the individual treatment conditions as baselines.

			Medium only	DMSO	Vinblastine	Compound	8 Gy radiation	Compound + radiation
ESE-16	Viable	M%±SD	93.89±2.45	93.93±1.31	54.74±8.89	90.79±4.99	84.60±2.75	73.68±2.22
		P-value when compared to:						
		DMSO	0.98	-	**1.26E-04**	0.27	**8.66E-04**	**4.19E-06**
		ESE-16						**1.55E-03**
		Radiation						**8.28E-04**
	Apoptosis	M%±SD	5.49±2.32	4.98±1.39	43.30±7.85	8.79±4.94	14.77±2.99	25.39±1.84
		P-value when compared to:						
		DMSO	0.73	-	**7.26E-05**	0.19	**1.01E-03**	**2.06E-06**
		ESE-16						**1.45E-03**
		Radiation						**9.16E-04**
	Necrosis	M%±SD	0.63±0.20	1.09±0.44	1.96±1.08	0.41±0.27	0.63±0.39	0.93±0.52
		P-value when compared to:						
		DMSO	0.16	-	0.18	0.07	0.17	0.66
		ESE-16						0.18
		Radiation						0.40
LimPyr1	Viable	M%±SD	96.89±0.84	97.10±0.64	31.62±7.02	91.32±0.59	85.65±4.80	67.01±8.34
		P-value when compared to:						
		DMSO	0.74	-	**8.71E-05**	**2.04E-03**	**1.49E-02**	**3.38E-03**
		LimPyr1						**0.03**
		Radiation						**0.03**
	Apoptosis	M%±SD	2.73±0.69	2.46±0.54	60.83±8.03	8.24±0.78	13.62±4.09	30.69±8.36
		P-value when compared to:						
		DMSO	0.62	-	**2.31E-04**	**2.11E-03**	**9.40E-03**	**4.29E-03**
		LimPyr1						**0.04**
		Radiation						**0.03**
	Necrosis	M%±SD	0.39±0.16	0.44±0.14	7.55±2.83	0.45±0.19	0.73±0.71	2.30±1.96
		P-value when compared to:						
		DMSO	0.70	-	**1.22E-02**	0.97	0.52	0.18
		LimPyr1						0.29
		Radiation						0.26

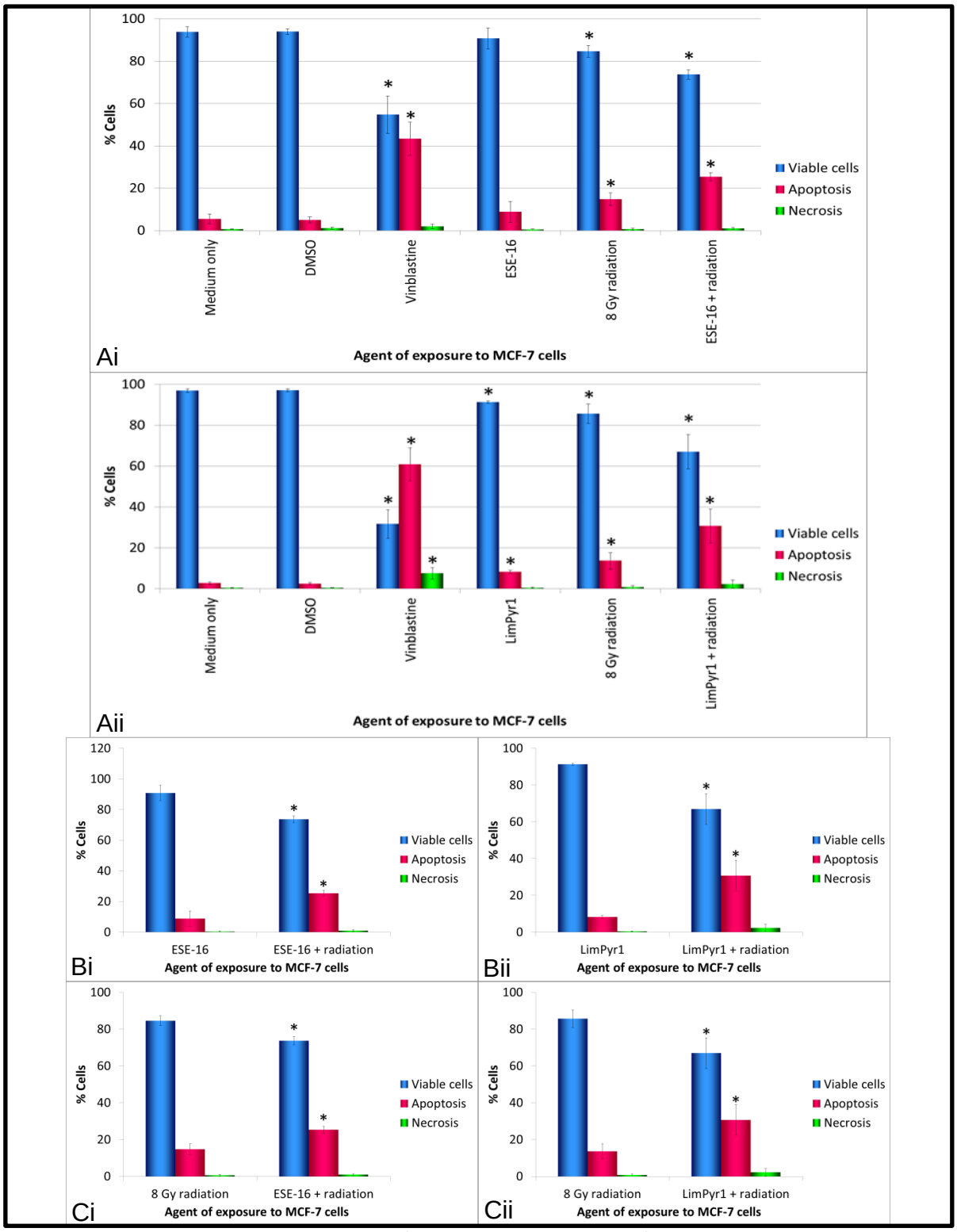

Figure 4.14: Graphical representation of annexin V-FITC quantification in MCF-7 cells exposed to various treatment conditions. MCF-7 cells exposed to LimPyr1, 8 Gy radiation, ESE-16 or LimPyr1 24 hours prior to radiation displayed a significant increase in apoptotic cells with a concurrent decrease in cell viability (Ai and Aii). MCF-7 cells pre-treated with ESE-16 and LimPyr1 displayed a significant increase in apoptosis induction compared to cells exposed to ESE-16 or LimPyr1 only (Bi and Bii) and cells exposed to 8 Gy radiation only (Ci and Cii). The

averages of viable, apoptotic and necrotic cells of three biological repeats are displayed on the bar graph and the standard deviations are indicated by T-bars. A *P*-value <0.05 was considered statistically significant and are indicated with an asterisk (*).

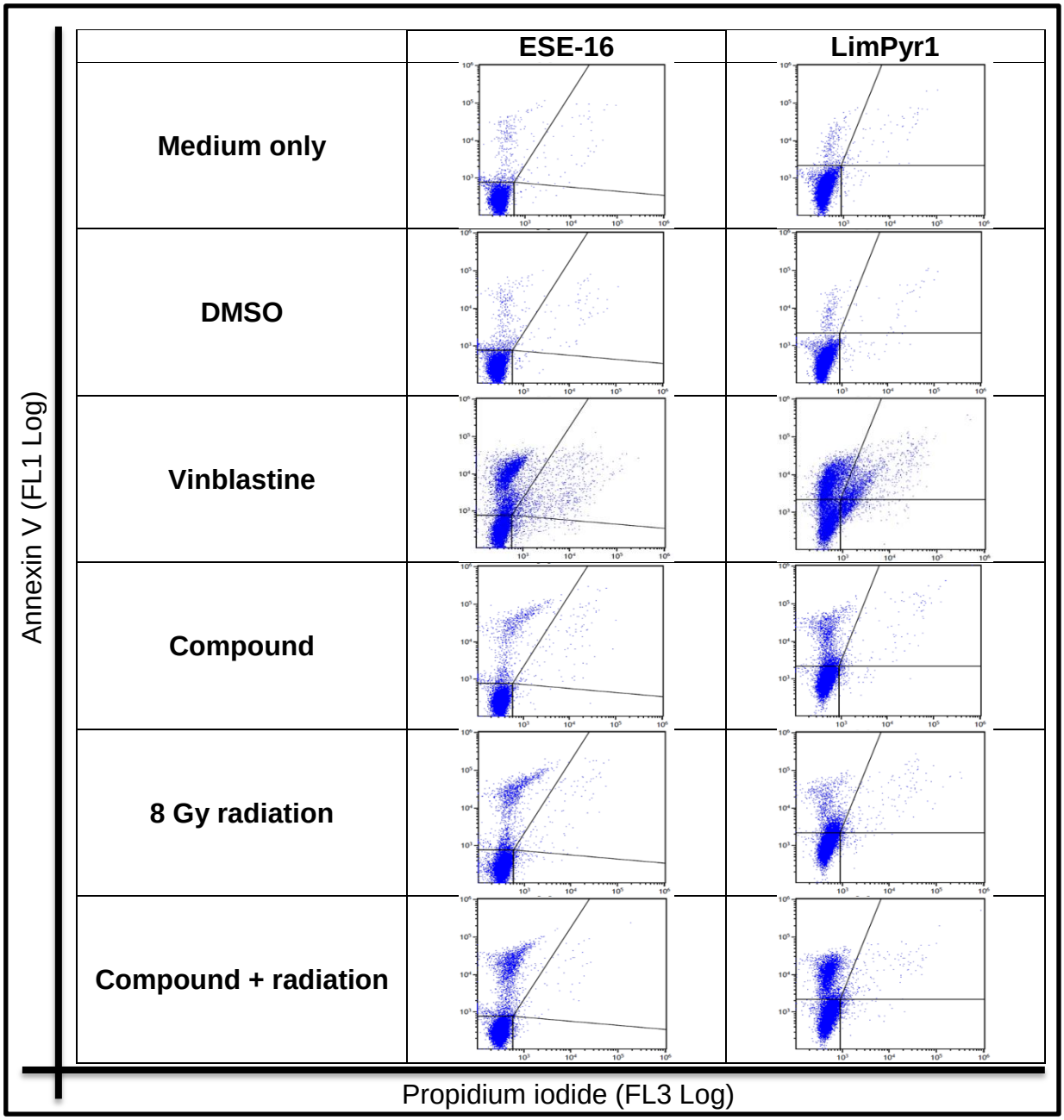

Figure 4.15: Representative flow cytometric dot plots of annexin V-FITC indicating apoptosis in MDA-MB-231 cells exposed to various treatment modalities. The dot plots were obtained from MDA-MB-231 cells exposed to DMSO as a vehicle control, vinblastine as a positive method control, ESE-16, LimPyr1, 8 Gy radiation and ESE-16 or LimPyr1 24 hours prior to radiation by plotting apoptotic cells (annexin V-FITC (FL1 Log)) against necrotic cells (propidium iodide (FL3 Log)). The bottom left corner: viable cells; top left and right quadrants: apoptotic cells; bottom right quadrant: necrotic cells.

Table 4.6: Apoptotic induction measured by annexin V-FITC quantification in MDA-MB-231 cells exposed to various treatment conditions. Data were generated and analyzed using Kaluza Analysis software version 1.5 (FL, USA) and the ANOVA-single factor model, respectively. A two-tailed Student's *t*-test was used to calculate statistical significance. The averaged percentage (M%) and standard deviations (SD) for viable, apoptotic and necrotic MDA-MB-231 cells are summarized in the table below. The vehicle control (DMSO) and cells exposed to the individual treatment conditions served as baselines for the calculation of statistical significance (*P*-value <0.05).

			Medium only	DMSO	Vinblastine	ESE-16	8 Gy radiation	ESE-16 + radiation
ESE-16	Viable	M%±SD	95.66±0.93	94.98±0.67	47.80±10.01	89.93±1.81	84.81±1.41	80.58±2.10
		P-value when compared to:						
		DMSO	0.36	-	**1.24E-03**	**1.06E-02**	**3.50E-04**	**3.45E-04**
		ESE-16						**4.27E-03**
		Radiation						**0.04**
	Apoptosis	M%±SD	4.14±0.90	4.70±0.56	50.37±10.77	9.69±1.89	14.37±1.70	18.76±2.04
		P-value when compared to:						
		DMSO	0.41	-	**1.84E-03**	**1.18E-02**	**7.28E-04**	**3.27E-04**
		ESE-16						**4.84E-03**
		Radiation						**4.59E-02**
	Necrosis	M%±SD	0.20±0.04	0.31±0.12	1.83±0.77	0.37±0.08	0.83±0.32	0.66±0.22
		P-value when compared to:						
		DMSO	0.21	-	**0.03**	0.50	0.06	0.07
		ESE-16						0.09
		Radiation						0.49
LimPyr1	Viable	M%±SD	95.81±3.13	96.75±0.93	33.12±12.39	87.73±4.50	77.82±3.66	68.79±1.65
		P-value when compared to:						
		DMSO	0.64	-	**8.92E-04**	**0.03**	**9.65E-04**	**1.39E-05**
		LimPyr1						**2.38E-03**
		Radiation						**1.76E-02**
	Apoptosis	M%±SD	3.61±2.74	2.67±1.01	58.69±13.27	11.51±4.28	21.43±3.71	29.55±2.44
		P-value when compared to:						
		DMSO	0.61	-	**1.88E-03**	**0.03**	**1.08E-03**	**6.12E-05**
		LimPyr1						**3.16E-03**
		Radiation						**3.40E-02**
	Necrosis	M%±SD	0.59±0.40	0.57±0.13	8.18±2.20	0.76±0.23	0.75±0.43	1.66±0.87
		P-value when compared to:						
		DMSO	0.93	-	**3.91E-03**	0.27	0.52	0.10
		LimPyr1						0.16
		Radiation						0.18

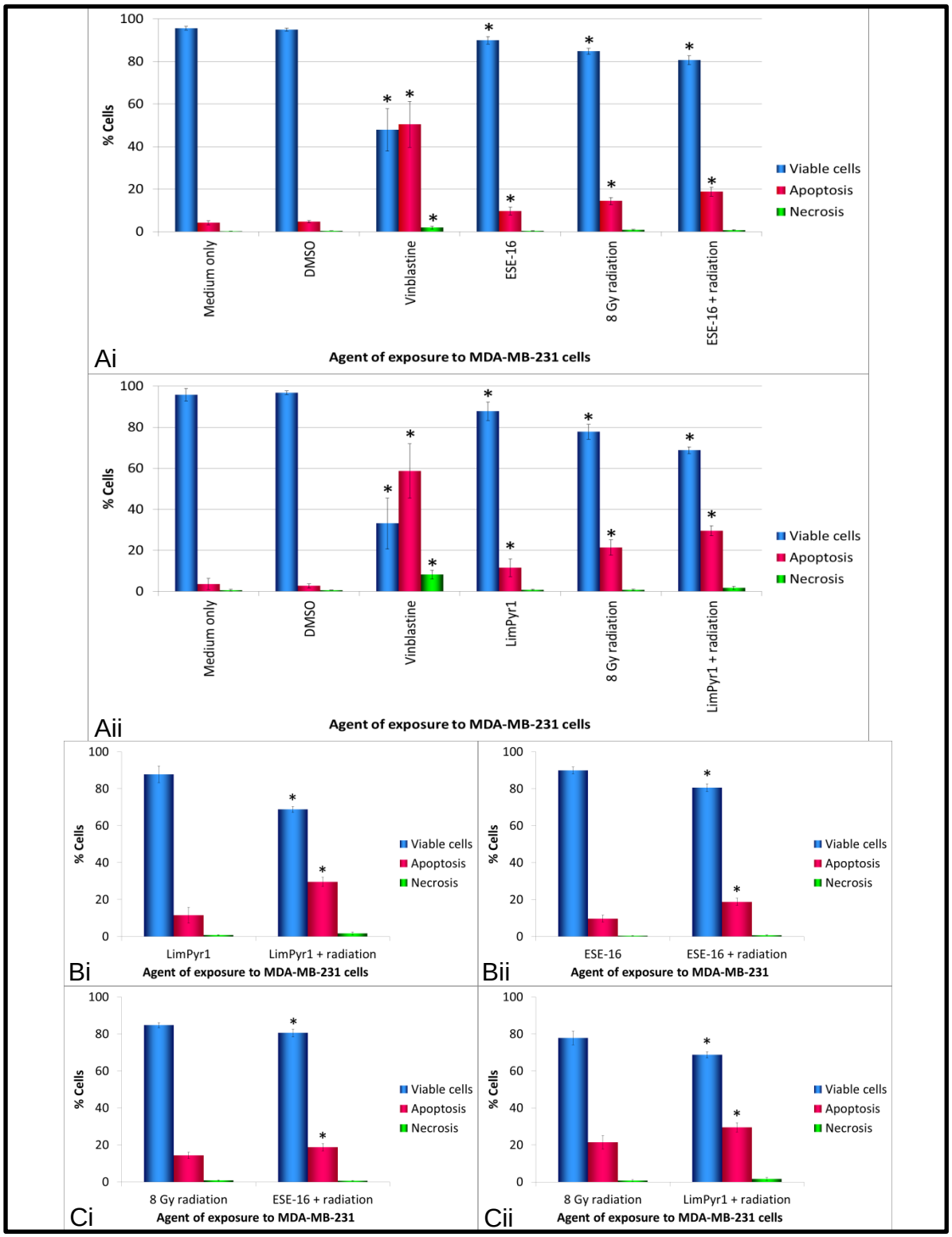

Figure 4.16: Graphical representation of annexin V-FITC quantification in MDA-MB-231 cells exposed to various treatment conditions. MDA-MB-231 cells exposed to ESE-16, LimPyr1, 8 Gy radiation and the combination treatment conditions displayed a significant increase in apoptosis (Ai and Aii). ESE-16 and LimPyr1 pre-treated MDA-MB-231 cells displayed a significant increase in apoptosis compared to cells exposed to the compounds alone (Bi and Bii) and 8 Gy radiation only (Ci and Cii). The bars represent the averages of viable, apoptotic and necrotic cells for three

biological repeats and the standard deviations are indicated by T-bars. A *P*-value <0.05 was considered statistically significant and are indicated with an asterisk (*).

4.2.2 Cell cycle analysis

The effect of microtubule regulating agents and radiation on the cell cycle progression of MCF-7-, MDA-MB-231- and BT-20 cells was evaluated 24 hours after radiation via flow cytometry. The G_2/M phase is the most radiosensitive phase of the cell cycle. Microtubule regulating drugs induce a mitotic block and expose the cells' chromosomes to radiation, resulting in increased DNA damage (414,417).

MCF-7-, MDA-MB-231- and BT-20 cells grown in medium only revealed no significant differences in the cell cycle distribution compared to cells exposed to DMSO (vehicle control). BT-20 cells were exposed to actinomycin D, and MCF-7- and MDA-MB-231 cells were exposed to vinblastine as positive controls for apoptosis. Cells exposed to the positive controls revealed a significant increase in the sub-G_1 apoptotic phase (Tables 4.7-4.9).

BT-20 cells displayed a statistically significant decrease in the G_1 phase with a concurrent increase in the sub-G_1 phase when exposed to ESE-15-one (50.95±1.84% and 16.96±6.01%), ESE-16 (48.29±0.64% and 23.77±0.75%), T4 (57.47±1.20% and 8.13±3.91%), LimPyr1 (48.49±6.48% and 5.92±2.38%) and 8 Gy radiation (33.13±11.34% and 20.49±5.37% (DMEM/F-12), 33.90±3.33% and 4.34±1.60% (RPMI)), compared to the vehicle control (57.17±3.49% and 7.87±3.74% (DMEM/F-12), 61.89±3.02% and 2.27±0.46% (RPMI). Additionally, the G_2/M phase was significantly increased in cells exposed to LimPyr1 (35.50±5.14%) and 8 Gy radiation (47.76±10.31% (DMEM/F-12) and 52.09±3.60% (RPMI)), compared to DMSO (27.87±4.74% (DMEM/F-12) and 27.96±1.20% (RPMI)) (Figure 4.17). BT-20 cells presented with a significant increase in the sub-G_1 and G_2/M phases, while the G_1 phase of was significantly decreased when pre-treated with ESE-15-one (15.68±5.87%, 48.77±9.94% and 28.00±3.01%, respectively) and ESE-16 (25.75±1.01%, 36.64±0.43% and

28.99±0.67%, respectively) (Table 4.7). ESE-15-one pre-treated cells displayed a significant decrease in the G_1 phase with a concurrent increase in the G_2/M phase, compared to cells exposed to ESE-15-one only. Similarly, cell cycle analysis of ESE-16 pre-treated cells displayed an increase in the G_2/M phase and a decrease in the G_1 population compared to the cells exposed to ESE-16 only. No significant differences were observed in the cell cycle distributions of the ESE-15-one and ESE-16/radiation combination therapies when compared to cells exposed to 8 Gy radiation only (Figure 4.18). As ESE-15-one pre-treated cells failed to increase the externalization of phosphatidylserine (as quantified by annexin V) more so than the individual treatments at these early time-points, ESE-16 was selected for all subsequent sensitization studies.

BT-20 cells displayed increased cell numbers in the sub-G_1 and G_2/M phases, while the percentage of cells in the G_1 phase was significantly decreased when exposed to T4 (7.97±4.23%, 41.14±10.48% and 41.21±11.68%, respectively) or LimPyr1 (4.65±1.21%, 63.63±6.61% and 23.69±5.47%, respectively) 24 hours prior to radiation. (Figure 4.17). Pre-treatment of BT-20 cells with T4 or LimPyr1 significantly decreased the G_1 phase, while increasing the G_2/M phase, compared to cells exposed to the compounds individually. T4 pre-treated BT-20 cells showed no changes in cell cycle distribution compared to cells exposed to 8 Gy radiation only. However, LimPyr1 pre-treated cells displayed a significant decrease in the G_1 phase, with a concurrent increase in the mitotic phase, compared to the 8 Gy radiation only sample (Figure 4.18). These results, in combination with results obtained from the annexin V quantification, identified LimPyr1 as the most successful candidate (compared to T4) to increase apoptotic cell death in combination with radiation. LimPyr1 was thus selected to pre-treat cells prior to radiation exposure for the remainder of the study.

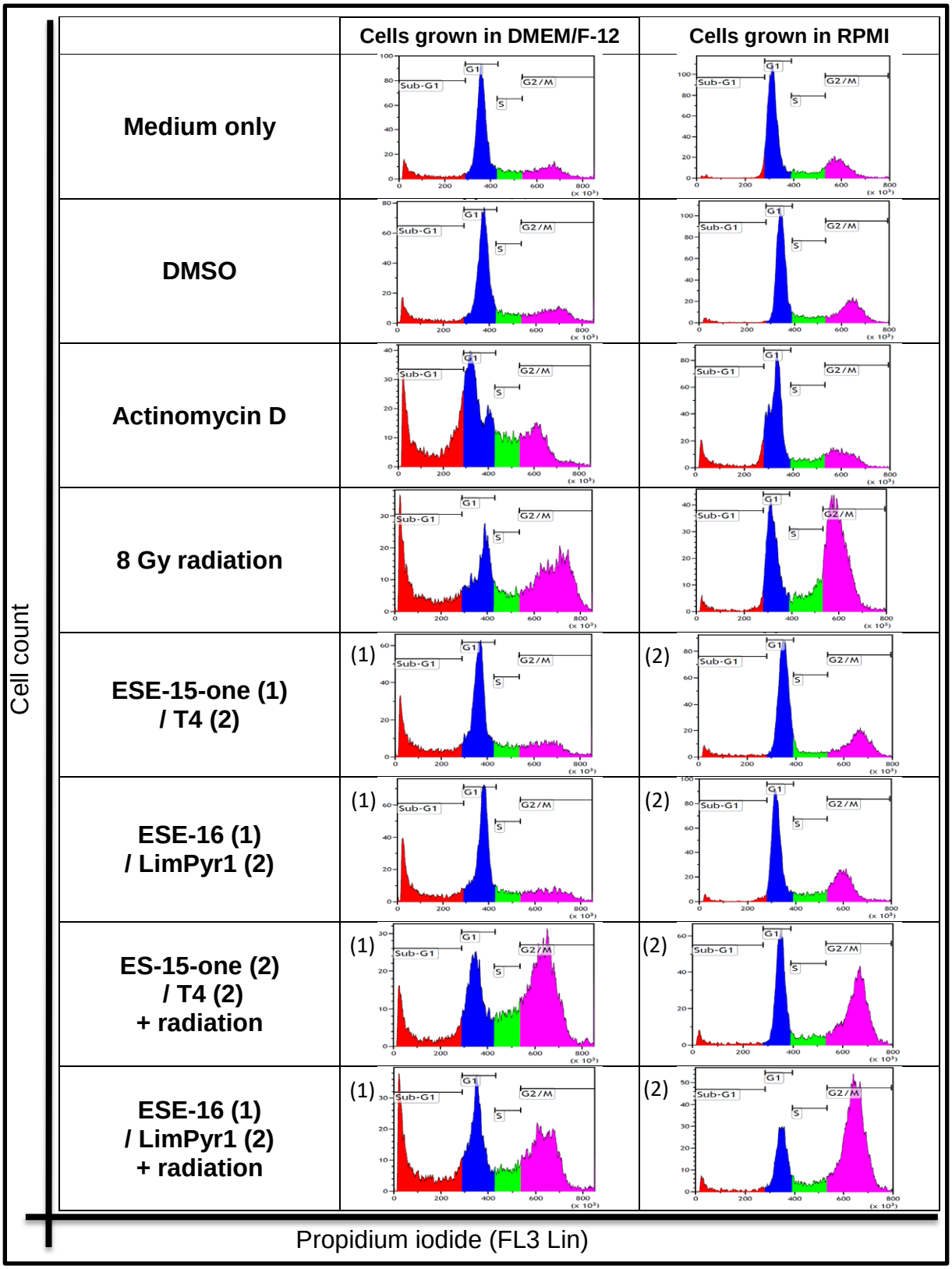

Figure 4.17: Histograms representing the cell cycle distributions of BT-20 cells exposed to various treatment conditions. Histograms were obtained by plotting the number of cells against propidium iodide (FL3 Lin). BT-20 cells were propagated in medium only (negative control) or exposed to DMSO as a vehicle control. Actinomycin D was used as a positive method control. BT-20 cells were exposed to various microtubule regulating agents and 8 Gy radiation.

Additionally, BT-20 cells were pre-treated with ESE-15-one, ESE-16, T4 or LimPyr1 24 hours prior to radiation.

MCF-7 cells exposed to ESE-16 displayed a small but statistically significant increase in the sub-G_1 phase (2.12±0.04%) compared to the vehicle control (1.52±0.07%). LimPyr1-exposure significantly increased the sub-G_1 (7.73±1.24%) and G_2/M phases (60.04±1.94%), while decreasing the G_1 population (16.81±0.54%) in MCF-7 cells, compared to DMSO (3.46±0.70%, 34.70±3.56% and 43.87±4.81%, respectively) (Figure 4.19). A significant increase in the sub-G_1 (3.89±0.24% (DMEM) and 8.70±0.86% (RPMI)) and G_2/M phase (62.98±6.61% (DMEM) and 64.11±0.00% (RPMI)) was observed in MCF-7 cells exposed to 8 Gy radiation, compared to DMSO (1.52±0.07% and 39.56±4.14 (DMEM), 3.46±0.70% and 34.70±3.56% (RPMI), respectively). Additionally, the S (5.00±0.81% (DMEM) and 10.03±3.73% (RPMI)) and G_1 phase (25.81±2.60% (DMEM) and 15.47±0.62% (RPMI)) was significantly decreased in MCF-7 cells 24 hours after radiation compared to DMSO (7.88±1.29% and 51.01±3.79% (DMEM), 17.97±2.47% and 43.87±4.81% (RPMI), respectively) (Table 4.8). MCF-7 cells exposed to ESE-16 24 hours prior to radiation displayed a significant increase in the sub-G_1 (6.27±0.72%) and G_2/M populations (61.38±6.94%) compared to DMSO as well as cells exposed to the compound only. A decrease in the S (5.02±0.41%) and G_1 phases (28.05±6.58%) were also observed in ESE-16 pre-treated cells when compared to the vehicle control and cells exposed to the compound only. Compared to cells exposed to radiation only, ESE-16 pre-treated MCF-7 cells displayed a statistically significant increase in the sub-G_1 apoptotic phase (Figure 4.20). LimPyr1 pre-treated MCF-7 cells displayed a significant increase in the sub-G_1 (7.80±1.00%) and G_2/M phases (72.81±1.60%), while the S (9.38±4.29%) and G_1 phases (8.44±0.04%) were significantly decreased. Compared to cells exposed to LimPyr1 or 8 Gy radiation only, LimPyr1 pre-treated MCF-7 cells displayed a significant increase in the G_2/M phase, with a concurrent decrease in the G_1 phase (Figure 4.20).

Table 4.7: Cell cycle analysis of BT-20 cells exposed to various treatment conditions. Data were generated using Kaluza Analysis software version 1.5 (FL, USA) and analyzed, using an ANOVA-single factor model. In the table below, the averaged percentages (M%) and standard deviations (SD) of three biological repeats are displayed for each phase of the cell cycle. Statistical significance (*P*-value <0.05) was calculated with a two-tailed Student's t-test using cells exposed to DMSO and the individual treatments as baselines.

		Medium only	DMSO	Actinomycin D	ESE-15-one	ESE-16	8 Gy radiation	ESE-15-one + radiation	ESE-16 + radiation
Sub-G_1	M%±SD	10.96±5.57	7.87±3.74	32.84±3.59	16.96±6.01	23.77±0.75	20.49±5.37	15.68±5.87	25.75±1.01
	P-value when compared to:								
	DMSO	0.33	-	**1.96E-05**	**0.03**	**1.93E-03**	**4.18E-03**	**0.04**	**7.66E-03**
	ESE-15-one							0.77	
	ESE-16								0.08
	Radiation							0.27	0.38
G_1	M%±SD	55.17±2.64	57.17±3.49	39.31±5.54	50.95±1.84	48.29±0.64	33.13±11.34	28.00±3.01	28.99±0.67
	P-value when compared to:								
	DMSO	0.34	-	**5.77E-04**	**1.51E-02**	**0.02**	**1.92E-03**	**3.33E-06**	**3.18E-03**
	ESE-15-one							**1.28E-05**	
	ESE-16								**6.42E-05**
	Radiation							0.41	0.58
S	M%±SD	7.25±1.59	7.33±1.48	8.95±3.13	7.42±1.46	7.88±1.36	7.01±1.95	7.92±3.57	9.15±0.35
	P-value when compared to:								
	DMSO	0.94	-	0.34	0.93	0.84	0.78	0.74	0.30
	ESE-15-one							0.80	
	ESE-16								0.31
	Radiation							0.64	0.45
G_2/M	M%±SD	26.85±5.98	27.87±4.74	20.04±5.87	24.94±6.49	20.41±2.14	47.76±10.31	48.77±9.94	36.64±0.43
	P-value when compared to:								
	DMSO	0.77	-	0.06	0.46	0.06	**6.06E-03**	**4.08E-03**	**4.27E-03**
	ESE-15-one							**7.00E-03**	
	ESE-16								**2.09E-03**
	Radiation							0.89	0.51

		Medium only	DMSO	Actinomycin D	T4	LimPyr1	8 Gy radiation	T4 + radiation	LimPyr1 + radiation
Sub-G_1	M%±SD	3.61±1.26	2.27±0.46	13.26±4.01	8.13±3.91	5.92±2.38	4.34±1.60	7.97±4.23	4.65±1.21
	P-value when compared to:								
	DMSO	0.09	-	**1.03E-03**	**0.02**	**0.02**	**0.04**	**0.03**	**1.06E-02**
	T4							0.96	
	LimPyr1								0.38
	Radiation							0.11	0.76
G_1	M%±SD	62.72±2.84	61.89±3.02	55.06±1.81	57.47±1.20	48.49±6.48	33.90±3.33	41.21±11.68	23.69±5.47
	P-value when compared to:								
	DMSO	0.68	-	**3.83E-03**	**0.03**	**9.50E-03**	**3.61E-06**	**1.13E-02**	**1.82E-05**
	T4							**0.03**	
	LimPyr1								**1.10E-03**
	Radiation							0.21	**1.03E-02**
S	M%±SD	7.50±1.58	7.70±1.56	8.62±3.00	6.23±1.52	10.01±3.16	9.66±2.57	9.64±2.56	7.91±1.49
	P-value when compared to:								
	DMSO	0.86	-	0.60	0.23	0.24	0.23	0.23	0.85
	T4							0.05	
	LimPyr1								0.27
	Radiation							0.99	0.27
G_2/M	M%±SD	26.20±3.34	27.96±1.20	23.09±2.80	28.04±2.99	35.50±5.14	52.09±3.60	41.14±10.48	63.63±6.61
	P-value when compared to:								
	DMSO	0.35	-	**1.48E-02**	0.96	**0.03**	**4.37E-06**	**0.04**	**4.11E-05**
	T4							4.81E-02	
	LimPyr1								**5.28E-04**
	Radiation							0.06	**1.20E-02**

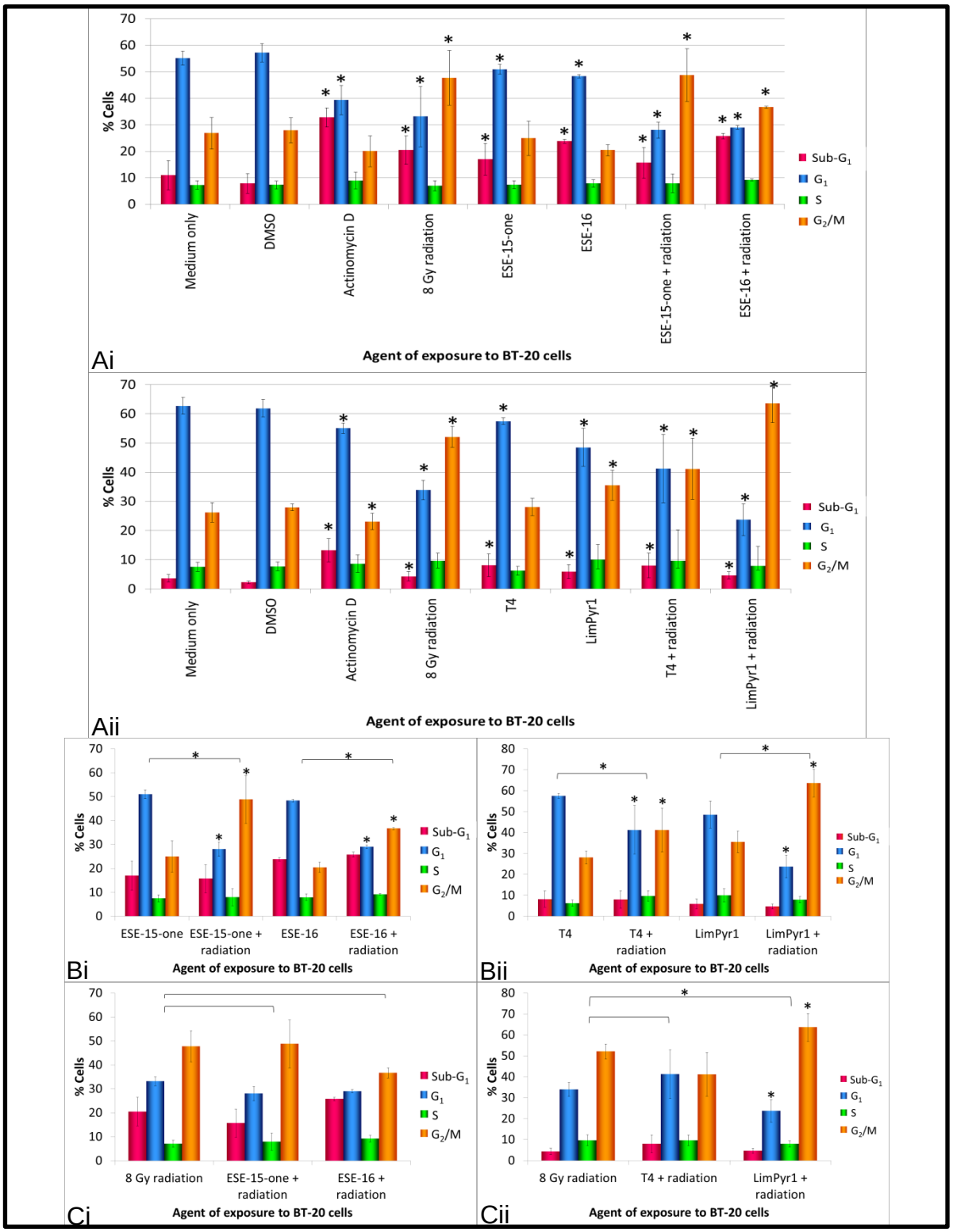

Figure 4.18: Graphical representation of cell cycle analysis in BT-20 cells exposed to various treatment conditions. BT-20 cells exposed to ESE-15-one or ESE-16 (Ai) and LimPyr1 or T4 (Aii) displayed a significant increase in the sub-G_1 apoptotic phase, with a concurrent decrease in the G_1 population. Additionally, LimPyr1-exposed cells displayed an increase in the G_2/M phase (Aii). Exposure to 8 Gy radiation significantly increased the sub-G_1 and G_2/M phases in addition to decreasing the G_1 population (Ai & Aii). ESE-15-one and ESE-16 pre-treated cells displayed a

significant increase in the G_2/M phase with a concurrent decrease in the G_1 phase compared to DMSO and cells exposed to the compounds only (Ai &Bi). Compared to DMSO, ESE-15-one and ESE-16 pre-treated cells displayed an increase in the sub-G_1 apoptotic phase. Exposure to T4 24 hours prior to radiation significantly increased the G_2/M phase while decreasing the G_1 population compared to DMSO and cells exposed to T4 only (Aii & Bii). T4 pre-treatment also significantly increased the sub-G_1 phase compared to DMSO. Similarly, LimPyr1 pre-treatment increased the sub-G_1 and G_2/M phases in addition to decreasing the G_1 phase compared to the vehicle control (Aii). Compared to cells exposed to LimPyr1 (Bii) or 8 Gy radiation only (Cii), cells exposed to the LimPyr1 and radiation treatment significantly increased the G_2/M phase, while decreasing the percentage of cells in the G_1 phase. Three biological repeats were completed for each experiment. The mean percentages of cells in each phase of the cell cycle are displayed in the bar graphs and the standard deviations are indicated by T-bars. A *P*-value <0.05 was considered statistically significant and are indicated with an asterisk (*).

MDA-MB-231 cells displayed a significant increase in the sub-G_1 phase with a concurrent decrease in the G_1 phase when exposed to ESE-16 (2.41±0.01% and 48.47±2.05%, respectively) and LimPyr1 (6.90±0.23% and 33.32±2.49%, respectively), compared to the vehicle control (1.31±0.45% and 54.22±0.91% (DMEM), 3.12±0.99% and 47.51±3.00% (RPMI), respectively). Additionally, LimPyr1-exposed MDA-MB-231 cells displayed a significant increase in the G_2/M phase (52.75±4.63%) compared to the vehicle control (36.18±1.28%) (Figure 4.21). Exposure to 8 Gy radiation significantly decreased the G_1 population (32.35±4.69% (DMEM) and 30.83±5.49% (RPMI)) and increased the G_2/M phase (54.89±9.06% (DMEM) and 54.91±5.20% (RPMI)) of MDA-MB-231 cells (Table 4.9). Compared to the vehicle control MDA-MB-231 cells displayed a significant increase in the sub-G_1 and G_2/M phases, in addition to a decreased G_1 phase when pre-treated with ESE-16 (5.90±2.22%, 55.35±5.77% and 30.90±1.96%, respectively) or LimPyr1 (6.28±0.74%, 76.64±0.34% and 12.58±1.29%, respectively) 24 hours prior to radiation. Additionally, LimPyr1 pre-treated MDA-MB-231 cells displayed a statistically significant decrease in the S phase (4.52±1.18%) compared to the vehicle control (13.22±4.16%) (Figure 4.21). Compared to cells exposed to the compounds only, ESE-16 and LimPyr1 pre-treated MDA-MB-231 cells displayed a significant decrease in the G_1 phase, with a concurrent increase in the G_2/M phase. LimPyr1 pre-treatment significantly decreased the G_1 population while increasing the G_2/M phase in MDA-MB-231 cells compared to cell exposed to 8 Gy radiation only (Figure 4.22).

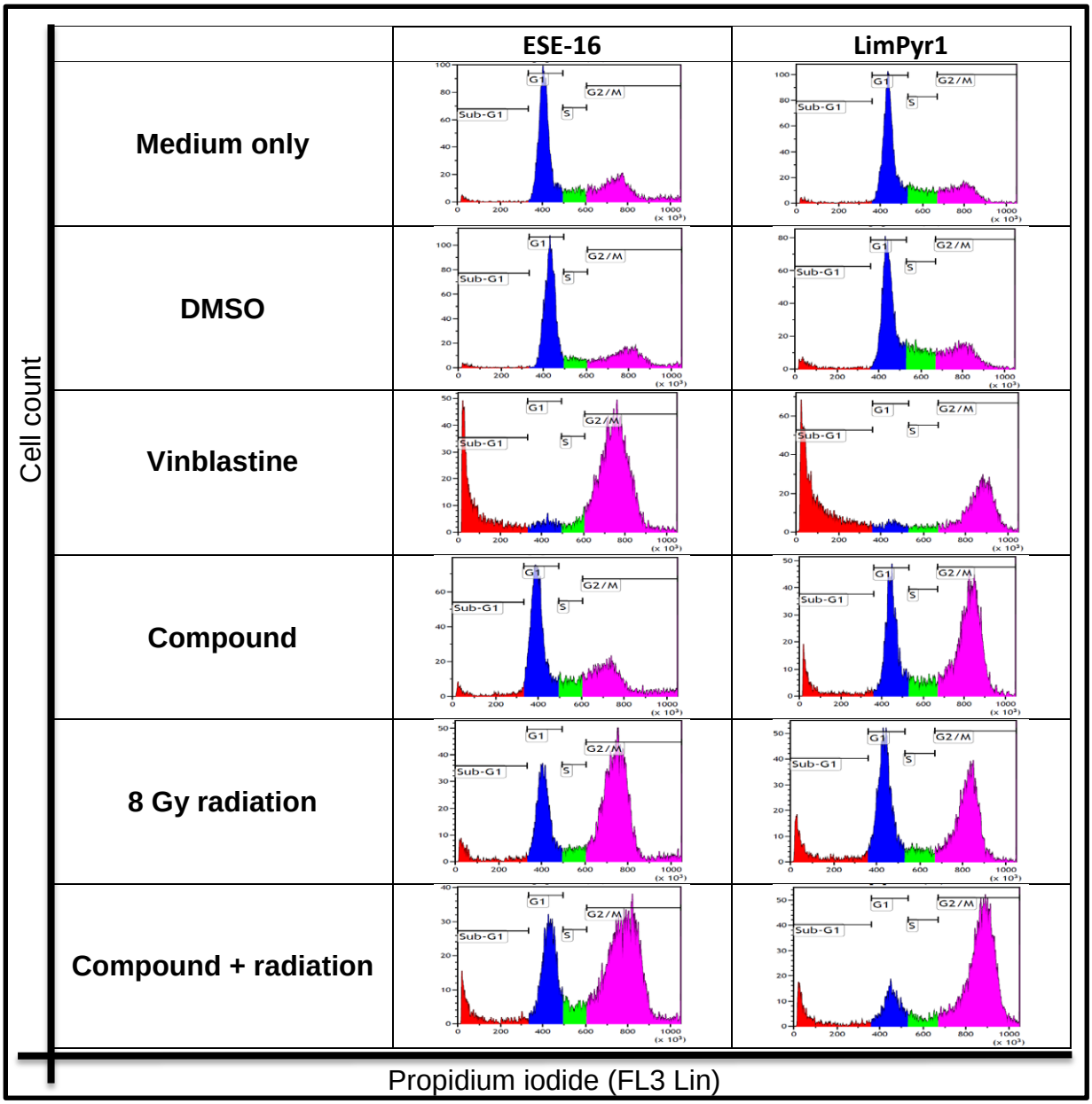

Figure 4.19: Histograms representing the cell cycle distributions of MCF-7 cells exposed to various treatment conditions. Cell counts were plotted against propidium iodide detection (FL3 Lin). MCF-7 cells propagated in medium only or exposed to DMSO served as negative and vehicle controls, respectively. A positive control, vinblastine, was included for apoptosis detection. MCF-7 cells were also exposed to ESE-16, LimPyr1, 8 Gy radiation and the combination treatment conditions.

Table 4.8: Cell cycle analysis of MCF-7 cells exposed to various treatment conditions. Data of three biological repeats were generated using Kaluza Analysis software version 1.5 (FL, USA). The ANOVA-single factor model and a two-tailed Student's *t*-test were used to analyze the data and calculate statistically significant differences, respectively. The table summarizes the averaged percentages (M%) and standard deviations (SD) of all cell cycle phases. Statistically significant differences (*P*-value <0.05) were calculated using the vehicle (DMSO) and cells exposed to the individual treatments as baselines.

			Medium only	DMSO	Vinblastine	Compound	8 Gy radiation	Compound + radiation
ESE-16	Sub-G_1	M%±SD	1.55±0.28	1.52±0.07	33.04±11.76	2.12±0.04	3.89±0.24	6.27±0.72
		P-value when compared to:						
		DMSO	0.90	-	**9.73E-03**	**2.00E-03**	**4.29E-04**	**1.14E-03**
		ESE-16						**1.48E-02**
		Radiation						**4.74E-02**
	G_1	M%±SD	46.51±9.68	51.01±3.79	5.19±1.18	47.74±2.32	25.81±2.60	28.05±6.58
		P-value when compared to:						
		DMSO	0.49	-	**3.70E-05**	0.27	**6.86E-04**	**6.35E-03**
		ESE-16						**8.10E-03**
		Radiation						0.61
	S	M%±SD	8.20±0.96	7.88±1.29	3.97±0.51	8.99±1.42	5.00±0.81	5.02±0.41
		P-value when compared to:						
		DMSO	0.75	-	**8.12E-03**	0.37	**0.03**	**0.02**
		ESE-16						**9.65E-03**
		Radiation						0.97
	G_2/M	M%±SD	41.64±7.03	39.56±4.14	63.87±11.49	40.47±3.52	62.98±6.61	61.38±6.94
		P-value when compared to:						
		DMSO	0.68	-	**0.04**	0.78	**6.51E-03**	**9.47E-03**
		ESE-16						**9.64E-03**
		Radiation						0.79
LimPyr1	Sub-G_1	M%±SD	3.22±0.60	3.46±0.70	36.81±8.69	7.73±1.24	8.70±0.86	7.80±1.00
		P-value when compared to:						
		DMSO	0.68	-	**2.69E-03**	**6.56E-03**	**1.20E-03**	**3.52E-03**
		LimPyr1						0.95
		Radiation						0.30
	G_1	M%±SD	43.72±9.64	43.87±4.81	7.57±1.52	16.81±0.54	15.47±0.62	8.44±0.04
		P-value when compared to:						
		DMSO	0.98	-	**2.38E-04**	**4.86E-03**	**4.24E-03**	**2.20E-03**
		LimPyr1						**2.07E-03**
		Radiation						**3.91E-03**
	S	M%±SD	17.51±3.45	17.97±2.47	7.28±3.35	11.56±3.80	10.03±3.73	9.38±4.29
		P-value when compared to:						
		DMSO	0.86	-	**1.13E-02**	0.07	**0.04**	**0.04**
		LimPyr1						0.54
		Radiation						0.85
	G_2/M	M%±SD	35.54±5.73	34.70±3.56	48.34±5.74	60.04±1.94	64.11±0.00	72.81±1.60
		P-value when compared to:						
		DMSO	0.84	-	**0.02**	**4.16E-04**	**1.58E-03**	**7.21E-05**
		LimPyr1						**9.28E-04**
		Radiation						**5.35E-03**

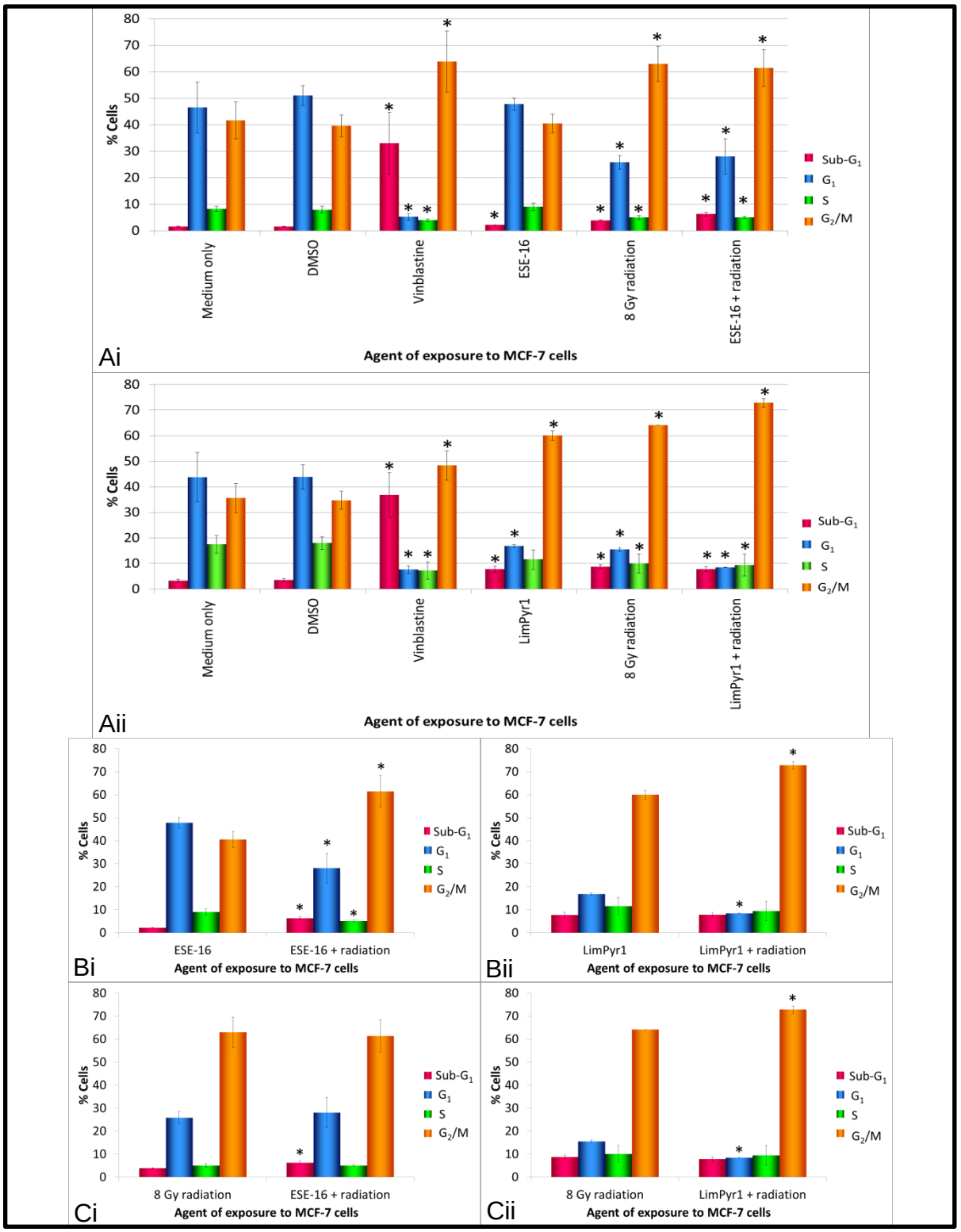

Figure 4.20: Graphical representation of cell cycle analysis in MCF-7 cells exposed to various treatment conditions. MCF-7 cells exposed to ESE-16 (Ai) and LimPyr1 (Aii) displayed a statistically significant increase in the sub-G_1 phase. Additionally, LimPyr1 exposure resulted in an increased G_2/M phase with a concurrent decrease in the G_1 population (Aii). Cells exposed to 8 Gy radiation, the ESE-16/radiation combination treatment and the LimPyr1/radiation combination treatment displayed a significant decrease in the G_1 and S phases, while the sub-G_1

and G_2/M phases were significantly increased (Ai & Aii). Similarly, ESE-16 pre-treated cells displayed an increase in the sub-G_1 and G_2/M phases, and a decrease in the G_1 and S phases compared to cells exposed to ESE-16 only (Bi). Compared to cells exposed to 8 Gy radiation only, ESE-16 pre-treated cells displayed a statistically significant increase in the sub-G_1 phase (Ci). Exposure to LimPyr1 24 hour prior to radiation resulted in a decreased G_1 population and increased G_2/M phase compared to the individual treatment conditions (Bii & Cii). The mean percentage cells present in the cell cycle phases are displayed in the bar graphs and the standard deviations indicated by T-bars. A *P*-value <0.05 was considered statistically significant and are indicated with an asterisk*.

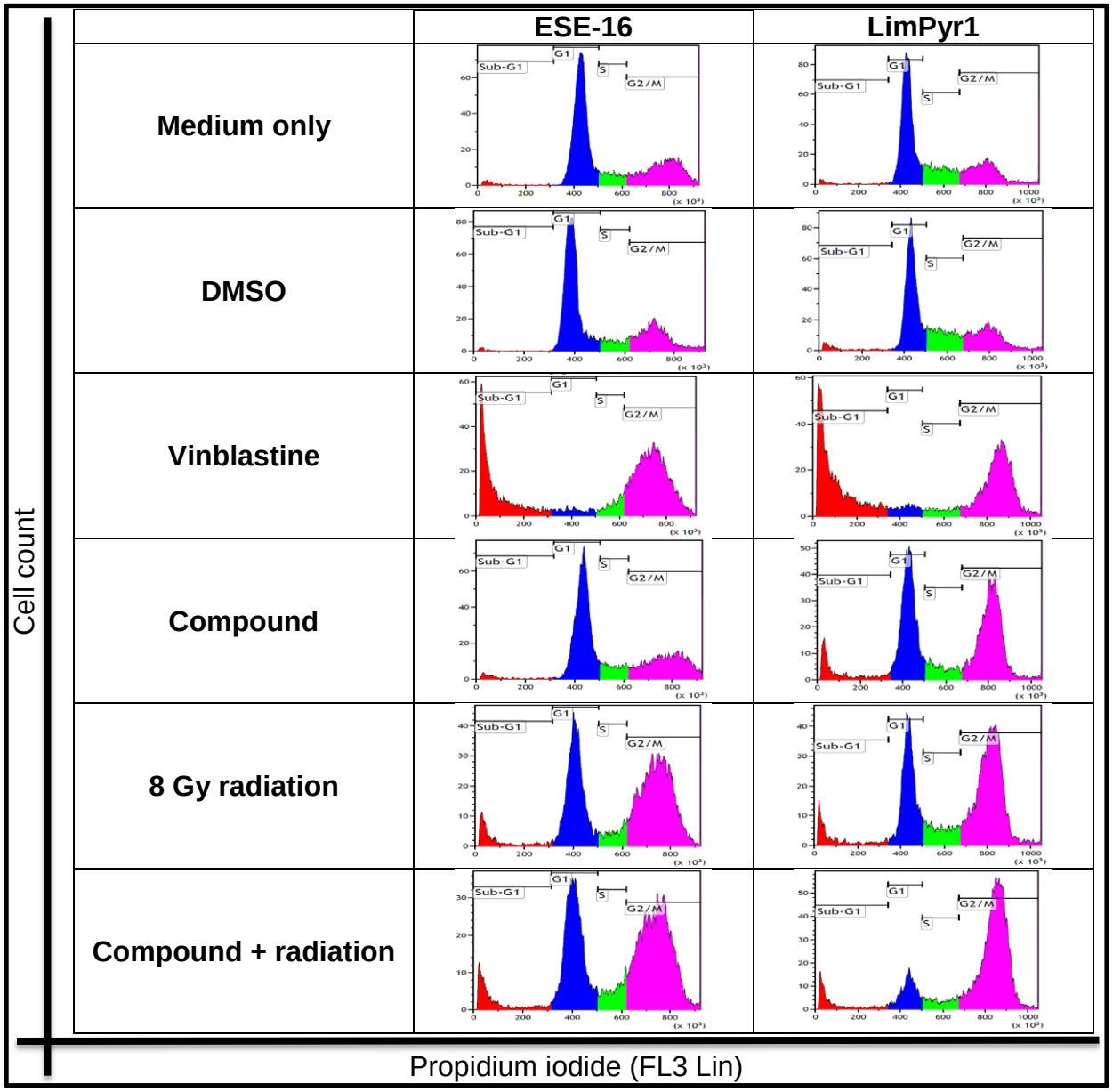

Figure 4.21: Histograms representing the cell cycle distributions of MDA-MB-231 cells exposed to various treatment conditions. Cell cycle distributions were visualized by plotting cell counts against propidium iodide (FL3 Lin) quantification. MDA-MB-231 cells exposed to DMSO served as a vehicle control and cells grown in medium only as a negative control. MDA-MB-231 cells

were exposed to the positive method control, vinblastine. MDA-MB-231 cells were exposed to ESE-16, LimPyr1 and 8 Gy radiation and the augmented effect of the compounds and radiation were observed in the combination treatment condition samples.

Table 4.9: Cell cycle analysis of MDA-MB-231 cells exposed to the various treatment conditions. Data were generated and analyzed, using Kaluza Analysis software version 1.5 (FL, USA) and the ANOVA-single factor model, respectively. A two-tailed Student's *t*-test was used to calculate statistical significance. The averaged percentage (M%) and the standard deviations (SD) of three biological repeats are summarized in the table below. The vehicle control (DMSO) and individual treatment samples served as baselines for the calculation of statistical significance (*P*-value <0.05).

			Medium only	DMSO	Vinblastine	Compound	8 Gy radiation	Compound + radiation
ESE-16	Sub-G_1	M%±SD	1.54±0.83	1.31±0.45	37.65±9.50	2.41±0.01	5.71±2.86	5.90±2.22
		P-value when compared to:						
		DMSO	0.69	-	**2.70E-03**	**4.60E-02**	0.06	**0.02**
		ESE-16						0.12
		Radiation						0.93
	G_1	M%±SD	52.50±4.81	54.22±0.91	5.39±1.05	48.47±2.05	32.35±4.69	30.90±1.96
		P-value when compared to:						
		DMSO	0.58	-	**4.36E-07**	**0.02**	**1.36E-03**	**4.84E-05**
		ESE-16						**2.35E-03**
		Radiation						0.65
	S	M%±SD	10.02±2.51	10.30±3.02	7.58±3.66	10.40±2.84	7.01±1.85	7.81±1.95
		P-value when compared to:						
		DMSO	0.91	-	0.38	0.97	0.18	0.30
		ESE-16						0.30
		Radiation						0.63
	G_2/M	M%±SD	35.92±6.48	34.16±3.33	49.34±10.91	38.69±4.89	54.89±9.06	55.35±5.77
		P-value when compared to:						
		DMSO	0.70	-	0.08	0.29	**0.02**	**0.01**
		ESE-16						**4.50E-02**
		Radiation						0.95
LimPyr1	Sub-G_1	M%±SD	3.17±2.48	3.12±0.99	41.29±4.33	6.90±0.23	6.56±2.02	6.28±0.74
		P-value when compared to:						
		DMSO	0.98	-	**1.19E-04**	**2.96E-03**	0.06	**1.13E-02**
		LimPyr1						0.24
		Radiation						0.83
	G_1	M%±SD	47.98±1.76	47.51±3.00	6.16±0.84	33.32±2.49	30.83±5.49	12.58±1.29
		P-value when compared to:						
		DMSO	0.83	-	**2.12E-05**	**3.23E-03**	**9.91E-03**	**4.99E-05**
		LimPyr1						**2.13E-04**
		Radiation						**4.98E-03**
	S	M%±SD	12.59±2.95	13.22±4.16	3.90±0.42	7.05±2.09	7.73±2.09	4.52±1.18
		P-value when compared to:						
		DMSO	0.84	-	**1.81E-02**	0.08	0.11	**0.03**
		LimPyr1						0.14
		Radiation						0.08
	G_2/M	M%±SD	36.30±1.96	36.18±1.28	48.66±4.00	52.75±4.63	54.91±5.20	76.64±0.34
		P-value when compared to:						
		DMSO	0.94	-	**6.74E-03**	**3.96E-03**	**3.75E-03**	**7.58E-07**
		LimPyr1						**8.80E-04**
		Radiation						**1.95E-03**

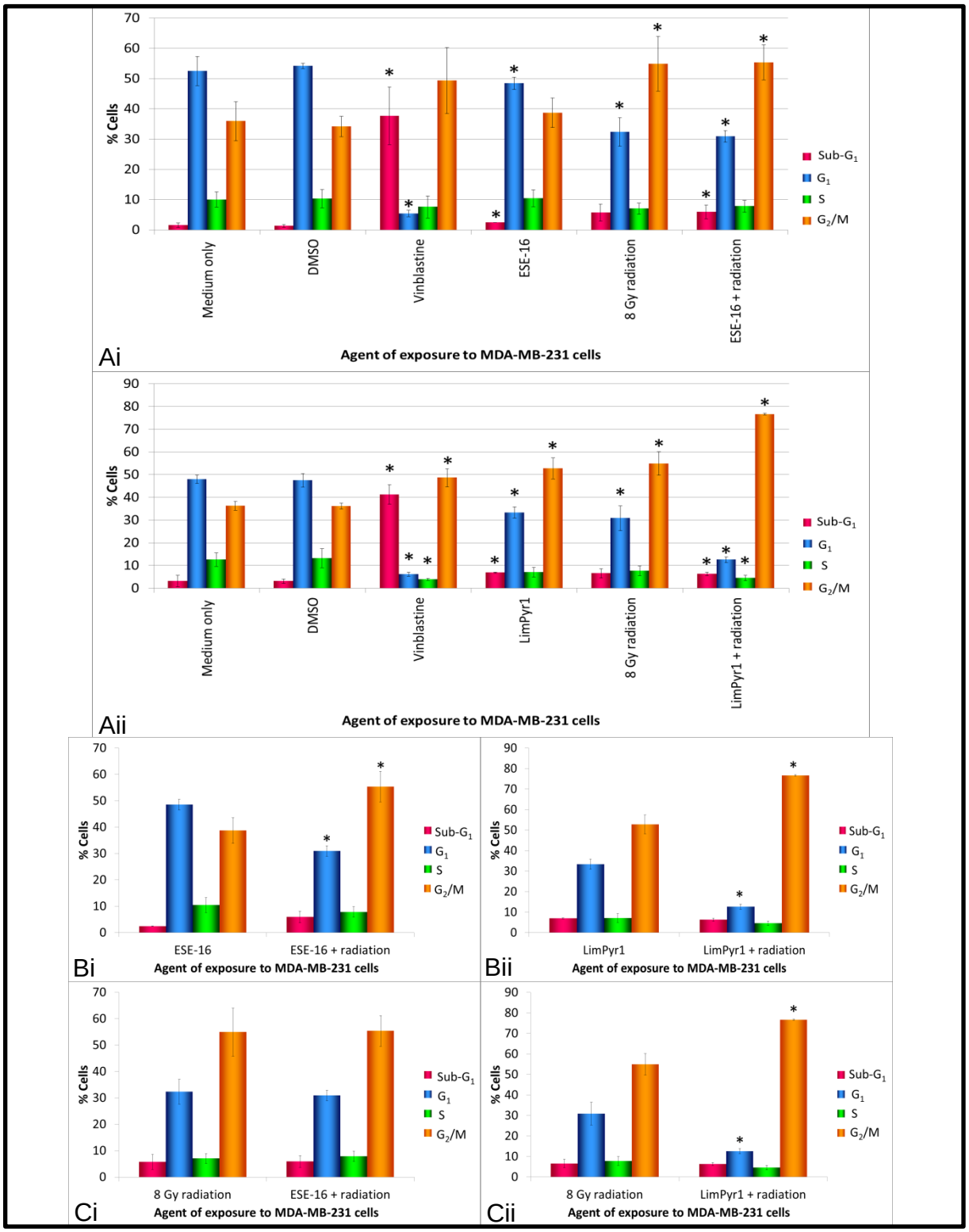

Figure 4.22: Graphical representation of the cell cycle analysis of MDA-MB-231 cells exposed to various treatment conditions. MDA-MB-231 cells exposed to ESE-16 (Ai) and LimPyr1 (Aii) displayed a significantly increase in the sub-G_1 phase with a concurrent decrease in the G_1 phase compared to DMSO. Additionally, LimPyr1 exposure resulted in an increased G_2/M population (Aii). Cells exposed to 8 Gy radiation displayed a significant increase in the G_2/M phase and a

decreased G_1 population (Ai & Aii). ESE-16 and LimPyr1 pre-treated cells displayed a decrease in the G_1 phase and an increase in the sub-G_1 and G_2/M phases, compared to DMSO (Ai & Aii). The S phase was also significantly decreased in LimPyr1 pre-treated cells (Aii). Compared to cells exposed to the compounds only, ESE-16 and LimPyr1 pre-treated cells displayed a decrease in the G_1 phase with a concurrent increase in the G_2/M phase (Bi & Bii). Similar observations were made in LimPyr1 pre-treated cells compared to cells exposed to 8 Gy radiation only (Cii). The bars represent the averaged percentage of three biological repeats and the standard deviations are indicated by T-bars. A *P*-value <0.05 was considered statistically significant and are indicated with an asterisk (*).

4.2.3 Intracellular signaling pathways induced by pre-exposing breast cancer cells to the novel compounds prior to radiation

4.2.3.1 Reactive oxygen species production: Flow cytometric quantification of superoxide employing hydroethidine

ROS generation exists in equilibrium with a variety of antioxidant defenses and is considered essential for normal physiological cellular functions. However, once ROS production is increased beyond this threshold, damage to various proteins, membranes, lipids and organelles occur resulting in apoptotic activation (481). The presence of ROS was quantified via flow cytometry, employing hydroethidine (superoxide detection) at different time points in breast cancer cells following exposure to different treatment conditions.

Breast cancer cells exposed to DMSO served as vehicle controls for this experiment. No statistically significant differences were observed at any time-point in superoxide formation when the vehicle control was compared to cells propagated in growth medium only (negative control). MCF-7-, MDA-MB-231- and BT-20 cells were exposed to rotenone as a positive control. Superoxide was significantly increased in all samples exposed to the positive control compared to the vehicle control.

MCF-7 cells exposed to ESE-16 displayed an increase in superoxide at the 4 hour termination point (1.22±0.18 fold increase) (Figure 4.23). Superoxide production was decreased at the

24- and 48 hour termination points, but not statistically significantly less than the levels quantified at 4 hours (Figure 4.24). LimPyr1-exposed MCF-7 cells displayed an increase in superoxide generation at the 4 (1.12±0.06 fold increase), 24 (1.48±0.17 fold increase) and 48 hours (1.42±0.18 fold increase) termination points, compared to the vehicle control. Additionally, LimPyr1-exposure resulted in a sustained increase in superoxide production over the 48 hour time frame (Figure 4.24). Superoxide generation was significantly increased 4 (1.20±0.13- and 1.22±0.19 fold increase), 24 (1.24±8.29E-04- and 1.59±0.42 fold increase) and 48 hours (1.57±0.46- and 1.21±0.08 fold increase) after 8 Gy radiation in cells propagated in DMEM and RPMI media, respectively (Table 4.10). MCF-7 cells exposed to ESE-16 24 hours prior to radiation displayed a significant increase in superoxide 4 (1.49±0.17-, 1.32±0.27- and 1.26±0.20 fold increase, respectively), 24 (1.44±0.19-, 1.54±0.24- and 1.24±0.11 fold increase, respectively) and 48 hours (1.73±0.45-, 1.77±0.36- and 1.06±0.01 fold increase, respectively) after radiation compared to DMSO, ESE-16-exposed cells and cells exposed to 8 Gy radiation only, respectively (Figure 4.23). Similarly, LimPyr1 pre-treated cells also displayed significantly higher levels of superoxide 4 (1.35±0.17-, 1.18±0.17- and 1.08±0.07 fold increase, respectively), 24 (1.75±0.36-, 1.18±0.14- and 1.28±0.07 fold increase, respectively) and 48 hours (1.64±0.40-, 1.24±0.17- and 1.49±0.36 fold increase, respectively) after radiation compared to DMSO and cells exposed to LimPyr1 or 8 Gy radiation only, respectively (Figure 4.23).

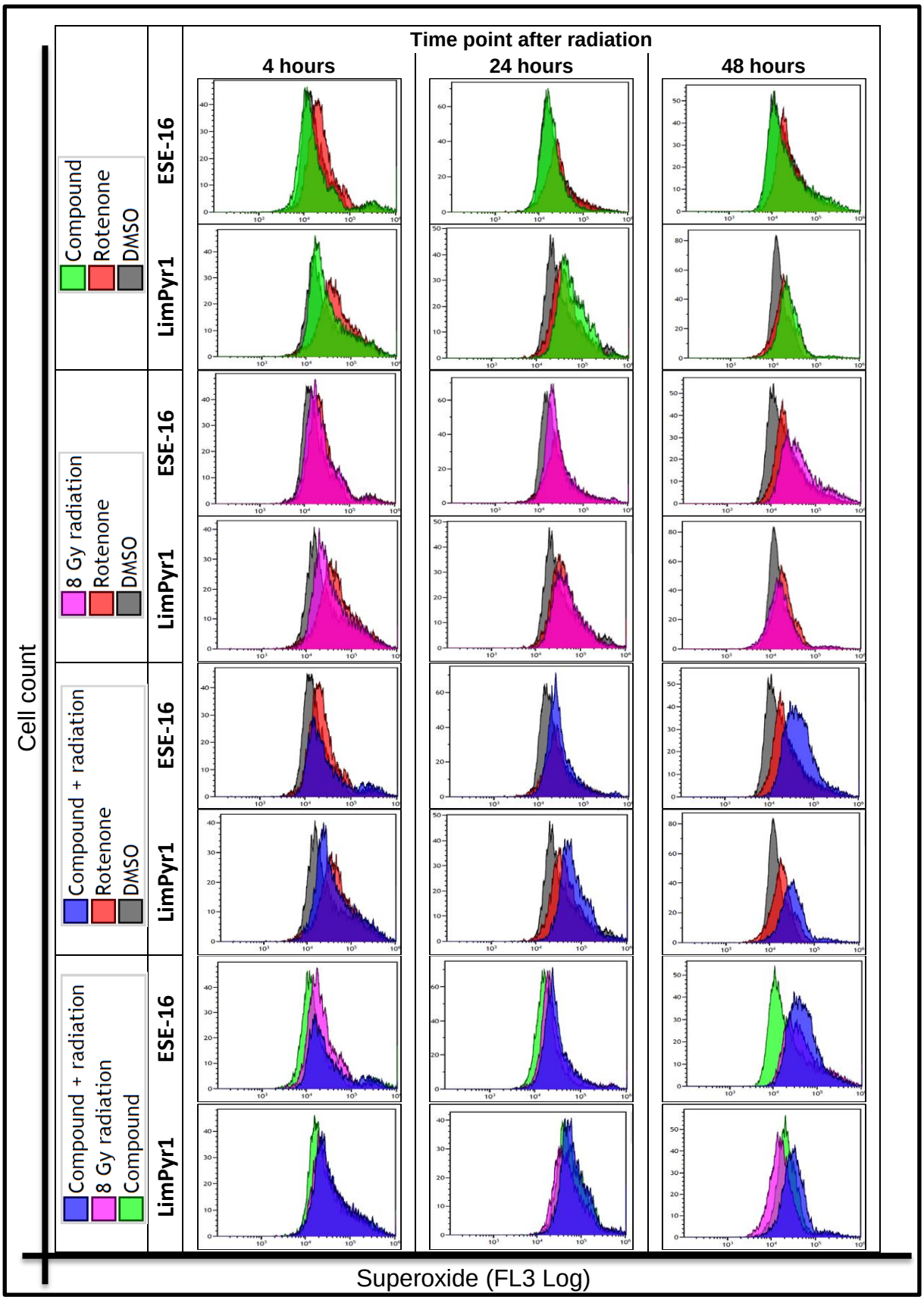

Figure 4.23: Representative overlay histograms of superoxide detection in MCF-7 cells. Histograms were obtained 4, 24 and 48 hours after radiation by plotting cell count against superoxide detection (FL3 Log). Overlay histograms displayed a right shift at all three time-

points in cells exposed to the combination treatment conditions, compared to the DMSO vehicle control and cells exposed to the individual treatment conditions.

Table 4.10: Superoxide detection in MCF-7 cells exposed to various treatment conditions. Data analyses were completed using the ANOVA-single factor model, using statistical data generated with Kaluza Analysis version 1.5 (FL, USA). The table displays the averaged fold change (FC) of three biological repeats at three different time-points after radiation and their standard deviations (SD). A two-tailed Student's *t*-test was used to calculate statistically significant differences (*P*-value <0.05) by using the vehicle control and cells exposed to the individual treatments as baselines.

			Medium only	DMSO	Rotenone	Compound	8 Gy radiation	Combination
Compared to DMSO								
4 hours	ESE-16	FC± SD	1.12±0.16	1	1.44±0.24	1.22±0.18	1.20±0.13	1.49±0.17
		P-value	0.14	-	**3.51E-03**	**0.03**	**0.01**	**2.22E-04**
	LimPyr1	FC± SD	1.09±0.09	1	1.55±0.28	1.12±0.06	1.22±0.19	1.35±0.17
		P-value	0.07	-	**2.42E-03**	**2.02E-03**	**0.04**	**1.97E-03**
24 hours	ESE-16	FC ± SD	1.10±0.18	1	1.22±0.11	0.95±0.08	1.24±8.29E-04	1.44±0.19
		P-value	0.40	-	**0.03**	0.33	**1.32E-08**	**0.02**
	LimPyr1	FC ± SD	1.34±0.37	1	1.50±0.30	1.48±0.17	1.59±0.42	1.75±0.36
		P-value	0.11	-	**0.02**	**1.27E-03**	**0.03**	**0.01**
48 hours	ESE-16	FC ± SD	1.05±0.12	1	1.56±0.16	1.11±0.12	1.57±0.46	1.73±0.45
		P-value	0.47	-	**4.08E-04**	0.11	**4.66E-02**	**0.02**
	LimPyr1	FC ± SD	1.02±0.17	1	1.57±0.35	1.42±0.18	1.21±0.08	1.64±0.40
		P-value	0.86	-	**0.02**	**3.53E-03**	**2.80E-03**	**0.02**
Compared to compound								
4 hours	ESE-16	FC ± SD				1		1.32±0.27
		P-value				-		**0.03**
	LimPyr1	FC ± SD				1		1.18±0.17
		P-value				-		**0.04**
24 hours	ESE-16	FC ± SD				1		1.54±0.24
		P-value				-		**0.02**
	LimPyr1	FC ± SD				1		1.18±0.14
		P-value				-		**0.04**
48 hours	ESE-16	FC ± SD				1		1.77±0.36
		P-value				-		**0.01**
	LimPyr1	FC ± SD				1		1.24±0.17
		P-value				-		**0.03**
Compared to 8 Gy radiation								
4 hours	ESE-16	FC ±S D					1	1.26±0.20
		P-value					-	**0.02**
	LimPyr1	FC ±S D					1	1.08±0.07
		P-value					-	**4.66E-02**
24 hours	ESE-16	FC ± SD					1	1.24±0.11
		P-value					-	**0.02**
	LimPyr1	FC ± SD					1	1.28±0.07
		P-value					-	**8.36E-04**
48 hours	ESE-16	FC ± SD					1	1.06±0.01
		P-value					-	**6.74E-06**
	LimPyr1	FC ± SD					1	1.49±0.36
		P-value					-	**0.03**

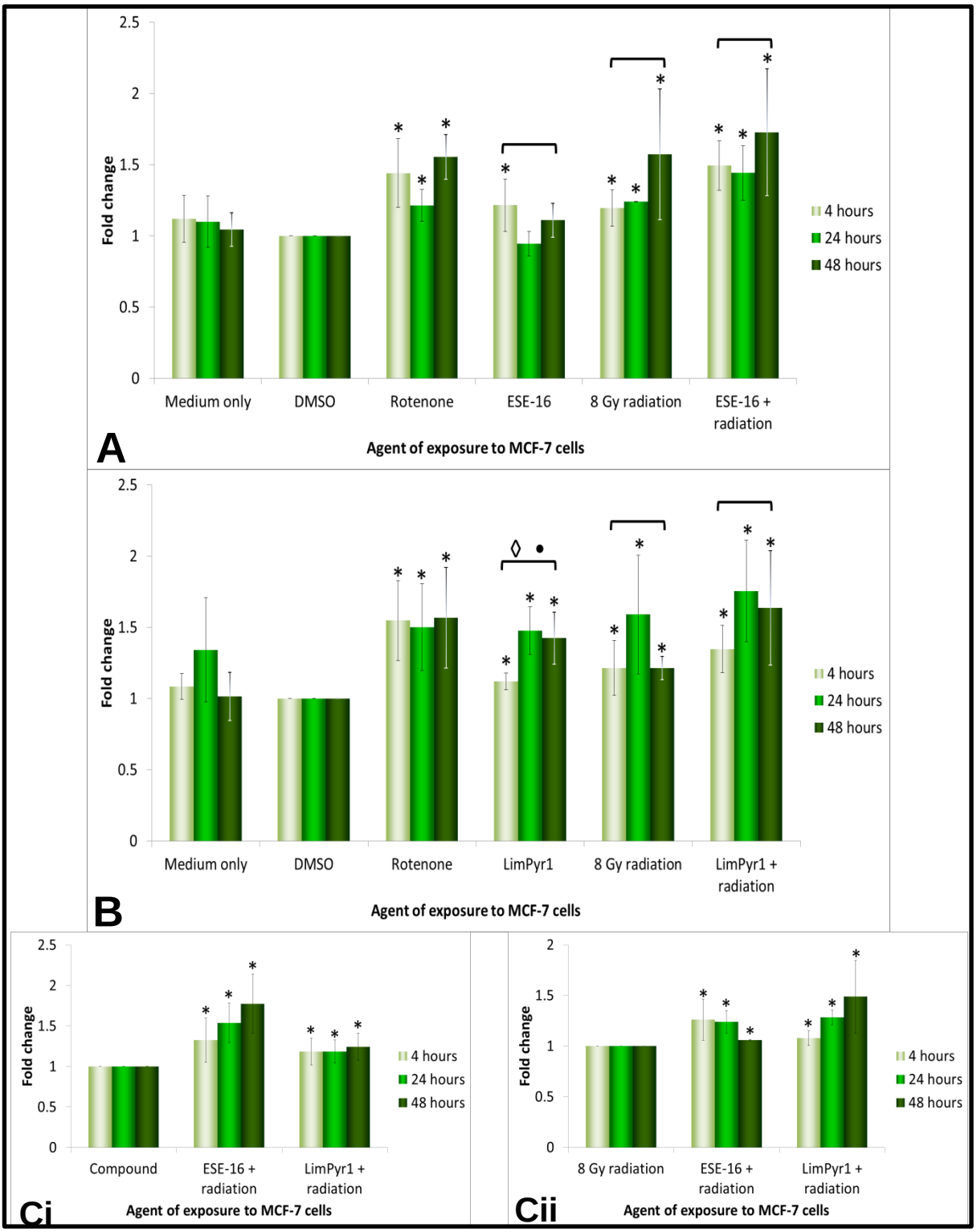

Figure 4.24: Graphical representation of superoxide quantification in MCF-7 cells after exposure to different treatment conditions. ESE-16 exposed MCF-7 cells displayed a significant increase in superoxide at the 4 hour termination point (A). LimPyr1 exposure significantly increased superoxide production at all three time points (B). Superoxide production increased over the 48 hour time frame in LimPyr1 exposed cells. MCF-7 cells exposed to 8 Gy radiation (A-B), and ESE-16 (A) or LimPyr1 (B) 24 hours prior to 8 Gy radiation displayed a significant increase

in superoxide 4-, 24- and 48 hours after radiation. Compared to cells exposed to the compounds (Ci) or 8 Gy radiation (Cii) only, ESE-16- and LimPyr1 pre-treated MCF-7 cells displayed significantly higher levels of superoxide at all three time-points in the experiment. The bar graph summarizes the mean fold increase of three biological repeats and standard deviations are represented by T-bars. Statistically significant differences are indicated with * (*P*-value <0.05) when compared to DMSO (A-B), cells exposed to ESE-16 and LimPyr1 only (Ci) or 8 Gy radiation only (Cii), ◊ when the 4 hour termination point was compared to the 24 hour termination point; and • when the 4 hour termination point was compared to the 48 hour termination point.

MDA-MB-231 cells exposed to ESE-16 (1.02±0.01 fold increase) or LimPyr1 (1.74±0.39 fold increase) displayed a significant increase in superoxide at the 24 hour termination point (Figure 4.25). Additionally, MDA-MB-231 cells exposed to LimPyr1 displayed significantly higher superoxide levels at the 48 hour termination point (1.16±0.13 fold increase) compared to DMSO. Exposure to 8 Gy radiation significantly increased superoxide in MDA-MB-231 cells 24 (1.40±0.20- and 2.12±0.53 fold increase) and 48 hours (1.48±0.25- and 1.32±0.18 fold increase) after radiation in cells propagated in DMEM and RPMI media, respectively (Table 4.11). This increase in superoxide was significantly higher 24 and 48 hours after radiation compared to superoxide levels measured at 4 hours after radiation (Figure 4.26). ESE-16 pre-treated cells displayed significantly higher superoxide levels 4 (1.16±0.10-, 1.10±0.06- and 1.20±0.12 fold increase), 24 (1.47±0.21-, 1.34±0.16- and 1.05±0.03 fold increase) and 48 hours (2.18±0.32-, 2.27±0.39- and 1.48±0.07 fold increase) after radiation compared to cells exposed to DMSO, ESE-16 and 8 Gy radiation only, respectively. Additionally, superoxide production progressively increased in the ESE-16 pre-treated MDA-MB-231 cells over the 48 hour time frame (Figure 4.26). Pre-treatment of MDA-MB-231 cells with LimPyr1 resulted in significantly higher superoxide levels 4 (1.54±0.35-, 1.22±0.13- and 1.28±0.20 fold increase), 24 (2.17±0.89-, 1.34±0.23- and 1.17±0.05 fold increase) and 48 hours (1.37±0.10-, 1.55±0.18- and 1.80±0.24 fold increase) after radiation compared to cells exposed to DMSO, LimPyr1 or 8 Gy radiation only, respectively.

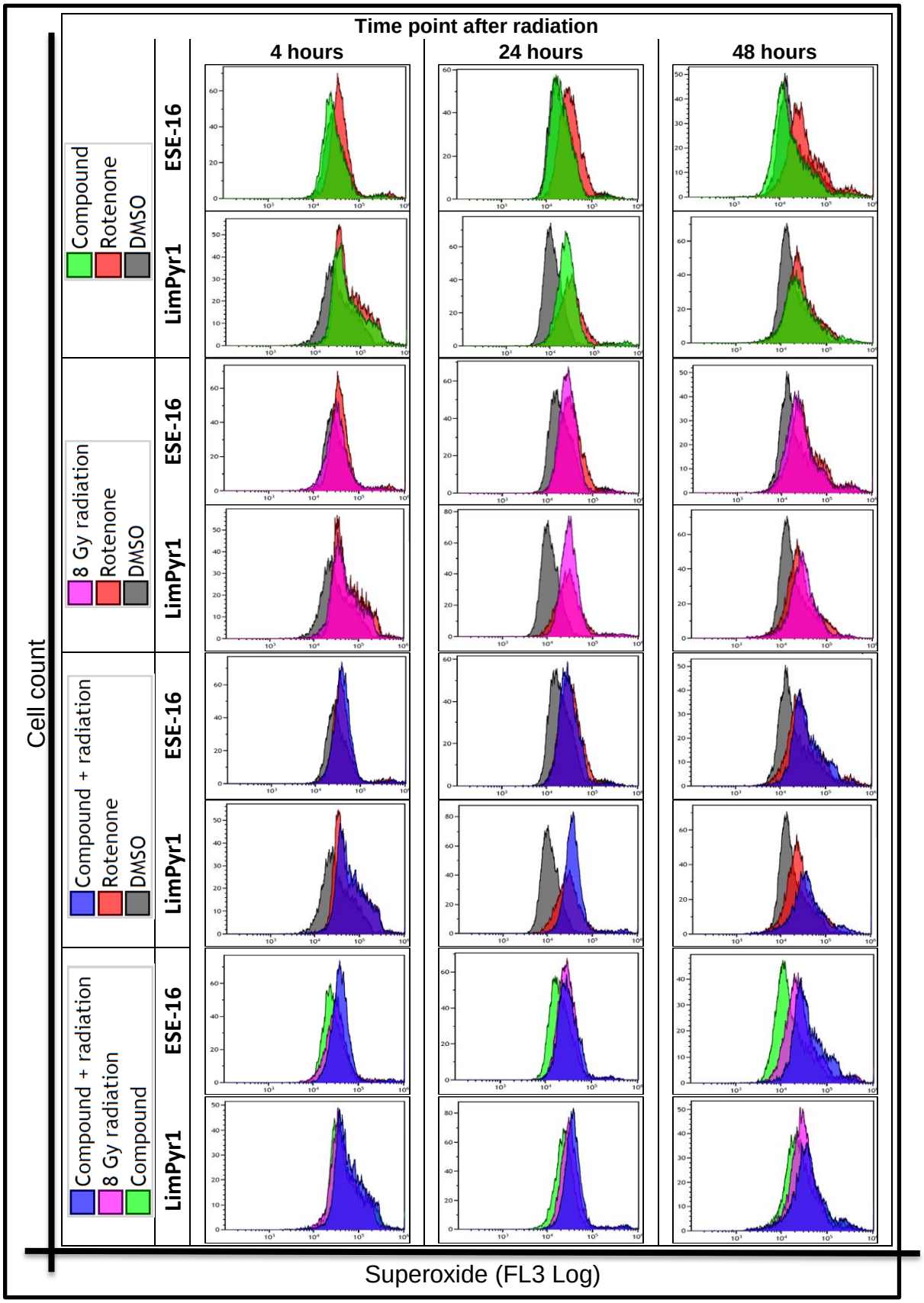

Figure 4.25: Representative overlay histograms of superoxide detection in MDA-MB-231 cells. Histograms were obtained 4, 24 and 48 hours after radiation by plotting cell counts against the generated superoxide production (FL3 Log). Overlay histograms displayed an increase in

superoxide via a right shift in cells exposed to the different treatment conditions, compared to the DMSO vehicle control.

Table 4.11: Superoxide detection in MDA-MB-231 cells exposed to various treatment conditions. Data were generated with Kaluza Analysis version 1.5 (FL, USA) and analyzed, using the ANOVA-single factor model. Three biological repeats were completed for each time-point. The table displays the averaged fold change (FC) and the standard deviations (SD). Statistically significant differences (*P*-value <0.05) were calculated with a two-tailed Student's *t*-test using the vehicle control and cells exposed to the individual treatments as baselines.

			Medium only	DMSO	Rotenone	Compound	8 Gy radiation	Combination
Compared to DMSO								
4 hours	ESE-16	FC± SD	0.95±0.07	1	1.36±0.26	0.99±0.13	1.05±0.05	1.16±0.10
		P-value	0.21	-	**0.03**	0.91	0.07	**0.02**
	LimPyr1	FC± SD	1.05±0.19	1	1.43±0.25	1.22±0.31	1.20±0.22	1.54±0.35
		P-value	0.62	-	**0.01**	0.21	0.11	**0.02**
24 hours	ESE-16	FC ± SD	0.97±0.10	1	1.58±0.28	1.02±0.01	1.40±0.20	1.47±0.21
		P-value	0.59	-	**0.02**	**4.92E-02**	**0.02**	**0.02**
	LimPyr1	FC ± SD	1.27±0.43	1	1.87±0.53	1.74±0.39	2.12±0.53	2.17±0.89
		P-value	0.26	-	**0.02**	**0.01**	**0.01**	**0.04**
48 hours	ESE-16	FC ± SD	1.05±0.20	1	1.67±0.22	0.97±0.16	1.48±0.25	2.18±0.32
		P-value	0.68	-	**0.01**	0.80	**0.03**	**3.14E-03**
	LimPyr1	FC ± SD	1.11±0.18	1	1.39±0.17	1.37±0.10	1.55±0.18	1.80±0.24
		P-value	0.27	-	**3.3598E-03**	**3.9522E-04**	**7.4212E-04**	**5.9314E-04**
Compared to compound								
4 hours	ESE-16	FC ± SD				1		1.10±0.06
		P-value				-		**0.02**
	LimPyr1	FC ± SD				1		1.22±0.13
		P-value				-		**0.02**
24 hours	ESE-16	FC ± SD				1		1.34±0.16
		P-value				-		**0.03**
	LimPyr1	FC ± SD				1		1.34±0.23
		P-value				-		**0.03**
48 hours	ESE-16	FC ± SD				1		2.27±0.39
		P-value				-		**4.92E-03**
	LimPyr1	FC ± SD				1		1.32±0.18
		P-value				-		**0.01**
Compared to 8 Gy radiation								
4 hours	ESE-16	FC ±S D					1	1.20±0.12
		P-value					-	**0.02**
	LimPyr1	FC ±S D					1	1.28±0.20
		P-value					-	**0.03**
24 hours	ESE-16	FC ± SD					1	1.05±0.03
		P-value					-	**0.04**
	LimPyr1	FC ± SD					1	1.17±0.05
		P-value					-	**3.5993E-04**
48 hours	ESE-16	FC ± SD					1	1.48±0.07
		P-value					-	**2.61E-04**
	LimPyr1	FC ± SD					1	1.16±0.13
		P-value					-	**4.6189E-02**

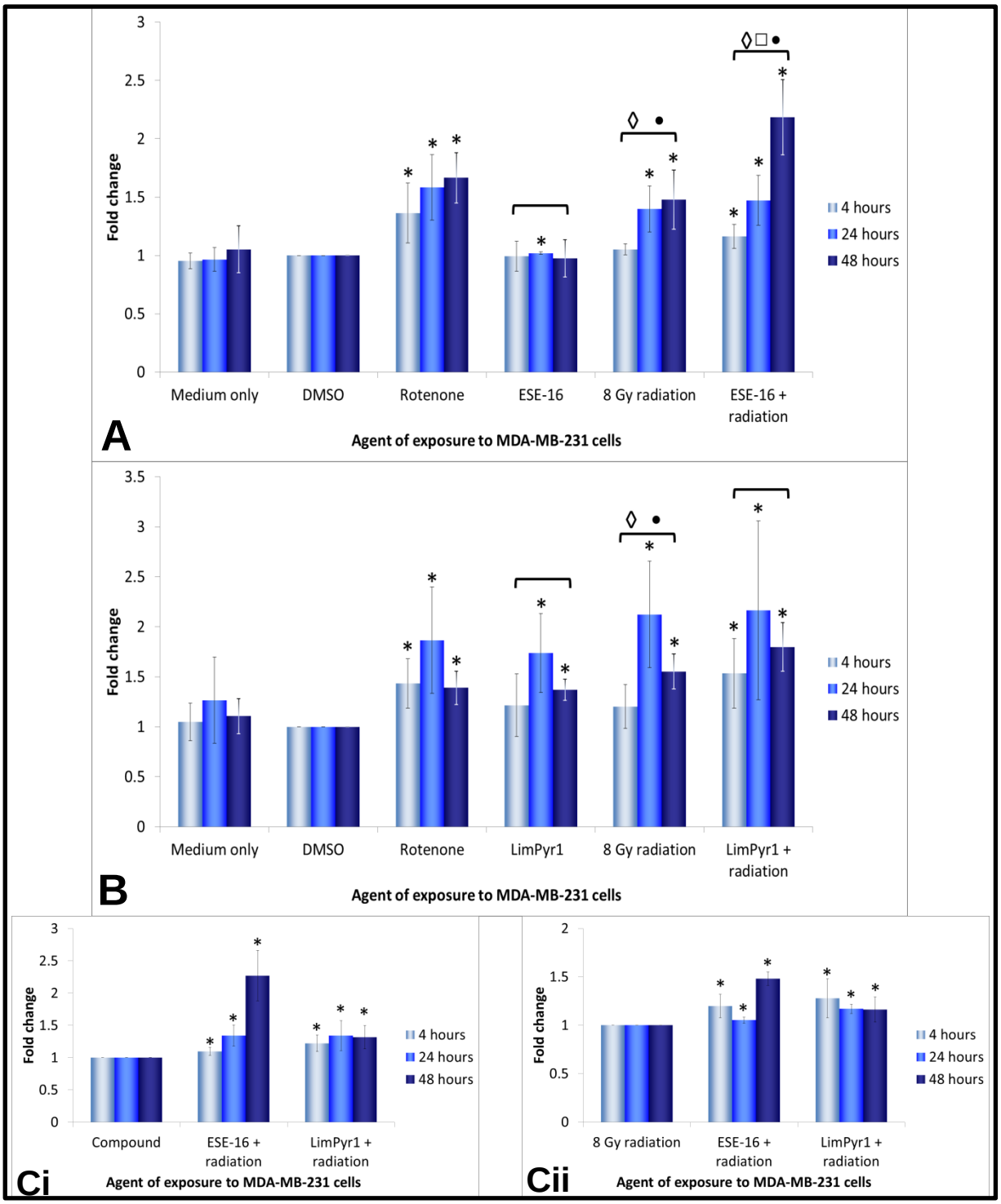

Figure 4.26: Graphical representation of superoxide quantification in MDA-MB-231 cells after exposure to the different treatment conditions. MDA-MB-231 cells exposed to ESE-16 displayed a very small increase in superoxide production at the 24 hour time point (A), whereas LimPyr1-exposure resulted in increased superoxide levels at the 24 and 48 hour time points (B). MDA-MB-231 cells displayed significantly higher levels of superoxide 24 and 48 hours after exposure to 8 Gy radiation (A-B). ESE-16 pre-treated MDA-MB-231 cells increased superoxide production over the 48 hour time frame (A). MDA-MB-231 cells pre-treated with LimPyr1 displayed significantly higher levels of superoxide at all three time-points. Compared to cells

exposed to the compound only (Ci) and cells exposed to 8 Gy radiation (Cii), the combination treatment conditions significantly increased superoxide production over a 48 hour time frame following radiation. The mean fold increases of three biological repeats are summarized in the bar graph. Standard deviations are represented by T-bars and statistically significant differences are indicated with * (*P*-value <0.05) when compared to DMSO (A-B), cells exposed to ESE-16 and LimPyr1 only (Ci) or 8 Gy radiation only (Cii), ◊ when the 4 hour termination point was compared to the 24 hour termination point, □ when the 24 hour termination point was compared to the 48-hour termination point; and • when the 4 hour termination point was compared to the 48 hour termination point.

Superoxide levels were significantly higher in BT-20 cells exposed to ESE-16 at the 4 (1.37±0.12 fold increase), 24 (1.05±0.02 fold increase) and 48 hour (1.24±0.12 fold increase) termination points, compared to DMSO (Figure 4.27). Superoxide production decreased from the 4 to the 24 hour termination point, but was restored at 48 hours (Figure 4.28). BT-20 cells exposed to LimPyr1 displayed a significant increase in superoxide production at the 4 (1.47±0.13 fold increase), 24 (1.37±0.06 fold increase) and 48 hour (1.24±0.05 fold increase) termination points compared to the vehicle control. This increase in superoxide observed in the LimPyr1-exposed BT-20 cells significantly decreased over the 48 hour time frame (Figure 4.28). Radiation exposure resulted in significantly higher superoxide levels in BT-20 cells at all three time points in the experiment (Table 4.12). Superoxide production significantly increased from 4 to 24 hours after radiation. Exposure of BT-20 cells to ESE-16 prior to radiation significant increased superoxide 4 (1.54±0.17-, 1.13±0.08- and 1.37±0.13 fold increase), 24 (1.38±0.04-, 1.32±0.06- and 1.08±0.02 fold increase) and 48 hours (1.51±0.27-, 1.22±0.09- and 1.04±0.02 fold increase) after radiation compared to DMSO and the compound or radiation only samples, respectively (Figure 4.27). LimPyr1 pre-treated BT-20 cells displayed a significant increase in superoxide production 4 (1.72±0.12 fold increase), 24 (2.28±0.44 fold increase) and 48 hours (2.56±0.59 fold increase) after radiation compared to DMSO. This increase in superoxide production was significantly higher 48 hours after radiation compared to the 4 hour quantification (Figure 4.28). Additionally, the superoxide production was significantly higher in the LimPyr1 pre-treated BT-20 cells 4 (1.18±0.15- and 1.26±0.17 fold increase), 24 (1.66±0.31- and 1.43±0.20 fold increase) and 48 hours (1.86±0.43- and 1.42±0.23 fold increase) after radiation compared to cells exposed to the compound or radiation only, respectively (Figure 4.27).

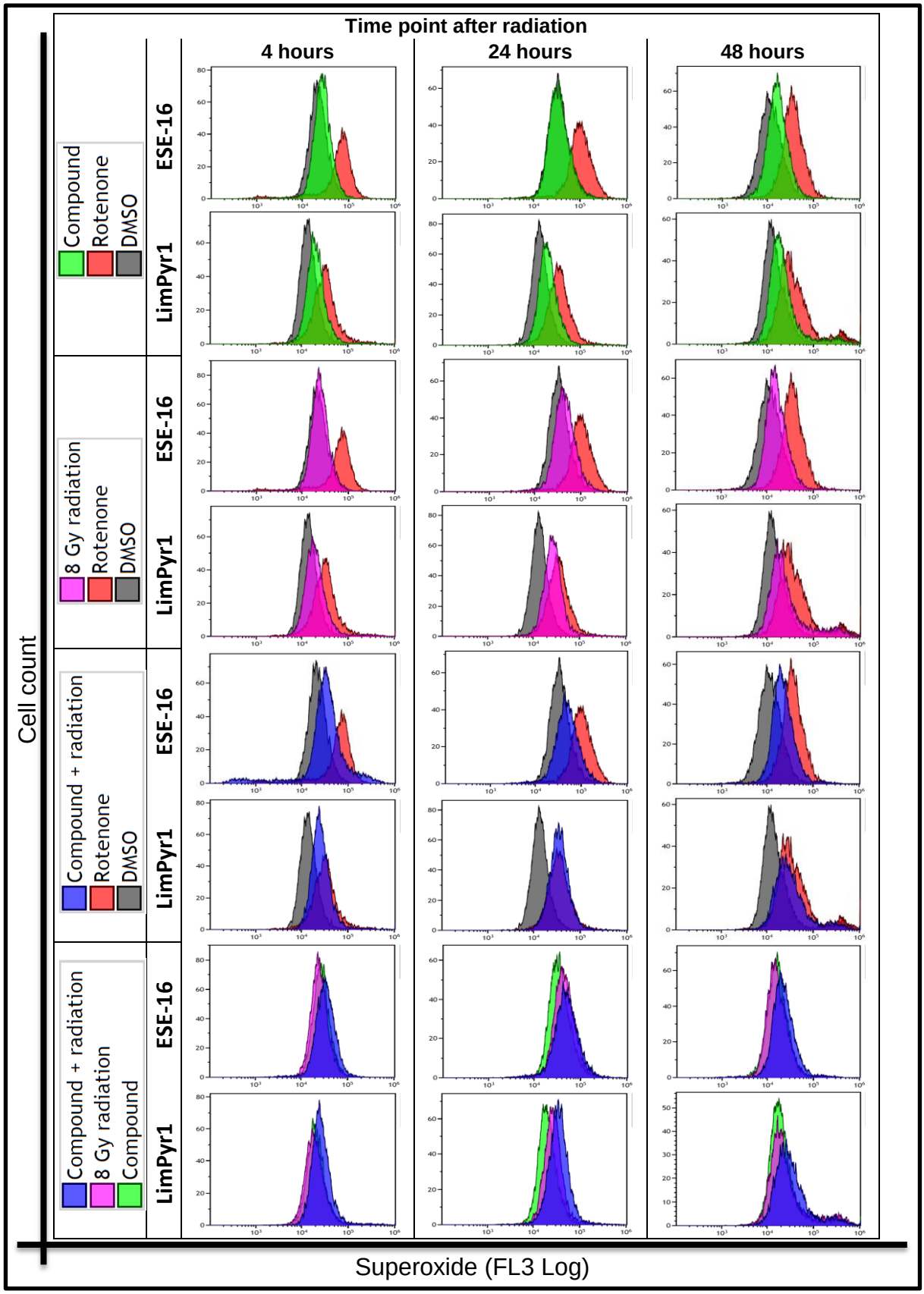

Figure 4.27: Representative overlay histograms of superoxide detection in BT-20 cells. Histograms were obtained over a 48 hour time frame following radiation exposure. Histograms were created by plotting cell counts against superoxide quantification (FL3 Log). Overlay

histograms displayed a right shift indicating increased superoxide production in cells exposed to the different treatment conditions, compared to the DMSO vehicle control.

Table 4.12: Superoxide detection in BT-20 cells exposed to various treatment conditions. Kaluza Analysis version 1.5 (FL, USA) was used to generate statistical data followed by analysis, using the ANOVA-single factor model. The average fold change (FC) is displayed in the table ± the standard deviations (SD). A two-tailed Student's *t*-test was employed to calculate statistically significant differences (*P*-value <0.05) using the vehicle control and cells exposed to the individual treatments as baselines.

			Medium only	DMSO	Rotenone	Compound	8 Gy radiation	Combination
Compared to DMSO								
4 hours	ESE-16	FC± SD	1.06±0.17	1	2.48±0.19	1.37±0.12	1.13±0.03	1.54±0.17
		P-value	0.50	-	**4.84E-06**	**7.37E-04**	**9.09E-05**	**6.02E-04**
	LimPyr1	FC± SD	1.11±0.16	1	2.03±0.43	1.47±0.13	1.46±0.25	1.72±0.12
		P-value	0.24	-	**2.95E-03**	**3.93E-04**	**0.01**	**1.87E-05**
24 hours	ESE-16	FC ± SD	1.05±0.09	1	2.91±0.47	1.05±0.02	1.31±0.06	1.38±0.04
		P-value	0.39	-	**2.17E-03**	**1.45E-02**	**1.10E-03**	**9.51E-05**
	LimPyr1	FC ± SD	1.06±0.07	1	2.28±0.21	1.37±0.06	1.88±0.22	2.28±0.44
		P-value	0.21	-	**4.60E-04**	**5.43E-04**	**2.30E-03**	**0.01**
48 hours	ESE-16	FC ± SD	1.30±0.36	1	3.02±0.25	1.24±0.12	1.34±0.07	1.51±0.27
		P-value	0.15	-	**3.66E-06**	**0.01**	**6.88E-05**	**0.01**
	LimPyr1	FC ± SD	1.07±0.09	1	2.00±0.25	1.24±0.05	1.56±0.31	2.56±0.59
		P-value	0.21	-	**2.15E-03**	**2.88E-03**	**0.03**	**0.01**
Compared to compound								
4 hours	ESE-16	FC ± SD				1		1.13±0.08
		P-value				-		**0.02**
	LimPyr1	FC ± SD				1		1.18±0.15
		P-value				-		**4.96E-02**
24 hours	ESE-16	FC ± SD				1		1.32±0.06
		P-value				-		**8.4549E-04**
	LimPyr1	FC ± SD				1		1.66±0.31
		P-value				-		**0.02**
48 hours	ESE-16	FC ± SD				1		1.22±0.09
		P-value				-		**3.13E-03**
	LimPyr1	FC ± SD				1		1.86±0.43
		P-value				-		**0.02**
Compared to 8 Gy radiation								
4 hours	ESE-16	FC ±S D					1	1.37±0.13
		P-value					-	**1.41E-03**
	LimPyr1	FC ±S D					1	1.26±0.17
		P-value					-	**0.02**
24 hours	ESE-16	FC ± SD					1	1.08±0.02
		P-value					-	**0.01**
	LimPyr1	FC ± SD					1	1.43±0.20
		P-value					-	**0.03**
48 hours	ESE-16	FC ± SD					1	1.04±0.02
		P-value					-	**0.01**
	LimPyr1	FC ± SD					1	1.42±0.23
		P-value					-	**0.04**

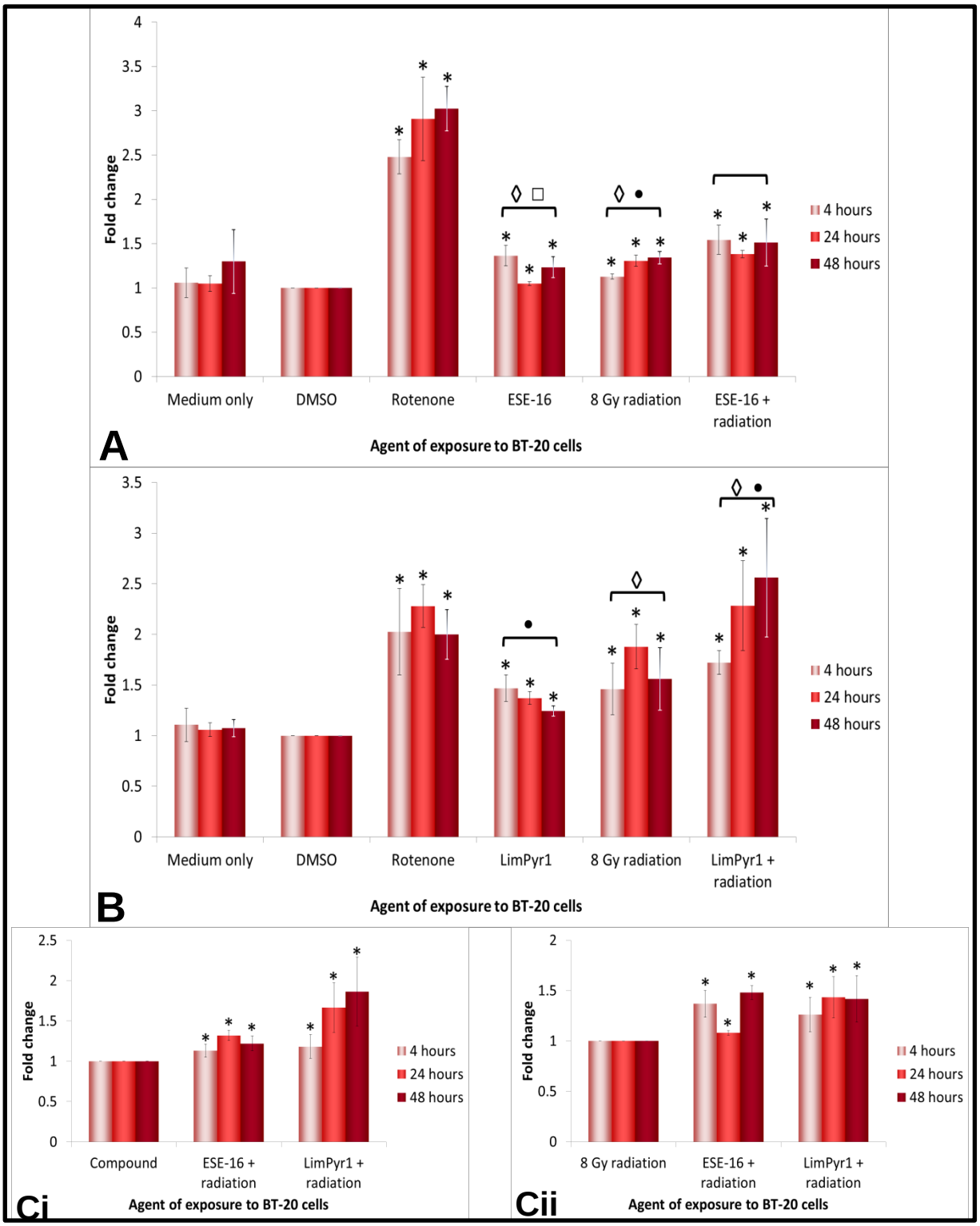

Figure 4.28: Graphical representation of superoxide quantification in BT-20 cells after exposure to different treatment conditions. ESE-16 and LimPyr1-exposed BT-20 cells displayed a significant increase in superoxide at the 4, 24 and 48 hour termination points (A+B). Superoxide production significantly decreased from 4 to 24 hours in ESE-16 exposed cells, but was restored after 48 hours (A). In contrast, superoxide production continuously decreased over the 48 hour time frame in LimPyr1 exposed BT-20 cells (B). BT-20 cells displayed a significant

increase in superoxide levels following 8 Gy radiation (A-B). ESE-16- and LimPyr1 pre-treated BT-20 cells displayed a significant increase in superoxide compared to the vehicle controls (A-B) and the individual treatments (C). The decrease in superoxide observed in LimPyr1 exposed cells was prevented in the combination therapy (B). The bar graph summarizes the mean fold increases of three biological repeats. Standard deviations are represented by T-bars and statistically significant differences are indicated with * (*P*-value <0.05) when compared to DMSO (A-B), cells exposed to ESE-16 and LimPyr1 only (Ci) or 8 Gy radiation only (Cii), ◊ when the 4 hour termination point was compared to the 24 hour termination point, □ when the 24 hour termination point was compared to the 48 hour termination point; and • when the 4 hour termination point was compared to the 48 hour termination point.

4.2.3.2 Mitochondrial transmembrane potential: Flow cytometric quantification of Mitocapture™

As an early intracellular apoptotic event, the mitochondrial transmembrane potential decreases (107). This increases the permeability of the outer membrane, resulting in the release of apoptotic proteins such as cytochrome *c* (108). The permeability of the mitochondrial transmembrane was quantified following exposure to the different treatments, via flow cytometry, employing the Mitocapture™ fluorometric kit.

MCF-7-, MDA-MB-231- and BT-20 cells grown in media only or exposed to DMSO served as negative- and vehicle controls, respectively. No statistically significant differences were observed in the permeability of the mitochondrial transmembrane in cells propagated in growth medium when compared the vehicle control (Table 4.13). A positive control for apoptosis was included, by exposing the cells to vinblastine. A significant increase in Mitocapture™ was observed in MCF-7-, MDA-MB-231- and BT-20 cells exposed to the positive control (Figure 4.29).

MCF-7 cells exposed to LimPyr1 revealed a significant increase (1.11±0.03 fold) in Mitocapture™, but no changes in the mitochondrial transmembrane potential was quantified in the ESE-16 exposed samples (Table 4.13). A statistically significant increase in

Mitocapture™ was observed in MDA-MB-231- (1.20±0.11- and 1.36±0.027 fold increases) and BT-20 cells (1.18±0.07- and 1.16±0.15 fold increase) exposed to ESE-16 and LimPyr1, respectively. Mitocapture™ was significantly increased in MCF-7- (1.47±0.29 (DMEM)- and 1.26±0.20 (RPMI) fold increases), MDA-MB-231- (1.32±0.19 (DMEM)- and 1.42±0.18 (RPMI) fold increases) and BT-20 cells (1.21±0.07 (DMEM/F-12)- and 1.32±0.19 (RPMI) fold increases) 24 hours after 8 Gy radiation, compared to the vehicle control. MCF-7 cells pre-treated with ESE-16 or LimPyr1 24 hours prior to 8 Gy radiation revealed a 1.74±0.29- and 1.43±0.17 fold increase in Mitocapture™, respectively. Similarly, ESE-16 and LimPyr1 pre-treated MDA-MB-231- (1.69±0.24- and 1.63±0.27 fold increases, respectively) and BT-20 cells (1.31±0.08- and 1.52±0.10 fold increases, respectively) displayed significant increases in Mitocapture™ 24 hours after radiation (Figure 4.29).

The augmented effect of ESE-16 and LimPyr1 in combination with radiation was observed when the combination therapy was compared to the individual treatments. A statistically significant increase in Mitocapture™ were observed in MCF-7- (1.57±0.06- and 1.19±0.08 fold increases, respectively), MDA-MB-231- (1.40±0.10- and 1.28±.15 fold increases, respectively) and BT-20 cells (1.29±0.09- and 1.08±0.04 fold increases, respectively) exposed to the ESE-16/radiation combination therapy when compared to cells exposed to ESE-16 and 8 Gy radiation only (Figure 4.30). Compared to cells exposed to LimPyr1 only, LimPyr1 pre-treated MCF-7-, MDA-MB-231-, and BT-20 cells displayed significant fold increases of 1.23±0.14, 1.22±0.15 and 1.29±0.20 in Mitocapture™, respectively (Table 4.13). Mitocapture™ was also significantly increased in the LimPyr1 pre-treated MCF-7- (1.15±0.07 fold increase), MDA-MB-231- (1.08±0.06 fold increase) and BT-20 cells (1.16±0.15 fold increase), compared to cells exposed to 8 Gy radiation only (Figure 4.30).

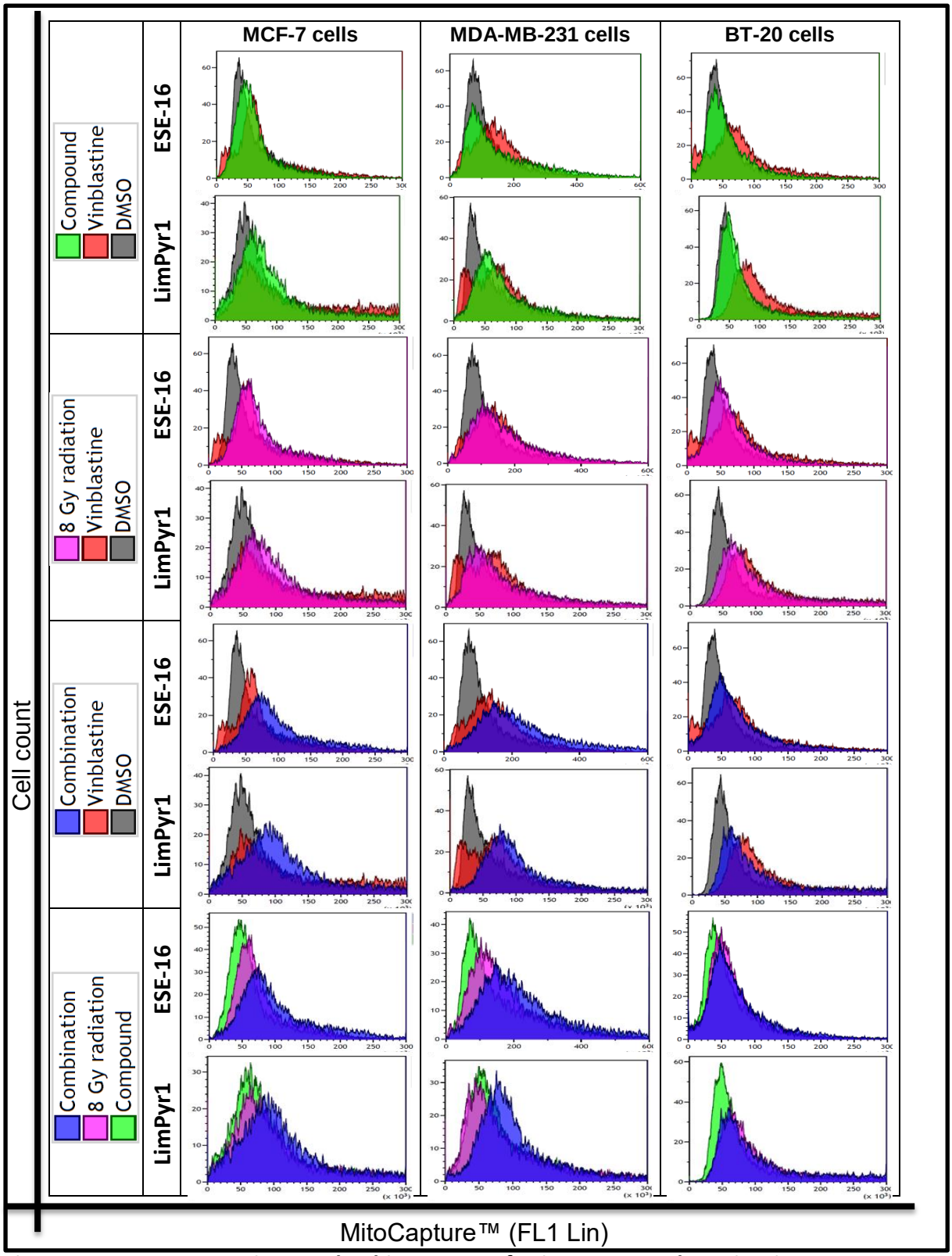

Figure 4.29: Representative overlay histograms of Mitocapture™ detection in MCF-7-, MDA-MB-231- and BT-20 cells exposed to appropriate controls and various treatment conditions. Histograms were obtained 24 hours after irradiation by plotting cell count against Mitocapture™ detection (FL1 Lin). Overlay histograms displayed a right shift in cells exposed to the different treatment conditions, compared to the DMSO vehicle control.

Table 4.13: Mitocapture™ quantification in breast cancer cells exposed to various treatment conditions. Data analyses were completed using the ANOVA-single factor model, using data generated with Kaluza Analysis version 1.5 (FL, USA). The table displays the averaged fold change (FC) of three biological repeats and the standard deviations (SD). A two-tailed Student's *t*-test was used to calculate statistically significant differences (*P*-value <0.05) by using the vehicle control and cells exposed to the individual treatments as baselines.

			Medium only	DMSO	Vinblastine	Compound	8 Gy radiation	Combination
Compared to DMSO								
MCF-7	ESE-16	FC± SD	1.12±0.29	1	1.14±0.05	1.11±0.20	1.47±0.29	1.74±0.29
		P-value	0.53	-	**1.09E-02**	0.41	**4.91E-02**	**1.16E-02**
	LimPyr1	FC± SD	0.97±0.27	1	1.65±0.33	1.11±0.03	1.26±0.20	1.43±0.17
		P-value	0.81	-	**1.05E-02**	**6.02E-04**	**0.04**	**2.63E-03**
MDA-MB-231	ESE-16	FC ± SD	1.07±0.11	1	1.80±0.39	1.20±0.11	1.32±0.19	1.69±0.24
		P-value	0.34	-	**0.02**	**0.04**	**0.04**	**7.67E-03**
	LimPyr1	FC ± SD	0.94±0.08	1	1.11±0.04	1.36±0.27	1.42±0.18	1.63±0.27
		P-value	0.19	-	**2.06E-03**	**0.04**	**3.50E-03**	**3.30E-03**
BT-20	ESE-16	FC ± SD	0.94±0.15	1	1.35±0.16	1.18±0.07	1.21±0.07	1.31±0.08
		P-value	0.54	-	**1.75E-02**	**1.78E-02**	**6.24E-03**	**3.01E-03**
	LimPyr1	FC ± SD	1.01±0.32	1	1.38±0.34	1.16±0.15	1.32±0.19	1.52±0.10
		P-value	0.96	-	**0.04**	**0.04**	**6.62E-03**	**5.66E-06**
Compared to compound								
MCF-7	ESE-16	FC ± SD				1		1.57±0.06
		P-value				-		**5.98E-05**
	LimPyr1	FC ± SD				1		1.23±0.14
		P-value				-		**1.65E-02**
MDA-MB-231	ESE-16	FC ± SD				1		1.40±0.10
		P-value				-		**2.51E-03**
	LimPyr1	FC ± SD				1		1.22±0.15
		P-value				-		**0.03**
BT-20	ESE-16	FC ± SD				1		1.29±0.09
		P-value				-		**7.49E-03**
	LimPyr1	FC ± SD				1		1.29±0.20
		P-value				-		**1.42E-02**
Compared to 8 Gy radiation								
MCF-7	ESE-16	FC ±S D					1	1.19±0.08
		P-value					-	**1.69E-02**
	LimPyr1	FC ±S D					1	1.15±0.07
		P-value					-	**5.30E-03**
MDA-MB-231	ESE-16	FC ± SD					1	1.28±0.15
		P-value					-	**0.03**
	LimPyr1	FC ± SD					1	1.08±0.06
		P-value					-	**0.03**
BT-20	ESE-16	FC ± SD					1	1.08±0.04
		P-value					-	**0.04**
	LimPyr1	FC ± SD					1	1.16±0.15
		P-value					-	**0.04**

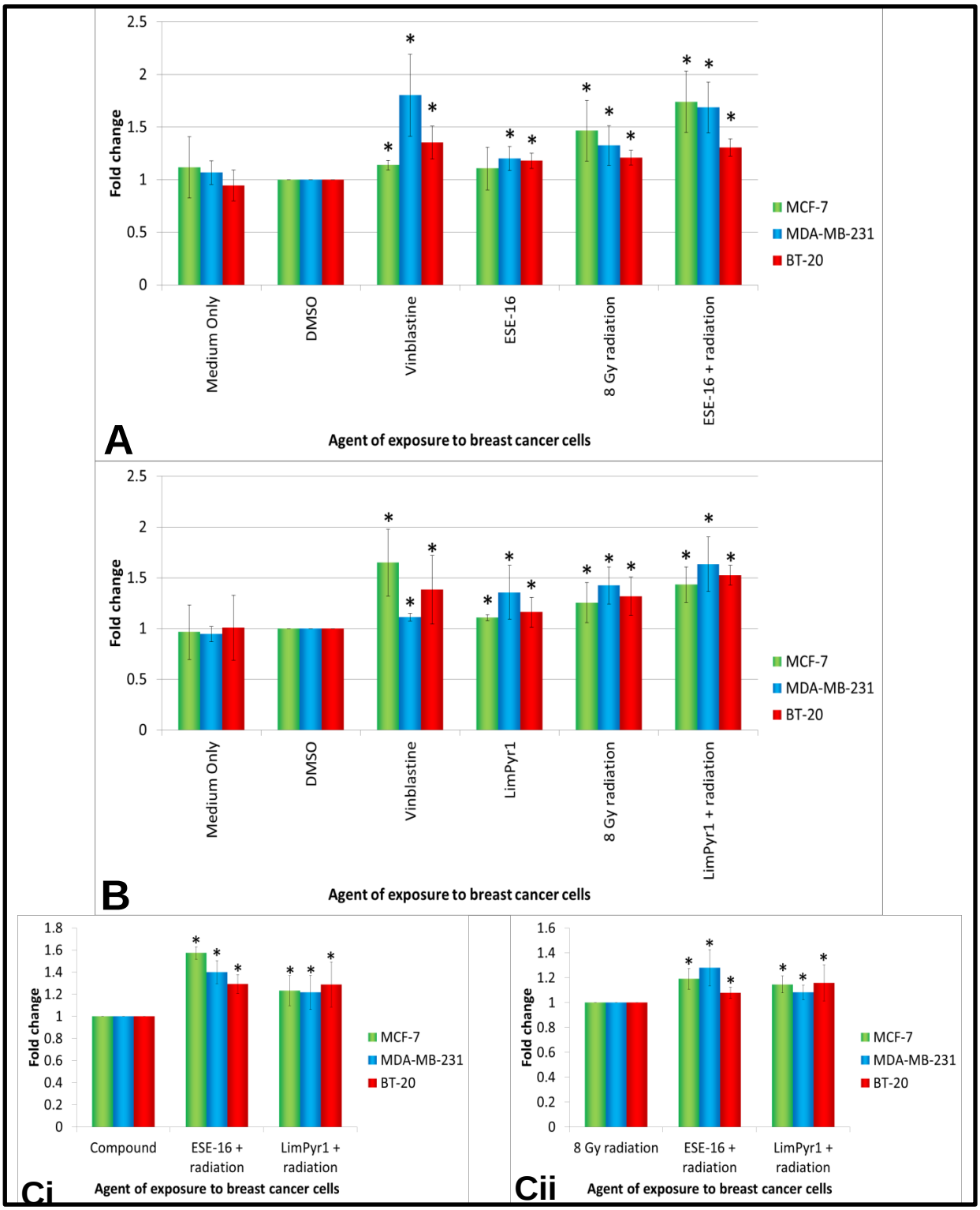

Figure 4.30: Graphical representation of Mitocapture™ quantification in MCF-7-, MDA-MB-231- and BT-20 cells after exposure to different treatment conditions. ESE-16 exposed MDA-MB-231- and BT-20 cells displayed a statistically significant increase in Mitocapture™ compared to DMSO (A). MCF-7-, MDA-MB-231- and BT-20 cells displayed a significant increase in Mitocapture™ when exposed to LimPyr1 (B) and 8 Gy radiation (A-B), respectively. Following exposure to either ESE-16 or LimPyr1 24 hours prior to 8 Gy radiation MCF-7-, MDA-MB-231-

and BT-20 cells displayed a significant increase in Mitocapture™ when compared to the vehicle controls (A-B) and the individual treatment conditions (C). The bar graph summarizes the mean fold increases of three biological repeats. Standard deviations are represented by T-bars and statistically significant differences are indicated with * (*P*-value <0.05) when compared to DMSO (A-B), cells exposed to ESE-16 and LimPyr1 only (Ci) or 8 Gy radiation only (Cii).

4.2.3.3 Western blot

4.2.3.3.1 Bax and cleaved caspase 3

Increased apoptotic cell death was confirmed in the combination treatments during annexin V quantification and cell cycle analysis. Activation of the intrinsic apoptotic pathway results in the activation of Bax which inserts pores into the mitochondrial outer membrane (482). The latter was quantified via Mitocapture™. Apoptosis can be induced via a caspase dependent or -independent route downstream of Bax (483). The effector caspase, caspase 3, has been identified as a key mediator for caspase dependent apoptotic cell death (483). In order to identify whether the combination therapies induce apoptosis via a caspase dependent or -independent manner, Bax and cleaved caspase 3 were quantified via a western blot in MDA-MB-231- and BT-20 cells, 24 hours after radiation. As MCF-7 cells do not express caspase 3 (484), only Bax was quantified for this cell line.

MCF-7 cells exposed to ESE-16 (2.59±0.87 fold increase), LimPyr1 (1.84±0.09 fold increase) and 8 Gy radiation (3.33±1.23- (DMEM) and 3.96±1.07 (RPMI) fold increases) displayed a significant increase in Bax expression compared to the vehicle control (Figure 4.31). ESE-16 pre-treated MCF-7 cells displaced a significant increase in Bax expression compared to DMSO (4.25±0.42 fold increase), cells exposed to ESE-16 (1.70±0.29 fold increase) and cells exposed to 8 Gy radiation only (1.13±0.06 fold increase) (Figure 4.32). Bax expression was also significantly increased in MCF-7 cells exposed to LimPyr1 24 hours prior to radiation compared to the vehicle control (5.04±0.50 fold increase) and cells exposed to the LimPyr1 (2.65±0.43 fold increase) or 8 Gy radiation only (1.44±0.22 fold increase) (Table 4.14).

Exposure to ESE-16 (1.16±0.06 fold increase), 8 Gy radiation (1.64±0.26 (DMEM)- and 2.36±0.81 (RPMI) fold increases), ESE-16 prior to radiation (2.78±0.67 fold increase) and LimPyr1 prior to radiation (3.74±1.11 fold increase) significantly increased Bax expression in MDA-MB-231 cells (Figure 4.31). Additionally, ESE-16- and LimPyr1 pre-treated cells displayed a significant increase in Bax expression compared to cells exposed to the compounds (2.47±0.66- and 2.95±0.98 fold increases, respectively) and 8 Gy radiation only (1.47±0.09- and 1.61±0.31 fold increases, respectively) (Table 4.14). BT-20 cells exposed to LimPyr1 (2.01±0.58 fold increase) and 8 Gy radiation (1.61±0.29 (DMEM/F-12)- and 2.29±0.44 (RPMI) fold increases) expressed significantly higher Bax levels compared to the vehicle control (Figure 4.33). ESE-16 pre-treated BT-20 cells displayed a significant increase in Bax compared to DMSO (2.37±0.36 fold increase), cells exposed to ESE-16 (1.51±0.14 fold increase) or 8 Gy radiation only (1.49±0.21 fold increase) (Table 4.14). Similarly, LimPyr1 pre-treated BT-20 cells displayed a significant increase in Bax expression compared to DMSO (2.40±0.01 fold increase), cells exposed to LimPyr1 (1.46±0.06 fold increase) and cells exposed to 8 Gy radiation only (1.18±0.03 fold increase) (Figure 4.34).

MDA-MB-231- and BT-20 cells exposed to ESE-16 (5.81±1.98- and 1.59±0.11 fold increases, respectively) and LimPyr1 (4.92±0.31- and 3.13±0.96 fold increases, respectively) displayed a significant increase in cleaved caspase 3 compared to DMSO (Table 4.15). Exposure to 8 Gy radiation significantly increased cleaved caspase 3 in MDA-MB-231- (9.81±5.49 (DMEM)- and 3.66±0.90 (RPMI) fold increases) and BT-20 cells (1.26±0.14 (DMEM)- and 3.35±0.61 (RPMI) fold increases). MDA-MB-231 cells pre-treated with ESE-16 (25.38±4.42 fold increase) and LimPyr1 (4.58±1.47 fold increase) displayed significantly higher cleaved caspase 3 levels compared to the vehicle control (Figure 4.33). Compared to DMSO treated cells, increased cleaved caspase 3 protein levels were also observed in BT-20 cells pre-treated with ESE-16 (1.42±0.20 fold increase) and LimPyr1 (4.33±1.08 fold increase) (Figure 4.34). ESE-16 pre-treated MDA-MB-231- (14.86±3.08 fold increase) and BT-20 cells (1.93±0.31 fold increase) displayed significantly higher cleaved caspase 3 protein levels compared to cells exposed to the compounds only. Additionally, MDA-MB-231- and BT-20 cells exposed to the ESE-16- (2.18±0.53- and 1.18±0.05 fold increases, respectively) and the

LimPyr1 (1.40±0.15- and 1.29±0.14 fold increases, respectively) combination therapies displayed a significant increase in cleaved caspase 3 compared to cells exposed to 8 Gy radiation only (Table 4.15).

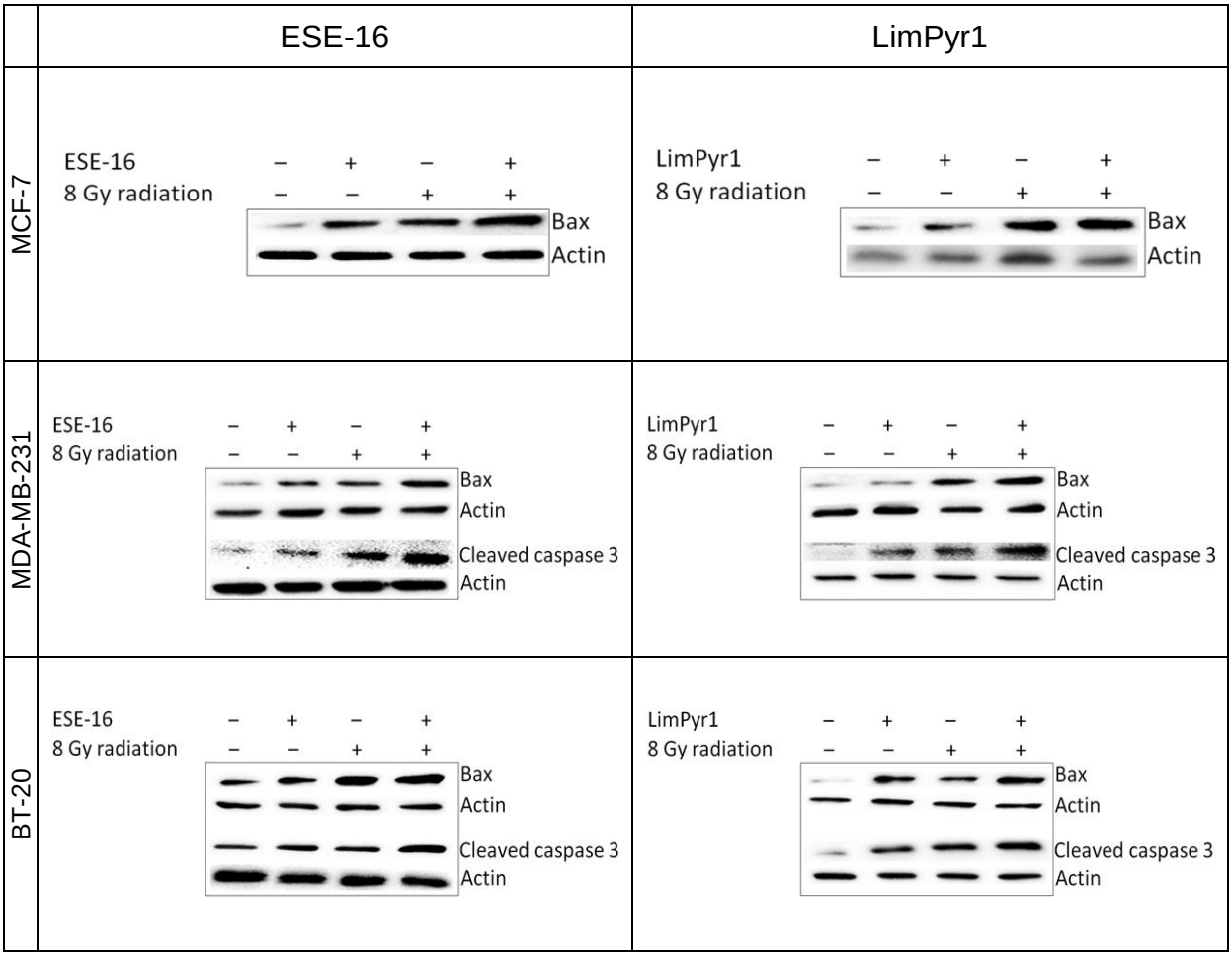

Figure 4.31: Western blots visualizing Bax and cleaved caspase 3 protein expressions in MCF-7-, MDA-MB-231- and BT-20 cells exposed to various treatment conditions. The expression of Bax was quantified in the MCF-7 cell line, whereas Bax and cleaved caspase 3 protein expressions were quantified in MDA-MB-231- and BT-20 cell exposed to ESE-16, LimPyr1 and 8 Gy radiation. Additionally, cells were pre-treated with ESE-16 or LimPyr1 24 hours prior to radiation.

Table 4.14: Bax expression in MCF-7-, MDA-MB-231- and BT-20 cells exposed to various treatment conditions. ChemiDoc MP (Bio-rad, CA, USA) was used to visualize proteins followed by analysis, using Image Lab Software Version 5.2.1 (Bio-rad, CA, USA). The ANOVA-single factor model and a two-tailed Student's t-test were used to analyze data. The mean fold change (FC) of three biological repeats is displayed in the table ± standard deviations (SD). Cells exposed to DMSO and the individual treatment conditions were used as baselines to calculate statistically significant differences (*P*-value <0.05).

			DMSO	Compound	8 Gy radiation	Combination
Compared to DMSO						
MCF-7	ESE-16	FC± SD	1	2.59±0.87	3.33±1.23	4.25±0.42
		P-value	-	**0.04**	**0.04**	**7.00E-04**
	LimPyr1	FC± SD	1	1.84±0.09	3.96±1.07	5.04±0.50
		P-value	-	**3.86E-04**	**0.01**	**1.52E-04**
MDA-MB-231	ESE-16	FC ± SD	1	1.16±0.06	1.64±0.26	2.78±0.67
		P-value	-	**0.01**	**0.02**	**0.01**
	LimPyr1	FC ± SD	1	1.08±0.08	2.36±0.81	3.74±1.11
		P-value	-	0.17	**0.04**	**0.01**
BT-20	ESE-16	FC ± SD	1	1.46±0.29	1.61±0.29	2.37±0.36
		P-value	-	0.06	**0.02**	**2.75E-03**
	LimPyr1	FC ± SD	1	2.01±0.58	2.29±0.44	2.40±0.01
		P-value	-	**4.54E-02**	**0.01**	**4.26E-08**
Compared to compound						
MCF-7	ESE-16	FC ± SD		1		1.70±0.29
		P-value		-		**0.01**
	LimPyr1	FC ± SD		1		2.65±0.43
		P-value		-		**0.01**
MDA-MB-231	ESE-16	FC ± SD		1		2.47±0.66
		P-value		-		**0.02**
	LimPyr1	FC ± SD		1		2.95±0.98
		P-value		-		**0.03**
BT-20	ESE-16	FC ± SD		1		1.51±0.14
		P-value		-		**0.01**
	LimPyr1	FC ± SD		1		1.46±0.06
		P-value		-		**6.19E-04**
Compared to 8 Gy radiation						
MCF-7	ESE-16	FC ±S D			1	1.13±0.06
		P-value			-	**0.03**
	LimPyr1	FC ±S D			1	1.44±0.22
		P-value			-	**0.03**
MDA-MB-231	ESE-16	FC ± SD			1	1.47±0.09
		P-value			-	**2.51E-03**
	LimPyr1	FC ± SD			1	1.61±0.31
		P-value			-	**0.03**
BT-20	ESE-16	FC ± SD			1	1.49±0.21
		P-value			-	**0.02**
	LimPyr1	FC ± SD			1	1.18±0.03
		P-value			-	**1.51E-03**

Table 4.15: Cleaved caspase 3 expression in MDA-MB-231 and BT-20 cells exposed to various treatment conditions. Proteins were visualized on a ChemiDoc MP (Bio-rad, CA, USA) and quantified, using Image Lab Software Version 5.2.1 (Bio-rad, CA, USA). Data were analyzed, using the ANOVA-single factor model and a two-tailed Student's *t*-test. Three biological repeats were completed. The mean fold change (FC) and standard deviations (SD) are displayed in the table. Statistically significant differences (*P*-value <0.05) were calculated using DMSO and cells exposed to the individual treatment conditions as baselines.

			DMSO	Compound	8 Gy radiation	Combination
Compared to DMSO						
MDA-MB-231	ESE-16	FC ± SD	1	5.81±1.98	9.81±5.49	25.38±4.42
		P-value	-	**0.01**	**4.99E-02**	**1.86E-03**
	LimPyr1	FC ± SD	1	4.92±0.31	3.66±0.90	4.58±1.47
		P-value	-	**1.58E-04**	**0.01**	**0.02**
BT-20	ESE-16	FC ± SD	1	1.59±0.11	1.26±0.14	1.42±0.20
		P-value	-	**1.97E-03**	**0.03**	**0.03**
	LimPyr1	FC ± SD	1	3.13±0.96	3.35±0.61	4.33±1.08
		P-value	-	**0.02**	**2.65E-03**	**0.01**
Compared to compound						
MDA-MB-231	ESE-16	FC ± SD		1		14.86±3.08
		P-value		-		**3.37E-03**
	LimPyr1	FC ± SD		1		2.41±0.46
		P-value		-		**0.01**
BT-20	ESE-16	FC ± SD		1		1.93±0.31
		P-value		-		**0.01**
	LimPyr1	FC ± SD		1		1.41±0.14
		P-value		-		**0.01**
Compared to 8 Gy radiation						
MDA-MB-231	ESE-16	FC ± SD			1	2.18±0.53
		P-value			-	**0.02**
	LimPyr1	FC ± SD			1	1.40±0.15
		P-value			-	**0.01**
BT-20	ESE-16	FC ± SD			1	1.18±0.05
		P-value			-	**4.85E-03**
	LimPyr1	FC ± SD			1	1.29±0.14
		P-value			-	**0.03**

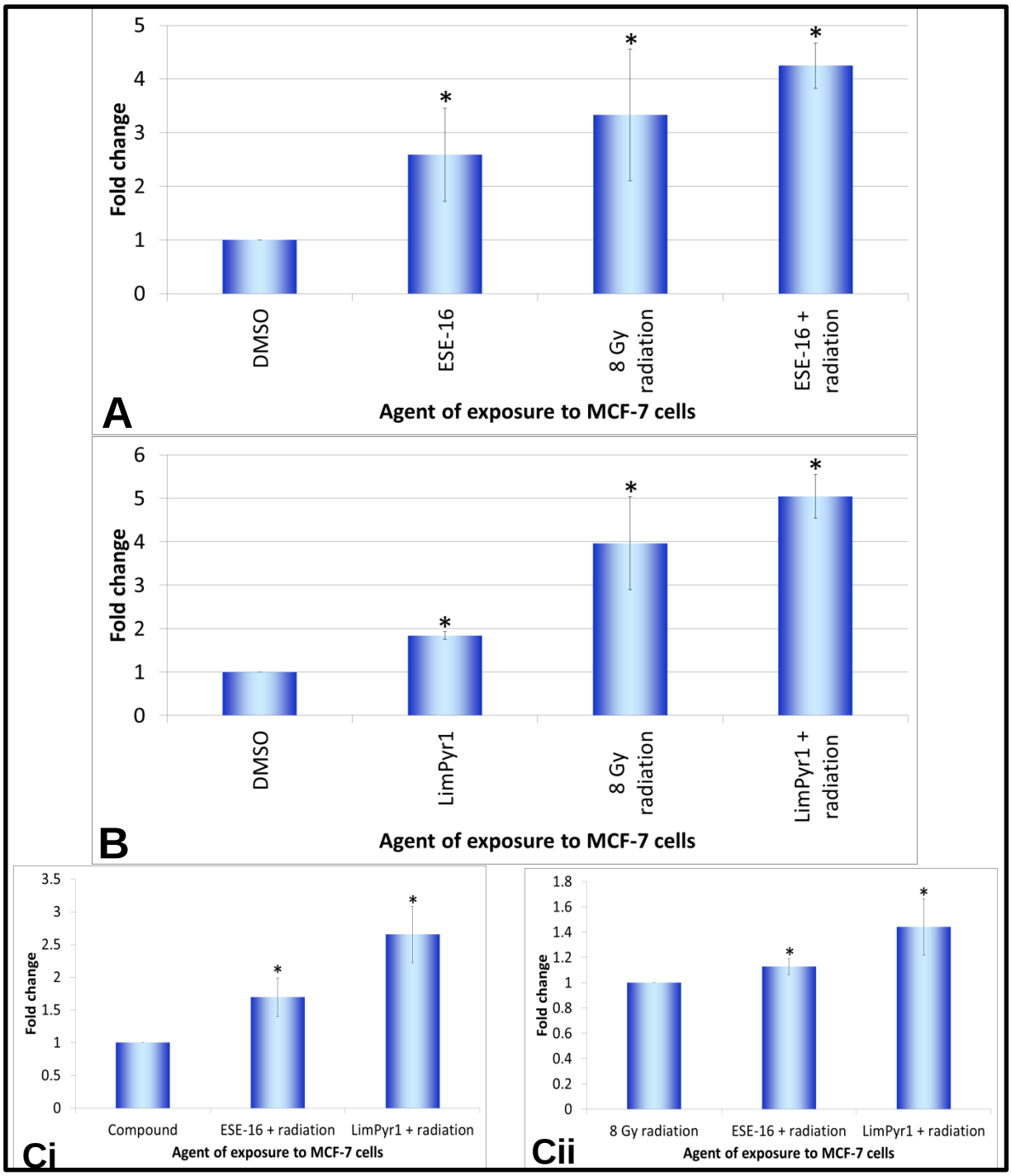

Figure 4.32: Graphical representation of Bax expression in MCF-7 cells exposed to different treatment conditions. MCF-7 cells exposed to ESE-16 (A) and LimPyr1 (B) displayed a significant increase in Bax expression. MCF-7 cells exposed to 8 Gy radiation (A-B), and ESE-16 (A) or LimPyr1 (B) 24 hours prior to 8 Gy radiation displayed a significant increase in Bax 24 hours after radiation. Compared to cells exposed to ESE-16 or LimPyr1 (Ci), or 8 Gy radiation (Cii) only, ESE-16- and LimPyr1 pre-treated MCF-7 cells displayed significantly higher Bax protein levels 24 hours after radiation. The bar graph summarizes the mean fold increases of three biological repeats and standard deviations are represented by T-bars. Statistically significant differences

are indicated with * (*P*-value <0.05) when compared to DMSO (A-B), cells exposed to ESE-16 and LimPyr1 (Ci) or 8 Gy radiation only (Cii).

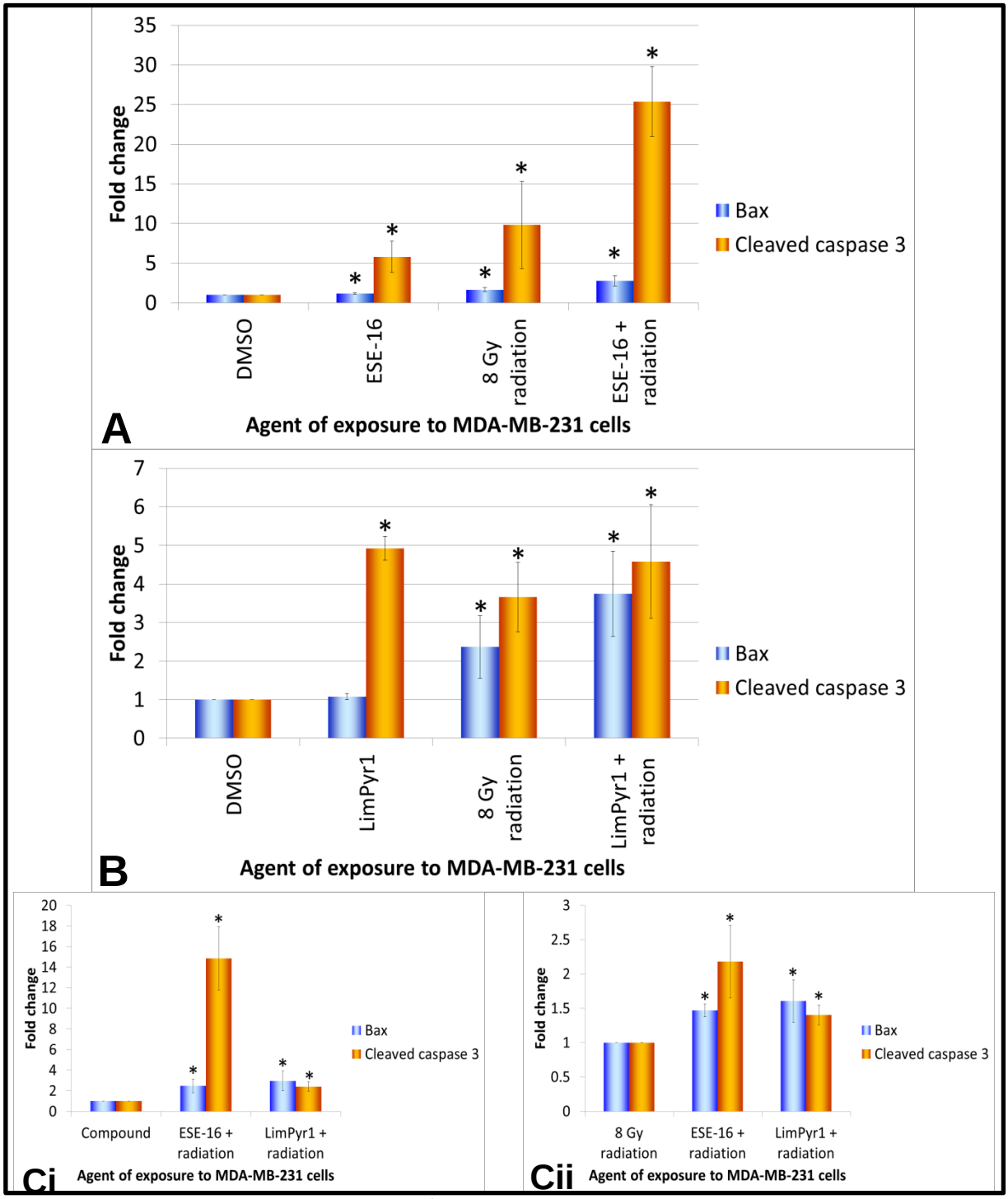

Figure 4.33: Graphical representation of Bax and cleaved caspase 3 proteins in MDA-MB-231 cells exposed to different treatment conditions. Bax and cleaved caspase 3 expressions was significantly increased in MDA-MB-231 cells exposed to ESE-16 and 8 Gy radiation, compared to DMSO (A-B). LimPyr1 exposed cells only expressed increased cleaved caspase 3 proteins levels (B). MDA-MB-231 cells exposed to ESE-16 (A) or LimPyr1 (B) 24 hours prior to radiation

expressed significantly higher Bax and cleaved caspase 3 protein levels compared to cells exposed to the vehicle (A-B), cells exposed to the compounds (Ci) and cells exposed to 8 Gy radiation only (Cii). The mean fold increases of three biological repeats are displayed in the bar graph. Standard deviations are represented by T-bars and statistically significant differences are indicated with * (P-value <0.05) when compared to DMSO (A-B), cells exposed to ESE-16 or LimPyr1 only (Ci) and 8 Gy radiation only (Cii).

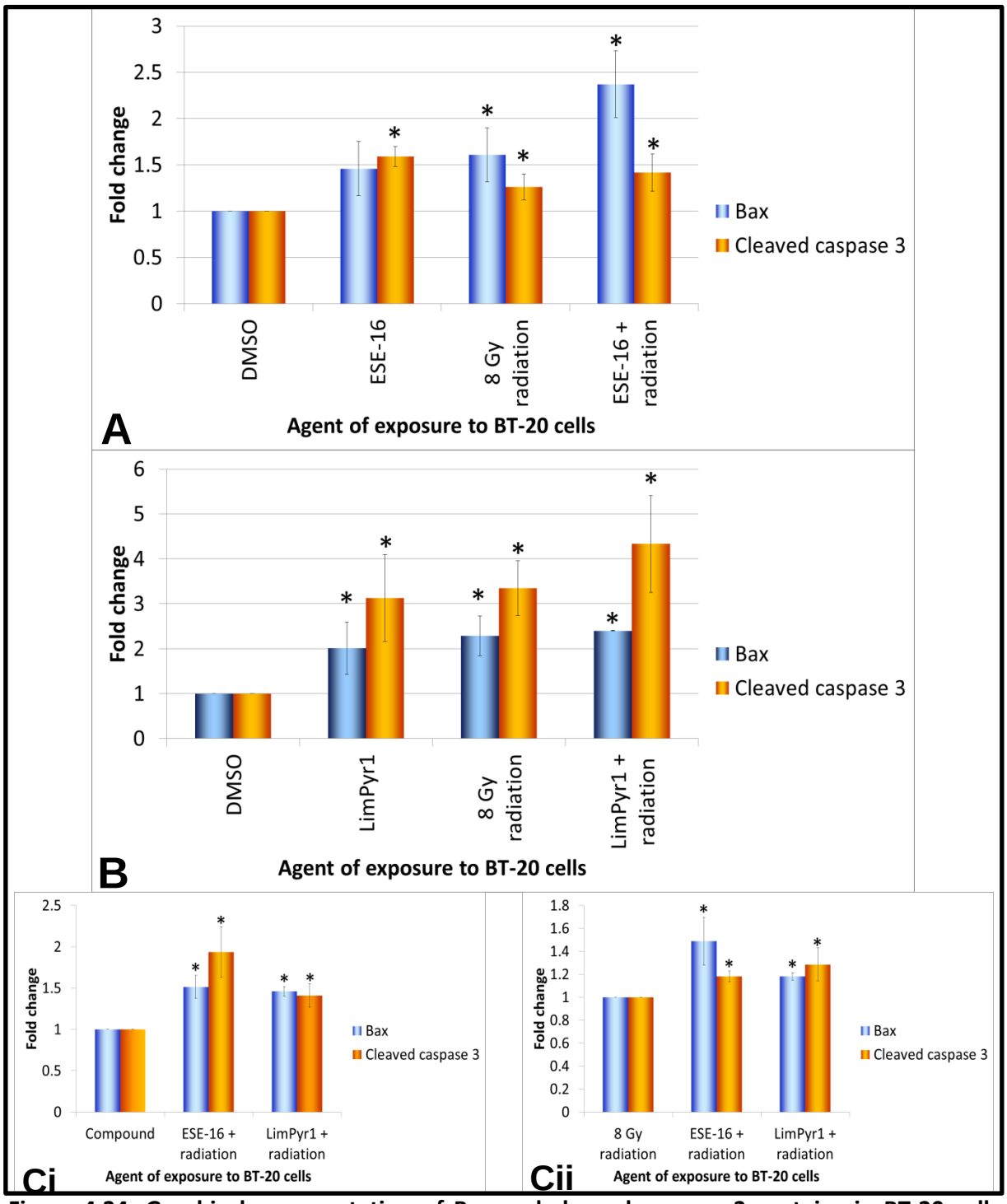

Figure 4.34: Graphical representation of Bax and cleaved caspase 3 proteins in BT-20 cells exposed to different treatment conditions. BT-20 cells exposed to ESE-16 displayed significantly

higher cleaved caspase 3 protein levels compared to the vehicle control (A). LimPyr1 (B) and 8 Gy radiation (A-B) exposure resulted in significantly higher Bax and cleaved caspase 3 protein levels compared to DMSO. Pre-treatment of BT-20 cells with ESE-16 (A) and LimPyr1 (B) resulted in elevated Bax and cleaved caspase 3 levels compared to DMSO (A-B) and cells exposed to the compounds (Ci) or 8 Gy radiation only (Cii). The bar graph illustrates the mean fold changes of three biological repeats, and the standard deviations are represented by T-bars. Statistically significant differences are indicated with * (P-value <0.05) when compared to DMSO (A-B), cells exposed to ESE-16 or LimPyr1 only (Ci) and 8 Gy radiation only (Cii).

4.2.3.3.2 p-Akt & p-FoxO1/3a

The protein, FoxO, is a downstream target of Akt/PKB and is tightly regulated by posttranslational modifications such as acetylation, ubiquitination and phosphorylation (485). Cell proliferation and -survival are regulated by the Akt kinase which inhibits the transcriptional functions of the pro-apoptotic FoxO proteins via phosphorylation. Phosphorylation of FoxO results in the translocation of the protein from the nucleus to the cytoplasm (457,485). In addition to decreasing the DNA binding activity and inducing cytoplasmic retention of FoxO, Akt/PKB also induces proteosomal degradation of FoxO in response to insulin and serum growth factors (486). The effect of microtubule regulators in combination with radiation on the Akt/FoxO pathway in breast cancer cells was evaluated via quantification of both proteins in their phosphorylated state, using western blot analysis 24 hours after irradiation.

MCF-7 cells exposed to ESE-16 (1.65±0.25- and 1.27±0.09 fold increase), LimPyr1 (2.06±0.19- and 2.52±0.66 fold increase) and 8 Gy (1.59±0.35- and 1.44±0.12 fold increase (DMEM), 1.42±0.21- and 1.93±0.49 fold increase (RPMI)) radiation displayed a significant increase in the phosphorylation of Akt and FoxO1/3a, respectively, compared to the vehicle control (Table 4.16 & 4.17). Interestingly, ESE-16- (0.61±0.12- and 0.54±0.08, respectively) and LimPyr1 (0.70±0.16- and 0.41±0.17, respectively) pre-treated MCF-7 cells displayed a significant decrease in phosphorylated Akt and FoxO1/3a proteins compared to the vehicle control taken as 1 (Table 4.16 & 4.17). Phosphorylation of Akt and FoxO1/3a was

significantly decreased in MCF-7 cells exposed to the ESE-16/radiation combination therapy compared to cells exposed to ESE-16 (0.37±0.01 and 0.37±0.15, respectively) or 8 Gy radiation only (0.45±0.06 and 0.41±0.03, respectively) taken as 1 (Figure 4.35). Similarly, LimPyr1 pre-treated MCF-7 cells displayed significantly lower phosphorylated Akt and FoxO1/3a levels compared to cells exposed to LimPyr1 (0.35±0.11 and 0.25±0.11, respectively) and 8 Gy radiation only (0.51±0.18 and 0.38±0.14, respectively) (Figure 4.36).

Exposure to ESE-16 (1.31±0.15- and 1.62±0.27 fold increase, respectively), LimPyr1 (1.31±0.15- and 1.62±0.27 fold increase, respectively) and 8 Gy radiation (1.20±0.03- and 1.78±0.29- (DMEM), 1.66±0.22- and 1.45±0.25 (RPMI) fold increase, respectively) significantly increased the phosphorylation of Akt and FoxO1/3a in MDA-MB-231 cells, whereas MDA-MB-231 cells exposed to ESE-16- (0.50±0.26 and 0.56±0.13, respectively) or LimPyr1 (0.91±0.02 and 0.76±0.12, respectively) 24 hours prior to radiation displayed a significant decrease in Akt and FoxO1/3a phosphorylation compared to DMSO (Figure 4.35). Pre-treated MDA-MB-231 cells displayed significantly lower phosphorylate Akt and FoxO1/3a protein levels compared to cells exposed to ESE-16 (0.35±0.27 and 0.31±0.08, respectively) or LimPyr1 (0.30±0.10 and 0.57±0.26, respectively) only (Table 4.16 & 4.17). Additionally, ESE-16 (0.42±0.22 and 0.42±0.14, respectively)- and LimPyr1 (0.37±0.11 and 0.64±0.20, respectively) pre-treated MDA-MB-231 cells displayed a significant decreased in the phosphorylation of Akt and FoxO1/3a compared to cells exposed to 8 Gy radiation only (Figure 4.37).

Phosphorylation of Akt was significantly increased in BT-20 cells exposed to ESE-16 (1.50±0.24 fold increase) and 8 Gy radiation (2.01±0.55- (DMEM/F-12) and 1.20±0.12 (RPMI) fold increase) compared to DMSO (Table 4.16). FoxO1/3a phosphorylation was significantly higher in BT-20 cells exposed to ESE-16 (1.09±0.05 fold increase), LimPyr1 (1.57±0.08 fold increase) and 8 Gy radiation (1.75±0.06- (DMEM/F-12) and 1.32±0.06 (RPMI) fold increase), compared to DMSO (Table 4.17). In contrast, pre-treatment of BT-20 cells with ESE-16 (0.85±0.03 and 0.70±0.11, respectively) or LimPyr1 (0.44±0.12 and 0.31±0.13, respectively)

significantly decrease the phosphorylation of Akt and FoxO1/3a compared to DMSO (Figure 4.35). Additionally, ESE-16- and LimPyr1 pre-treated BT-20 cells displayed a significant decrease in Akt and FoxO1/3a phosphorylation compared to cells exposed to ESE-16 (0.56±0.08 and 0.78±0.13, respectively) or LimPyr1 only (0.54±0.24 and 0.29±0.22, respectively). ESE-16 (0.50±0.06 and 0.44±0.10, respectively)- and LimPyr1 (0.80±0.03 and 0.22±0.13, respectively) pre-treated BT-20 cells also displayed significantly lower levels of phosphorylated Akt and FoxO1/3a compared to cells exposed to 8 Gy radiation only (Figure 4.38).

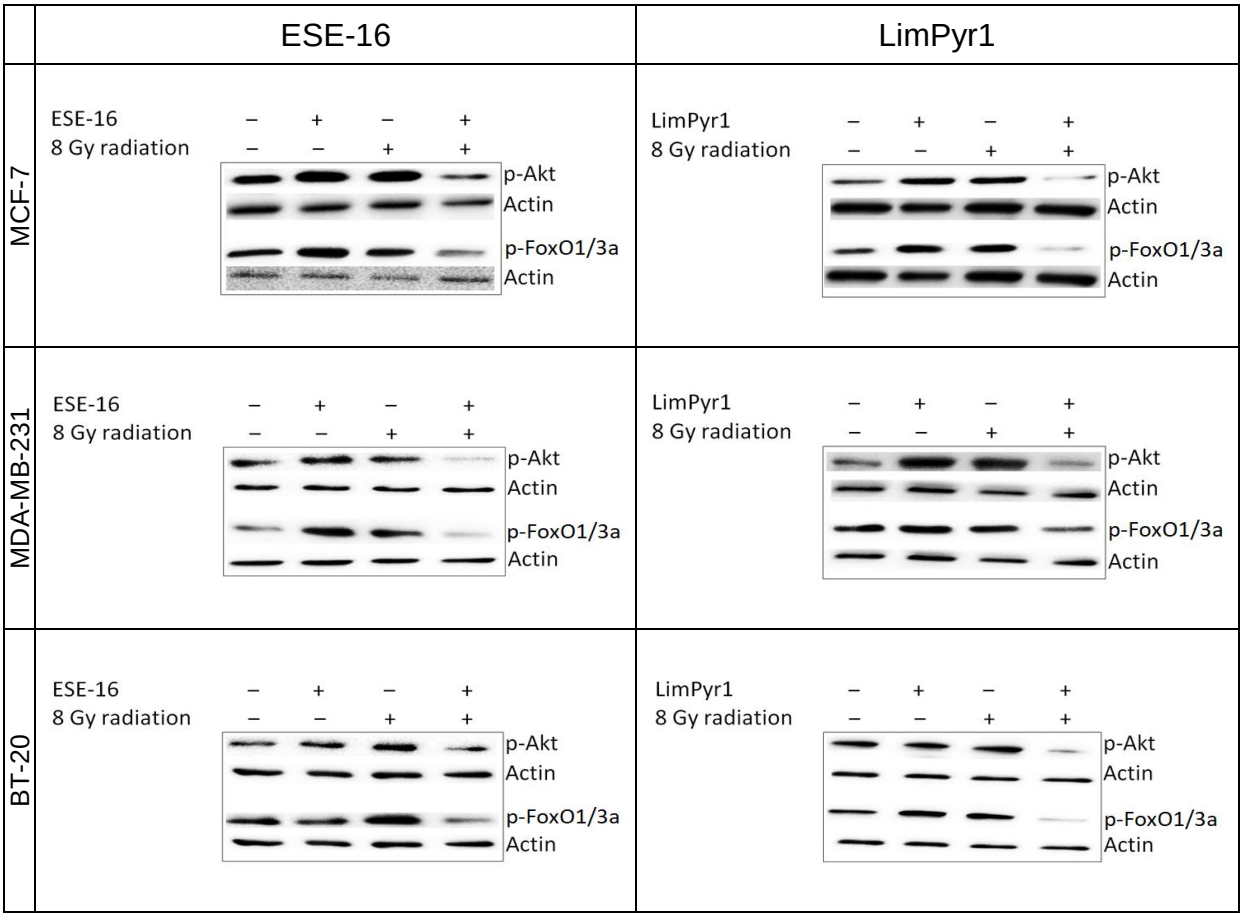

Figure 4.35: Western blots visualizing phosphorylated Akt and FoxO1/3a protein levels in MCF-7-, MDA-MB-231- and BT-20 cells exposed to various treatment conditions. Breast cancer cells were exposed to ESE-16, LimPyr1, 8 Gy radiation, ESE-16 24 hours prior to radiation and LimPyr1 24 hours prior to radiation. Phosphorylated Akt and FoxO1/3a proteins were quantified 24 hours after radiation.

Table 4.16: Akt phosphorylation in MCF-7-, MDA-MB-231- and BT-20 cells exposed to various treatment conditions. Phosphorylated proteins were visualized with a ChemiDoc MP (Bio-rad, CA, USA) followed by analysis, using Image Lab Software Version 5.2.1 (Bio-rad, CA, USA). Data were analyzed using an ANOVA-single factor model and a two-tailed Student's *t*-test. The mean fold changes (FC) of three biological repeats are displayed in the table ± standard deviations (SD). Cells exposed to DMSO and the individual treatment conditions were used as baselines to calculate statistically significant differences (*P*-value <0.05).

			DMSO	Compound	8 Gy radiation	Combination
Compared to DMSO						
MCF-7	ESE-16	FC± SD	1	1.65±0.25	1.59±0.35	0.61±0.12
		P-value	-	**0.02**	**0.04**	**0.01**
	LimPyr1	FC± SD	1	2.06±0.19	1.42±0.21	0.70±0.16
		P-value	-	**7.11E-04**	**0.02**	**0.03**
MDA-MB-231	ESE-16	FC ± SD	1	1.31±0.15	1.20±0.03	0.50±0.26
		P-value	-	**0.03**	**1.75E-04**	**0.03**
	LimPyr1	FC ± SD	1	3.20±1.13	1.66±0.22	0.91±0.02
		P-value	-	**0.03**	**0.01**	**2.48E-03**
BT-20	ESE-16	FC ± SD	1	1.50±0.24	2.01±0.55	0.85±0.03
		P-value	-	**0.03**	**0.03**	**3.01E-03**
	LimPyr1	FC ± SD	1	0.94±0.19	1.20±0.12	0.44±0.12
		P-value	-	0.63	**4.94E-02**	**2.93E-03**
Compared to compound						
MCF-7	ESE-16	FC ± SD		1		0.37±0.01
		P-value		-		**4.35E-06**
	LimPyr1	FC ± SD		1		0.35±0.11
		P-value		-		**4.67E-04**
MDA-MB-231	ESE-16	FC ± SD		1		0.35±0.27
		P-value		-		**0.01**
	LimPyr1	FC ± SD		1		0.30±0.10
		P-value		-		**9.60E-04**
BT-20	ESE-16	FC ± SD		1		0.56±0.08
		P-value		-		**8.40E-04**
	LimPyr1	FC ± SD		1		0.54±0.24
		P-value		-		**0.04**
Compared to 8 Gy radiation						
MCF-7	ESE-16	FC ±S D			1	0.45±0.06
		P-value			-	**6.80E-05**
	LimPyr1	FC ±S D			1	0.51±0.18
		P-value			-	**0.01**
MDA-MB-231	ESE-16	FC ± SD			1	0.42±0.22
		P-value			-	**0.01**
	LimPyr1	FC ± SD			1	0.37±0.11
		P-value			-	**6.26E-04**
BT-20	ESE-16	FC ± SD			1	0.50±0.06
		P-value			-	**1.32E-04**
	LimPyr1	FC ± SD			1	0.80±0.03
		P-value			-	**1.17E-03**

Table 4.17: FoxO1/3a phosphorylation in MCF-7-, MDA-MB-231- and BT-20 cells exposed to various treatment conditions. A ChemiDoc MP (Bio-rad, CA, USA) was used to visualize the phosphorylated proteins. Bands were quantified using Image Lab Software Version 5.2.1 (Bio-rad, CA, USA). The ANOVA-single factor model and a two-tailed Student's *t*-test were used to analyze the data of three biological repeats. The mean fold change (FC) and standard deviations (SD) are presented in the table. Statistically significant differences (*P*-value <0.05) were calculated using cells exposed to DMSO and the individual treatment conditions as baselines.

			DMSO	Compound	8 Gy radiation	Combination
Compared to DMSO						
MCF-7	ESE-16	FC± SD	1	1.27±0.09	1.44±0.12	0.54±0.08
		P-value	-	**0.01**	**0.01**	**5.74E-04**
	LimPyr1	FC± SD	1	2.52±0.66	1.93±0.49	0.41±0.17
		P-value	-	**0.02**	**0.04**	**0.01**
MDA-MB-231	ESE-16	FC ± SD	1	1.62±0.27	1.78±0.29	0.56±0.13
		P-value	-	**0.02**	**0.01**	**0.01**
	LimPyr1	FC ± SD	1	2.11±0.23	1.45±0.25	0.76±0.12
		P-value	-	**2.92E-03**	**0.04**	**0.03**
BT-20	ESE-16	FC ± SD	1	1.09±0.05	1.75±0.06	0.70±0.11
		P-value	-	**0.03**	**2.48E-05**	**0.01**
	LimPyr1	FC ± SD	1	1.57±0.08	1.32±0.06	0.31±0.13
		P-value	-	**9.36E-04**	**2.50E-03**	**7.99E-04**
Compared to compound						
MCF-7	ESE-16	FC ± SD		1		0.37±0.15
		P-value		-		**1.91E-03**
	LimPyr1	FC ± SD		1		0.25±0.11
		P-value		-		**3.43E-04**
MDA-MB-231	ESE-16	FC ± SD		1		0.31±0.08
		P-value		**-**		**4.33E-04**
	LimPyr1	FC ± SD		1		0.57±0.26
		P-value		**-**		**0.04**
BT-20	ESE-16	FC ± SD		1		0.78±0.13
		P-value		-		**0.04**
	LimPyr1	FC ± SD		1		0.29±0.22
		P-value		-		**0.01**
Compared to 8 Gy radiation						
MCF-7	ESE-16	FC ±S D			1	0.41±0.03
		P-value			**-**	**3.65E-06**
	LimPyr1	FC ±S D			1	0.38±0.14
		P-value			**-**	**1.63E-03**
MDA-MB-231	ESE-16	FC ± SD			1	0.42±0.14
		P-value			**-**	**2.21E-03**
	LimPyr1	FC ± SD			1	0.64±0.20
		P-value			**-**	**0.04**
BT-20	ESE-16	FC ± SD			1	0.44±0.10
		P-value			-	**5.29E-04**
	LimPyr1	FC ± SD			1	0.22±0.13
		P-value			-	**4.70E-04**

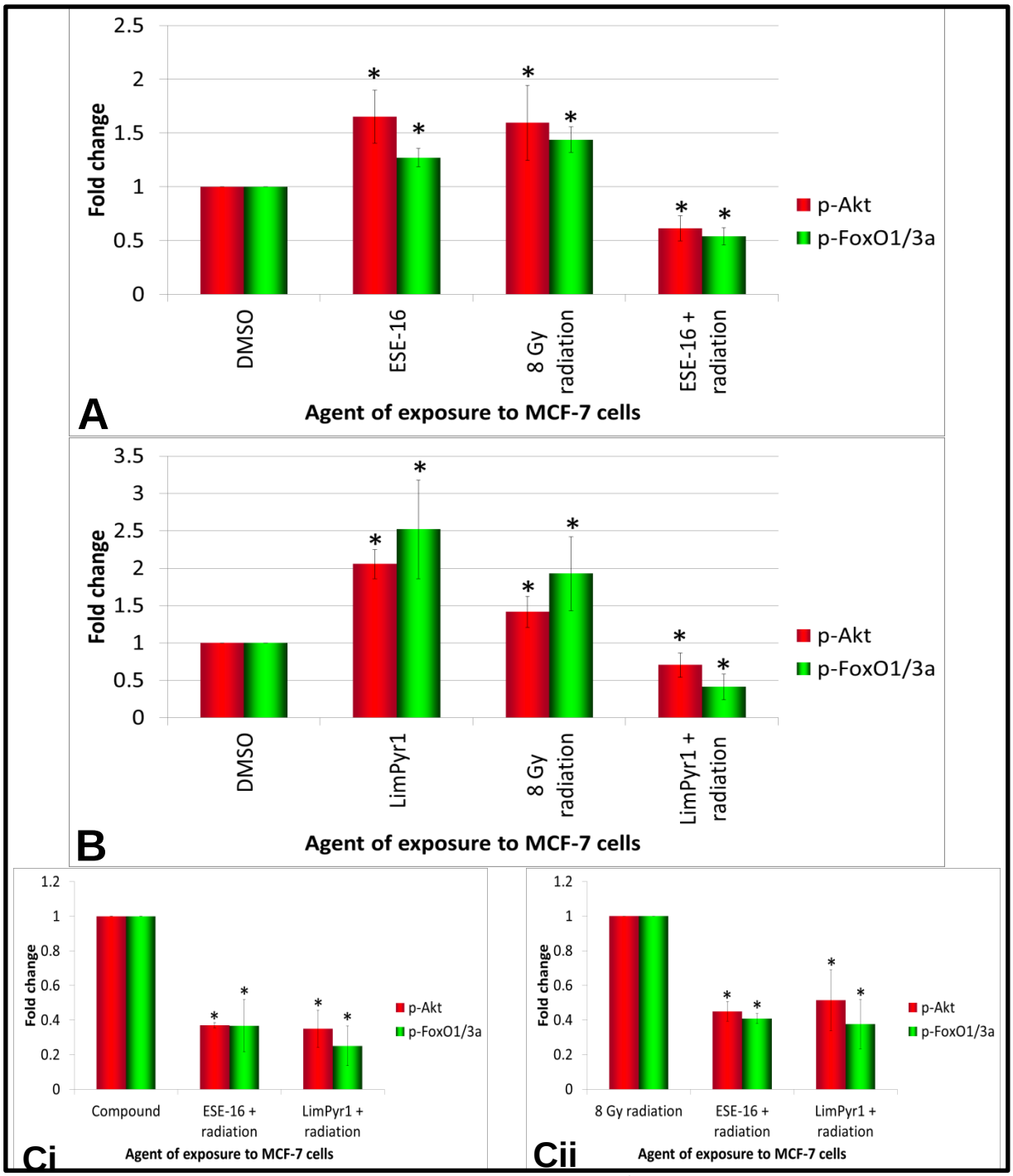

Figure 4.36: Graphical representation of Akt and FoxO1/3a phosphorylation in MCF-7 cells exposed to different treatment conditions. MCF-7 cells exposed to ESE-16 (A) and LimPyr1 (B) displayed a significant increase in Akt and FoxO1/3a phosphorylation, compared to DMSO. Similarly, exposure to 8 Gy radiation increased the phosphorylation of Akt and FoxO1/3a. Akt and FoxO1/3a phosphorylation was significantly decreased in MCF-7 cells exposed to ESE-16 or LimPyr1 24 hours prior to radiation compared to the vehicle control (A&B) and cells exposed to the compounds (Ci) or 8 Gy radiation only (Cii). The bar graph summarizes the mean fold changes of three biological repeats and standard deviations are represented by T-bars.

Statistically significant differences are indicated with * (P-value <0.05) when compared to DMSO (A-B), cells exposed to ESE-16 or LimPyr1 only (Ci) and cells exposed to 8 Gy radiation only (Cii).

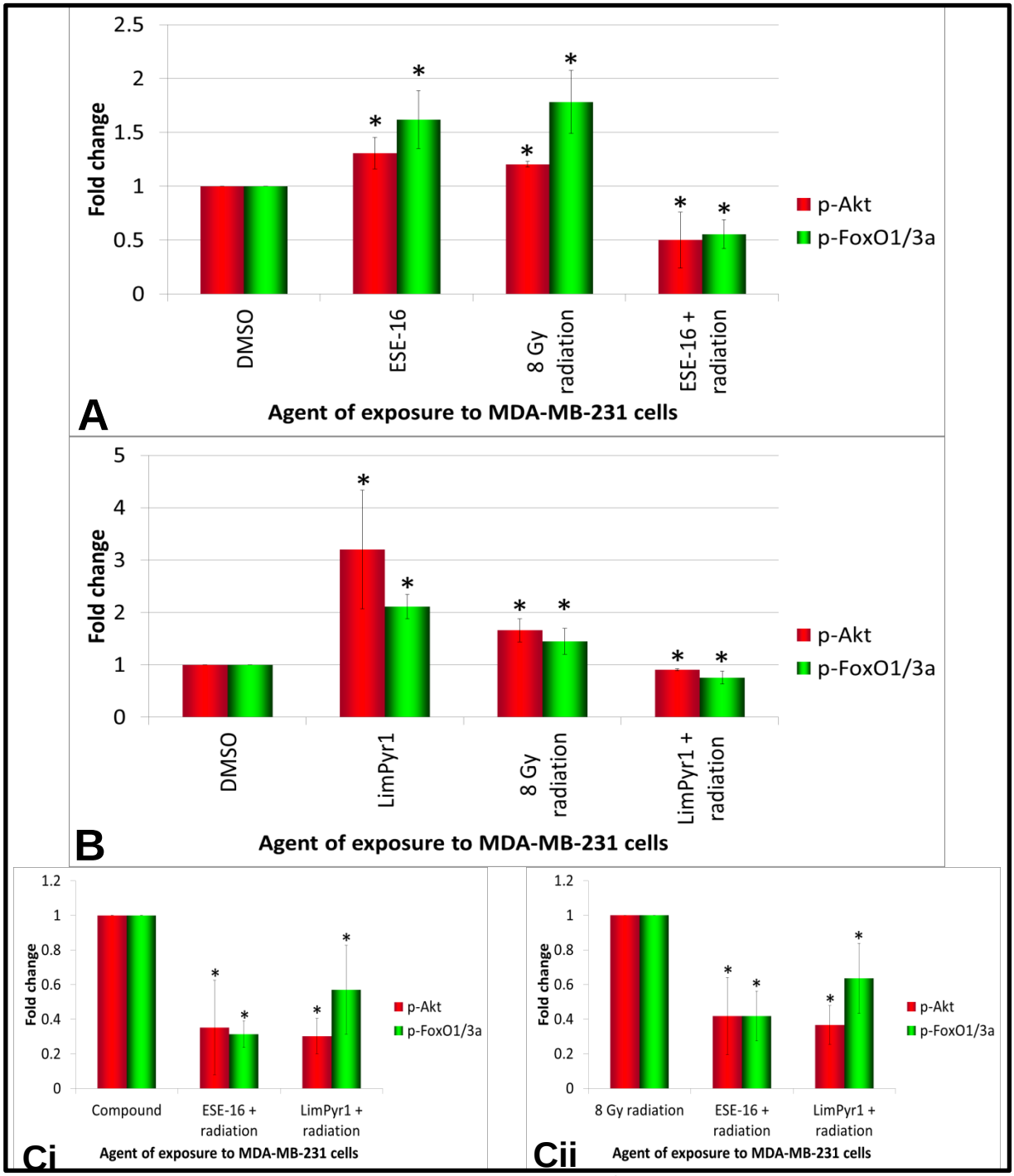

Figure 4.37: Graphical representation of Akt and FoxO1/3a phosphorylation in MDA-MB-231 cells exposed to different treatment conditions. MDA-MB-231 cells displayed a significant increase in the phosphorylation of Akt and FoxO1/3a following exposure to ESE-16 (A) and LimPyr1 (B). Phosphorylation of Akt and FoxO1/3a was also significantly increased after 8 Gy radiation (A&B). ESE-16- and LimPyr1 pre-treated MDA-MB-231 cells displayed a significant decrease in Akt and FoxO1/3a phosphorylation compared to DMSO (A&B), cells exposed to ESE-

16 or LimPyr1 only (Ci) and cells exposed to 8 Gy radiation only (Cii). The averaged fold changes of three biological repeats are displayed in the bar graph with standard deviations represented by T-bars. Statistically significant differences are indicated with * (P-value <0.05) when compared to DMSO (A-B), cells exposed to ESE-16 or LimPyr1 only (Ci) and cells exposed to 8 Gy radiation only (Cii).

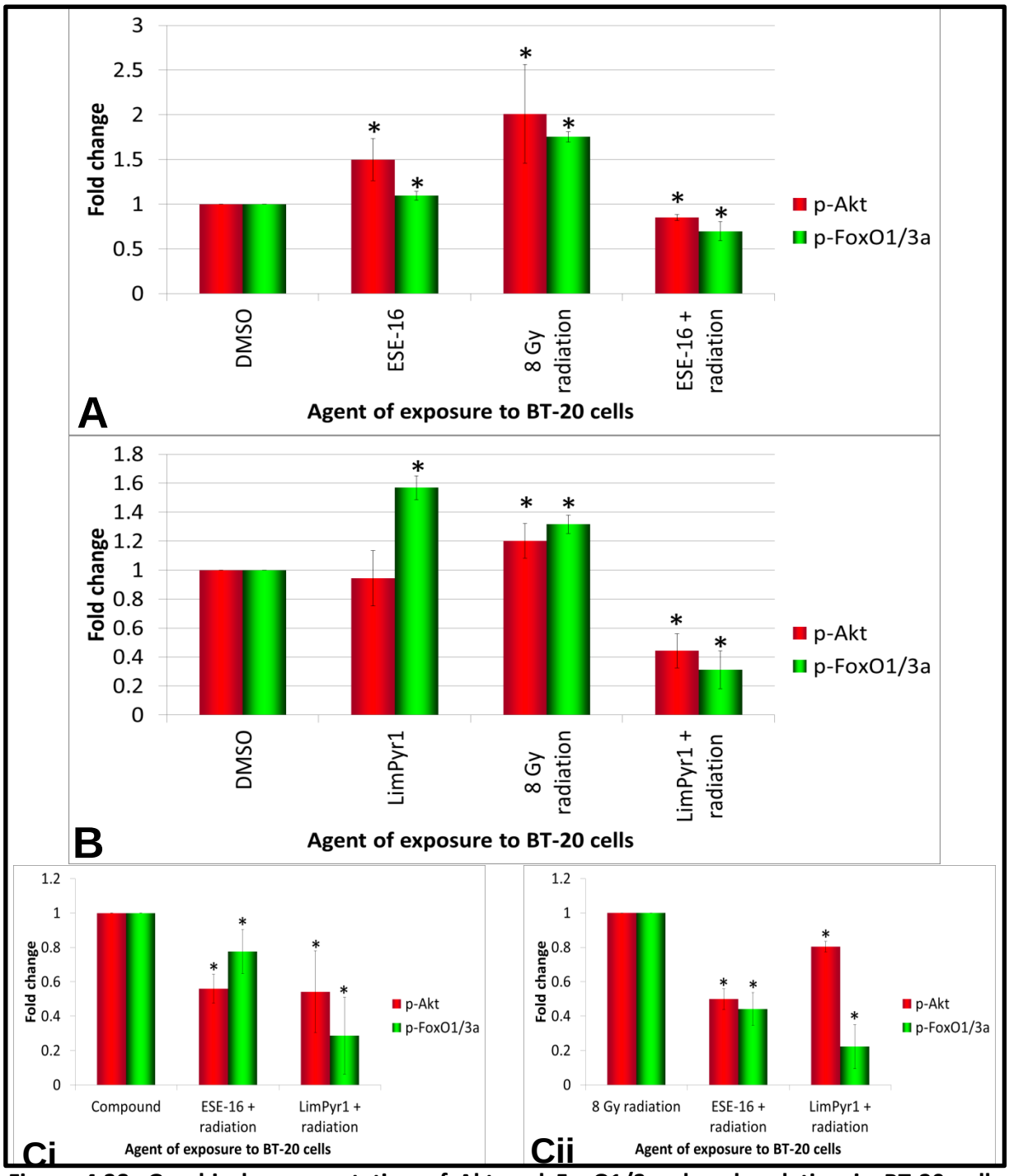

Figure 4.38: Graphical representation of Akt and FoxO1/3a phosphorylation in BT-20 cells exposed to different treatment conditions. The phosphorylation of Akt and FoxO1/3a was significantly increased in BT-20 cells exposed to ESE-16 (A) and 8 Gy radiation (A&B). Compared

to DMSO LimPyr1 exposed BT-20 cells displayed an increase in the phosphorylation of FoxO1/3a (B). However, BT-20 cells exposed to ESE-16 and LimPyr1 prior to radiation displayed a significant decrease in Akt and FoxO1/3a phosphorylation compared to DMSO (A&B) and cells exposed to the individual treatment conditions (C). Three biological repeats were completed for this experiment. Fold change was calculated against DMSO and cells exposed to the individual treatment conditions taken as one and the mean fold changes are represented in the bar graph. Standard deviations are represented by T-bars and statistically significant differences are indicated with * (P-value <0.05) when compared to DMSO (A-B), cells exposed to ESE-16 or LimPyr1 only (Ci) and cells exposed to 8 Gy radiation only (Cii).

4.2.3.3.3 Cyclin B1

Cell cycle analysis of pre-treated breast cancer cells illustrated a mitotic block. Exposure to radiation results in DNA damage and the activation of the ATM kinase. The ATM kinase regulates the cells biological response to the increased DNA damage by phosphorylating checkpoint kinase 1 and 2 (Chk 1/2) (487). These kinases inhibit the downstream effector cyclin B1 and delay the activation of cyclin B1/Cdk1, an essential step for G_2/M progression (488). This phenomenon is referred to as radiation-induced mitotic delay (489). In order to evaluate radiation-induced mitotic delay in pre-treated breast cancer cells cyclin B1 protein levels were quantified 24 hours after irradiation via a western blot.

MCF-7-, MDA-MB-231- and BT-20 cells exposed to ESE-16 (0.46±0.33, 0.33±0.14 and 0.67±0.19) and LimPyr1 (0.64±0.17, 0.20±0.03 and 0.61±0.20), respectively, displayed significantly lower cyclin B1 levels compared to the vehicle taken as 1 (Figure 4.39). Exposure to 8 Gy radiation significantly lowered cyclin B1 levels in MCF-7- (0.61±0.10 (DMEM) and 0.63±0.22 (RPMI)), MDA-MB-231- (0.37±0.21 (DMEM) and 0.52±0.18 (RPMI)) and BT-20 cells (0.45±0.16 (DMEM/F-12) and 0.50±0.10 (RPMI)) compared to DMSO (Table 4.18). Pre-treatment of MCF-7-, MDA-MB-231- and BT-20 cells with ESE-16 24 hour prior to radiation significantly lowered the expression of cyclin B1 significantly compared to DMSO (0.28±0.23, 0.17±0.17 and 0.29±0.15, respectively), cells exposed to ESE-16 (0.34±0.06, 0.19±0.10 and 0.44±0.21, respectively) and cells exposed to 8 Gy radiation only (0.43±0.30, 0.37±0.23 and 0.61±0.14, respectively) taken as 1 (Table 4.18). Similarly, LimPyr1 pre-

treated MCF-7-, MDA-MB-231- and BT-20 cells displayed significantly lower cyclin B1 levels compared to DMSO (0.50±0.12, 0.12±0.02 and 0.27±0.17, respectively), LimPyr1-exposed cells (0.70±0.13, 0.63±0.20 and 0.70±0.02, respectively) and cells exposed to 8 Gy radiation only (0.68±0.16, 0.26±0.15 and 0.40±0.15, respectively), taken as 1 (Figure 4.39).

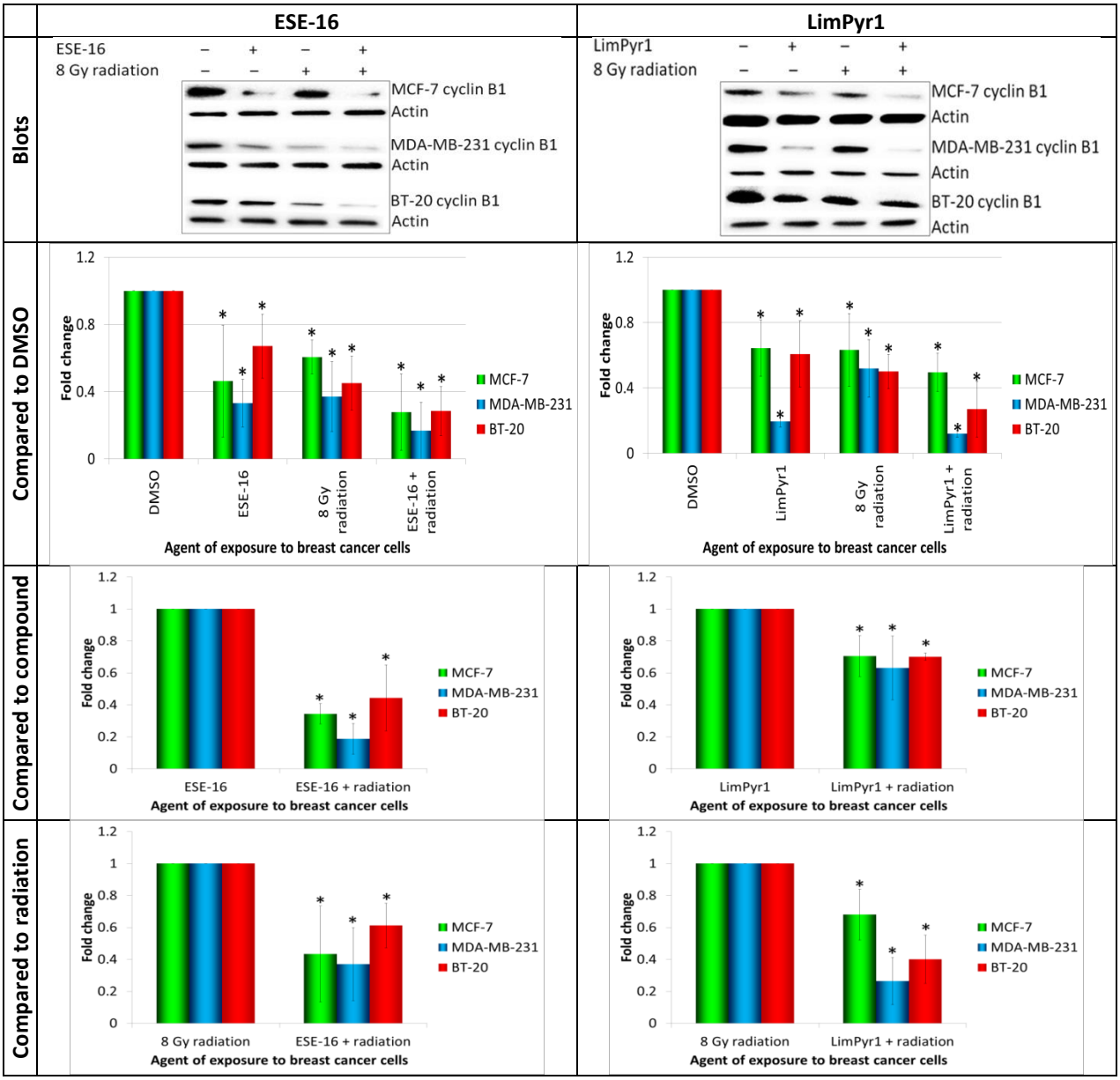

Figure 4.39: Cyclin B1 quantification in MCF-7-, MDA-MB-231- and BT-20 cells exposed to various treatment conditions. Breast cancer cells exposed to ESE-16, LimPyr1 and 8 Gy radiation displayed significantly lower cyclin B1 levels compared to the DMSO vehicle control. The augmented effect of ESE-16 and LimPyr1 in combination with radiation is evident in the significantly decreased cyclin B1 levels in pre-treated cells compared to the vehicle control and cells exposed to the individual treatments. Bars graphs indicate the average of three biological repeats, with standard deviations represented by T-bars. Statistically significant differences are

indicated with * (*P*-value <0.05) when were compared to DMSO, cells exposed to the compounds only and cells exposed to 8 Gy radiation only.

Table 4.18: Cyclin B1 quantification in MCF-7-, MDA-MB-231- and BT-20 cells exposed to various treatment conditions. Proteins were visualized on a ChemiDoc MP (Bio-rad, CA, USA) and quantified using Image Lab Software Version 5.2.1 (Bio-rad, CA, USA). Data were analyzed using the ANOVA-single factor model and a two-tailed Student's *t*-test. The fold changes (FC) and standard deviations (SD) of three biological repeats are displayed in the table. Statistically significant differences (*P*-value <0.05) were calculated using the vehicle control and cells exposed to the individual treatments as baselines.

			DMSO	Compound	8 Gy radiation	Combination
Compared to DMSO						
MCF-7	ESE-16	FC± SD	1	0.46±0.33	0.61±0.10	0.28±0.23
		P-value	-	**4.89E-02**	**2.37E-03**	**0.01**
	LimPyr1	FC± SD	1	0.64±0.17	0.63±0.22	0.50±0.12
		P-value	-	**0.02**	**4.56E-02**	**1.69E-03**
MDA-MB-231	ESE-16	FC ± SD	1	0.33±0.14	0.37±0.21	0.17±0.17
		P-value	-	**1.21E-03**	**0.01**	**1.02E-03**
	LimPyr1	FC ± SD	1	0.20±0.03	0.52±0.18	0.12±0.02
		P-value	-	**2.23E-06**	**0.01**	**1.76E-07**
BT-20	ESE-16	FC ± SD	1	0.67±0.19	0.45±0.16	0.29±0.15
		P-value	-	**0.04**	**3.93E-03**	**1.05E-03**
	LimPyr1	FC ± SD	1	0.61±0.20	0.50±0.10	0.27±0.17
		P-value	-	**0.03**	**2.85E-03**	**1.77E-03**
Compared to compound						
MCF-7	ESE-16	FC ± SD		1		0.34±0.06
		P-value		-		**2.94E-04**
	LimPyr1	FC ± SD		1		0.70±0.13
		P-value		-		**0.02**
MDA-MB-231	ESE-16	FC ± SD		1		0.19±0.10
		P-value		**-**		**5.24E-04**
	LimPyr1	FC ± SD		1		0.63±0.20
		P-value		**-**		**0.03**
BT-20	ESE-16	FC ± SD		1		0.44±0.21
		P-value		-		**0.01**
	LimPyr1	FC ± SD		1		0.70±0.02
		P-value		-		**1.43E-04**
Compared to 8 Gy radiation						
MCF-7	ESE-16	FC ±S D			1	0.43±0.30
		P-value			**-**	**0.03**
	LimPyr1	FC ±S D			1	0.68±0.16
		P-value			**-**	**0.03**
MDA-MB-231	ESE-16	FC ± SD			1	0.37±0.23
		P-value			**-**	**0.01**
	LimPyr1	FC ± SD			1	0.26±0.15
		P-value			**-**	**9.81E-04**
BT-20	ESE-16	FC ± SD			1	0.61±0.14
		P-value			-	**0.01**
	LimPyr1	FC ± SD			1	0.40±0.15
		P-value			-	**2.31E-03**

4.2.4 Morphological studies: Polarization-optical transmitted light differential interference contrast microscopy

Morphological changes such as cellular fragmentation into membrane bound apoptotic bodies, cell shrinkage and -detachment are observed in cells undergoing apoptosis via light microscopy (467). To visualize the morphological response of MCF-7-, MDA-MB-231-, and BT-20 cells exposed to the various treatment conditions PlasDIC images were taken 4-, 24- and 48 hours after radiation.

MCF-7-, MDA-MB-231- and BT-20 cells propagated in medium only served as negative controls. The negative controls displayed a health cell population with most cells present in interphase (Figure 4.40-4.42). Cell proliferation is evident in the increased cell density from 4- to 48 hours. Breast cancer cells exposed to DMSO served as a vehicle control. Similar morphology was observed in MCF-7-, MDA-MB-231- and BT-20 cells exposed to the vehicle control when compared to the negative control. Vinblastine and actinomycin D served as positive controls for apoptosis. Decreased cell density with concomitant apoptotic body formation was observed in all three cell lines when exposed to the positive control.

MCF-7-, MDA-MB-231- and BT-20 cells exposed to ESE-16 and LimPyr1, respectively, displayed some rounded cells with apoptotic body formation. Additionally, a decrease in cell density was observed over the 48 hour time frame when compared to the vehicle control. No morphological changes were observed in all three cell lines 4 hours after exposed to 8 Gy radiation (Figure 4.40-4.42). Cell rounding and apoptotic body formation were observed 24- and 48 hours after irradiation. MCF-7-, MDA-MB-231- and BT-20 cells pre-treated with ESE-16 or LimPyr1 24 hours prior to 8 Gy radiation presented with rounded morphology at all three time points in the experiment. Apoptotic body formation was observed 24- and 48 hours after irradiation accompanied by a decrease in cell density over the 48-hour time frame (Figure 4.40-4.42).

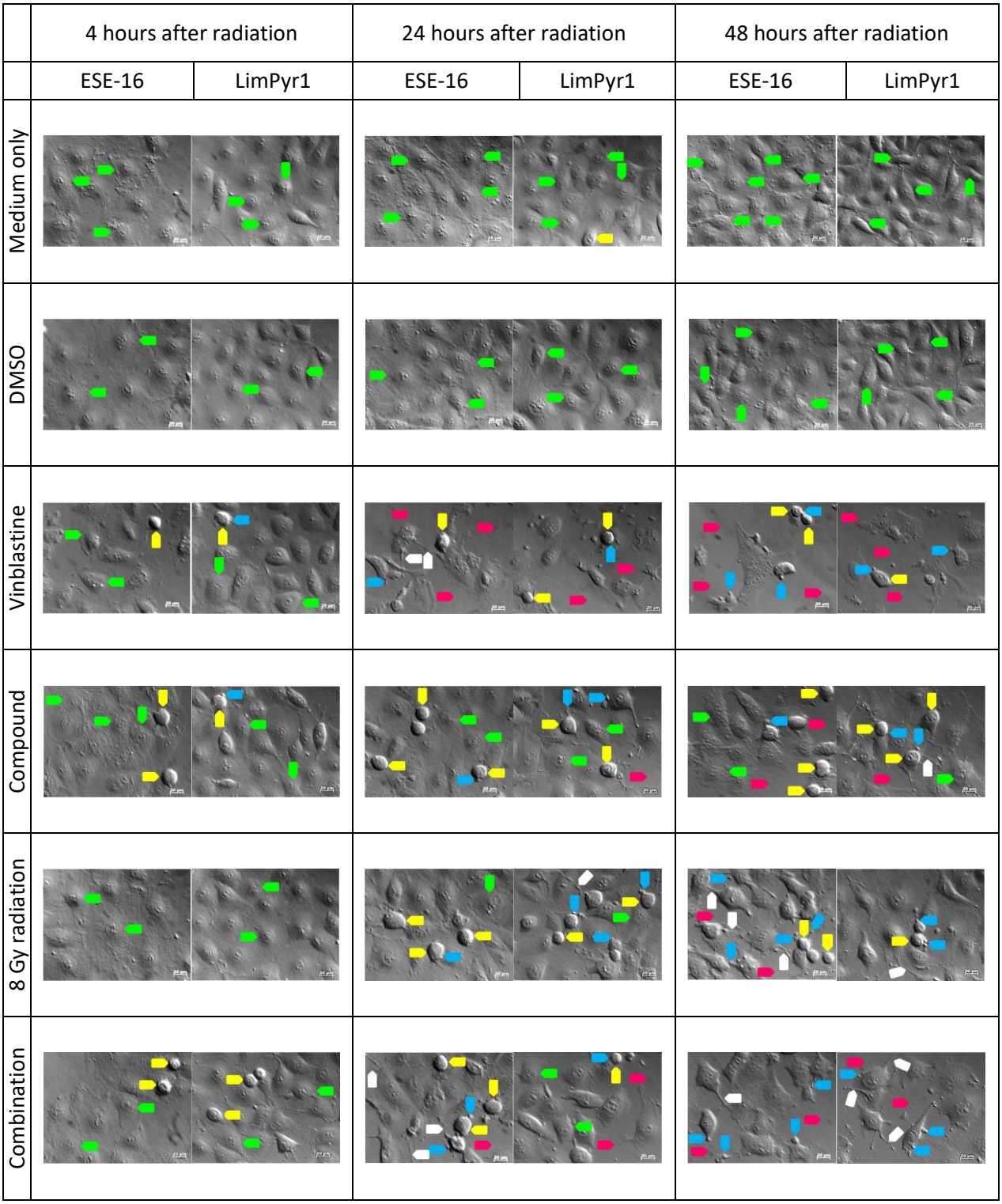

Figure 4.40: PlasDIC micrographs of MCF-7 cells exposed to various treatment conditions. MCF-7 cells were exposed to appropriate controls and various treatment conditions and images were taken over a 48-hour time frame after irradiation. Micrographs illustrated cells present in interphase (green arrows), rounded cells proposed to be in metaphase (yellow arrows), apoptotic bodies (blue arrows), cell protrusions indicating cellular distress (white arrows) and decreased cell density (pink arrows).

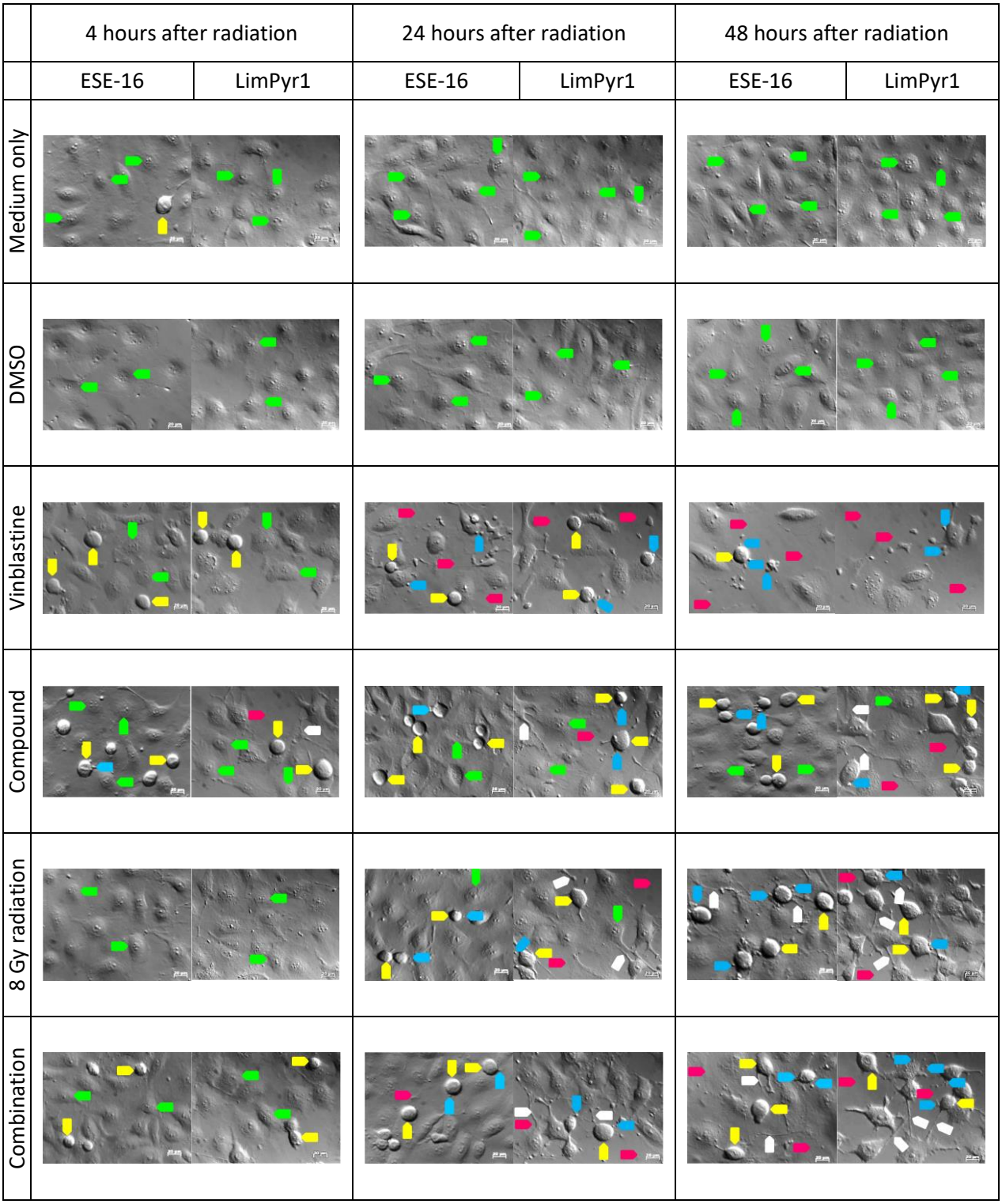

Figure 4.41: PlasDIC micrographs of MDA-MB-231 cells exposed to various treatment conditions. MDA-MB-231 cells were exposed to various treatment conditions and images were taken 4-, 24- and 48 hours after irradiation. Images illustrated cells present in interphase (green arrows), rounded cells proposed to be in metaphase (yellow arrows), apoptotic bodies (blue arrows), cell protrusions indicating cellular distress (white arrows) and decreased cell density (pink arrows).

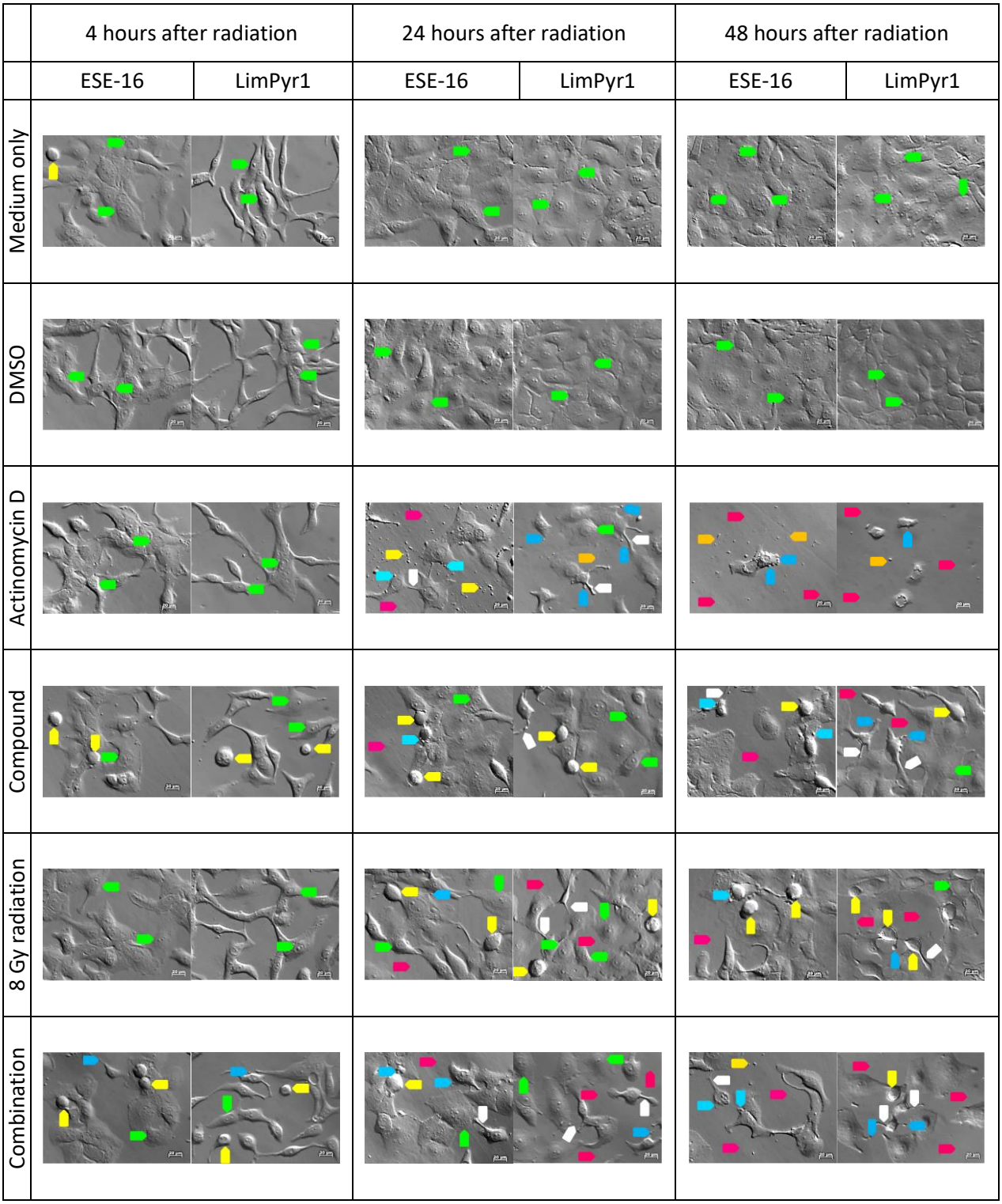

Figure 4.42: PlasDIC micrographs of BT-20 cells exposed various treatment conditions. BT-20 cells were exposed to ESE-16, LimPyr1 and 8 Gy radiation. Additionally BT-20 cells were pre-treated with ESE-16 or LimPyr1 24 hours prior to irradiation. Images were taken 4-, 24- and 48 hours after radiation. Images illustrated cells present in interphase (green arrows), rounded cells proposed to be in metaphase (yellow arrows), apoptotic bodies (blue arrows), cell protrusions indicating cellular distress (white arrows) and decreased cell density (pink arrows).

4.2.5 Long term cellular proliferation quantified via a crystal violet stain

Colony formation represents the long-term cell fate following treatment (468). The ability of breast cancer cells to survive, restore and proliferate following exposure to the various treatment modalities was quantified using a crystal violet stain 14 days after irradiation. Cells were exposed to ESE-16, LimPyr1, 4 Gy radiation and ESE-16 or LimPyr1 in combination with 4 Gy radiation. Due to cells being seeded at very low densities for this experiment the dose of radiation was decreased to 4 Gy and kept constant throughout this experiment.

Breast cancer cells propagated in medium only served as a negative control and cells exposed to DMSO as a vehicle control. No significant differences were observed in cell proliferation when the negative control was compared to the vehicle control (Figure 4.43). The positive method control (vinblastine) significantly decreased the ability of the cells to proliferate post exposure. MCF-7- (0.77±0.05) and MDA-MB-231 cells (0.89±0.06) exposed to ESE-16, and BT-20 cells exposed to LimPyr1 (0.89±0.07) displayed a significant decrease is cell proliferation compared to DMSO taken as 1. MCF-7- (0.19±0.03 (DMEM), 0.29±0.03 (RPMI)), MDA-MB-231- (0.33±0.02 (DMEM), 0.36±0.12 (RPMI)) and BT-20 cells (0.23±0.01 (DMEM/F-12), 0.27±0.01 (RPMI)) exposed to 4 Gy radiation also displayed a significant decrease in long term cellular proliferation (Table 4.19). MCF-7-, MDA-MB-231- and BT-20 cells exposed to ESE-16 24 hours prior to radiation displayed a significant decrease in cell growth compared to DMSO taken as 1 (0.14±0.01, 0.18±0.02, 0.17±0.01, respectively) (Figure 4.44). A similar decrease in cell proliferation was observed in MCF-7- (0.22±0.01), MDA-MB-231- (0.26±0.03) and BT-20 cells (0.19±0.02) pre-treated with LimPyr1 24 hours prior to radiation (Figure 4.44).

In order to evaluate whether the combination treatment were more effective in decreasing cell survival the results obtained from cells exposed to the combination therapies were compared to the individual treatment conditions taken as 1. ESE-16 pre-treated MCF-7-, MDA-MB-231- and BT-20 cells displayed a significant decrease in long term cellular

proliferation compared to cells exposed to ESE-16 (0.19±0.01, 0.20±0.03, 0.18±0.03, respectively) or 4 Gy radiation (0.78±0.10, 0.55±0.10, 0.75±0.05, respectively) (Figure 4.44). Similarly, MCF-7-, MDA-MB-231- and BT-20 cells pre-treated with LimPyr1 displayed a significant decrease in cell survival compared to LimPyr1 (0.23±0.03, 0.27±0.02 and 0.22±0.01, respectively) or 4 Gy radiation (0.76±0.11, .98±0.01 and 0.70±0.08, respectively) samples (Figure 4.44).

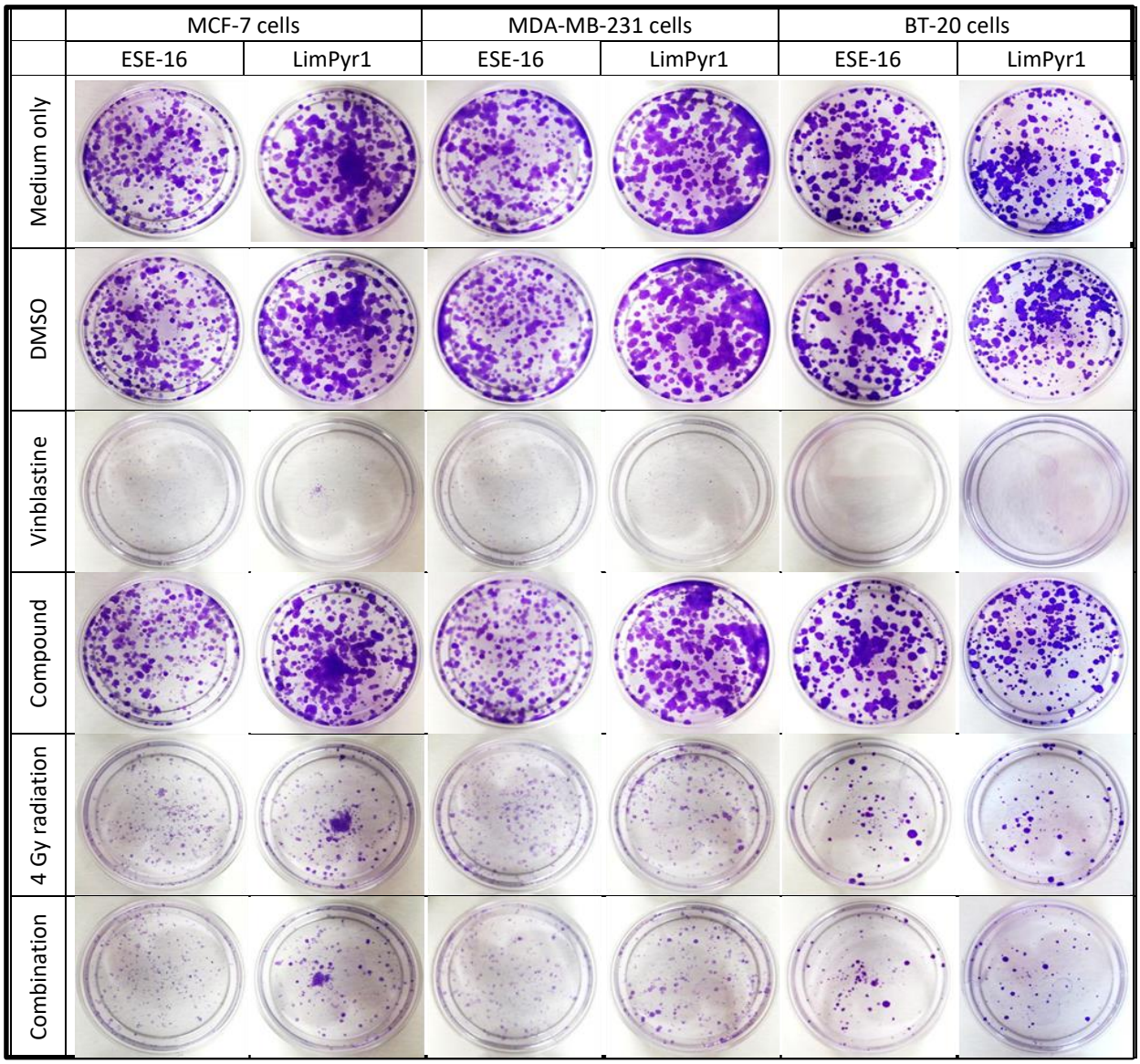

Figure 4.43: Cellular proliferation 14 days after radiation in MCF-7-, MDA-MB-231- and BT-20 cells exposed to various treatment conditions. Cellular proliferation was quantified in MCF-7-, MDA-MB-231- and BT20 cells exposed to ESE-16, LimPyr1 and 4 Gy radiation. Additionally, breast cancer cells were exposed to ESE-16 or LimPyr1 24 hours prior to 4 Gy radiation in order to evaluate whether an augmented effect can be obtained in the combination therapies.

Table 4.19: Cellular proliferation measure 14 days after radiation in MCF-7-, MDA-MB-231- and BT-20 cells following exposure to various treatment conditions. The crystal violet stain was solubilized and the optical density was measured at 570 nm. Cellular proliferation is expressed as fold change and was calculated relative to the vehicle control taken as 1. In the table below the averaged fold change (FC) and standard deviations (SD) of three biological repeats (n=3) are displayed. A two-tailed Student's *t*-test was used to calculate statistically significant differences (*P*-value <0.05) using the vehicle control and individual treatments conditions as baselines.

			Medium only	DMSO	Vinblastine	Compound	4 Gy radiation	Combination
Compared to DMSO								
MCF-7	ESE-16	FC± SD	1.01±0.02	1	0.08±0.01	0.77±0.05	0.19±0.03	0.14±0.01
		P-value	0.30	-	**6.24E-10**	**1.12E-03**	**7.55E-07**	**7.93E-09**
	LimPyr1	FC± SD	1.03±0.04	1	0.04±0.01	0.97±0.09	0.29±0.03	0.22±0.01
		P-value	0.21	-	**1.05E-09**	0.56	**3.60E-06**	**1.75E-08**
MDA-MB-231	ESE-16	FC ± SD	1.03±0.09	1	0.09±3.58E-03	0.89±0.06	0.33±0.02	0.18±0.02
		P-value	0.64	-	**1.56E-10**	**0.04**	**8.52E-07**	**2.79E-07**
	LimPyr1	FC ± SD	0.99±0.02	1	0.07±0.03	0.99±0.10	0.36±0.12	0.26±0.03
		P-value	0.48	-	**6.52E-07**	0.85	**8.49E-04**	**1.82E-06**
BT-20	ESE-16	FC ± SD	1.00±4.25E-03	1	0.04±0.01	1.00±0.09	0.23±0.01	0.17±0.01
		P-value	0.89	-	**5.29E-10**	0.99	**9.13E-08**	**7.04E-08**
	LimPyr1	FC ± SD	1.01±0.01	1	0.07±0.01	0.89±0.07	0.27±0.01	0.19±0.02
		P-value	0.18	-	**1.33E-08**	**4.81E-02**	**2.78E-09**	**6.10E-07**
Compared to compound								
MCF-7	ESE-16	FC ± SD				1		0.19±0.01
		P-value				-		**5.63E-09**
	LimPyr1	FC ± SD				1		0.23±0.03
		P-value				-		**2.40E-06**
MDA-MB-231	ESE-16	FC ± SD				1		0.20±0.03
		P-value				-		**2.00E-06**
	LimPyr1	FC ± SD				1		0.27±0.02
		P-value				-		**7.27E-07**
BT-20	ESE-16	FC ± SD				1		0.18±0.03
		P-value				-		**6.94E-07**
	LimPyr1	FC ± SD				1		0.22±0.01
		P-value				-		**2.61E-08**
Compared to 4 Gy radiation								
MCF-7	ESE-16	FC ±S D					1	0.78±0.10
		P-value					-	**1.93E-02**
	LimPyr1	FC ±S D					1	0.76±0.11
		P-value					-	**1.76E-02**
MDA-MB-231	ESE-16	FC ± SD					1	0.55±0.10
		P-value					-	**1.25E-03**
	LimPyr1	FC ± SD					1	0.98±0.01
		P-value					-	**0.03**
BT-20	ESE-16	FC ± SD					1	0.75±0.05
		P-value					-	**9.52E-04**
	LimPyr1	FC ± SD					1	0.70±0.08
		P-value					-	**3.21E-03**

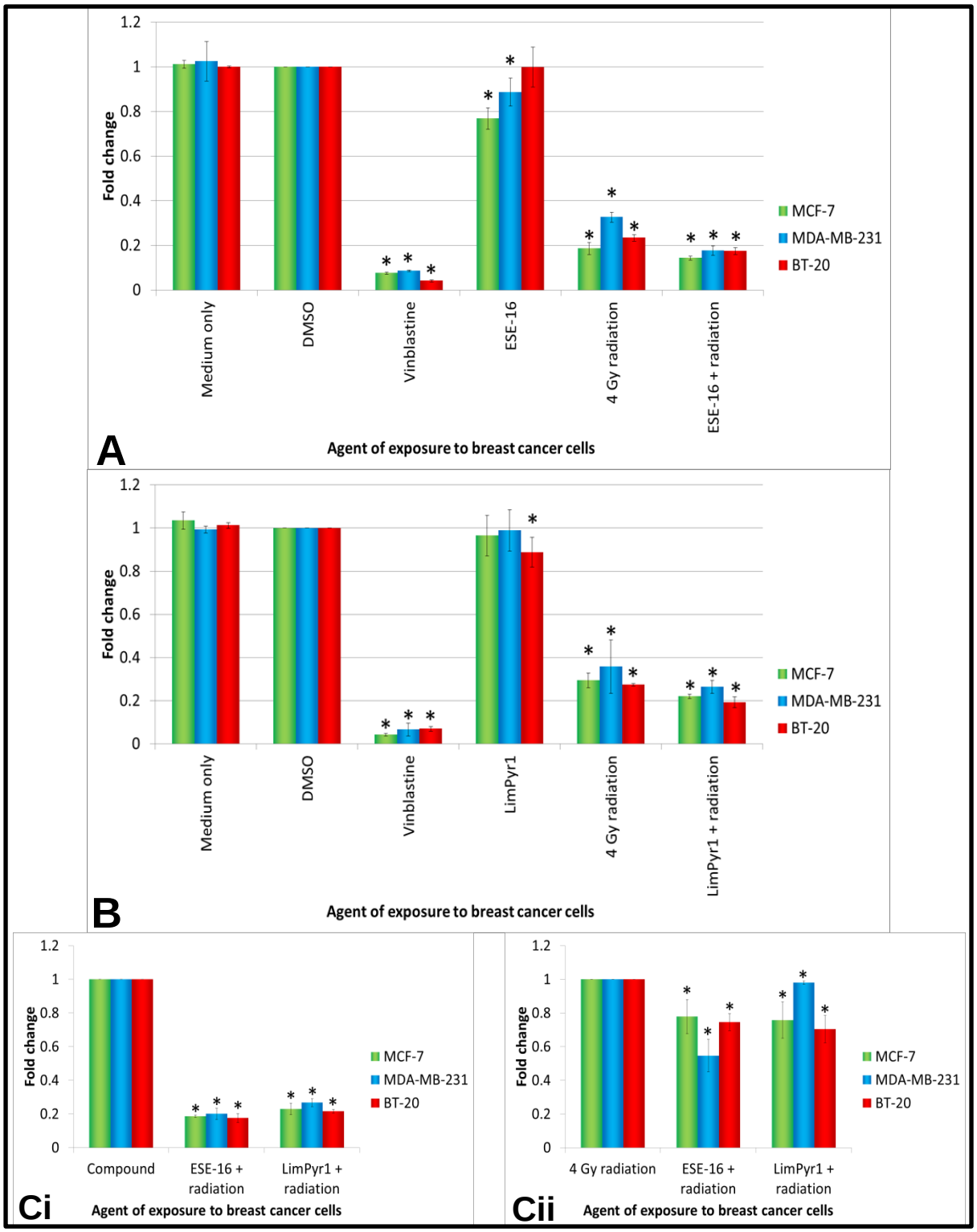

Figure 4.44: Graphical representation of long term cellular proliferation 14 days after radiation in MCF-7-, MDA-MB-231- and BT-20 cells exposed to various treatment conditions. The vehicle control (DMSO) revealed no significant difference in cell proliferation compared to cells propagated in media only (A-B). This confirms that DMSO had no influence on proliferation. MCF-7- and MDA-MB-231 cells displayed a significant decrease in proliferation following exposure to ESE-16 (A), 4 Gy radiation and the combination treatment conditions (A-B). BT-20

cells exposed to LimPyr1 (B), 4 Gy radiation and the combination treatments displayed a significant decrease in cell proliferation 14 days after radiation (A-B). Pre-treated MCF-7-, MDA-MB-231 and BT-20 cells revealed a significant decrease in proliferation compared to cells exposed to the compounds (Ci) or 4 Gy radiation (Cii) only. The bar graphs display the mean fold changes of three biological repeats and standard deviations are represented by T-bars. Statistically significant differences are indicated with * (*P*-value <0.05) when compared to DMSO (A-B), cells exposed to the compounds (Ci) or 4 Gy radiation only (Cii).

4.2.6 DNA damage and repair

4.2.6.1 Quantification of phosphorylated H2AX via flow cytometry

Ionizing radiation and genotoxic drugs induce DNA double-strand breaks which can be repaired via nonhomologous end-joining (NHEJ) and/or homologous recombination (490,491). These DNA double-strand breaks are detected rapidly via the cellular DNA damage response network, involving PI3-like kinases ATM, ATR and DNA-PK (492). These proteins phosphorylate a downstream histone known as H2AX. Phosphorylation of the SQE motif of H2AX at serine 139 produces γH2AX foci along megabase chromatin domains neighboring the site of damage. γH2AX serves as a docking site for DNA repair proteins, thus promoting DNA repair via NHEJ (493). The levels of phosphorylation of H2AX in breast cancer cells pre-treated with microtubule inhibitors and then irradiated were compared to those in cells exposed to the compounds or radiation only, following quantification via flow cytometry 2 and 24 hours after irradiation.

MCF-7-, MDA-MB-231- and BT-20 cells were propagated in growth medium only as negative controls. Data collected from the negative controls revealed no significant differences compared to data obtained from cells exposed to DMSO as vehicle controls. This confirmed that the vehicle does not induce DNA double-strand breaks in the breast cancer cell lines. As a positive control for DNA damage cells were exposed to etoposide for 2 hours prior to termination. Phosphorylation of H2AX was significantly increased in all samples exposed to the positive control (Table 4.20-4.22).

DNA double-strand breaks were significantly increased in MCF-7 cells 2 hours (3.87±1.72- (DMEM) and 1.42±0.19 fold increase (RPMI)) and 24 hours (5.96±1.86- (DMEM) and 2.63±0.21 fold increase (RPMI)) after 8 Gy radiation, compared to DMSO (Figure 4.45). DNA repair was evident in the radiation exposed samples as the DNA damage detected at 24 hours after radiation were significantly lower compared to the earlier time point (Figure 4.46). MCF-7 cells exposed to ESE-16 24 hours prior to radiation displayed a significant increase in γH2AX 2 hours (4.51±1.36 fold increase) and 24 hours (1.83±0.22 fold increase) after radiation. Similar to the 8 Gy radiation sample ESE-16 pre-treated cells displayed significantly lower levels of γH2AX 24 hours after radiation compared to 2 hours after radiation (Figure 4.46). LimPyr1 pre-treatment resulted in elevated phosphorylated H2AX proteins 2 hours after radiation (4.39±0.45 fold increase) and was maintained until 24 hours after radiation (4.20±0.85 fold increase). Compared to cells exposed to ESE-16 or LimPyr1 only, pre-treated ESE-16 and -LimPyr1 cells displayed a significant increase in γH2AX 2 hours (2.73±6.86E-04- and 1.81±0.12 fold increase, respectively) and 24 hours (1.77±0.46- and 2.63±0.76 fold increase, respectively) after radiation (Table 4.20). DNA damage was not elevated in ESE-16 pre-treated MCF-7 cells 2 hours after radiation compared to cells exposed to 8 Gy radiation only. However, 24 hours after radiation H2AX phosphorylation was significantly increased in the ESE-16 pre-treated cells (1.29±0.06 fold increase) compared to cells exposed to radiation only. MCF-7 cells pre-treated with LimPyr1 displayed a significant decrease in γH2AX 2 hours after radiation (0.65±0.19) compared to the radiation only sample taken as 1 (Figure 4.46). These γH2AX levels remained constant resulting in γH2AX levels being increased in LimPyr1 pre-treated cells 24 hours after radiation (1.86±0.02 fold increase) compared to cells exposed to 8 Gy radiation only (Figure 4.46).

MDA-MB-231 cells exposed to LimPyr1 displayed a significantly increase in γH2AX (2.14±0.66 fold increase) at the 24 hour termination point compared to DMSO. Exposure to 8 Gy radiation (2.04±0.15- (DMEM) and 16.85±5.38 fold increase (RPMI) (2 hours); 1.51±0.02- (DMEM) and 2.38±0.53 fold increase (RPMI) (24 hours)), ESE-16 in combination with radiation (2.08±0.14- (2 hours) and 2.65±0.50 fold increase (24 hours)) and LimPyr1 in

combination with radiation (6.81±3.56- (2 hours) and 7.62±2.90 fold increase (24 hours)) resulted in elevated γH2AX levels 2 and 24 hours after radiation compared to the vehicle control (Figure 4.47). MDA-MB-231 cells exposed to 8 Gy radiation only presented with significantly lower γH2AX levels 24 hours after radiation compared to the earlier time-point, indicating DNA repair (Figure 4.48). The phosphorylation of H2AX was significantly increased in MDA-MB-231 cells exposed to ESE-16 or LimPyr1 24 hours prior to radiation 2 hours (2.01±0.20- and 1.90±0.30 fold increase, respectively) and 24 hours after radiation (2.91±0.68- and 3.51±0.45 fold increase, respectively) compared to cells exposed to the compounds only. Compared to cells exposed to 8 Gy radiation only ESE-16- (2.12±0.42 fold increase) and LimPyr1 pre-treated (3.13±0.49 fold increase) MDA-MB-231 cells displayed a significant increase in H2AX phosphorylation 24 hours after radiation (Table 4.21). Interesting LimPyr1 pre-treated cells displayed a significant decrease in γH2AX 2 hours after radiation (0.46±0.10) compared to the radiation only sample taken as 1 (Figure 4.48).

LimPyr1-exposure resulted in a significant increase in γH2AX in BT-20 cells at the 2 hours (1.53±0.20 fold increase) and 24 hour (1.49±0.29 fold increase) termination points, compared to DMSO. BT-20 cells exposed to 8 Gy radiation (3.44±0.65- and 1.23±0.07 fold increase (DMEM), 3.09±0.61- and 2.25±0.01 fold increase (RPMI)), the ESE-16/radiation combination treatment (2.35±0.24- and 1.21±0.11 fold increase) and the LimPyr1/radiation combination treatment (2.77±0.67- and 2.92±0.39 fold increase) displayed a significant increase in γH2AX 2 and 24 hours after radiation compared to the vehicle control (Figure 4.49). DNA repair was evident in BT-20 cells exposed to 8 Gy radiation and the ESE-16/radiation combination treatment as the phosphorylation of H2AX was significantly lower in the samples terminated 24 hours after radiation compared to the 2 hour quantification (Figure 4.50). BT-20 cells exposed to ESE-16 (3.11±0.68- and 1.24±0.03 fold increase) or LimPry1 (1.59±0.33- and 2.15±0.13 fold increase) 24 hours prior to radiation displayed a significant increase in γH2AX 2 and 24 hours after radiation, compared to cells exposed to the compounds only. Compared to cells exposed to 8 Gy radiation only (taken as 1) ESE-16- (0.70±0.12) and LimPyr1 (0.89±0.06) pre-treated BT-20 cells displayed a significant decrease in DNA double strand breaks 2 hours after radiation (Table 4.22). Quantification of H2AX

phosphorylation 24 hours after radiation revealed a significant increase in BT-20 cells pre-treated with LimPyr1 (1.40±0.22 fold increase) compared to the radiation only sample, whereas ESE-16 pre-treated cells were similar to the cells exposed to 8 Gy radiation only (Figure 4.50).

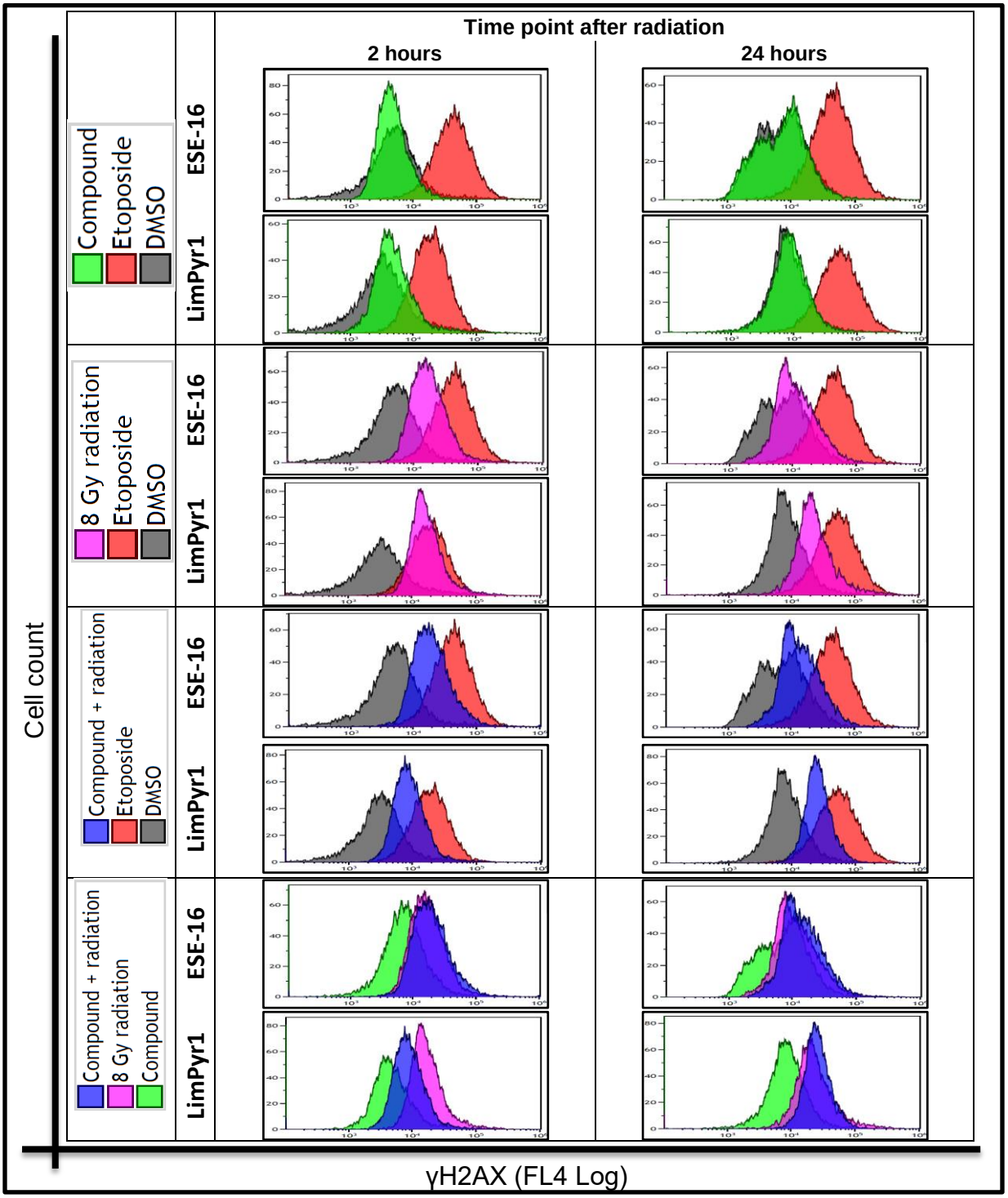

Figure 4.45: Representative overlay histograms of γH2AX detection in MCF-7 cells. Histograms were obtained 2 and 24 hours after radiation by plotting cell count against γH2AX (FL4 Log).

Overlay histograms displayed a right shift 24 hours after irradiation in cells exposed to the combination treatment conditions, compared to the vehicle control and cells exposed to the individual treatment conditions.

Table 4.20: Quantification of γH2AX in MCF-7 cells exposed to various treatment conditions. Data were generated 2 and 24 hours after irradiation with Kaluza Analysis version 1.5 (FL, USA). Data analysis was completed using the ANOVA-single factor model. The table displays the averaged fold changes (FC) of three biological repeats and the standard deviations (SD). A two-tailed Student's *t*-test was used to calculate statistically significant differences (*P*-value <0.05) by using the vehicle control and cells exposed to the individual treatments as baselines.

			Medium only	DMSO	Etoposide	Compound	8 Gy radiation	Combination
Compared to DMSO								
2 hours	ESE-16	FC± SD	0.82±0.64	1	11.31±1.38	1.44±0.49	3.87±1.72	4.51±1.36
		P-value	0.64	-	**7.55E-04**	0.18	**0.04**	**0.01**
	LimPyr1	FC± SD	1.67±1.11	1	11.44±2.93	1.60±0.76	5.96±1.86	4.39±0.45
		P-value	0.35	-	**3.49E-03**	0.23	**0.01**	**7.30E-04**
24 hours	ESE-16	FC ± SD	1.06±0.28	1	5.46±0.60	1.09±0.37	1.42±0.19	1.83±0.22
		P-value	0.72	-	**2.15E-04**	0.69	**0.02**	**2.75E-03**
	LimPyr1	FC ± SD	1.06±0.22	1	10.12±0.11	1.60±0.82	2.63±0.21	4.20±0.85
		P-value	0.63	-	**6.11E-07**	0.26	**1.91E-04**	**2.90E-03**
Compared to compound								
2 hours	ESE-16	FC ± SD				1		2.73±6.86E-04
		P-value				-		**2.00E-11**
	LimPyr1	FC ± SD				1		1.81±0.12
		P-value				-		**1.12E-03**
24 hours	ESE-16	FC ± SD				1		1.77±0.46
		P-value				-		**0.04**
	LimPyr1	FC ± SD				1		2.63±0.76
		P-value				-		**0.03**
Compared to 8 Gy radiation								
2 hours	ESE-16	FC ±S D					1	1.10±0.06
		P-value					-	0.06
	LimPyr1	FC ±S D					1	0.65±0.19
		P-value					-	**0.04**
24 hours	ESE-16	FC ± SD					1	1.29±0.06
		P-value					-	**8.40E-04**
	LimPyr1	FC ± SD					1	1.86±0.02
		P-value					-	**5.32E-06**

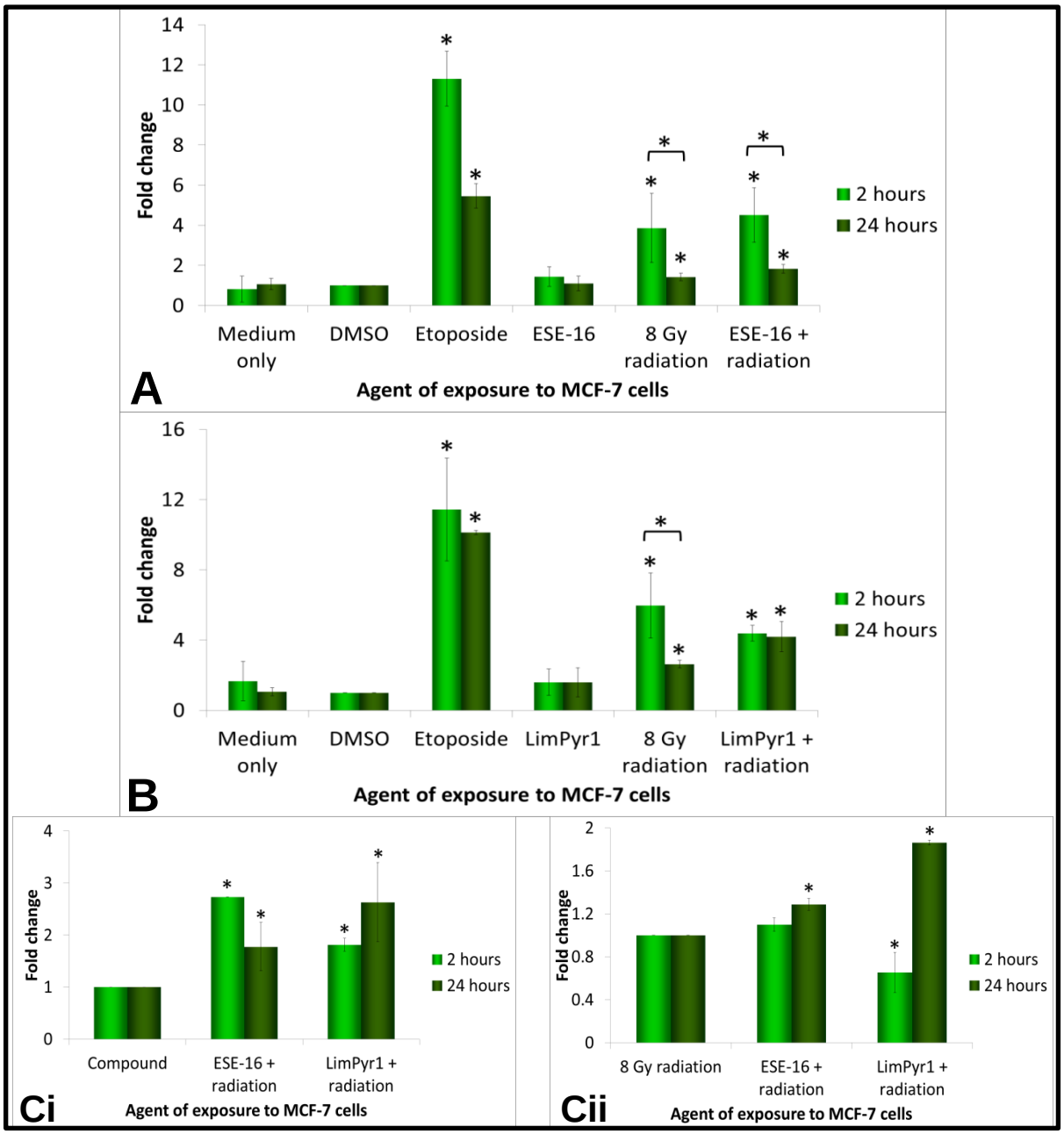

Figure 4.46: Graphical representation of γH2AX quantification in MCF-7 cells exposed to different treatment conditions. MCF-7 cells exposed to ESE-16 (A) and LimPyr1 (B) displayed no increase in γH2AX, whereas 8 Gy radiation exposure resulted in significantly higher γH2AX levels 2 and 24 hours after irradiation (A&B). ESE-16- (A) and LimPyr1 (B) pre-treatment of MCF-7 cells resulted in elevated γH2AX levels 2 and 24 hours after irradiation compared to DMSO and cells exposed to the compounds only (Ci). Data obtained from cells exposed to 8 Gy radiation and the ESE-16/radiation combination therapy displayed a significant decrease in γH2AX 24 hours after irradiation compared to the 2 hour quantification, indicating DNA repair (A&B). ESE-16 pre-treated cells displayed higher γH2AX levels 24 hours after irradiation compared to cells exposed to radiation only (Cii). DNA damage was significantly lower in LimPyr1 pre-treated cells 2 hours after irradiation compared to the radiation only sample (Cii). However, 24 hours after irradiation γH2AX was significantly higher in MCF-7 cells exposed to LimPyr1 24 hours prior to irradiation,

compared to cells exposed to 8 Gy radiation only (Cii). The bar graph summarizes the mean fold increases of three biological repeats and standard deviations are represented by T-bars. Statistically significant differences are indicated with * (*P*-value <0.05) when compared to DMSO (A-B), cells exposed to ESE-16 and LimPyr1 (Ci) or 8 Gy radiation only (Cii).

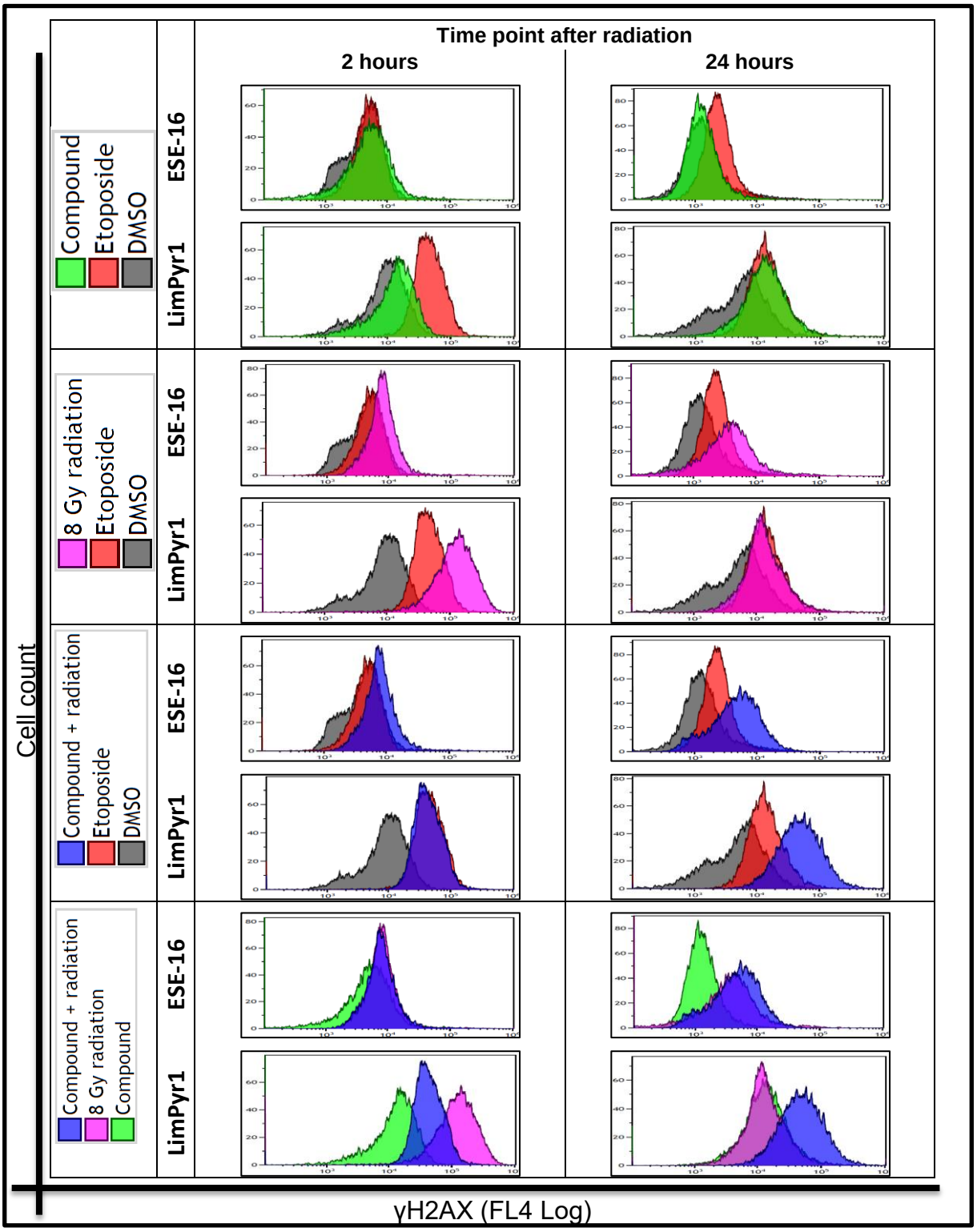

Figure 4.47: Representative overlay histograms of γH2AX detection in MDA-MB-231 cells. Histograms were obtained 2 and 24 hours after radiation by plotting data points obtained from

flow cytometry of the cell count against γH2AX (FL4 Log). Overlay histograms displayed an increase in γH2AX 2 and 24 hours after irradiation via a clear right shift in cells exposed to the different treatment conditions, compared to the DMSO vehicle control.

Table 4.21: Quantification of γH2AX in MDA-MB-231 cells exposed to various treatment conditions. Data were generated with Kaluza Analysis version 1.5 (FL, USA) (2 and 24 hours after irradiation) and analyzed using the ANOVA-single factor model. Three biological repeats were completed for each time-point. The table displays the averaged fold changes (FC) and the standard deviations (SD). Statistically significant differences (*P*-value <0.05) were calculated with a two-tailed Student's *t*-test using the vehicle control and cells exposed to the individual treatments as baselines.

			Medium only	DMSO	Etoposide	Compound	8 Gy radiation	Combination
Compared to DMSO								
2 hours	ESE-16	FC± SD	0.85±0.31	1	1.42±0.14	1.04±0.03	2.04±0.15	2.08±0.14
		P-value	0.45	-	**0.01**	0.16	**2.46E-04**	**1.76E-04**
	LimPyr1	FC± SD	0.90±0.07	1	6.60±1.89	1.73±0.56	16.85±5.38	6.81±3.56
		P-value	0.07	-	**0.01**	0.09	**0.01**	**4.75E-02**
24 hours	ESE-16	FC ± SD	1.00±0.31	1	1.58±0.16	0.92±0.12	1.51±0.02	2.65±0.50
		P-value	0.99	-	**0.01**	0.31	**1.66E-05**	**4.78E-03**
	LimPyr1	FC ± SD	0.91±0.09	1	3.00±0.23	2.14±0.66	2.38±0.53	7.62±2.90
		P-value	0.17	-	**5.10E-04**	**0.04**	**0.01**	**0.02**
	Compared to compound							
2 hours	ESE-16	FC ± SD				1		2.01±0.20
		P-value				-		**8.73E-04**
	LimPyr1	FC ± SD				1		1.90±0.30
		P-value				-		**0.01**
24 hours	ESE-16	FC ± SD				1		2.91±0.68
		P-value				-		**0.01**
	LimPyr1	FC ± SD				1		3.51±0.45
		P-value				-		**6.16E-04**
Compared to 8 Gy radiation								
2 hours	ESE-16	FC ±S D					1	1.02±0.04
		P-value					-	0.45
	LimPyr1	FC ±S D					1	0.46±0.10
		P-value					-	**1.99E-03**
24 hours	ESE-16	FC ± SD					1	2.12±0.42
		P-value					-	**0.01**
	LimPyr1	FC ± SD					1	3.13±0.49
		P-value					-	**1.68E-03**

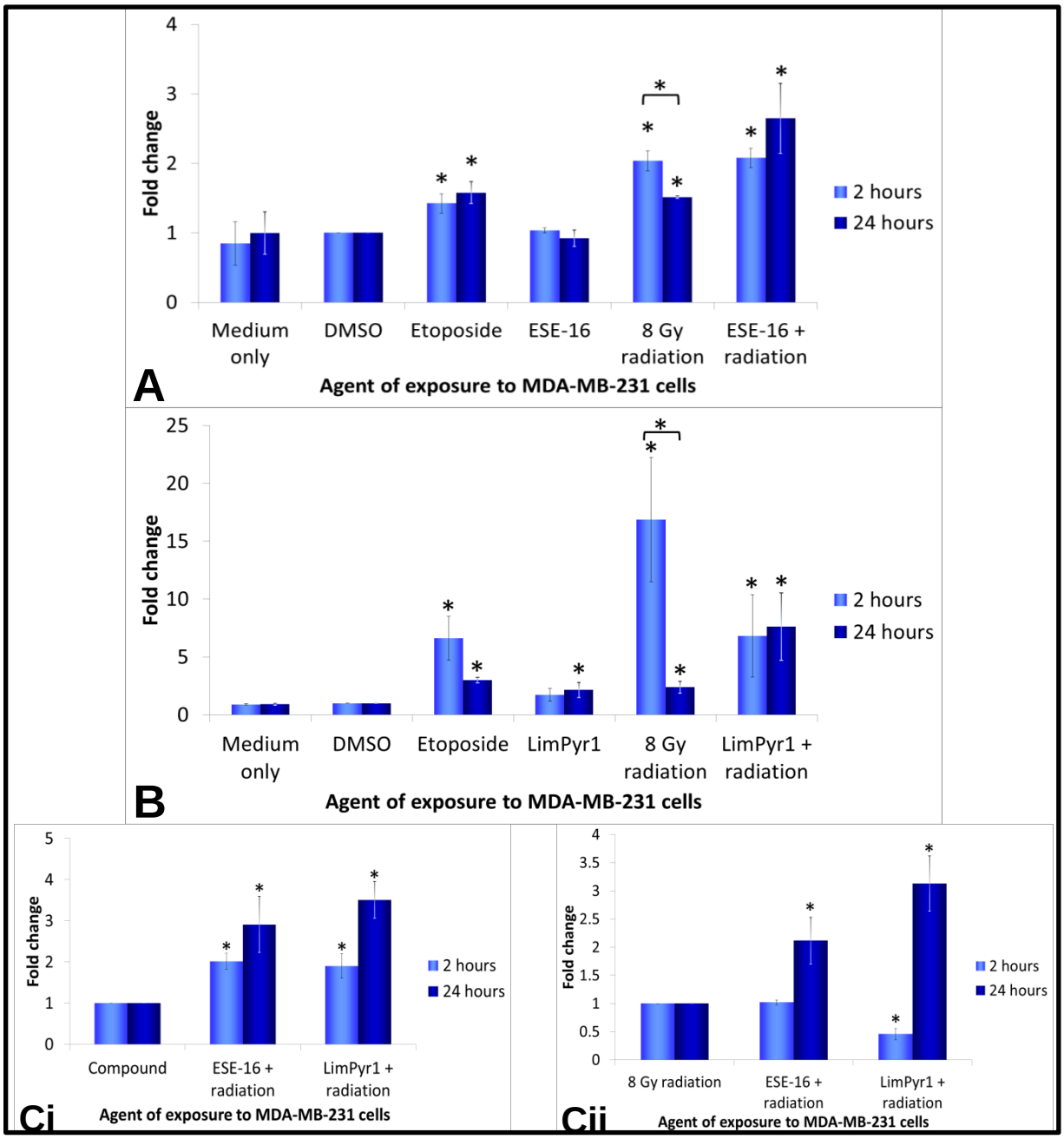

Figure 4.48: Graphical representation of γH2AX quantification in MDA-MB-231 cells exposed to different treatment conditions. MDA-MB-231 cells exposed to ESE-16 displayed no significant increase in γH2AX at the 2 and 24 hour termination points (A). Exposure to LimPyr1 resulted in elevated γH2AX levels at the 24 hour termination point, compared to DMSO (B). DNA damage was significantly increased 2 and 24 hours after 8 Gy radiation (A&B). DNA repair was observed in cells exposed to 8 Gy radiation whereas the 24 hour quantification of γH2AX was significantly lower compared to the earlier time point. MDA-MB-231 cells exposed to ESE-16 or LimPyr1 24 hours prior to irradiation displayed a significant increase in γH2AX 2 and 24 hours after irradiation compared to the vehicle control (A&B) and cells exposed to compounds only (Ci). Phosphorylation of H2AX was significantly decreased in LimPyr1 pre-treated cells 2 hours after irradiation compared to cells exposed to radiation only (Cii). However, γH2AX was significantly higher in LimPyr1 pre-treated cells 24 hours after irradiation compared to levels in

radiation only sample (Cii). The mean fold increases of three biological repeats are summarized in the bar graph. Standard deviations are represented by T-bars and statistically significant differences are indicated with * (*P*-value <0.05) when compared to DMSO (A-B), cells exposed to ESE-16 and LimPyr1 (Ci) or 8 Gy radiation only (Cii).

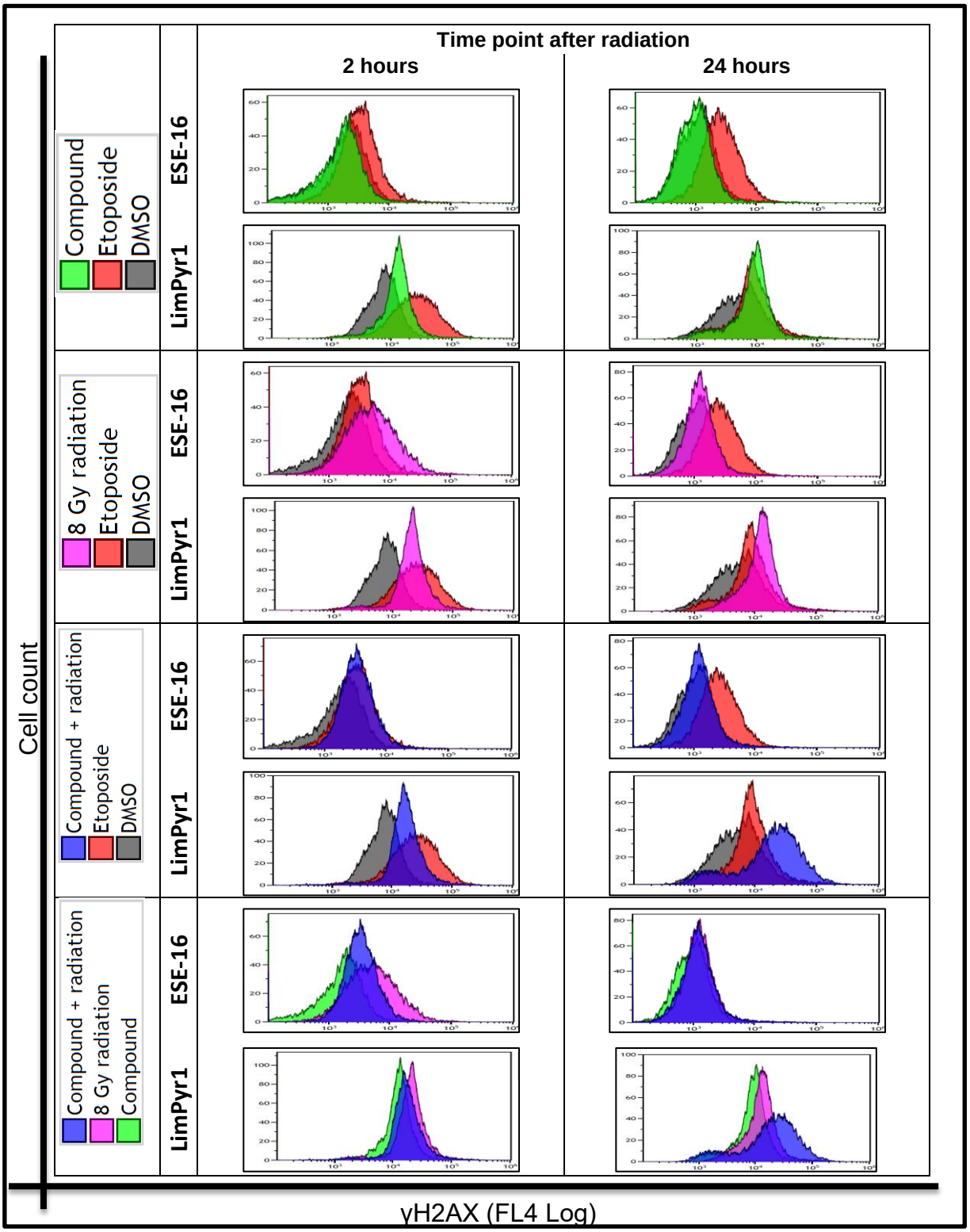

Figure 4.49: Representative overlay histograms of γH2AX detection in BT-20 cells. Histograms were obtained 2 and 24 hours after irradiation exposure. Histograms were created by plotting

cell count against γH2AX (FL4 Log). Overlay histograms displayed a right shift indicating increased double strand breaks in cells exposed to the different treatment conditions, compared to the DMSO vehicle control.

Table 4.22: Quantification of γH2AX in BT-20 cells exposed to various treatment conditions. Kaluza Analysis version 1.5 (FL, USA) was used to generate statistical data 2 and 24 hours after irradiation followed by analysis using the ANOVA-single factor model. The average fold change (FC) is displayed in the table ± the standard deviations (SD). A two-tailed Student's *t*-test was used to calculate statistically significant differences (*P*-value <0.05) using the vehicle control and cells exposed to the individual treatments as baselines.

			Medium only	DMSO	Etoposide	Compound	8 Gy radiation	Combination
Compared to DMSO								
2 hours	ESE-16	FC± SD	0.89±0.20	1	2.84±0.62	0.78±0.17	3.44±0.65	2.35±0.24
		P-value	0.38	-	**0.01**	0.09	**2.93E-03**	**6.06E-04**
	LimPyr1	FC± SD	0.86±0.28	1	2.72±0.64	1.53±0.20	3.09±0.61	2.77±0.67
		P-value	0.42	-	**0.01**	**0.01**	**4.01E-03**	**0.01**
24 hours	ESE-16	FC ± SD	1.06±0.04	1	2.50±0.12	1.08±0.18	1.23±0.07	1.21±0.11
		P-value	0.07	-	**2.69E-05**	0.48	**0.01**	**0.04**
	LimPyr1	FC ± SD	1.15±0.12	1	6.66±1.80	1.49±0.29	2.25±0.01	2.92±0.39
		P-value	0.10	-	**0.01**	**0.04**	**4.45E-07**	**2.54E-03**
Compared to compound								
2 hours	ESE-16	FC ± SD				1		3.11±0.68
		P-value				-		**0.01**
	LimPyr1	FC ± SD				1		1.59±0.33
		P-value				-		**0.04**
24 hours	ESE-16	FC ± SD				1		1.24±0.03
		P-value				-		**1.74E-04**
	LimPyr1	FC ± SD				1		2.15±0.13
		P-value				-		**4.45E-04**
Compared to 8 Gy radiation								
2 hours	ESE-16	FC ±S D					1	0.70±0.12
		P-value					-	**0.01**
	LimPyr1	FC ±S D					1	0.89±0.06
		P-value					-	**0.03**
24 hours	ESE-16	FC ± SD					1	0.98±0.03
		P-value					-	0.22
	LimPyr1	FC ± SD					1	1.40±0.22
		P-value					-	**0.03**

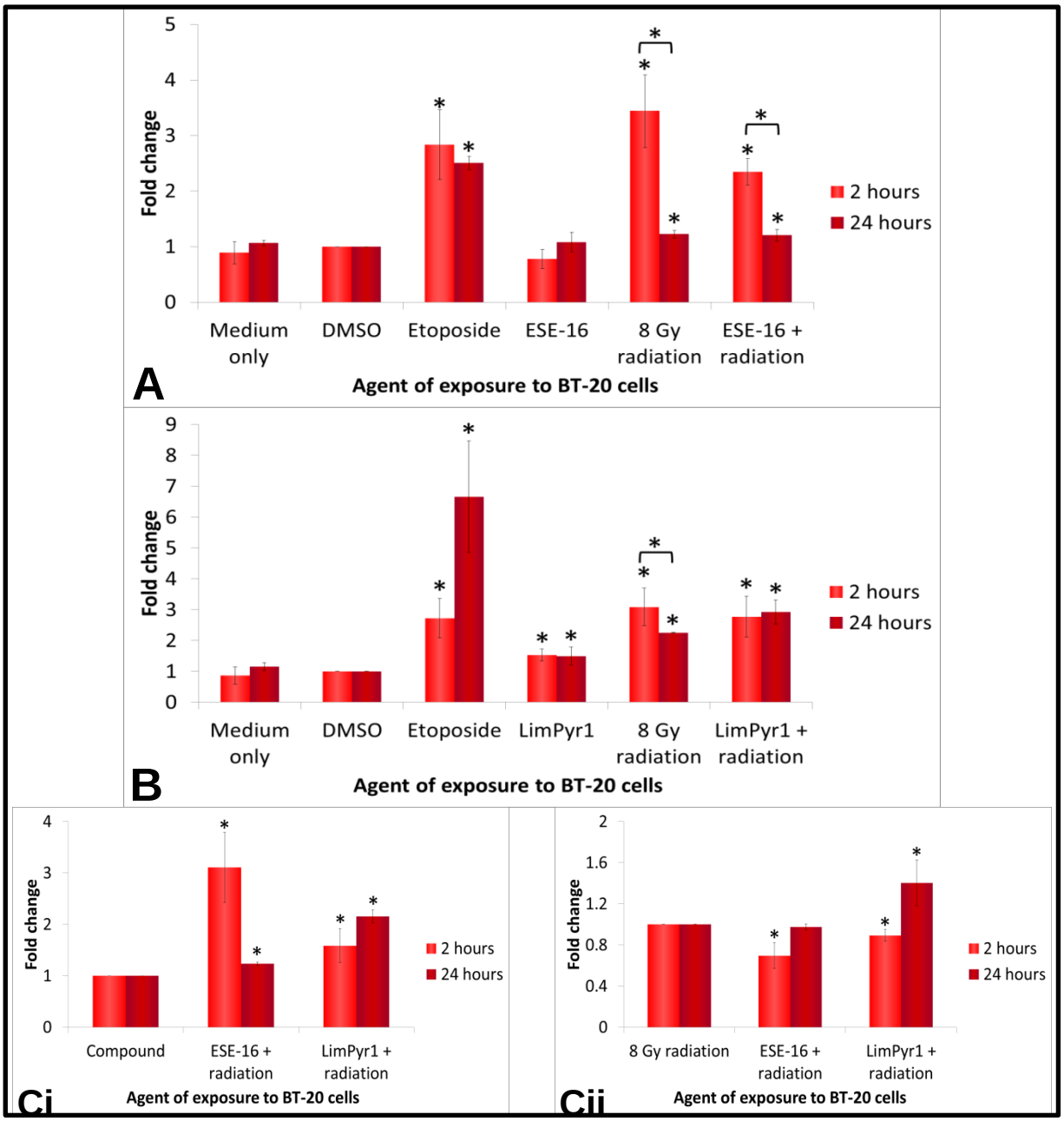

Figure 4.50: Graphical representation of γH2AX quantification in BT-20 cells exposed to different treatment conditions. Phosphorylation of H2AX was significantly increased 2 and 24 hours after irradiation in BT-20 cells exposed to LimPyr1 (B), 8 Gy radiation (A&B), the ESE-16/radiation combination treatment (A) and the LimPyr1/radiation combination treatment (B), compared to DMSO. Additionally, ESE-16- and LimPyr1 pre-treated cells displayed a significant increase in γH2AX 2 and 24 hours after irradiation compared to cells exposed to the compound only (Ci). Pre-treatment of BT-20 cells with ESE-16 or LimPyr1 resulted in decreased γH2AX levels 2 hours after irradiation, but increased γH2AX levels 24 hours after irradiation, compared to cells exposed to 8 Gy radiation only (Cii). The bar graph summarizes the mean fold increases of three biological repeats. Standard deviations are represented by T-bars and statistically significant differences are indicated with * (*P*-value <0.05) when compared to DMSO (A-B), cells exposed to ESE-16 and LimPyr1 (Ci) or 8 Gy radiation only (Cii).

4.2.6.2 Micronuclei quantification

An essential part of genetic toxicology is the study of DNA damage at the chromosome level. Micronuclei quantification is a preferred method for assessing chromosome damage (494). Failure of chromosome fragments or whole chromosomes to bind to the mitotic spindles prevent their inclusion into the nucleus post division, resulting in micronuclei formation (136). Unlike the quantification of γH2AX via flow cytometry, which evaluates DNA damage within a cell population, the cytokinesis-block micronucleus assay allows for the assessment of DNA damage within individual cells.

Breast cancer cells exposed to DMSO served as a vehicle control for this experiment. Micronuclei was not significantly increased in breast cancer cells exposed to DMSO compared to cells propagated in medium only, indicating that the vehicle had no effect on chromosome damage (Table 4.23-4.25).

Quantification of micronuclei revealed no significantly increase in DNA damage in MCF-7 cells exposed to ESE-16 (24±5 and 22±5, respectively) or LimPyr1 (14±5 and 18±6, respectively) at the 2 and 24 hour termination points, compared to DMSO (22±13 and 17±6 (DMEM), 13±7 and 11±7 (RPMI), respectively). Exposure to 8 Gy radiation significantly increased the number of micronuclei 2 hours (349±12 (DMEM) and 362±6 (RPMI)) and 24 hours (317±6 (DMEM) and 296±8 (RPMI)) after radiation. The presence of micronuclei significantly decreased from 2 to 24 hours after radiation in MCF-7 cells exposed to 8 Gy radiation only (Figure 4.51). This may suggest that the damage DNA is being repaired. Pre-treatment of MCF-7 cells with ESE-16 (361±19 and 328±4, respectively) or LimPyr1 (380±17 and 385±10, respectively) resulted in a significant increase in micronuclei formation 2 and 24 hours after radiation, compared to DMSO. Similar to cells exposed to 8 Gy radaition only, ESE-16 pre-treated MCF-7 cells displayed a significant decrease in micronuclei 24 hours after radiation compared to the earlier time-point. The number of micronuclei formed in LimPyr1 pre-treated MCF-7 cells remained unchanged over the 24 hour time frame. The formation of

micronuclei was significantly higher 2 and 24 hours after radiation in ESE-16- and LimPyr1 pre-treated cells compared to cells exposed to the compounds only (Table 4.23). DNA damage was equally induced as measured 2 hours after radiation in MCF-7 cells exposed to 8 Gy radiation and cells exposed to ESE-16 or LimPyr1 prior to radiation. However, micronuclei quantification in pre-treated cells was significantly higher 24 hours after radiation compared to cells exposed to 8 Gy radiation only (Figure 4.51).

MDA-MB-231 cells exposed to ESE-16 displayed no increase in micronuclei formation at the 2 hours (29±8) or 24 hour (25±7) termination points compared to DMSO (30±4 and 25±4, respectively). LimPyr1-exposure did not increase micronuclei formation at the 2 hour termination point (21±15), however at the 24 hour termination point the presence of micronuclei was significantly increased (35±6) compared to the vehicle control (18±7 and 17±9, respectively) (Table 4.24). DNA damage was significantly induced 2 hours (279±6 (DMEM) and 370±23 (RPMI)) and 24 hours (255±6 (DMEM) and 301±15 (RPMI)) after 8 Gy radiation in MDA-MB-231 cells. Some repair of the damaged DNA was observed in the significant decrease of micronuclei presence 24 hours after radiation compared to the earlier termination point (Figure 4.52). MDA-MB-231 cells exposed to ESE-16 24 hours prior to radiation displayed a significant increase in micronuclei formation 2 hours (285±11) and 24 hours (285±11) after radiation compared to DMSO and cells exposed to ESE-16 only. Similarly, LimPyr1 pre-treatment significantly increased micronuclei formation 2 hours (372±9) and 24 hours (392±19) after radiation compared to the vehicle control and cells exposed to LimPyr1 only. Quantification of micronuclei 2 hours after radiation revealed that DNA damage was equally induced in cells exposed to 8 Gy radiation only and cells exposed to the combination therapies. However, the presence of micronuclei was significantly increased 24 hours after radiation compared to cells exposed to 8 Gy radiation only (Figure 4.52).

Micronuclei formation was not significantly increased at the 2 hours (72±3) or 24 hour (77±23) termination point in BT-20 cells exposed to ESE-16, compared to the vehicle control

(69±27 and 58±18, respectively). BT-20 cells exposed to LimPyr1 displayed a significant increase in micronuclei expression at the 2 hours (95±21) and 24 hour (112±6) termination points compared to DMSO (49±17 and 64±16, respectively). A significant increase in the presence of micronuclei was observed in BT-20 cells exposed to 8 Gy radiation as quantified 2 hours (344±7 (DMEM/F-12) and 342±4 (RPMI)) and 24 hours (271±10 (DMEM/F-12) and 283±13 (RPMI)) after radiation (Table 4.25). Pre-treatment of BT-20 cells with ESE-16 resulted in a significant increase in micronuclei formation 2 hours (365±30) and 24 hours (280±21) after radiation, compared to DMSO. Quantification of micronuclei illustrated a significant decrease in micronuclei presence in BT-20 cells exposed to 8 Gy radiation only and the ESE-16/radiation combination therapy 24 hours after radiation compared to those quantified 2 hours after radiation (Figure 4.53). This may indicate the activation of DNA repair mechanisms in these samples. ESE-16 pre-treated BT-20 cells displayed a significant increase in micronuclei formation 2 and 24 hours after radiation compared to cells exposed to ESE-16 only. However, micronuclei were not significantly increased at any time-point in ESE-16 pre-treated BT-20 cells compared to cells exposed to 8 Gy radiation only (Table 4.25). Micronuclei quantification in BT-20 cells exposed to LimPyr1 24 hours prior to radiation revealed a significant increase 2 and 24 hours after radiation, compared to the vehicle control. The quantity of micronuclei observed 2 hours after radiation in LimPyr1 pre-treated cells remained constant compared to the 24 hour quantification. Additionally, LimPyr1 pre-treated BT-20 cells displayed a significantly increase in micronuclei formation 2 and 24 hours after radiation compared to cells exposed to LimPyr1 or 8 Gy radiation only (Figure 4.53).

MCF-7-, MDA-MB-231- and BT-20 cells pre-treated with ESE-16 (Appendix B (Table B1)) or LimPyr1 (Appendix B (Table B2)) displayed increased micronuclei formation 24 hours after radiation compared to cells exposed to 8 Gy radiation only. Interesting to note is that the number of cells that displayed micronuclei was not increased in the pre-treated cells. It was in fact the number of micronuclei present within a single cell that was increased in the pre-treated samples (Figure 4.54). Thus, the number of cells that obtained DNA damage was similar in cells exposed to the combination treatments and cells exposed to radiation only,

but pre-treated cells obtained more damage per cell compared to the cells exposed to radiation only.

Table 4.23: Micronuclei quantification in MCF-7 cells 2 and 24 hours after radiation. Micronuclei were quantified 2 and 24 hours after irradiation via light microscopy. Three biological repeats were included for each time-point where 500 binucleated cells were quantified for each repeat. The ANOVA-single factor model and a two-tailed Student's *t*-test were used to analyze the data and calculate statistically significant differences, respectively. The table summarizes the average number of micronuclei per 500 binucleated cells (M%) ± standard deviations (SD). Statistically significant differences (*P*-value <0.05) were calculated using the vehicle (DMSO) and cells exposed to the individual treatment condition as baselines.

			Medium only	DMSO	Compound	8 Gy radiation	Compound + radiation
ESE-16	2 hours	M%±SD	20±3	22±13	24±5	349±12	361±19
		P-value when compared to:					
		DMSO	0.83	-	0.75	**5.63E-06**	**1.37E-05**
		ESE-16					**7.89E-06**
		Radiation					0.43
	24 hours	M%±SD	14±6	17±6	22±5	317±6	328±4
		P-value when compared to:					
		DMSO	0.60	-	0.28	**3.11E-07**	**1.38E-07**
		ESE-16					**1.06E-07**
		Radiation					**0.04**
LimPyr1	2 hours	M%±SD	13±5	13±7	14±5	362±6	380±17
		P-value when compared to:					
		DMSO	0.95	-	0.81	**3.57E-07**	**4.27E-06**
		ESE-16					**3.68E-06**
		Radiation					0.16
	24 hours	M%±SD	15±2	11±7	18±6	296±8	385±10
		P-value when compared to:					
		DMSO	0.41	-	0.26	**1.28E-06**	**6.66E-07**
		LimPyr1					**6.30E-07**
		Radiation					**2.77E-04**

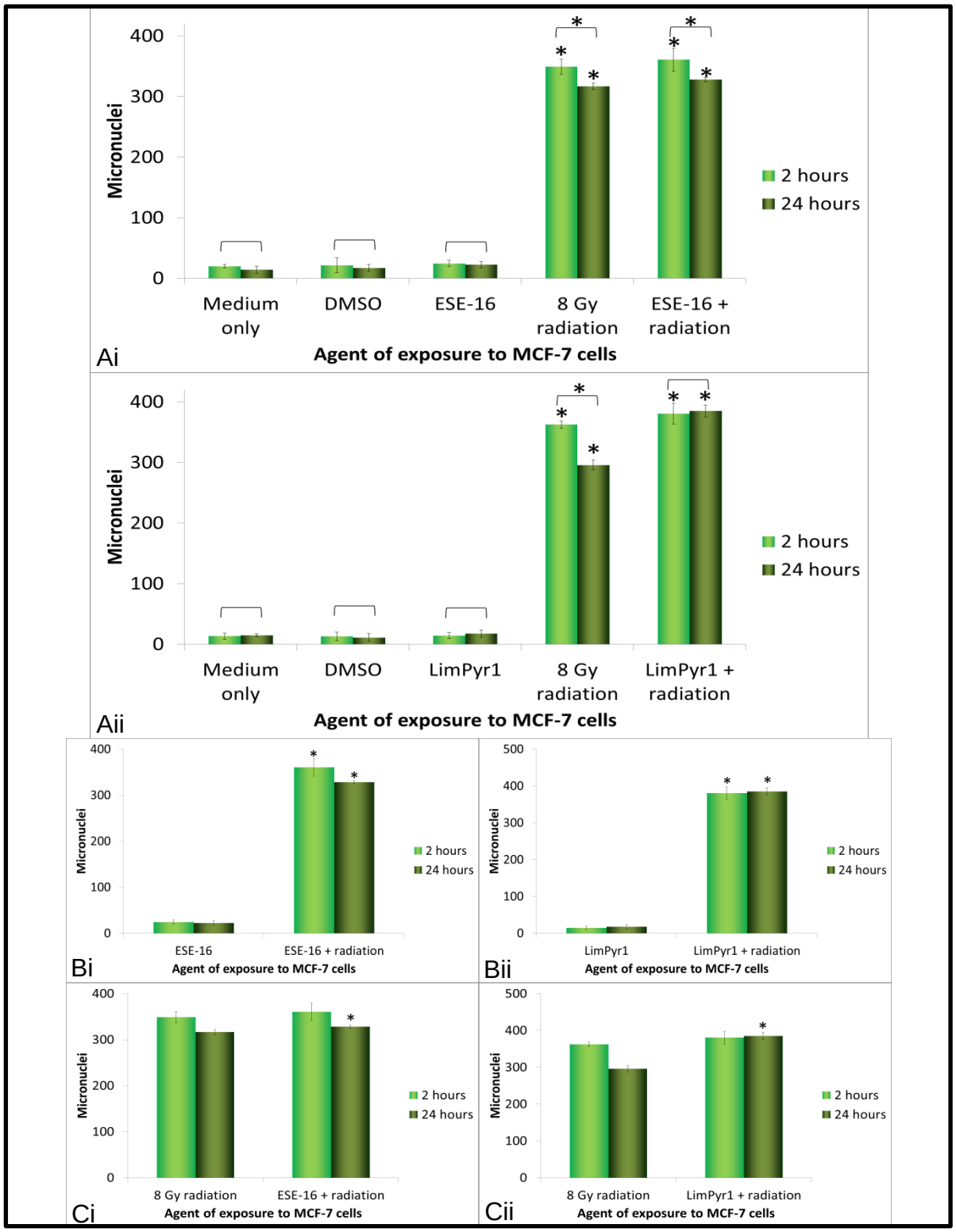

Figure 4.51: Graphical representation of micronuclei quantification in MCF-7 cells exposed to various treatment conditions. MCF-7 cells exposed to ESE-16 (Ai) and LimPyr1 (Aii) displayed no significant increase in micronuclei formation compared to DMSO. Exposure to 8 Gy radiation resulted in a significant increase in micronuclei formation (Ai & Aii). A decrease in micronuclei was observed 24 hours after irradiation compared to the data obtained from the 2 hour quantification (Ai & Aii). This may indicate the activation of DNA repair mechanisms. Pre-

treatment of MCF-7 cells with ESE-16 or LimPyr1 resulted in a significant increase in micronuclei 2 and 24 hours after irradiation compared to DMSO (A&B) and cells exposed to the compounds only (Bi & Bii). Similar to the 8 Gy radiation only sample ESE-16 pre-treated MCF-7 cells also displayed a significant decrease in micronuclei formation over the 24 hour time frame (Ai). DNA damage was equally measured 2 hours after radiation in MCF-7 cells exposed to ESE-16 or LimPyr1 24 hours prior to irradiation compared to cells exposed to 8 Gy radiation only (Ci & Cii). However, 24 hours after radiation the presence of micronuclei was significantly increase in the combination treatments compared to the radiation only sample (Ci & Cii). The bar graph illustrates the average micronuclei quantified per 500 binucleated cells for three biological repeats with the standard deviations represented by T-bars. A *P*-value <0.05 was considered statistically significant and are indicated with an * when compared to DMSO (Ai & Aii), cells exposed to ESE-16 and LimPyr1 only (Bi & Bii) and cells exposed to 8 Gy radiation only (Ci & Cii).

Table 4.24: Micronuclei quantification in MDA-MB-231 cells 2 and 24 hours after radiation. Micronuclei were manually quantified 2 and 24 hours after radiation in 500 binucleated cells per repeat. Three biological repeats were included in this experiment for samples terminated 2 and 24 hours after irradiation. The data were analyzed using an ANOVA-single factor model. Statistical significance (*P*-value <0.05) was calculated with a two-tailed Student's *t*-test using cells exposed to DMSO or the individual treatment conditions as baselines. The average number of micronuclei per 500 binucleated cells (M%) and standard deviation (SD) of the repeat are displayed in the table below.

			Medium only	DMSO	Compound	8 Gy radiation	Compound + radiation
ESE-16	2 hours	M%±SD	27±8	30±4	29±8	279±6	285±11
		P-value when compared to:					
		DMSO	0.62	-	0.90	**3.86E-07**	**2.85E-06**
		ESE-16					**4.92E-06**
		Radiation					0.50
	24 hours	M%±SD	30±10	25±4	25±7	255±6	291±15
		P-value when compared to:					
		DMSO	0.46	-	0.95	**6.55E-07**	**7.30E-06**
		ESE-16					**9.53E-06**
		Radiation					**0.02**
LimPyr1	2 hours	M%±SD	25±10	18±7	21±15	370±23	372±9
		P-value when compared to:					
		DMSO	0.38	-	0.76	**1.31E-05**	**5.77E-07**
		ESE-16					**3.67E-06**
		Radiation					0.86
	24 hours	M%±SD	27±14	17±9	35±6	301±15	392±19
		P-value when compared to:					
		DMSO	0.35	-	**0.04**	**9.84E-06**	**6.54E-06**
		LimPyr1					**6.32E-06**
		Radiation					**2.85E-03**

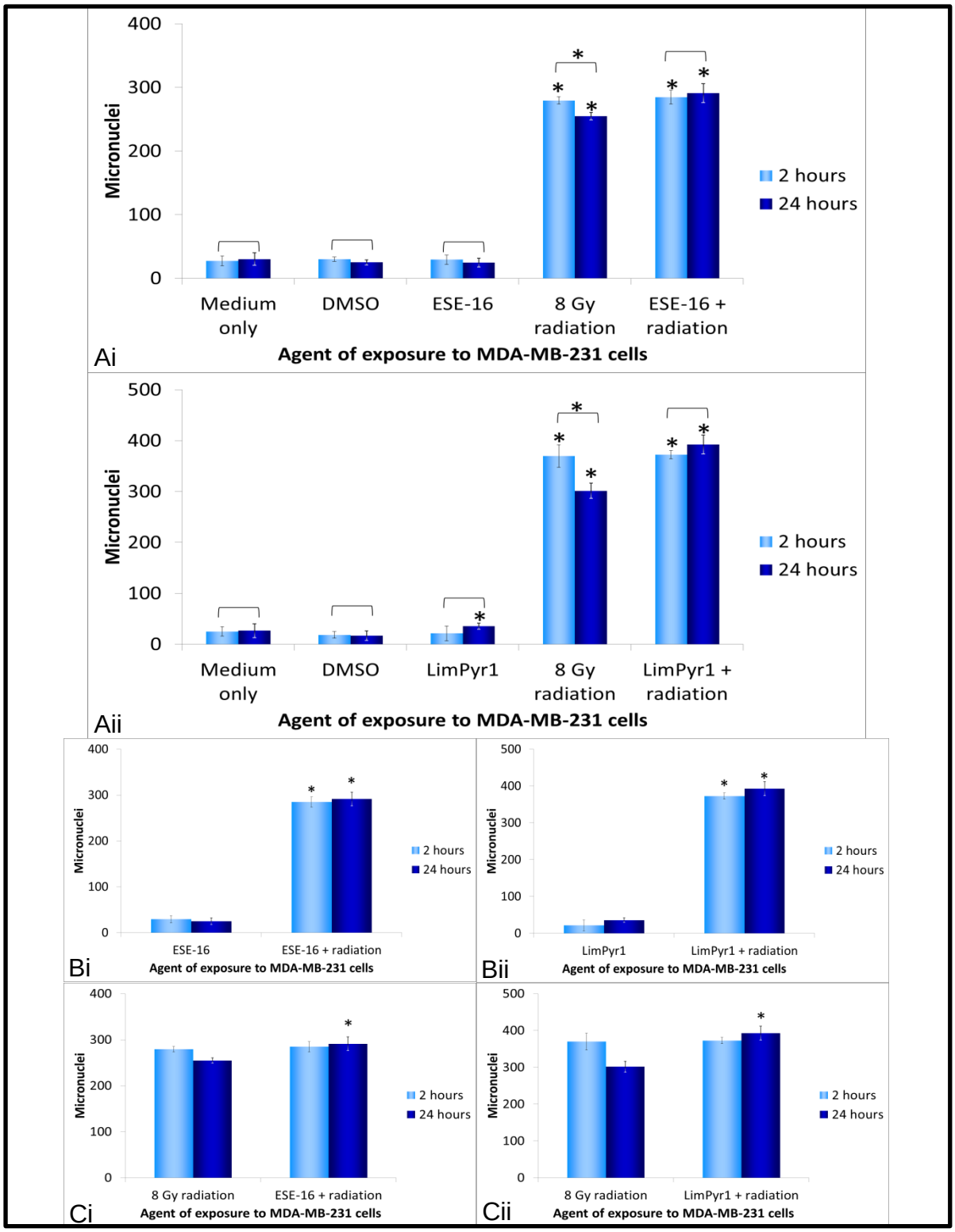

Figure 4.52: Graphical representation of micronuclei quantification in MDA-MB-231 cells exposed to various treatment conditions. MDA-MB-231 cells exposed to ESE-16 displayed no increase in micronuclei formation at the 2 or 24 hour termination points compared to DMSO (Ai). LimPyr1-exposure did not increase micronuclei formation at the 2-hour termination point, but micronuclei detection at the 24 hour termination point was significantly increased compared to DMSO (Aii). MDA-MB-231 cells exposed to 8 Gy radiation displayed a significant

increase in micronuclei formation 2 and 24 hours after irradiation. Cells exposed to 8 Gy radiation displayed a significant decrease in micronuclei presence 24 hours after irradiation compared to the 2 hours quantification, indicating the repair of the damaged DNA (Ai & Aii). ESE-16- and LimPyr1 pre-treatment resulted in significantly higher micronuclei numbers 2 and 24 hours after irradiation compared to the vehicle control (Ai & Aii) and cells exposed to the compounds only (Bi & Bii). No significant differences were observed in pre-treated cells 2 hours after irradiation compared to cells exposed to 8 Gy radiation only, however 24 hours after irradiation micronuclei yield was significantly higher in the pre-treated cells (Ci & Cii). The averaged micronuclei per 500 binucleated cells of three biological repeats are displayed in the bar graph for each time-point. Standard deviations are represented by T-bars and statistically significant differences (*P*-value <0.05) are indicated by an asterisk (*) when compared to DMSO (Ai & Aii), cells exposed to ESE-16 and LimPyr1 only (Bi & Bii) and cells exposed to 8 Gy radiation only (Ci & Cii).

Table 4.25: Micronuclei quantification in BT-20 cells 2 and 24 hours after radiation. The ANOVA-single factor model was used to analyze the data obtained from manual micronuclei quantification 2 and 24 hours after irradiation. Three biological repeats were included for each time-point. A total of 500 binucleated cells were examined for micronuclei per repeat. Using cells exposed to DMSO or the individual treatment conditions a two-tailed Student's *t*-test was employed to calculate statistically significant differences (*P*-value <0.05). The table summarizes the average number of micronuclei per 500 binucleated cells (M%) and standard deviations (SD).

			Medium only	DMSO	Compound	8 Gy radiation	Compound + radiation
ESE-16	2 hours	M%±SD	65±9	69±27	72±3	344±7	365±30
		P-value when compared to:					
		DMSO	0.82	-	0.88	**8.54E-04**	**2.15E-04**
		ESE-16					**9.70E-04**
		Radiation					0.42
	24 hours	M%±SD	70±12	58±18	77±23	271±10	280±21
		P-value when compared to:					
		DMSO	0.40	-	0.44	**4.47E-03**	**0.01**
		ESE-16					**0.01**
		Radiation					0.65
LimPyr1	2 hours	M%±SD	55±13	49±17	95±21	342±4	413±27
		P-value when compared to:					
		DMSO	0.68	-	**0.04**	**1.73E-04**	**3.64E-05**
		ESE-16					**8.62E-05**
		Radiation					**0.04**
	24 hours	M%±SD	63±23	64±16	112±6	283±13	372±25
		P-value when compared to:					
		DMSO	0.94	-	**0.01**	**5.50E-05**	**5.59E-05**
		LimPyr1					**5.88E-05**
		Radiation					**0.01**

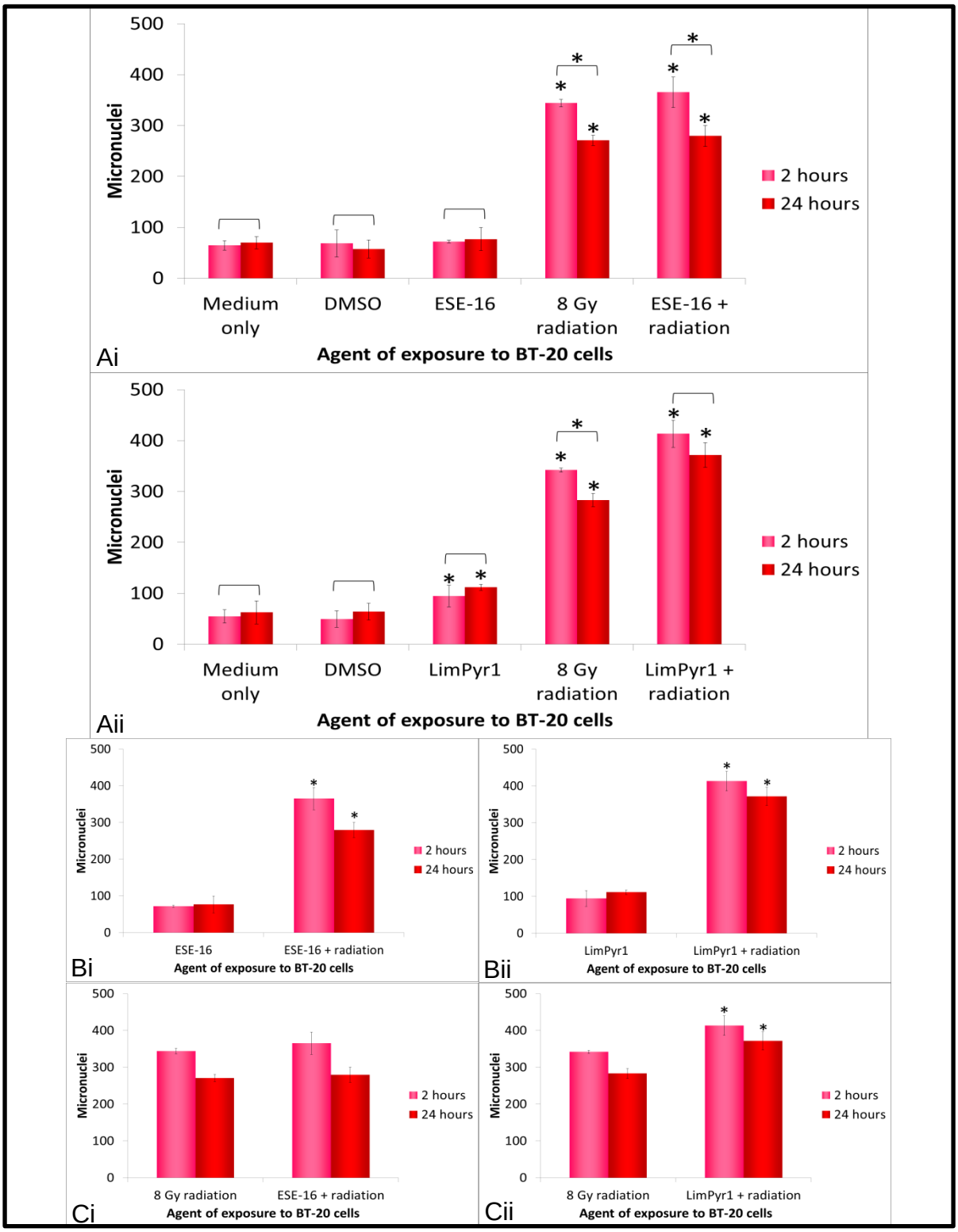

Figure 4.53: Graphical representation of micronuclei quantification in BT-20 cells exposed to various treatment conditions. BT-20 cells exposed to ESE-16 displayed no increase in micronuclei formation compared to DMSO (Ai), whereas LimPyr1-exposure resulted in an increase in micronuclei at the 2 and 24 hour termination points (Aii). Micronuclei formation was significantly increased in BT-20 cells exposed to 8 Gy radiation only, however DNA repair mechanisms were activated as illustrate by the decrease in micronuclei detection 24 hours after

radiation compared to that quantified at the earlier time-point (Ai & Aii). Pre-treatment of BT-20 cells with ESE-16 or LimPyr1 resulted in a significant increase in micronuclei presence 2 and 24 hours after irradiation compared to cells exposed to DMSO (Ai & Aii) or the compounds only (Bi & Bii). Similar to the radiation only sample ESE-16 pre-treated cells displayed significantly lower micronuclei numbers 24 hours after irradiation compared to the data obtained 2 hours after irradiation (Ai). Compared to cells exposed to 8 Gy radiation only ESE-16 pre-treated cells displayed no significant differences 2 or 24 hours after irradiation (Ci). LimPyr1 pre-treatment significantly increased micronuclei formation 2 and 24 hours after irradiation compared to cells exposed to radiation only (Cii). The average micronuclei quantified per 500 binucleated cells in three biological repeats are displayed on the bar graph with standard deviations indicated by T-bars. A *P*-value <0.05 was considered statistically significant and are indicated with an * when compared to DMSO (Ai & Aii), cells exposed to ESE-16 and LimPyr1 (Bi & Bii) or 8 Gy radiation only (Ci & Cii).

4.2.6.3 Quantification of the DNA repair response via Western blot analysis of Ku70 expression

DNA double strand breaks are the most critical DNA damage which can lead to chromosomal truncations and translocations if improperly repaired (495). Additionally, if DNA double strand breaks remain unrepaired the cell is rendered apoptotic (496). DNA double strand breaks are repair rapidly via NHEJ, a process instigated by the binding of the Ku complex (Ku70/Ku80) to the site of damage (497). A sensitive method for quantifying DNA double strand breaks is the measuring of H2AX phosphorylation (γH2AX). Exposure of breast cancer cells to the microtubule regulating agents delay the phosphorylation of H2AX, 2 hours after irradiation, compared to cells exposed to radiation only. However, micronuclei studies did confirm no significant differences in DNA damage induced by the combination treatments compared to 8 Gy radiation only samples, 2 hours after irradiation. As the binding of the Ku complex is signaled by γH2AX, the repair of the damage will thus theoretically be delayed in the combination therapy due to decreased H2AX phosphorylation. In order to confirm this hypothesis Ku70 protein quantification was done 2 and 24 hours after irradiation in order to investigate early and late DNA repair via a standard western blot.

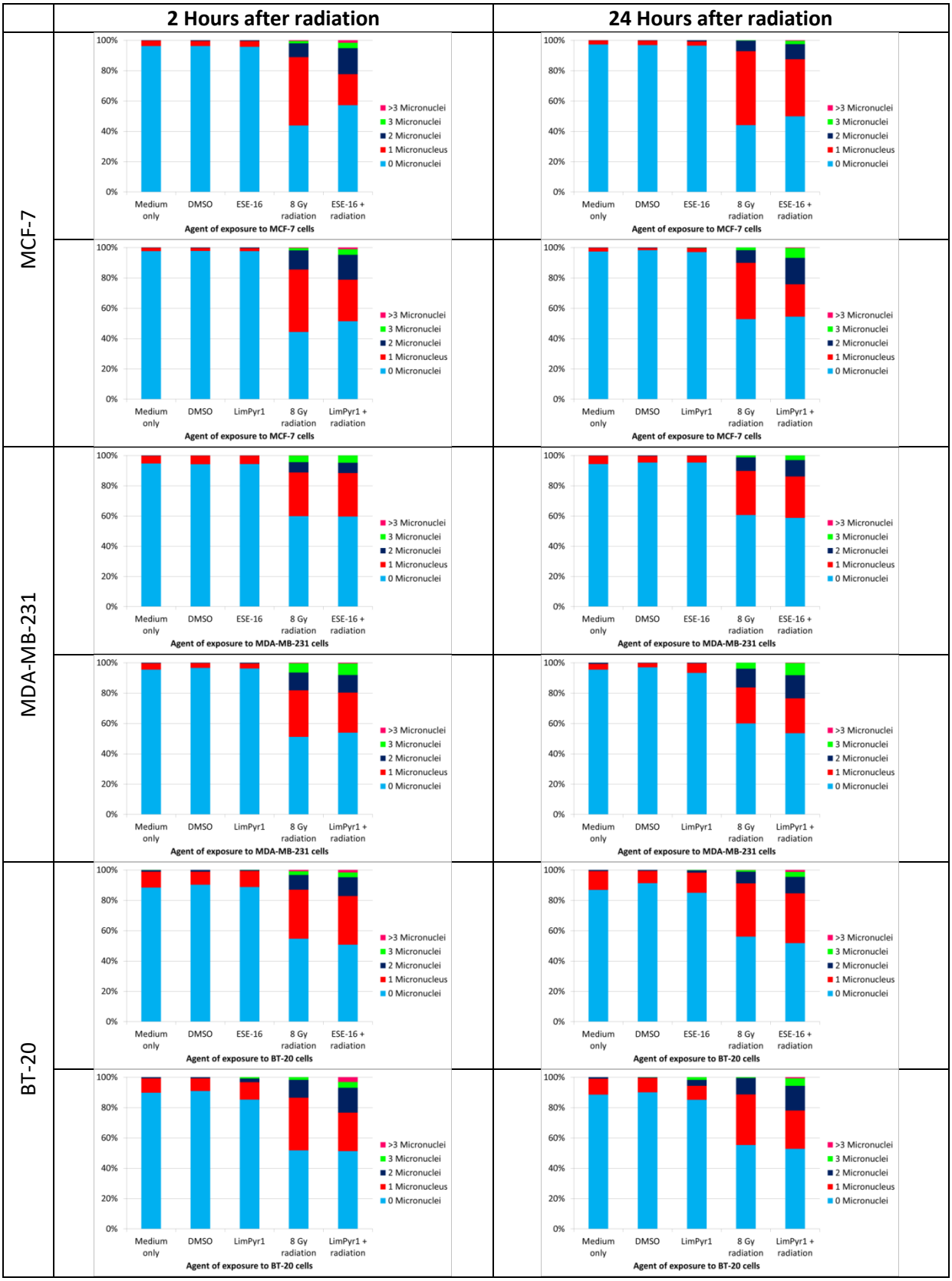

Figure 4.54: Distribution of micronuclei in MCF-7-, MDA-MB-231- and BT-20 cells exposed to various treatment condition. Micronuclei quantification followed 2 and 24 hours after irradiation. Increased micronuclei was observed in ESE-16- and LimPyr1 pre-treated cells 24

hours after irradiation compared to cells exposed to 8 Gy radiation only. The number of cells that obtained DNA damage was not increased in the pre-treated samples, however the DNA damage obtained by the pre-treated cells were more severe, as illustrated by increased micronuclei per cell.

MCF-7 cells exposed to LimPyr1 (2.33±0.64 fold increase), 8 Gy radiation (2.05±0.51- (DMEM) and 2.83±0.22 (RPMI) fold increase), ESE-16 24 hours prior to radiation (1.13±0.07 fold increase) and LimPyr1 24 hours prior to radiation (2.08±0.29 fold increase) displayed a significant increase in Ku70 at the 2 hour termination point compared to the vehicle control (Figure 4.55). MCF-7 cells pre-treated with LimPyr1 significantly increased Ku70 2 hour after radiation (1.32±0.19 fold increase) compared to cells exposed to the compound only. Ku70 expression was significantly increased at the 24 hour termination point in MCF-7 cells exposed to 8 Gy radiation (1.60±0.27- (DMEM) and 1.74±0.19 (RPMI) fold increase), the ESE-16/radiation combination treatment (2.26±0.78 fold increase) and the LimPyr1/radiation combination treatment (2.22±0.73fold increase), compared to DMSO (Table 4.26). Compared to cells exposed to the compound only ESE-16- (2.59±0.24fold increase) and LimPyr1 (1.78±0.45 fold increase) pre-treated MCF-7 cells displayed significantly higher Ku70 protein levels. Interesting, ESE-16- (0.58±0.16) and LimPry1 (0.68±0.16) pre-treated cells displayed a significant decrease in Ku70 expression 2 hours after radiation compared to cells exposed to 8 Gy radiation only taken as 1. In contrast, Ku70 expression was significantly increased in ESE-16- (1.23±0.08 fold increase) and LimPyr1 (1.73±0.19 fold increase) pre-treated cells 24 hours after radiation compared to the radiation only exposed samples (Figure 4.56).

Elevated Ku70 protein levels were observed at the 2 hour termination point in MDA-MB-231 cells exposed to ESE-16 (1.65±0.24 fold increase), LimPyr1 (1.68±0.34 fold increase) and 8 Gy radiation (1.95±0.13- (DMEM) and 1.98±0.04 (RPMI) fold increase), compared to DMSO. Additionally, ESE-16- (1.83±0.45 fold increase) and LimPyr1 (1.71±0.01 fold increase) pre-treated MDA-MB-231 cells displayed significantly higher Ku70 protein levels 2 hours after radiation compared to the vehicle control (Figure 4.55). ESE-16 pre-treated MDA-MB-231

cells expressed significantly higher Ku70 levels (1.19±0.06 fold increase) 2 hours after radiation compared to cells exposed to the compound only. Ku70 protein levels were significantly decreased 2 hours after radiation in ESE-16- (0.74±0.11) and LimPyr1 (0.86±0.02) pre-treated MDA-MB-231 cells compared to cells exposed to 8 Gy radiation only taken as 1. A significant increase in Ku70 expression was observed at the 24 hour termination point in LimPyr1 (1.20±0.07 fold increase) and 8 Gy radiation (1.57±0.17- (DMEM) and 1.32±0.12 (RPMI) fold increase) exposed MDA-MB-231 cells (Table 4.27). ESE-16 pre-treated MDA-MB-231 cells displayed a significantly increase 24 hours after radiation in Ku70 compared to DMSO (1.53±0.29 fold increase), cells exposed to ESE-16 (1.22±4.77E-04 fold increase) or 8 Gy radiation only (1.19±0.10 fold increase). Similarly, MDA-MB-231 cells exposed to LimPyr1 24 hours prior to radiation displayed a significant increase in Ku70 expression 24 hours after radiation compared to the vehicle control (1.60±0.28 fold increase) and cells exposed to LimPyr1 (1.20±0.11 fold increase) or 8 Gy radiation only (1.21±0.10 fold increase) (Figure 4.57).

BT-20 cells exposed to LimPyr1 (1.20±0.11- and 1.35±0.21 fold increase), 8 Gy radiation (1.72±0.26- and 1.37±0.17 fold increase (DMEM/F-12), 1.99±0.48- and 1.69±0.37 fold increase (RPMI), ESE-16 in combination with radiation (1.32±0.08- and 1.53±0.22 fold increase) and LimPyr1 in combination with radiation (1.73±0.27- and 2.34±0.83 fold increase) displayed a significant increase in Ku70 protein levels at the 2 and 24 hours termination points, respectively, compared to DMSO (Figure 4.55). ESE-16- (1.48±0.28- and 1.34±0.06 fold increase) and LimPyr1 (1.43±0.09- and 1.71±0.39 fold increase) pre-treated BT-20 cells displayed a significant increase in Ku70 2 and 24 hours after radiation compared to cells exposed to ESE-16 or LimPyr1 only (Table 4.28). Ku70 expression was significantly decreased 2 hours after radiation in BT-20 cells exposed to the ESE-16- (0.78±0.11) and LimPyr1 (0.88±0.07) combination therapies, compared to cells exposed to 8 Gy radiation only taken as 1. However, 24 hours after radiation Ku70 expression was significantly higher in ESE-16- (1.11±0.02 fold increase) and LimPyr1 (2.21±0.03 fold increase) pre-treated BT-20 cells compared to the 8 Gy radiation only samples (Figure 4.58).

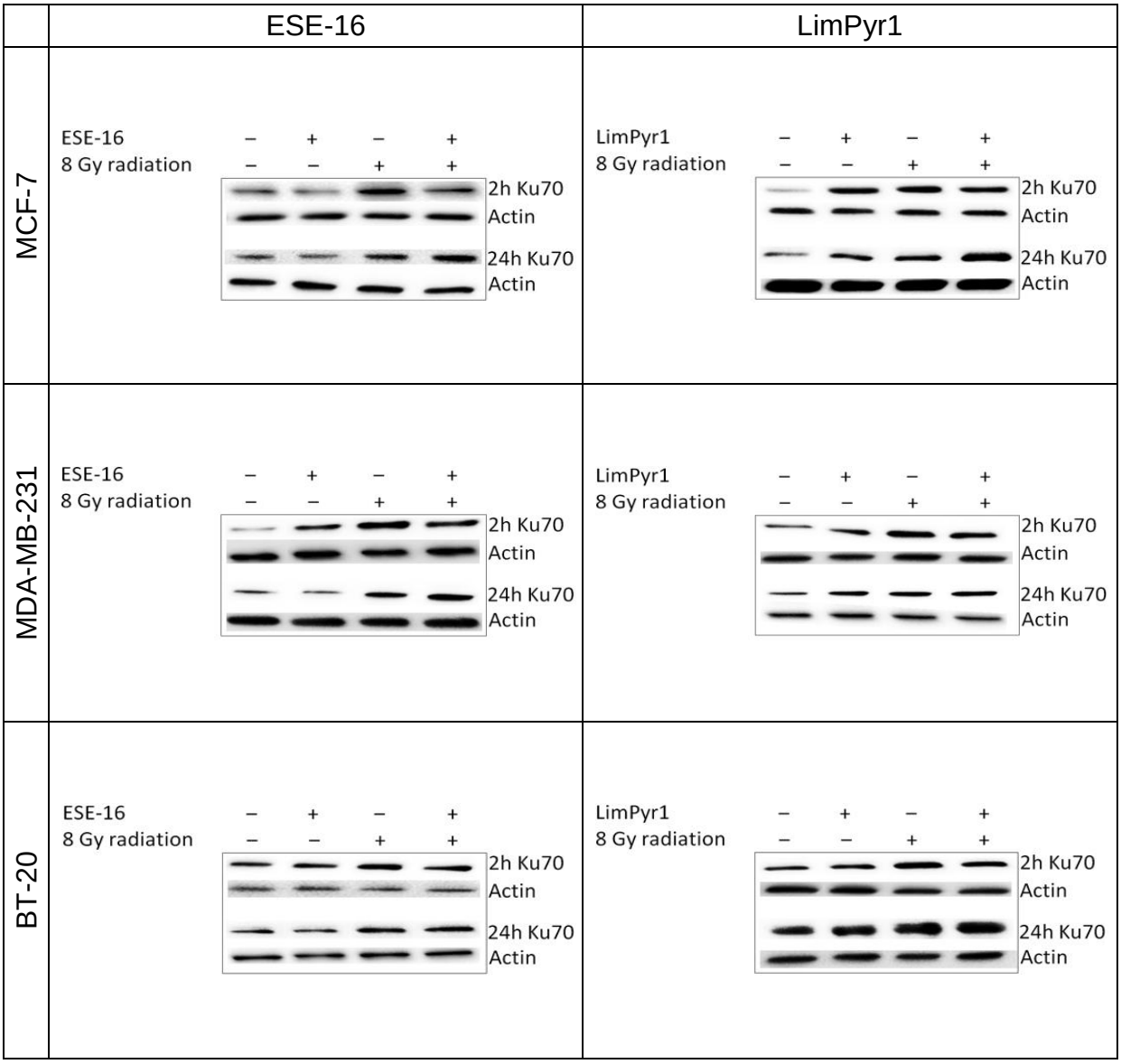

Figure 4.55: Western blots illustrating Ku70 protein expression in MCF-7-, MDA-MB-231- and BT-20 cells 2 and 24 hours after radiation. Breast cancer cells were exposed to ESE-16 or LimPyr1, 8 Gy radiation and ESE-16 or LimPyr1 24 hours prior to irradiation. Quantification of Ku70 followed 2 and 24 hours after irradiation.

Table 4.26: Ku70 expression in MCF-7 cells 2 and 24 hours after irradiation. Ku70 proteins were visualized with a ChemiDoc MP (Bio-rad, CA, USA) followed by analysis using Image Lab Software Version 5.2.1 (Bio-rad, CA, USA). Data were analyzed using an ANOVA-single factor model and a two-tailed Student's t-test. The mean fold changes (FC) of three biological repeats are displayed in the table ± standard deviations (SD). Cells exposed to DMSO and the individual treatment conditions were used as baselines to calculate statistically significant differences (*P*-value <0.05).

			DMSO	Compound	8 Gy radiation	Combination
Compared to DMSO						
2 hours	ESE-16	FC± SD	1	0.88±0.42	2.05±0.51	1.13±0.07
		P-value	-	0.64	**0.02**	**0.03**
	LimPyr1	FC± SD	1	2.33±0.64	2.83±0.22	2.08±0.29
		P-value	-	**0.02**	**5.88E-04**	**0.01**
24 hours	ESE-16	FC ± SD	1	1.11±0.21	1.60±0.27	2.26±0.78
		P-value	-	0.42	**0.02**	**4.88E-02**
	LimPyr1	FC ± SD	1	1.01±0.11	1.74±0.19	2.22±0.73
		P-value	-	0.83	**4.98E-03**	**0.04**
Compared to compound						
2 hours	ESE-16	FC ± SD		1		1.13±0.30
		P-value		-		0.47
	LimPyr1	FC ± SD		1		1.32±0.19
		P-value		-		**4.92E-02**
24 hours	ESE-16	FC ± SD		1		2.59±0.24
		P-value		**-**		**1.12E-03**
	LimPyr1	FC ± SD		1		1.78±0.45
		P-value		**-**		**0.04**
Compared to 8 Gy radiation						
2 hours	ESE-16	FC ±S D			1	0.58±0.16
		P-value			**-**	**0.01**
	LimPyr1	FC ±S D			1	0.68±0.16
		P-value			**-**	**0.03**
24 hours	ESE-16	FC ± SD			1	1.23±0.08
		P-value			**-**	**0.01**
	LimPyr1	FC ± SD			1	1.73±0.19
		P-value			**-**	**0.01**

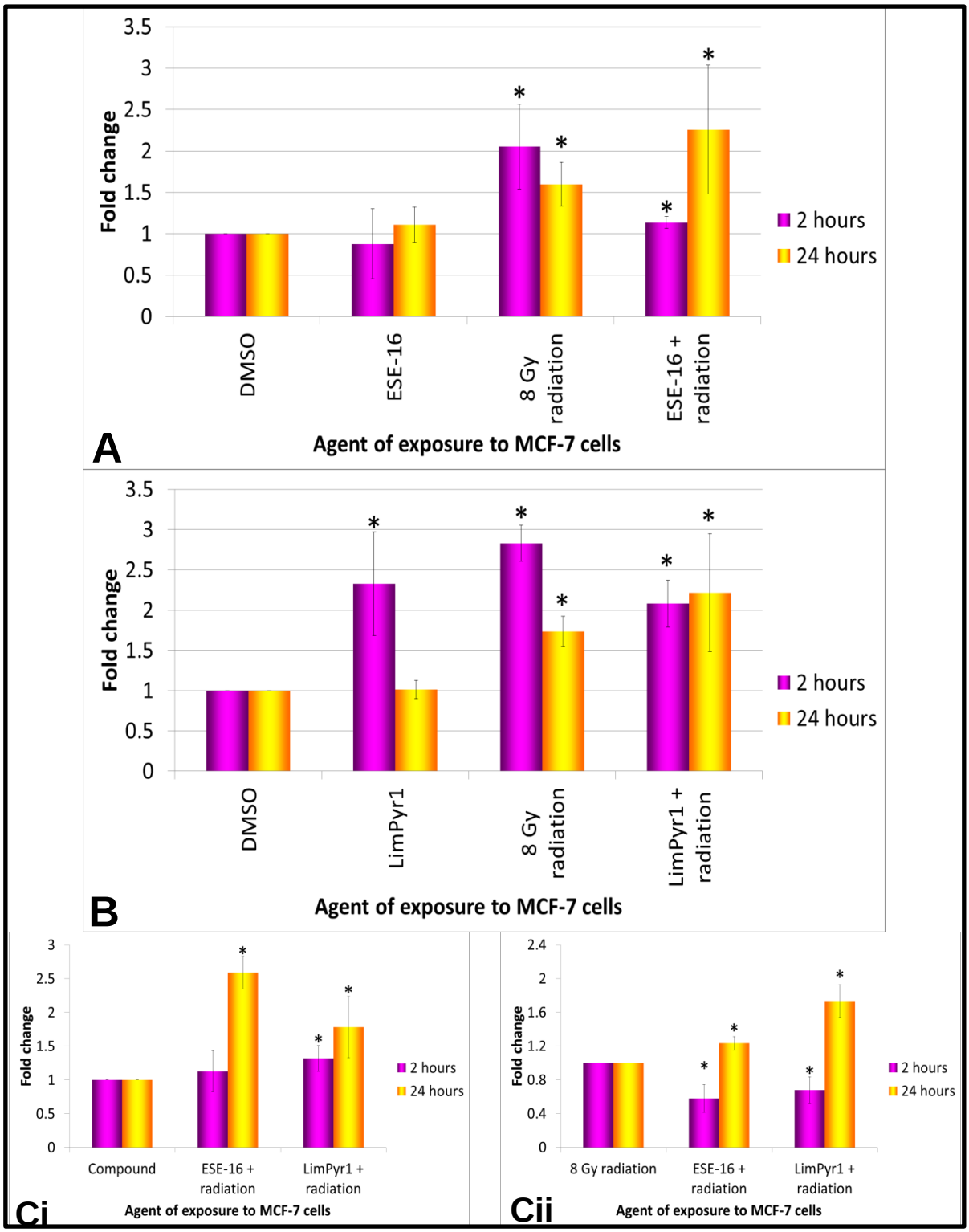

Figure 4.56: Graphical representation of Ku70 protein expression in MCF-7 cells 2 and 24 hours after irradiation. MCF-7 cells exposed to 8 Gy radiation (A&B), LimPyr1 (B), ESE-16 24 hours prior to radiation (A) and LimPyr1 24 hours prior to irradiation (B) displayed a significant increase in Ku70 at the 2 hour termination point. Exposure to 8 Gy radiation (A&B), the ESE-16/radiation combination treatment (A) and the LimPyr1/radiation combination treatment (B) significantly increased Ku70 expression 24 hours after irradiation. ESE-16- and LimPyr1 pre-

treated MCF-7 cells displayed a significant increase in Ku70 24 hours after irradiation compared to cell exposed to the compounds only (Ci). Additionally, LimPyr1 pre-treatment significantly increased Ku70 expression 2 hours after irradiation compared to cells exposed to LimPyr1 only. Ku70 expression was significantly decreased in ESE-16- and LimPyr1 pre-treated cells 2 hours after irradiation compared to cells exposed to 8 Gy radiation only. However, 24 hours after irradiation Ku70 was significantly increased in the pre-treated cells compared to the radiation only samples (Cii). The bar graph summarizes the mean fold changes of three biological repeats and standard deviations are represented by T-bars. Statistically significant differences are indicated with * (*P*-value <0.05) when compared to DMSO (A-B), cells exposed to ESE-16 or LimPyr1 only (Ci) and cells exposed to 8 Gy radiation only (Cii).

Table 4.27: Ku70 expression in MDA-MB-231 cells 2 and 24 hours after irradiation. A ChemiDoc MP (Bio-rad, CA, USA) was used to visualize Ku70 proteins 2 and 24 hours after irradiation. Bands were quantified using Image Lab Software Version 5.2.1 (Bio-rad, CA, USA) and data were analyzed using an ANOVA-single factor model. A two-tailed Student's *t*-test was used to calculate statistical significance (*P*-value <0.05) using DMSO and cells exposed to the individual treatment conditions as baselines. The mean fold change (FC) of three biological repeats is displayed in the table ± standard deviations (SD).

			DMSO	Compound	8 Gy radiation	Combination
Compared to DMSO						
2 hours	ESE-16	FC± SD	1	1.65±0.24	1.95±0.13	1.83±0.45
		P-value	-	**0.01**	**8.41E-04**	**0.03**
	LimPyr1	FC± SD	1	1.68±0.34	1.98±0.04	1.71±0.01
		P-value	-	**0.03**	**2.03E-05**	**1.54E-07**
24 hours	ESE-16	FC ± SD	1	0.95±0.10	1.57±0.17	1.53±0.29
		P-value	-	0.46	**0.01**	**0.04**
	LimPyr1	FC ± SD	1	1.20±0.07	1.32±0.12	1.60±0.28
		P-value	-	**0.01**	**0.01**	**0.02**
Compared to compound						
2 hours	ESE-16	FC ± SD		1		1.19±0.06
		P-value		-		**0.01**
	LimPyr1	FC ± SD		1		1.07±0.16
		P-value		-		0.49
24 hours	ESE-16	FC ± SD		1		1.22±4.77E-04
		P-value		**-**		**3.37E-09**
	LimPyr1	FC ± SD		1		1.20±0.11
		P-value		-		**0.04**
Compared to 8 Gy radiation						
2 hours	ESE-16	FC ±S D			1	0.74±0.11
		P-value			-	**0.02**
	LimPyr1	FC ±S D			1	0.86±0.02
		P-value			**-**	**9.31E-04**
24 hours	ESE-16	FC ± SD			1	1.19±0.10
		P-value			-	**0.04**
	LimPyr1	FC ± SD			1	1.21±0.10
		P-value			-	**0.03**

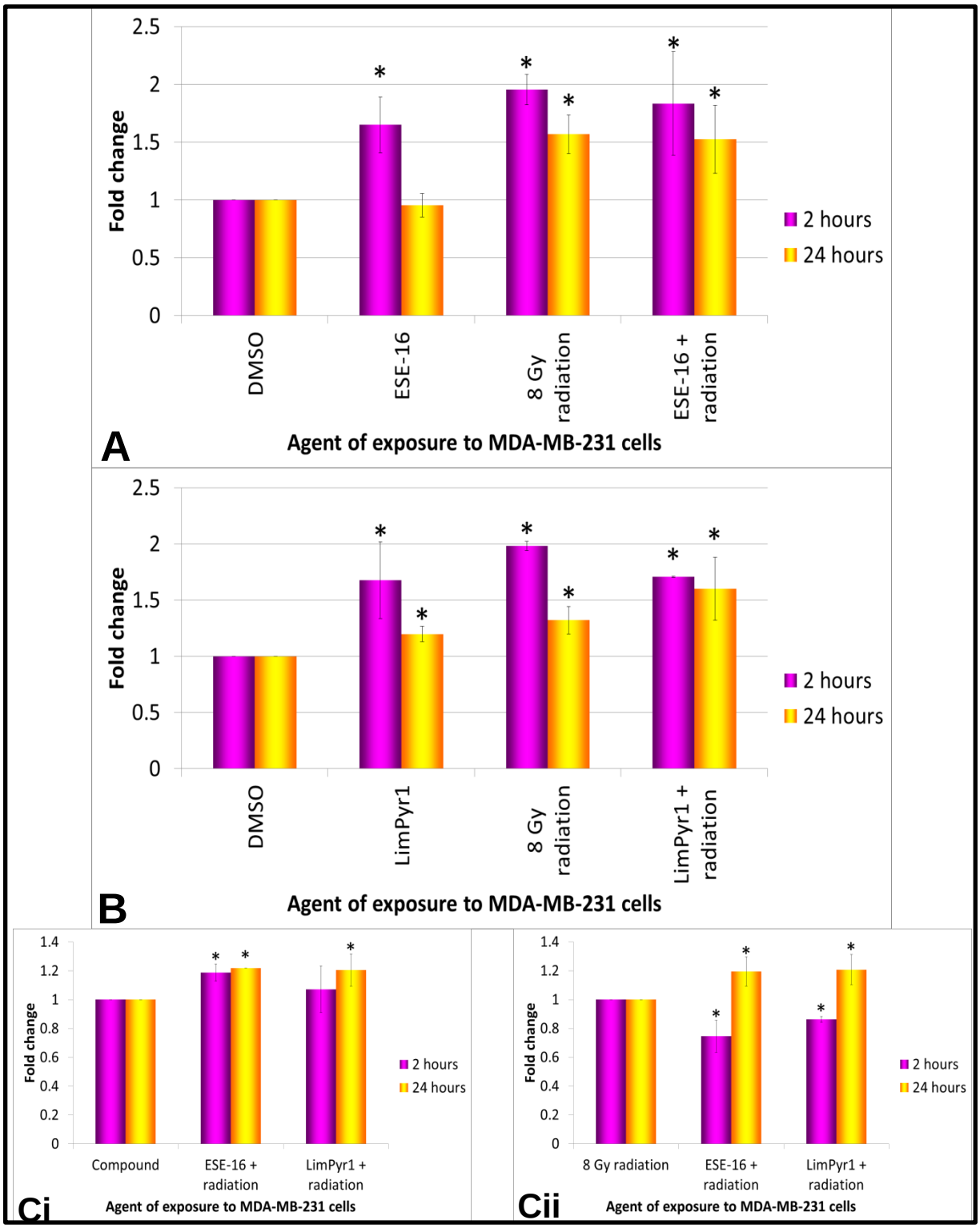

Figure 4.57: Graphical representation of Ku70 protein expression in MDA-MB-231 cells 2 and 24 hours after irradiation. MDA-MB-231 cells exposed to ESE-16 (A), LimPyr1 (B) and 8 Gy radiation (A&B) displayed significantly higher Ku70 protein levels at the 2 hour termination point. Additionally, Ku70 was significantly increased at the 24 hour termination point following exposure to LimPyr1 (B) and 8 Gy radiation (A&B). MDA-MB-231 cells pre-treated with ESE-16 displayed elevated Ku70 protein levels 2 and 24 hours after irradiation compared to the vehicle

control (A) and cells exposed to ESE-16 only (Ci). LimPyr1 presentation resulted in elevated Ku70 protein levels in MDA-MB-231 cells 2 hours after irradiation compared to DMSO (B), and 24 hours after irradiation compared to DMSO (B) and cells exposed to LimPyr1 only (Cii). MDA-MB-231 cells exposed to ESE-16 or LimPyr1 24 hours prior to irradiation displayed significantly lower Ku70 levels compared to cells exposed to 8 Gy radiation only (Cii). Ku70 protein levels was significantly higher in pre-treated cells 24 hours after irradiation compared to cells exposed to radiation only (Cii). The mean fold increases of three biological repeats are summarized in the bar graph. Standard deviations are represented by T-bars and statistically significant differences are indicated with * (*P*-value <0.05) when compared to DMSO (A-B), cells exposed to ESE-16 or LimPyr1 only (Ci) and cells exposed to 8 Gy radiation only (Cii).

Table 4.28: Ku70 expression in BT-20 cells 2 and 24 hours after irradiation. Ku70 protein bands were obtained using a ChemiDoc MP (Bio-rad, CA, USA) followed by band quantification using Image Lab Software Version 5.2.1 (Bio-rad, CA, USA). The ANOVA-single factor model was used to analyze the data and statistical significance (*P*-value <0.05) were calculated using a two-tailed Student's *t*-test. The mean fold changes (FC) of three biological repeats are displayed in the table ± standard deviations (SD).

			DMSO	Compound	8 Gy radiation	Combination
Compared to DMSO						
2 hours	ESE-16	FC± SD	1	1.06±0.29	1.72±0.26	1.32±0.08
		P-value	-	0.73	**0.01**	**2.27E-03**
	LimPyr1	FC± SD	1	1.20±0.11	1.99±0.48	1.73±0.27
		P-value	-	**0.03**	**0.02**	**0.01**
24 hours	ESE-16	FC ± SD	1	1.14±0.21	1.37±0.17	1.53±0.22
		P-value	-	0.31	**0.02**	**0.01**
	LimPyr1	FC ± SD	1	1.35±0.21	1.69±0.37	2.34±0.83
		P-value	-	**4.73E-02**	**0.04**	**4.87E-02**
Compared to compound						
2 hours	ESE-16	FC ± SD		1		1.48±0.28
		P-value		-		**4.66E-02**
	LimPyr1	FC ± SD		1		1.43±0.09
		P-value		-		**1.33E-03**
24 hours	ESE-16	FC ± SD		1		1.34±0.06
		P-value		-		**7.68E-04**
	LimPyr1	FC ± SD		1		1.71±0.39
		P-value		-		**0.04**
Compared to 8 Gy radiation						
2 hours	ESE-16	FC ±S D			1	0.78±0.11
		P-value			-	**0.02**
	LimPyr1	FC ±S D			1	0.88±0.07
		P-value			-	**0.04**
24 hours	ESE-16	FC ± SD			1	1.11±0.02
		P-value			-	**6.54E-04**
	LimPyr1	FC ± SD			1	2.21±0.03
		P-value			-	**6.76E-06**

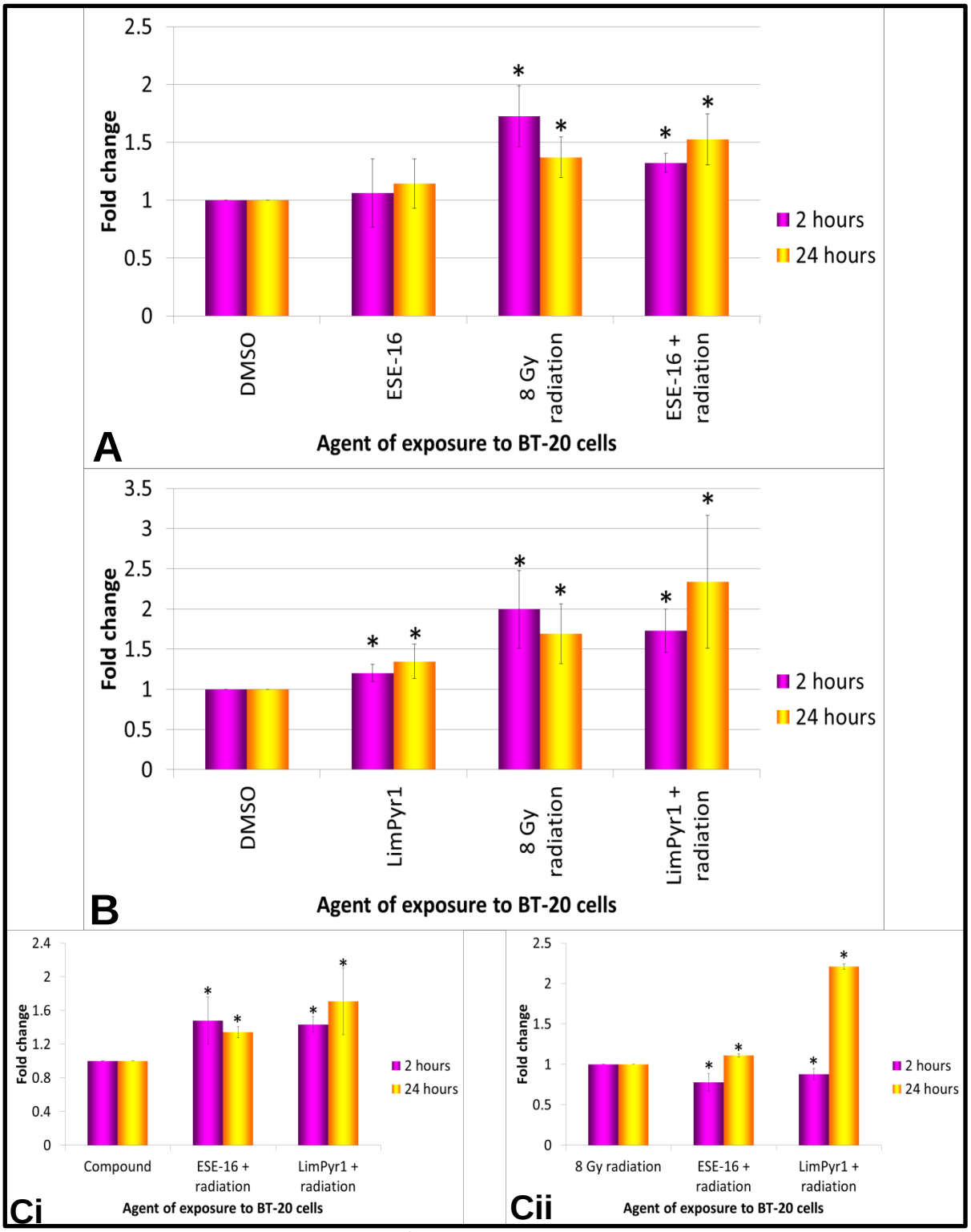

Figure 4.58: Graphical representation of Ku70 protein expression in BT-20 cells 2 and 24 hours after irradiation. BT-20 cells exposed to 8 Gy radiation (A&B), LimPyr1 (B), ESE-16 prior to irradiation (A) and LimPyr1 prior to irradiation (B) displayed elevated Ku70 protein levels 2 and 24 hours after radiation. Additionally, ESE-16- and LimPyr1 pre-treated BT-20 cells displayed an increase in Ku70 2 and 24 hours after irradiation compared to cells exposed to the compounds only (Ci). Compared to cells exposed to 8 Gy radiation only BT-20 cells exposed to the

combination treatments displayed significantly lower Ku70 protein levels 2 hours after irradiation, but elevated Ku70 protein levels 24 hours after irradiation (Cii). The bar graph summarizes the mean fold increases of three biological repeats. Standard deviations are represented by T-bars and statistically significant differences are indicated with * (*P*-value <0.05) when compared to DMSO (A-B), cells exposed to ESE-16 or LimPyr1 only (Ci) and cells exposed to 8 Gy radiation only (Cii).

4.3 Evaluation of the bystander effect induced by irradiated cells

4.3.1 Reactive oxygen species production: Flow cytometric quantification of superoxide employing hydroethidine

Superoxide formation was quantified by means of flow cytometry employing hydroethidine. Untreated BT-20 cells were measured for ROS generation 48 hours after exposure to conditioned media obtained from BT-20 cells exposed to appropriate controls and various treatment conditions.

BT-20 cells propagated in conditioned media obtained from cells exposed to DMSO and rotenone served as vehicle- and positive controls, respectively. Cells propagated in DMEM/F-12 (for the investigation of ESE-16) or RPMI (for the investigation of LimPyr1) served as negative controls. No statistically significant differences were calculated between the negative- and vehicle controls. Superoxide quantification was significantly increased in the positive controls (Table 4.29).

Conditioned media obtained from cells exposed to ESE-16 and LimPyr1 did not induce superoxide generation in untreated BT-20 cells (Figure 4.59). Superoxide quantification was significantly increased in untreated BT-20 cells following a 48 hour exposure to conditioned media obtained from cells exposed to 8 Gy radiation (1.21±0.12 (DMEM/F-12)- and 1.16±0.11 (RPMI) fold increase). Media transferred from the ESE-16- and LimPyr1/radiation combination treatments significantly increased ROS production in untreated BT-20 cells

(1.39±0.09 - and 1.29±0.17 fold increase, respectively), compared to the vehicle control (Figure 4.60). Additionally, cells exposed to the combination treatments' conditioned media revealed a significant increase in superoxide production compare to cells propagated in ESE-16 or LimPyr1 (1.33±0.04- and 1.29±0.15 fold increase, respectively)- and 8 Gy radiation (1.16±0.10- and 1.16±0.06 fold increase, respectively) conditioned media (Table 4.29).

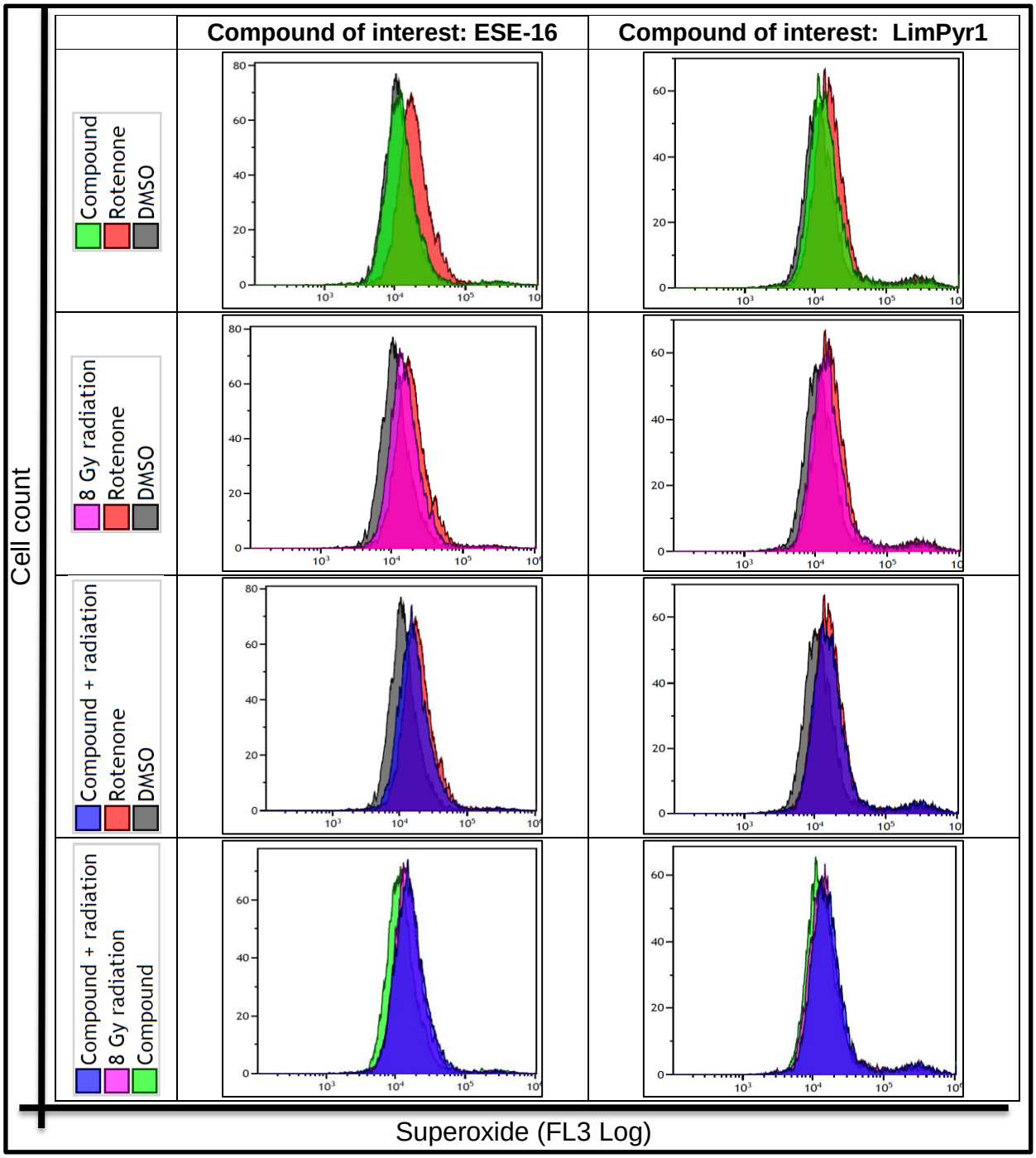

Figure 4.59: Representative overlay histograms of superoxide detection in untreated BT-20 cells propagated in conditioned media obtained from cells exposed to appropriate controls

and different treatment conditions for 48 hours. Histograms were obtained by plotting the cell count against superoxide detection (FL3 Log). A right shift is observed in untreated BT-20 cells propagated in conditioned media obtained from cells exposed to different treatment conditions.

Table 4.29: Superoxide detection in untreated breast cancer cells exposed to conditioned media obtained from treated cells for 48 hours. Data were generated and analyzed using Kaluza Analysis version 1.5 (FL, USA) and an ANOVA-single factor model. The averaged fold change (FC) and standard deviations (SD) of three biological repeats are displayed in the table. A two-tailed Student's *t*-test was used to calculate statistically significant differences (*P*-value <0.05) using cells propagated in DMSO (vehicle control) conditioned media as a baseline. Additionally, *P*-values were also calculated for the combination treatment conditions when compared to individual treatments.

			Medium only	DMSO	Rotenone	Compound	8 Gy radiation	Compound + radiation
BT-20 cells	Compared to DMSO							
	ESE-16	FC± SD	1.12±0.16	1	1.54±0.31	1.05±0.10	1.21±0.12	1.39±0.09
		P-value	0.28	-	**0.04**	0.46	**0.04**	**1.45E-03**
	LimPyr1	FC ± SD	1.13±0.20	1	1.21±0.14	1.00±0.10	1.16±0.11	1.29±0.17
		P-value	0.24	-	**0.03**	0.99	**0.02**	**1.35E-02**
	Compared to compound							
	ESE-16	FC ± SD				1		1.33±0.04
		P-value				-		**1.92E-04**
	LimPyr1	FC ± SD				1		1.29±0.15
		P-value				-		**8.80E-03**
	Compared to radiation							
	ESE-16	FC ±S D					1	1.16±0.10
		P-value					-	**4.99E-02**
	LimPyr1	FC ± SD					1	1.16±0.06
		P-value					-	**2.61E-03**

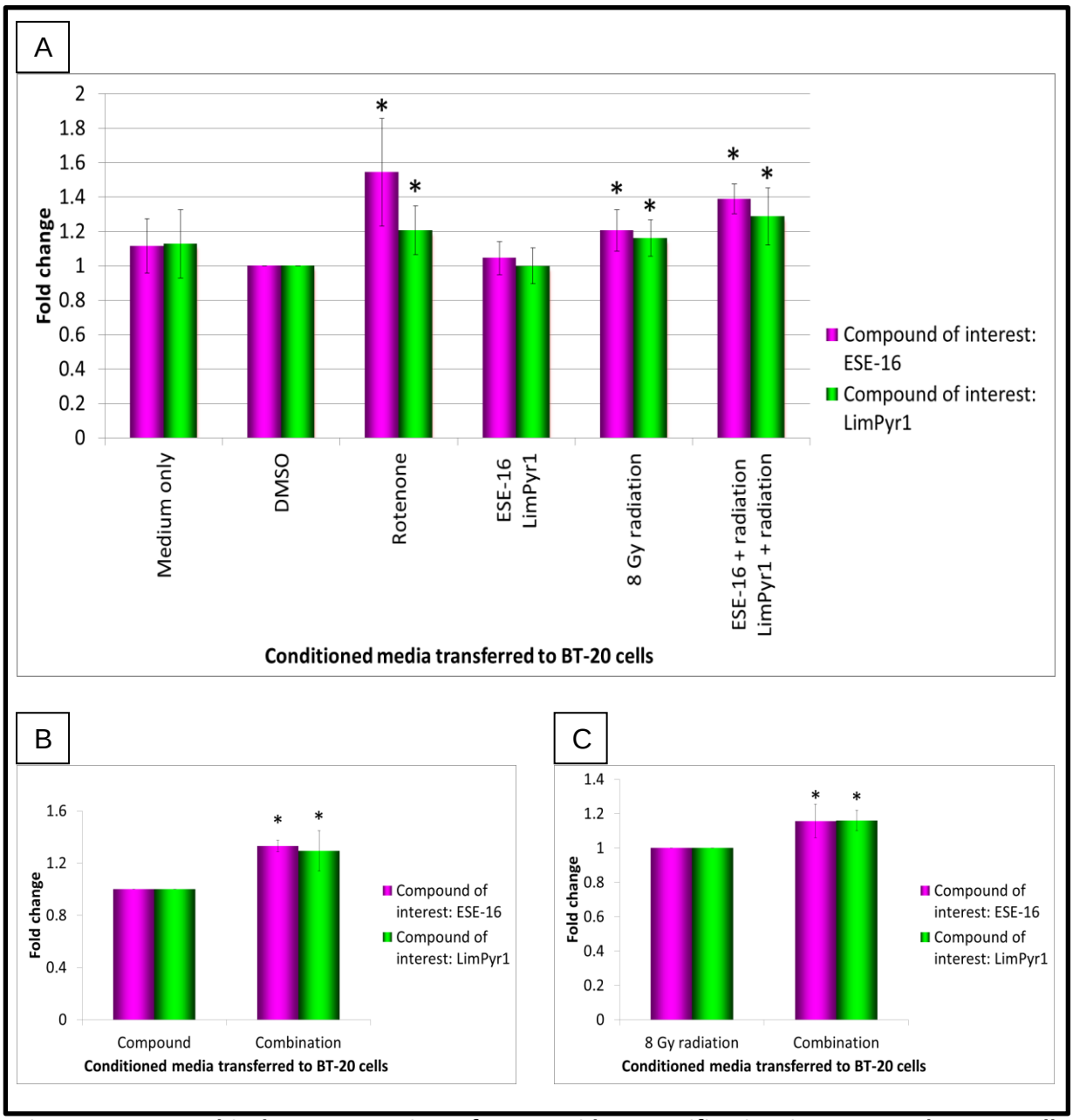

Figure 4.60: Graphical representation of superoxide quantification in untreated BT-20 cells propagated in conditioned media obtained from cells exposed to various treatment conditions for 48 hours. Superoxide was not significantly increased in untreated BT-20 cells propagated in ESE-16- and LimPyr1 conditioned media. Conditioned media obtained from cells exposed to 8 Gy radiation revealed a significant increase in superoxide generation in untreated BT-20 cells when compared to the vehicle control. Untreated BT-20 cells propagated in conditioned media obtained from pre-treated BT-20 cells revealed a significant increase in superoxide when compared to cells propagated in conditioned media obtained from the vehicle control and individual treatment conditions. The mean fold increases of three biological repeats are represented in the bar graph. Standard deviations are represented by T-bars. Statistically significant differences are indicated with * (*P*-value <0.05) when compared to DMSO (A), cells exposed to ESE-16 or LimPyr1 only (B) and 8 Gy radiation only (C).

4.3.2 Mitochondrial transmembrane potential: Flow cytometric quantification of Mitocapture™

The mitochondrial transmembrane permeability was quantified in untreated BT-20 cells propagated in conditioned media obtained from cells exposed to various controls and treatment conditions for 48 hours using the Mitocapture™ flow cytometric fluorometric kit.

BT-20 cells propagated in growth media served as negative controls. Conditioned media transferred from cells exposed to DMSO and vinblastine served as vehicle- and positive apoptotic controls, respectively. No statistically significant differences were calculated when the vehicle controls were compared to the negative controls. The positive apoptotic controls revealed a significant increase in mitochondrial transmembrane permeability (Table 4.30).

Conditioned media obtained from cells exposed to ESE-16 and LimPyr1 revealed no significant increase in Mitocapture™ when exposed to untreated BT-20 cells (Figure 4.61). Untreated BT-20 cells displayed a significant increase in Mitocapture™ quantification when exposed to conditioned media transferred from cells exposed to 8 Gy radiation (1.37±0.21-(DMEM/F-12) and 1.26±0.16 (RPMI) fold increase), compared to the vehicle control (Figure 4.62). BT-20 cells propagated in the media obtained from ESE-16- and LimPyr1 pre-treated cells revealed a significant increase in Mitocapture™ compared to the negative control (1.54±0.22- and 1.44±0.22 fold increase, respectively), cells exposed to ESE-16 or LimPyr1 conditioned media (1.61±0.22- and 1.17±0.11 fold increase, respectively) and 8 Gy radiation conditioned media (1.08±4.44E-03- and 1.14±0.08 fold increase, respectively) (Table 4.30).

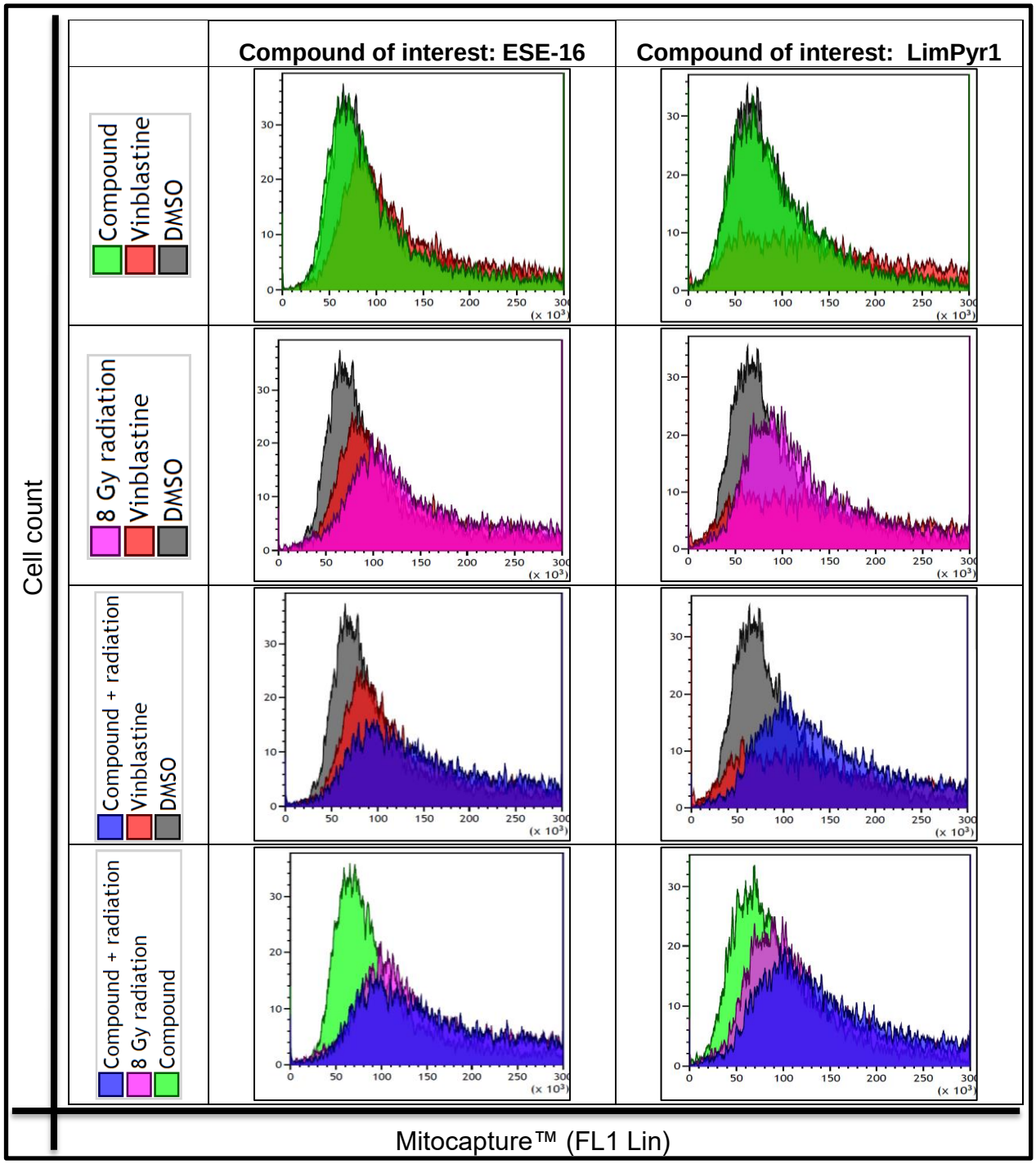

Figure 4.61: Representative overlay histograms of Mitocapture™ detection in untreated BT-20 cells exposed to conditioned media obtained from cells exposed to appropriate controls and different treatment conditions. Histograms were obtained by plotting the cell count against Mitocapture™ detection (FL1 Lin) using data points obtained by flow cytometry. Untreated BT-20 cells displayed a right shift when exposed to conditioned media obtained from BT-20 cells exposed to different treatment conditions for 48 hours.

Table 4.30: Mitocapture™ detection in untreated breast cancer cells following a 48 hour exposure to conditioned media obtained from treated cells. Kaluza Analysis version 1.5 (FL, USA) was used to generate data following analysis using an ANOVA-single factor model. The averaged fold change (FC) and standard deviations (SD) of three biological repeats are displayed. A two-tailed Student's *t*-test was used to calculate statistically significant differences (*P*-value <0.05) using cells propagated in conditioned media obtained from BT-20 cells exposed to the vehicle control as a baseline. *P*-values were also calculated for the combination treatment condition when compared to individual treatments.

			Medium only	DMSO	Vinblastine	Compound	8 Gy radiation	Compound + radiation
BT-20 cells	Compared to DMSO							
	ESE-16	FC± SD	1.03±0.05	1	1.27±0.15	0.96±0.05	1.37±0.21	1.54±0.22
		P-value	0.32	-	**0.03**	0.20	**0.04**	**1.25E-02**
	LimPyr1	FC ± SD	1.26±0.27	1	1.76±0.33	1.11±0.15	1.26±0.16	1.44±0.22
		P-value	0.10	-	**3.81E-03**	0.18	**1.78E-02**	**6.34E-03**
	Compared to compound							
	ESE-16	FC ± SD				1		1.61±0.22
		P-value				-		**8.87E-03**
	LimPyr1	FC ± SD				1		1.17±0.11
		P-value				**-**		**0.02**
	Compared to radiation							
	ESE-16	FC ±S D					1	1.08±4.44E-03
		P-value					**-**	**6.33E-05**
	LimPyr1	FC ± SD					1	1.14±0.08
		P-value					**-**	**1.02E-02**

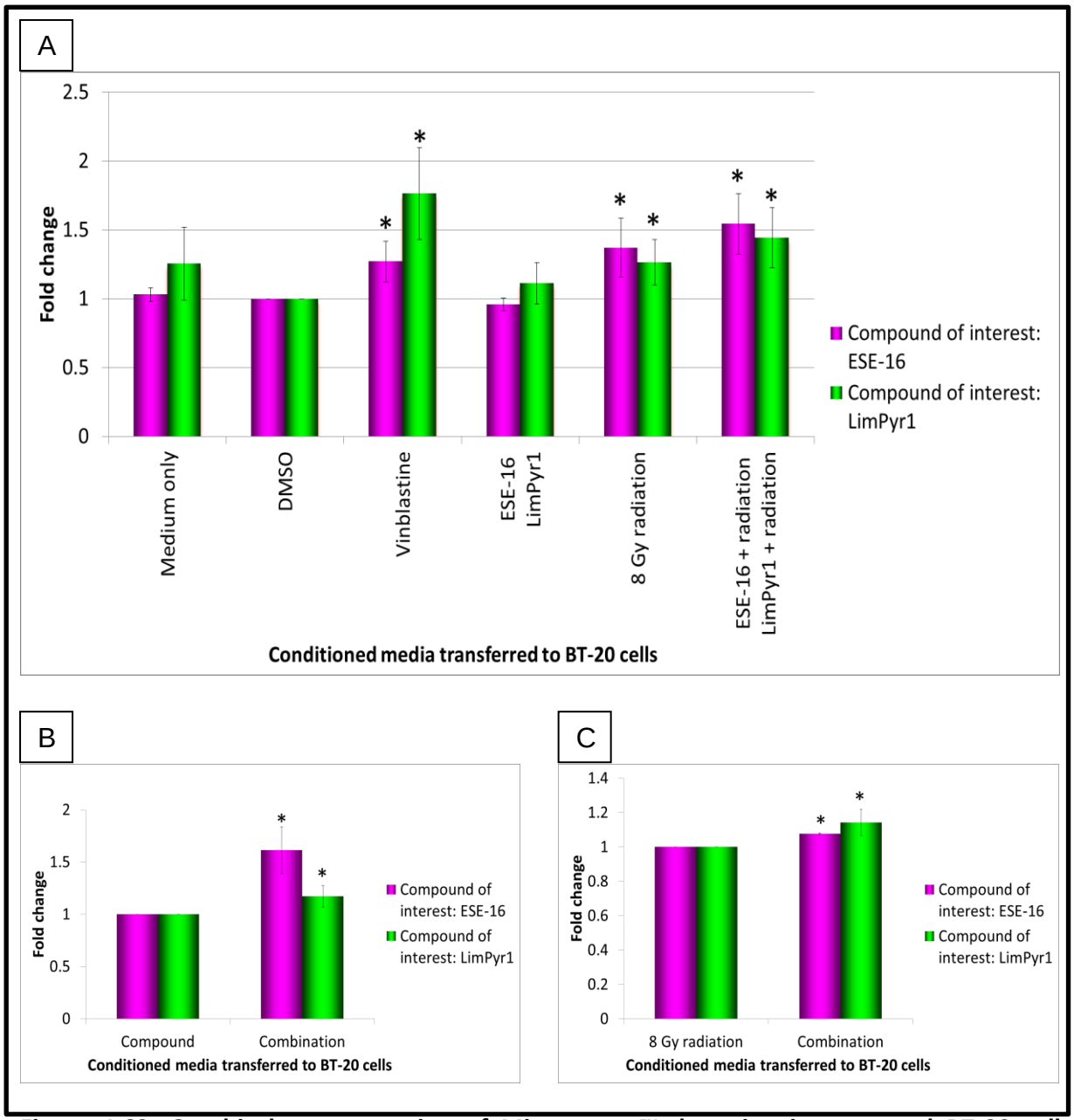

Figure 4.62: Graphical representation of Mitocapture™ detection in untreated BT-20 cells following a 48 hour exposure to conditioned media obtained from cells exposed to various treatment modalities. BT-20 cells propagated in conditioned media obtained from cells exposed to ESE-16 and LimPyr1, respectively, revealed no significant increase in Mitocapture™ compared to the vehicle controls. Conditioned media obtained from cells exposed to 8 Gy radiation revealed a significant increase in mitochondria transmembrane permeability in untreated BT-20 cells. Additionally, untreated BT-20 cells propagated in conditioned media obtained from pre-treated BT-20 cells revealed a significant increase in Mitocapture™ quantification when compared to cells propagated in conditioned media obtained from vehicle controls, as well as the individual treatment conditions. The bar graph illustrates the mean fold increase of three biological repeats, with standard deviations represented by T-bars. Statistically significant differences are indicated with * (*P*-value <0.05) when compared to DMSO (A), cells exposed to ESE-16 or LimPyr1 only (B) and 8 Gy radiation only (C).

4.3.3 Long term cellular proliferation quantified by crystal violet staining.

Long term cell proliferation was evaluated in BT-20 cells exposed to conditioned media transferred from cells exposed to ESE-16, LimPyr1, 8 Gy radiation or pre-treated with either ESE-16 or LimPyr1 24 hours prior to 8 Gy radiation.

BT-20 cells exposed to conditioned medium obtained from cells exposed to DMSO and doxorubicin served as vehicle- and positive controls. Cell proliferation was significantly decreased in BT-20 cells propagated in doxorubicin conditioned media compared to the vehicle control (Figure 4.63). No statistically significant differences were observed between the vehicle control and cells propagated in medium only (Table 4.31).

Cell proliferation remained uninterrupted in BT-20 cells propagated in ESE-16 conditioned media compared to the vehicle control (Figure 4.63). BT-20 cells exposed to LimPyr1 (0.89±0.07) and 8 Gy radiation (0.37±0.02 (DMEM/F-12) and 0.27±0.01 (RPMI)) conditioned media revealed a significant decrease in cell proliferation (Table 4.31) compared to DMSO taken as 1. Conditioned media obtained from BT-20 cells expose to either ESE-16 or LimPyr1 24 hours prior to radiation reduced cell proliferation significantly (0.34±0.02 and 0.19±0.02, respectively) in untreated BT-20 cells over a period of 14 days compared to DMSO taken as 1 (Figure 4.64). Untreated BT-20 cells propagated in media obtained from ESE-16- or LimPyr1 pre-treated cells significantly decreased cell proliferation compared to cells propagated in conditioned media obtained from samples exposed to the compounds only (0.36±0.02 and 0.22±0.01, respectively) and 8 Gy radiation conditioned media (0.90±0.02 and 0.70±0.08, respectively) taken as 1 (Table 4.31).

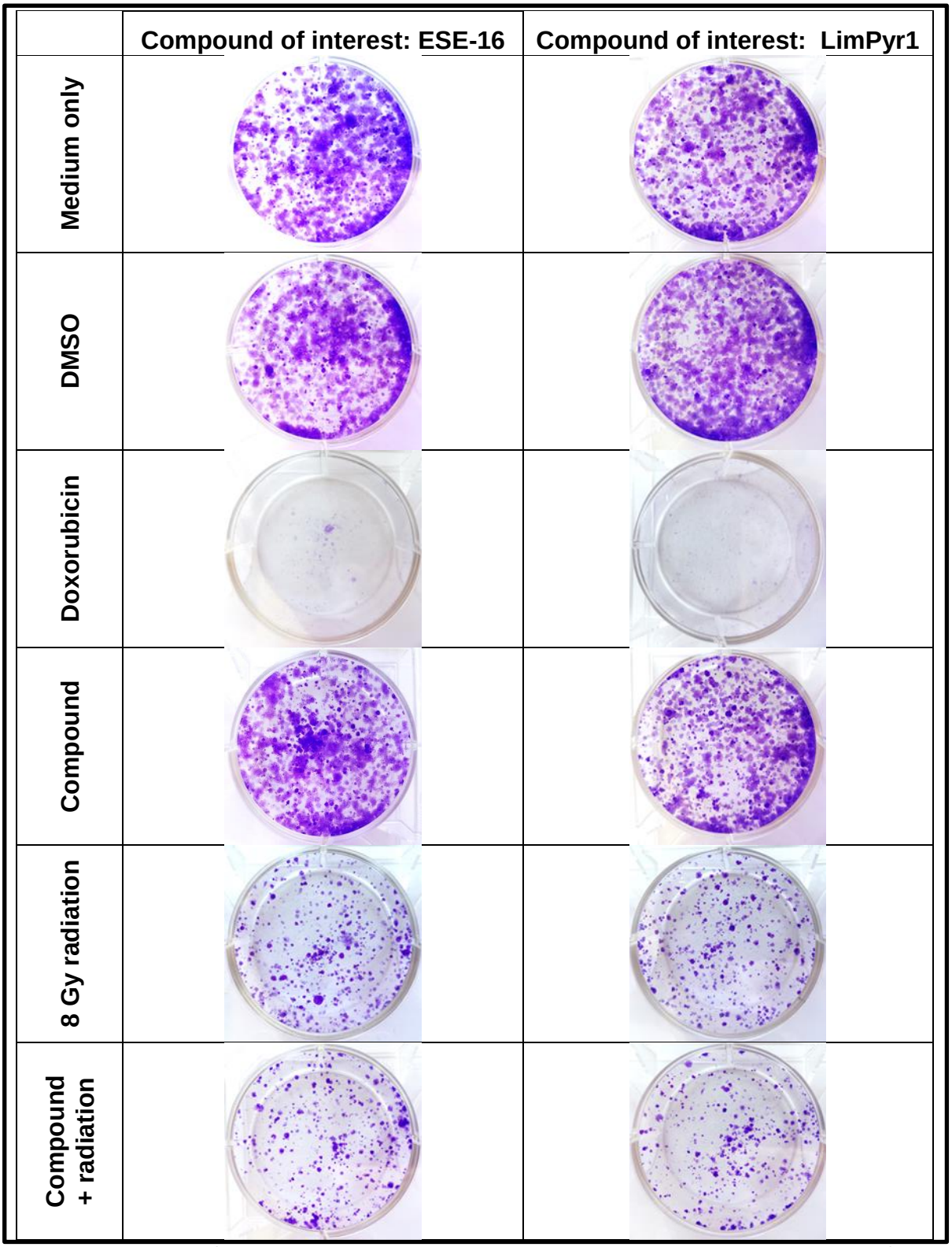

Figure 4.63: Cell proliferation in untreated BT-20 cells propagated in conditioned media for 14 days obtained from cells exposed to various controls and treatment conditions. Conditioned media transferred from BT-20 cells exposed to LimPyr1, 8 Gy radiation and the combination therapies decreased cell proliferation via the bystander effect in untreated BT-20 cells.

Table 4.31: Cellular survival in untreated BT-20 cells exposed to conditioned media obtained from BT-20 cells exposed to various controls and treatment conditions. Data were generated by solubilizing the crystal violet dye and reading the absorbance at 570 nm. Cell survival was calculated relative to the vehicle control and expressed as fold change. The averaged fold change (FC) and standard deviation (SD) of three biological repeats (n=3) are displayed in the table. A two-tailed Student's *t*-test was used to calculate statistically significant differences (*P*-value <0.05) using the vehicle control and individual treatments conditions as baselines.

			Medium only	DMSO	Doxorubicin	Compound	8 Gy radiation	Compound + radiation
BT-20 cells	Compared to DMSO							
	ESE-16	FC± SD	1.00±0.01	1	0.03±0.01	0.95±0.07	0.37±0.02	0.34±0.02
		P-value	0.78	-	**3.28E-08**	0.28	**1.19E-06**	**5.26E-07**
	LimPyr1	FC ± SD	1.01±0.01	1	0.07±0.01	0.89±0.07	0.27±0.01	0.19±0.02
		P-value	0.18	-	**1.33E-08**	**4.81E-02**	**2.78E-09**	**6.10E-07**
	Compared to compound							
	ESE-16	FC ± SD				1		0.36±0.02
		P-value				-		**1.42E-06**
	LimPyr1	FC ± SD				1		0.22±0.01
		P-value				**-**		**2.61E-08**
	Compared to radiation							
	ESE-16	FC ±S D					1	0.90±0.02
		P-value					-	**1.51E-03**
	LimPyr1	FC ± SD					1	0.70±0.08
		P-value					-	**3.21E-03**

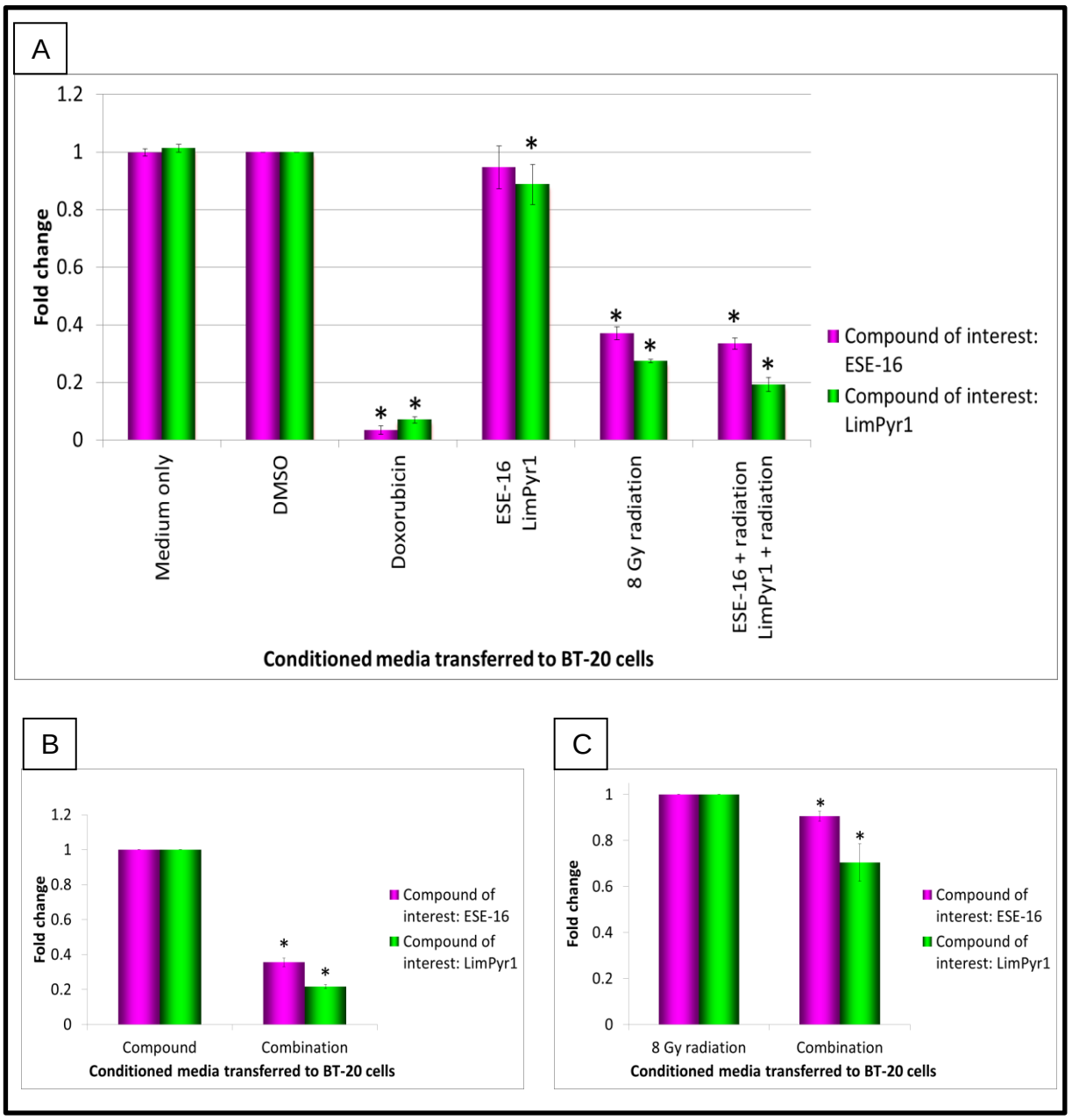

Figure 4.64: Graphical representation of cell survival in untreated BT-20 cells propagated for 14 days in conditioned media obtained from treated cells. No significant difference was observed in untreated BT-20 cells propagated in ESE-16 conditioned media. Untreated BT-20 cells propagated in conditioned media obtained from LimPyr1, 8 Gy radiation and cells pre-treated with either ESE-16 or LimPyr1 24 hours prior to radiation revealed a significant decrease in cell proliferation. Conditioned media transferred from the combination therapies decreased cell proliferation significantly compared to cells propagated in conditioned media obtained from BT-20 cells exposed to the individual treatment conditions. Bars represent the mean fold changes of three biological repeats, with standard deviations represented by T-bars. Statistically significant differences are indicated with * (*P*-value <0.05) when compared to DMSO (A), cells exposed to ESE-16 or LimPyr1 only (B) or 8 Gy radiation only (C).

4.3.4 DNA damage and repair: Quantification of γH2AX and Ku70 proteins via a western blot

The induction of DNA damage (γH2AX) and the recruitment of DNA repair proteins (Ku70) in untreated BT-20 cells propagated in conditioned media obtained from cells exposed to various treatment conditions were quantified 2 hours after transfer via a western blot. This experiment illustrated the intercellular communication between cells directly exposed to radiotherapy (donors) and non-exposed cells which are recipients of possible factors released from the donors.

Untreated BT-20 cells propagated in DMSO conditioned media served as a vehicle control. Conditioned media transferred from BT-20 cells exposed to ESE-16 (1.21±0.11 fold increase) and LimPyr1 (4.05±0.55 fold increase) significantly increased the expression of γH2AX in untreated BT-20 cells, compared to DMSO. Ku70 expression remained unchanged in BT-20 cells propagated in ESE-16 conditioned media, whereas the expression of Ku70 was significantly increased in cells propagated in LimPyr1 conditioned media (1.58±0.04 fold increase) (Figure 4.65). A statistically significant increase in γH2AX (2.08±0.63-(DMEM/F-12) and 4.18±0.55 fold increase (RPMI)) and Ku70 (1.21±0.03- (DMEM/F-12) and 1.89±0.41 fold increase (RPMI)) expression were observed in untreated BT-20 cells propagated in conditioned media obtained from samples exposed to 8 Gy radiation, compared to the vehicle control (Table 4.32). Untreated B-20 cells propagated in conditioned media obtained from ESE-16- or LimPyr1 pre-treated cells revealed a statistically significant increase in γH2AX and Ku70 expression when compared to cells propagated in DMSO- (2.28±0.53- and 2.62±0.24 fold increase, 5.57±0.93- and 1.84±0.30 fold increase), ESE-16- (1.67±0.20- and 2.42±0.67 fold increase), LimPyr1- (1.37±0.08- and 1.49±0.11 fold increase) and 8 Gy radiation conditioned media (1.34±0.21- and 2.10±0.18 fold increase, 1.16±0.03- and 1.13±0.03 fold increase), respectively (Figure 4.66).

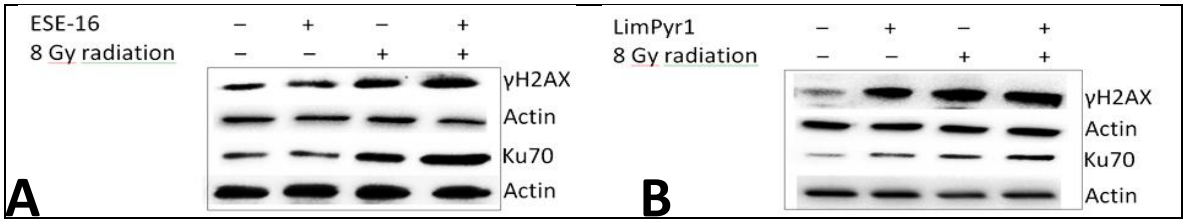

Figure 4.65: Western blots visualizing γH2AX and Ku70 protein expressions in untreated BT-20 cells propagated in conditioned media obtained from cells exposed to various treatment conditions for 2 hours. Untreated BT-20 cells propagated in conditioned media obtained from cells exposed to ESE-16 (A) and LimPyr1 (B) 24 hours prior to irradiation increased the expression of DNA damage and repair proteins compared to the individual treatments.

Table 4.32: Expression of DNA damage (γH2AX) and DNA repair (Ku70) proteins in untreated BT-20 via the bystander effect 2 hours post transfer. Proteins were visualized by ChemiDoc MP (Bio-rad, CA, USA) and analyzed using Image Lab Software Version 5.2.1 (Bio-rad, CA, USA). Data were analyzed using the ANOVA-single factor model and a two-tailed Student's *t*-test. The fold change (FC) and standard deviation (SD) of three biological repeats are displayed in the table. Statistically significant differences (*P*-value <0.05) were calculated using the vehicle control as a baseline. *P*-values were also calculated for the combination treatment conditions when compared to the individual treatments.

			DMSO	Compound	8 Gy radiation	Compound + radiation
Compound of interest: ESE-16	Compared to DMSO					
	γH2AX	FC± SD	1	1.21±0.11	2.08±0.63	2.28±0.53
		P-value	-	**0.04**	**4.70E-02**	**1.38E-02**
	Ku70	FC ± SD	1	1.00±0.12	1.21±0.03	2.62±0.24
		P-value	-	0.95	**9.42E-04**	**3.00E-04**
	Compared to compound					
	γH2AX	FC ± SD		1		1.67±0.20
		P-value		-		**7.41E-03**
	Ku70	FC ± SD		1		2.42±0.67
		P-value		-		**0.02**
	Compared to radiation					
	γH2AX	FC ±S D			1	1.34±0.21
		P-value			-	**4.62E-02**
	Ku70	FC ± SD			1	2.10±0.18
		P-value			-	**1.35E-03**
Compound of interest: LimPyr1	Compared to DMSO					
	γH2AX	FC± SD	1	4.05±0.55	4.18±0.55	5.57±0.93
		P-value	-	**6.40E-04**	**5.68E-04**	**1.03E-03**
	Ku70	FC ± SD	1	1.58±0.04	1.89±0.41	1.84±0.30
		P-value	-	**1.31E-04**	**1.98E-02**	**7.92E-03**
	Compared to compound					
	γH2AX	FC ± SD		1		1.37±0.08
		P-value		-		**1.02E-03**
	Ku70	FC ± SD		1		1.49±0.11
		P-value		-		**3.94E-03**
	Compared to radiation					
	γH2AX	FC ±S D			1	1.16±0.03
		P-value			-	**2.17E-03**
	Ku70	FC ± SD			1	1.13±0.03
		P-value			-	**2.39E-03**

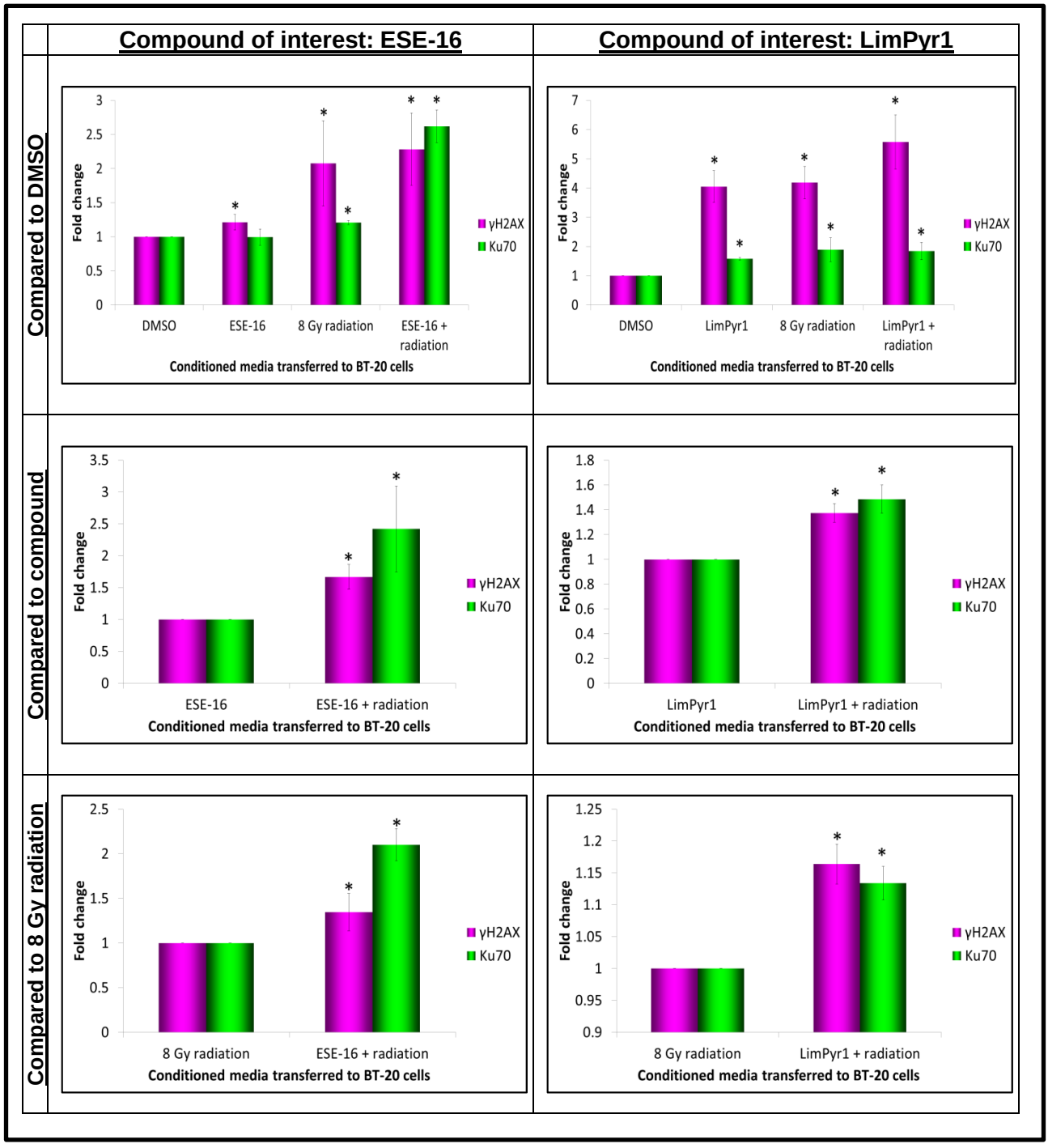

Figure 4.66: Graphical representation of γH2AX and Ku70 expression in untreated BT-20 cells exposed for 2 hours to conditioned media transferred from cells exposed to various treatment conditions. Untreated BT-20 cells propagated in conditioned media obtained from cells exposed to LimPyr1, 8 Gy radiation and the combination treatments displayed a significant increase in γH2AX and Ku70 expression. The conditioned media obtained from the combination treatment conditions significantly increased the expression of γH2AX and Ku70 in untreated BT-20 cells compared to the individual treatments. Bars indicate the average of three biological repeats, with standard deviations represented by T-bars. Statistically significant differences are indicated with * (*P*-value <0.05) when compared to DMSO, cells exposed to the compounds or radiation only.

4.4 Evaluation of radiation-induced resistance due to dose fractionation in irradiated cells

4.4.1 Reactive oxygen species production: Flow cytometric quantification of superoxide employing hydroethidine

Reactive oxygen species production was quantified in BT-20 cells exposed to microtubule regulating agents, single dose and fractionated radiotherapy. Exposure of cancer cells to low radiation doses over a period of time may lead to the development of radioresistance. The aim of this study was to identify a potential anti-cancer compound that will decrease the development of radiation resistance in triple negative breast cancer cells.

Various controls were included in the study. BT-20 cells exposed to DMSO served as a vehicle control while rotenone exposure served as a positive control for ROS production. Compared to cells propagated in medium only the vehicle control displayed no significant increase in superoxide production. Rotenone significantly induced ROS production 24 hours after exposure compared to the vehicle control (Table 4.33).

Superoxide production was significantly increased in BT-20 cells exposed to ESE-16 (1.05±0.02 fold increase), a single radiation dose of 8 Gy (1.25±0.11 fold increase) and fractionated radiotherapy (2 Gy for 4 consecutive days) (1.20±0.15 fold increase) compared to DMSO (Figure 4.67). BT-20 cells exposed to ESE-16 prior to 8 Gy radiation displayed a significant increase (1.39±0.06 fold increase) in ROS production compared to the vehicle control. Additionally, cells exposed to the single dose combination therapy produced significantly more superoxide compared to cells exposed to ESE-16 (1.35±0.08 fold increase) and 8 Gy radiation (1.12±0.05 fold increase) only. Cells exposed to ESE-16 prior to fractionated radiotherapy revealed a significant increase in ROS generation compared to the vehicle control (1.29±0.10 fold increase), cells exposed to ESE-16 (1.25±0.13 fold increase) and cells exposed to fractionated radiotherapy (1.10±0.08 fold increase) (Figure 4.68).

Breast cancer cells exposed to fractionate radiotherapy as well as the combination fractionated therapy (ESE-16 prior to fractionated radiotherapy) produced significantly lower levels of superoxide compared to cells exposed to a single radiation dose (8 Gy) (0.93±0.05) and cells exposed to the single dose combination therapy (0.92±0.04), taken as 1 (Table 4.33). This illustrated the inability of ESE-16 to prevent the development of radiation resistance in BT-20 cells.

Compared to the vehicle control a significant fold increase in ROS production of 1.40±0.27, 1.29±0.17, 1.19±0.06, 1.84±0.15 and 2.20±0.42 was observed in BT-20 cells exposed to LimPyr1, 8 Gy radiation (single dose), fractionated radiation doses, pre-treated BT-20 cells exposed to 8 Gy radiation and BT-20 cells pre-treated prior to fractionated radiotherapy (Table 4.33), respectively. Compared to LimPyr1 treatment alone the combination therapy was more successful in inducing ROS production following exposure to a single radiation dose (1.38±0.12 fold increase) or fractionated radiation doses (1.73±0.49 fold increase). By pre-treating BT-20 cells with LimPyr1 prior to single dose (1.38±0.12 fold increase)- or fractionated (1.73±0.49 fold increase) radiotherapy resulted in increased superoxide production compared to cells exposed to the unsensitized equivalents (Figure 4.68). A decrease in superoxide was observed in cells exposed to fractionated radiotherapy compared to the single dose samples (0.84±0.09) taken as 1. This indicated a decrease in apoptosis activation and possible development of radiation resistance. The latter was prevented with the addition of LimPyr1 as observed by the increased ROS production in BT-20 cells exposed to LimPyr1 prior to fractionated radiotherapy compared to the single dose combination therapy samples (1.24±0.16 fold increase) (Figure 4.67).

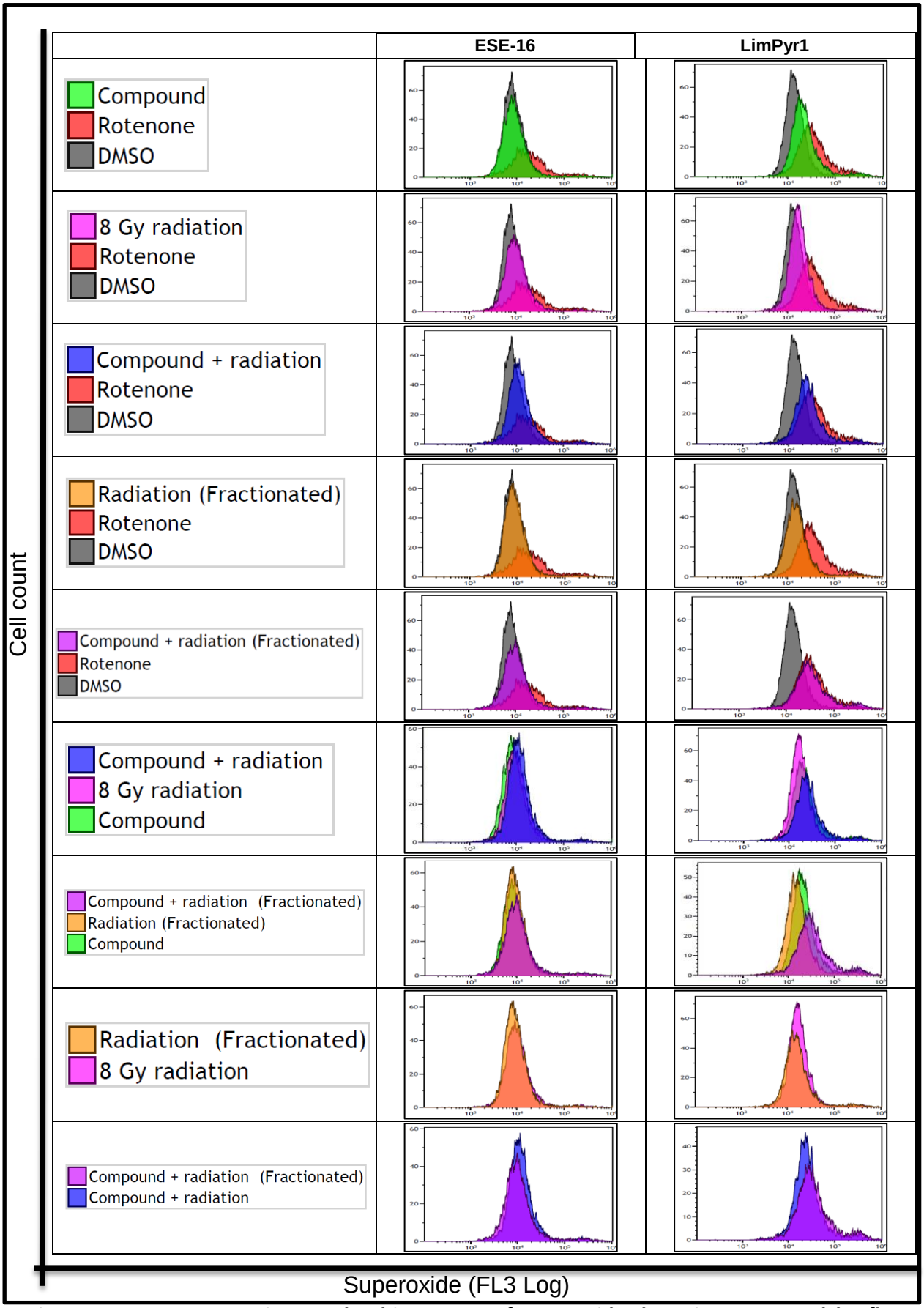

Figure 4.67: Representative overlay histograms of superoxide detection measured by flow cytometry in BT-20 cells exposed to ESE-16 or LimPyr1, single dose and fractionated

radiotherapy. Histograms were obtained by plotting the cell count against the generated superoxide (FL3 Log) using data obtained from flow cytometry. BT-20 cells exposed to the various treatment condition display a right sift, indicating increased superoxide production. Decreased ROS quantification was observed in cells exposed to fractionated radiotherapy compared to cells exposed to single dose radiation, indicating the induction of radiation-induced resistance due to dose fractionation. BT-20 cells pre-treated with ESE-16 prior to fractionated radiotherapy did not succeed in preventing the induction of radiation-induced resistance, however the addition of LimPry1 prior to fractionate radiotherapy increased superoxide production compared to pre-treated cells exposed to a single radiation dose.

Table 4.33: Superoxide detection by means of flow cytometry employing hydroethidine in BT-20 cells exposed to single dose and fractionated radiotherapy. Data were analyzed using an ANOVA-single factor model from data points generated using Kaluza Analysis version 1.5 (FL, USA). The averaged fold change (FC) and standard deviations (SD) of three biological repeats are displayed. Using DMSO as baseline statistically significant differences (*P*-value <0.05) were calculated using a two-tailed Student's *t*-test. Additionally, *P*-values were also calculated for cells exposed to the combination treatments (single- or fractionated radiation dose exposure) when compared to cells exposed to the individual treatment conditions.

			Medium only	DMSO	Rotenone	Compound	8 Gy radiation (Single dose)	8 Gy radiation (Fractionated)	Compound + radiation (Single dose)	Compound + radiation (Fractionated)
BT-20 cells	**Compared to DMSO**									
	ESE-16	FC± SD	1.04±0.13	1	1.82±0.40	1.05±0.02	1.25±0.11	1.20±0.15	1.39±0.06	1.29±0.10
		P-value	0.55	-	**6.09E-03**	**5.73E-03**	**3.65E-03**	**0.04**	**1.17E-05**	**1.23E-03**
	LimPyr1	FC ± SD	1.05±0.07	1	1.84±0.50	1.40±0.27	1.29±0.17	1.19±0.06	1.84±0.15	2.20±0.42
		P-value	0.21	-	**1.80E-02**	**0.02**	**1.43E-02**	**1.04E-03**	**7.94E-05**	**2.07E-03**
	Compared to compound									
	ESE-16	FC± SD				1			1.35±0.08	1.25±0.13
		P-value				-			**1.48E-04**	**8.22E-03**
	LimPyr1	FC± SD				1			1.20±0.06	1.38±0.21
		P-value				-			**6.91E-04**	**1.07E-02**
	Compared to radiation									
	ESE-16	FC± SD					1		1.12±0.05	
		P-value					-		**4.80E-03**	
		FC± SD						1		1.10±0.08
		P-value						-		**4.74E-02**
	LimPyr1	FC± SD					1		1.38±0.12	
		P-value					-		**1.08E-03**	
		FC± SD						1		1.73±0.49
		P-value						-		**0.02**
	Fractionated dose compared to single dose									
	ESE-16	FC± SD					1	0.93±0.05		
		P-value					-	**4.51E-02**		
		FC± SD							1	0.92±0.04
		P-value							-	**9.50E-03**
	LimPyr1	FC± SD					1	0.84±0.09		
		P-value					-	**1.11E-02**		
		FC± SD							1	1.24±0.16
		P-value							-	**0.02**

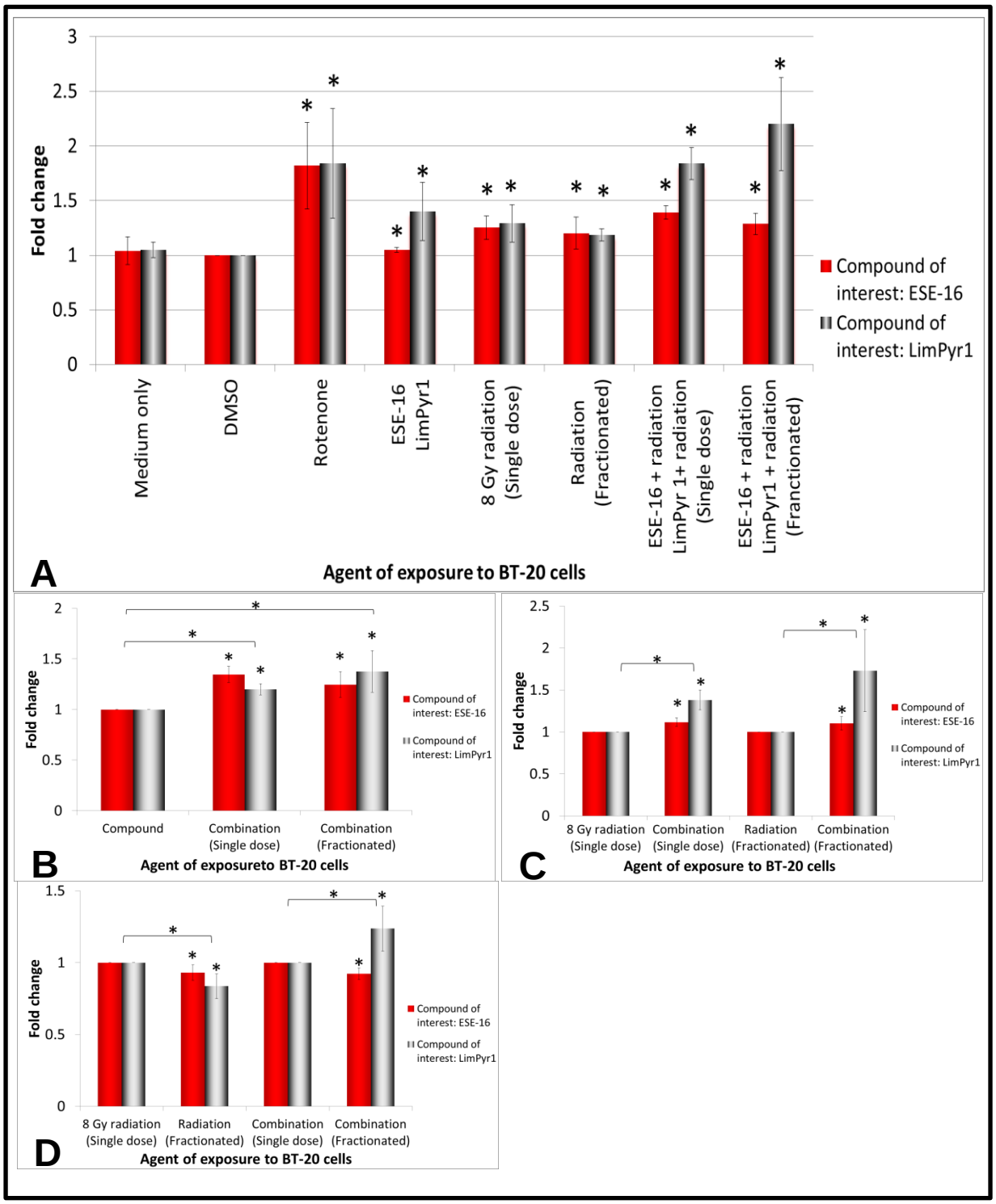

Figure 4.68: Graphical representation of superoxide quantification in BT-20 cells exposed to single dose or fractionated radiotherapy. BT-20 cells exposed to microtubule regulating agents, radiotherapy (single dose and fractionated doses) and a combination therapy revealed a significant increase in superoxide quantification compared to the vehicle control. BT-20 cells exposed to the combination therapy (single dose or fractionated radiation exposure) were more sufficient in inducing superoxide production compared to the individual treatments. Fractionated radiotherapy produced less superoxide compared to the samples exposed to the

single dose of 8 Gy. This indicated the induction of radiation resistance, resulting in a decreased apoptotic signal. The addition of LimPyr1 prior to fractionated radiotherapy prevented the induction of radiation-induced resistance, however pre-treatment with ESE-16 failed to produce similar results. The bar graph illustrates the average fold change of three biological repeats. Standard deviations are represented by T-bars. Statistically significant differences are indicated with * (*P*-value <0.05) when compared to DMSO (A), cells exposed to ESE-16 or LimPyr1 only (B) or radiation only (C). Statistically significant differences were also calculated for cells exposed to the fractionated combination therapy compared to pre-treated cells exposed to a single radiation dose (D).

4.4.2 Mitochondrial transmembrane potential: Flow cytometric quantification of MitoCapture™

Changes in the mitochondrial transmembrane potential were quantified in BT-20 cells exposed to fractionated radiotherapy. The aim of this experiment was to evaluate whether exposure to fractionated radiotherapy will result in the development of radioresistance by decreasing the induction of apoptosis, and whether the addition of the compounds will prevent the latter.

BT-20 cells were propagated in medium as a negative control or exposed to DMSO as a vehicle control. No significant difference in the mitochondrial transmembrane potential was quantified when the negative control was compared to the vehicle control. As a positive apoptotic control cells were exposed to vinblastine for 24 hours. A statistically significant increase in the permeability of the mitochondrial transmembrane was displayed in cells exposed to the positive control (Table 4.34).

BT-20 cells exposed to ESE-16 for 72 hours revealed a significant increase in MitoCapture™ when compared to the vehicle control (1.12±0.08 fold increase) (Figure 4.69). MitoCapture™ was significantly increased in cells exposed to 8 Gy radiation (one dose) (1.38±0.13 fold increase), fractionated radiotherapy (total exposure of 8 Gy over a period of 4 days) (1.31±0.14 fold increase), cells pre-treated with ESE-16 prior to 8 Gy radiation (single dose)

(1.63±0.18 fold increase) and cells exposed to ESE-16 prior to fractionated radiotherapy (1.39±0.22 fold increase). Compared to cells exposed to ESE-16 only pre-treated BT-20 cells displayed a significant 1.51±0.25- and 1.27±0.17 fold increase in MitoCapture™ following exposure to a single radiation dose and fractionated radiotherapy, respectively (Figure 4.70). Compared to cells exposed to a single dose of 8 Gy radiation pre-treated cells displayed a significant increase in the permeability of the mitochondrial transmembrane (1.18±0.11 fold increase). BT-20 cells exposed to ESE-16 prior to fractionated radiotherapy also displayed increased MitoCapture™ quantification (1.09±0.04 fold increase) compared to cells exposed to fractionate radiotherapy (Table 4.34). The development of radioresistance was observed when cells exposed to fractionated radiotherapy displayed as significant decrease in MitoCapture™ detection (0.94±0.02) compared to cells exposed to a single radiation dose taken as 1. The latter was not prevented with the addition of ESE-16, as a decrease in MitoCapture™ (0.85±0.11) was also observed in cells exposed to the fractionated combination therapy when compared to the single dose combination therapy taken as 1 (Figure 4.70).

A statistically significant fold increase of 1.64±0.26, 1.47±0.17 and 1.16±0.01 in MitoCapture™ quantification was observed in BT-20 cells exposed to LimPyr1, a single dose of 8 Gy radiation and fractionated radiation doses, compared to the vehicle control (Table 4.34). BT-20 cells exposed to LimPyr1 prior to single dose radiotherapy revealed a significant increase in the permeability of the mitochondrial transmembrane when compared to the vehicle control (2.06±0.44 fold increase), cells exposed to LimPyr1 (1.25±0.13 fold increase) and BT-20 cells exposed to 8 Gy radiation (single dose) (1.19±0.09 fold increase). Additionally, BT-20 cells exposed to the fractionated combination therapy also displayed a significant fold increase of 2.60±0.75, 1.57±0.22 and 2.04±0.35 in MitoCapture™ when compared to the vehicle control, cells exposed to LimPyr1 or fractionated radiotherapy, respectively (Figure 4.70). BT-20 cells exposed to fractionated radiotherapy revealed a significant decrease in MitoCapture™ detection compared to cells exposed to the single radiation dose (Figure 4.69). This indicated that radiation-induced resistance was initiated in cells exposed to the fractionated radiotherapy, decreasing the induction of apoptosis. This

development of radiation resistance was prevented with the addition of LimPyr1, where cells exposed to LimPyr1 prior to fractionated radiotherapy displayed a significant 1.25±0.13 fold increase in MitoCapture™ detention compared too cells exposed LimPyr1 prior to a single radiation dose of 8 Gy (Table 4.34).

Table 4.34: MitoCapture™ quantification in breast cancer cells exposed to single dose and fractionated radiotherapy. Data points were generated using Kaluza Analysis version 1.5 (FL, USA) followed by analysis using an ANOVA-single factor model. The averaged fold change (FC) and standard deviations (SD) of three biological repeats are displayed. A two-tailed Student's *t*-test was used to calculate statistically significant differences (*P*-value <0.05) using cells exposed to DMSO as a baseline. *P*-values were also calculated for cells exposed to the combination treatment condition (single- or fractionated radiation dose exposure) when compared to cells exposed to the individual treatment conditions.

			Medium only	DMSO	Vinblastine	Compound	8 Gy radiation (Single dose)	8 Gy radiation (Fractionated)	Compound + radiation (Single dose)	Compound + radiation (Fractionated)
BT-20 cells	**Compared to DMSO**									
	ESE-16	FC± SD	0.94±0.09	1	2.27±0.70	1.12±0.08	1.38±0.13	1.31±0.14	1.63±0.18	1.39±0.22
		P-value	0.22	-	**1.29E-02**	**0.02**	**1.30E-03**	**4.55E-03**	**4.25E-04**	**1.26E-02**
	LimPyr1	FC ± SD	1.17±0.17	1	2.63±0.69	1.64±0.26	1.47±0.17	1.16±0.01	2.06±0.44	2.60±0.75
		P-value	0.16	-	**0.02**	**1.23E-02**	**1.26E-02**	**3.03E-05**	**1.41E-02**	**0.02**
	Compared to compound									
	ESE-16	FC± SD				1			1.51±0.25	1.27±0.17
		P-value				-			**6.40E-03**	**1.92E-02**
	LimPyr1	FC± SD				1			1.25±0.13	1.57±0.22
		P-value				-			**0.03**	**1.17E-02**
	Compared to radiation									
	ESE-16	FC± SD					1		1.18±0.11	
		P-value					-		**1.77E-02**	
		FC± SD						1		1.09±0.04
		P-value						-		**4.74E-03**
	LimPyr1	FC± SD					1		1.19±0.09	
		P-value					-		**0.02**	
		FC± SD						1		2.04±0.35
		P-value						-		**6.62E-03**
	Fractionated dose compared to single dose									
	ESE-16	FC± SD					1	0.94±0.02		
		P-value					-	**3.58E-04**		
		FC± SD							1	0.85±0.11
		P-value							-	**0.04**
	LimPyr1	FC± SD					1	0.74±0.11		
		P-value					-	**1.46E-02**		
		FC± SD							1	1.25±0.13
		P-value							-	**0.03**

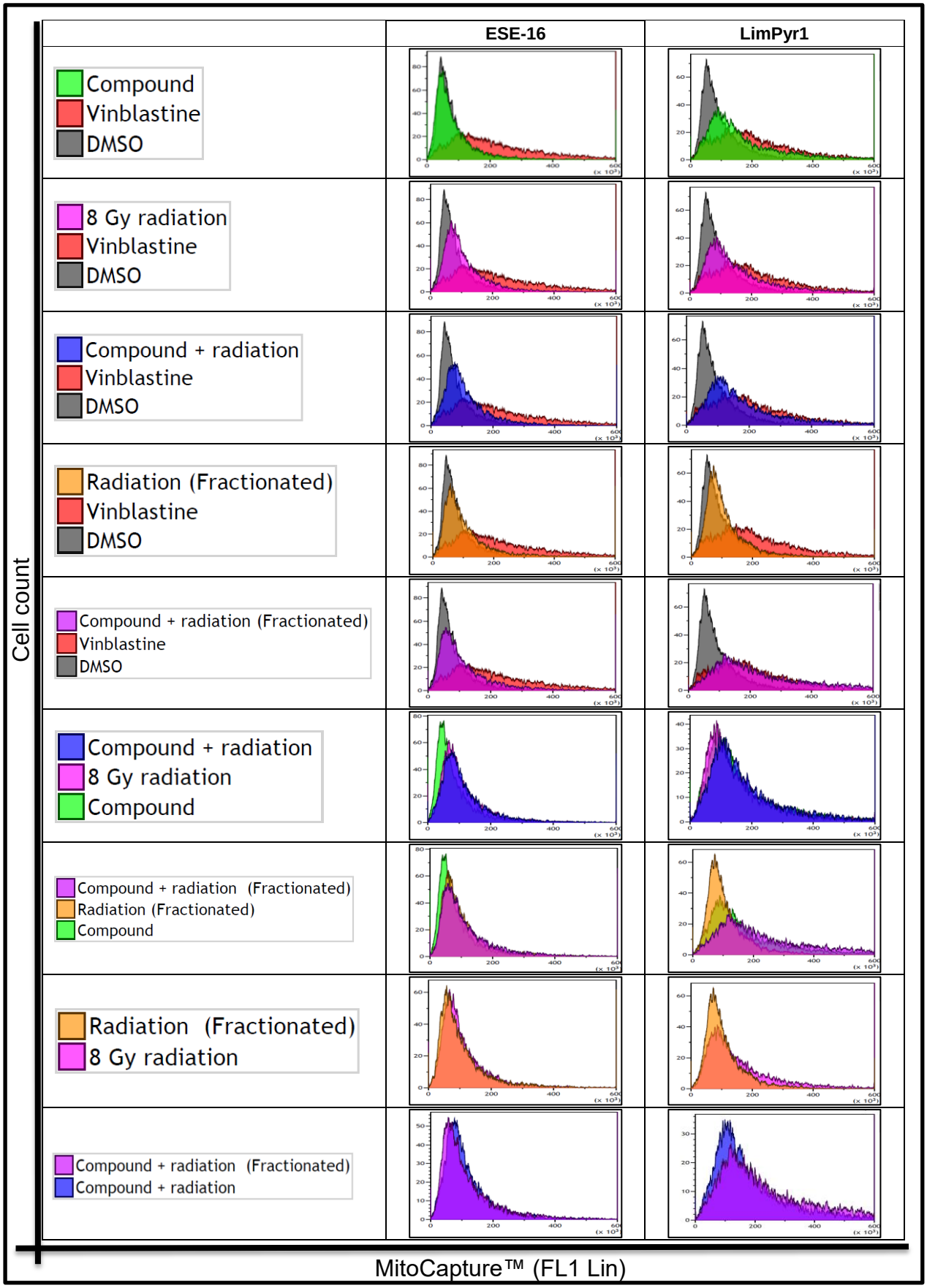

Figure 4.69: Representative overlay histograms of MitoCapture™ in BT-20 cells exposed to microtubule regulating agents, single dose and fractionated radiotherapy. Histograms were

obtained by plotting the cell count against MitoCapture™ quantification (FL1 Lin). A right shift is observed in MitoCapture™ in BT-20 cells exposed to single dose or fractionated radiotherapy. Development of radioresistance is illustrated in the left shift of histograms obtained from cells exposed to fractionated radiotherapy compared to cells exposed to a single dose of 8 Gy radiation. The addition of ESE-16 prior to radiation did not prevent the latter, however the addition of LimPyr1 prior to fractionated radiotherapy display a right shift (increase in MitoCapture™) compared to the single dose combination therapy.

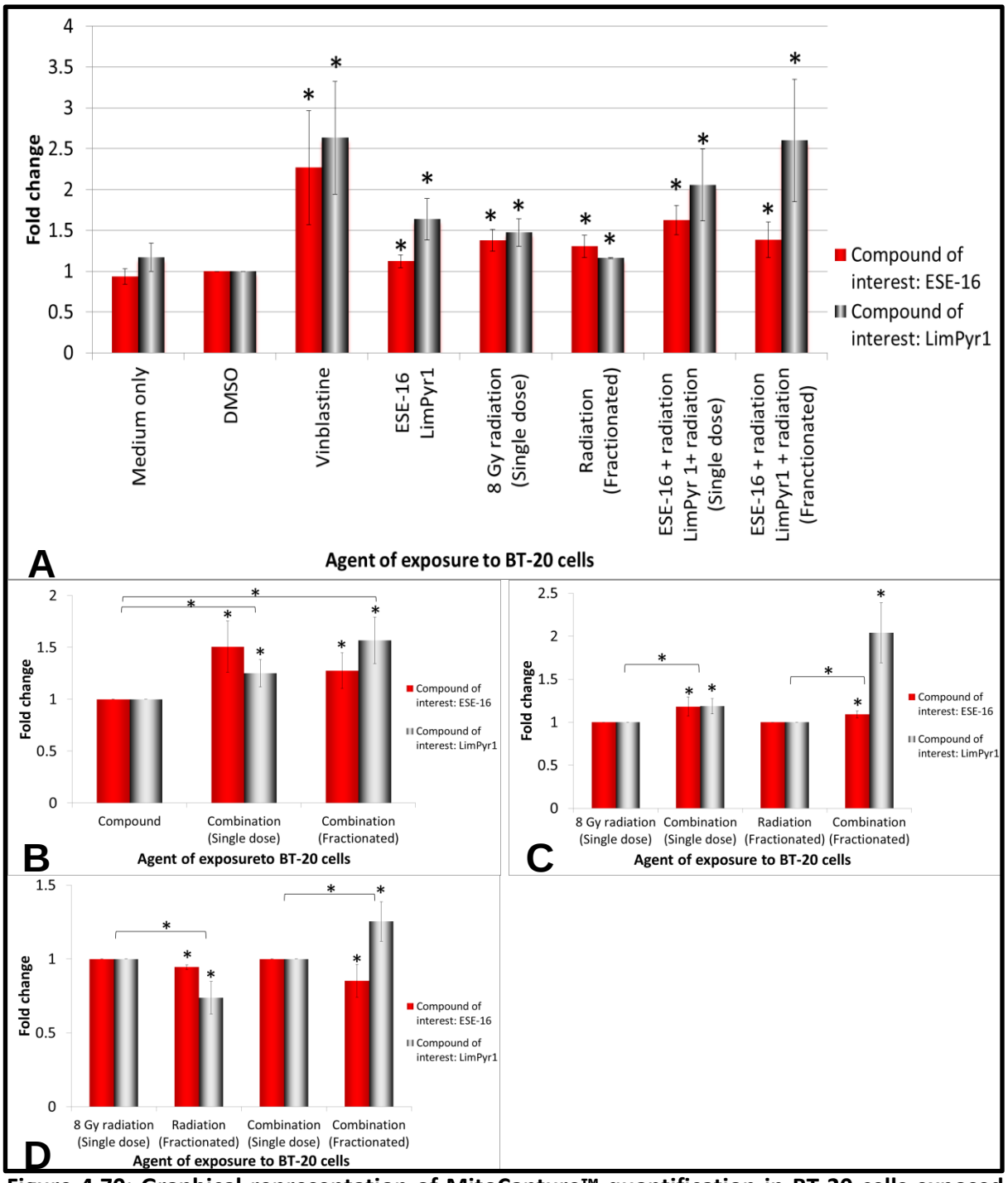

Figure 4.70: Graphical representation of MitoCapture™ quantification in BT-20 cells exposed to microtubule regulating agents, single dose or fractionated radiotherapy. BT-20 cells

exposed to ESE-16 and LimPyr1, respectively, revealed a significant increase in MitoCapture™. Single dose and fractionated radiotherapy also increased the permeability of the mitochondrial transmembrane, as did the combination therapies. MitoCapture™ was significantly increased in BT-20 cells exposed to the combination treatment conditions compared to the individual treatments. The permeability of the mitochondrial transmembrane was significantly decreased in cells exposed to fractionated radiotherapy compared to cells exposed to the single dose of 8 Gy radiation. This indicated the induction of radiation resistance due to dose fractionation, resulting in a decreased apoptotic signal. The latter was prevented with the addition of LimPyr1 prior to radiation, however ESE-16 refrain from preventing the development of radiation resistance. The bar graph illustrates the mean fold increase of three biological repeats, with standard deviations represented by T-bars. Statistically significant differences are indicated with * (*P*-value <0.05) when compared to DMSO (A), cells exposed to ESE-16 or LimPyr1 only (B) or 8 Gy radiation only (C), as well as cells exposed to the compounds prior to fractionated radiotherapy compared to cells exposed to the compounds prior to single radiation dose delivery (D).

5. Discussion

"If I have seen further than others, it is by standing upon the shoulders of giants."

~Sir Isaac Newton~

"While there are several chronic diseases more destructive to life than cancer, none is more feared"- Charles Mayo

Breast cancer is one of the most frequently diagnosed cancer types among women worldwide (498). Treatment regimens for breast cancer usually include chemotherapy and radiation therapy (7). However, with the alarming increase of breast cancer diagnosis each year a more cost and clinically effective method for treating these patients is imperative. Additionally, the development of chemo- and radiation resistance among South African and French patients remains problematic in both countries. Among the breast cancers, triple receptor-negative breast cancers, which do not express hormonal receptors, are aggressive and are resistant to treatments (499). Ideally, a pharmaceutical agent which selectively sensitizes cancer cells to radiation would allow administration of lower doses of each treatment modality, yielding synergistic anti-cancer benefits and lower metastasis occurrence, in addition to decreasing the side-effect profiles and recovery time of patients. This *in vitro* study aimed to identify and evaluate the potential of novel compounds to radiosensitize breast cancer cells with various receptor statuses.

Biological material is composed of atoms joined by bonds to form molecules. Exposure of biological material to ionizing radiation results in displacement of these atoms, breaking the bonds joining the electrons (500). This process induces damage to various parts of the cell,

but it is the damage to the cellular DNA that is very important (500). Upon damage the enzyme responsible for DNA replication, DNA polymerase, becomes inactive. Consequently the DNA replication fork is stalled, preventing DNA replication (501). The cell has various DNA repair mechanisms. However, when the damage obtained by ionizing radiation is too severe the repair mechanisms are rendered ineffective (502). This causes the replication fork to collapse. In order to prevent this damaged DNA being passed on to the next generation of cells, programmed cell death is induced (503).

Radiation therapy is an effective treatment modality for cancer. Radiation can be used as a single agent or in combination with chemotherapy or surgery. Radiation may be prescribed for patients prior to surgery in order to decrease the tumor size (502). Radiation therapy can also be administered after the surgical procedure. This post-surgical radiation regime aims to eliminate any malignant cells which were not removed during surgery (502). Theoretically, radiation is a very effective treatment option for cancer, however there are some challenges in a clinical setting. The main challenge of radiotherapy is to maximize the radiation dose delivered to the malignant cells while the dose received by the normal cells is kept to a minimum (504). As cancer cells are surrounded by normal cells, best practices on dose- and method delivery of the radiotherapy remains a research question in order to minimize these side-effects. DNA damage is obtained by the malignant cells as well as the surrounding non-cancerous cells during radiotherapy. Rapidly dividing cells, such as cancer cells, are more susceptible to the effects of radiation due to their decreased capability to repair the damaged DNA (501,505). Normal cells can, to a certain extent, repair the damage to regain normal function after radiotherapy, keeping radiotherapy a viable treatment option (505).

Different types of radiation are used in the treatment of cancer. The extent of the damage obtained by the genome is not the same with equivalent physical doses delivered by different radiation types (506). The relative biological effectiveness is a scaling factor used in the radiation biology field in order to account for these differences (506). The relative

biological effectiveness is defined as “the ratio of the doses required by two radiations to cause the same level of effect” and depends on the radiation dose, fractionation rate, linear energy transfer and biological endpoint which is influenced by the cell’s sensitivity to radiation (507,508). The therapeutic effect of radiation therapy largely depends on the induction of double strand breaks and the subsequent induction of cell death (509). The ATM-p53-Bax-cytochrome *c* cascade pathway is activated in radiation-exposed cells resulting in mitotic catastrophe and apoptotic cell death (163,510,511). Furthermore, cells may enter a state of terminal proliferation arrest. These cells are said to be in senescence and will be rendered apoptotic if the DNA damage is too severe to be repaired (512).

Radiosensitization is the process through which the lethal effect of radiation is increased by physical, chemical or pharmacological interventions (513). The aim of radiosensitizers is to increase the sensitivity of tumor cells to radiation. However, radiosensitization is only beneficial in a clinical setting if a differential effect between malignant- and non-malignant cells can be demonstrated.

Numerous approaches have been investigated to increase the efficacy of radiation therapy. Increased sensitivity has been achieved by halogenated pyrimidine treatment prior to radiation. This approach utilizes halogenated pyrimidines such as 5-bromodeoxyuridine to increase the DNA damage induced by radiation (513,514). This is achieved by exploiting the mechanism of action of these compounds which weakens the DNA molecule, thus making the genome more vulnerable to radiation damage (515). Another approach to radiosensitize cells by targeting the cellular DNA is to inhibit the repair mechanisms involved in DNA damage repair. Platinum chemotherapeutics, such as cisplastin, have the ability to crosslink purine bases in the DNA strands. This interferes with the efficiency of DNA repair mechanisms, thereby contributing to increased DNA damage (513,514).

Radiosensitization can also be achieved by using biological response modifiers such as interferons and tyrosine kinase inhibitors (513,516). As these modifiers regulate various biological and biochemical processes such as the cell cycle, metabolism, stress response, the cytokine network, DNA repair, and programmed cell death, their mechanism of action may be exploited to increase cellular radiosensitivity. Overexpression of epidermal growth factor receptor (EGFR) has been linked to radiation resistance. Thus, inhibition of the receptor as well as its associated ligand, epidermal growth factor (EGF), significantly increases the sensitivity of cells to radiation (513,516). Alternatively, cytokines can be used to alter cellular radiosensitivity. The aforementioned signaling molecules are responsible for a number of cell fate decisions following radiation damage such as DNA repair activation, cellular proliferation and differentiation, as well as cell death. The mechanism of action of these different signaling molecules can be exploited to increase radiosensitivity (513,516). Additionally, bioreducible cytokines such as mitomycin C and tirapazaine are activated to form cytokines and are toxic to hypoxic cells (513,514). Since hypoxia confers radioresistance the aforementioned molecules are used to eliminate the hypoxic cells and increase the radiosensitivity of the tumors. Furthermore, reoxygenation can be employed to increase oxygen levels within the tumor micromilieu, counteracting hypoxia and in turn radiosensitize the tumor cells (513,514).

The biological mechanisms involving the enzyme COX-2 has been extensively studied as a potential mechanism for radiosensitization (513). Studies have highlighted the involvement of COX-2 in cell proliferation in breast-, prostrate-, colorectal- and hematological malignancies (517-519). These findings prompted the investigation of COX-2 inhibitors as potential radiosensitizing agents. Human cervical carcinoma cells (HeLa) as well as human prostate carcinoma (PC3) displayed an increase of radiosensitivity following siRNA silencing of COX-2 (520). The current study was based on published data characterizing taxanes and other microtubule targeting agents as radiosensitizing agents (513,514). By inducing a metaphase block taxanes, such as paclitaxel, expose the cellular DNA to the damaging effects of ionizing radiation. This resulted in the G_2/M phase being labeled as 'the most radiosensitive phase of the cell cycle'. Due to the fact that rapidly dividing malignant cells

are susceptible to the effects of microtubule targeting agents, they may provide a potential mechanism to promote radiosensitization within the clinical setting (414).

Cancer treatment relies on a multidisciplinary treatment approach for an optimal outcome. Although surgery and radiotherapy remain the treatments of choice for the local control of cancer, treatment and prevention of metastatic cancers requires systemic therapy. Moreover, systemic therapy can be administered in combination with the aforementioned treatment modalities as part of a primary treatment regime with curative intent. There are many classes of systemic drugs available for the treatment of cancer. However, for the past three decades research has been shifted to the development and implementation of systemic drugs with improved dose-responses (521). As a result several new approaches have been investigated and resulted in new therapeutic agents. A group of drugs that affect the cellular microtubule cytoskeleton by associating with α- or β tubulin dimers (522,523) has been integrated into the treatment of ovarian-, breast-, lung-, lymphoid derived- and head- and neck cancers (524,525). These microtubule targeting agents can either be classified as microtubule stabilizing agents (such as taxanes and epothiliones) or microtubule destabilizing agents (such as colchicine and vinblastine) (283,526,527). Once cells enter metaphase in the presence of a microtubule targeting agent the SAC becomes activated, halting the transition to anaphase (73,528). This is due to the inability of chromosomes to properly attach to the spindle microtubules. Thus, as long as the microtubules are defunct the SAC activity will be elevated, resulting in a prolonged metaphase block and the subsequent induction of apoptosis (526).

2-ME is a microtubule targeting agent naturally synthesized by the body via estrogen methylation facilitated by COMT activity (529). This microtubule targeting agent exerts its effect by inducing an extended metaphase block by binding to the colchicine binding sites on tubulin with an inhibitor constant (Ki)-value of 22 ± 2 μM (270,273). This leads to the cytotoxic induction of programmed cell death type 1, a mechanism which is retained in PgP-overexpressing multiple drug resistant cell lines (286,290,530). The anti-proliferative effect

of 2-ME has been established *in vitro* in prostate- (276,277), lung- (302-304), cervical- (275), breast- (278-280), ovarian- (274,301) and esophageal cancers (300). A study conducted by Kuo *et al.* highlighted another important property of 2-ME (531). Apoptosis was induced in urothelial carcinoma cells *in vitro* 24 hours after exposure to 2 µM 2-ME. However, cell death was not induced in non-tumorigenic transformed urothelial cells under the same conditions. These results suggested that the anti-proliferative effect of 2-ME is targeted at rapidly dividing malignant cells, while slow dividing or quiescent cells are less affected (274,531). Furthermore, the anti-mitotic activity of 2-ME is not dependent on the estrogen receptor status of cells (532). Mechanistic studies confirmed that the induction of apoptosis in human acute leukaemia Jurkat T cells exposed to 2-ME at a concentration of 1 µM for 24 hours was initiated by microtubule disruption and occurred in an estrogen-independent manner (532). Additionally, results obtained *in vivo* confirmed the *in vitro* results. Estrogen receptor negative breast- (308) and lung cancer (309) mouse models displayed a significant reduction in tumor growth after 2-ME treatment, in addition to displaying a favorable side-effect profile. These findings postulated that 2-ME could clinically be used for the treatment of triple receptor-negative breast cancers and clinical trials commenced. 2-ME, registered as Panzem® (533), has undergone numerous clinical trials as a chemotherapeutic agent and displayed positive results during a phase II clinical trial on hormone-refractory prostate cancer, with minimal hepatic toxicity (292). These results were achieved in spite of 2-ME's low bioavailability. Due to 17β-hydroxy-steriod dehydrogenase-mediated metabolism 2-ME is rapidly broken down in the body, limiting its anti-cancer effect (292). This stumbling block led to the design and development of several 2-ME analogues, which aimed to increase the bioavailability of the parent compound, while retaining or enhancing its cytotoxicity.

The pharmacokinetic limitations associated with 2-ME encouraged the design of a range of novel 2-ME analogues in our laboratory. During the *in silico* design of these analogues Stander *et al.* mainly focused on improving the cytotoxicity and bioavailability of the parent compound, in addition to localizing the analogues to the acidic tumor microenvironments (312). Increased cytotoxicity was achieved by C2' and C3' modifications, whereas D ring modifications ensured decreased 17β-hydroxysteroid dehydrogenase metabolism. Additionally, erythrocyte CAII binding was achieved by steroid sulphamoylation which aimed

to further increase the half-life and bioavailability of these analogues by bypassing the first liver metabolism. These analogues were also designed to preferentially bind to CAIX. CAIX is overexpressed in the tumor micromilieu, thus the design aimed to localize these analogues to tumor cells (312,534). Data published by Leese *et al.* indicated that an ethyl substitution at the position C2 of estrogen yielded the highest binding to tubulin at the colchicine-binding sites (272). By incorporating the latter into the design of our novel *in silico*-designed analogues Stander *et al.* synthesized ESE-15-one and ESE-16 based on the successful docking of these ligands into the colchicine-binding sites between the α- and β tubulin dimers (312). In the current study this computer simulated mechanism of action was translated into an experimental evaluation by exposing ESE-16 to purified tubulin in competition with [^{3}H] colchicine. In the presence of ESE-16 [^{3}H] colchicine-tubulin binding was significantly decreased which confirms the ability of ESE-16 to bind to tubulin utilizing the colchicine binding sites. As the chemical structure of ESE-16 and ESE-15-one only differ at the C'17 and C'16 positions of the D-ring (312), it is theorized that the aforementioned mechanism of action is also employed by ESE-15-one. These novel compounds have polar moieties which would potentially increase their solubility in more acceptable excipients than what is possible for their hydrophobic parent compound, 2-ME (535).

These two non-commercially available analogues were assessed for their cytotoxicity and radiosensitization potential in breast cancer cell lines in the current study. Spectrophotometric quantification of MTT revealed nanomolar GI_{50} concentrations for both compounds in estrogen receptor positive (MCF-7)-, estrogen receptor negative (MDA-MB-231)- and triple receptor-negative (BT-20) breast cancer cell lines. Thus, nanomolar GI_{50} values were obtained irrespective of the receptor status of the cell lines. This indicated that the analogues retained the characteristic of 2-ME of exerting its anti-proliferative effect independently of hormone receptor status (289,293,312,536). The GI_{50} values obtained from this study revealed a cytotoxicity that is increased tenfold when compared to the GI_{50} values obtained from various cell lines exposed to the parent compound (537). These findings concurred with data published by our laboratory which reported effective cytotoxicity of these two compounds in additional cell lines including the non-keratinising

squamous epithelial esophageal cancer cells (SNO), cervical adenocarcinoma cells (HeLa), uterine sarcoma cells (MES-SA) and lung epithelial cancer cells (A549) (289,312). The multiple drug-resistant uterine sarcoma cell line, MES-SA/DX5, has also demonstrated cytotoxicity when treated with ESE-15-one and ESE-16, suggesting that these compound do not act as substrates of the PgP pumps and may be able to overcome drug resistance associated with PgP overexpression (289,538). The dose-response curves generated during a cytotoxicity screening test of 17 of the *in silico*-designed analogues displayed significantly lower GI_{50} values for the sulpahmoylated compounds compared to the non-sulphamoylated intermediates. This demonstrated that the addition of the sulpahmoylated group to the parent compound confers the observed increased cytotoxicity (289).

LIM kinases are emerging targets for the treatment of cancer due to their involvement in the regulation of the cellular cytoskeleton. LIM kinases coordinate actin dynamics by interacting with ADF/cofilin (539). In its active unphosphorylated state, cofilin hydrolyses F-actin filaments and sequesters G-actin monomers from the polymerizing end, promoting actin depolymerization. Upon phosphorylation, cofilin dissociates from actin and polymerization of filamental actin commences (539). LIM kinase is activated upon phosphorylation by downstream Rho GTPases such as ROCK, Pak1 and 4, whereas SSH-IL and bone morphogenetic protein receptor II (BMPRII) inhibit LIM kinase activity. Additionally, LIM kinase is associated with microtubule destabilization which promotes actin stress fiber formation and enhances cell contractility (540). Furthermore, co-localization of phosphorylated LIM kinases and gamma-tubulin was observed in the centrosomes of human breast- and prostate cancer cells during the early stages of mitosis, suggesting their involvement in mitotic spindle assembly (541).

Metastatic cancer cells spread from the primary tumor to distant parts of the body, mostly after local invasion. Cell motility involves the protrusion of the leading edge of the cell membrane, forward propelment of the cell body and the retraction of the cell rear. This process is largely controlled by actin polymerization at the leading cell edge, promoting membrane protrusion (542,543). Thus, the actin binding protein cofilin is essential for cellular movement and is under the cyclic control of LIM kinase. This led to the hypothesis

that LIM kinase is involved in the motility of cells by regulating the actin treadmilling process. Upon investigation of this hypothesis it was found that locally invasive breast- and prostate cancer cells, as well as metastatic breast-, skin-, prostate- and colon tumors express elevated levels of LIM kinase (544). Furthermore, it was noted that cells expressing elevated LIM kinase levels also displayed increased serine protease urokinase type plasminogen activator (uPA) and its receptor (uPAR). This led to the conclusion that LIM kinase increases the secretion of uPA, which is responsible for the degradation of the extracellular matrix, and in turn enhances cell motility and tumor invasion (544).

The aforementioned characteristics of LIM kinase made it a potential target for the treatment of cancer and led to the design of several LIM kinase inhibitors. Inhibition of LIM kinase can be achieved via gene knockdown techniques or by biochemical means (545,546). Inhibition of LIM kinase resulted in a significant decrease in breast- and lung cancer cell division, invasion and migration. Furthermore, inhibition of LIM kinase resulted in altered actin dynamics and disruption of the microtubule network which decreased tumor proliferation (547-550).

The research team lead by Prof. L Lafanechère in Grenoble, France, employed a cell-based assay to screen a diverse chemical library in an attempt to identify chemicals that interact with microtubule regulators (548). This cell-based assay recognized the polymerization state of microtubules in the presence of these chemicals and led to the discovery of a microtubule modifier called LimPyr1. Furthermore, it was discovered that LimPyr1 was a LIM kinase 1/2 inhibitor. By inhibiting the phosphorylation of cofilin LimPyr1 inhibited the dynamic activity of actin microfilaments (548). A comprehensive study was conducted by Prudent *et al.* which identified alterations in microtubule dynamics in the presence of LimPyr1. Data generated from the study revealed that LimPyr1 induced a stable microtubule network with mostly detyrosinated tubulin (548). Additionally, microtubules treated with LimPyr1 were resistant to the depolymerizing effect of nocodazole.

The microtubule stabilizing properties of LimPyr1 was shared by other LIM kinase inhibitors that were both structurally similar and different to LimPyr1 (548). This suggests that the

stabilizing effect produced by the LIM kinase inhibitors is the result of direct LIM kinase inhibition and not due to off-target effects. Furthermore, the ability of LimPyr1 to stabilize the microtubules occured independent of its effect on the actin cytoskeleton (548). This observation was made in HeLa cells exposed to the actin microfilament depolymerizing agent cytochalasin prior to the addition of LimPyr1. Addition of LimPyr1 still resulted in the stabilization of the microtubule network in these cytochalasin treated HeLa cells as measured by the formation of detyrosinated microtubules. LimPyr1 retained its cytotoxicity and anti-proliferative activity in paclitaxel resistant cell lines, and displayed anti-cancer activity *in vivo* with limited side-effects (547,548). Clinical application of LimPyr1 is limited due to its four ring scaffold structure. This structure renders the inhibitor poorly soluble and limits further pharmacological development in its current structure (318).

Invasive breast cancer cells often express higher levels of endogenous LIMK1 (219,551). Western blot analysis of the invasive breast cancer cell lines TS/A-pGL3 and MDA-MB-231-ZNF217rvLuc2 revealed an endogenous LIMK1 level that was at least 50% higher when compared to non-invasive cells such as the MCF-7 cells (219,552). As LimPyr1 is a LIM kinase inhibitor, these cells were used for the evaluation of the toxcicity of LimPyr1. Utilizing the MTT cytotoxicity assay toxicity profiles were generated after a 48 hour exposure to a LimPyr1 dose-response curve (0-25 µM). The proliferation of these invasive breast cancer cells were decreased to around 90% with GI_{50} values calculated at 1.4 µM for TS/A-pGL3- and 7 µM for MDA-MB-231-ZNF217rvLuc2 cells (547). The cytotoxic effect of LimPyr1 was confirmed in the currently study. Spectrophotometric quantification of MTT revealed higher GI_{50} concentrations for LimPyr1 when exposed to BT-20 cells (16.38±0.55 µM), MCF-7 cells (19.50±1.41 µM) and MDA-MB-231 cells (19.50±0.71 µM) for 48 hours.

Other on-going phenotypic studies conducted by the IAB research team aim to identify compounds that sensitize cells to non-lethal doses of paclitaxel. Paclitaxel is one of the most well-known naturally sourced anti-cancer drugs and is frequently prescribed for the treatment of breast- and ovarian cancer (553). By targeting cellular microtubules, paclitaxel prevents the transition between the G_2 phase and the mitotic phase, subsequently preventing cellular division (554). This results in a prolonged mitotic block and the cell is

rendered apoptotic. This form of cell death is desirable as it does not activate an immune response (74). However, paclitaxel treatment is associated with various side effects such as neutropenia and peripheral neuropathies (555). Additionally, the development of drug resistance is a major limitation in paclitaxel treatment (556). Paclitaxel and other pharmaceutical agents have been studied and employed in combined cancer treatment regimes. This aimed to increase the cancer cell's sensitivity to paclitaxel, allowing lower dose administration in order to decrease the side-effects and the development of drug resistance, whilst retaining the anti-cancer effect of paclitaxel.

Using a cell based assay the IAB research team combined 8000 molecules with sub-lethal doses of paclitaxel. Based on these cytotoxicity studies, the compound T4 was selected for further analysis as it showed the most potential to sensitize cells to paclitaxel (unpublished data). The ability of T4 to increase paclitaxel sensitivity was also observed in yeast, indicating that its target is conserved among species (unpublished data). In the quest for identifying the target of T4, it was established during a preliminary *in vitro* study that T4 exerts its effect by binding to the coldhidine binding sites on tubulin, resulting in abnormal mitotic spindle formation. The abnormal mitotic spindle formation may also be due to the activation of the SAC, as T4 treatment did result in the accumulation of multinucleated cells (unpublished data). The cytotoxicity of T4 in the absence of paclitaxel was quantified in the current study where a GI_{50} value of 36.00±1.10 µM was obtained in BT-20 cells following a 48 hour exposure.

5.1 Drug properties and cytotoxicity

By binding to the colchicine binding sites on tubulin 2-ME induces a mitotic arrest by supressing microtubule dynamics or preventing tubulin polymerization (270). The mechanism through which 2-ME induces mitotic arrest depends on the concentration of the anti-mitotic drug (557). 2-ME was evaluated for its effect on microtubule depolymerization and dynamic instability at various concentrations. Assembly of purified tubulin was stalled in

the presence of 2-ME (5-100 µM) in a dose-dependent manner. However, the substitution of purified tubulin with microtubule-associated protein-containing microtubules required a significantly higher concentration of 2-ME (only 13% of the polymer mass was decreased with 500 µM) to depolymerize the microtubules (557). Microtubule dynamic instability was observed in an *in vitro* tubulin assay (assembled to a steady state prior to 2-ME exposure) following exposure to a low dose 2-ME (4 µM) where a decrease of 17% and 27% was detected in the mean growth rate and dynamicity, respectively. These results correlated with the data obtained from MCF-7 exposed 2-ME cells and led to the conclusion that 2-ME induces a mitotic arrest by supressing microtubule dynamics at low doses, whereas the mitotic arrest seen at higher doses is a result of microtubule depolymerization (557).

The ability of ESE-16 to bind to the colchicine binding sites on tubulin was confirmed during the *in vitro* colchicine binding assay in the present study. An ESE-16-induced metaphase block was visualized in autofluorescent HeLa Kyoto cells. The time-lapsed video microscopy revealed a marked delay in metaphase progression in HeLa Kyoto cells exposed to ESE-16 compared to the vehicle control. ESE-16-treated HeLa Kyoto cells spend an average of 367.85±19.89 minutes in metaphase compared to the 26.3±2.4 minutes of DMSO-exposed cells. These results confirmed a significant G_2/M phase block induced by the sulpahmoylated 2-ME analogues. Radiosensitization has been demonstrated in cells blocked in the G_2/M phase (414,417). Tubulin assembly assays confirmed the inhibition of tubulin polymerization of ESE-16 at low concentrations (5 µM), however a higher concentration of ESE-15-one (25 µM) was required to achieve the same effect (558). Still, the ability of these compounds to disrupt the stability of assembled purified tubulin has not been investigated to date.

Several modifications were made to the 2-ME molecule during the design of our novel analogues which aimed to increase the cytotoxicity of the parent compound. The importance of the sulpha-group added to the C3' position was highlighted in a compound screening test utilizing various cancer cell lines (558). Cytotoxicity studies indicated that the non-sulphamoylated analogues displayed a significantly higher GI_{50} value compared to those

with the added moiety. However, conformational changes to the D-ring at positions C16' and C17' did not influence the cytotoxicity of the compounds significantly (558). By using the IncuCyte® system in conjunction with the DNA binding agent, IncuCyte® Cytotox Green, the cytotoxic effect of the two potential radiosensitizing agents, ESE-15-one and ESE-16, was measured in HeLa cells over a 72 hour time frame. The real-time imaging showed an early increase in rounded cells following exposure to the two compounds. The rounding of the cells may suggest a mitotic block induced by the microtubule abrogative effect of the compounds. The prolonged mitotic block prevented the proliferation of the HeLa cells and resulted in higher green fluorescence levels, indicating cell death. This real time imaging indicated a time-dependent increase in cell death, confirming that the cytotoxicity of the parent compound, 2-ME, was retained during the design of the novel sulphamoylated analogues.

Treatment of metastatic breast cancer remains suboptimal. Thus, a potential radiosensitizing agent that prevents the migration of tumor cells would be beneficial to any cancer treatment regime. The ability of cancer cells to migrate and invade local and distant tissues distant from the primary tumor is facilitated by chemotactic migration (477). Chemotactic migration is guided by protruding cellular membranes which form pseudopodia. These pseudopodia attach to the extracellular matrix in order to initiate the forward propelment of the cell (477). Additionally, cell migration also contributes to the formation of new blood vessels, a process known as angiogenesis (438). Thus, by preventing cell migration a potential anti-cancer agent should, in theory, not only prevent cancer metastasis but can also inhibit the vascularization of newly formed tumors. Cell migration necessitates the rearrangement of the cellular actin skeleton (439). Previously reported data from our laboratory visualized the ability of ESE-15-one and ESE-16 to alter the actin morphology of HeLa- and MDA-MB-231 cells using fluorescent microscopy (559). Furthermore, the ability of HeLa- and MDA-MB-231 cells to migrate was significantly decreased in the presence of ESE-15-one and ESE-16 during a scratch assay (559).

By using a slightly different technique the ability of ESE-15-one and ESE-16 to decrease the migration of HeLa cells at different concentrations were assessed in this study. Scratch assays were performed on confluent HeLa cells. Scratch assays provide vital information with regards to cell migration, cell-cell adhesion and ECM remodelling (560). Cells were exposed to 0.2 and 0.4 µM of ESE-15-one and ESE-16, respectively, whereafter wound closure was measured by the IncuCyte® system every 2 hours. The experiment was conducted in a time-frame less than the doubling time of the cells. A delay in wound closure was already observed for both compounds after 8 hours exposure to the higher concentration. An increased number of rounded cells were observed for the duration of the experiment. However, cells that have undergone apoptosis cannot migrate. Therefore it is important to evaluate the effect of cellular migration using lower concetrations. These lower doses may affect cellular migration without inducing apoptotic cell death. The mitotic block was also observed to a lesser extend at the lower doses. However, only ESE-15-one was able to delay wound closure at the 10 hour time point at the lower dose. These results suggest that ESE-16 has less of an effect on the polymerization of tubulin at lower concentrations and its anti-mitotic properties may also result from the alteration of microtubule dynamics, a characteristic observed in the parent compound (557).

Pharmaceutical agents, such as 2-ME, that bind to the colchicine binding sites on tubulin cause microtubule abrogation which subsequently induce a G_2/M phase block as a result of the SAC being activated (270). This can be visualized using fluorescent microscopy. Incubation of 2-ME treated cells with a fluorescently-labeled antibody allows the visualization of microtubule alterations induced by the microtubule targeting agent. Oocytes treated with 2-ME (5-7.5 µM for 20 hours) revealed perturbations in spindle formation (561). Additionally, 20 µM of 2-ME significantly disrupted the cellular microtubule structure of HK-1 nasopharyngeal carcinoma cells after 48 hours (562). Subsequently a mitotic block was induced and the nucleus duplicated in the absence of mitosis due to the up-regulation of MAPK. Florescent microscopy was also used to visualize the microtubule effect induced by paclitaxel in endothelial cells. At concentrations ranging from 1-10 nM, paclitaxel stabilized the microtubule network. However, such stabilization was not observed in cells exposed to lower concentrations (0.1-100 pM) (563).

Confocal microscopy employing anti-alpha-tubulin antibodies conjugated with an Alexa-488 fluorescent probe was used to visualize the effect of the two novel 2-ME analogues ESE-15-one and ESE-16 on the cytoskeletal microtubule architecture of MDA-MB-231 cells. ESE-15-one- and ESE-16-treated MDA-MB-231 cells displayed abnormal mitotic spindle formation 24 hours after exposure (312). Similar results were observed in ESE-16-treated HeLa cells. Disintegration of the tubulin structure was observed in HeLa cells exposed to 0.5 µM of ESE-16 for 24 hours (564). These results confirmed that the 2-ME analogues are anti-mitotic and the spindle disrupting ability of the parent compound was retained.

LimPyr1 was discovered during the screening of a chemical library focused on the identification of chemicals that interfered with microtubule dynamics (548). As LimPyr1 is a LIM kinase inhibitor it was unexpected that this compound altered the microtubule network, as LIM kinase is a known actin regulator. However, this microtubule-actin filament co-dependency phenomenon was described by Vasiliev about 45 years ago (565). Vasiliev observed that the polarized actin-dependent protrusions located at the leading edge of translocating fibroblasts are maintained by microtubules (565). This led to subsequent studies attempting to identify possible mechanisms through which the three cytoskeletal substructures (actin, microtubules and intermediate filaments) engage in extensive cross communication that is particularly important to coordinate core biological processes such as regulating cell polarity and shape during cell migration, as well as polarizing cells for division by promoting a symmetry break. It is hypothesized that the cytoskeletal crosstalk between the actin skeleton, more specifically F-actin, and the microtubule network occurs mainly through direct structure-based contact mediated by microtubule-actin cross linkers or via signaling pathways such as the activation/inactivation of RhoA/ Ras-related C3 botulinum toxin substrate 1 (Rac1) (566).

In an attempt to locate the cellular target of LimPyr1 the research team in Grenoble assessed the effect of LimPry1 on the cellular cytoskeleton of HeLa cells. It was found that LimPyr1 supresses microtubule dynamic instability. This however was achieved without targeting tubulin directly (548). During an *in vitro* tubulin assembly assay, LimPyr1 did not

induce tubulin assembly on pure tubulin or in the presence of associated microtubule proteins (548). Further analysis did confirm the stabilization effect of LimPyr1 on the microtubule network. A total of 82.9% of cells exposed to LimPyr1 for 2 hours presented with abnormal mitotic spindles with disorganized asters, a significant increase compared to the abnormal spindle formation observed in 12.8% of DMSO-treated cells (548). Furthermore, they evaluated the effect of LimPyr1 on microtubule dynamic instability parameters. Green fluorescent protein (GFP) microtubule-associated protein RP/EB family member 3 (EB3)-transfected cells exposed to LimPyr1 for 2 hours were assessed via fluorescent time-lapse microscopy. Data revealed an increase in the distance-based catastrophe frequency in a dose dependent manner (548). This illustrated the ability of LimPyr1 to suppress microtubule dynamic instability and subsequently decreased the growth rate of microtubules.

As previously mentioned, the actin and microtubule networks are interconnected. The effect of LimPyr1 was assessed on the actin cytoskeleton. Using fluorescein-phalloidin, the F-actin of HeLa cells exposed to LimPyr1 for 2 hours were stained. Fluorescent micrographs demonstrated that LimPyr1 significantly affected the organization of the actin microfilaments, while time-lapsed video migration assays confirmed the inhibition of MCF10A migration following LimPyr1 exposure at low concentrations (10 µM) (548). Similar to the effect observed during the *in vitro* tubulin assembly assay, it was noted during an actin-pyrene polymerization assay that LimPyr1 does not directly affect the assembly of actin monomers, confirming that the alterations observed in the actin organization of LimPyr1-treated cells were not due to the direct interaction between LimPyr1 and actin, but rather through the inhibition of LIM kinase (548).

It has been established that the novel 2-ME analogues cause alternations in the microtubule network of various cells lines *in vitro*. With the continued increase in publications illustrating the cross-talk between the actin skeleton and microtubule network, the effect of the novel 2-ME analogues on the actin cytoskeleton was recently investigated by our laboratory. Examination of F-actin-phalloidin labeled MDA-MB-231 cells exposed to ESE-15-one and ESE-16 for 2 hours revealed an increased number of thickened stress fibres (559).

Additionally, the stress fibres observed at the leading edges of DMSO-exposed cells (cell polarity) were not observed in cells exposed to the sulphamoylated analogues. After a 24-hour-treatment with the respective compounds, HeLa cells demonstrated no stress fibre formation but did present with a peripheral actin network (559). This peripheral actin network may be the subsequent result of the metaphase block induced by these novel compounds.

To investigate the effect of ESE-15-one, ESE-16, LimPyr1 and T4 on the actin and microtubule cytoskeletons simultaneously, a dual fluorescent stain was used in the current study. MCF-7-, MDA-MB-231- and BT-20 cells were exposed to the various compounds (GI_{50} concentrations) for 24 hours. MCF-7- and MDA-MB-231 cells exposed to ESE-16 displayed a depolymerized microtubule network most likely due to the binding of the colchicine binding sites on tubulin. This was accompanied by increased stress fibre formation. Similar actin morphology was observed in dihydromotuporamine C treated MDA-MB-231 cells (567). Dihydromotuporamine C is known for its anti-invasive activity and in addition to the induced stable stress fibres in the MDA-MB-231 cells, treatment resulted in the prolonged activation of RhoA-ROCK signaling molecules. This subsequently led to the formation of enlarged focal adhesions located on the periphery of the cell (567). Similar actin stress filaments were observed at the leading edges of the DMSO-treated cells in the current study. This migration polarity was disrupted in the treated MCF-7- and MDA-MB-231 breast cancer cells indicating that ESE-16 could potentially prevent cell migration by stabilizing and accumulating F-actin. The triple receptor-negative breast cancer cell line, BT-20, displayed depolymerized microtubules following exposure to ESE-15-one and ESE-16, similar to those observed in the MCF-7- and MDA-MB-231 cells. However, BT-20 cells displayed peripheral radial arrangements of actin filaments following exposure to ESE-15-one and ESE-16. This radial arrangement of the actin network is indicative of the rounding of the ridged actomyosin cortex (568). The latter promotes cell rounding via de-adhesion of the cell from the extracellular matrix in order to progress and complete cell division. Furthermore, actin stress fibre formation was not evident in BT-20 treated cells and cell polarity was disrupted in the same manner as observed in the MCF-7- and MDA-MB-231 cells.

No published data illustrating the effects of T4 on the cellular cytoskeleton are available. In the current study BT-20 cells exposed to T4 for 24 hours revealed a slight increase in the stabilization of the microtubule network accompanied by a few actin stress fibres. Unpublished preliminary data collected by the IAB research team demonstrated a delay in chromosome alignment in T4 treated HeLa Kyoto cells resulting in the induction of a metaphase block. Additionally, T4 demonstrated the ability to block cells in pro-metaphase at higher concentrations. The target for T4 is currently under investigation by the IAB research team.

Similar to previously published data, micrographs in the current study illustrated the depolymerizing effect of LimPyr1 on the actin skeleton of all three cell lines. The latter is achieved by LIM kinase inhibition by LimPyr1 activity. The inhibition of cofilin phosphorylation subsequently inhibits the dynamic activity of actin microfilament, resulting in depolymerization (559). Additionally, LimPyr1-exposure diminished cell migration polarity while stabilizing the microtubule network. Although it has been documented that the microtubule stabilizing effect of LimPyr1 occurs independently of its effect on the actin network, the mechanism through which LimPyr1 induces the microtubule stabilization remains unclear (548). Polymerization of microtubules is facilitated by p25 and can be inhibited upon p25 phosphorylation by LIMK1 (569). Therefore, it is hypothesized that LimPyr1 could potentially induce dephosphorylation of p25, resulting in stabilization of microtubules (548).

The design behind this study necessitated the determination of the lowest compound- and radiation doses that significantly induced apoptotic cell death. In order to determine these experimental parameters a range of does-reponse curve experiments were conducted. The GI_{50} concentrations of ESE-15-one, ESE-16, T4 and LimPyr1 were obtained via spectrophotometric quantification of MTT and provided a starting point for a more refined compound dose-response curve (GI_{50}, ¾ GI_{50}, ½ GI_{50}, ¼ GI_{50} and ⅛ GI_{50}). BT-20 cells were exposed to ESE-15-one, ESE-16, T4 and LimPyr1 dose curves. BT-20 cells were selected for the evaluation of the toxicity of all four microtubule regulating agents as these cells are the most resistant to anti-cancer agents. MCF-7- and MDA-MB-231 cells were exposed to ESE-16

and LimPyr1 dose curves. Cells were exposed to the compounds for 48 hours as this was the total exposure-time during the radiosensitization experiments. The samples were analysed for the induction of apoptosis by means of flow cytometry employing Annexin V. Additionally, the effect on the cell cycle was also assessed via flow cytometry, where the apoptotic sub-G_1 peak was quantified using propidium iodide staining. Together, these techniques enabled the identification of the lowest compound doses that significantly induced apoptosis in the various breast cancer cells lines. Apoptosis was significantly induced in BT-20 cells following exposure to 0.06 µM ESE-15-one, 0.112 µM ESE-16, 18 µM T4 and 1.638 µM LimPyr1 for 48 hour. In the MCF-7- and MDA-MB-231 cells apoptotic cells were signficantly increase by ESE-16 at the concentrations of 0.157 µM and 0.137 µM, respectively. The LIM kinase inhibitor, LimPyr1 significantly decreased MCF-7 and MDA-MB-231 cell viability at 2.437 µM.

By employing the same experimental setup, the lowest radiation dose that significantly increased apoptosis in MCF-7-, MDA-MB-231- and BT-20 cells was determine following exposure to a radiation dose-response curve. Apoptosis was signficantly increased after 8 Gy radiation exposure in MCF-7- and MDA-MB-231 cells, whereas 6 Gy radiation significantly increased BT-20 cell death. Although the BT-20 cell line displayed an increase in apoptosis after 6 Gy radiation, it was decided that 8 Gy would be used for all subsequent radiation exposure, in order to keep the radiation delivery protocol constant for all cell lines.

5.2 Regulation of the cell cycle

The radiosensitivity of cancer cells may vary in accordance to the phase of the cell cycle. Cells are most radiosensitive in the G_2/M phase and less sensitive in the G_1 phase, while the latter part of the S phase is considered the least radiosensitive (570). This understanding has led to the realization that chemotherapeutic agents, such as 2-ME, that induce a mitotic block may sensitize cells to radiation and produce a greater therapeutic effect (414). This hypothesis was tested in a study conducted by Casarez *et al.* where prostate cancer cells

were pre-treated with 2-ME in an attempt to increase their radiosensitivity (418). The study was conducted based on previously published data that demonstrated the efficacy of 2-ME as a single agent against human prostate cancer cells (571), as well as its ability to radiosensitize non-small lung cancer models (572,573). A significant decrease in MAPK phosphorylation had been observed in noncancerous cells exposed to 2-ME (574,575). Furthermore, the selective inhibition of the MAPK pathway significantly increased the sensitivity of cells to radiation (576-578). These results prompted Casarez *et al.* to evaluate the effect of 2-ME on MAPK phosphorylation in human prostate cancer cells (418). Exposure of PC3 prostate cancer cells to 1.5 µM 2-ME (the dose that increased the sensitivity of the cells to radiation) for 18 hours resulted in dose-dependent decrease in MAPK phosphorylation *in vitro*. Furthermore, the team was unable to increase the radiosensitivity of cells which expressed constitutively active MEK (upstream effector of MAPK) with 2-ME pre-exposure. A decrease in MAPK phosphorylation was accompanied by a decrease in cellular survival (as asses by clonogenic studies) in PC3 cells pre-treated with 2-ME (418).

The radiosensitizing ability of 2-ME was further investigated *in vivo* (418). Subcutaneous prostate cancer (PC3) mice xerograph models were treated with 2-ME only (75 mg/kg), radiation only (10 Gy fractionated over 5 consecutive days) or a combination treatment where 2-ME was administered 4 hours prior to radiation. Tumor growth was not significantly effected by 2-ME treatment alone, whereas a slight decrease in tumor growth was observed in the radiation-only specimens (418). Mice treated with 2-ME prior to radiation exposure displayed a superadditive effect (*P*-value < 0.0001) resulting in a significant decrease in tumor growth in these mouse models (418). These promising results prompted further *in vivo* investigation utilizing orthotropic prostate murine models which are more physiologically appropriate compared to the subcutaneous models. Log-phase PC-3M-luc-C6 cells were surgically injected into the dorsolateral lobes of prostate glands of nude mice. Tumor growth was monitored for 2 weeks whereafter treatment commenced (418). Bioluminescence imaging revealed a delay in the orthotropic tumor growth in mice treated with the combination therapy. The combination therapy protocol entailed oral administration of 2-ME 4 hours prior to radiaton treatment. Compared to the untreated control group, no significant change in tumor growth was observed in mice treated with

only 2-ME, whereas radiation treatment alone did result in a significant decrease in tumor growth. However, an f-test did confirm a superadditive effect on tumor size reduction after treatment with the combination treatment when compared to the individual treatment conditions. The authors therefore concluded that 2-ME does radiosensitize prostate cancer cells *in vitro* and *in vivo* via the decrease in MAPK phosphorylation (418).

The effects of ESE-16, LimPyr1 and their combination with radiation were investigated in this *in vitro* study by quantifying cyclin B1 expression using Western blot analysis, as well as determining the subsequent effects on the cell cycle progression via flow cytometry. CDK and cyclins are highly conserved proteins and form complexes in order to regulate cell cycle progression in eukaryotes. Cyclin B1 is the regulatory subunit for CDK1 (catalytic subunit) which regulates the transition from the G_2 phase to the M phase (579). Various human tumors such as head and neck-, gastric-, cervical-, colorectal- and breast carcinomas display significantly higher levels of cyclin B1 which contributes to the aggressive proliferation of these neoplastic tissues (580-586). Furthermore, head and neck squamous cell carcinomas that express high levels of cyclin B1 have been shown to be resistant to radiotherapy (584), whereas breast carcinomas which overexpress nuclear cyclin B1 levels are resistant to adjuvant therapy (587). Overexpression of cyclin B1 is also linked to aneuploidy and an increased proliferation rate in human mammary carcinomas (588). The latter may be attributed to the ability of cyclin B1 overexpressed cells to override the DNA damage checkpoint located in the G_2 phase . Thus, deregulation of cyclin B1 contributes to neoplastic transformation in addition to promoting tumor cell proliferation (589). Therefore, down regulation of cyclin B1 will reduce the effect of CDK1/cyclin B1 and potentially decrease the proliferation of human cancer cells (590,591).

Eukaryotic cells exposed to radiation demonstrated a pause in the G_2 phase. The mechanism responsible for this delay has been identified as a decrease in cyclin B1 expression most likely under p53 control, and is known as the radiation induced mitotic delay (592). DNA damage activates ATM kinase which phosphorylates CDK1/2. This prevents the activation and nuclear import of cyclin B1/CDK1 from the cytoplasm, inducing a metaphase block (593). HeLa cells exposed to radiation displayed a dose-dependent decrease in cyclin B1

expression, which alongside the activation of the DNA damage checkpoint was responsible for the G_2 delay (594). Similar results were obtained in the current study. MCF-7-, MDA-MB-231- and BT-20 cells exposed to 8 Gy radiation displayed a significant decrease in cyclin B1 protein expression 24 hours after radiation. This was accompanied by a significant increase in cells present in the G_2/M phase as assessed by flow cytometry. MCF-7-, MDA-MB-231 and BT-20 cells exposed to low doses of ESE-16 and LimPyr1 also displayed a significant decrease in cyclin B1 expression. Although the effect of LimPyr1 on the expression of cyclin B1 has not been previously investigated Prudent *et al*. did report a G_2/M cell cycle arrest in LimPyr1 treated HeLa cells (353). Similarly a 48 hour exposure to LimPyr1 significantly delayed the progression from the G_2 phase to mitosis in the three breast cancer cell lines in this study. ESE-16 increases the expression of cyclin B1 in HeLa cells following a 24 hour exposure to 0.5 µM of ESE-16 (595). This was followed by a significant delay in the transition from the G_2 phase to the M phase. These results did not correlate with the decreased cyclin B1 expression observed in the current study. A study conducted by Newman *et al.* demonstrated an initial increase in cyclin B1 expression in MCF-7 cells exposed to 500 nM of 2-ME (596). The elevated cyclin B1 expression prevented the progression of the cell cycle by inducing a mitotic block. These levels deteriorated in the MCF-7 cells after 48 hours of exposure resulting in the induction of apoptosis (596). These finding suggest that the sulphamoylated analogue ESE-16 may initially increase the expression of cyclin B1 which deteriorates after a prolonged exposure. As published previously, the G_2/M phase block observed in ESE-16 treated HeLa cells was accompanied by elevated cyclin B1 levels 24 hours after exposure (595). In the current study the cells were exposed to ESE-16 for 48 hours and presented with decreased cyclin B levels. No mitotic block was observed in MCF7-, MDA-MB-231- or BT-20 cells exposed to ESE-16 for 48 hours, however the induction of cell death was illustrated by an increase in cells present in the sub-G_1 apoptotic phase.

Cell cycle analysis of MCF-7-, MDA-MB-231, and BT-20 cells exposed to the ESE-16 and LimPyr1/radiation combination treatments displayed a significant increase in the G_2/M phase with a concurrent decrease in the G_1 phase. The apoptotic sub-G_1 peak was also significantly increased in the combination treatment samples and correlated with the apoptotic hallmarks observed in the PlasDIC micrographs. Compared to cells exposed to the

compounds only, ESE-16 and LimPyr1 pre-treated MCF-7-, MDA-MB-231- and BT-20 cells displayed a significant increase in the G_2/M phase. Furthermore, breast cancer cells presensitized with LimPyr1 displayed an increased number of cells in the G_2/M phase compared to cells exposed to radiation only. The BT-20- and MDA-MB-231 cell lines displayed no significant differences in the cell cycle of cells presensitized with ESE-16 compared to the radiation control. However, a significant increase in the sub-G_1 apoptotic phase was observed in the ESE-16 pre-treated MCF-7 breast cancer cell line when compared to cells exposed to radiation only. Induction of a G_2/M block is followed by p53-mediated apoptotic cell death in cells exposed to ionizing radiation (597). This mechanism however may vary according to cell type as seen in the above mentioned results.

5.3 Cellular survival and apoptotic cell death

The FoxO family of transcription factors is an important class of tumor suppressor proteins expressed in a variety of cancers. The FoxO subfamily of forkhead transcription factors, FoxO1 and FoxO3a, are downstream targets of the serine/threonine Akt (598). Under the regulation of the Akt kinase, these FoxO transcription factors are positive regulators of cell proliferation and survival (599). Furthermore, emerging evidence suggests that genes involved in various cellular processes including cell death, metabolism, cell cycle progression, oxidative stress protection and neoplastic transformation are associated with FoxO protein activity (599). In their unphosphorylated state, FoxOs inhibit cellular growth and replication while promoting apoptotic cell death (600). The latter is achieved by increasing the expression of cyclin-dependent kinase inhibitors (CDKIs), facilitating the induction of the extrinsic apoptotic pathway by increasing the expression of death receptor ligands such as TRAIL and Fas, and inducing mitochondrial apoptosis by increasing the expression of mitochondria-targeting proteins such as the pro-apoptotic members of the Bcl-2 family (599,601,602). Phosphorylation of FoxOs on highly conserved serine and threonine residues are facilitated by the Akt kinase. Upon phosphorylation the association between FoxOs and DNA is hindered and the cytoplasmic translocation of FoxO is facilitated by the chaperone protein 14-3-3σ (603). Nuclear exportation and cytoplasmic retention of

phosphorylated FoxOs inhibit the FoxO-dependent transcription of genes, such as $p27^{Kip1}$ and Bcl-2-like protein 11 (Bim), which are involved in apoptosis and cell cycle arrest (604).

FoxO1/3a-induced apoptosis was investigated in MCF-7-, MDA-MB-231- and BT-20 cells following exposure to the various treatment conditions in the current study. Western blot analysis revealed a significant increase in phosphorylated Akt and FoxO1/3a in MCF-7-, MDA-MB-231- and BT-20 cells exposed to 8 Gy radiation only. The cytoplasmic sequestering of FoxO3a in non-melanoma skin cancer (NMSC) following ultraviolet B (UVB) irradiation was found to be mTORC2-dependent (605). The negative regulation of Foxo3a is mediated by Akt, which is downstream of mTORC2. Furthermore, this negative regulation of FoxO3a contributed to cell survival after radiation exposure. By inhibiting mTORC2 activity the authors demonstrated an increase in radiation-induced apoptosis due to the nuclear localization of FoxO3a (605). The role of the Akt pathway following radiation exposure was also investigated in a study utilizing glioblastoma cell lines (606). A single radiation dose of 6 Gy significantly increased the phosphorylation of Akt in U87MG, MO59J, and LN18 cells. Moreover, it was demonstrated that the phosphorylation of Akt in U87MG cells was significantly decreased when cells were cultured in serum-free medium compared to those grown in medium supplemented with 10% serum. The latter suggested that radiation-induced Akt phosphorylation was dependent upon the presence of a serum factor and was inhibited upon the addition of the EGFR inhibitor, AG1478 (606). These results confirmed that the activation of Akt in U87MG cells is dependent on the activation of the EGFR, and thus the team was able to increase the radiosensitivity of highly radioresistant U87MG cells by inhibiting the activation of the PI3k, EGFR and Akt signaling pathways (606).

Three main radiation resistance mechanisms, including intrinsic radiosensitivity, tumor cell proliferation and hypoxia, are associated with the activation of the PI3K/Akt pathway (607). Firstly, the intrinsic radiosensitivity of a tumor cell is altered by the activation and translocation of Akt from the cytoplasm to the nucleus after irradiation (608). Additionally, the MRE11-ATM pathway can activate the human homologue, Akt1, in the nucleus upon radiation-induced DNA damage (609). In the nucleus Akt1 forms a functional complex with DNA repair proteins namely DNA-dependent protein kinase catalytic subunits (DNA-PKcs),

and promotes the autophoshorylation of DNA-PKcs, stimulates DNA-PKcs kinase activity and increases the accumulation of DNA-PKcs at the DNA double strand breaks (610,611). The recruitment and activation of these DNA repair proteins facilitated by Akt1 ensure efficient repair of the double strand breaks induced by the radiation and consequently confers radioresistance to the cells (612).

Secondly, the PI3K/Akt pathway can confer radioresistance due to its involvement in tumor cell proliferation. Long-term exposure to fractionated radiotherapy activates the Akt pathway (613). Akt is responsible for the inactivation of synthase kinase-3β (GSK3β) (614). GSK3β is responsible for the degradation of cyclin D1 at the G_1/S transition point of the cell cycle. Due to its inactivation by Akt, GSK3β no longer facilitates the nuclear export and cytoplasmic degradation of the cyclin D1, resulting in the overexpression of cyclin D1 (614). Since lower cyclin D1 levels are required for sufficient DNA synthesis the overexpressed cyclin D1 level induces DNA damage (613). Subsequently, DNA-PK is activated which in turn inactivates GSK3β and activates Akt (613), creating a positive feedback loop of cyclin D1 overexpression (613,615,616). The cyclin D-dependent DNA damage activates the DNA damage checkpoint and HR, allowing the cells exposed to fractionated radiation to repair the damaged DNA (617).

Thirdly, the PI3K/Akt pathway confers radiation resistance to cells via its involvement in tumor hypoxia. Hypoxic conditions promote the transcription and expression of HIF-1α, a process regulated by the PI3K/Akt pathway (618). HIF-1α is a central transcription mediator that plays a crucial role in the cellular response to hypoxia. In addition to being significantly increased under hypoxic conditions, HIF-1α is responsible for the transcription of a cluster of about 60 genes, including enzymes of glucose metabolism and VEGF, which is highly expressed in cancer cells (619,620). VEGF exerts its effect on endothelial cells via VEGF receptors. Binding of the receptor activates a tyrosine kinase pathway which results in the activation of angiogenesis. In addition to stimulating angiogenesis and vasculogenesis, VEGF increases the permeability of the vasculature, enhances tumor growth and promotes tumor metastasis (618,619). Additionally, genes involved in cell proliferation and survival have been linked to the activation of HIF-1α,

which results in increased tumor aggressiveness, cancer recurrence and resistance to treatment (621).

Similar to the results obtained from cells exposed to 8 Gy radiation Western blot analysis revealed a significant increase in phosphorylated Akt in MCF-7-, MDA-MB-231- and BT-20 cells exposed to ESE-16 only. LimPyr1 exposure resulted in elevated levels of phosphorylated Akt in MCF-7- and MDA-MB-231 cells, but had no effect on the BT-20 cell line. Furthermore, Western blot analysis confirmed the subsequent increase in phosphorylated FoxO1/3a in all three breast cancer cell lines exposed to ESE-16 and LimPyr1. Results published in an article which focused on the nongenomic action of 2-ME at physiological levels were similar to those observed in the ESE-16 exposed samples (622). When exposed to a low dose of 2-ME (50 nmol/L) for 5 minutes, ER-positive MCF-7- and T-47D breast cancer cells displayed a 2.5-fold increase in Akt phosphorylation. Furthermore exposure of MCF-7- and T-47D cells to low doses of 2-ME (10 to 500 nmol/L) resulted in increased proliferation of these cells, suggesting that the survival pathway was activated via Akt phosphorylation (622). Results published by Chen *et al.* revealed similar results in HUVEC cells (623). A dose-dependent increase in Akt phosphorylation was observed in HUVEC cells exposed to low doses of 2-ME ranging from 10^{-7} M to 10^{-5} M for 20 minute. The increase in Akt phosphorylation was accompanied by an increase in endothelial nitric oxide synthase (eNOS) phosphorylation at Ser1177 with a concurrent increase in nitric oxide (NO) release from HUVEC cells. NO can promote tumor cell survival and angiogenesis at moderate concentrations (623).

Although Akt phosphorylation was increased at low doses of 2-ME, 2-ME-induced cell death is associated with the down regulation of the cytoprotective Akt pathway (624). A study conducted by Gao *et al*. on human leukemia cells (Jurkat- and U937 cells) investigated the effect of high doses of 2-ME (2 and 4 µM) on the induction of apoptosis (624). Data revealed a dose-dependent increase in the release of mitochondrial proteins such as cytochrome *c* and apoptosis inducing factor (AIF). In addition, ROS generation was significantly increased in Jurkat- and U937 cells exposed to these concentrations of 2-ME and was accompanied by the dephosphorylation of Akt (624). Furthermore, the lethal effect of 2-ME was potentiated

after the PI3K pathway was inhibited by the PI3K inhibitor, LY294002 (624). The addition of the SOD mimetic, tetrabutylammonium phosphate, and catalase, a H_2O_2 scavenger, prevented the induction of 2-ME-mediated apoptosis while preventing the dephosphorylation of Akt (624). These results demonstrated a mechanism of action employed by 2-ME in human leukemia cells where 2-ME induces oxidative injury as a primary event. This is followed by the inactivation of the survival pathway (Akt dephosphorylation) leading to mitochondrial injury and apoptotic cell death. Additionally, the authors concluded that the Akt pathway plays a crucial role in the lethality of 2-ME by mediating the cellular response to 2-ME induced oxidative stress (624).

The serine/threonine-protein kinase PAK 1 is involved in the intracellular signaling pathways involved in cell proliferation, survival and migration (625). Cell proliferation is mediated via PAK activation of the Ras/Raf/Mek/ERK pathway, whereas cell survival is mediated via PAK signaling to the Bad/Bcl-2 pathway (626). Additionally, a concurrent activation of the Akt pathway is facilitated by PAK 1. Furthermore, LIM kinase can be phosphorylated by PAK 1 and PAK 4 at its 508 threonine residue (627). This stimulates LIM kinase activity resulting in the phosphorylation of cofilin. In its phosphorylated state cofilin prevents actin depolymerization, thus by phosphorylating LIM kinase, PAK regulates actin filament turnover and assembly. Data obtained from this *in vitro* study indicated that phosphorylated Akt is increased in MCF-7- and MDA-MB-231 cells following exposure to a low dose of the LIM kinase inhibitor, LimPyr1. This may suggest that the inhibition of LIM kinase enhances the phosphorylation of Akt facilitated by their mutual upstream regulator PAK, which activates the cell survival pathway and inhibits apoptosis via FoxO phosphorylation. Furthermore, LIMK maintains the ERK signaling pathway during the G_1 phase of the cells cycle. As the ERK pathway is another target for the PAK 1 kinase, the PAK 1-mediated phosphorylation of Akt may be increased in the cancer cells upon LIM kinase inhibition in an attempt to evade the effect of the inhibitor and maintain cell survival. However, the precise mechanics of this molecular crosstalk needs to be further investigated. The BT-20 cell line did not illustrate an increase in Akt phosphorylation 24 hours after radiation. However, the phosphorylation levels of FoxO1/3a was significantly increased. This may be due to the Akt phosphorylation levels being decreased to background levels after a

24-hour-exposure to LimPyr1, or that the phosphorylation of FoxO1/3a is facilitated by other kinases. SGK has been reported to increase FoxO phosphorylation at the same sites as Akt, resulting in decreased FoxO-DNA binding and FoxO being translocated to the cytoplasm (628).

In addition to its inhibitory effect on FoxO, Akt inhibits the induction of apoptosis by decreasing the expression of Bax, a pro-apoptotic protein, while it enhances the expression of anti-apoptotic proteins such as Bcl-2 (629). Interestingly, in spite of the increased Akt phosphorylation levels observed in the current study MCF-7-, MDA-MB-231- and BT-20 cells exposed to 8 Gy radiation (as a single agent) displayed a significant increase in Bax expression. Similarly, previously published data revealed a dose-dependent increase in Bax expression in MCF-7 cells exposed to 1.5-4.5 Gy radiation (630). Furthermore, the expression of the anti-apoptotic protein Bcl-2 was significantly decreased by 22% and 17% in MCF-7 cells 48 hours after 3 and 4.5 Gy irradiation, respectively (630). ESE-16 exposure significantly increased Bax expression in MCF-7- and MDA-MB-231 cells, while LimPyr1 exposure resulted in elevated Bax levels in MCF-7- and BT-20 cells. The expression of Bax has not previously been quantified in ESE-16- or LimPyr1-exposed cells *in vitro*, however previous experiments indicated that the ratio of pro-apoptotic Bax and anti-apoptotic Bcl-2 plays an important role in the induction of apoptosis in HeLa and esophageal carcinoma cells following exposure to 1 µM of 2-ME (631). As published by Day *et al.* microtubule damage induced by various microtubule disrupting agents, such as paclitaxel, 2-ME and 2-MEbisMATE, resulted in Bcl-2 deactivation in A2780 human ovarian cancer cells, which suggests that the microtubule damaging agents are similar in the activation of the intrinsic apoptotic pathway (632). Exposure of MDA-MB-231 cells to LimPyr1 and BT-20 cells to ESE-16 did not increase the expression of Bax at these low doses, therefore future studies are recommended to identify changes in the expression and phosphorylation of Bax and Bcl-2, as the Bax/Bcl-2 ratio is more important in determining the induction of apoptosis than either protein alone. The activation may be time- and dose-dependent.

The levels of intracellular ROS can be increased by hyperactive Akt via the stimulation of oxidative metabolism (due to raised metabolic activity) in the mitochondria. Furthermore

phosphorylated Akt elevates ROS levels by repressing the transcription of antioxidant genes via FoxO phosphorylation and cytoplasmic sequestering (633). A study conducted on the effect of malonate on SH-SY5Y neuroblastoma cells and primary cerebellar granule neurons illustrated a link between elevated ROS levels and the activation of Bax (634). Upon activation, Bax translocates to the mitochondria and oligomerizes to form channels in the mitochondrial membrane or regulates the activity of pre-exciting channels. The latter results in a decrease in the outer mitochondrial membrane potential resulting in the release of cytochrome *c* from the mitochondria into the cytosol, and initiating the intrinsic apoptotic pathway. Cytosolic cytochrome *c* activates a caspase cascade by complexing with Apaf-1 and caspase 9 to form the apoptosome. The latter leads to the activation of the executioner caspases, such as caspase 3, resulting in the induction of cell death. The induction of the intrinsic apoptotic pathway via ROS-mediated mitochondrial injury was observed in SK-N-SH and SH-SY5Y neuroblastoma cells exposed to 2-ME (634). 2-ME treated SK-N-SH and SH-SY5Y cells displayed elevated ROS levels with a concurrent decrease in the mitochondrial transmembrane potential. The compromised mitochondrial membrane resulted in the activation of the initiator caspase 9 which in turn activated the executioner caspase 3 in SK-N-SH cells, resulting in the induction of apoptosis (634).

The effect of LimPyr1 on the microtubule dynamics, cellular motility and *in vivo* tumor morphology and proliferation has been studied extensively. Mice with MDA-MB-231 Dendra2 tumors displayed a less 'packed' cellular morphology when treated with 10 mg/kg LimPyr1 for 8 days compared to the vehicle-treated mice (547). To quantify these morphological changes the team measured the area of fluorescent-labeled cells and concluded that there was a statistically significantly decreased in the mice treated with LimPyr1 (547). These results correlated with those obtained from Ki67 staining which indicated a decrease in cellular proliferation in the subcutaneous MDA-MB-231 xenografts treated with LimPyr1, with an increase in apoptotic cells (detected using terminal deoxynucleotidyl transferase deoxyuridine triphosphate nick end labeling (TUNEL) staining) (547). These results did confirm the anti-tumor effect of LimPyr1, however the precise mechanism of apoptotic induction via LimPyr1 remains unclear.

ROS contributes to the radiosensitivity of cells (635). The latter was observed in a study conducted on PC3- and DU145 prostate cancer cell lines (636). Although maximum levels of ROS production were measured 15 minutes after 4- and 8 Gy radiation, the radiosensitive PC3 cells displayed a significant increase in cytosolic ROS compared to the more radioresistant DU145 cell line (636). Next, the team evaluated the involvement of intracellular antioxidants such as glutathione (GSH) in the cellular reaction to radiation, as this antioxidant counteracts the effects of ROS, contributing to cellular homeostasis. The GSH levels as well as the levels of glutathione disulphide (GSSG) were measured in radiation-exposed cells. GSSG is a disulphide derived from two GSH molecules. By establishing the GSH:GSSG ratio the team could identify the oxidative state of both cell types following radiation exposure (636). The radioresistant DU145 cell line presented with a higher GSH:GSSG ratio compared to the PC3 cell line. The PC3 cell line displayed low basal levels of GSH which were rapidly depleted after radiation exposure, whereas the DU145 cells were able to recover rapidly from the oxidative stress due to higher antioxidant level (636). The team attributed the sensitivity of the PC3 cells to the accumulation of ROS and depletion of GSH.

As mentioned above, increased ROS production can be activated by phosphorylated Akt (633). Furthermore, ROS mediated activation of Akt increases the induction of apoptosis (637). Thus, by increasing ROS, Akt could initiate the activation and translocation of Bax to the mitochondria, contributing to the induction of the intracellular apoptotic pathway. An increase in Akt phosphorylation (survival pathway) as well as an increase in Bax expression (apoptotic pathway) was observed in MCF-7-, MDA-MB-231- and BT-20 cells exposed to the individual treatment conditions. We therefore measured the production of ROS in these cells in order to identify the mechanism through which Bax was activated, and whether this led to the induction of mitochondrial apoptosis.

Flow cytometric analysis revealed a significant increase in ROS in ESE-16 treated MCF-7-, MDA-MB-231- and BT-20 cells at various time frames. The ROS production in ESE-16 treated MCF-7 and MDA-MB-231 cells returned to basal levels at 24 and 48 hours respectively, whereas the ROS production in BT-20 cells was elevated up to 48 hours. These results

correlated with previously published data where ESE-16 significanly increased superoxide levels in MDA-MB-231- and MCF-7 cells (38). The study indicated elevated superoxide levels 6 and 18 hours in response to higher ESE-16 doses in the MDA-MB-231- and MCF-7 cell lines, respectively. Furthermore, ESE-16 exposure resulted in depolymerization of the mitochondrial membrane in MDA-MB-231- and MCF-7 cells in addition to activating caspase 3 and -7 (38). Similar results were obtained in the current study. MDA-MB-231 cells exposed to low doses of ESE-16 displayed an increase in Mitocapture™, illustrating a decrease in the mitochondrial transmembrane potential. This could be attributed to the increased Bax expression and was followed by the activation of caspase 3. Quantification of cleaved caspase 3 was significantly increased in MDA-MB-231 cells exposed to low ESE-16 doses. Apoptotic cell death was quantified by flow cytometry employing annexin V. ESE-16 exposed MDA-MB-231 cells displayed a significant increase in annexin V-stained apoptotic cells as well as an increase in the sub-G_1 apoptotic phase. The ROS production of MCF-7 cells was only elevated at the earliest time point, however the expression of Bax was still significantly increased. The latter did not result in increased mitochondrial transmembrane permeability as Mitocapture™ detection did not reveal an increase in the fluorescent signal. Furthermore, no increase in annexin V staining was observed in MCF-7 cells exposed to low doses of ESE-16, but a small increase in the sub-G_1 phase was observed. ESE-16 induced the intrinsic apoptotic pathway in the BT-20 cells by significantly increasing the expression of ROS and decreasing the mitochondrial transmembrane potential. Temporal and cell-specific differences must be taken into account when examining these data.

The induction of the intrinsic apoptotic pathway was confirmed in LimPyr1-treated MCF-7-, MDA-MB-231- and BT-20 cells. Low doses of LimPyr1 significantly increased ROS in all three cell lines over the 48 hour time frame. The permeability of the mitochondrial transmembrane was significantly increased in MCF-7-, MDA-MB-231- and BT-20 cells exposed to LimPyr1. The activation of cleaved caspase 3 was quantified in MDA-MB-231- and BT-20 cells exposed to LimPyr1 and displayed a significant increase compared to the negative controls. Apoptotic cell death was significantly increased in all three cell lines, confirming the induction of mitochondria-mediated apoptosis.

MCF-7- and BT-20 cells exposed to 8 Gy radiation displayed similar effects. An increase in ROS was observed at all three experimental time points resulting in the increase expression of Bax. Bax expression increased the mitochondrial transmembrane permeability (as measured by Mitocapture™) resulting in the activation of initiator caspases which resulted in elevated levels and activation of caspase 3 (BT-20 cells). Annexin V quantification revealed a significant increase in apoptotic cells 24 hours after irradiation in MCF-7- and BT-20 cells exposed to 8 Gy radiation. MDA-MB-231 cells exposed to 8 Gy radiation displayed similar but delayed effects after radiation exposure. ROS production was only significantly increased in MDA-MB-231 cells 24 hours after irradiation. Although Bax expression and mitochondrial permeability were increased in this cell line, the cell cycle analysis revealed no significant increase in the sub-G_1 phase. However, the G_2/M phase was significantly elevated. Annexin V quantification did reveal an increase in the number of apoptotic cells, which may indicate that MDA-MB-231 cells exposed to 8 Gy radiation induced a prolonged mitotic block which resulted in the induction of cell death at a later time point compared to the other two cell lines.

The data above demonstrated that low doses ESE-16, LimPyr1 and 8 Gy radiation activated the Akt and FoxO pathway, while simultaneously inducing mitochondrial apoptosis. As apoptotic cell death was observed in the cells exposed to the individual treatment conditions, the assumption can be made that the apoptotic signaling was more pronounced but could have been delayed by the activation of the survival pathway. As increased levels of phosphorylated Akt and ROS are linked to autophagic cell death (638,639), it is possible that autophagy was induced in cells exposed to the individual treatment conditions. Experiments evaluating the time-dependent induction of autophagy alongside the activation of Akt would provide insight into the mechanisms involved in the delayed apoptosis observed in cells exposed to the individual treatment conditions.

Activation of the survival pathway was not observed in MCF-7-, MDA-MB-231- and BT-20 cells exposed to ESE-16 and LimPyr1 24 hours prior to irradiation. The phosphorylation of Akt and FoxO was significantly decreased in ESE-16 and LimPyr1 presensitized MCF-7-, MDA-MB-231- and BT-20 cells compared to cells exposed to the vehicle control and cells exposed

to the individual conditions. Thus, the survival pathway was inhibited in pre-treated cells which resulted in the induction of the intrinsic apoptotic pathway at an earlier time point compared to cells exposed to the compounds or radiation only. By preventing the phosphorylation of Akt, FoxO can promote the induction of apoptosis and Bax activity was not inhibited. Therefore, Bax was rapidly activated by the increased ROS observed in the combination treatments. This was seen in Bax levels being significantly increased in pre-treated cells compared to the individual treatment conditions. Subsequently the permeabilization of the mitochondria occurred more rapidly in pre-treated cells, as measured by the increase in Mitocapture™. This ultimately increased the activation of the caspase cascade as seen in elevated cleaved caspase 3 levels which resulted in a significant increase in apoptosis (annexin V quantification) in the combination-treated cells compared to the individual treatment conditions. Results obtained from annexin V quantification were visualized using PlasDIC where an increased number of apoptotic bodies were observed in breast cancer cells exposed to the combination treatment conditions. Thus, by preventing the activation of the survival pathway ESE-16 and LimPyr1 pre-treatment induced cell death more rapidly compared to the individual treatment conditions.

By staining cell populations with crystal violet 14 days after exposure to the individual treatment conditions, a significant decrease in long term cellular proliferation was observed. This illustrated that the ability of cells to survive, restore and proliferate was not regained after exposure to LimPyr1, ESE-16 and 4 Gy radiation. These results correlate with previously published data illustrating a significant decrease in colony formation in human colon carcinoma cells (HCT116 and SW613-B3 cells) when exposed to 2-ME for 24 hours (267). The authors did note that the long-term proliferation of the SW613-B3 was less affected by 2-ME exposure when compared to HCT116 cells and attributed it to the intrinsic resistance displayed by SW613-B3 cells when exposed to a panel of drugs (267). A study conducted by Cazarez *et al.* demonstrated increased radiosensitvity in human prostate carcinoma cells (PC3 cells) following pre-treatment with 2-ME (418). Furthermore, a study conducted in our laboratory evaluated the effect of another 2-ME analogue, ESE-15-ol, and radiation on colony survival in a human lung adenocarcinoma epithelial cell line (A549) and an estrogen receptor-positive tumorigenic human epithelial breast cancer cell line (MCF-7)

(640). A549- and MCF-7 cells exposed to low doses ESE-15-ol or 6 Gy radiation revealed a significant decrease in colony formation 10 days after irradiation (640). This suggested that the ability of 2-ME to decrease colony survival was retained in the novel analogues. Although the effect of LimPyr1 has not been evaluated previously it has been published that LimPyr1 has a significant effect on cellular proliferation (547). These findings correlate with those observed in the current study, suggesting that cell death was induced in ESE-16 and LimPyr1 exposed MCF-7-, MDA-MB-231- and BT-20 cells despite the cellular survival pathway being activated.

MCF-7-, MDA-MB-231- and BT-20 cells exposed to ESE-16 and LimPyr1 24 hours prior to radiation revelead a significant decrease in long term cellular proliferation compared to cells exposed to the compounds or 4 Gy radiation only. These finding correlate with the augmented apoptotic signaling, in addition to the decreased expression of survival proteins, observed in pre-treated cells.

5.4 DNA damage and repair

DNA double strand breaks are the most harmful DNA lesions obtained by a cell exposed to radiation (641). These DNA double strand breaks can be repaired via NHEJ and HR (642). DNA double strand breaks are repaired much slower via HR, thus the majority of the double strand breaks are repaired via rapid NHEJ. Furthermore, NHEJ can repair DNA damage throughout the cell cycle, whereas HR is only active in the S and G_2/M phases (642). Damage to the cellular genome is rapidly detected by various DNA damage proteins such as ATM, ATR and DNA-PK (643). The nuclear foci of H2AX are located along the megabase chromatin domains which neighbour the sites of damage. H2AX is rapidly phosphorylated (known as γH2AX in its phosphorylated state) by the aforementioned proteins, and accumulates at the site of damage and serves as a docking site for DNA repair proteins in order to facilitate NHEJ (644). γH2AX foci can be detected by immunofluorescence and are used as a marker of DNA damage since increased levels of foci have been reported to correlate with the degree

of genotoxic insult (644). Once the damaged DNA has been identified, recruitment of DNA repair proteins such as the Ku complex (Ku70/Ku80) is initiated. The Ku complex keeps both ends of the damaged DNA in close proximity, allowing the direct re-joining of the DNA strand by NHEJ. Once the repair of the damaged DNA is complete the Ku complex dissociates from the DNA end and cell cycle progression commences (644).

Genetic toxicity is also studied at a chromosomal level by quantifying micronuclei (645). Damaged chromosomes fail to bind correctly to the mitotic spindles during cellular division. This results in the exclusion of either chromatid fragments or whole chromosomes from the newly formed daughter-cell nuclei. These are then enclosed in nuclear membranes to form micronuclei. Micronuclei exhibit a similar morphology to the main nucleus, apart from being smaller in size (645).

The extent of DNA damage incurred within the cells in the current study was assessed via flow cytometric quantification of γH2AX foci and micronuclei formation. Furthermore, activation of the DNA repair mechanisms was quantified via Ku70 expression using a Western blot. DNA damage and repair experiments were conducted 2 and 24 hours after irradiation to assess whether the combination treatment increased cell death signaling via the increased occurrence of DNA damage, or whether the effect was due to an ineffective damage repair mechanism. MCF-7-, MDA-MB-231- and BT-20 cells exposed to the ESE-16 drug control displayed no significant increase in γH2AX or micronuclei formation over the 24 hour time frame. Additionally, the MCF-7- and BT-20 cells revealed no increase in Ku70, indicating that ESE-16 in itself did not induce DNA damage at low doses. MDA-MB-231 cells displayed a significant increase in Ku70 at the 2 hour termination point, which decreased to basal level after 24 hours. The exact reason for this increase remains to be fully elucidated, as this increase did not coincide with an increase of γH2AX or micronuclei.

MCF-7-, MDA-MB-231- and BT-20 cells pre-treated with ESE-16 24 hours prior to irradiation displayed a significant increase in γH2AX and micronuclei at 2 and 24 hours after irradiation. Furthermore, the expression of Ku70 was significantly increased in all three cell lines, illustrating the activation of DNA repair mechanisms. These DNA repair mechanisms seem to be successful in their execution in MCF-7- and BT-20 cells as was evident by the decreased γH2AX and micronuclei quantification at 24 hours when compared to the earlier time point. This, however, was not observed in ESE-16 pre-treated MDA-MB-231 cells, suggesting that the damage obtained by the MDA-MB-231 cells due to the ESE-16/radiation combination therapy was ineffectively repaired. γH2AX and micronuclei formation were significantly increased in MCF-7-, MDA-MB-231- and BT-20 cells exposed to ESE-16 prior to irradiation compared to the compound only-treated samples. Since DNA damage was not induced in cells exposed to ESE-16 only, it is hypothesized that the damage observed in the ESE-16/radiation combination treatment stems from the radiation. Nevertheless the DNA repair mechanisms were rapidly activated in MDA-MB-231 and BT-20 cells as illustrated by the increased Ku70 expression 2 and 24 hours after irradiation. ESE-16 pre-treated MCF-7 cells displayed an elevation in the Ku70 protein levels only 24 hours after irradiation, suggesting that the activation of the repair mechanism was slightly delayed in this cell line.

The LimPyr1 exposure caused an increase in DNA damage which appeared to be cell line specific. MCF-7 cells exposed to the LimPyr1 drug control displayed no significant increase in DNA damage, whereas LimPyr1 treated MDA-MB-231 cells displayed a significant increase in γH2AX and micronuclei at the 24 hour termination point. The BT-20 cell line appeared to be the most sensitive to the nuclear damaged induced by LimPyr1, as observed at both the 2 and 24 hour termination points. The expression of Ku70 was increased in MDA-MB-231- and BT-20 cells indicating that the DNA damage response was activated and DNA repair proteins were recruited to the site of damage. MCF-7-, MDA-MB-231 and BT-20 cells pre-treated with LimPyr1 24 hours prior to 8 Gy radiation displayed a significant increase in DNA damage as quantified by γH2AX and micronuclei formation 2 and 24 hours after irradiation compared to the vehicle controls. Furthermore, the DNA damage observed in these LimPyr1 pre-treated cells was significantly increased compared to cells exposed to LimPyr1 only. As

MCF-7 cells did not sustain DNA damage due to exposure to the compound, the damage obtained in the LimPyr1/radiation combination therapy is thus proposed to be due to the radiation exposure. However, MDA-MB-231 and BT-20 cells did display increased γH2AX and micronuclei formation in LimPyr1-only treated samples, thus potentially potentiating the damaging effects of the radiation in these cell lines. Compared to the vehicle control, the LimPyr1/radiation treatment significantly increased the expression of Ku70 in all three cell lines 2 and 24 hours after irradiation. The expression of Ku70 was also significantly increased 2 and 24 hours after irradiation in LimPyr1 pre-treated MCF-7- and BT-20 cell lines when compared to cells exposed to the compound only. The MDA-MB-231 cells displayed elevated Ku70 levels 24 hours after irradiation when compared to the compound only.

Essentially, H2AX phosphorylation appeared to be decreased at 2 hours, but increased during the following 24 hours in the combination-treated cells when they were compared to the 8 Gy radiation only-exposed cells. Counterintuitively, micronuclei studies show that the amount of damage induced is equal at 2 hours after irradiation. Thus, the hypothesis was formed that the combination therapy decreased the phosphorylation of H2AX, which in turn decreased the recruitment of Ku70. Initial postulates included an ineffective shuttling of the DNA repair proteins from the cytoplasm to the nucleolus due to the abrogation of the microtubule and actin dynamics. Following irradiation, EGFRs are translocated to the cell nucleus from the cytoplasm (646). Nuclear EGFRs are localized to uncoiled chromatin, allowing DNA repair proteins to rapidly access the site of damage (646). The transport of EGFR form the cytoplasm to the cell nucleus is associated with the Ku complex (Ku70/Ku80). Furthermore, EGFR cytoplasm-nuclear transport is assisted by protein phosphatase 1, which is significantly increased in the nucleus following irradiation. EGFR regulates the activity of DNA-PK by forming a complex with the DNA repair protein kinase (646). Once activated DNA-PK associates with the Ku complex. The Ku complexes are responsible for kinase activation by binding DNA-PK to the broken DNA ends, assisting in the repair of the damaged DNA via NHEJ (647,648). Previously published data illustrated an increase in the sensitivity of A549 cells to radiation by inhibiting the translocation of EGFR into the nucleus

(646). This prevented the activation of DNA-PK, resulting in a decrease in DNA repair, subsequently radiosensitizing A539 cells.

The importance of translocating the mismatch repair proteins, malate dehydrogenase (MDH)2 and 6 into the nucleus following exposure to alkylating agents was highlighted by Christmann *et al.* (649). Mismatches in the DNA base sequences may be induced by base instability or acquired during replication (650). These mismatches are repaired via a process called DNA mismatch repair, which can also process chemical-induced DNA damaged (649). MDH2 plays various roles in the repair of DNA mismatches depending on its binding partner. MDH2 can form a complex with MDH3 in the nucleus to form the mutator S (MutS)β repair complex (651,652). A complex of MDH2 and 6 is known as MutSα (653). MutSα initiates repair in an ATP-dependent manner by binding to base-base mismatches (654,655), whereas MutSβ repairs long mutant loops by binding to longer inserted or deleted mismatches (649). Various cell lines displayed an increase in nuclear MDH2 and 6 levels following exposure to agents that induce O^6-methylguanine (O^6-MeG) lesions in the DNA (649). Following exposure to alkylating agents, O^6-MeG lesions initiated the translocation of MutSα into the nucleus. In the nucleus MutSα binds to the mismatches and complexed with MutLα, which consist of MutL mismatch repair proteins (MutL homolog 1 (MLH1)) and mismatch repair endonuclease (PMS1 homolog 2 (PMS2)) (656). However, in cells expressing a DNA repair protein known as O^6-MeG-DNA methyltransferase (MGMT), no translocation of MutSα was observed. Translocation of MutSα was restored in these cells by inhibiting MGMT (649). The results from this study highlighted the importance of nuclear translocation of MSH2 and 6 in base damage repair, a mechanism initiated by O^6-MeG lesions. Moreover, the mutagenic and carcinogenic response to endogenous methylating species formation or methylating drug exposure may be altered due to defects in the nuclear transport of mismatch proteins (649). By altering the microtubule and actin dynamics ESE-16 and LimPyr1 may affect the cytoplasmic-nuclear trafficking of these molecules. This may result in the induction of cell death due to the damaged DNA not being repaired.

Nuclear repair mechanisms may also be inhibited by ESE-16 and LimPyr1 at a transcriptional or posttranscriptional level. The PI3K-Akt-mTOR pathway plays an important role in cell migration and adhesion, metastasis, cell survival and proliferation, and radioresistance (657-660). A study conducted by Chang *et al.* investigated the effect of DNA repair mechanisms following the inhibition of the Pl3K-Akt-mTOR pathway in radioresistant prostate cancer cells (661). Three radioresistant cell lines (PC-3RR, DU145RR and LNCaPRR) associated with autophagy, inhibition of apoptosis, G_0/G_1 and S phase cell cycle arrest and DNA repair proteins involved in NHEJ and HR were developed by the research team (661). By exposing these radioresistant cell lines to single-agent PI3K-Akt-mTOR inhibitors such as BMK120 (PI3K inhibitor) and Rapamycin (mTOR inhibitor) or dual inhibitors (BEZ235 and PI103) the research team was able to increase the sensitivity of the cells to radiation. Similar results were reported for normal prostate cancer cell lines (DU145, PC-3 and LNCaP) exposed to PI3K-Akt-mTOR pathway inhibitors (661). Moreover, the human prostate epithelial cell line, RWPE-1 was less sensitive to the effects of single or dual PI3K-Akt-mTOR inhibitors, suggesting that these inhibitors target cancer cells, while leaving normal cells less affected (661). The combination of the dual inhibitors (BE2235 and PI103) with radiation resulted in a decrease in colony formation in the resistant cell lines compared to the results obtained from cells treated with a combination of the individual inhibitors prior to irradiation. The decreased colony formation was accompanied by the decrease in the nuclear protein associated with proliferation, Ki67 (661). This led to a significant increase in apoptotic cell death. Due to the fact that the dual PI3K-mTOR inhibitors have a broader effect on genotypes with pro-apoptotic effects compared to the individual inhibitors, an increase in apoptotic cell death was observed is cells treated with the dual inhibitors prior to radiation (662,663).

Results obtained from the aforementioned *in vitro* study revealed an increase in apoptotic cell death, whereas pro-survival mechanisms associated with autophagy were inhibited in radioresistant prostate cancer cells treated with PI3K and mTOR dual inhibitors prior to 6 Gy radiation (661). PI3K-mTOR inhibition significantly increased radiation induced DNA damage, while the NHEJ and HR pathways were diminished under these experimental conditions. Furthermore, the study conducted by Chang *et al.* illustrated the mechanisms involved in

the increased radiosensitivity of radioresistant prostate cancer cells treated with dual PI3K-mTOR inhibitors (661). Results revealed that increased radiosensitivity lies in the redistribution of the cell cycle to the radiosensitive G_2/M phase, while the G_0/G_1 and S cell cycle arrest associated with these radioresistant prostate cancer cells were abolished (661).

A study conducted on acute pancreatitis demonstrated a link between cell death and oxidative DNA damage (664). It has been hypothesized that a decrease in the Ku complex may result due to oxidative stress. The lack of these DNA repair proteins at the DNA damaged site was linked to an increase in p53 and Bax expression, and decreased Bcl-2 expression. This resulted in the activation of the intrinsic apoptotic pathway (664). A combination of the aforementioned mechanisms may be employed by ESE-16 and LimPyr1 to decrease DNA repair, rendering breast cancer cells more radiosensitive. However, further experiments are needed to identify the precise mechanisms involved in the sensitization abilities of these anti-mitotics.

Although potentially contributing to the initial observations, the ineffective cytoplasmic-nuclear shuttling of the DNA repair proteins may not be the exclusive answer to the observation. Signaling molecules released by cells exposed to the combination treatment may be fundamental to the decrease in long-term survival, as demonstrated in clonongenic studies in which cells were treated with conditioned medium. A significant decreased in long term cellular proliferation, together with an increase in the mitochondrial transmembrane permeability and γH2AX and Ku70 expression were observed in cells propgated in the conditioned media obtained from the combination therapy, compared to cells propogated in conditioned media obtained from cells exposed to the individual treatment conditions. Due to the results demonstrating the bystander effect, signaling molecules which may extravasate or be part of an intercellular crosstalk are proposed to play a significant role in the long-term survival of the cells exposed to both treatment modalities. Future investigations will aim to identify this signaling pathway and the molecules involved more specifically. Differences in results from pre-exposure to the microtubule disrupting agent and the LIM kinase inhibitor which depolymerizes actin also highlights the possibility of alternative mechanistic and signaling pathways.

5.5 Radiation-induced resistance due to dose fractionation and radiation-induced bystander effect

As part of a pilot study, ESE-16 and LimPyr1 were assessed for their ability to prevent the development of radiation resistance in a triple receptor-negative breast cancer cell line (BT-20). Furthermore, the radiation-induced bystander effect was assessed in BT-20 cells propogated in conditioned media obtained from cells exposed to ESE-16 and LimPyr1 24 hours prior to irradiation.

Exposure of cells to repetitive smaller doses of ionizing radiation may decrease the cellular response upon subsequent exposure, increasing radiation resistance (665). The cellular mechanisms responsible for the development of radiation resistance are not fully know, however several possible mechanisms have been published in the literature. Radiation resistance may arise from abnormal DNA damage responses, epigenetic modifications in cancer subpopulations (such as cancer stem cells), deregulation of signaling pathways and oncogenic miRNA overproduction (666). The PI3K/Akt and MAPK/nuclear factor kappa-light-chain-enhancer of activated B cells (NF-κB) regulate various cellular signaling pathways such as DNA repair and apoptosis which can be deregulated in radioresistant cells. Additionally, miRNAs are involved in the regulation of signaling pathways induced by radiation and can modulate key components in the above mentioned pathways, further decreasing the sensitivity of cancer cells to radiation (666).

In the current study BT-20 cells were exposed to 8 Gy radiation as a single dose, or fractionated over 4 days (2 Gy per day). Apoptotic signaling was measured via superoxide production as well as changes in the mitochondrial transmembrane potential using flow cytometry. BT-20 cells exposed to fractionated radiation displayed a significant decrease in apoptotic signaling when compared to cells exposed to a single dose of 8 Gy. This indicated the induction of radiation resistance due to dose fractionation, resulting in a decreased apoptotic signal. Similar results were obtained in the differentiated counterparts of human neural progenitor stem cells and normal human fibroblasts (667). Enhanced mitochondrial activity was observed in differentiated cells exposed to long term fractionated radiotherapy

(0.01 and 0.05 Gy/fraction for 31 days). These cells displayed an increase in the mitochondrial transmembrane potential in addition to elevated mitochondrial complex IV activity (667). This enhanced mitochondrial activity replenished the energy demands stemming from chronic DNA damage. Furthermore, a reduction of glutathione (an antioxidant) was observed in differentiated cells exposed to the long term fractionated radiotherapy due to the continuous activation of mitochondrial oxidative phosphorylation. This resulted in increased oxidative stress along with genomic instability (667). In contrast, the mitochondrial activity of human neural progenitor stem cells were not affected by long term fractionated radiotherapy. These cells were resistant to the radiation therapy due to their ability to efficiently repair the damaged DNA (667).

The decreased apoptotic signaling (possible development of radiation resistance) observed in BT-20 cells exposed to fractionated radiotherapy was prevented with the addition of LimPyr1 prior to irradiation. ESE-16, however, did not prevent this response. The mechanism through which LimPyr1 potentially prevents the development of radiation resistance requires additional experiments to identify the signaling pathway involved. It has been published that cancer stem cells display increased activation of the DNA damage checkpoint, conferring resistance to radiation (668), whereas telomere shortening enhances radiosensitivity (669). Therefore, the involvement of telomere damage and cancer stem cells should be investigate as part of the effect of not developing radiation resistance.

The radiation-induced bystander effect is the phenomenon which illustrates the relationship between non-irradiated cells and cells exposed to radiation (670). Non-irradiated cells may exhibit effects such as changes in processes of translation, apoptotic cell death, changes in cell proliferation and gene expression due to signals received from irradiated cells (671).

The cellular response to the bystander signal is cell line specific (672). A study conducted by Gómez-Millán *et al.* used apoptosis and colony survival assays to demonstrate the sensitivity of umbilical-cord stromal stem cells and melanoma skin cancer cells to radiation-induced

bystander signaling (673). Results demonstrated that umbilical-cord stromal stem cells were not sensitive to radiation-conditioned medium, whereas melanoma skin cancer cells displayed increased apoptotic signaling and decreased colony survival (673). Literature suggests that non-neoplastic cells are resistant to radiation-induced bystander signaling. By assessing DNA damage and apoptotic cell death in human bone marrow mesenchymal stem cells and embryonic stem cells exposed to a range of radiation (0.2 to 10 Gy), Sokolov *et al*. demonstrated no evidence of radiation-induced bystander effects when compared to their non-irradiated counterparts (674). This provides a possible mechanism for using human stem cells for regenerative therapy and could assist in the repopulation of normal cells and tissues following radiation-induced damage. The radiation-induced bystander effect was also observed in cancer stem-like cells of the human HT1080 fibrosarcoma cell line which displayed a decrease in colony survival in addition to increased DNA damage (675). These effects were not observed in the normal primary fibroblasts, which were resistant to bystander signaling following low and high LET irradiation (676).

The response generated due to bystander signaling may also depend on the genetic status of the cells. The gene responsible for cell survival after irradiation, known as tumor protein p53 (TP53), is often mutated in cancer cells (677). Colorectal carcinoma cells (HCT116) with wild type TP53 and cells with knockout TP53 genes were exposed to a range of X-ray radiation. Both cells lines, wild-type and knockout, displayed a decrease in cell viability with increased radiation doses (0 to 8 Gy) (677). However, the mode of cell death differed. Cells with knocked out genes displayed an increase in apoptotic cell death, whereas wild type cells were more susceptible to radiation-induced senescence associated with the NFκB pathway (677).

In the current study, the radiation-induced bystander effect was evaluated by transferring conditioned media obtained from cells exposed to radiation and the combination therapies to non-exposed cells. Results illustrated a significant increase in mitochondrial transmembrane permeability and superoxide formation in BT-20 cells propagated in

conditioned media obtained from cells exposed to the ESE-16 and LimPyr1/radiation combination therapies compared to the individual treatment conditions. Furthermore, long term cellular survival was significantly decreased in cells propagated in medium from the combination treatment conditions, compared to cells exposed to the compounds or radiation only. These results suggest that the combination therapies produced a greater apoptotic signal and released soluble factors which are transferred to non-exposed cells, inducing apoptosis via the radiation-induced bystander effect. These molecules may include ROS, cytokines and lipid peroxide products (678). However, further analysis of the radiation-induced bystander effect induced by ESE-16 and LimPyr1/radiation combination therapies are needed to identify the molecules involved in this process.

6. Conclusion

"I may not have gone where I intended to go,

but I think I have ended up where I needed to be."

-Douglas Adams-

Pre-treatment of MCF-7-, MDA-MB-231- and BT-20 cells with ESE-16 and LimPyr1 24 hours prior to 8 Gy radiation resulted in more cell death compared to the individual treatments alone. This effect was highlighted in the long-term proliferation studies, with alternations in signaling evident at 2 and 24 hours post irradiation. ESE-16 and LimPyr1 pre-treatment of breast cancer cells inhibited the activation of the survival pathway by decreasing the phosphorylation of Akt. In its unphosphorylated state, Akt is unable to phosphorylate FoxO1/3a and is thus unable to inhibit the induction of apoptosis via the FoxO1/3a pathway (679). The activation and translocation of Bax to the mitochondria is permitted upon Akt phosphorylation (680). Apoptotic induction was further enhanced in the combination treatments by an increased ROS production, which may initiate the oligomerization of Bax/Bak via tBid (681). The latter inserts megapores into the mitochondrial membrane, reducing the mitochondrial transmembrane potential (681). Subsequently cytochrome *c* is released from the mitochondria into the cytoplasm where it complexes with Apaf-1 in order to form the procaspase-9-activating apoptosome. The latter activates the initiator caspase 9 which initiates a caspase cascade culminating in the activation of the executer caspase 3 (680).

Radiation-induced DNA double strand breaks result in the activation of the DNA damage response (682). The latter results in the phosphorylation of H2AX which accumulates at the site of damage and recruits DNA repair proteins such as Ku70/Ku80 (682). The anti-mitotic effect of LimPyr1 and ESE-16 may theoretically have rendered the chromosomes more exposed to radiation damage (increased micronuclei), although the differences between the

combination effect and radiation alone at the 24 hour time point was not marked. However, by altering the cytoskeleton dynamics, phosphorylation of H2AX may be delayed resulting in decreased Ku70 binding to DNA breaks. This potential delay in DNA repair may possibly account for the increase in apoptosis (683).

Interestingly, γH2AX and Ku70 expression were also increased indirectly as seen in experiments examining the radiation-induced bystander effect. This illustrates the production of extracellular molecule(s) which are potentially present in conditioned medium without the direct effects of the treatment, and alludes to an additional mechanism other than the direct effect on cytoskeletal dynamics. Elevated ROS production with a concomitant decrease in the mitochondrial transmembrane potential was demonstrated in these cells, which ultimately led to a decrease in long term cellular survival as assessed via long term proliferation studies. Furthermore, LimPyr1, but not ESE-16, was able to prevent the development of radiation resistance in BT-20 cells.

Thus, the working hypothesis was formed that MCF-7-, MDA-MB-231-, and BT-20 cells exposed to the ESE-16 and LimPyr1/radiation combination therapy exhibit significantly increased apoptotic cell death compared to the individual treatment conditions (Figure 6.1). The mechanisms involved prevent the activation of the survival pathway, increase the induction of the intrinsic apoptotic pathway and delay the repair of radiation-induced DNA damage. The precise mechanisms by which ESE-16 and LymPyr1 increased the sensitivity of breast cancer cells to radiation, and the identification of the molecules transferred from treated cells to non-exposed cells, as well as those that prevent radioresistance need to be further studied. Future molecular and mechanistic studies over increased time points post-exposure should aim to elucidate the molecular mechanisms responsible for ESE-16 and LimPyr1 radiosensitization, as well as aim to validate the safety and efficacy of this combination treatment *in vivo*.

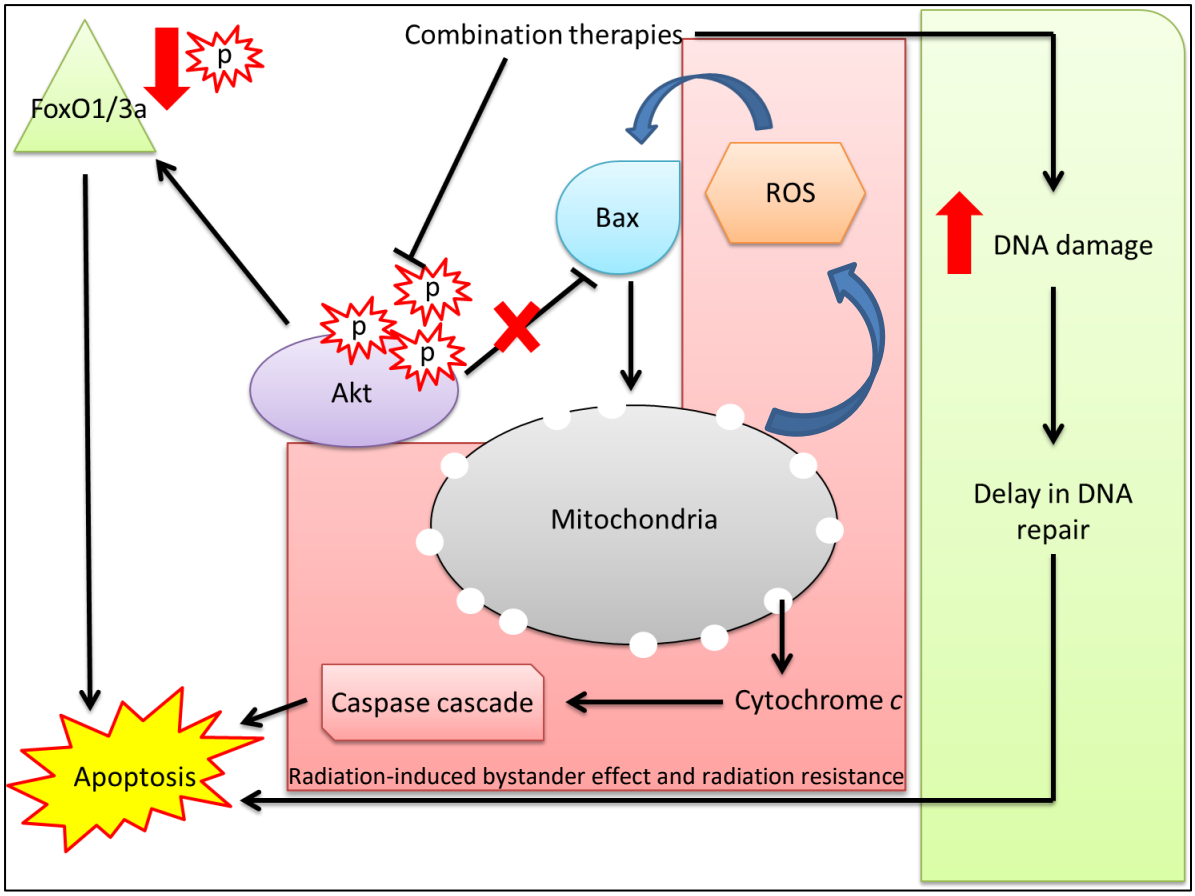

Figure 6.1: Summary of proposed signaling pathways induced by ESE-16 and LimPyr1 to increase the sensitivity of breast cancer cells to radiation. Pre-treatment of MCF-7-, MDA-MB-231- and BT-20 cells resulted in the inhibition of Akt phosphorylation. A decrease in Akt phosphorylation decreased the phosphorylation of FoxO1/03, resulting in the induction of apoptosis. This, in addition to an increased ROS production may permit the activation and translocation of Bax to the mitochondrial. The latter initiates the insertion of pores into the mitochondrial membrane resulting in the release of cytochrome *c*. The resultant caspase cascade increased apoptotic cell death, and is executed by caspase 3. The combination treatment conditions induced more DNA damage 24 hours after irradiation in BT-20 cells compared to the individual treatment conditions, however the recruitment of DNA repair mechanisms may be delayed. A resultant prolonged mitotic block may contribute in rendering the cells more susceptible to apoptotic induction. Unknown extracellular messengers also appear to have a transferrable effect on non-exposed cells, decreasing their long-term survival. Image created using Microsoft Power Point 2010.

7. Acknowledgement of funding

The study was financially supported by the National Research Foundation (NRF), the Cancer Association of South Africa (CANSA), the Medical Research Council (MRC), the Research Committee (School of Medicine) of the University of Pretoria (RESCOM), the Struwig-Germeshuysen Trust, the French Embassy and La Ligne Foundation Arc. Academic achievement bursaries were awarded by the University of Pretoria during the completion of the project.

8. References

(1) Breasted JH. The Edwin Smith Surgical Papyrus: published in facsimile and hieroglyphic transliteration with translation and commentary in two volumes. University of Chicago Press Chicago; 1930.

(2) Brawanski A. On the myth of the Edwin Smith papyrus: is it magic or science? Acta. Neurochir. 2012;154(12):2285-2291.

(3) Rayter Z, Mansi J. Medical therapy of breast cancer. Cambridge University Press; 2003.

(4) Porter R. The Greatest Benefit to Mankind: A Medical History of Humanity (The Norton History of Science). WW Norton & Company; 1999.

(5) Papavramidou N, Papavramidis T, Demetriou T. Ancient Greek and Greco–Roman methods in modern surgical treatment of cancer. Ann. Surg. Oncol. 2010;17(3):665-667.

(6) Cotlar AM, Dubose JJ, Rose DM. History of surgery for breast cancer: radical to the sublime. Curr. Surg. 2003;60(3):329-337.

(7) Mayoclinic.org [Internet]. Breast cancer Treatments and drugs - Mayo Clinic. [cited 2014 March 23]. Available from: http://www.mayoclinic.org/diseases-conditions/breast-cancer/basics/treatment/con-20029275.

(8) World Health Organization.int [Internet]. Cancer [cited 2018 August]. Available from: https://www.who.int/news-room/fact-sheets/detail/cancer.

(9) Breastcancer.org. [Internet]. What Is Breast Cancer? [updated 2015 Oct. 23; cited 2015 Dec. 7]. Available from: http://www.breastcancer.org/symptoms/understand_bc/what_is_bc.

(10) National Cancer Institute at the National Institutes of Health [Internet]. BRCA1 and BRCA2: Cancer risk and Genetic Testing. Maryland: National Cancer Institute; [updated 2014 Jan. 22; cited 2014 Mar. 23]. Available from: http://www.cancer.gov/cancertopics/factsheet/Risk/BRCA.

(11) Kelsey JL, Bernstein L. Epidemiology and prevention of breast cancer. Annu. Rev. Public Health. 1996;17(1):47-67.

(12) Runnebaum IB, Nagarajan M, Bowman M, Soto D, Sukumar S. Mutations in p53 as potential molecular markers for human breast cancer. Proc. Natl. Acad. Sci. U.S.A. 1991;88(23):10657-10661.

(13) Armstrong B, Doll R. Environmental factors and cancer incidence and mortality in different countries, with special reference to dietary practices. Int. J. Cancer. 1975;15(4):617-631.

(14) Ramalho I, Campos S, Rebelo T, Figueiredo Dias M. A scary onset of a rare and aggressive type of primary breast sarcoma: A case report. Case Rep. Oncol. 2016;9(3):796-801.

(15) Xiao Y, Ma D, Ruan M, Zhao S, Liu X, Jiang Y, et al. Mixed invasive ductal and lobular carcinoma has distinct clinical features and predicts worse prognosis when stratified by estrogen receptor status. Sci. Rep. 2017;7(1):10380.

(16) Rakha EA, Reis-Filho J, Baehner F, Dabbs DJ, Decker T, Eusebi V, et al. Breast cancer prognostic classification in the molecular era: the role of histological grade. Breast Cancer Res. 2010;12(4):207.

(17) breastcancer.org [Internet]. Breast cancer stages. [cited 2018 November]. Available from: https://www.breastcancer.org/symptoms/diagnosis/staging.

(18) Kwan ML, Kushi LH, Weltzien E, Maring B, Kutner SE, Fulton RS, et al. Epidemiology of breast cancer subtypes in two prospective cohort studies of breast cancer survivors. Breast Cancer Res. 2009;11(3):R31.

(19) Wood AJJ, Shapiro CL, Recht A. Side effects of adjuvant treatment of breast cancer. N. Engl. J. Med. 2001;344(26):1997-2008.

(20) Bland KI, Copeland EM, Klimberg VS, Gradishar WJ. The breast: comprehensive management of benign and malignant diseases. 5th ed. Elsevier Inc.; 2017. p.1113.

(21) Chen S, Masri S, Wang X, Phung S, Yuan Y, Wu X. What do we know about the mechanisms of aromatase inhibitor resistance? J. Steroid Biochem. Mol. Biol. 2006;102(1):232-240.

(22) Reed MJ, Purohit A, Woo L, Newman SP, Potter BVL. Steroid sulfatase: molecular biology, regulation, and inhibition. Endocr. Rev. 2005;26(2):171-202.

(23) Alberts B, Bray D, Hopkin K, Johnson A, Lewis J, Raff M, et al. Essential cell biology. 4th ed. New York: Garland Science; 2013. p. 603-604.

(24) Cooper GM. The Cell: A Molecular Approach. 6th ed. Washington, DC: ASM press; 2000.

(25) Budirahardja Y, Gonczy P. Coupling the cell cycle to development. Development. 2009;136(17):2861-2872.

(26) Sridhar J, Akula N, Pattabiraman N. Selectivity and potency of cyclin-dependent kinase inhibitors. AAPS J. 2006;8(1):E204-221.

(27) Sánchez I, Dynlacht BD. New insights into cyclins, CDKs, and cell cycle control. Semin. Cell Dev. Biol. 2005; 16(3): 311-321.

(28) Malumbres M, Barbacid M. Cell cycle, CDKs and cancer: a changing paradigm. Nat. Rev. Cancer. 2009;9(3):153-166.

(29) Vermeulen K, Van Bockstaele DR, Berneman ZN. The cell cycle: a review of regulation, deregulation and therapeutic targets in cancer. Cell Prolif. 2003;36(3):131-149.

(30) Salaun P, Rannou Y, Claude P. Cdk1, Plks, Auroras, and Neks: the mitotic bodyguards. Adv. Exp. Med. Biol. 2008;617:41-56.

(31) Neganova I, Lako M. G_1 to S phase cell cycle transition in somatic and embryonic stem cells. J. Anat. 2008;213(1):30-44.

(32) Zetterberg A, Larsson O. Kinetic analysis of regulatory events in G_1 leading to proliferation or quiescence of Swiss 3T3 cells. Proc. Natl. Acad. Sci. U.S.A. 1985;82(16):5365-5369.

(33) Williams GH, Stoeber K. Cell cycle markers in clinical oncology. Curr. Opin. Cell Biol. 2007;19(6):672-679.

(34) Weinberg RA. The retinoblastoma protein and cell cycle control. Cell. 1995;81(3):323-330.

(35) Malumbres M, Barbacid M. Mammalian cyclin-dependent kinases. Trends Biochem. Sci. 2005;30(11):630-641.

(36) VanArsdale T, Boshoff C, Arndt KT, Abraham RT. Molecular pathways: Targeting the cyclin D-CDK4/6 axis for cancer treatment. Clin. Cancer Res. 2015;21(13):2905-2910.

(37) Adams PD. Regulation of the retinoblastoma tumor suppressor protein by cyclin/cdks. Biochim. Biophys. Acta. 2001;1471(3):M123-M133.

(38) Stander BA, Joubert F, Tu C, Sippel KH, McKenna R, Joubert AM. Signaling pathways of ESE-16, an antimitotic and anticarbonic anhydrase estradiol analog, in breast cancer cells. PLoS ONE. 2013;8(1):e53853.

(39) Tessema M, Lehmann U, Kreipe H. Cell cycle and no end. Virchows Arch. 2004;444(4):313-323.

(40) Ford HL, Pardee AB. Cancer and the cell cycle. J. Cell. Biochem. 1999; Suppl 32-33:166-172.

(41) DesMarais V, Macaluso F, Condeelis J, Bailly M. Synergistic interaction between the Arp2/3 complex and cofilin drives stimulated lamellipod extension. J. Cell. Sci. 2004;117:3499-3510.

(42) Planas-Silva MD, Weinberg RA. The restriction point and control of cell proliferation. Curr. Opin. Cell Biol. 1997;9(6):768-772.

(43) Schafer KA. The cell cycle: a review. Vet. Pathol. 1998;35(6):461-478.

(44) Bell SP, Dutta A. DNA replication in eukaryotic cells. Annu. Rev. Biochem. 2002;71(1):333-374.

(45) Henneke G, Koundrioukoff S, Hubscher U. Multiple roles for kinases in DNA replication. EMBO Rep. 2003;4(3):252-256.

(46) Lei M, Tye BK. Initiating DNA synthesis: from recruiting to activating the MCM complex. J. Cell. Sci. 2001;114:1447-1454.

(47) Kishimoto T. Entry into mitosis: a solution to the decades-long enigma of MPF. Chromosoma. 2015;124(4):417-428.

(48) Schottenfeld D, Fraumeni Jr JF. Cancer epidemiology and prevention. 3rd ed. New York: Oxford University Press; 2006.

(49) Ferrari S. Protein kinases controlling the onset of mitosis. Cell. Mol. Life Sci. 2006;63(7-8):781-795.

(50) Nigg EA. Cell division: mitotic kinases as regulators of cell division and its checkpoints. Nat. Rev. Mol. Cell Biol. 2001;2(1):21-32.

(51) Hermeking H, Benzinger A. 14-3-3 proteins in cell cycle regulation. Semin. Cancer Biol. 2006;16(3):183-192.

(52) Dai W, Huang X, Ruan Q. Polo-like kinases in cell cycle checkpoint control. Front. Biosci. 2003;8:d1128-d1133.

(53) Okouneva T, Azarenko O, Wilson L, Littlefield BA, Jordan MA. Inhibition of centromere dynamics by eribulin (E7389) during mitotic metaphase. Mol. Cancer Ther. 2008;7(7):2003-2011.

(54) Skibbens RV, Skeen VP, Salmon ED. Directional instability of kinetochore motility during chromosome congression and segregation in mitotic newt lung cells: a push-pull mechanism. J. Cell Biol. 1993;122(4):859-875.

(55) Hartwell LH, Weinert TA. Checkpoints: controls that ensure the order of cell cycle events. Science. 1989;246(4930):629-634.

(56) Bartek J, Lukas C, Lukas J. Checking on DNA damage in S phase. Nat. Rev. Mol. Cell Biol. 2004;5(10):792-804.

(57) Thornton TM, Rincon M. Non-classical p38 map kinase functions: cell cycle checkpoints and survival. Int. J. Biol. Sci. 2009;5(1):44-51.

(58) Agarwal ML, Taylor WR, Chernov MV, Chernova OB, Stark GR. The p53 network. J. Biol. Chem. 1998;273(1):1-4.

(59) Levine AJ. p53, the cellular gatekeeper for growth and division. Cell. 1997;88(3):323-331.

(60) Fang G, Yu H, Kirschner MW. The checkpoint protein MAD2 and the mitotic regulator CDC20 form a ternary complex with the anaphase-promoting complex to control anaphase initiation. Genes Dev. 1998;12(12):1871-1883.

(61) Taylor WR, Stark GR. Regulation of the G2/M transition by p53. Oncogene. 2001;20(15):1803-1815.

(62) Tyner A. A new year, a new role for p21: Mediating degradation of Cyclin B1. Cell Cycle. 2009;8(2):183-184.

(63) Lopez-Girona A, Furnari B, Mondesert O, Russell P. Nuclear localization of Cdc25 is regulated by DNA damage and a 14-3-3 protein. Nature. 1999;397(6715):172-175.

(64) Shibata A, Barton O, Noon AT, Dahm K, Deckbar D, Goodarzi AA, et al. Role of ATM and the damage response mediator proteins 53BP1 and MDC1 in the maintenance of G(2)/M checkpoint arrest. Mol. Cell Biol. 2010;30(13):3371-3383.

(65) Roshak AK, Capper EA, Imburgia C, Fornwald J, Scott G, Marshall LA. The human polo-like kinase, PLK, regulates cdc2/cyclin B through phosphorylation and activation of the cdc25C phosphatase. Cell Signal. 2000;12(6):405-411.

(66) Skaar JR, Pagano M. Control of cell growth by the SCF and APC/C ubiquitin ligases. Curr. Opin. Cell Biol. 2009;21(6):816-824.

(67) Peters J. The anaphase promoting complex/cyclosome: a machine designed to destroy. Nat. Rev. Mol. Cell Biol. 2006;7(9):644-656.

(68) Potapova TA, Daum JR, Pittman BD, Hudson JR, Jones TN, Satinover DL, et al. The reversibility of mitotic exit in vertebrate cells. Nature. 2006;440(7086):954-958.

(69) Sudakin V, Chan GK, Yen TJ. Checkpoint inhibition of the APC/C in HeLa cells is mediated by a complex of BUBR1, BUB3, CDC20, and MAD2. J. Cell Biol. 2001;154(5):925-936.

(70) Li R, Murray AW. Feedback control of mitosis in budding yeast. Cell. 1991;66(3):519-531.

(71) Hoyt MA, Totis L, Roberts BT. *S. cerevisiae* genes required for cell cycle arrest in response to loss of microtubule function. Cell. 1991;66(3):507-517.

(72) Herzog F, Primorac I, Dube P, Lenart P, Sander B, Mechtler K, et al. Structure of the anaphase-promoting complex/cyclosome interacting with a mitotic checkpoint complex. Science. 2009;323(5920):1477-1481.

(73) Matson DR, Stukenberg PT. Spindle poisons and cell fate: a tale of two pathways. Mol. Interv. 2011;11(2):141-150.

(74) Kroemer G, El-Deiry W, Golstein P, Peter ME, Vaux D, Vandenabeele P, et al. Classification of cell death: recommendations of the Nomenclature Committee on Cell Death. Cell Death Differ. 2005;12 (Suppl 2):1463-1467.

(75) Kumar V, Abbas AK, Fausto N. Robbins and Cotran Pathologic Basis of Disease. 7th ed. Philadelphia: Elsevier;2005:p.3-46.

(76) Lemasters JJ. Dying a thousand deaths: redundant pathways from different organelles to apoptosis and necrosis. Gastroenterology. 2005;129(1):351-360.

(77) Luke CJ, Pak SC, Askew YS, Naviglia TL, Askew DJ, Nobar SM, et al. An intracellular serpin regulates necrosis by inhibiting the induction and sequelae of lysosomal injury. Cell. 2007;130(6):1108-1119.

(78) Turk B, Stoka V. Protease signalling in cell death: caspases versus cysteine cathepsins. FEBS Lett. 2007;581(15):2761-2767.

(79) Zong WX, Thompson CB. Necrotic death as a cell fate. Genes Dev. 2006;20(1):1-15.

(80) Malhi H, Gores GJ, Lemasters JJ. Apoptosis and necrosis in the liver: a tale of two deaths? Hepatology. 2006;43:S31-S44.

(81) Leist M, Single B, Castoldi AF, Kuhnle S, Nicotera P. Intracellular adenosine triphosphate (ATP) concentration: a switch in the decision between apoptosis and necrosis. J. Exp. Med. 1997;185(8):1481-1486.

(82) Conus S, Simon H. Cathepsins: key modulators of cell death and inflammatory responses. Biochem. Pharmacol. 2008;76(11):1374-1382.

(83) Conus S, Perozzo R, Reinheckel T, Peters C, Scapozza L, Yousefi S, et al. Caspase-8 is activated by cathepsin D initiating neutrophil apoptosis during the resolution of inflammation. J. Exp. Med. 2008;205(3):685-698.

(84) Jagtap P, Szabó C. Poly (ADP-ribose) polymerase and the therapeutic effects of its inhibitors. Nat. Rev. Drug Discov. 2005;4(5):421-440.

(85) Los M, Mozoluk M, Ferrari D, Stepczynska A, Stroh C, Renz A, et al. Activation and caspase-mediated inhibition of PARP: a molecular switch between fibroblast necrosis and apoptosis in death receptor signaling. Mol. Cell Biol. 2002;13(3):978-988.

(86) Martin SJ, Reutelingsperger CP, McGahon AJ, Rader JA, van Schie RC, LaFace DM, et al. Early redistribution of plasma membrane phosphatidylserine is a general feature of apoptosis regardless of the initiating stimulus: inhibition by overexpression of Bcl-2 and Abl. J. Exp. Med. 1995;182(5):1545-1556.

(87) Ziegler U, Groscurth P. Morphological features of cell death. Physiology. 2004;19(3):124-128.

(88) Elmore S. Apoptosis: a review of programmed cell death. Toxicol. Pathol. 2007;35(4):495-516.

(89) Savill J, Fadok V. Corpse clearance defines the meaning of cell death. Nature. 2000;407(6805):784-788.

(90) Kurosaka K, Takahashi M, Watanabe N, Kobayashi Y. Silent cleanup of very early apoptotic cells by macrophages. J. Immunol. 2003;171(9):4672-4679.

(91) Koopman G, Reutelingsperger CP, Kuijten GA, Keehnen RM, Pals ST, van Oers MH. Annexin V for flow cytometric detection of phosphatidylserine expression on B cells undergoing apoptosis. Blood. 1994;84(5):1415-1420.

(92) Werdehausen R, Braun S, Essmann F, Schulze-Osthoff K, Walczak H, Lipfert P, et al. Lidocaine induces apoptosis via the mitochondrial pathway independently of death receptor signaling. Anesthesiology. 2007;107(1):136-143.

(93) Thorburn A. Apoptosis and autophagy: regulatory connections between two supposedly different processes. Apoptosis. 2008;13(1):1-9.

(94) Boldin MP, Goncharov TM, Goltseve YV, Wallach D. Involvement of MACH, a novel MORT1/FADD-interacting protease, in Fas/APO-1-and TNF receptor–induced cell death. Cell. 1996;85(6):803-815.

(95) Muzio M, Chinnaiyan AM, Kischkel FC, O'Rourke K, Shevchenko A, Ni J, et al. FLICE, a novel FADD-homologous ICE/CED-3–like protease, is recruited to the CD95 (Fas/APO-1) death-inducing signaling complex. Cell. 1996;85(6):817-827.

(96) Li P, Nijhawan D, Budihardjo I, Srinivasula SM, Ahmad M, Alnemri ES, et al. Cytochrome c and dATP-dependent formation of Apaf-1/caspase-9 complex initiates an apoptotic protease cascade. Cell. 1997;91(4):479-489.

(97) Ashkenazi A, Dixit VM. Apoptosis control by death and decoy receptors. Curr. Opin. Cell Biol. 1999;11(2):255-260.

(98) Locksley RM, Killeen N, Lenardo MJ. The TNF and TNF receptor superfamilies: integrating mammalian biology. Cell. 2001;104(4):487-501.

(99) Wang L, Yang JK, Kabaleeswaran V, Rice AJ, Cruz AC, Park AY, et al. The Fas-FADD death domain complex structure reveals the basis of DISC assembly and disease mutations. Nat. Struct. Mol. Biol. 2010;17(11):1324-1329.

(100) de Vries EG, Gietema JA, de Jong S. Tumor necrosis factor-related apoptosis-inducing ligand pathway and its therapeutic implications. Clin. Cancer Res. 2006;12(8):2390-2393.

(101) Bensaad K, Cheung EC, Vousden KH. Modulation of intracellular ROS levels by TIGAR controls autophagy. EMBO J. 2009;28(19):3015-3026.

(102) Cai H. Hydrogen peroxide regulation of endothelial function: origins, mechanisms, and consequences. Cardiovasc. Res. 2005;68(1):26-36.

(103) Pelicano H, Feng L, Zhou Y, Carew JS, Hileman EO, Plunkett W, et al. Inhibition of mitochondrial respiration: a novel strategy to enhance drug-induced apoptosis in human leukemia cells by a reactive oxygen species-mediated mechanism. J. Biol. Chem. 2003;278(39):37832-37839.

(104) Pan J, Hong M, Ren J. Reactive oxygen species: a double-edged sword in oncogenesis. World J. Gastroenterol. 2009;15(14):1702-1707.

(105) Sena LA, Chandel NS. Physiological roles of mitochondrial reactive oxygen species. Mol. Cell. 2012;48(2):158-167.

(106) Deeb D, Gao X, Jiang H, Janic B, Arbab AS, Rojanasakul Y, et al. Oleanane triterpenoid CDDO-Me inhibits growth and induces apoptosis in prostate cancer cells through a ROS-dependent mechanism. Biochem. Pharmacol. 2010;79(3):350-360.

(107) Eskes R, Desagher S, Antonsson B, Martinou JC. Bid induces the oligomerization and insertion of Bax into the outer mitochondrial membrane. Mol. Cell Biol. 2000;20(3):929-935.

(108) Ryter SW, Kim HP, Hoetzel A, Park JW, Nakahira K, Wang X, et al. Mechanisms of cell death in oxidative stress. Antioxid. Redox Signal. 2007;9(1):49-89.

(109) Eisenberg-Lerner A, Kimchi A. The paradox of autophagy and its implication in cancer etiology and therapy. Apoptosis. 2009;14(4):376-391.

(110) Zhao Y, Yang J, Liao W, Liu X, Zhang H, Wang S, et al. Cytosolic FoxO1 is essential for the induction of autophagy and tumour suppressor activity. Nat. Cell Biol. 2010;12(7):665-675.

(111) Begg AC, Stewart FA, Vens C. Strategies to improve radiotherapy with targeted drugs. Nat. Rev. Cancer. 2011;11(4):239-253.

(112) Delaney G, Jacob S, Featherstone C, Barton M. The role of radiotherapy in cancer treatment: estimating optimal utilization from a review of evidence-based clinical guidelines. Cancer. 2005;104(6):1129-1137.

(113) Durante M, Loeffler JS. Charged particles in radiation oncology. Nat. Rev. Clin. Oncol. 2010;7(1):37-43.

(114) Peters LJ, Withers HR, Thames HD,J, Fletcher GH. Tumor radioresistance in clinical radiotherapy. Int. J. Radiat. Oncol. Biol. Phys. 1982;8(1):101-108.

(115) West CM, Davidson SE, Hendry JH, Hunter RD. Prediction of cervical carcinoma response to radiotherapy. Lancet. 1991;338(8770):818.

(116) Maier P, Hartmann L, Wenz F, Herskind C. Cellular pathways in response to ionizing radiation and their targetability for tumor radiosensitization. Int. J. Mol. Sci. 2016;17(1):102.

(117) Feyer PC, Steingraeber M. Radiotherapy of Bone Metastasis in Breast Cancer Patients - Current Approaches. Breast Care (Basel). 2012;7(2):108-112.

(118) Prise KM, O'Sullivan JM. Radiation-induced bystander signalling in cancer therapy. Nat. Rev. Cancer. 2009;9(5):351-360.

(119) Maier P, Wenz F, Herskind C. Radioprotection of normal tissue cells. Strahlenther Onkol. 2014;190(8):745-752.

(120) Emami B, Lyman J, Brown A, Cola L, Goitein M, Munzenrider JE, et al. Tolerance of normal tissue to therapeutic irradiation. Int. J. Radiat. Oncol. Biol. Phys. 1991;21(1):109-122.

(121) Herskind C, Wenz F. Radiobiological aspects of intraoperative tumour-bed irradiation with low-energy X-rays (LEX-IORT). Transl. Cancer Res. 2014;3(1):3-17.

(122) Han W, Yu KN. Ionizing radiation, DNA double strand break and mutation. Adv. Genet. 2010;4:197-210.

(123) Kane SA. Introduction to physics in modern medicine. 2nd ed. USA: Taylor & Francis; 2009. p. 313-314.

(124) Herskind C, Westergaard O. Inactivation of a single eucaryotic gene irradiated *in vitro* in transcriptionally active chromatin form. Radiat. Res. 1986;106(3):331-344.

(125) Herskind C, Westergaard O. Variable protection by OH scavengers against radiation-induced inactivation of isolated transcriptionally active chromatin: the influence of secondary radicals. Radiat. Res. 1988;114(1):28-41.

(126) Shiloh Y. ATM and related protein kinases: safeguarding genome integrity. Nat. Rev. Cancer. 2003;3(3):155-168.

(127) Abraham RT. Cell cycle checkpoint signaling through the ATM and ATR kinases. Genes Dev. 2001;15(17):2177-2196.

(128) Stracker TH, Roig I, Knobel PA, Marjanovic M. The ATM signaling network in development and disease. Front Genet. 2013;4:37.

(129) Stokes MP, Rush J, Macneill J, Ren JM, Sprott K, Nardone J, et al. Profiling of UV-induced ATM/ATR signaling pathways. Proc. Natl. Acad. Sci. U.S.A. 2007;104(50):19855-19860.

(130) Lukas J, Lukas C, Bartek J. Mammalian cell cycle checkpoints: signalling pathways and their organization in space and time. DNA repair. 2004;3(8-9):997-1007.

(131) Zhou BS, Bartek J. Targeting the checkpoint kinases: chemosensitization versus chemoprotection. Nat. Rev. Cancer. 2004;4(3):216-225.

(132) Zhang XP, Liu F, Wang W. Two-phase dynamics of p53 in the DNA damage response. Proc. Natl. Acad. Sci. U.S.A. 2011;108(22):8990-8995.

(133) Gudkov AV, Komarova EA. The role of p53 in determining sensitivity to radiotherapy. Nat. Rev. Cancer. 2003;3(2):117-129.

(134) Lane DP, Benchimol S. p53: oncogene or anti-oncogene. Genes Dev. 1990;4(1):1-8.

(135) Chapman JR, Taylor MRG, Boulton SJ. Playing the end game: DNA double-strand break repair pathway choice. Mol. Cell. 2012;47(4):497-510.

(136) Fenech M, Kirsch-Volders M, Natarajan AT, Surralles J, Crott JW, Parry J, et al. Molecular mechanisms of micronucleus, nucleoplasmic bridge and nuclear bud formation in mammalian and human cells. Mutagenesis. 2011;26(1):125-132.

(137) Lieber MR. The mechanism of double-strand DNA break repair by the nonhomologous DNA end-joining pathway. Annu. Rev. Biochem. 2010;79:181-211.

(138) Ma Y, Pannicke U, Schwarz K, Lieber MR. Hairpin opening and overhang processing by an Artemis/DNA-dependent protein kinase complex in nonhomologous end joining and V (D) J recombination. Cell. 2002;108(6):781-794.

(139) Chernikova SB, Game JC, Brown JM. Inhibiting homologous recombination for cancer therapy. Cancer Biol. Ther. 2012;13(2):61-68.

(140) Bunting SF, Callén E, Wong N, Chen H, Polato F, Gunn A, et al. 53BP1 inhibits homologous recombination in Brca1-deficient cells by blocking resection of DNA breaks. Cell. 2010;141(2):243-254.

(141) Bouwman P, Aly A, Escandell JM, Pieterse M, Bartkova J, van dG, et al. 53BP1 loss rescues BRCA1 deficiency and is associated with triple-negative and BRCA-mutated breast cancers. Nat. Struct. Mol. Biol. 2010;17(6):688-695.

(142) Ianzini F, Bertoldo A, Kosmacek EA, Phillips SL, Mackey MA. Lack of p53 function promotes radiation-induced mitotic catastrophe in mouse embryonic fibroblast cells. Cancer Cell Int. 2006;6(11):p1-8.

(143) Eriksson D, Stigbrand T. Radiation-induced cell death mechanisms. Tumor Biol. 2010;31(4):363-372.

(144) Eriksson D, Lofroth PO, Johansson L, Riklund KA, Stigbrand T. Cell cycle disturbances and mitotic catastrophes in HeLa Hep2 cells following 2.5 to 10 Gy of ionizing radiation. Clin. Cancer Res. 2007;13(18):5501s-5508s.

(145) Dodson H, Wheatley SP, Morrison CG. Involvement of centrosome amplification in radiation-induced mitotic catastrophe. Cell Cycle. 2007;6(3):364-370.

(146) Löffler H, Lukas J, Bartek J, Krämer A. Structure meets function—centrosomes, genome maintenance and the DNA damage response. Exp. Cell Res. 2006;312(14):2633-2640.

(147) Farhat M, Poissonnier A, Hamze A, Ouk-Martin C, Brion JD, Alami M, et al. Reversion of apoptotic resistance of TP53-mutated Burkitt lymphoma B-cells to spindle poisons by exogenous activation of JNK and p38 MAP kinases. Cell Death Dis. 2014;5(5):e1201.

(148) Castedo M, Perfettini J, Roumier T, Andreau K, Medema R, Kroemer G. Cell death by mitotic catastrophe: a molecular definition. Oncogene. 2004;23(16):2825-2837.

(149) Erenpreisa J, Kalejs M, Ianzini F, Kosmacek EA, Mackey MA, Emzinsh D, et al. Segregation of genomes in polyploid tumour cells following mitotic catastrophe. Cell Biol. Int. 2005;29(12):1005-1011.

(150) Fenech M. The *in vitro* micronucleus technique. Mutat. Res. 2000;455(1):81-95.

(151) Holland N, Bolognesi C, Kirsch-Volders M, Bonassi S, Zeiger E, Knasmueller S, et al. The micronucleus assay in human buccal cells as a tool for biomonitoring DNA damage: the HUMN project perspective on current status and knowledge gaps. Mutat. Res. 2008;659(1):93-108.

(152) Samanta S, Dey P. Micronucleus and its applications. Diagn. Cytopathol. 2012;40(1):84-90.

(153) Alvarez S, Drané P, Meiller A, Bras M, Deguin-Chambon V, Bouvard V, et al. A comprehensive study of p53 transcriptional activity in thymus and spleen of γ irradiated

mouse: High sensitivity of genes involved in the two main apoptotic pathways. Int. J. Radiat. Biol. 2006;82(11):761-770.

(154) Findley HW, Gu L, Yeager AM, Zhou M. Expression and regulation of Bcl-2, Bcl-xl, and Bax correlate with p53 status and sensitivity to apoptosis in childhood acute lymphoblastic leukemia. Blood. 1997;89(8):2986-2993.

(155) Zhan Q, Fan S, Bae I, Guillouf C, Liebermann DA, O'Connor PM, et al. Induction of bax by genotoxic stress in human cells correlates with normal p53 status and apoptosis. Oncogene. 1994;9(12):3743-3751.

(156) Michalak EM, Villunger A, Adams JM, Strasser A. In several cell types tumour suppressor p53 induces apoptosis largely via Puma but Noxa can contribute. Cell Death Differ. 2008;15(6):1019-1029.

(157) Erlacher M, Michalak EM, Kelly PN, Labi V, Niederegger H, Coultas L, et al. BH3-only proteins Puma and Bim are rate-limiting for gamma-radiation- and glucocorticoid-induced apoptosis of lymphoid cells *in vivo*. Blood. 2005;106(13):4131-4138.

(158) Jeffers JR, Parganas E, Lee Y, Yang C, Wang J, Brennan J, et al. Puma is an essential mediator of p53-dependent and-independent apoptotic pathways. Cancer Cell 2003;4(4):321-328.

(159) Jin Z, El-Deiry W. Overview of cell death signaling pathways. Cancer Biol. Ther. 2005;4(2):147-171.

(160) Riedl SJ, Shi Y. Molecular mechanisms of caspase regulation during apoptosis. Nat. Rev. Mol. Cell Biol. 2004;5(11):897-907.

(161) Clark AC, MacKenzie SH. Targeting cell death in tumors by activating caspases. Curr. Cancer Drug Targets. 2008;8(2):98-109.

(162) Rodriguez J, Lazebnik Y. Caspase-9 and APAF-1 form an active holoenzyme. Genes Dev. 1999;13(24):3179-3184.

(163) Schmitt CA. Senescence, apoptosis and therapy—cutting the lifelines of cancer. Nat. Rev. Cancer. 2003;3(4):286-295.

(164) Lehmann BD, McCubrey JA, Jefferson HS, Paine MS, Chappell WH, Terrian DM. A dominant role for p53-dependent cellular senescence in radiosensitization of human prostate cancer cells. Cell cycle. 2007;6(5):595-605.

(165) Gewirtz DA, Holt SE, Elmore LW. Accelerated senescence: an emerging role in tumor cell response to chemotherapy and radiation. Biochem. Pharmacol. 2008;76(8):947-957.

(166) Stein GH, Dulić V. Origins of G1 arrest in senescent human fibroblasts. Bioessays. 1995;17(6):537-543.

(167) Rodier F, Coppé J, Patil CK, Hoeijmakers WAM, Muñoz DP, Raza SR, et al. Persistent DNA damage signalling triggers senescence-associated inflammatory cytokine secretion. Nat. Cell. Biol. 2009;11(8):973-979.

(168) Suzuki K, Mori I, Nakayama Y, Miyakoda M, Kodama S, Watanabe M. Radiation-induced senescence-like growth arrest requires TP53 function but not telomere shortening. Radiat. Res. 2001;155(1):248-253.

(169) Bao S, Wu Q, McLendon RE, Hao Y, Shi Q, Hjelmeland AB, et al. Glioma stem cells promote radioresistance by preferential activation of the DNA damage response. Nature. 2006;444(7120):756-760.

(170) Luo M, Ding L, Li Q, Yao H. miR-668 enhances the radioresistance of human breast cancer cell by targeting IκBα. Breast Cancer. 2017;24(5):673-682.

(171) Huang T, Yin L, Wu J, Gu J, Wu J, Chen D, et al. MicroRNA-19b-3p regulates nasopharyngeal carcinoma radiosensitivity by targeting TNFAIP3/NF-κB axis. J. Exp. Clin. Cancer Res. 2016;35(1):188.

(172) Toulany M, Schickfluß T, Eicheler W, Kehlbach R, Schittek B, Rodemann HP. Impact of oncogenic K-RAS on YB-1 phosphorylation induced by ionizing radiation. Breast Cancer Res. 2011;13(2):R28.

(173) Bur H, Haapasaari K, Turpeenniemi-Hujanen T, Kuittinen O, Auvinen P, Marin K, et al. Low Rap1-interacting factor 1 and sirtuin 6 expression predict poor outcome in radiotherapy-treated Hodgkin lymphoma patients. Leuk. Lymphoma. 2018;59(3):679-689.

(174) Jang NY, Kim DH, Cho BJ, Choi EJ, Lee J, Wu H, et al. Radiosensitization with combined use of olaparib and PI-103 in triple-negative breast cancer. BMC Cancer 2015;15(1):89.

(175) Sousa MML, Bjørås KØ, Hanssen-Bauer A, Solvang-Garten K, Otterlei M. p38 MAPK signaling and phosphorylations in the BRCT1 domain regulate XRCC1 recruitment to sites of DNA damage. Sci. Rep. 2017;7(1):6322.

(176) Chen Y, Li Z, Dong Z, Beebe J, Yang K, Fu L, et al. 14-3-3sigma Contributes to Radioresistance By Regulating DNA Repair and Cell Cycle via PARP1 and CHK2. Mol. Cancer Res. 2017;15(4):418-428.

(177) Gogineni VR, Nalla AK, Gupta R, Dinh DH, Klopfenstein JD, Rao JS. Chk2-mediated G2/M cell cycle arrest maintains radiation resistance in malignant meningioma cells. Cancer Lett. 2011;313(1):64-75.

(178) Wei F, Wu Y, Tang L, He Y, Shi L, Xiong F, et al. BPIFB1 (LPLUNC1) inhibits migration and invasion of nasopharyngeal carcinoma by interacting with VTN and VIM. Br. J. Cancer 2018;118(2):233-247.

(179) Wei F, Tang L, He Y, Wu Y, Shi L, Xiong F, et al. BPIFB1 (LPLUNC1) inhibits radioresistance in nasopharyngeal carcinoma by inhibiting VTN expression. Cell Death Dis. 2018;9(4):432.

(180) Zhou R, Wu Y, Wang W, Su W, Liu Y, Wang Y, et al. Circular RNAs (circRNAs) in cancer. Cancer Lett. 2018;425:134-142.

(181) Zhang X, Li Y, Wang D, Wei X. miR-22 suppresses tumorigenesis and improves radiosensitivity of breast cancer cells by targeting Sirt1. Biol. Res. 2017;50(1):27.

(182) Tang L, Wei F, Wu Y, He Y, Shi L, Xiong F, et al. Role of metabolism in cancer cell radioresistance and radiosensitization methods. J. Exp. Clin. Cancer Res. 2018;37(1):87.

(183) Tang Y, He Y, Shi L, Yang L, Wang J, Lian Y, et al. Co-expression of AFAP1-AS1 and PD-1 predicts poor prognosis in nasopharyngeal carcinoma. Oncotarget. 2017;8(24):39001-39011.

(184) Goffart N, Lombard A, Lallemand F, Kroonen J, Nassen J, Di Valentin E, et al. CXCL12 mediates glioblastoma resistance to radiotherapy in the subventricular zone. Neuro-oncology. 2016;19(1):66-77.

(185) Zhang Y, Xia M, Jin K, Wang S, Wei H, Fan C, et al. Function of the c-Met receptor tyrosine kinase in carcinogenesis and associated therapeutic opportunities. Mol. Cancer. 2018;17(1):45.

(186) Zhang H, Luo H, Jiang Z, Yue J, Hou Q, Xie R, et al. Fractionated irradiation-induced EMT-like phenotype conferred radioresistance in esophageal squamous cell carcinoma. J. Radiat. Res. 2016;57(4):370-380.

(187) Xie G, Liu Y, Yao Q, Zheng R, Zhang L, Lin J, et al. Hypoxia-induced angiotensin II by the lactate-chymase-dependent mechanism mediates radioresistance of hypoxic tumor cells. Sci. Rep. 2017;7:42396.

(188) Yoshida GJ, Saya H. Therapeutic strategies targeting cancer stem cells. Cancer Sci. 2016;107(1):5-11.

(189) Chang L, Graham PH, Hao J, Ni J, Bucci J, Cozzi PJ, et al. PI3K/Akt/mTOR pathway inhibitors enhance radiosensitivity in radioresistant prostate cancer cells through inducing apoptosis, reducing autophagy, suppressing NHEJ and HR repair pathways. Cell Death Dis. 2014;5(10):e1437.

(190) Chen X, Wang P, Guo F, Wang X, Wang J, Xu J, et al. Autophagy enhanced the radioresistance of non-small cell lung cancer by regulating ROS level under hypoxia condition. Int. J. Radiat. Biol. 2017;93(8):764-770.

(191) Pitroda SP, Wakim BT, Sood RF, Beveridge MG, Beckett MA, MacDermed DM, et al. STAT1-dependent expression of energy metabolic pathways links tumour growth and radioresistance to the Warburg effect. BMC medicine. 2009;7(1):68.

(192) Shimura T, Noma N, Sano Y, Ochiai Y, Oikawa T, Fukumoto M, et al. AKT-mediated enhanced aerobic glycolysis causes acquired radioresistance by human tumor cells. Radiother. Oncol. 2014;112(2):302-307.

(193) Yu L, Sun Y, Li J, Wang Y, Zhu Y, Shi Y, et al. Silencing the Girdin gene enhances radio-sensitivity of hepatocellular carcinoma via suppression of glycolytic metabolism. J. Exp. Clin. Cancer Res. 2017;36(1):110.

(194) Chan R, Sethi P, Jyoti A, McGarry R, Upreti M. Investigating the radioresistant properties of lung cancer stem cells in the context of the tumor microenvironment. Radiat. Res. 2016;185(2):169-181.

(195) Li F, Zhou K, Gao L, Zhang B, Li W, Yan W, et al. Radiation induces the generation of cancer stem cells: A novel mechanism for cancer radioresistance. Oncol. Lett. 2016;12(5):3059-3065.

(196) Chi H, Tsai C, Tsai M, Yeh C, Lin K. Roles of long noncoding rnas in recurrence and metastasis of radiotherapy-resistant cancer stem cells. Int. J. Mol. Sci. 2017;18(9):1903.

(197) Prise KM, O'sullivan JM. Radiation-induced bystander signalling in cancer therapy. Nat. Rev. Cancer. 2009;9(5):351-360.

(198) Belyakov OV, Malcolmson AM, Folkard M, Prise KM, Michael B, thD. Direct evidence for a bystander effect of ionizing radiation in primary human fibroblasts. Br. J. Cancer. 2001;84(5):674-679.

(199) Nagasawa H, Little JB. Induction of sister chromatid exchanges by extremely low doses of alpha-particles. Cancer Res. 1992;52(22):6394-6396.

(200) Schettino G, Folkard M, Michael BD, Prise KM. Low-dose binary behavior of bystander cell killing after microbeam irradiation of a single cell with focused CK X rays. Radiat. Res. 2005;163(3):332-336.

(201) Schettino G, Folkard M, Prise KM, Vojnovic B, Held KD, Michael BD. Low-dose studies of bystander cell killing with targeted soft X rays. Radiat. Res. 2003;160(5):505-511.

(202) Shareef MM, Cui N, Burikhanov R, Gupta S, Satishkumar S, Shajahan S, et al. Role of tumor necrosis factor-alpha and TRAIL in high-dose radiation-induced bystander signaling in lung adenocarcinoma. Cancer Res. 2007;67(24):11811-11820.

(203) Gaugler M, Neunlist M, Bonnaud S, Aubert P, Benderitter M, Paris F. Intestinal epithelial cell dysfunction is mediated by an endothelial-specific radiation-induced bystander effect. Radiat. Res. 2007;167(2):185-193.

(204) Prise KM. Studies of bystander effects in human fibroblasts using a charged particle microbeam. Int. J. Radiat. Biol. 1998;74(6):793-798.

(205) Kadhim MA, Lee R, Moore SR, Macdonald DA, Chapman KL, Patel G, Prise KM. Genomic instability after targeted irradiation of human lymphocytes: evidence for inter-individual differences under bystander conditions. Mutat. Res. 2010;688(1-2):91-94.

(206) Shao C, Furusawa Y, Aoki M, Matsumoto H, Ando K. Nitric oxide-mediated bystander effect induced by heavy-ions in human salivary gland tumour cells. Int. J. Radiat. Biol. 2002;78(9):837-844.

(207) Huo L, Nagasawa H, Little JB. HPRT mutants induced in bystander cells by very low fluences of alpha particles result primarily from point mutations. Radiat. Res. 2001;156(5):521-525.

(208) Yang H, Asaad N, Held KD. Medium-mediated intercellular communication is involved in bystander responses of X-ray-irradiated normal human fibroblasts. Oncogene. 2005;24(12):2096-2103.

(209) Mothersill C, Seymour C. Medium from irradiated human epithelial cells but not human fibroblasts reduces the clonogenic survival of unirradiated cells. Int. J. Radiat. Biol. 1997;71(4):421-427.

(210) Iyer R, Lehnert BE. Low dose, low-LET ionizing radiation-induced radioadaptation and associated early responses in unirradiated cells. Mutat. Res. 2002;503(1):1-9.

(211) Belyakov OV, Folkard M, Mothersill C, Prise KM, Michael BD. Bystander-induced differentiation: a major response to targeted irradiation of a urothelial explant model. Mutat. Res. 2006;597(1):43-49.

(212) Lyng FM, Seymour CB, Mothersill C. Initiation of apoptosis in cells exposed to medium from the progeny of irradiated cells: a possible mechanism for bystander-induced genomic instability? Radiat. Res. 2002;157(4):365-370.

(213) Coates PJ, Lorimore SA, Wright EG. Damaging and protective cell signalling in the untargeted effects of ionizing radiation. Mutat. Res. 2004;568(1):5-20.

(214) Hervé J, Bourmeyster N, Sarrouilhe D, Duffy HS. Gap junctional complexes: from partners to functions. Prog. Biophys. Mol. Biol. 2007;94(1-2):29-65.

(215) Oyamada M, Oyamada Y, Takamatsu T. Regulation of connexin expression. Biochim. Biophys. Acta. 2005;1719(1-2):6-23.

(216) Trosko JE, Ruch RJ. Cell-cell communication in carcinogenesis. Front. Biosci. 1998;3(3):d208-236.

(217) Emerit I. Reactive oxygen species, chromosome mutation, and cancer: possible role of clastogenic factors in carcinogenesis. Free Radic. Biol. Med. 1994;16(1):99-109.

(218) Emerit I, Garban F, Vassy J, Levy A, Filipe P, Freitas J. Superoxide-mediated clastogenesis and anticlastogenic effects of exogenous superoxide dismutase. Proc. Natl. Acad. Sci. U.S.A. 1996;93(23):12799-12804.

(219) Yoshioka K, Foletta V, Bernard O, Itoh K. A role for LIM kinase in cancer invasion. Proc. Natl. Acad. Sci. U.S.A. 2003;100(12):7247-7252.

(220) Auclair C, Gouyette A, Levy A, Emerit I. Clastogenic inosine nucleotide as components of the chromosome breakage factor in scleroderma patients. Arch. Biochem. Biophys. 1990;278(1):238-244.

(221) Chou CH, Chen PJ, Lee PH, Cheng AL, Hsu HC, Cheng JC. Radiation-induced hepatitis B virus reactivation in liver mediated by the bystander effect from irradiated endothelial cells. Clin. Cancer Res. 2007;13(3):851-857.

(222) Narayanan PK, LaRue K, Goodwin EH, Lehnert BE. Alpha particles induce the production of interleukin-8 by human cells. Radiat. Res. 1999;152(1):57-63.

(223) Zhou H, Ivanov VN, Gillespie J, Geard CR, Amundson SA, Brenner DJ, et al. Mechanism of radiation-induced bystander effect: role of the cyclooxygenase-2 signaling pathway. Proc. Natl. Acad. Sci. U.S.A. 2005;102(41):14641-14646.

(224) Iyer R, Lehnert BE, Svensson R. Factors underlying the cell growth-related bystander responses to alpha particles. Cancer Res. 2000;60(5):1290-1298.

(225) Lehnert BE, Goodwin EH, Deshpande A. Extracellular factor(s) following exposure to alpha particles can cause sister chromatid exchanges in normal human cells. Cancer Res. 1997;57(11):2164-2171.

(226) Shao C, Stewart V, Folkard M, Michael BD, Prise KM. Nitric oxide-mediated signaling in the bystander response of individually targeted glioma cells. Cancer Res. 2003;63(23):8437-8442.

(227) Coates PJ, Robinson JI, Lorimore SA, Wright EG. Ongoing activation of p53 pathway responses is a long-term consequence of radiation exposure *in vivo* and associates with altered macrophage activities. J. Pathol. 2008;214(5):610-616.

(228) Shao C, Folkard M, Michael BD, Prise KM. Targeted cytoplasmic irradiation induces bystander responses. Proc. Natl. Acad. Sci. U.S.A. 2004;101(37):13495-13500.

(229) Wu LJ, Randers-Pehrson G, Xu A, Waldren CA, Geard CR, Yu Z, et al. Targeted cytoplasmic irradiation with alpha particles induces mutations in mammalian cells. Proc. Natl. Acad. Sci. U.S.A. 1999;96(9):4959-4964.

(230) Tartier L, Gilchrist S, Burdak-Rothkamm S, Folkard M, Prise KM. Cytoplasmic irradiation induces mitochondrial-dependent 53BP1 protein relocalization in irradiated and bystander cells. Cancer Res. 2007;67(12):5872-5879.

(231) Nugent SME, Mothersill CE, Seymour C, McClean B, Lyng FM, Murphy JEJ. Increased mitochondrial mass in cells with functionally compromised mitochondria after exposure to both direct γ radiation and bystander factors. Radiat. Res. 2007;168(1):134-142.

(232) Wade RH. On and around microtubules: an overview. Mol. Biotechnol. 2009;43(2):177-191.

(233) Gan PP, McCarroll JA, Po'uha ST, Kamath K, Jordan MA, Kavallaris M. Microtubule dynamics, mitotic arrest, and apoptosis: drug-induced differential effects of betaIII-tubulin. Mol. Cancer Ther. 2010;9(5):1339-1348.

(234) de Forges H, Bouissou A, Perez F. Interplay between microtubule dynamics and intracellular organization. Int. J. Biochem. Cell. Biol. 2012;44(2):266-274.

(235) Riehlman TD, Olmsted ZT, Branca CN, Winnie AM, Seo L, Cruz LO, et al. Functional replacement of fission yeast gamma-tubulin small complex proteins Alp4 and Alp6 by human GCP2 and GCP3. J. Cell Sci. 2013;126:4406-4413.

(236) Mitchison T, Kirschner M. Dynamic instability of microtubule growth. Nature. 1984;312(5991):237-242.

(237) Kirschner MW, Mitchison T. Microtubule dynamics. Nature. 1986;324(6098):621.

(238) Conde C, Cáceres A. Microtubule assembly, organization and dynamics in axons and dendrites. Nat. Rev. Neurosci. 2009;10(5):319-332.

(239) Mandelkow EM, Mandelkow E, Milligan RA. Microtubule dynamics and microtubule caps: a time-resolved cryo-electron microscopy study. J. Cell Biol. 1991;114(5):977-991.

(240) Howard J, Hyman AA. Growth, fluctuation and switching at microtubule plus ends. Nat. Rev. Mol. Cell Biol. 2009;10(8):569-574.

(241) Zhang D, Rogers GC, Buster DW, Sharp DJ. Three microtubule severing enzymes contribute to the "Pacman-flux" machinery that moves chromosomes. J. Cell Biol. 2007;177(2):231-242.

(242) Noda Y, Sato-Yoshitake R, Kondo S, Nangaku M, Hirokawa N. KIF2 is a new microtubule-based anterograde motor that transports membranous organelles distinct from those carried by kinesin heavy chain or KIF3A/B. J. Cell Biol. 1995;129(1):157-167.

(243) Wordeman L, Wagenbach M, von Dassow G. MCAK facilitates chromosome movement by promoting kinetochore microtubule turnover. J. Cell Biol. 2007;179(5):869-879.

(244) Ems-McClung SC, Walczak CE. Kinesin-13s in mitosis: Key players in the spatial and temporal organization of spindle microtubules. Semin. Cell Dev. Biol. 2010;21(3):276-282.

(245) Walczak CE, Mitchison TJ, Desai A. XKCM1: a Xenopus kinesin-related protein that regulates microtubule dynamics during mitotic spindle assembly. Cell. 1996;84(1):37-47.

(246) Kline-Smith S, Walczak CE. The microtubule-destabilizing kinesin XKCM1 regulates microtubule dynamic instability in cells. Mol. Biol. Cell. 2002;13(8):2718-2731.

(247) Ohi R, Burbank K, Liu Q, Mitchison TJ. Nonredundant functions of Kinesin-13s during meiotic spindle assembly. Curr. Biol. 2007;17(11):953-959.

(248) Perez F, Diamantopoulos GS, Stalder R, Kreis TE. CLIP-170 highlights growing microtubule ends *in vivo*. Cell. 1999;96(4):517-527.

(249) Komarova YA, Akhmanova AS, Kojima S, Galjart N, Borisy GG. Cytoplasmic linker proteins promote microtubule rescue *in vivo*. J. Cell Biol. 2002;159(4):589-599.

(250) Nakano A, Kato H, Watanabe T, Min K, Yamazaki S, Asano Y, et al. AMPK controls the speed of microtubule polymerization and directional cell migration through CLIP-170 phosphorylation. Nat. Cell Biol. 2010;12(6):583-590.

(251) Lee HS, Komarova YA, Nadezhdina ES, Anjum R, Peloquin JG, Schober JM, et al. Phosphorylation controls autoinhibition of cytoplasmic linker protein-170. Mol. Biol. Cell .2010;21(15):2661-2673.

(252) Jordan MA, Wilson L. Microtubules as a target for anticancer drugs. Nat. Rev. Cancer. 2004;4(4):253-265.

(253) Duflos A, Kruczynski A, Barret J. Novel aspects of natural and modified vinca alkaloids. Curr. Med. Chem. Anticancer Agents. 2002;2(1):55-70.

(254) Skoufias DA, Wilson L. Mechanism of inhibition of microtubule polymerization by colchicine: inhibitory potencies of unliganded colchicine and tubulin-colchicine complexes. Biochemistry. 1992;31(3):738-746.

(255) Diaz JF, Andreu JM. Assembly of purified GDP-tubulin into microtubules induced by taxol and taxotere: reversibility, ligand stoichiometry, and competition. Biochemistry. 1993;32(11):2747-2755.

(256) Horwitz SB. How to make taxol from scratch. Nature. 1994;367(6464):593-594.

(257) Hayden JH, Bowser SS, Rieder CL. Kinetochores capture astral microtubules during chromosome attachment to the mitotic spindle: direct visualization in live newt lung cells. J. Cell Biol. 1990;111(3):1039-1045.

(258) Jordan MA, Wendell K, Gardiner S, Derry WB, Copp H, Wilson L. Mitotic block induced in HeLa cells by low concentrations of paclitaxel (Taxol) results in abnormal mitotic exit and apoptotic cell death. Cancer Res. 1996;56(4):816-825.

(259) Tsuchiya Y, Nakajima M, Yokoi T. Cytochrome P450-mediated metabolism of estrogens and its regulation in human. Cancer Lett. 2005;227(2):115-124.

(260) Kristensen VN, Børresen-Dale AL. Molecular epidemiology of breast cancer: genetic variation in steroid hormone metabolism. Mutat. Res. Rev. Mutat. Res. 2000;462(2):323-333.

(261) Lee AJ, Cai MX, Thomas PE, Conney AH, Zhu BT. Characterization of the oxidative metabolites of 17β-estradiol and estrone formed by 15 selectively expressed human cytochrome P450 isoforms. Endocrinology. 2003;144(8):3382-3398.

(262) Weisz J, Bui QD, Roy D, Liehr JG. Elevated 4-hydroxylation of estradiol by hamster kidney microsomes: a potential pathway of metabolic activation of estrogens. Endocrinology. 1992;131(2):655-661.

(263) Shou M, Korzekwa KR, Brooks EN, Krausz KW, Gonzalez FJ, Gelboin HV. Role of human hepatic cytochrome P450 1A2 and 3A4 in the metabolic activation of estrone. Carcinogenesis. 1997;18(1):207-214.

(264) Guengerich FP. Oxidation of 17 alpha-ethynylestradiol by human liver cytochrome P-450. Mol. Pharmacol. 1988;33(5):500-508.

(265) Martucci CP, Fishman J. P450 enzymes of estrogen metabolism. Pharmacol. Ther. 1993;57(2):237-257.

(266) Hernandez JS, Watson RW, Wood TC, Weinshilboum RM. Sulfation of estrone and 17 beta-estradiol in human liver. Catalysis by thermostable phenol sulfotransferase and by dehydroepiandrosterone sulfotransferase. Drug Metab. Dispos. 1992;20(3):413-422.

(267) Parks M, Tillhon M, Dona F, Prosperi E, Scovassi AI. 2-Methoxyestradiol: new perspectives in colon carcinoma treatment. Mol. Cell Endocrinol. 2011;331(1):119-128.

(268) Tevaarwerk AJ, Holen KD, Alberti DB, Sidor C, Arnott J, Quon C, et al. Phase I trial of 2-methoxyestradiol NanoCrystal dispersion in advanced solid malignancies. Clin. Cancer Res. 2009;15(4):1460-1465.

(269) Matei D, Schilder J, Sutton G, Perkins S, Breen T, Quon C, et al. Activity of 2 methoxyestradiol (Panzem® NCD) in advanced, platinum-resistant ovarian cancer and primary peritoneal carcinomatosis: A hoosier oncology group trial. Gynecol. Oncol. 2009;115(1):90-96.

(270) Mooberry SL. Mechanism of action of 2-methoxyestradiol: new developments. Drug Resist. Updat. 2003;6(6):355-361.

(271) Dunn JF, Merriam GR, Eil C, Kono S, Loriaux DL, Nisula BC. Testosterone-estradiol binding globulin binds to 2-methoxyestradiol with greater affinity than to testosterone. J. Clin. Endocrinol. Metab. 1980;51(2):404-406.

(272) Leese MP, Leblond B, Smith A, Newman SP, Di Fiore A, De Simone G, et al. 2-substituted estradiol bis-sulfamates, multitargeted antitumor agents: synthesis, *in vitro* SAR, protein crystallography, and *in vivo* activity. J. Med. Chem. 2006;49(26):7683-7696.

(273) D'Amato RJ, Lin CM, Flynn E, Folkman J, Hamel E. 2-Methoxyestradiol, an endogenous mammalian metabolite, inhibits tubulin polymerization by interacting at the colchicine site. Proc. Natl. Acad. Sci. U.S.A. 1994;91(9):3964-3968.

(274) Cushman M, He H, Katzenellenbogen JA, Lin CM, Hamel E. Synthesis, antitubulin and antimitotic activity, and cytotoxicity of analogs of 2-methoxyestradiol, an endogenous

mammalian metabolite of estradiol that inhibits tubulin polymerization by binding to the colchicine binding site. J. Med. Chem. 1995;38(12):2041-2049.

(275) Joubert A, Maritz C, Joubert F. Influence of prostaglandin A2 and 2-methoxyestradiol on Bax and Bcl-2 expression levels in cervical carcinoma cells. Biomed. Res. 2005;26(2):87-90.

(276) Davoodpour P, Landstrom M. 2-Methoxyestradiol-induced apoptosis in prostate cancer cells requires Smad7. J. Biol. Chem. 2005;280(15):14773-14779.

(277) Montgomery RB, Bonham M, Nelson PS, Grim J, Makary E, Vessella R, et al. Estrogen effects on tubulin expression and taxane mediated cytotoxicity in prostate cancer cells. Prostate. 2005;65(2):141-150.

(278) Amorino GP, Freeman ML, Choy H. Enhancement of radiation effects *in vitro* by the estrogen metabolite 2-methoxyestradiol. Radiat. Res. 2000;153(4):384-391.

(279) Liu ZJ, Lee WJ, Zhu BT. Selective insensitivity of ZR-75-1 human breast cancer cells to 2-methoxyestradiol: evidence for type II 17beta-hydroxysteroid dehydrogenase as the underlying cause. Cancer Res. 2005;65(13):5802-5811.

(280) Lippert C, Seeger H, Mueck AO. The effect of endogenous estradiol metabolites on the proliferation of human breast cancer cells. Life Sci. 2003;72(8):877-883.

(281) Mabjeesh NJ, Escuin D, LaVallee TM, Pribluda VS, Swartz GM, Johnson MS, et al. 2ME2 inhibits tumor growth and angiogenesis by disrupting microtubules and dysregulating HIF. Cancer cell. 2003;3(4):363-375.

(282) Kerbel R, Folkman J. Clinical translation of angiogenesis inhibitors. Nat. Rev. Cancer. 2002;2(10):727-739.

(283) Perez EA, Mooberry S, Twelves C, Rugo HS. New frontiers and treatment paradigms for metastatic breast cancer. Clin. Adv. Hematol. Oncol. 2011;9(8 Suppl 20):1-15.

(284) Semenza GL. HIF-1 and tumor progression: pathophysiology and therapeutics. Trends. Mol. Med. 2002;8(4):S62-S67.

(285) Becker CM, Rohwer N, Funakoshi T, Cramer T, Bernhardt W, Birsner A, et al. 2-Methoxyestradiol inhibits hypoxia-inducible factor-1α and suppresses growth of lesions in a mouse model of endometriosis. Am. J. Pathol. 2008 2;172(2):534-544.

(286) Childs S, Ling V. The MDR superfamily of genes and its biological implications. Important Adv. Oncol. 1994:21-36.

(287) Klappe K, Hummel I, Hoekstra D, Kok JW. Lipid dependence of ABC transporter localization and function. Chem. Phys. Lipids 2009;161(2):57-64.

(288) Stavrovskaya AA. Cellular mechanisms of multidrug resistance of tumor cells. Biochemistry (Mosc). 2000;65(1):95-106.

(289) Theron A, Prudent R, Nolte E, van den Bout I, Punchoo R, Marais S, et al. Novel *in silico*-designed estradiol analogues are cytotoxic to a multidrug-resistant cell line at nanomolar concentrations. Cancer Chemother. Pharmacol. 2015;75(2):431-437.

(290) Chauhan D, Catley L, Hideshima T, Li G, Leblanc R, Gupta D, et al. 2-Methoxyestradiol overcomes drug resistance in multiple myeloma cells. Blood. 2002;100(6):2187-2194.

(291) Rajkumar SV, Richardson PG, Lacy MQ, Dispenzieri A, Greipp PR, Witzig TE, et al. Novel therapy with 2-methoxyestradiol for the treatment of relapsed and plateau phase multiple myeloma. Clin. Cancer Res. 2007;13(20):6162-6167.

(292) Sweeney C, Liu G, Yiannoutsos C, Kolesar J, Horvath D, Staab MJ, et al. A phase II multicenter, randomized, double-blind, safety trial assessing the pharmacokinetics, pharmacodynamics, and efficacy of oral 2-methoxyestradiol capsules in hormone-refractory prostate cancer. Clin. Cancer Res. 2005;11(18):6625-6633.

(293) LaVallee TM, Zhan XH, Herbstritt CJ, Kough EC, Green SJ, Pribluda VS. 2-Methoxyestradiol inhibits proliferation and induces apoptosis independently of estrogen receptors alpha and beta. Cancer Res. 2002;62(13):3691-3697.

(294) Kim PKM, Mahidhara R, Seol D. The role of caspase-8 in resistance to cancer chemotherapy. Drug Resist. Updat. 2001;4(5):293-296.

(295) Chauhan D, Li G, Hideshima T, Podar K, Mitsiades C, Mitsiades N, et al. JNK-dependent release of mitochondrial protein, Smac, during apoptosis in multiple myeloma (MM) cells. J. Biol. Chem. 2003;278(20):17593-17596.

(296) Djavaheri-Mergny M, Wietzerbin J, Besancon F. 2-Methoxyestradiol induces apoptosis in Ewing sarcoma cells through mitochondrial hydrogen peroxide production. Oncogene. 2003;22(17):2558-2567.

(297) Huang P, Feng L, Oldham EA, Keating MJ, Plunkett W. Superoxide dismutase as a target for the selective killing of cancer cells. Nature. 2000;407(6802):390-395.

(298) Hagen T, D'Amico G, Quintero M, Palacios-Callender M, Hollis V, Lam F, et al. Inhibition of mitochondrial respiration by the anticancer agent 2-methoxyestradiol. Biochem. Biophys. Res. Commun. 2004;322(3):923-929.

(299) Tinley TL, Leal RM, Randall-Hlubek D, Cessac JW, Wilkens LR, Rao PN, et al. Novel 2-methoxyestradiol analogues with antitumor activity. Cancer Res. 2003;63(7):1538-1549.

(300) Joubert A, Maritz C, Joubert F. Bax/Bcl-2 expression levels of 2-methoxyestradiol-exposed esophageal cancer cells. Biomed. Res. 2005;26(3):131-134.

(301) Day JM, Newman SP, Comninos A, Solomon C, Purohit A, Leese MP, et al. The effects of 2-substituted oestrogen sulphamates on the growth of prostate and ovarian cancer cells. J. Steroid Biochem. Mol. Bio.l 2003;84(2):317-325.

(302) Mukhopadhyay T, Roth JA. Superinduction of wild-type p53 protein after 2-methoxyestradiol treatment of Ad5p53-transduced cells induces tumor cell apoptosis. Oncogene. 1998;17(2):241-246.

(303) Mukhopadhyay T, Roth JA. Induction of apoptosis in human lung cancer cells after wild-type p53 activation by methoxyestradiol. Oncogene. 1997;14(3):379-384.

(304) Maxwell SA, Roth JA, Mukhopadhyay T. Analysis of phosphorylated isoforms of the p53 tumor suppressor protein in human lung carcinoma cells undergoing apoptosis. Electrophoresis. 1996;17(11):1772-1775.

(305) Stander BA, Marais S, Vorster CJ, Joubert AM. *In vitro* effects of 2-methoxyestradiol on morphology, cell cycle progression, cell death and gene expression changes in the tumorigenic MCF-7 breast epithelial cell line. J. Steroid Biochem. Mol. Biol. 2010;119(3-5):149-160.

(306) Kirches E, Warich-Kirches M. 2-methoxyestradiol as a potential cytostatic drug in gliomas? Med. Chem. 2009;9(1):55-65.

(307) Chen Y, McMillan-Ward E, Kong J, Israels SJ, Gibson SB. Oxidative stress induces autophagic cell death independent of apoptosis in transformed and cancer cells. Cell Death Differ. 2008;15(1):171-182.

(308) Klauber N, Parangi S, Flynn E, Hamel E, D'Amato RJ. Inhibition of angiogenesis and breast cancer in mice by the microtubule inhibitors 2-methoxyestradiol and taxol. Cancer Res. 1997;57(1):81-86.

(309) Kataoka M, Schumacher G, Cristiano RJ, Atkinson EN, Roth JA, Mukhopadhyay T. An agent that increases tumor suppressor transgene product coupled with systemic transgene delivery inhibits growth of metastatic lung cancer *in vivo*. Cancer Res. 1998;58(21):4761-4765.

(310) Newman SP, Ireson CR, Tutill HJ, Day JM, Parsons MF, Leese MP, et al. The role of 17beta-hydroxysteroid dehydrogenases in modulating the activity of 2-methoxyestradiol in breast cancer cells. Cancer Res. 2006;66(1):324-330.

(311) Sweeney C, Liu G, Yiannoutsos C, Kolesar J, Horvath D, Staab MJ, et al. A phase II multicenter, randomized, double-blind, safety trial assessing the pharmacokinetics, pharmacodynamics, and efficacy of oral 2-methoxyestradiol capsules in hormone-refractory prostate cancer. Clin. Cancer Res. 2005;11(18):6625-6633.

(312) Stander A, Joubert F, Joubert A. Docking, synthesis, and *in vitro* evaluation of antimitotic estrone analogs. Chem. Biol. Drug Des. 2011 03;77(3):173-181.

(313) Gorovoy M, Niu J, Bernard O, Profirovic J, Minshall R, Neamu R, et al. LIM kinase 1 coordinates microtubule stability and actin polymerization in human endothelial cells. J. Biol. Chem. 2005;280(28):26533-26542.

(314) Ray S, Fanti JA, Macedo DP, Larsen M. LIM kinase regulation of cytoskeletal dynamics is required for salivary gland branching morphogenesis. Mol. Biol. Cell. 2014;25(16):2393-2407.

(315) Manetti F. LIM kinases are attractive targets with many macromolecular partners and only a few small molecule regulators. Med. Res. Rev. 2012;32(5):968-998.

(316) Toshima J, Toshima JY, Takeuchi K, Mori R, Mizuno K. Cofilin phosphorylation and actin reorganization activities of testicular protein kinase 2 and its predominant expression in testicular Sertoli cells. J. Biol. Chem. 2001;276(33):31449-58.

(317) Scott RW, Olson MF. LIM kinases: function, regulation and association with human disease. J. Mol. Med. 2007;85(6):555-568.

(318) Prunier C, Prudent R, Kapur R, Sadoul K, Lafanechere L. LIM kinases: cofilin and beyond. Oncotarget. 2017;8(25):41749-41763.

(319) Aggelou H, Chadla P, Nikou S, Karteri S, Maroulis I, Kalofonos HP, et al. LIMK/cofilin pathway and Slingshot are implicated in human colorectal cancer progression and chemoresistance. Virchows Arch. 2018;472(5): 727–737.

(320) Vartiainen MK, Mustonen T, Mattila PK, Ojala PJ, Thesleff I, Partanen J, et al. The three mouse actin-depolymerizing factor/cofilins evolved to fulfill cell-type–specific tequirements for actin dynamics. Mol. Biol. Cell. 2002;13(1):183-194.

(321) Szabó A, Oláh J, Szunyogh S, Lehotzky A, Szénási T, Csaplár M, et al. Modulation of microtubule acetylation by the interplay of TPPP/p25, SIRT2 and new anticancer agents with anti-SIRT2 potency. Sci. Rep. 2017;7(1):17070.

(322) Acevedo K, Li R, Soo P, Suryadinata R, Sarcevic B, Valova VA, et al. The phosphorylation of p25/TPPP by LIM kinase 1 inhibits its ability to assemble microtubules. Exp. Cell Res. 2007;313(20):4091-4106.

(323) Schofield AV, Steel R, Bernard O. Rho-associated coiled-coil kinase (ROCK) protein controls microtubule dynamics in a novel signaling pathway that regulates cell migration. J. Biol. Chem. 2012;287(52):43620-43629.

(324) Bhardwaj A, Srivastava SK, Singh S, Arora S, Tyagi N, Andrews J, et al. CXCL12/CXCR4 signaling counteracts docetaxel-induced microtubule stabilization via p21-activated kinase 4-dependent activation of LIM domain kinase 1. Oncotarget. 2014;5(22):11490-11500.

(325) Fourest-Lieuvin A, Peris L, Gache V, Garcia-Saez I, Juillan-Binard C, Lantez V, et al. Microtubule regulation in mitosis: tubulin phosphorylation by the cyclin-dependent kinase Cdk1. Mol. Biol. Cell. 2006;17(3):1041-1050.

(326) Sinclair WK, Morton RA. X-ray sensitivity during the cell generation cycle of cultured Chinese hamster cells. Radiat. Res. 1966;29(3):450-474.

(327) Ritchey L, Ottman R, Roumanos M, Chakrabarti R. A functional cooperativity between Aurora A kinase and LIM kinase1: implication in the mitotic process. Cell Cycle. 2012;11(2):296-309.

(328) Lorenzo C, Liao Q, Hardwicke MA, Ducommun B. Pharmacological inhibition of aurora-A but not aurora-B impairs interphase microtubule dynamics. Cell Cycle. 2009;8(11):1733-1737.

(329) Kosoff RE, Aslan JE, Kostyak JC, Dulaimi E, Chow HY, Prudnikova TY, et al. Pak2 restrains endomitosis during megakaryopoiesis and alters cytoskeleton organization. Blood. 2015;125(19):2995-3005.

(330) Devreotes P, Janetopoulos C. Eukaryotic chemotaxis: distinctions between directional sensing and polarization. J. Biol. Chem. 2003;278(23):20445-20448.

(331) Sidani M, Wessels D, Mouneimne G, Ghosh M, Goswami S, Sarmiento C, et al. Cofilin determines the migration behavior and turning frequency of metastatic cancer cells. J. Cell Biol. 2007;179(4):777-791.

(332) Manetti F. LIM kinases are attractive targets with many macromolecular partners and only a few small molecule regulators. Med. Res. Rev. 2012;32(5):968-998.

(333) Kiuchi T, Ohashi K, Kurita S, Mizuno K. Cofilin promotes stimulus-induced lamellipodium formation by generating an abundant supply of actin monomers. J. Cell Biol. 2007;177(3):465-476.

(334) Yamaguchi H, Condeelis J. Regulation of the actin cytoskeleton in cancer cell migration and invasion. Biochim. Biophys. Acta. 2007;1773(5):642-652.

(335) Wang W, Eddy R, Condeelis J. The cofilin pathway in breast cancer invasion and metastasis. Nat. Rev. Cancer. 2007;7(6):429-440.

(336) Ghosh M, Song X, Mouneimne G, Sidani M, Lawrence DS, Condeelis JS. Cofilin promotes actin polymerization and defines the direction of cell motility. Science. 2004;304(5671):743-746.

(337) Mouneimne G, DesMarais V, Sidani M, Scemes E, Wang W, Song X, et al. Spatial and temporal control of cofilin activity is required for directional sensing during chemotaxis. Curr. Biol. 2006;16(22):2193-2205.

(338) Arber S, Barbayannis FA, Hanser H, Schneider C, Stanyon CA, Bernard O, et al. Regulation of actin dynamics through phosphorylation of cofilin by LIM-kinase. Nature. 1998;393(6687):805-809.

(339) Sumi T, Matsumoto K, Takai Y, Nakamura T. Cofilin phosphorylation and actin cytoskeletal dynamics regulated by rho- and Cdc42-activated LIM-kinase 2. J. Cell Biol. 1999;147(7):1519-1532.

(340) Yang N, Higuchi O, Ohashi K, Nagata K, Wada A, Kangawa K, et al. Cofilin phosphorylation by LIM-kinase 1 and its role in Rac-mediated actin reorganization. Nature. 1998;393(6687):809-812.

(341) Dan C, Kelly A, Bernard O, Minden A. Cytoskeletal changes regulated by the PAK4 serine/threonine kinase are mediated by LIM kinase 1 and cofilin. J. Biol. Chem. 2001;276(34):32115-32121.

(342) Edwards DC, Sanders LC, Bokoch GM, Gill GN. Activation of LIM-kinase by Pak1 couples Rac/Cdc42 GTPase signalling to actin cytoskeletal dynamics. Nat. Cell Biol. 1999;1(5):253-259.

(343) Maekawa M, Ishizaki T, Boku S, Watanabe N, Fujita A, Iwamatsu A, et al. Signaling from Rho to the actin cytoskeleton through protein kinases ROCK and LIM-kinase. Science. 1999;285(5429):895-898.

(344) Bamburg JR. Proteins of the ADF/cofilin family: essential regulators of actin dynamics. Annu. Rev. Cell Dev. Biol. 1999;15(1):185-230.

(345) Gohla A, Birkenfeld J, Bokoch GM. Chronophin, a novel HAD-type serine protein phosphatase, regulates cofilin-dependent actin dynamics. Nat. Cell Biol. 2005;7(1):21-29.

(346) Huang TY, Minamide LS, Bamburg JR, Bokoch GM. Chronophin mediates an ATP-sensing mechanism for cofilin dephosphorylation and neuronal cofilin-actin rod formation. Dev. Cell. 2008;15(5):691-703.

(347) Niwa R, Nagata-Ohashi K, Takeichi M, Mizuno K, Uemura T. Control of actin reorganization by Slingshot, a family of phosphatases that dephosphorylate ADF/cofilin. Cell. 2002;108(2):233-246.

(348) Sumi T, Hashigasako A, Matsumoto K, Nakamura T. Different activity regulation and subcellular localization of LIMK1 and LIMK2 during cell cycle transition. Exp. Cell Res. 2006;312(7):1021-1030.

(349) Sumi T, Matsumoto K, Nakamura T. Mitosis-dependent phosphorylation and activation of LIM-kinase 1. Biochem. Biophys. Res. Commun. 2002;290(4):1315-1320.

(350) Chakrabarti R, Jones JL, Oelschlager DK, Tapia T, Tousson A, Grizzle WE. Phosphorylated LIM kinases colocalize with gamma-tubulin in centrosomes during early stages of mitosis. Cell Cycle. 2007;6(23):2944-2952.

(351) Dumontet C, Jordan MA. Microtubule-binding agents: a dynamic field of cancer therapeutics. Nat. Rev. Drug Discov. 2010;9(10):790-803.

(352) Zhou J, Giannakakou P. Targeting microtubules for cancer chemotherapy. Curr. Med. Chem. Anticancer Agents. 2005;5(1):65-71.

(353) Prudent R, Vassal-Stermann E, Nguyen CH, Pillet C, Martinez A, Prunier C, et al. Pharmacological inhibition of LIM kinase stabilizes microtubules and inhibits neoplastic growth. Cancer Res. 2012;72(17):4429-4439.

(354) Li R, Doherty J, Antonipillai J, Chen S, Devlin M, Visser K, et al. LIM kinase inhibition reduces breast cancer growth and invasiveness but systemic inhibition does not reduce metastasis in mice. Clin. Exp. Metastasis 2013;30(4):483-495.

(355) Scott RW, Hooper S, Crighton D, Li A, Konig I, Munro J, et al. LIM kinases are required for invasive path generation by tumor and tumor-associated stromal cells. J. Cell Biol. 2010;191(1):169-185.

(356) Wani MC, Taylor HL, Wall ME, Coggon P, McPhail AT. Plant antitumor agents. VI. Isolation and structure of taxol, a novel antileukemic and antitumor agent from Taxus brevifolia. J. Am. Chem. Soc. 1971;93(9):2325-2327.

(357) Schiff PB, Fant J, Horwitz SB. Promotion of microtubule assembly *in vitro* by taxol. Nature. 1979;277(5698):665.

(358) Schiff PB, Horwitz SB. Taxol stabilizes microtubules in mouse fibroblast cells. Proc. Natl. Acad. Sci. U.S.A. 1980;77(3):1561-1565.

(359) Ganesh T, Yang C, Norris A, Glass T, Bane S, Ravindra R, et al. Evaluation of the tubulin-bound paclitaxel conformation: Synthesis, biology, and SAR studies of C-4 to C-3 'bridged paclitaxel analogues'. J. Med. Chem. 2007;50(4):713-725.

(360) Yang C, Horwitz S. Taxol®: The first microtubule stabilizing agent. Int. J. Mol. Sci. 2017;18(8):1733.

(361) Marupudi NI, Han JE, Li KW, Renard VM, Tyler BM, Brem H. Paclitaxel: a review of adverse toxicities and novel delivery strategies. Expert Opin. Drug. Saf. 2007;6(5):609-621.

(362) Gottesman MM. Mechanisms of cancer drug resistance. Annu. Rev. Med. 2002;53(1):615-627.

(363) Hari M, Loganzo F, Annable T, Tan X, Musto S, Morilla DB, et al. Paclitaxel-resistant cells have a mutation in the paclitaxel-binding region of beta-tubulin (Asp26Glu) and less stable microtubules. Mol. Cancer Ther. 2006;5(2):270-278.

(364) Yusuf RZ, Duan Z, Lamendola DE, Penson RT, Seiden MV. Paclitaxel resistance: molecular mechanisms and pharmacologic manipulation. Curr. Cancer Drug Targets. 2003;3(1):1-19.

(365) Barbuti AM, Chen Z. Paclitaxel through the ages of anticancer therapy: exploring its role in chemoresistance and radiation therapy. Cancers. 2015;7(4):2360-2371.

(366) Juliano RL, Ling V. A surface glycoprotein modulating drug permeability in Chinese hamster ovary cell mutants. Biochim. Biophys. Acta. 1976;455(1):152-162.

(367) Kathawala RJ, Gupta P, Ashby Jr CR, Chen Z. The modulation of ABC transporter-mediated multidrug resistance in cancer: a review of the past decade. Drug Resist. Updat. 2015;18:1-17.

(368) Sodani K, Patel A, Kathawala RJ, Chen ZS. Multidrug resistance associated proteins in multidrug resistance. Chin. J. Cancer 2012;31(2):58-72.

(369) Takayanagi S, Kataoka T, Ohara O, Oishi M, Kuo MT, Ishikawa T. Human ATP-binding cassette transporter ABCC10: expression profile and p53-dependent upregulation. J. Exp. Ther. Oncol. 2004;4(3): 239-246.

(370) Hopper E, Belinsky MG, Zeng H, Tosolini A, Testa JR, Kruh GD. Analysis of the structure and expression pattern of MRP7 (ABCC10), a new member of the MRP subfamily. Cancer Lett. 2001;162(2):181-191.

(371) Chen ZS, Hopper-Borge E, Belinsky MG, Shchaveleva I, Kotova E, Kruh GD. Characterization of the transport properties of human multidrug resistance protein 7 (MRP7, ABCC10). Mol. Pharmacol. 2003;63(2):351-358.

(372) Mitchison T, Kirschner M. Dynamic instability of microtubule growth. Nature. 1984;312(5991):237-242.

(373) Ganguly A, Cabral F. New insights into mechanisms of resistance to microtubule inhibitors. Biochim. Biophys. Acta. 2011;1816(2):164-171.

(374) Ganguly A, Yang H, Cabral F. Paclitaxel-dependent cell lines reveal a novel drug activity. Mol. Cancer Ther. 2010;9(11):2914-2923.

(375) Bhattacharya R, Cabral F. Molecular basis for class V beta-tubulin effects on microtubule assembly and paclitaxel resistance. J. Biol. Chem. 2009;284(19):13023-13032.

(376) Kamath K, Wilson L, Cabral F, Jordan MA. BetaIII-tubulin induces paclitaxel resistance in association with reduced effects on microtubule dynamic instability. J. Biol. Chem. 2005;280(13):12902-12907.

(377) Orr GA, Verdier-Pinard P, McDaid H, Horwitz SB. Mechanisms of Taxol resistance related to microtubules. Oncogene. 2003;22(47):7280-7295.

(378) Rath O, Kozielski F. Kinesins and cancer. Nat. Rev. Cancer. 2012;12(8):527-539.

(379) Ganguly A, Yang H, Pedroza M, Bhattacharya R, Cabral F. Mitotic centromere-associated kinesin (MCAK) mediates paclitaxel resistance. J. Biol. Chem. 2011;286(42):36378-36384.

(380) Ganguly A, Yang H, Cabral F. Overexpression of mitotic centromere-associated Kinesin stimulates microtubule detachment and confers resistance to paclitaxel. Mol. Cancer. Ther. 2011;10(6):929-937.

(381) E Eisenhauer EA, ten Bokkel Huinink WW, Swenerton KD, Gianni L, Myles J, Van der Burg ME, Kerr I, Vermorken JB, Buser K, Colombo N. European-Canadian randomized trial of paclitaxel in relapsed ovarian cancer: high-dose versus low-dose and long versus short infusion. J. Clin. Oncol. 1994;12(12):2654-66..

(382) Holmes FA, Walters RS, Theriault RL, Buzdar AU, Frye DK, Hortobagyi GN, et al. Phase II trial of taxol, an active drug in the treatment of metastatic breast cancer. JNCI. 1991;83(24):1797-1805.

(383) Seidman AD, Hudis CA, Norton L. Memorial Sloan-Kettering Cancer Center experience with paclitaxel in the treatment of breast cancer: from advanced disease to adjuvant therapy. Semin. Oncol. 1995;22(4):3-8.

(384) Seidman AD, Reichman BS, Crown JP, Yao TJ, Currie V, Hakes TB, Hudis CA, Gilewski TA, Baselga J, Forsythe P. Paclitaxel as second and subsequent therapy for metastatic breast cancer: activity independent of prior anthracycline response. J. Clin. Oncol. 1995;13(5):1152-1159.

(385) Gelmon KA. Biweekly paclitaxel in the treatment of patients with metastatic breast cancer. Semin. Oncol. 1995;22(5):117-122.

(386) Abrams JS, Vena DA, Baltz J. Paclitaxel activity in heavily pretreated breast cancer: a National Cancer Institute Treatment Referral Center trial. J. Clin. Oncol. 1995;13(8):2056-2065.

(387) Dieras V, Marty M, Tubiana N, Corette L, Morvan F, Serin D, Mignot L, Chazard M, Garet F, Onetto N. Phase II randomized study of paclitaxel versus mitomycin in advanced breast cancer. Semin. Oncol. 1995;22(4):33-39.

(388) Wilson WH, Berg SL, Bryant G, Wittes RE, Bates S, Fojo A, et al. Paclitaxel in doxorubicin-refractory or mitoxantrone-refractory breast cancer: a phase I/II trial of 96-hour infusion. J. Clin. Oncol. 1994;12(8):1621-1629.

(389) Jahanzeb M, Frankel C, Elkersh M, Koletsky A, Radice P, Vogel CL. Rationale for trials studying pegylated liposomal doxorubicin in metastatic breast cancer. Breast Cancer. 1997;11(10).

(390) Holmes FA. Update: the M.D. Anderson Cancer Center experience with paclitaxel in the management of breast carcinoma. Semin. Oncol. 1995;22(4):9-15.

(391) Holmes FA, Newman RA, Madden V. Schedule dependent pharmacokinetics (PK) in a phase I trial of Taxol and doxorubicin as initial chemotherapy for metastatic breast cancer. Ann. Oncol. Suppl. 1994;5:489.

(392) O'Shaughnessy JA, Fisherman JS, Cowan KH. Combination paclitaxel (Taxol) and doxorubicin therapy for metastatic breast cancer. Semin. Oncol. 1994;21(5):19-23.

(393) Fisherman JS, McCabe M, Noone M, Ognibene FP, Goldspiel B, Venzon DJ, et al. Phase I study of Taxol, doxorubicin, plus granulocyte-colony stimulating factor in patients with metastatic breast cancer. J. Natl. Cancer Inst. Monogr. 1993;(15):189-194.

(394) Holmes FA, Frye D, Valero V, Walters RS, Theriault RL, Booser D, Vadan-Raj S, Hortobagyi GN. Phase I study of taxol and doxorubicin with G-CSF in patients without prior chemotherapy for metastatic breast cancer. Proc. Am. Soc. Clin. Oncol. 1992;11: 60.

(395) Sledge GW,J, Robert N, Sparano JA, Cogleigh M, Goldstein LJ, Neuberg D, et al. Eastern Cooperative Oncology Group studies of paclitaxel and doxorubicin in advanced breast cancer. Semin. Onco.l 1995;22(3):105-108.

(396) Sledge Jr GW. Doxorubicin/paclitaxel combination chemotherapy for metastatic breast cancer: the Eastern Cooperative Oncology Group experience. Semin. Oncol. 1995 Oct;22(5 suppl 12):123-125; discussion 126-129.

(397) Sledge Jr GW, Sparano J, McCaskill-Stevens W, Cobleigh M, Robert N, Baughman C, Neuberg D, Rowinsky E. Pilot trial of alternating taxol and adriamycin for metastatic breast cancer. Proc. Am. Soc. Clin. Oncol. 1993;12: 71.

(398) Gianni L, Munzone E, Capri G, Fulfaro F, Tarenzi E, Villani F, et al. Paclitaxel by 3-hour infusion in combination with bolus doxorubicin in women with untreated metastatic breast cancer: high antitumor efficacy and cardiac effects in a dose-finding and sequence-finding study. J. Clin. Oncol. 1995;13(11):2688-2699.

(399) Biganzoli L, Cufer T, Bruning P, Coleman RE, Duchateau L, Rapoport B, Nooij M, Delhaye F, Miles D, Sulkes A, Hamilton A. Doxorubicin-paclitaxel: A safe regimen in terms of cardiac toxicity in metastatic breast carcinoma patients. Int. J. Cancer. 2003 1;97(1):40-45.

(400) Gianni L, Dombernowsky P, Sledge G, Martin M, Amadori D, Arbuck S, et al. Cardiac function following combination therapy with paclitaxel and doxorubicin: an analysis of 657 women with advanced breast cancer. Ann. Oncol. 2001;12(8):1067-1073.

(401) Sledge Jr GW, Neuberg D, Bernardo P, Ingle JN, Martino S, Rowinsky EK, et al. Phase III trial of doxorubicin, paclitaxel, and the combination of doxorubicin and paclitaxel as front-line chemotherapy for metastatic breast cancer: an intergroup trial (E1193). J. Clin. Oncol. 2003;21(4):588-592.

(402) Sledge GW,J. Cisplatin and platinum analogues in breast cancer. Semin. Oncol. 1992;19(1):78-82.

(403) Hortobagyi GN. Paclitaxel-based combination chemotherapy for breast cancer. Breast Cancer. 1997;11(3).

(404) Gelmon KA, O'Reilly SE, Tolcher AW, Campbell C, Bryce C, Ragaz J, et al. Phase I/II trial of biweekly paclitaxel and cisplatin in the treatment of metastatic breast cancer. J. Clin. Oncol. 1996;14(4):1185-1191.

(405) Wasserheit C, Frazein A, Oratz R, Sorich J, Downey A, Hochster H, et al. Phase II trial of paclitaxel and cisplatin in women with advanced breast cancer: an active regimen with limiting neurotoxicity. J. Clin. Oncol. 1996;14(7):1993-1999.

(406) Tolcher AW, Cowan KH, Noone MH, Denicoff AM, Kohler DR, Goldspiel BR, et al. Phase I study of paclitaxel in combination with cyclophosphamide and granulocyte colony-stimulating factor in metastatic breast cancer patients. J. Clin. Oncol. 1996;14(1):95-102.

(407) Johnson SA, Harper P, Hortobagyi GN, Pouillart P. Vinorelbine: an overview. Cancer Treat. Rev. 1996;22(2):127-142.

(408) Adams DJ. Synergy of Navelbine-Taxol combination treatment in two human breast cancer cell lines. Proc. Am. Assoc. Cancer Res. 1994;35(327): I994.

(409) Ibrahim N, Hortobagyi GN, Valero V, Dhingra K, Willey J, Hohneker J, Buzdar AV. Phase I study of vinorelbine (Navelbine) and paclitaxel by simultaneous 3-hour infusion for untreated metastatic breast cancer. Proc. Am. Assoc. Cancer Res. 1995; 36:242.

(410) Ibrahim NK, Hortobagyi GN, Valero V. Phase I study of vinorelbine (Navelbine) and paclitaxel (Taxol) by simultaneous 3-hour infusion with G-CSF support, for untreated metastatic breast cancer. Breast Cancer Res. Treat. 1996;37:44.

(411) Conte PF, Michelotti A, Baldini E, Tibaldi C, DaPrato M, Salvadori B, et al. Activity and safety of epirubicin plus paclitaxel in advanced breast cancer. Semin. Oncol. 1996;23(1):28-32.

(412) Chang AY, Garrow GC. Pilot study of vinorelbine (Navelbine) and paclitaxel (Taxol) in patients with refractory breast cancer and lung cancer. Semin. Oncol. 1995;22(2):66-70; discussion 70-71.

(413) Dittrich C, Zifko U, Fazeny B, Fiegl M, Grisold W, Huber H. Vinorelbine after paclitaxel in breast cancer: cross resistance and cumulative neurotoxicity? Ann. Oncol. 1994;5(5):473-474.

(414) Masunaga S, Ono K, Suzuki M, Nishimura Y, Kinashi Y, Takagaki M, et al. Radiosensitization effect by combination with paclitaxel *in vivo*, including the effect on intratumor quiescent cells. Int. J. Radiat. Oncol. Biol. Phys. 2001;50(4):1063-1072.

(415) Luo Y, Chen X, Luo L, Zhang Q, Gao C, Zhuang X, et al. [6]-Gingerol enhances the radiosensitivity of gastric cancer via G2/M phase arrest and apoptosis induction. Oncol. Rep. 2018;39(5):2252-2260.

(416) Vavrova J, Marekova-Rezacova M, Vokurkova D, Psutka J. Cell cycle alteration, apoptosis and response of leukemic cell lines to gamma radiation with high-and low-dose rate. Physiol. Res. 2004;53:335-342.

(417) Jin C, Wu H, Liu J, Bai L, Guo G. The effect of paclitaxel-loaded nanoparticles with radiation on hypoxic MCF-7 cells. J. Clin. Pharm. Ther. 2007;32(1):41-47.

(418) Casarez EV, Dunlap-Brown M, Conaway MR, Amorino GP. Radiosensitization and modulation of p44/42 mitogen-activated protein kinase by 2-Methoxyestradiol in prostate cancer models. Cancer Res. 2007;67(17):8316-8324.

(419) Zou H, Zhao S, Zhang J, Lv G, Zhang X, Yu H, et al. Enhanced radiation-induced cytotoxic effect by 2-ME in glioma cells is mediated by induction of cell cycle arrest and DNA damage via activation of ATM pathways. Brain Res. 2007;1185:231-238.

(420) Liu C, Chang H, Chen I, Chen C, Hsu M, Fu S, et al. Costunolide causes mitotic arrest and enhances radiosensitivity in human hepatocellular carcinoma cells. Radiat Oncol. 2011;6(1):56.

(421) ATCC: The Essentials of Life Science Research [Internet]. MCF7 (ATCC ® HTB-22™). Available from: http://www.atcc.org/products/all/HTB-22.aspx

(422) ATCC: The Essentials of Life Science Research [Internet]. MDA-MB-231 (ATCC ® HTB-26™). Available from: https://www.atcc.org/products/all/HTB-26.aspx

(423) ATCC: The Essentials of Life Science Research [Internet]. BT-20 (ATCC ® HTB-19™). Available from: https://www.atcc.org/products/all/HTB-19.aspx

(424) ATCC: The Essentials of Life Science Research [Internet]. SOP: Thawing, propagating and cryopreserving protocol: MCF-7 breast adenocarcinoma (ATCC® HTB-22™) . Available at: https://physics.cancer.gov/docs/bioresource/breast/NCI-PBCF-HTB22_MCF7_SOP-508.pdf.

(425) ATCC: The Essentials of Life Science Research [Internet]. SOP: Thawing, propagating and cryopreserving protocol: NCI-PBCF-HTB26 (MDA-MB-231) breast adenocarcinoma(ATCC®HTB-26™). Available at: https://physics.cancer.gov/docs/bioresource/breast/NCI-PBCF-HTB26_MDA-MB-231_SOP-508.pdf.

(426) Oncolines [Internet]. BT-20-data-sheet. Available at: https://www.ntrc.nl/wp-content/uploads/2016/04/Oncolines-2.0-BT-20-data-sheet.pdf.

(427) ATCC: The Essentials of Life Science Research [Internet]. HeLa S3 (ATCC ® CCL-2.2™). Available from: https://www.atcc.org/products/all/CCL-2.2.aspx.

(428) ATCC: The Essentials of Life Science Research [Internet]. Protocol to cryopreserve cell cultures-50. Available from: https://www.atcc.org/support/faqs/03401/Protocol+to+cryopreserve+cell+cultures-50.aspx

(429) abcam [Internet]. Counting cells using a hemocytometer. Available from: https://www.abcam.com/protocols/counting-cells-using-a-haemocytometer.

(430) Strober W. Trypan blue exclusion test of cell viability. Curr. Protoc. Immunol. 2001;Appendix 3:Appendix 3B. doi: 10.1002/0471142735.ima03bs21.

(431) Adefolaju GA, Theron KE, Hosie MJ. BAX/BCL-2 mRNA and protein expression in human breast MCF-7 cells exposed to drug vehicles-methanol and dimethyl sulfoxide (DMSO) for 24 hrs. Niger. Med. J. 2015;56(3):169-174.

(432) Bai R, Covell DG, Taylor GF, Kepler JA, Copeland TD, Nguyen NY, et al. Direct photoaffinity labeling by dolastatin 10 of the amino-terminal peptide of beta-tubulin containing cysteine 12. J. Biol. Chem. 2004;279(29):30731-30740.

(433) Paturle-Lafanechere L, Edde B, Denoulet P, Van Dorsselaer A, Mazarguil H, Le Caer JP, et al. Characterization of a major brain tubulin variant which cannot be tyrosinated. Biochemistry. 1991;30(43):10523-10528.

(434) Di Sante G, Casimiro MC, Pestell TG, Pestell RG. Time-lapse video microscopy for assessment of EYFP-Parkin aggregation as a marker for cellular mitophagy. J. Vis. Exp. 2016;(111). doi(111):10.3791/53657.

(435) Burke RT, Orth JD. Through the looking glass: Time-lapse microscopy and longitudinal tracking of single cells to study anti-cancer therapeutics. J. Vis. Exp. 2016;(111). doi(111):10.3791/53994.

(436) Lovell G, Dale NB, Trezise D. Real-time visualization and quantification of neutrophil extracellular traps. J Immunol. 2018;200 (1): 49-50

(437) Guan X. Cancer metastases: challenges and opportunities. Acta. Pharm. Sin. B. 2015;5(5):402-418.

(438) Bossi F, Tripodo C, Rizzi L, Bulla R, Agostinis C, Guarnotta C, et al. C1q as a unique player in angiogenesis with therapeutic implication in wound healing. Proc. Natl. Acad. Sci. U.S.A. 2014;111(11):4209-4214.

(439) Akhshi TK, Wernike D, Piekny A. Microtubules and actin crosstalk in cell migration and division. Cytoskeleton. 2014;71(1):1-23.

(440) American Type Culture Collection [Internet]. MTT Cell Proliferation Assay. Manassas: ATCC; [updated 2011; cited 2014 Mar. 23]. Available from: http://www.atcc.org/~/media/DA5285A1F52C414E864C966FD78C9A79.ashx

(441) Lim SW, Loh HS, Ting KN, Bradshaw TD, Allaudin ZN. Reduction of MTT to purple formazan by vitamin E isomers in the absence of cells. Trop. Life. Sci. Res. 2015;26(1):111-120.

(442) Hussey PJ, Hashimoto T. The cytoskeleton and signal transduction: Role and regulation of plant actin-and microtubule-binding proteins. Annu. Rev. Plant Biol. 2018:244-272.

(443) Frismantiene A, Kyriakakis E, Dasen B, Erne P, Resink TJ, Philippova M. Actin cytoskeleton regulates functional anchorage-migration switch during T-cadherin-induced phenotype modulation of vascular smooth muscle cells. Cell Adh. Migr. 2018;12(1):69-85.

(444) Lopata A, Hughes R, Tiede C, Heissler SM, Sellers JR, Knight PJ, et al. Affimer proteins for F-actin: novel affinity reagents that label F-actin in live and fixed cells. Sci. Rep. 2018;8(1):6572.

(445) Mirsaeidi M, Gidfar S, Vu A, Schraufnagel D. Annexins family: insights into their functions and potential role in pathogenesis of sarcoidosis. J. Transl. Med. 2016;14(1):89

(446) M. H. Visagie. *In vitro* cell signalling events of 2-methoxyestradiol-bis-sulphamate in a breast adenocarcinoma- and a non-tumorigenic breast epithelial cell line. [Masters of Science]. University of Pretoria; 2010.

(447) Krysko DV, Vanden Berghe T, D'Herde K, Vandenabeele P. Apoptosis and necrosis: detection, discrimination and phagocytosis. Methods. 2008;44(3):205-221.

(448) Brown M, Wittwer C. Flow cytometry: principles and clinical applications in hematology. Clin. Chem. 2000;46(8):1221-1229.

(449) Nunez R. DNA measurement and cell cycle analysis by flow cytometry. Curr. Issues Mol. Biol. 2001;3(3):67-70.

(450) Tanida I, Ueno T, Kominami E. LC3 and Autophagy. Methods Mol. Biol. 2008;445:77-88. doi: 10.1007/978-1-59745-157-4_4.

(451) Suzuki T, Fujikura K, Higashiyama T, Takata K. DNA staining for fluorescence and laser confocal microscopy. J. Histochem. Cytochem. 1997;45(1):49-53.

(452) Maiuri MC, Malik SA, Morselli E, Kepp O, Criollo A, Mouchel P, et al. Stimulation of autophagy by the p53 target gene Sestrin2. Cell cycle. 2009;8(10):1571-1576.

(453) Wojtala A, Bonora M, Malinska D, Pinton P, Duszynski J, Wieckowski MR. Methods to monitor ROS production by fluorescence microscopy and fluorometry. Meth. Enzymol. 2014;542: 243-262.

(454) Chaturvedi R, Cheng Y, Asim M, Bussiere FI, Xu H, Gobert AP, et al. Induction of polyamine oxidase 1 by Helicobacter pylori causes macrophage apoptosis by hydrogen peroxide release and mitochondrial membrane depolarization. J. Biol. Chem. 2004;279(38):40161-40173.

(455) Mahmood T, Yang PC. Western blot: technique, theory, and trouble shooting. N. Am. J. Med. Sci. 2012;4(9):429-434.

(456) Gross A, Jockel J, Wei MC, Korsmeyer SJ. Enforced dimerization of BAX results in its translocation, mitochondrial dysfunction and apoptosis. EMBO J. 1998;17(14):3878-3885.

(457) Zhang X, Tang N, Hadden TJ, Rishi AK. Akt, FoxO and regulation of apoptosis. Biochim. Biophys. Acta. 2011;1813(11):1978-1986.

(458) Schmidt M, Fernandez dM, van dH, Klompmaker R, Kops GJ, Lam EW, et al. Cell cycle inhibition by FoxO forkhead transcription factors involves downregulation of cyclin D. Mol. Cell Biol. 2002;22(22):7842-7852.

(459) Maiese K, Chong ZZ, Hou J, Shang YC. The “O” class: crafting clinical care with FoxO transcription factors. Adv. Exp. Med. Biol. 2009; 665:242–260.

(460) Lindqvist A, van Zon W, Rosenthal CK, Wolthuis RMF. Cyclin B1–Cdk1 activation continues after centrosome separation to control mitotic progression. PLoS Biol. 2007;5(5):e123.

(461) Miller KM, Tjeertes JV, Coates J, Legube G, Polo SE, Britton S, et al. Human HDAC1 and HDAC2 function in the DNA-damage response to promote DNA nonhomologous end-joining. Nat. Struct. Mol. Biol. 2010;17(99):1144-1151.

(462) Gottlieb TM, Jackson SP. The DNA-dependent protein kinase: requirement for DNA ends and association with Ku antigen. Cell. 1993;72(1):131-142.

(463) Danz R, Dietrich P, Soell A, Hoyer C, Wagener M, inventors; Jenoptik AG, assignee. Arrangement and method for polarization-optical interference contrast. United States patent US 7,046,436. 2006 May 16.

(464) Joubert A, Marais S, Maritz C. Influence of 2-methoxyestradiol on MCF-7 cells: an improved differential interference contrasting technique and Bcl-2 and Bax protein expression levels. Biocell. 2009;33(1):67-70.

(465) Danz R, Vogelsang A [Internet]. PlasDIC- a useful modification of the differential interference contrast according to Smith/Nomarski in transmitted light arrangement.

Gottingen: Photonik; [cited 2014 Mar. 23]. Available from: http://www.carlzeiss.co.uk/C12567BE00472A5C/EmbedTitelIntern/Article-PlasDic_Photonic_e/$File/PlasDIC_Photonik_2004March_e.pdf.

(466) El Arnaout T, Kurki L, Vaarala T, Ojala K, Cullen PJ, Sullivan C. Crystallization monitoring using simultaneous bright field and PlasDIC imaging. Chem. Eng. J. 2016;300:64-74.

(467) Visagie MH, Joubert AM. 2-Methoxyestradiol-bis-sulfamate induces apoptosis and autophagy in a tumorigenic breast epithelial cell line. Mol. Cell. Biochem. 2011;357(1-2):343-352.

(468) Munshi A, Hobbs M, Meyn RE. Clonogenic cell survival assay. Methods Mol. Med. 2005;110:21-28.

(469) Rafehi H, Orlowski C, Georgiadis GT, Ververis K, El-Osta A, Karagiannis TC. Clonogenic assay: adherent cells. J. Vis. Exp. 2011;(49). pii: 2573. doi: 10.3791/2573.

(470) Puck TT, Marcus PI. Action of x-rays on mammalian cells. J. Exp. Med. 1956;103(5):653-666.

(471) Tanaka T, Huang X, Halicka HD, Zhao H, Traganos F, Albino AP, et al. Cytometry of ATM activation and histone H2AX phosphorylation to estimate extent of DNA damage induced by exogenous agents. Cytometry Part A. 2007;71(9):648-661.

(472) Ewald B, Sampath D, Plunkett W. H2AX phosphorylation marks gemcitabine-induced stalled replication forks and their collapse upon S-phase checkpoint abrogation. Mol. Cancer Ther. 2007;6(4):1239-1248.

(473) Najafi M, Fardid R, Hadadi G, Fardid M. The mechanisms of radiation-induced bystander effect. JBPE. 2014;4(4): 163–172.

(474) Nagasawa H, Little JB. Induction of sister chromatid exchanges by extremely low doses of alpha-particles. Cancer Res. 1992;52(22):6394-6396.

(475) Sawant SG, Randers-Pehrson G, Metting NF, Hall EJ. Adaptive response and the bystander effect induced by radiation in C3H 10T1/2 cells in culture. Radiat Res. 2001;156(2):177-180.

(476) Dimova EG, Bryant PE, Chankova SG. Adaptive response: some underlying mechanisms and open questions. Genet. Mol. Biol. 2008;31(2):396-408.

(477) Martin TA, Ye L, Sanders AJ, Lane J, Jiang WG. Cancer invasion and metastasis: molecular and cellular perspective. Landes Bioscience: Madame Curie Bioscience Database [Internet]; 2013.

(478) Ishizaki T, Morishima Y, Okamoto M, Furuyashiki T, Kato T, Narumiya S. Coordination of microtubules and the actin cytoskeleton by the Rho effector mDia1. Nat. Cell. Biol. 2001;3(1):8-14.

(479) Raftopoulou M, Hall A. Cell migration: Rho GTPases lead the way. Dev. Biol. 2004;265(1):23-32.

(480) Small JV, Kaverina I. Microtubules meet substrate adhesions to arrange cell polarity. Curr. Opin. Cell. Biol. 2003;15(1):40-47.

(481) Redza-Dutordoir M, Averill-Bates D. Activation of apoptosis signalling pathways by reactive oxygen species. Biochim. Biophys. Acta. 2016;1863(12):2977-2992.

(482) Westphal D, Dewson G, Czabotar PE, Kluck RM. Molecular biology of Bax and Bak activation and action. Biochim. Biophys. Acta. 2011;1813(4):521-531.

(483) Didonna A, Sussman J, Benetti F, Legname G. The role of Bax and caspase-3 in doppel-induced apoptosis of cerebellar granule cells. Prion. 2012;6(3):309-316.

(484) Jänicke RU. MCF-7 breast carcinoma cells do not express caspase-3. Breast Cancer Res. Treat. 2009;117(1):219-221.

(485) Daitoku H, Sakamaki J, Fukamizu A. Regulation of FoxO transcription factors by acetylation and protein–protein interactions. Biochim. Biophys. Acta. 2011;1813(11):1954-1960.

(486) Zhao Y, Wang Y, Zhu W. Applications of post-translational modifications of FoxO family proteins in biological functions. J. Cell Biol. 2011;3(5):276-282.

(487) Muschel RJ, Zhang HB, Iliakis G, McKenna WG. Cyclin B expression in HeLa cells during the G2 block induced by ionizing radiation. Cancer Res. 1991;51(19):5113-5117.

(488) Fisher CJ, Goswami PC. Mitochondria-targeted antioxidant enzyme activity regulates radioresistance in human pancreatic cancer cells. Cancer Biol. Ther. 2008;7(8):1271-1279.

(489) Hallahan DE. Radiation-mediated gene expression in the pathogenesis of the clinical radiation response. Semin. Radiat. Oncol. 1996;6(4):250-267.

(490) Cromie GA, Connelly JC, Leach DRF. Recombination at double-strand breaks and DNA ends: conserved mechanisms from phage to humans. Mol. Cell. 2001;8(6):1163-1174.

(491) Hoeijmakers JHJ. Genome maintenance mechanisms for preventing cancer. Nature. 2001;411(6835):366-374.

(492) Shiloh Y. ATM: expanding roles as a chief guardian of genome stability. Exp. Cell Res. 2014;329(1):154-161.

(493) Franco S, Gostissa M, Zha S, Lombard DB, Murphy MM, Zarrin AA, et al. H2AX prevents DNA breaks from progressing to chromosome breaks and translocations. Mol. Cell. 2006;21(2):201-214.

(494) Sheikh MS, Burns TF, Huang Y, Wu GS, Amundson S, Brooks KS, et al. p53-dependent and -independent regulation of the death receptor KILLER/DR5 gene expression in response to genotoxic stress and tumor necrosis factor alpha. Cancer Res. 1998;58(8):1593-1598.

(495) Khanna KK, Jackson SP. DNA double-strand breaks: signaling, repair and the cancer connection. Nat. Genet. 2001;27(3):247-254.

(496) Koike M, Yutoku Y, Koike A. The defect of Ku70 affects sensitivity to x-ray and radiation-induced caspase-dependent apoptosis in lung cells. J. Vet. Sci. 2013;75(4):415-420.

(497) Tak H, Mhatre M. Molecular characterization of DNA repair protein Ku70 from Vitis vinifera and its purification from transgenic tobacco. Transgenic Res. 2013;22(4):839-848.

(498) CANSA - The Cancer Association of South Africa [Internet]. Prevalence Cancer. Available from: https://www.cansa.org.za/south-african-cancer-statistics/

(499) Yao H, He G, Yan S, Chen C, Song L, Rosol TJ, et al. Triple-negative breast cancer: is there a treatment on the horizon? Oncotarget. 2017;8(1):1913-1924.

(500) Cannan WJ, Pederson DS. Mechanisms and consequences of double-strand DNA break formation in chromatin. J. Cell Physiol. 2016;231(1):3-14.

(501) Nickoloff JA. DNA repair dysregulation in cancer: From molecular mechanisms to synthetic lethal opportunities. Stress Response Pathways in Cancer. 2015: 7-28. doi:10.1007/978-94-017-9421-3_2

(502) Baskar R, Lee KA, Yeo R, Yeoh KW. Cancer and radiation therapy: current advances and future directions. Int. J. Med. Sci. 2012;9(3):193-199.

(503) Jackson SP, Bartek J. The DNA-damage response in human biology and disease. Nature. 2009;461(7267):1071-1078.

(504) Emami B, Lyman J, Brown A, Cola L, Goitein M, Munzenrider JE, et al. Tolerance of normal tissue to therapeutic irradiation. Int. J. Radiat. Oncol. Biol. Phys. 1991;21(1):109-122.

(505) Begg AC, Stewart FA, Vens C. Strategies to improve radiotherapy with targeted drugs. Nat. Rev. Cancer. 2011;11(4):239-253.

(506) Howard M, Beltran C, Sarkaria J, Herman MG. Characterization of relative biological effectiveness for conventional radiation therapy: a comparison of clinical 6 MV X-rays and 137Cs. J. Radiat. Res. 2017;58(5):608-613.

(507) Baskar R. Emerging role of radiation induced bystander effects: Cell communications and carcinogenesis. Genome Integr. 2010;1(1):13.

(508) Guo JY, Chen HY, Mathew R, Fan J, Strohecker AM, Karsli-Uzunbas G, et al. Activated Ras requires autophagy to maintain oxidative metabolism and tumorigenesis. Genes Dev. 2011;25(5):460-470.

(509) Verheij M. Clinical biomarkers and imaging for radiotherapy-induced cell death. Cancer Metastasis Rev. 2008;27(3):471-480.

(510) Dewey WC, Ling CC, Meyn RE. Radiation-induced apoptosis: relevance to radiotherapy. Int. J. Radiat. Oncol. Biol. Phys. 1995;33(4):781-796.

(511) Cragg MS, Harris C, Strasser A, Scott CL. Unleashing the power of inhibitors of oncogenic kinases through BH3 mimetics. Nat. Rev. Cancer. 2009;9(5):321-326.

(512) Roninson IB. Tumor cell senescence in cancer treatment. Cancer Res. 2003;63(11):2705-2715.

(513) Gallez B. Radiosensitization. Schwab M. (eds) Encyclopedia of Cancer. Berlin: Springer; 2011

(514) Wasserman TH, Chapman JD. Radiation response modulation. Part A. Chemical sensitizers and protectors. Principles and Practice of Radiation Oncology. 4th ed. Philadelphia: Lippincott; 2004.

(515) Thomas SR, Khuntia D. Motexafin gadolinium injection for the treatment of brain metastases in patients with non-small cell lung cancer. Int J Nanomedicine. 2007;2(1):79-87.

(516) Chung TD, Schmidt-Ullrich RK. Radiation response modulation. Part B. Biologic response modifiers. Perez CA, Brady LW, Halperin EC, Schmidt-Ullrich (eds) Principles and practice of radiation oncology, 4th ed. Philadelphia: Lippincott Williams & Wilkins; 2004.

(517) Dennis LK, Lynch CF, Torner JC. Epidemiologic association between prostatitis and prostate cancer. Urology. 2002;60(1):78-83.

(518) Howe LR. Inflammation and breast cancer. Cyclooxygenase/prostaglandin signaling and breast cancer. Breast Cancer Res. 2007;9(4):210.

(519) Coussens LM, Werb Z. Inflammation and cancer. Nature. 2002;420(6917):860-867.

(520) Palayoor ST, Arayankalayil MJ, Shoaibi A, Coleman CN. Radiation sensitivity of human carcinoma cells transfected with small interfering RNA targeted against cyclooxygenase-2. Clin. Cancer Res. 2005;11(19):6980-6986.

(521) Wood KW, Cornwell WD, Jackson JR. Past and future of the mitotic spindle as an oncology target. Curr. Opin. Pharmacol. 2001;1(4):370-377.

(522) Downing KH. Structural basis for the interaction of tubulin with proteins and drugs that affect microtubule dynamics 1. Annu. Rev. Cell Dev. Biol. 2000;16(1):89-111.

(523) Nettles JH, Li H, Cornett B, Krahn JM, Snyder JP, Downing KH. The binding mode of epothilone A on α, ß-tubulin by electron crystallography. Science. 2004;305(5685):866-869.

(524) Hadfield JA, Ducki S, Hirst N, McGown AT. Tubulin and microtubules as targets for anticancer drugs. Prog. Cell Cycle Res. 2003;5:309-325.

(525) Pellegrini F, Budman DR. Tubulin function, action of antitubulin drugs, and new drug development. Cancer Invest. 2005;23(3):264-273.

(526) Schiff PB, Horwitz SB. Taxol stabilizes microtubules in mouse fibroblast cells. Proc. Natl. Acad. Sci. U.S.A. 1980;77(3):1561-1565.

(527) Hunt JT. Discovery of ixabepilone. Mol. Cancer Ther. 2009;8(2):275-281.

(528) Clute P, Pines J. Temporal and spatial control of cyclin B1 destruction in metaphase. Nat. Cell Biol. 1999;1(2):82-87.

(529) Ball P, Haupt M, Knuppen R. Biogenesis and metabolism of catechol estrogens *in vitro*. Catechol Estrogens. 1983:91-104.

(530) De Vries E,F.J., Doorduin J, Vellinga NAR, Van Waarde A, Dierckx RA, Klein HC. Can celecoxib affect P-glycoprotein-mediated drug efflux? A microPET study. Nucl. Med. Biol. 2008;35(4):459-466.

(531) Kuo KL, Lin WC, Ho IL, Chang HC, Lee PY, Chung YT, Hsieh JT, Pu YS, Shi CS, Huang KH. 2-methoxyestradiol induces mitotic arrest, apoptosis, and synergistic cytotoxicity with arsenic trioxide in human urothelial carcinoma cells. PLoS One. 2013;8(8):e68703.

(532) Lee ST, Lee JY, Han CR, Kim YH, Taub D, Kim YH. Dependency of 2-methoxyestradiol-induced mitochondrial apoptosis on mitotic spindle network impairment and prometaphase arrest in human Jurkat T cells. Biochem. Pharmacol. 2015;94(4):257-269.

(533) Kulke MH, Chan JA, Meyerhardt JA, Zhu AX, Abrams TA, Blaszkowsky LS, et al. A prospective phase II study of 2-methoxyestradiol administered in combination with bevacizumab in patients with metastatic carcinoid tumors. Cancer Chemother. Pharmacol. 2011;68(2):293-300.

(534) Chiche J, Ilc K, Laferriere J, Trottier E, Dayan F, Mazure NM, et al. Hypoxia-inducible carbonic anhydrase IX and XII promote tumor cell growth by counteracting acidosis through the regulation of the intracellular pH. Cancer Res. 2009;69(1):358-368.

(535) Desai KGH, Mallery SR, Schwendeman SP. Effect of formulation parameters on 2-methoxyestradiol release from injectable cylindrical poly (DL-lactide-co-glycolide) implants. Eur. J. Pharm. Biopharm. 2008;70(1):187-198.

(536) Leese MP, Leblond B, Smith A, Newman SP, Di Fiore A, De Simone G, et al. 2-substituted estradiol bis-sulfamates, multitargeted antitumor agents: synthesis, *in vitro* SAR, protein crystallography, and *in vivo* activity. J. Med. Chem. 2006;49(26):7683-7696.

(537) Van Zijl C, Lottering M, Steffens F, Joubert A. *In vitro* effects of 2-methoxyestradiol on MCF-12A and MCF-7 cell growth, morphology and mitotic spindle formation. Cell Biochem. Funct. 2008;26(5):632-642.

(538) Wesolowska O, Paprocka M, Kozlak J, Motohashi N, Dus D, Michalak K. Human sarcoma cell lines MES-SA and MES-SA/Dx5 as a model for multidrug resistance modulators screening. Anticancer Res. 2005;25(1):383-389.

(539) Antonipillai J, Francis SL. Inhibition of LIM kinase inhibits cancer growth. J. Biochem. Biotechnol. 2018;1(1).

(540) Gorovoy M, Niu J, Bernard O, Profirovic J, Minshall R, Neamu R, et al. LIM kinase 1 coordinates microtubule stability and actin polymerization in human endothelial cells. J. Biol. Chem. 2005;280(28):26533-26542.

(541) Chakrabarti R, Jones JL, Oelschlager DK, Tapia T, Tousson A, Grizzle WE. Phosphorylated LIM kinases colocalize with gamma-tubulin in centrosomes during early stages of mitosis. Cell Cycle. 2007;6(23):2944-2952.

(542) Worthylake RA, Burridge K. RhoA and ROCK promote migration by limiting membrane protrusions. J. Biol. Chem. 2003;278(15):13578-13584.

(543) Wang W, Mouneimne G, Sidani M, Wyckoff J, Chen X, Makris A, et al. The activity status of cofilin is directly related to invasion, intravasation, and metastasis of mammary tumors. J. Cell Biol. 2006;173(3):395-404.

(544) Bagheri-Yarmand R, Mazumdar A, Sahin AA, Kumar R. LIM kinase 1 increases tumor metastasis of human breast cancer cells via regulation of the urokinase-type plasminogen activator system. Int. J. Cancer. 2006;118(11):2703-2710.

(545) Xia H, Sun S, Wang B, Wang T, Liang C, Li G, et al. miR-143 inhibits NSCLC cell growth and metastasis by targeting Limk1. Int. J. Mol. Sci. 2014;15(7):11973-11983.

(546) Li R, Doherty J, Antonipillai J, Chen S, Devlin M, Visser K, et al. LIM kinase inhibition reduces breast cancer growth and invasiveness but systemic inhibition does not reduce metastasis in mice. Clin. Exp. Metastasis. 2013;30(4):483-495.

(547) Prunier C, Josserand V, Vollaire J, Beerling E, Petropoulos C, Destaing O, et al. LIM Kinase Inhibitor Pyr1 Reduces the Growth and Metastatic Load of Breast Cancers. Cancer Res. 2016;76(12):3541-3552.

(548) Prudent R, Vassal-Stermann E, Nguyen CH, Pillet C, Martinez A, Prunier C, et al. Pharmacological inhibition of LIM kinase stabilizes microtubules and inhibits neoplastic growth. Cancer Res. 2012;72(17):4429-4439.

(549) Mardilovich K, Baugh M, Crighton D, Kowalczyk D, Gabrielsen M, Munro J, et al. LIM kinase inhibitors disrupt mitotic microtubule organization and impair tumor cell proliferation. Oncotarget. 2015;6(36):38469-38486.

(550) Chen Q, Jiao D, Hu H, Song J, Yan J, Wu L, et al. Downregulation of LIMK1 level inhibits migration of lung cancer cells and enhances sensitivity to chemotherapy drugs. Oncol. Res. 2013;20(11):491-498.

(551) Wang W, Eddy R, Condeelis J. The cofilin pathway in breast cancer invasion and metastasis. Nat. Rev. Cancer. 2007;7(6):429-440.

(552) Shibue T, Brooks MW, Inan MF, Reinhardt F, Weinberg RA. The outgrowth of micrometastases is enabled by the formation of filopodium-like protrusions. Cancer Discov. 2012;2(8):706-721

(553) Weaver BA. How Taxol/paclitaxel kills cancer cells. Mol. Biol. Cell. 2014;25(18):2677-2681.

(554) Wang X, Pan L, Mao N, Sun L, Qin X, Yin J. Cell-cycle synchronization reverses Taxol resistance of human ovarian cancer cell lines. Cancer Cell Int. 2013;13(1):77.

(555) Rivera E, Cianfrocca M. Overview of neuropathy associated with taxanes for the treatment of metastatic breast cancer. Cancer Chemother. Pharmacol. 2015;75(4):659-670.

(556) Patel N, Chatterjee SK, Vrbanac V, Chung I, Mu CJ, Olsen RR, et al. Rescue of paclitaxel sensitivity by repression of Prohibitin1 in drug-resistant cancer cells. Proc. Natl. Acad. Sci. U.S.A. 2010;107(6):2503-2508.

(557) Kamath K, Okouneva T, Larson G, Panda D, Wilson L, Jordan MA. 2-Methoxyestradiol suppresses microtubule dynamics and arrests mitosis without depolymerizing microtubules. Mol. Cancer Ther. 2006;5(9):2225-2233.

(558) Theron A, Prudent R, Nolte E, van dB, Punchoo R, Marais S, et al. Novel *in silico*-designed estradiol analogues are cytotoxic to a multidrug-resistant cell line at nanomolar concentrations. Cancer Chemother. Pharmacol. 2015;75(2):431-437.

(559) A. E. Theron. *In vitro* and *in vivo* anti-cancer properties of novel spindle disruptors. [PhD thesis]. University of Pretoria; 2016.

(560) Zraikat M, Shnyder S, Sheldrake H, Patterson L. Tumour Dissemination And Assays Involved. Arch. Can. Res. 2017;5(2):144.

(561) Eichenlaub-Ritter U, Winterscheidt U, Vogt E, Shen Y, Tinneberg H, Sorensen R. 2-Methoxyestradiol induces spindle aberrations, chromosome congression failure, and nondisjunction in mouse oocytes. Biol. Reprod. 2007;76(5):784-793.

(562) Ting CM, Lee YM, Wong C, Wong AS, Lung HL, Lung ML, et al. 2-Methoxyestradiol induces endoreduplication through the induction of mitochondrial oxidative stress and the activation of MAPK signaling pathways. Biochem. Pharmacol. 2010;79(6):825-841.

(563) Wang J, Lou P, Lesniewski R, Henkin J. Paclitaxel at ultra low concentrations inhibits angiogenesis without affecting cellular microtubule assembly. Anticancer Drugs. 2003;14(1):13-19.

(564) Theron AE, Nolte EM, Lafanechere L, Joubert AM. Molecular crosstalk between apoptosis and autophagy induced by a novel 2-methoxyestradiol analogue in cervical adenocarcinoma cells. Cancer Cell Int. 2013;13(1):87.

(565) Vasiliev JM, Gelfand IM, Domnina LV, Ivanova OY, Komm SG, Olshevskaja LV. Effect of colcemid on the locomotory behaviour of fibroblasts. J. Embryol. Exp. Morphol. 1970;24(3):625-640.

(566) Ning W, Yu Y, Xu H, Liu X, Wang D, Wang J, et al. The CAMSAP3-ACF7 complex couples noncentrosomal microtubules with actin filaments to coordinate their dynamics. Dev. Cell. 2016;39(1):61-74.

(567) McHardy LM, Sinotte R, Troussard A, Sheldon C, Church J, Williams DE, et al. The tumor invasion inhibitor dihydromotuporamine C activates RHO, remodels stress fibers and focal adhesions, and stimulates sodium-proton exchange. Cancer Res. 2004;64(4):1468-1474.

(568) Maddox AS, Burridge K. RhoA is required for cortical retraction and rigidity during mitotic cell rounding. J. Cell Biol. 2003;160(2):255-265.

(569) Acevedo K, Li R, Soo P, Suryadinata R, Sarcevic B, Valova VA, et al. The phosphorylation of p25/TPPP by LIM kinase 1 inhibits its ability to assemble microtubules. Exp. Cell Res. 2007;313(20):4091-4106.

(570) Tsuchida E, Kaida A, Pratama E, Ikeda M, Suzuki K, Harada K, et al. Effect of x-irradiation at different stages in the cell cycle on individual cell–based kinetics in an asynchronous cell population. PloS ONE. 2015;10(6):e0128090.

(571) Freytag SO, Paielli D, Wing M, Rogulski K, Brown S, Kolozsvary A, et al. Efficacy and toxicity of replication-competent adenovirus-mediated double suicide gene therapy in combination with radiation therapy in an orthotopic mouse prostate cancer model. Int. J. Radiat. Oncol. Biol. Phys. 2002;54(3):873-885.

(572) Amorino GP, Freeman ML, Choy H. Enhancement of radiation effects *in vitro* by the estrogen metabolite 2-methoxyestradiol. Radiat. Res. 2000;153(4):384-391.

(573) Huober JB, Nakamura S, Meyn R, Roth JA, Mukhopadhyay T. Oral administration of an estrogen metabolite-induced potentiation of radiation antitumor effects in presence of wild-type p53 in non–small-cell lung cancer. Int. J. Radiat. Oncol. Biol. Phys. 2000;48(4):1127-1137.

(574) Barchiesi F, Jackson EK, Fingerle J, Gillespie DG, Odermatt B, Dubey RK. 2-Methoxyestradiol, an estradiol metabolite, inhibits neointima formation and smooth muscle cell growth via double blockade of the cell cycle. Circ. Res. 2006;99(3):266-274.

(575) Dubey RK, Jackson EK, Keller PJ, Imthurn B, Rosselli M. Estradiol metabolites inhibit endothelin synthesis by an estrogen receptor-independent mechanism. Hypertension. 2001;37(2 Pt 2):640-644.

(576) Dent P, Reardon DB, Park JS, Bowers G, Logsdon C, Valerie K, et al. Radiation-induced release of transforming growth factor alpha activates the epidermal growth factor receptor and mitogen-activated protein kinase pathway in carcinoma cells, leading to increased proliferation and protection from radiation-induced cell death. Mol. Biol. Cell. 1999;10(8):2493-2506.

(577) Carter S, Auer KL, Reardon DB, Birrer M, Fisher PB, Valerie K, et al. Inhibition of the mitogen activated protein (MAP) kinase cascade potentiates cell killing by low dose ionizing radiation in A431 human squamous carcinoma cells. Oncogene. 1998;16(21):2787-2796.

(578) Reardon DB, Contessa JN, Mikkelsen RB, Valerie K, Amir C, Dent P, et al. Dominant negative EGFR-CD533 and inhibition of MAPK modify JNK1 activation and enhance radiation toxicity of human mammary carcinoma cells. Oncogene. 1999;18(33):4756-4766.

(579) Androic I, Krämer A, Yan R, Rödel F, Gätje R, Kaufmann M, et al. Targeting cyclin B1 inhibits proliferation and sensitizes breast cancer cells to taxol. BMC Cancer. 2008;8(1):391.

(580) Wang A, Yoshimi N, Ino N, Tanaka T, Mori H. Overexpression of cyclin B1 in human colorectal cancers. J. Cancer Res. Clin. Oncol. 1997;123(2):124-127.

(581) Kawamoto H, Koizumi H, Uchikoshi T. Expression of the G2-M checkpoint regulators cyclin B1 and cdc2 in nonmalignant and malignant human breast lesions: immunocytochemical and quantitative image analyses. Am. J. Pathol. 1997;150(1):15-23.

(582) Soria JC, Jang SJ, Khuri FR, Hassan K, Liu D, Hong WK, et al. Overexpression of cyclin B1 in early-stage non-small cell lung cancer and its clinical implication. Cancer Res. 2000;60(15):4000-4004.

(583) Banerjee SK, Weston AP, Zoubine MN, Campbell DR, Cherian R. Expression of cdc2 and cyclin B1 in Helicobacter pylori-associated gastric MALT and MALT lymphoma: relationship to cell death, proliferation, and transformation. Am. J. Pathol. 2000;156(1):217-225.

(584) Hassan KA, Ang KK, El-Naggar AK, Story MD, Lee JI, Liu D, et al. Cyclin B1 overexpression and resistance to radiotherapy in head and neck squamous cell carcinoma. Cancer Res. 2002;62(22):6414-6417.

(585) Rudolph P, Kühling H, Alm P, Fernö M, Baldetorp B, Olsson H, et al. Differential prognostic impact of the cyclins E and B in premenopausal and postmenopausal women with lymph node-negative breast cancer. Int. J. Cancer. 2003;105(5):674-680.

(586) Zhao M, Kim Y, Yoon B, Kim S, Kang M, Kim S, et al. Expression profiling of cyclin B1 and D1 in cervical carcinoma. Exp Oncol. 2006;28(1):44-48.

(587) Suzuki T, Urano T, Miki Y, Moriya T, Akahira J, Ishida T, et al. Nuclear cyclin B1 in human breast carcinoma as a potent prognostic factor. Cancer Sci. 2007;98(5):644-651.

(588) Collecchi P, Santoni T, Gnesi E, Naccarato AG, Passoni A, Rocchetta M, et al. Cyclins of phases G1, S and G2/M are overexpressed in aneuploid mammary carcinomas. Cytometry. 2000;42(4):254-260.

(589) Shen M, Feng Y, Gao C, Tao D, Hu J, Reed E, et al. Detection of cyclin b1 expression in g(1)-phase cancer cell lines and cancer tissues by postsorting Western blot analysis. Cancer Res. 2004;64(5):1607-1610.

(590) Yuan J, Krämer A, Matthess Y, Yan R, Spänkuch B, Gätje R, et al. Stable gene silencing of cyclin B1 in tumor cells increases susceptibility to taxol and leads to growth arrest *in vivo*. Oncogene. 2006;25(12):1753-1762.

(591) Yuan J, Yan R, Krämer A, Eckerdt F, Roller M, Kaufmann M, et al. Cyclin B1 depletion inhibits proliferation and induces apoptosis in human tumor cells. Oncogene. 2004;23(34):5843-5852.

(592) Maity A, McKenna WG, Muschel RJ. The molecular basis for cell cycle delays following ionizing radiation: a review. Radiother. Oncol. 1994;31(1):1-13.

(593) Yang C, Lee M, Hao J, Cui X, Guo X, Smal C, et al. Deoxycytidine kinase regulates the G2/M checkpoint through interaction with cyclin-dependent kinase 1 in response to DNA damage. Nucleic Acids Res. 2012;40(19):9621-9632.

(594) Bernhard EJ, Maity A, Muschel RJ, McKenna WG. Effects of ionizing radiation on cell cycle progression. Radiat. Environ. Biophys. 1995;34(2):79-83.

(595) Theron AE, Nolte EM, Lafanechère L, Joubert AM. Molecular crosstalk between apoptosis and autophagy induced by a novel 2-methoxyestradiol analogue in cervical adenocarcinoma cells. Cancer Cell Int. 2013;13(1):87.

(596) Newman SP, Foster PA, Stengel C, Day JM, Ho YT, Judde JG, et al. STX140 is efficacious *in vitro* and *in vivo* in taxane-resistant breast carcinoma cells. Clin. Cancer Res. 2008;14(2):597-606.

(597) Murr R, Vaissiere T, Sawan C, Shukla V, Herceg Z. Orchestration of chromatin-based processes: mind the TRRAP. Oncogene. 2007;26(37):5358-5372.

(598) Hay N. Interplay between FOXO, TOR, and Akt. Biochim. Biophys. Acta. 2011;1813(11):1965-1970.

(599) Zhang X, Tang N, Hadden TJ, Rishi AK. Akt, FoxO and regulation of apoptosis. Biochim. Biophys. Acta. 2011;1813(11):1978-1986.

(600) Lam EW, Francis RE, Petkovic M. FOXO transcription factors: key regulators of cell fate. Biochem. Soc. Trans. 2006;34(Pt 5):722-726.

(601) Datta SR, Dudek H, Tao X, Masters S, Fu H, Gotoh Y, et al. Akt phosphorylation of BAD couples survival signals to the cell-intrinsic death machinery. Cell. 1997;91(2):231-241.

(602) Brunet A, Bonni A, Zigmond MJ, Lin MZ, Juo P, Hu LS, et al. Akt promotes cell survival by phosphorylating and inhibiting a Forkhead transcription factor. Cell. 1999;96(6):857-868.

(603) Tsuchiya K, Ogawa Y. Forkhead box class O family member proteins: The biology and pathophysiological roles in diabetes. J. Diabetes Investig. 2017;8(6):726-734.

(604) Fu Z, Tindall D. FOXOs, cancer and regulation of apoptosis. Oncogene. 2008;27(16):2312-2319.

(605) Feehan RP, Shantz LM. Negative regulation of the FOXO3a transcription factor by mTORC2 induces a pro-survival response following exposure to ultraviolet-B irradiation. Cell Signal. 2016;28(8):798-809.

(606) Li H, Kim J, Waldman T. Radiation-induced Akt activation modulates radioresistance in human glioblastoma cells. Radiat. Oncol. 2009;4(1):43.

(607) Schuurbiers OC, Kaanders JH, van der Heijden, Henricus FM, Dekhuijzen RP, Oyen WJ, Bussink J. The PI3-K/AKT-pathway and radiation resistance mechanisms in non-small cell lung cancer. J. Thorac. Oncol. 2009;4(6):761-767.

(608) Wang R, Brattain MG. AKT can be activated in the nucleus. Cell Signal. 2006;18(10):1722-1731.

(609) Viniegra JG, Martinez N, Modirassari P, Hernandez Losa J, Parada Cobo C, Sanchez-Arevalo Lobo VJ, et al. Full activation of PKB/Akt in response to insulin or ionizing radiation is mediated through ATM. J. Biol. Chem. 2005;280(6):4029-4036.

(610) Bozulic L, Surucu B, Hynx D, Hemmings BA. PKBα/Akt1 acts downstream of DNA-PK in the DNA double-strand break response and promotes survival. Mol. Cell. 2008;30(2):203-213.

(611) Toulany M, Lee KJ, Fattah KR, Lin YF, Fehrenbacher B, Schaller M, et al. Akt promotes post-irradiation survival of human tumor cells through initiation, progression, and termination of DNA-PKcs-dependent DNA double-strand break repair. Mol. Cancer Res. 2012;10(7):945-957.

(612) Toulany M, Rodemann HP. Potential of Akt mediated DNA repair in radioresistance of solid tumors overexpressing erbB-PI3K-Akt pathway. Transl. Cancer Res. 2013;2(3):190-202.

(613) Shimura T, Kakuda S, Ochiai Y, Nakagawa H, Kuwahara Y, Takai Y, et al. Acquired radioresistance of human tumor cells by DNA-PK/AKT/GSK3β-mediated cyclin D1 overexpression. Oncogene. 2010;29(34):4826-4837.

(614) Alt JR, Cleveland JL, Hannink M, Diehl JA. Phosphorylation-dependent regulation of cyclin D1 nuclear export and cyclin D1-dependent cellular transformation. Genes Dev. 2000;14(24):3102-3114.

(615) Alao JP. The regulation of cyclin D1 degradation: roles in cancer development and the potential for therapeutic invention. Mol. Cancer. 2007;6(1):24.

(616) Takahashi-Yanaga F, Sasaguri T. GSK-3β regulates cyclin D1 expression: a new target for chemotherapy. Cell Signal. 2008;20(4):581-589.

(617) Arnaudeau C, Lundin C, Helleday T. DNA double-strand breaks associated with replication forks are predominantly repaired by homologous recombination involving an exchange mechanism in mammalian cells1. J. Mol. Biol. 2001;307(5):1235-1245.

(618) Lerman OZ, Greives MR, Singh SP, Thanik VD, Chang CC, Seiser N, et al. Low-dose radiation augments vasculogenesis signaling through HIF-1-dependent and -independent SDF-1 induction. Blood. 2010;116(18):3669-3676.

(619) Semenza GL. Hypoxia-inducible factor 1: master regulator of O_2 homeostasis. Curr. Opin. Genet. Dev. 1998;8(5):588-594.

(620) Semenza GL. Signal transduction to hypoxia-inducible factor 1. Biochem. Pharmacol. 2002;64(5-6):993-998.

(621) Qing G, Simon MC. Hypoxia inducible factor-2α: a critical mediator of aggressive tumor phenotypes. Curr. Opin. Genet. Dev. 2009;19(1):60-66.

(622) Vijayanathan V, Venkiteswaran S, Nair SK, Verma A, Thomas TJ, Zhu BT, et al. Physiologic levels of 2-methoxyestradiol interfere with nongenomic signaling of 17beta-estradiol in human breast cancer cells. Clin. Cancer Res. 2006;12(7 Pt 1):2038-2048.

(623) Chen Z, Peng IC, Sun W, Su MI, Hsu PH, Fu Y, et al. AMP-activated protein kinase functionally phosphorylates endothelial nitric oxide synthase Ser633. Circ. Res. 2009;104(4):496-505.

(624) Gao N, Rahmani M, Dent P, Grant S. 2-Methoxyestradiol-induced apoptosis in human leukemia cells proceeds through a reactive oxygen species and Akt-dependent process. Oncogene. 2005;24(23):3797-3809.

(625) Ye DZ, Field J. PAK signaling in cancer. Cellular logistics. 2012;2(2):105-116.

(626) Tang Y, Zhou H, Chen A, Pittman RN, Field J. The Akt proto-oncogene links Ras to Pak and cell survival signals. J. Biol. Chem. 2000;275(13):9106-9109.

(627) Edwards DC, Sanders LC, Bokoch GM, Gill GN. Activation of LIM-kinase by Pak1 couples Rac/Cdc42 GTPase signalling to actin cytoskeletal dynamics. Nat. Cell. Biol. 1999;1(5):253-259.

(628) Wang X, Hu S, Liu L. Phosphorylation and acetylation modifications of FOXO3a: Independently or synergistically? Oncol. Lett. 2017;13(5):2867-2872.

(629) Tsuruta F, Masuyama N, Gotoh Y. The phosphatidylinositol 3-kinase (PI3K)-Akt pathway suppresses Bax translocation to mitochondria. J. Biol. Chem. 2002;277(16):14040-14047.

(630) Chorna I, Datsyuk L, Stoika R. Expression of Bax, Bad and Bcl-2 proteins under x-radiation effect towards human breast carcinoma MCF-7 cells and their doxorubicin-resistant derivatives. Exp. Oncol. 2005;27(3):196-201.

(631) Joubert A, Marais S, Maritz C. Influence of 2-methoxyestradiol on MCF-7 cells: An improved differential interference contrasting technique and Bcl-2 and Bax protein expression levels. Biocell. 2009;33(1):67-70.

(632) Day J, Foster P, Tutill H, Newman S, Ho Y, Leese M, et al. BCRP expression does not result in resistance to STX140 *in vivo*, despite the increased expression of BCRP in A2780 cells *in vitro* after long-term STX140 exposure. Br. J. Cancer. 2009;100(3):476-486.

(633) Salih DA, Brunet A. FoxO transcription factors in the maintenance of cellular homeostasis during aging. Curr. Opin. Cell Biol. 2008;20(2):126-136.

(634) Gelmon KA, O'reilly S, Tolcher AW, Campbell C, Bryce C, Ragaz J, et al. Phase I/II trial of biweekly paclitaxel and cisplatin in the treatment of metastatic breast cancer. J. Clin. Oncol. 1996;14(4):1185-1191.

(635) Dayal R, Singh A, Pandey A, Mishra KP. Reactive oxygen species as mediator of tumor radiosensitivity. J. Cancer Res. Ther. 2014;10(4):811-818.

(636) Jayakumar S, Kunwar A, Sandur SK, Pandey BN, Chaubey RC. Differential response of DU145 and PC3 prostate cancer cells to ionizing radiation: role of reactive oxygen species, GSH and Nrf2 in radiosensitivity. Biochim. Biophys. Acta. 2014;1840(1):485-494.

(637) Chetram MA, Bethea DA, Odero-Marah VA, Don-Salu-Hewage AS, Jones KJ, Hinton CV. ROS-mediated activation of AKT induces apoptosis via pVHL in prostate cancer cells. Mol. Cell Biochem. 2013;376(1-2):63-71.

(638) Filomeni G, De Zio D, Cecconi F. Oxidative stress and autophagy: the clash between damage and metabolic needs. Cell Death Differ. 2015;22(3):377-388.

(639) Shao X, Lai D, Zhang L, Xu H. Induction of autophagy and apoptosis via PI3K/AKT/TOR pathways by azadirachtin a in spodoptera litura cells. Sci. Rep. 2016;6:35482.

(640) Nolte E, Joubert A, Lakier R, van Rensburg A, Mercier A. Exposure of breast and lung Ccncer cells to a novel estrone analog prior to radiation enhances Bcl-2-mediated cell Death. Int. J. Mol. Sci. 2018;19(10):2887.

(641) Barnard S, Bouffler S, Rothkamm K. The shape of the radiation dose response for DNA double-strand break induction and repair. Genome Integr. 2013;4(1):1.

(642) Mao Z, Bozzella M, Seluanov A, Gorbunova V. Comparison of nonhomologous end joining and homologous recombination in human cells. DNA repair. 2008;7(10):1765-1771.

(643) Enriquez-Rios V, Dumitrache LC, Downing SM, Li Y, Brown EJ, Russell HR, et al. DNA-PKcs, ATM, and ATR Interplay Maintains Genome Integrity during Neurogenesis. J. Neurosci. 2017;37(4):893-905.

(644) Meyer B, Voss K, Tobias F, Jakob B, Durante M, Taucher-Scholz G. Clustered DNA damage induces pan-nuclear H2AX phosphorylation mediated by ATM and DNA–PK. Nucleic Acids Res. 2013;41(12):6109-6118.

(645) Luzhna L, Kathiria P, Kovalchuk O. Micronuclei in genotoxicity assessment: from genetics to epigenetics and beyond. Front. Genet. 2013;4:131.

(646) Dittmann K, Mayer C, Fehrenbacher B, Schaller M, Raju U, Milas L, et al. Radiation-induced epidermal growth factor receptor nuclear import is linked to activation of DNA-dependent protein kinase. J. Biol. Chem. 2005;280(35):31182-31189.

(647) Gu Y, Jin S, Gao Y, Weaver DT, Alt FW. Ku70-deficient embryonic stem cells have increased ionizing radiosensitivity, defective DNA end-binding activity, and inability to support V(D)J recombination. Proc. Natl. Acad. Sci. U.S.A 1997;94(15):8076-8081.

(648) Harari PM, Huang SM. Radiation response modification following molecular inhibition of epidermal growth factor receptor signaling. Semin. Radiat. Oncol. 2001;11(4):281-289.

(649) Christmann M, Kaina B. Nuclear translocation of mismatch repair proteins MSH2 and MSH6 as a response of cells to alkylating agents. J. Biol. Chem. 2000;275(46):36256-36262.

(650) Modrich P. Strand-specific mismatch repair in mammalian cells. J. Biol. Chem. 1997;272(40):24727-24730.

(651) Acharya S, Wilson T, Gradia S, Kane MF, Guerrette S, Marsischky GT, et al. hMSH2 forms specific mispair-binding complexes with hMSH3 and hMSH6. Proc. Natl. Acad. Sci. U.S.A. 1996;93(24):13629-13634.

(652) Palombo F, Iaccarino I, Nakajima E, Ikejima M, Shimada T, Jiricny J. hMutSβ, a heterodimer of hMSH2 and hMSH3, binds to insertion/deletion loops in DNA. Curr. Biol. 1996;6(9):1181-1184.

(653) Fishel R, Lescoe MK, Rao M, Copeland NG, Jenkins NA, Garber J, et al. The human mutator gene homolog MSH2 and its association with hereditary nonpolyposis colon cancer. Cell. 1993;75(5):1027-1038.

(654) Umar A, Boyer JC, Kunkel TA. DNA loop repair by human cell extracts. Science. 1994;266(5186):814-816.

(655) Li GM, Modrich P. Restoration of mismatch repair to nuclear extracts of H6 colorectal tumor cells by a heterodimer of human MutL homologs. Proc. Natl. Acad. Sci. U.S.A. 1995;92(6):1950-1954.

(656) Nicolaides NC, Papadopoulos N, Liu B, Weit Y, Carter KC, Ruben SM, et al. Mutations of two P/WS homologues in hereditary nonpolyposis colon cancer. Nature. 1994;371(6492):75-80.

(657) Vo BT, Morton D, Komaragiri S, Millena AC, Khan SA. TGF-β Effects on prostate cancer cell migration are mediated by PGE2 through activation of PI3K/AKT/mTOR pathway. Cancer Res. 2013;73(8):4080.

(658) Ni J, Cozzi P, Hao J, Beretov J, Chang L, Duan W, et al. Epithelial cell adhesion molecule (EpCAM) is associated with prostate cancer metastasis and chemo/radioresistance via the PI3K/Akt/mTOR signaling pathway. Int. J. Biochem. Cell Biol. 2013;45(12):2736-2748.

(659) Chang L, Graham PH, Hao J, Ni J, Bucci J, Cozzi PJ, et al. Acquisition of epithelial–mesenchymal transition and cancer stem cell phenotypes is associated with activation of the PI3K/Akt/mTOR pathway in prostate cancer radioresistance. Cell death & disease. 2013;4(10):e875.

(660) Chang L, Graham PH, Hao J, Bucci J, Cozzi PJ, Kearsley JH, et al. Emerging roles of radioresistance in prostate cancer metastasis and radiation therapy. Cancer Metastasis Rev. 2014;33(2-3):469-496.

(661) Chang L, Graham PH, Hao J, Ni J, Bucci J, Cozzi PJ, et al. PI3K/Akt/mTOR pathway inhibitors enhance radiosensitivity in radioresistant prostate cancer cells through inducing apoptosis, reducing autophagy, suppressing NHEJ and HR repair pathways. Cell death & disease. 2014;5(10):e1437.

(662) Serra V, Markman B, Scaltriti M, Eichhorn PJ, Valero V, Guzman M, et al. NVP-BEZ235, a dual PI3K/mTOR inhibitor, prevents PI3K signaling and inhibits the growth of cancer cells with activating PI3K mutations. Cancer Res. 2008;68(19):8022-8030.

(663) Wallin JJ, Edgar KA, Guan J, Berry M, Prior WW, Lee L, et al. GDC-0980 is a novel class I PI3K/mTOR kinase inhibitor with robust activity in cancer models driven by the PI3K pathway. Mol. Cancer Ther. 2011;10(12):2426-2436.

(664) Song JY, Lim JW, Kim H, Morio T, Kim KH. Oxidative stress induces nuclear loss of DNA repair proteins Ku70 and Ku80 and apoptosis in pancreatic acinar AR42J cells. J. Biol. Chem. 2003;278(38):36676-36687.

(665) Feinendegen LE, Pollycove M, Sondhaus CA. Responses to low doses of ionizing radiation in biological systems. Nonlinearity Biol. Toxicol. Med. 2004;2(3): 143-171.

(666) Wu T, Lin B, Chang H, Chang C. Radio resistance mechanisms of cancers: An overview and future perspectives. Biol. Med. S. 2015;S2.

(667) Shimura T, Sasatani M, Kawai H, Kamiya K, Kobayashi J, Komatsu K, et al. A comparison of radiation-induced mitochondrial damage between neural progenitor stem cells and differentiated cells. Cell cycle. 2017;16(6):565-573.

(668) Rich JN. Cancer stem cells in radiation resistance. Cancer Res. 2007;67(19):8980-8984.

(669) Drissi R, Wu J, Hu Y, Bockhold C, Dome JS. Telomere shortening alters the kinetics of the DNA damage response after ionizing radiation in human cells. Cancer Prev. Res. (Phila). 2011;4(12):1973-1981.

(670) Hei TK, Zhou H, Ivanov VN, Hong M, Lieberman HB, Brenner DJ, et al. Mechanism of radiation-induced bystander effects: a unifying model. J. Pharm. Pharmacol. 2008;60(8):943-950.

(671) Najafi M, Fardid R, Hadadi G, Fardid M. The mechanisms of radiation-induced bystander effect. J. Biomed. Phys. Eng. 2014;4(4):163-172.

(672) Mothersill C, Seymour C. Medium from irradiated human epithelial cells but not human fibroblasts reduces the clonogenic survival of unirradiated cells. Int. J. Radiat. Biol. 1997;71(4):421-427.

(673) Gómez-Millán J, Katz ISS, de Araujo Farias V, Linares-Fernández J, López-Peñalver J, Ortiz-Ferrón G, et al. The importance of bystander effects in radiation therapy in melanoma

skin-cancer cells and umbilical-cord stromal stem cells. Radiother. Oncol. 2012;102(3):450-458.

(674) Sokolov MV, Neumann RD. Radiation-induced bystander effects in cultured human stem cells. PLoS ONE. 2010;5(12):e14195.

(675) Liu Y, Kobayashi A, Maeda T, Fu Q, Oikawa M, Yang G, et al. Target irradiation induced bystander effects between stem-like and non stem-like cancer cells. Mutat. Res. 2015;773:43-47.

(676) Widel M, Przybyszewski WM, Cieslar-Pobuda A, Saenko YV, Rzeszowska-Wolny J. Bystander normal human fibroblasts reduce damage response in radiation targeted cancer cells through intercellular ROS level modulation. Mutat. Res. 2012;731(1-2):117-124.

(677) Widel M, Lalik A, Krzywon A, Poleszczuk J, Fujarewicz K, Rzeszowska-Wolny J. The different radiation response and radiation-induced bystander effects in colorectal carcinoma cells differing in p53 status. Mutat. Res. 2015;778:61-70.

(678) Sawal HA, Asghar K, Bureik M, Jalal N. Bystander signaling via oxidative metabolism. Onco. Targets Ther. 2017;10:3925-3940.

(679) Seiler F, Hellberg J, Lepper PM, Kamyschnikow A, Herr C, Bischoff M, et al. FOXO transcription factors regulate innate immune mechanisms in respiratory epithelial cells. J. Immunol. 2013;190(4):1603-1613.

(680) Kennedy SG, Kandel ES, Cross TK, Hay N. Akt/Protein kinase B inhibits cell death by preventing the release of cytochrome c from mitochondria. Mol. Cell Biol. 1999;19(8):5800-5810.

(681) Kuriyama S, Tsuji T, Sakuma T, Yamamoto T, Tanaka M. PLEKHN1 promotes apoptosis by enhancing Bax-Bak hetro-oligomerization through interaction with Bid in human colon cancer. Cell Death Dis. 2018;4(1):11.

(682) Nickoloff JA, Boss M, Allen CP, LaRue SM. Translational research in radiation-induced DNA damage signaling and repair. Transl. Cancer Res. 2017;6(Suppl 5):S875-891.

(683) Chang C, Leu J, Lee Y. The actin depolymerizing factor (ADF)/cofilin signaling pathway and DNA damage responses in cancer. Int. J. Mol. Sci. 2015;16(2):4095-4120.

(684) Kitazumi I, Tsukahara M. Regulation of DNA fragmentation: the role of caspases and phosphorylation. FEBS 2011;278(3):427-441.

9. Additional file 1

9.1 Radiation dose response curve: Flow cytometric quantification of apoptosis induction

The study design necessitated the determination of the lowest radiation dose that significantly induced apoptosis. In order to do so, MCF-7-, MDA-MB-231- and BT-20 cells were exposed to a radiation dose-response curve (0 Gy, 2 Gy, 4 Gy, 6 Gy, 8 Gy and 10 Gy). The selected radiation dose was used in all subsequent radiosensitization experiments.

MCF-7-, MDA-MB-231- and BT-20 cells propagated in medium only served as a negative control. The cell population consisted of 92.03±1.88%, 91.88±1.48% and 89.97±2.62% viable MCF-7-, MDA-MB-231- and BT-20 cells, respectively (Figure 1A). Cells undergoing apoptosis were quantified at 5.50±1.62% (MCF-7 cells), 5.85±1.08% (MDA-MB-231 cells) and 8.67±3.01% (BT-20 cells). No vehicle control was needed in this experiment as the cells were not exposed to the compounds. MCF-7- and MDA-MB-231 cells exposed to vinblastine, and BT-20 cells exposed to actinomycin D served as positive apoptotic controls. Cell viability was significantly decreased with a concurrent increase in apoptotic cells in all positive method control samples (Table 1A). MCF-7 cells exposed to the radiation dose-response curve revealed no significant difference in apoptosis induction (Figure 1A & 1B). Cell viability was significantly decreased after 6 Gy radiation in BT-20 cells (84.20±1.64%), with a concurrent increase in apoptosis (14.42±0.82%). MDA-MB-231- and BT-20 cells exposed to 8 Gy radiation revealed a significant decrease in cell viability (86.42±1.34% and 82.34±1.51%, respectively) and increased apoptosis (9.24±1.70% and 14.84±2.05%, respectively) (Table 1A). Cell viability was significantly decreased after 10 Gy radiation in MDA-MB-231- and BT-20 cells (83.85±3.43% and 80.91±0.47%, respectively), whereas apoptotic cells were significantly increased (11.10±2.65% and 16.92±0.55%, respectively). Additionally, MDA-MB-231 cells exposed to 10 Gy radiation revealed a significant increase in necrosis (5.06±1.44%) compared to the vehicle control (2.28±0.42%) (Figure 1B).

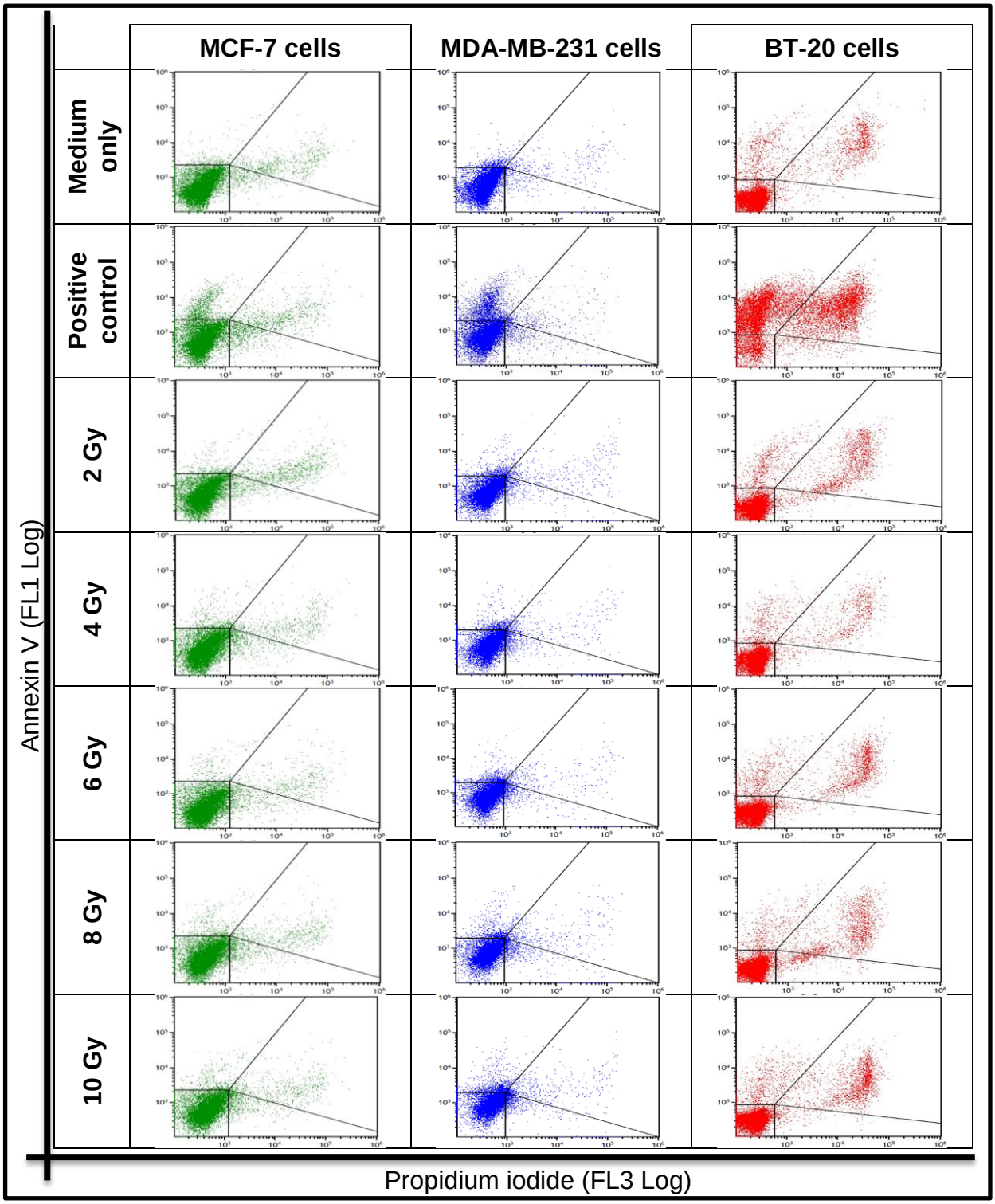

Figure 1A: Representative flow cytometric dot plots of annexin V-FITC of breast cancer cells exposed to a radiation dose range. Apoptotic cells were stained with annexin V-FITC (FL1 Log) and were plotted against propidium iodide (FL3 Log) that measured cells in late apoptosis and necrosis. MCF-7-, MDA-MB-231- and BT-20 cells were propagated in medium only (negative control), exposed to vinblastine (MCF-7- and MDA-MB-231 cells) or actinomycin D (BT-20 cells) as positive controls for apoptosis and exposed to a radiation dose-response curve: 2 Gy, 4 Gy, 6

Gy , 8 Gy and 10 Gy. The bottom left corner: viable cells; top left and right quadrants: apoptotic cells; bottom right quadrant: necrotic cells.

Table 1A: Annexin V-FITC analysis of MCF-7-, MDA-MB-231- and BT-20 breast cancer cells following exposure to a radiation dose range. Kaluza Analysis software version 1.5 (FL, USA) was used to generate the statistical data. The ANOVA-single factor model was used to analyze the data and statistical significance was calculated using a two-tailed Student's *t*-test. The averaged percentage (M%) and standard deviations (SD) of three biological repeats are displayed for viable-, apoptotic- and necrotic cells. Statistically significant differences (*P*-value <0.05) were calculated using cells propagated in medium only as a baseline.

			Medium only	Positive control	2 Gy	4 Gy	6 Gy	8 Gy	10 Gy
MCF-7	Viable	M%±SD	92.03±1.88	82.23±1.75	89.87±1.85	90.49±4.14	91.3±0.91	90.11±1.76	89.47±2.45
		P-value	-	**1.00E-02**	0.23	0.59	0.58	0.27	0.22
	Apoptosis	M%±SD	5.50±1.62	11.18±1.46	7.59±1.56	6.02±2.50	5.77±1.78	6.10±0.77	6.65±1.50
		P-value	-	**0.03**	0.18	0.78	0.86	0.59	0.42
	Necrosis	M%±SD	2.47±0.30	6.60±3.21	2.54±0.35	3.49±1.66	2.93±0.96	3.79±1.00	3.88±1.01
		P-value	-	0.09	0.80	0.35	0.47	0.09	0.08
MDA-MB-231	Viable	M%±SD	91.88±1.48	81.42±4.6	89.49±2.46	88.68±3.51	88.99±2.47	86.42±1.34	83.85±3.43
		P-value	-	**0.02**	0.22	0.22	0.16	**9.09E-03**	**0.02**
	Apoptosis	M%±SD	5.85±1.08	15.08±4.63	7.11±1.56	8.31±2.91	7.47±1.79	9.24±1.70	11.10±2.65
		P-value	-	**0.03**	0.31	0.24	0.25	**0.04**	**0.03**
	Necrosis	M%±SD	2.28±0.42	3.50±0.93	3.4±0.90	3.02±1.60	3.55±0.92	4.34±1.81	5.06±1.44
		P-value	-	0.11	0.12	0.48	0.10	0.13	**0.03**
BT-20	Viable	M%±SD	89.97±2.62	17.16±3.10	86.67±2.21	88.99±2.50	84.20±1.64	82.34±1.51	80.91±0.47
		P-value	-	**6.39E-06**	0.17	0.71	**0.03**	**1.20E-02**	**1.93E-02**
	Apoptosis	M%±SD	8.67±3.01	81.37±3.48	11.81±2.20	9.51±1.75	14.42±0.82	14.84±2.05	16.92±0.55
		P-value	-	**1.07E-05**	0.22	0.75	**0.03**	**0.04**	**0.04**
	Necrosis	M%±SD	1.36±0.49	1.47±0.81	1.52±0.67	1.50±0.75	1.38±0.83	2.82±2.00	2.17±1.03
		P-value	-	0.85	0.76	0.82	0.98	0.29	0.31

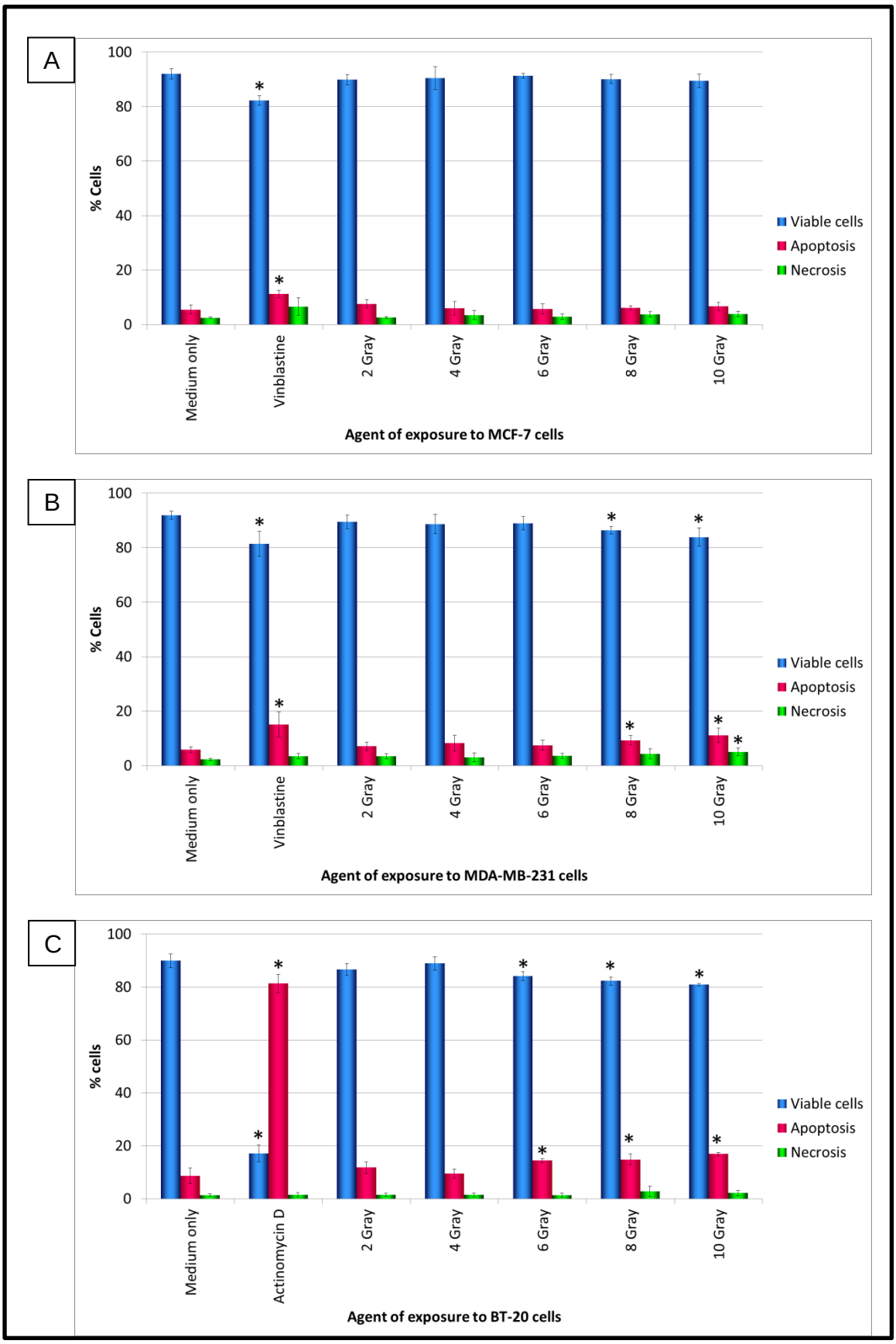

Figure 1B: Graphical representation of annexin V-FITC analysis of MCF-7-, MDA-MB-231- and BT-20 breast cancer cells exposed to a radiation dose range. MCF-7 cells displayed no

significant increase in apoptosis upon radiation exposure (A). The lowest radiation dose that significantly induced apoptosis was calculate at 8 Gy for MDA-MB-231 cells (B) and 6 Gy for BT-20 cells (C). The averages of three biological repeats are displayed on the bar graphs with the standard deviations represented by T-bars. Statistically significant differences are indicated with * (*P*-value <0.05).

Results obtained from the quantification of annexin V-FITC revealed the lowest radiation doses to increase apoptosis to be 6 Gy in BT-20 cells and 8 Gy in MDA-MB-231 cells. MCF-7 cells revealed no significant increase in annexin V-FITC staining following radiation exposure at the measured time point. These results were used in conjunction with results obtained from cell cycle analysis in order to determine the radiation dose that were used in all subsequent experiments.

9.2 Radiation dose response curve: Flow cytometric analysis of cell cycle progression

MCF-7-, MDA-MB-231- and BT-20 cells were stained with propidium iodide following exposure to a radiation dose-response curve (0 Gy, 2 Gy, 4 Gy, 6 Gy, 8 Gy and 10 Gy). The results obtained from this experiment indicated the effect of the different radiation doses on the cell cycle distribution. Additionally, the induction of cell death (cells present in the sub-G_1 phase) was used to select a radiation dose that was used for all subsequent experiments.

MCF-7-, MDA-MB-231- and BT-20 cells propagated in growth medium served as negative controls. A total of 54.26±2.89%, 45.48±4.06% and 64.26±2.44% MCF-7-, MDA-MB-231- and BT-20 cells, respectively, were present in the G_1 phase (Figure 1C). Negative controls revealed 29.73±5.04%, 39.53±7.34% and 24.23±1.63% of cells in the G_2/M phase, and 12.69±2.84%, 10.95±2.78% and 9.87±3.69% of MCF-7-, MDA-MB-231- and BT-20 cells present in the S phase. Only 3.46±1.19%, 4.05±1.67% and 1.72±0.91% of MCF-7-, MDA-MB-231- and BT-20 cells were present in the sub-G_1 phase (Figure 1D).

MCF-7- and MDA-MB-231 cells exposed to vinblastine served as a positive control for apoptosis. The positive control for the BT-20 cell line comprised of cells exposed to actinomycin D. All positive controls revealed a statistically significant increase in the percentage of cells present in the sub-G_1 phase, with a concurrent decrease in the G_1 phase (Table 1B). MCF-7- and BT-20 cells exposed to 2 Gy radiation revealed no significant differences in the cell cycle distribution, however MDA-MB-231 cells revealed a significant decrease in the G_1 phase (35.99±3.38%), compared to the negative control (Figure 1D). MDA-MB-231- and BT-20 cells exposed to 4 Gy radiation revealed a statistically significant decrease in the G_1 phase (28.42±6.27% and 57.50±3.01%, respectively). Additionally, BT-20 cells present in the G_2/M phase were significantly increased (33.26±1.79%) following 4 Gy radiation.

MCF-7 cells displayed a significant decrease in the G_1 phase following 6 Gy (37.70±8.25%)-, 8 Gy (31.11±9.86%)- and 10 Gy (15.43±8.50%) radiation. Additionally, MCF-7 cells present in the sub-G_1 phase were significantly increased when exposed to 8 Gy (10.93±5.18%) and 10 Gy (8.19±1.43%). Exposure of MCF-7 cells to 8 Gy (7.35±1.40%)- and 10 Gy (5.45±0.88%) radiation significantly decreased cells present in the S phase, with a concurrent increase in cells present in the G_2/M phase (50.74±13.95% and 71.03±10.08%, respectively) (Table 1B). MDA-MB-231 cells displayed a significant decrease in the G_1 phase following exposure to 6 Gy (20.96±1.01%)-, 8 Gy (15.80±3.19%)- and 10 Gy (13.25±1.41%) radiation (Figure 1D). This was accompanied by a significant increase in cells present in the G_2/M phase (62.14±0.88%, 69.74±6.99% and 72.17±1.67%, respectively). BT-20 cells revealed a significant decrease in the G_1 phase when exposed to 6 Gy (41.50±11.97%), 8 Gy (37.01±1.35%) and 10 Gy (24.83±5.75%). A statistically significant increase in the G_2/M- and sub-G_1 phases were observed in BT-20 cells exposed to 6 Gy (45.71±11.12% and 5.32±1.17%, respectively), 8 Gy (54.34±8.09% and 6.67±2.26%) and 10 Gy (62.11±6.53% and 6.70±2.52%) (Figure 1C).

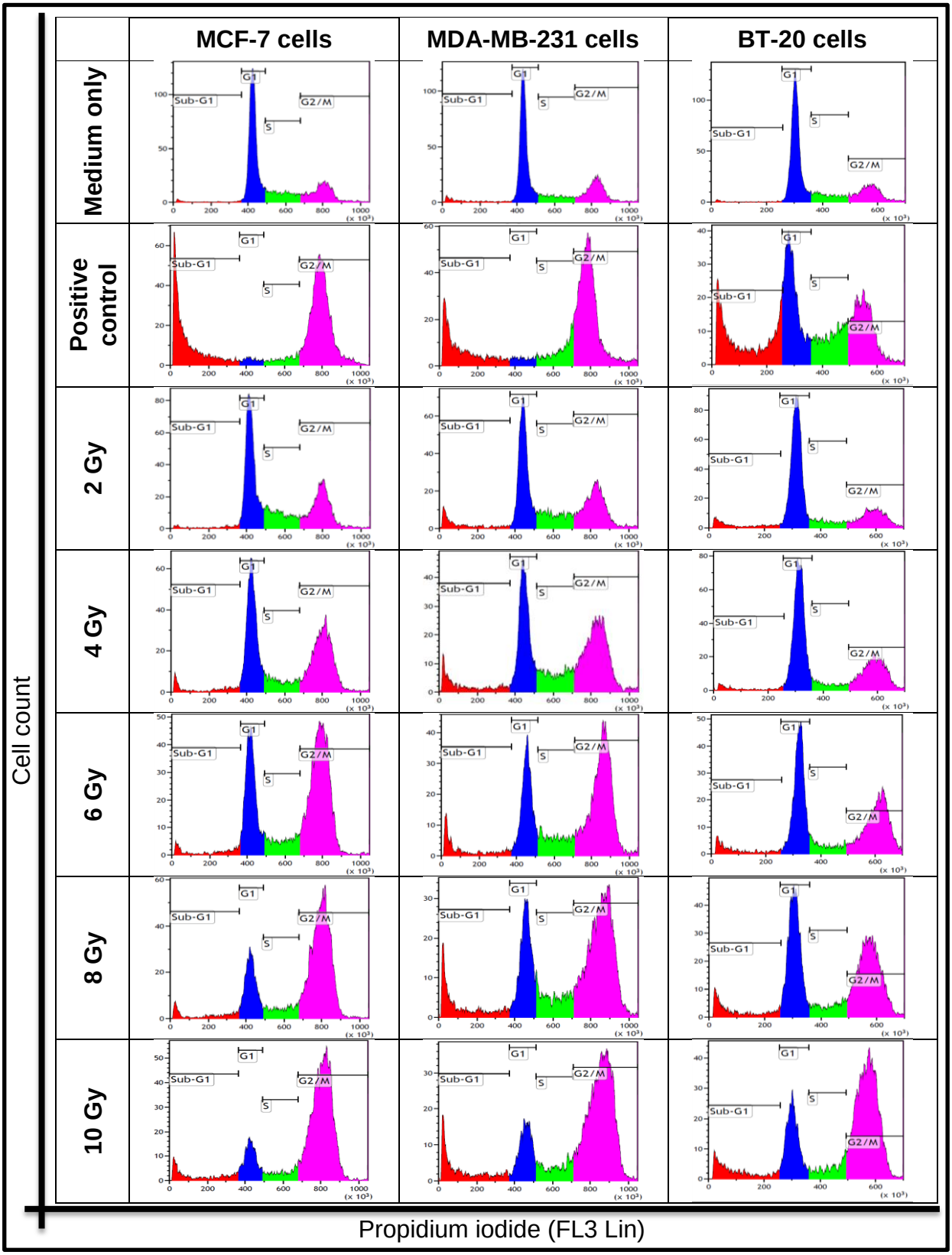

Figure 1C: Histograms representing the cell cycle distributions of MCF-7-, MDA-MB-231- and BT-20 cells exposed to a radiation dose-response curve. The number of cells was plotted against propidium iodide (FL3 Lin). Cells propagated in medium only served as a negative control, while vinblastine (MCF-7- and MDA-MB-231 cells) or actinomycin D (BT-20 cells) exposed cells

provided positive method controls for apoptosis. MCF-7-, MDA-MB-231- and BT-20 cells were exposed to a radiation dose-response curve (2 gray (Gy), 4 Gy, 6 Gy , 8 Gy, 10 Gy) in order to identify the lowest dose that significantly increase apoptosis.

Table 1B: Cell cycle analysis of three breast cancer cell lines after exposure to a radiation dose-response curve. Data were generated using Kaluza Analysis software version 1.5 (FL, USA). Data were analyzed using ANOVA-single factor model and a two-tailed Student's *t*-test. The averaged percentage (M%) and standard deviations (SD) of three biological repeats are displayed for cells present in the different phases of the cell cycle. Using cells propagated in medium only as a baseline, statistical significance (*P*-value <0.05) was calculated.

			Medium only	Positive control	2 Gy	4 Gy	6 Gy	8 Gy	10 Gy
MCF-7	Sub-G_1	M%±SD	3.46±1.19	40.36±11.31	5.03±2.57	4.79±0.77	10.13±6.92	10.93±5.18	8.19±1.43
		P-value	-	**1.77E-03**	0.31	0.15	0.11	**0.03**	**4.92E-03**
	G_1	M%±SD	54.26±2.89	4.51±1.70	49.35±10.73	38.33±15.71	37.70±8.25	31.11±9.86	15.43±8.50
		P-value	-	**2.66E-05**	0.41	0.10	**1.24E-02**	**5.97E-03**	**3.26E-04**
	S	M%±SD	12.69±2.84	5.08±0.57	11.92±4.19	10.35±0.38	8.14±1.46	7.35±1.40	5.45±0.88
		P-value	-	**0.02**	0.77	0.23	0.05	**0.03**	**8.64E-03**
	G_2/M	M%±SD	29.73±5.04	50.13±12.44	33.81±13.11	46.66±14.72	44.11±12.52	50.74±13.95	71.03±10.08
		P-value	-	**0.04**	0.58	0.08	0.09	**0.04**	**7.87E-04**
MDA-MB-231	Sub-G_1	M%±SD	4.05±1.67	20.31±0.67	5.59±1.23	6.19±1.12	6.32±2.85	6.25±2.68	7.09±2.65
		P-value	-	**1.09E-03**	0.27	0.14	0.30	0.29	0.17
	G_1	M%±SD	45.48±4.06	3.99±0.08	35.99±3.38	28.42±6.27	20.96±1.01	15.80±3.19	13.25±1.41
		P-value	-	**8.40E-04**	**0.04**	**1.68E-02**	**5.31E-04**	**5.72E-04**	**2.03E-04**
	S	M%±SD	10.95±2.78	9.09±3.16	14.94±1.08	11.18±0.80	10.57±1.26	8.27±1.17	7.49±1.31
		P-value	-	0.53	0.08	0.90	0.84	0.20	0.12
	G_2/M	M%±SD	39.53±7.34	66.66±3.75	43.52±3.48	54.22±6.30	62.14±0.88	69.74±6.99	72.17±1.67
		P-value	-	**1.86E-02**	0.44	0.06	**6.10E-03**	**6.69E-03**	**1.68E-03**
BT-20	Sub-G_1	M%±SD	1.72±0.91	21.57±7.87	4.47±2.86	2.36±1.50	5.32±1.17	6.67±2.26	6.70±2.52
		P-value	-	**1.22E-02**	0.19	0.56	**1.37E-02**	**0.04**	**0.03**
	G_1	M%±SD	64.26±2.44	33.21±3.69	61.44±2.24	57.50±3.01	41.50±11.97	37.01±1.35	24.83±5.75
		P-value	-	**2.64E-04**	0.21	**0.04**	**0.03**	**8.00E-04**	**3.98E-04**
	S	M%±SD	9.87±3.69	17.99±4.52	7.32±2.11	6.85±0.86	7.52±1.13	10.71±7.46	6.35±1.29
		P-value	-	0.07	0.36	0.24	0.35	0.87	0.19
	G_2/M	M%±SD	24.23±1.63	27.29±8.40	26.89±4.16	33.26±1.79	45.71±11.12	54.34±8.09	62.11±6.53
		P-value	-	0.57	0.36	**2.95E-03**	**0.03**	**3.21E-03**	**6.20E-04**

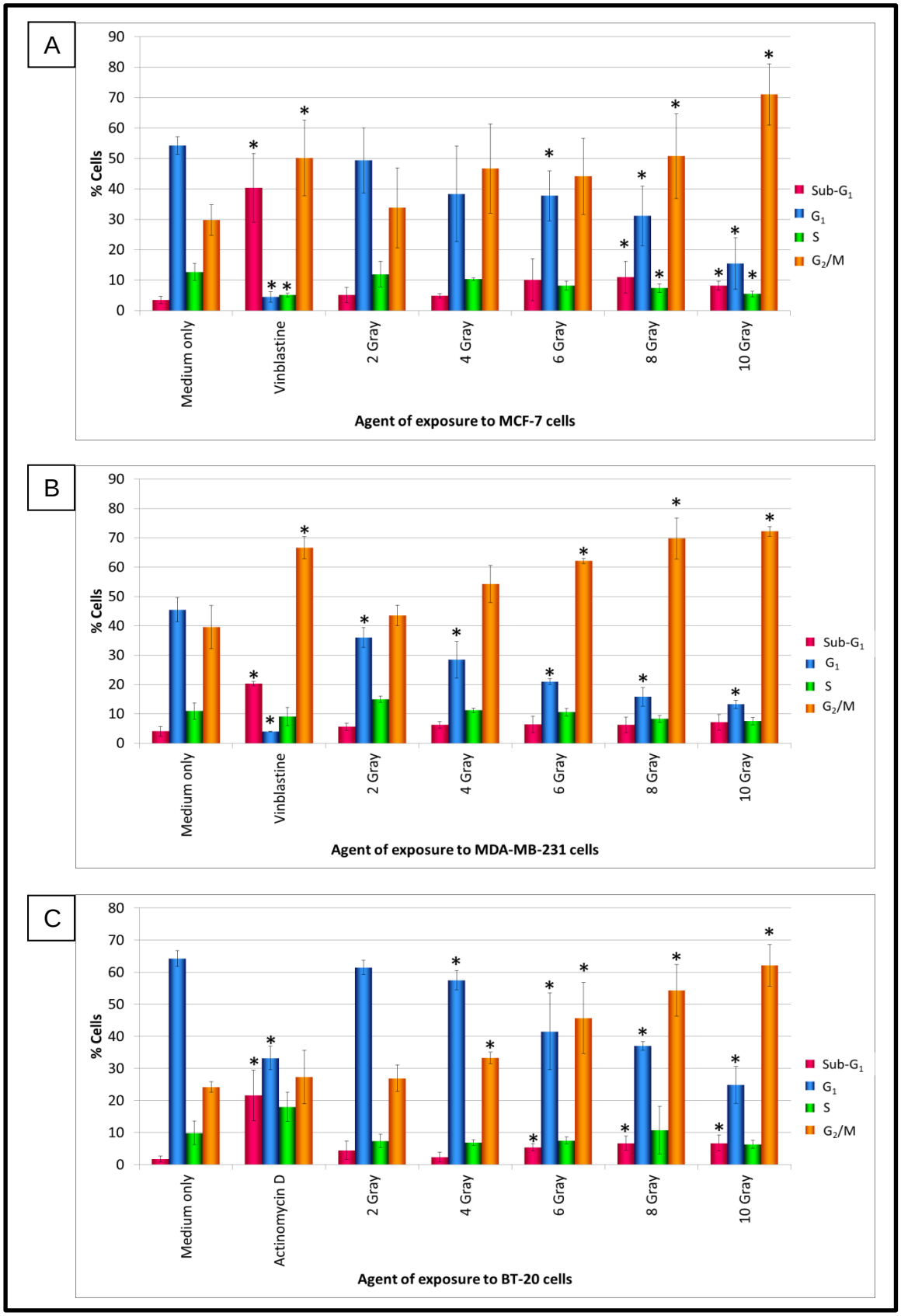

Figure 1D: Graphical representation of the cell cycle analysis of MCF-7-, MDA-MB-231- and BT-20 cells exposed to a radiation dose range. MDA-MB-231 cells displayed no significant increase in the sub-G_1 phase of the cell cycle upon exposure to the radiation dose-response curve. The

lowest radiation dose that significantly increased the sub-G_1 phase in MCF-7 cells was 8 Gy and 6 Gy in the BT-20 cell line. Bars indicate the mean of three biological repeats, with standard deviations represented by T-bars. Statistical significant differences are indicated with * (*P*-value <0.05).

The cell cycle analysis revealed that the lowest radiation dose that increased the sub-G_1 phase was 6 Gy for the BT-20 cell line and 8 Gy for the MCF-7 cell line. This suggests that the BT-20 cell line is more sensitive to radiation compared to the MCF-7- and MDA-MB-231 cell line. No statistically significant increase in sub-G_1 phase was observed in the MDA-MB-231 cells upon exposure to the radiation dose-response curve. However, annexin V-FITC results did indicate that apoptosis were significantly increased in the MDA-MB-231 cells after 8 Gy radiation. This may suggest that apoptosis is induced in MDA-MB-231 cells present in the G_2/M phase (metaphase block) after 8 Gy radiation. Thus, in order to keep the radiation dose delivery protocol constant 8 Gy was selected to be used in all the cell lines for the subsequent radiosensitization experiments.

10. Additional file 2

10.1 Compound dose response curve: Flow cytometric quantification of apoptosis induction

Breast cancer cells were exposed to the lowest compound dose that significantly increased apoptosis in an attempt to sensitize the cells to radiation. These doses were determined by exposing the cells to a compound dose-response curve (Table 2A) (using the GI_{50} concentration as a starting point (Table 4.3)) followed by quantification of apoptosis 48 hours after exposure via flow cytometry employing annexin V.

Table 2A: Compound dose-response curve concentrations exposed to BT-20-, MCF-7- and MDA-MB-231 cells. The concentration range of each compound to which the breast cancer cells were exposed to displayed in µM.

	BT-20 cells				MCF-7 cells		MDA-MB-231 cells	
	ESE-15-one	ESE-16	T4	LimPyr1	ESE-16	LimPyr1	ESE-16	LimPyr1
	µM							
Concentration 1	0.08	0.223	36	4.096	0.313	4.875	0.274	4.875
Concentration 2	0.06	0.167	27	2.73	0.235	3.25	0.206	3.25
Concentration 3	0.04	0.112	18	2.048	0.157	2.437	0.137	2.437
Concentration 4	0.02	0.056	9	1.638	0.078	1.95	0.069	1.95
Concentration 5	0.013	0.037	6	1.365	0.052	1.62	0.046	1.62

Breast cancer cells were exposed to DMSO as a vehicle control and actinomycin D (BT-20 cells) or vinblastine (MCF-7- and MDA-MB-231 cells) as positive controls for apoptosis. No statistically significant differences were observed in cell viability or apoptosis when DMSO samples were compared to cells propagated in medium only. Cells exposed to the positive apoptotic controls displayed a decrease in cell viability in addition to an increase in apoptotic cells (Table 2B & 2C).

BT-20 cell viability was significantly decreased (84.04±2.37% and 85.31±1.76%) with an increase in apoptotic cells (13.70±2.19% and 13.11±2.39%) when exposed to 0.08 µM and

0.06 µM ESE-15-one, compared to the vehicle control (91.06±1.83% and 7.69±2.36%, respectively) (Figure 2A). Following a 48 hour exposure to 0.223 µM, 0.167 µM and 0.112 µM ESE-16 BT-20 cells displayed a significant decrease in cell viability (76.33±3.16%, 87.74±0.72% and 86.22±3.89%, respectively) in addition to increased apoptosis (22.49±3.58%, 10.74±1.59% and 11.76±3.12%, respectively), compared to DMSO (93.45±1.77% and 5.46±1.25%). Compared to the vehicle control (91.22±1.35% and 6.92±2.21%, respectively) the compound T4 significantly decreased BT-20 cell viability to 75.58±4.94% at 36 µM due to an increase in apoptosis (21.65±3.19%). BT-20 cells exposed to the Lim kinase inhibitor, LimPyr1, displayed a significant decrease in cell viability with a concurrent increase in apoptosis at concentrations of 4.096 µM (85.27±2.11% and 13.40±1.97%), 2.73 µM (86.38±3.22% and 12.53±2.86%), 2.048 µM (83.15±2.05% and 15.55±2.39%) and 1.638 µM (84.27±0.79% and 14.82±1.14%), compared to the vehicle control (92.00±1.53% and 6.95±1.43%) (Table 2B).

This experiment indicated that 0.06 µM ESE-15-one, 0.167 µM ESE-16, 36 µM T4 and 1.638 µM LimPyr1 were the lowest concentrations to significantly increase apoptosis in BT-20 cells (Figure 2B). These results were compared to the cell cycle analysis of BT-20 cells exposed to the same dose-response curve before determining the pre-treatment concentrations.

The four candidate microtubule regulating agents were tested for their radiosensitizing abilities in BT-20 cells. BT-20 cells were exposed to the lowest compound doses that significantly increased apoptosis for 24 hours prior to radiation. Cells were analyzed 24 hours after radiation for apoptotic induction and cell cycle disturbances via flow cytometry employing annexin V and propidium iodide, respectively. After the completion of these studies ESE-16 and LimPyr1 showed the most potential to sensitize cells to radiation in this experimental setup. Thus, for the remainder of the study only these two compounds were included in the experiments.

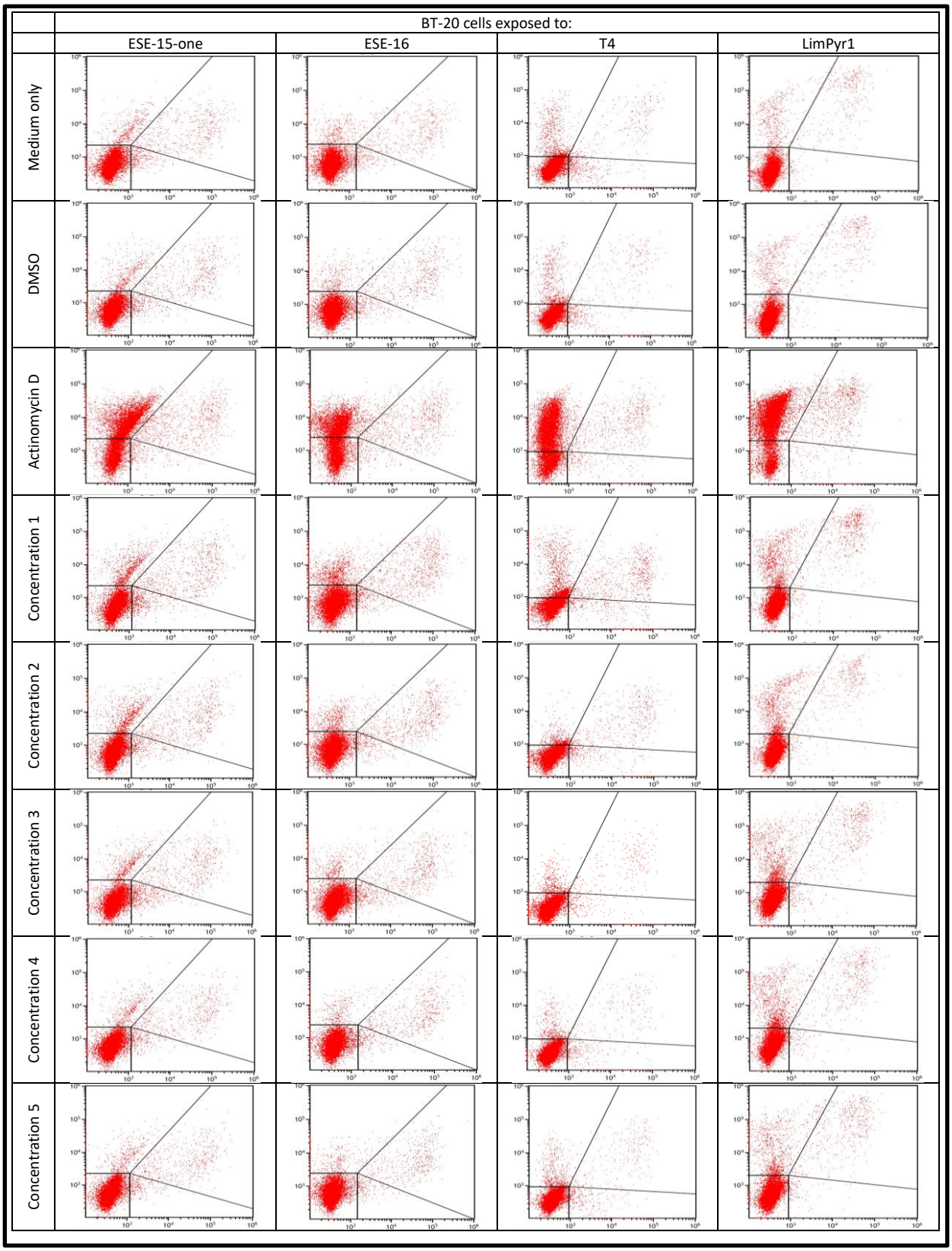

Figure 2A: Apoptotic cell death in BT-20 cells exposed to compound dose-response curves as illustrated by flow cytometric dot plots of annexin V-FITC. Apoptotic cells were labeled with annexin V-FITC (FL1 Log) and were plotted against cells stained with propidium iodide (FL3 Log). BT-20 cells were propagated in growth media only (negative control), exposed to DMSO as a

vehicle control or actinomycin D as a positive apoptotic control. Additionally, BT-20 cells were exposed to ESE-15-one, ESE-16, T4 and LimPyr1 dose-response curves (Table 2A). The bottom left corner: viable cells; top left and right quadrants: apoptotic cells; bottom right quadrant: necrotic cells.

Table 2B: Annexin V-FITC quantification in BT-20 cells exposed to compound dose-response curves. Kaluza Analysis software version 1.5 (FL, USA) were used to obtained the data, which were analyzed using the ANOVA-single factor model. Statistical significance was calculated using a two-tailed Student's *t*-test. The averaged percentage of three biological repeats (M%) and standard deviations (SD) are displayed for viable-, apoptotic- and necrotic BT-20 cells. Cells exposed to DMSO served as a baseline when statistically significant differences (*P*-value <0.05) were calculated.

						Drug concentrations				
			Medium only	**DMSO**	**Actinomycin D**	**0.08 µM**	**0.06 µM**	**0.04 µM**	**0.02 µM**	**0.013 µM**
ESE-15-one	Viable	M%±SD	90.34±2.31	91.06±1.83	34.87±7.50	84.04±2.37	85.31±1.76	88.11±0.64	91.92±2.42	91.87±2.13
		P-value	0.69	-	**2.28E-04**	**1.54E-02**	**1.72E-02**	0.06	0.65	0.64
	Apoptosis	M%±SD	8.21±2.97	7.69±2.36	63.88±8.01	13.70±2.19	13.11±2.39	9.65±2.32	6.98±2.79	7.00±2.53
		P-value	0.83	-	**3.10E-04**	**0.03**	**4.90E-02**	0.36	0.75	0.75
	Necrosis	M%±SD	1.45±0.65	1.24±0.64	1.25±0.51	2.27±1.61	1.58±0.69	2.24±1.69	1.10±0.57	1.14±0.55
		P-value	0.71	-	0.99	0.36	0.57	0.39	0.79	0.84
						0.223 µM	**0.167 µM**	**0.112 µM**	**0.056 µM**	**0.037 µM**
ESE-16	Viable	M%±SD	91.69±2.90	93.45±1.77	32.01±10.04	76.33±3.16	87.74±0.72	86.22±3.89	91.35±2.71	91.48±2.13
		P-value	0.40	-	**1.53E-04**	**1.21E-03**	**6.59E-03**	**0.03**	0.30	0.25
	Apoptosis	M%±SD	7.03±2.96	5.46±1.25	66.89±10.60	22.49±3.58	10.74±1.59	11.76±3.12	7.26±3.11	7.35±2.64
		P-value	0.44	-	**1.93E-04**	**1.48E-03**	**1.06E-02**	**0.02**	0.40	0.31
	Necrosis	M%±SD	1.29±0.76	1.09±0.64	1.10±0.68	1.19±0.47	1.52±1.05	2.02±1.49	1.39±1.04	1.17±0.71
		P-value	0.74	-	0.99	0.85	0.58	0.37	0.68	0.89
						36 µM	**27 µM**	**18 µM**	**9 µM**	**6 µM**
T4	Viable	M%±SD	90.03±0.56	91.22±1.35	25.36±3.46	75.58±4.94	88.56±4.84	92.76±1.55	92.88±2.19	93.35±2.31
		P-value	0.23	-	**6.67E-06**	**6.14E-03**	0.41	0.26	0.33	0.24
	Apoptosis	M%±SD	8.10±1.02	6.92±2.21	71.26±4.06	21.65±3.19	9.51±5.22	5.83±2.19	5.60±2.74	5.14±2.73
		P-value	0.45	-	**1.75E-05**	**2.76E-03**	0.47	0.58	0.55	0.43
	Necrosis	M%±SD	1.88±1.16	1.87±0.93	3.37±4.17	2.78±1.80	1.94±0.42	1.41±0.72	1.53±0.55	1.50±0.85
		P-value	0.99	-	0.57	0.48	0.91	0.54	0.62	0.64
						4.096 µM	**2.73 µM**	**2.048 µM**	**1.638 µM**	**1.365 µM**
LimPyr1	Viable	M%±SD	92.26±1.73	92.00±1.53	30.05±11.56	85.27±2.11	86.38±3.22	83.15±2.05	84.27±0.79	88.00±1.36
		P-value	0.82	-	**1.35E-07**	**4.50E-03**	**0.03**	**4.99E-03**	**7.61E-03**	0.09
	Apoptosis	M%±SD	6.95±1.43	7.28±1.49	68.78±11.65	13.40±1.97	12.53±2.86	15.55±2.39	14.82±1.14	10.93±1.11
		P-value	0.76	-	**1.55E-07**	**4.62E-03**	**0.02**	**1.09E-02**	**1.45E-02**	0.12
	Necrosis	M%±SD	0.79±0.30	0.73±0.29	1.17±0.76	1.33±0.59	1.09±0.42	1.30±0.35	0.92±0.35	1.08±0.25
		P-value	0.77	-	0.21	0.12	0.16	0.17	0.82	0.44

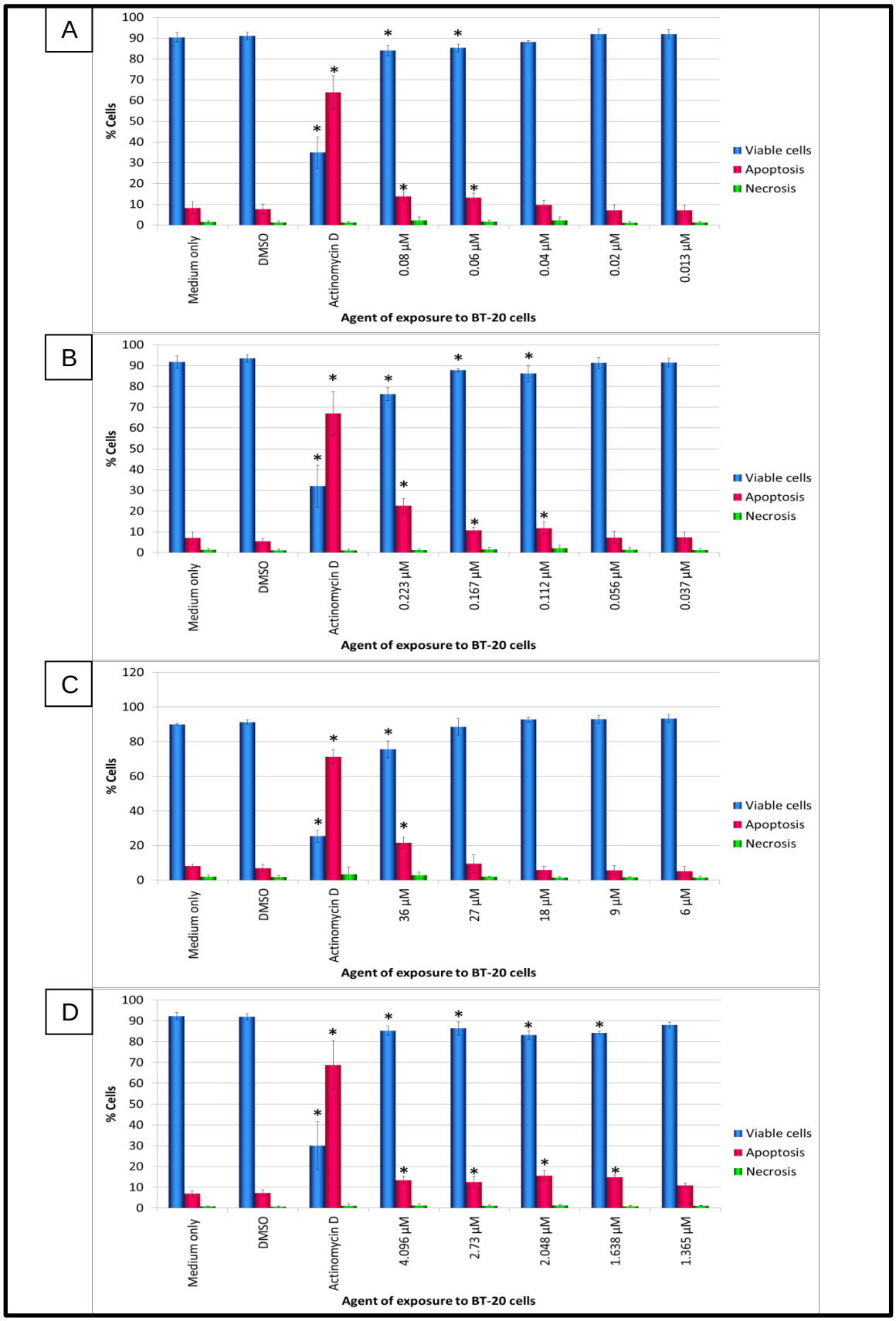

Figure 2B: Graphical representation of annexin V-FITC quantification in BT-20 cells exposed to compound dose-response curves. BT-20 cells were exposed to ESE-15-one (A), ESE-16 (B), T4 (C)

and LimPyr1 (D) dose-response curves. The lowest concentrations that significantly increased apoptosis were measured to be 0.06 µM ESE-15-one, 0.167 µM ESE-16, 36 µM T4 and 1.638 µM LimPyr1. Three biological repeats were completed for each dose-response curve. The averages of viable-, apoptotic and necrotic cells are displayed on the bar graphs and the standard deviations are indicated by T-bars. A *P*-value <0.05 was considered statistically significant and is indicated with an *.

MCF-7- and MDA-MB-231 cells were exposed to ESE-16- and LimPyr1 dose-response curves in order to identify the lowest concentration that significantly increase apoptosis. Annexin V-FITC analysis revealed a significant increase in apoptotic cells when MCF-7 cells were exposed to 0.313 µM (54.24±2.52%) and 0.235 µM (25.25±2.00%) ESE-16, compared to DMSO (4.66±3.18%). MDA-MB-231 cell viability was significantly decreased with a concurrent increase in apoptosis following a 48 hour exposure to ESE-16 at concentrations of 0.274 µM (26.11±7.22% viable cells and 72.84±6.52% apoptotic cells), 0.206 µM (28.97±5.32% viable cells and 69.75±5.88% apoptotic cells) and 0.137 µM (85.05±1.25% viable cells and 14.35±0.85% apoptotic cells), compared to the vehicle control (92.35±1.68% viable cells and 7.05±1.50% apoptotic cells) (Figure 2C). MCF-7- and MDA-MB-231 cells displayed a significant decrease in cell viability (81.69±3.42%, 85.54±1.65% and 88.76±3.21% (MCF-7), 60.91±11.68%, 85.21±2.69% and 84.20±0.66% (MDA-MB-231)) with increased apoptotic cells (17.45±5.14%, 9.90±5.04% and 10.21±2.33% (MCF-7), 38.86±11.97%, 14.29±2.88% and 13.50±2.32% (MDA-MB-231)) when exposed to 4.875 µM, 3.25 µM and 2.439 µM LimPyr1, respectively (Table 2C).

The lowest ESE-16 doses that significant increased apoptotic cell death were determined to be 0.235 µM and 0.137 µM in MCF-7- and MDA-MB-231 cells, respectively. LimPyr1 significantly increased apoptosis at 2.437 µM in both cell lines following a 48 hour exposure time (Figure 2D). These results were taken into consideration (with results obtained from cell cycle analysis) when the doses that were used to pre-treat the cells prior to radiation were selected.

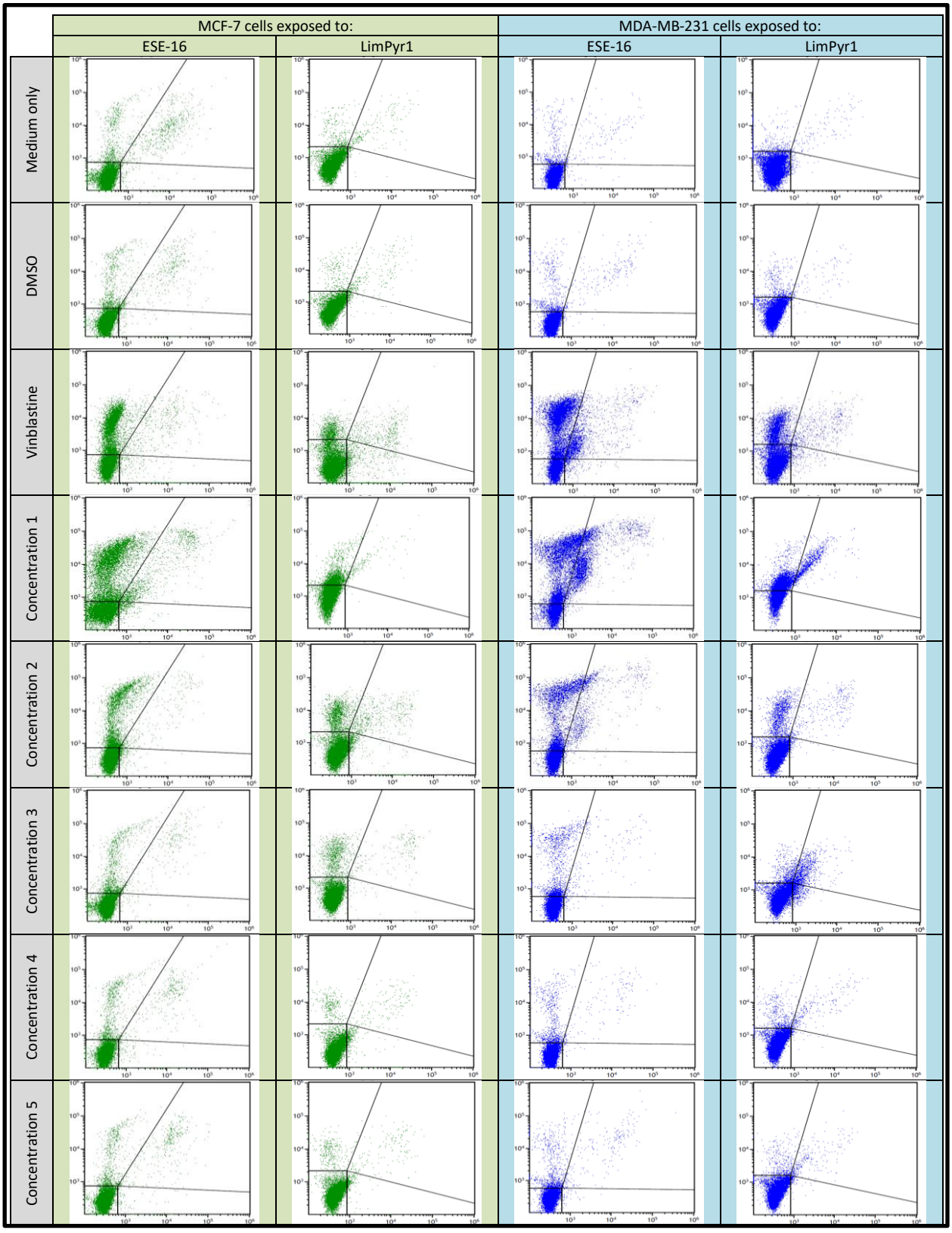

Figure 2C: Apoptotic cell death in MCF-7- and MDA-MB-231 cells exposed to compound dose-response curves as illustrated by flow cytometric dot plots of annexin V-FITC. Dot plots were obtained by plotting apoptotic cells (annexin V-FITC (FL1 Log)) against necrotic cells (propidium

iodide (FL3 Log)). MCF-7- and MDA-MB-231 cells were propagated in growth media only (negative control), exposed to DMSO as a vehicle control or vinblastine as positive apoptotic controls. MCF-7- and MDA-MB-231 cells were exposed to an ESE-16 and a LimPyr1 compound dose-response curve (Table 2A) to determine the lowest dose of each compound that significantly induced apoptosis. The bottom left corner: viable cells; top left and right quadrants: apoptotic cells; bottom right quadrant: necrotic cells.

Table 2C: Annexin V-FITC quantification in MCF-7- and MDA-MB-231 cells exposed to compound dose-response curves. Data were acquired and analyzed using Kaluza Analysis software version 1.5 (FL, USA) and an ANOVA-single factor model. Statistical significance was calculated using a two-tailed Student's *t*-test. The averaged percentage of three biological repeats (M%) and standard deviations (SD) are displayed for viable-, apoptotic- and necrotic cells. Statistically significant differences (*P*-value <0.05) were calculated using cells exposed to DMSO as a baseline.

							Drug concentrations				
				Medium only	**DMSO**	**Vinblastine**	**0.313 µM**	**0.235 µM**	**0.157 µM**	**0.078 µM**	**0.052 µM**
MCF-7	ESE-16	Viable	M%±SD	93.99±2.56	94.84±3.50	52.20±5.13	43.94±1.90	73.73±1.03	92.10±3.23	93.83±2.15	94.24±1.80
			P-value	0.75	-	**1.47E-03**	**3.59E-04**	**4.18E-03**	0.44	0.69	0.80
		Apoptosis	M%±SD	5.50±2.34	4.66±3.18	46.06±5.06	54.24±2.52	25.25±2.00	7.55±3.13	5.75±1.67	5.42±1.48
			P-value	0.73	-	**1.38E-03**	**3.60E-04**	**4.18E-03**	0.39	0.63	0.73
		Necrosis	M%±SD	0.51±0.31	0.50±0.33	1.75±0.06	1.82±0.64	1.02±0.97	0.36±0.10	0.41±0.49	0.34±0.32
			P-value	0.97	-	**0.02**	0.05	0.43	0.63	0.81	0.59
							4.875 µM	**3.25 µM**	**2.437 µM**	**1.95 µM**	**1.625 µM**
	LimPyr1	Viable	M%±SD	95.79±1.54	95.79±0.64	73.43±9.47	81.69±3.42	85.54±1.65	88.76±3.21	92.69±4.67	94.40±2.56
			P-value	0.99	-	**1.41E-03**	**2.17E-03**	**5.98E-04**	**0.02**	0.29	0.35
		Apoptosis	M%±SD	3.48±1.22	3.22±0.66	22.30±11.11	17.45±5.14	9.90±5.04	10.21±2.33	6.17±3.65	5.23±2.72
			P-value	0.69	-	**0.01**	**0.03**	**5.85E-04**	**0.01**	0.19	0.20
		Necrosis	M%±SD	0.73±0.44	0.99±0.72	4.26±1.66	0.28±0.36	4.55±4.86	1.03±0.93	1.15±1.18	0.38±0.19
			P-value	0.52	-	**0.01**	0.22	0.24	0.86	0.98	0.21
							0.274 µM	**0.206 µM**	**0.137 µM**	**0.069 µM**	**0.046µM**
MDA-MB-231	ESE-16	Viable	M%±SD	92.53±3.40	92.35±1.68	47.03±10.59	26.11±7.22	28.97±5.32	85.05±1.25	90.87±2.23	91.32±0.69
			P-value	0.94	-	1.85E-03	1.02E-04	2.49E-04	0.01	0.41	0.38
		Apoptosis	M%±SD	6.61±3.22	7.05±1.50	49.38±11.54	72.84±6.52	69.75±5.88	14.35±0.85	8.77±2.07	8.18±0.49
			P-value	0.84	-	3.25E-03	6.95E-05	3.17E-04	0.01	0.31	0.28
		Necrosis	M%±SD	0.86±0.54	0.60±0.32	2.10±0.74	1.06±0.97	1.29±0.56	0.61±0.40	0.35±0.18	0.49±0.22
			P-value	0.51	-	4.59E-02	0.47	0.17	0.97	0.32	0.65
							4.875 µM	**3.25 µM**	**2.437 µM**	**1.95 µM**	**1.625 µM**
	LimPyr1	Viable	M%±SD	96.51±0.73	95.67±2.74	71.15±9.37	60.91±11.68	85.21±2.69	84.20±0.66	91.40±5.05	94.55±0.48
			P-value	0.53	-	**5.00E-04**	**0.01**	**2.10E-03**	**0.02**	0.38	0.89
		Apoptosis	M%±SD	3.05±0.67	3.96±2.63	24.30±9.59	38.86±11.97	14.29±2.88	13.50±2.32	8.22±5.23	5.05±0.72
			P-value	0.48	-	**1.81E-03**	**0.01**	**2.96E-03**	**4.70E-02**	0.38	0.86
		Necrosis	M%±SD	0.45±0.21	0.38±0.31	4.55±2.24	0.23±0.36	0.50±0.45	2.31±2.98	0.38±0.18	0.39±0.37
			P-value	0.68	-	**3.28E-03**	0.84	0.30	0.33	0.73	0.82

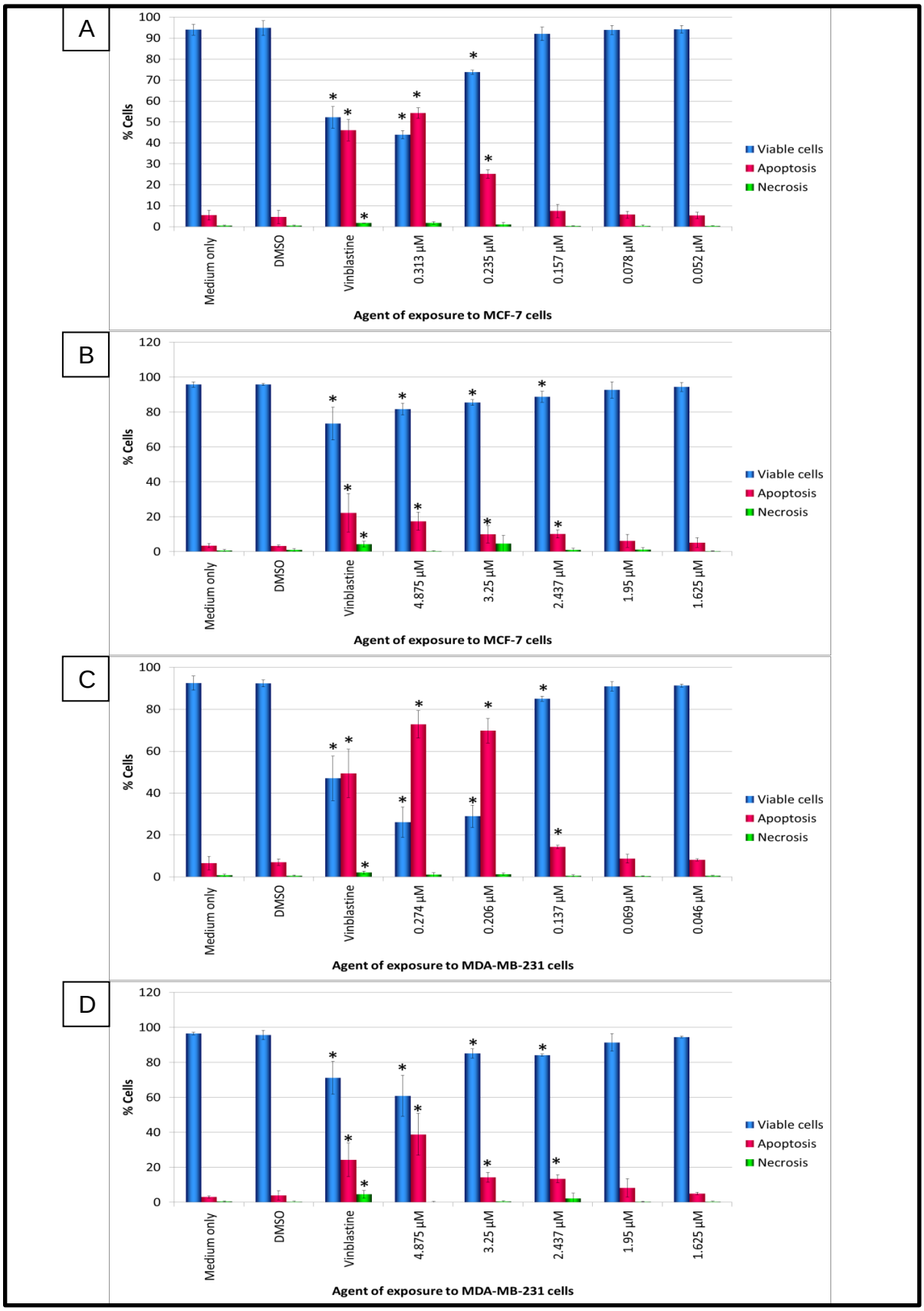

Figure 2D: Graphical representation of annexin V-FITC quantification in MCF-7- and MDA-MB-231 cells exposed to compound dose-response curves. MCF-7- and MDA-MB-231 cells were

exposed to an ESE-16 (A & C) and a LimPyr1 (B & D) dose-response curve. The lowest concentrations that significantly increased apoptosis were 0.235 µM ESE-16 and 2.437 µM LimPyr1 in the MCF-7 cell line, and 0.137 µM ESE-16 and 2.437 µM LimPyr1 in the MDA-MB-231 cell line. Three biological repeats were completed for each dose-response curve. The averages of viable-, apoptotic and necrotic cells are displayed on the bar graphs and the standard deviations indicated by T-bars. *P*-values <0.05 was considered statistically significant and indicated with an asterisk (*).

10.2 Compound dose response curve: Flow cytometric analysis of cell cycle progression

The ability of breast cancer cells to progress through the cell cycle following exposure to ESE-15-one-, ESE-16-, T4- or LimPyr1 dose-response curves (Table 2A) were examined to determine the lowest dose of the compounds that affect cell proliferation. These doses were used to pre-treat the cells prior to radiation in order to determine whether an augmented effect could be obtained in the combination therapy. Cell cycle analysis was performed 48 hours after exposure via flow cytometry employing propidium iodide.

Breast cancer cells were exposed to DMSO as a vehicle control and showed no significant difference in cell cycle distribution compared to cells propagated in growth medium only (Table 2D & 2E). As positive method controls BT-20 cells were exposed to actinomycin D, while MCF-7- and MDA-MB-231 cells were exposed to vinblastine. The positive apoptotic controls displayed a significant increase in sub-G_1 apoptotic cells with a decrease in the G_1 population (Figure 2E & 2G).

BT-20 cells exposed to 0.08 µM (33.67±8.73% G_1 phase and 20.93±8.70% sub-G_1 phase, respectively) and 0.06 µM (39.16±0.56% G_1 phase and 18.81±7.62% sub-G_1 phase, respectively) ESE-15-one displayed a significant decrease in the G_1 phase with a concurrent increase in the sub-G_1 apoptotic phase, compared to DMSO (49.84±3.47% G_1 phase and 6.19±1.56% sub-G_1 phase, respectively). Compared to the vehicle control (6.77±1.47% and

53.23±2.63%, respectively) a 48 hour exposure to ESE-16 at concentrations of 0.223 µM, 0.167 µM and 0.112 µM significantly increased the sub-G_1 phase (44.55±2.07%, 26.38±8.16% and 18.90±3.54, respectively) while decreasing the G_1 population (21.25±1.65%, 37.60±3.09% and 42.56±4.19%, respectively) (Figure 2E). The compound T4 significantly decreased the G_1- (40.53±6.07%), S- (7.40±0.60%) and G_2/M phases (16.11±1.37%) of BT-20 cells at 36 µM, compared to DMSO (56.15±2.32%, 12.35±1.07% and 25.03±2.52%, respectively). Additionally, the sub-G_1 phase was significantly increased in BT-20 cells exposed to 36 µM T4 for 48 hours (36.09±7.03%), compared to the vehicle control (6.62±4.39%). At concentrations of 27 µM and 18 µM T4 significantly increased the apoptotic sub-G_1 phase (32.23±1.01% and 17.98±5.44%, respectively) while decreasing the G_1 phase (33.15±3.39% and 50.85±2.07%, respectively), in addition to decreasing the S phase at 27 µM (9.16±0.40%) (Table 2D). BT-20 cells exposed to 4.096 µM, 2.73 µM, 2.048 µM and 1.638 µM LimPyr1 displayed a significant decrease in the G_1 phase (26.22±1.86%, 36.05±4.44%, 44.34±4.68% and 45.34±5.95%, respectively), while the sub-G_1- (15.00±3.99%, 13.67±2.95%, 7.21±1.63% and 7.68±1.49%, respectively) and G_2/M phases (48.35±2.74%, 39.15±9.14%, 39.65±4.79% and 36.37±4.08%, respectively) were significantly increased, compared to the vehicle control (62.95±4.37%, 5.54±2.35% and 24.02±3.17%, respectively) (Figure 2F).

These results suggested that the lowest dose of ESE-15-one and LimPyr1 that significantly increased the sub-G_1 apoptotic phase was 0.06 µM and 1.638 µM, respectively. This correlated with the results obtained from annexin V quantification and was used to pre-treat BT-20 cells 24 hours prior to radiation in the radiosensitization studies. Annexin V studies revealed a significant increase in apoptotic BT-20 cells when exposed to T4 at 36 µM, however the sub-G_1 phase was significantly increased at 18 µM. Similarly, the lowest dose that significantly increased annexin V staining in ESE-16-exposed BT-20 cells was 0.167 µM, but the sub-G_1 phase was significantly increased at 0.112 µM. These results suggested that there was a delay in the externalization of phosphatidylserine at the lower compound doses. As cells are permeabilized during the cell cycle protocol one may potentially observe DNA fragmentation at earlier stages which is represented in the increased sub-G_1 peak. This

is indicative of apoptosis (684), thus 0.112 µM ESE-16 and 18 µM T4 were used to pre-treat BT-20 cells.

The four compounds were tested for their ability to sensitized BT-20 cells to radiation. BT-20 cells were exposed to the lowest doses of all four compounds, respectively, 24 hours prior to radiation. Cell cycle analysis and annexin V studies revealed that ESE-16 and LimPyr1 hold the most promise to sensitize cells to radiation in this experimental set-up. These two compounds were thus selected to complete the study.

Cell cycle analyses were also performed on MCF-7- and MDA-MB-231 cells exposed to ESE-16- and LimPyr1 dose-response curves. MCF-7 cells displayed a significant increase in the sub-G_1- (34.81±9.96%) and G_2/M phases (47.23±11.49%), while the G_1 phase (14.32±4.61%) was significantly decreased following a 48 hour exposure to 0.313 µM ESE-16, compared to DMSO (0.33±0.10%, 65.28±9.39% and 25.79±4.73%, respectively). Additionally, ESE-16-exposure increased the sub-G_1 population of MCF-7 cells at concentrations of 0.235 µM (11.81±6.92%) and 0.157 µM (1.05±0.32%) (Figure 2G). A significant increase in the sub-G_1 phase with a concurrent decrease in the G_1 phase was observed in MDA-MB-231 cells exposed to 0.274 µM (34.22±6.75% and 3.60±1.17%, respectively), 0.206 µM (31.18±5.35% and 8.41±2.23%, respectively) and 0.137 µM (7.83±0.08% and 49.33±4.15%, respectively) ESE-16, compared to the vehicle control (0.62±0.32% and 65.57±4.75%, respectively). MDA-MB-231 cells also displayed a significant decrease in the S phase (2.08±0.30% and 2.64±1.03%) and an increase in the G_2/M population (53.05±5.88% and 49.41±4.16%) following ESE-16-exposure at 0.274 µM and 0.206 µM, respectively, compared to DMSO (5.62±0.93% and 25.11±3.99%, respectively) (Table 2E).

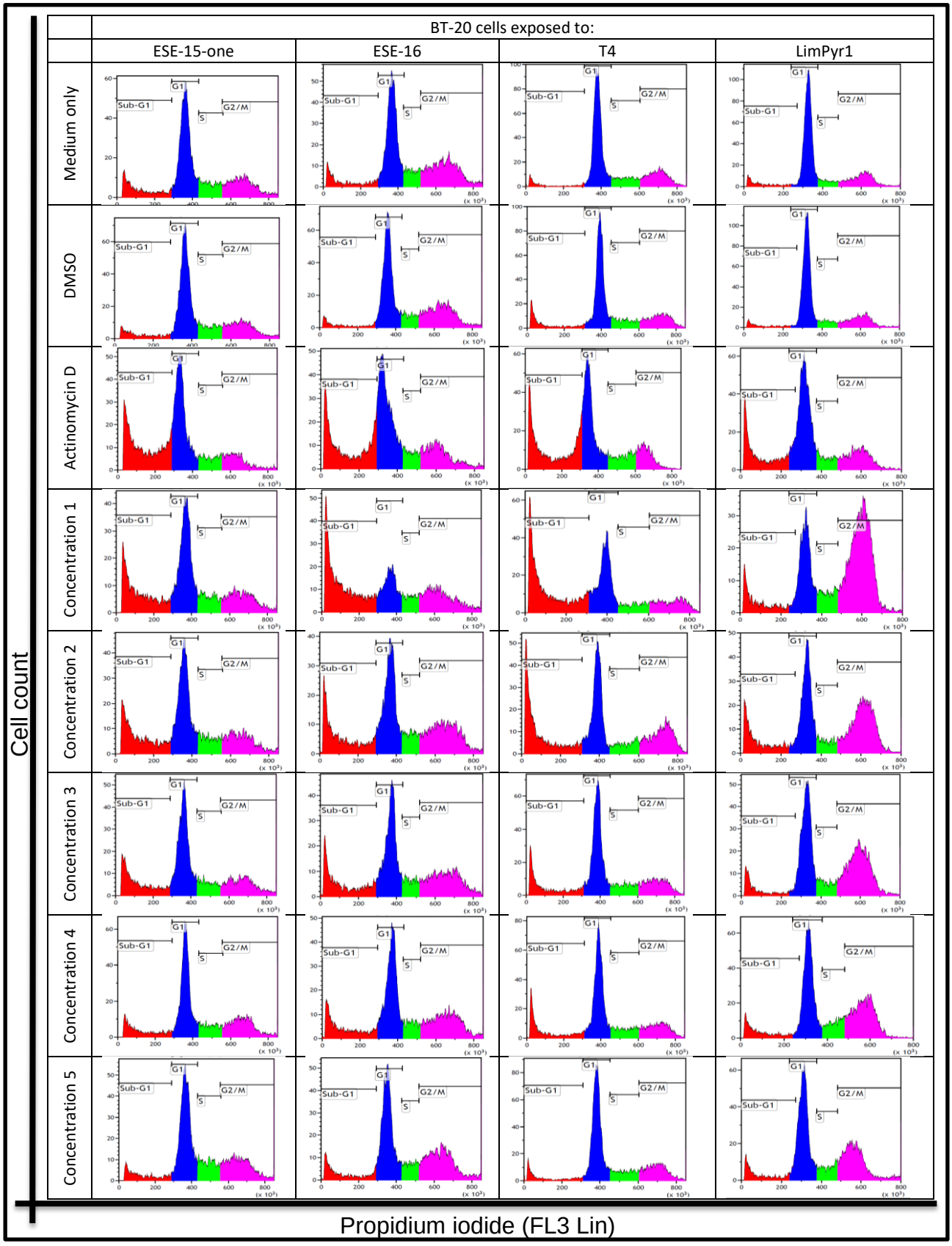

Figure 2E: Histograms representing the cell cycle distributions of BT-20 cells exposed to compound dose-response curves. Histograms were obtained by plotting the number of cells

against propidium iodide (FL3 Lin). BT-20 cells were propagated in growth media only (negative control), exposed to DMSO as vehicle controls or actinomycin D as positive apoptotic controls. BT-20 cells were exposed to ESE-15-one, ESE-16, T4 and LimPyr1 dose-response curves (Table 2A) to determine the lowest dose of each compound that significantly increase the sub-G_1 phase.

The Lim kinase inhibitor, LimPyr1, significantly increased the sub-G_1 phase of MCF-7- (3.28±0.64%, 2.95±0.50% and 3.67±1.35%, respectively) and MDA-MB-231 cells (3.45±0.55%, 2.00±0.11% and 3.00±0.90%, respectively) exposed to 4.875 µM, 3.25 µM and 2.437 µM, compared to the 1.59±0.49% and 1.30±0.36% observed in the MCF-7- and MDA-MB-231 vehicle controls. The percentage cells in the G_2/M phase was significantly increased in MCF-7- and MDA-MB-231 cells when exposed to LimPyr1 at concentrations of 4.875 µM (80.90±2.17% MCF-7 cells and 66.63±5.65% MDA-MB-231 cells), 3.25 µM (76.61±1.90% MCF-7 cells and 69.62±4.67% MDA-MB-231 cells) and 2.437 µM (48.47±3.45% MCF-7 cells and 60.49±2.60% MDA-MB-231 cells) when compared to the MCF-7- (32.43±5.23%) and MDA-MB-231 DMSO samples (32.85±7.74%). The G_1 phase of MCF-7- (8.92±3.44%, 11.84±1.44% and 43.12±3.52%, respectively) and MDA-MB-231 cells (8.17±3.07%, 7.02±3.42% and 35.61±5.48%, respectively) were significantly decreased in samples exposed to 4.875 µM, 3.25 µM and 2.437 µM LimPyr1,respectively, compared to the MCF-7- (56.57±4.87%) and MDA-MB-231 DMSO controls (49.99±7.12%). MCF-7 cells exposed to 4.875 µM LimPyr1 displayed a significant decrease in cells present in the S phase (6.93±2.05%) compared to the 9.43±5.87% observed in the vehicle control (Figure 2H).

The lowest dose LimPyr1 that significantly increased the amount of cells present in the sub-G_1 apoptotic phase of MCF-7- and MDA-MB-231 cells was 2.437 µM. This was confirmed with annexin V experiments and was used to pre-treat cells prior to radiation for the remainder of the investigations. Additionally, cell cycle analysis and annexin V studies revealed 0.137 µM ESE-16 to be the lowest dose to significantly increase apoptotic cell death in MDA-MB-231 cells, thus this dose was used to pre-treat MDA-MB-231 cells prior to radiation in further experiments. Cell cycle analysis of ESE-16-exposed MCF-7 cells

displayed a significant increase in the sub-G_1 phase following exposure to 0.157 µM, however apoptosis was only significant at 0.235 µM when quantified by annexin V. This may suggest increased DNA fragmentation at the lower concentration, which can be observed in cell cycle analysis via increased sub-G_1 peaks. DNA fragmentation is a hallmark of apoptotic cell death (684), thus 0.157 µM ESE-16 was used to pre-treat MCF-7 cells 24 hour prior to radiation in sensitization investigations.

Table 2D: Flow cytometric analysis of BT-20 cells exposed to compound dose-response curves. Data were acquired using Kaluza Analysis software version 1.5 (FL, USA) and analyzed using an ANOVA-single factor model. Statistical significance was calculated using a two-tailed Student's *t*-test. The averaged percentage of three biological repeats (M%) and their standard deviations (SD) are displayed for each phase of the cell cycle. Statistically significant differences (*P*-value <0.05) were calculated using the DMSO sample as a baseline.

						Drug concentrations				
			Medium only	DMSO	Actinomycin D	0.08 µM	0.06 µM	0.04 µM	0.02 µM	0.013 µM
ESE-15-one	Sub-G_1	M%±SD	9.00±3.37	6.19±1.56	32.62±3.63	20.93±8.70	18.81±7.62	13.78±5.62	9.71±2.26	7.02±1.07
		P-value	0.26	-	**3.17E-04**	**0.04**	**4.83E-02**	0.09	0.09	0.49
	G_1	M%±SD	47.62±6.68	49.84±3.47	39.69±4.41	33.67±8.73	39.16±0.56	43.58±5.24	44.98±4.60	44.49±7.17
		P-value	0.64	-	**0.04**	**0.04**	**0.01**	0.16	0.22	0.31
	S	M%±SD	10.73±1.14	10.21±1.48	9.50±1.93	9.72±0.21	12.62±4.07	8.89±0.74	10.34±1.09	12.23±1.44
		P-value	0.66	-	0.64	0.60	0.39	0.24	0.91	0.16
	G_2/M	M%±SD	32.80±6.99	33.85±4.86	18.39±3.42	35.83±8.64	29.68±10.88	33.88±7.41	35.13±5.77	36.42±8.44
		P-value	0.84	-	**0.01**	0.75	0.58	1.00	0.78	0.67
						0.223 µM	**0.167 µM**	**0.112 µM**	**0.056 µM**	**0.037 µM**
ESE-16	Sub-G_1	M%±SD	9.85±3.54	6.77±1.47	34.22±2.61	44.55±2.07	26.38±8.16	18.90±3.54	15.60±5.86	12.82±3.64
		P-value	0.24	-	**9.22E-05**	**1.51E-04**	**0.01**	**0.01**	0.06	0.06
	G_1	M%±SD	50.90±5.48	53.23±2.63	39.30±3.98	21.25±1.65	37.60±3.09	42.56±4.19	48.03±7.11	48.12±4.04
		P-value	0.54	-	**0.01**	**5.81E-05**	**2.61E-03**	**0.04**	0.30	0.14
	S	M%±SD	9.86±0.67	9.55±1.51	7.86±0.63	7.81±0.87	7.81±1.45	8.32±1.46	8.89±0.42	9.68±0.94
		P-value	0.76	-	0.15	0.23	0.22	0.37	0.51	0.90
	G_2/M	M%±SD	29.36±4.81	30.41±4.13	18.57±4.03	24.91±2.31	28.17±6.18	27.00±3.93	27.39±3.67	29.32±5.75
		P-value	0.79	-	0.02	0.20	0.63	0.36	0.40	0.80
						36 µM	**27 µM**	**18 µM**	**9 µM**	**6 µM**
T4	Sub-G_1	M%±SD	3.52±2.08	6.62±4.39	38.80±3.62	36.09±7.03	32.23±1.01	17.98±5.44	11.93±4.28	5.85±2.13
		P-value	0.43	-	**6.08E-04**	**3.52E-03**	**4.50E-03**	**4.80E-02**	0.21	0.80
	G_1	M%±SD	57.58±3.52	56.15±2.32	37.74±1.91	40.53±6.07	33.15±3.39	50.85±2.07	48.75±7.84	58.20±2.65
		P-value	0.59	-	**4.45E-04**	**0.01**	**2.66E-03**	**0.04**	0.19	0.37
	S	M%±SD	11.68±1.79	12.35±1.07	10.86±1.47	7.40±0.60	9.16±0.40	11.25±1.15	13.26±1.51	13.26±0.89
		P-value	0.61	-	0.23	**2.18E-03**	**0.03**	0.29	0.44	0.32
	G_2/M	M%±SD	22.89±2.88	25.03±2.52	12.98±1.33	16.11±1.37	25.55±1.99	20.09±2.98	26.19±7.96	22.92±3.44
		P-value	0.39	-	**1.84E-03**	**0.01**	0.83	0.09	0.82	0.44
						4.096 µM	**2.73 µM**	**2.048 µM**	**1.638 µM**	**1.365 µM**
LimPyr1	Sub-G_1	M%±SD	7.22±2.29	5.54±2.35	26.72±1.59	15.00±3.99	13.67±2.95	7.21±1.63	7.68±1.49	5.25±1.59
		P-value	0.85		**4.85E-04**	**4.52E-02**	**4.54E-02**	**4.76E-02**	**0.02**	0.41
	G_1	M%±SD	62.44±2.71	62.95±4.37	48.93±2.55	26.22±1.86	36.05±4.44	44.34±4.68	45.34±5.95	54.03±6.36
		P-value	0.77		**0.02**	**5.51E-04**	**3.27E-03**	**4.76E-03**	**0.01**	0.11
	S	M%±SD	7.50±1.55	7.59±0.61	7.70±0.78	10.32±2.12	11.04±5.61	9.06±4.69	11.11±4.01	7.67±1.31
		P-value	0.94		0.68	0.09	0.33	0.66	0.23	0.92
	G_2/M	M%±SD	22.89±2.76	24.02±3.17	16.82±0.37	48.35±2.74	39.15±9.14	39.65±4.79	36.37±4.08	32.16±5.43
		P-value	0.75		**0.04**	**3.82E-04**	**0.04**	**0.01**	**0.02**	0.14

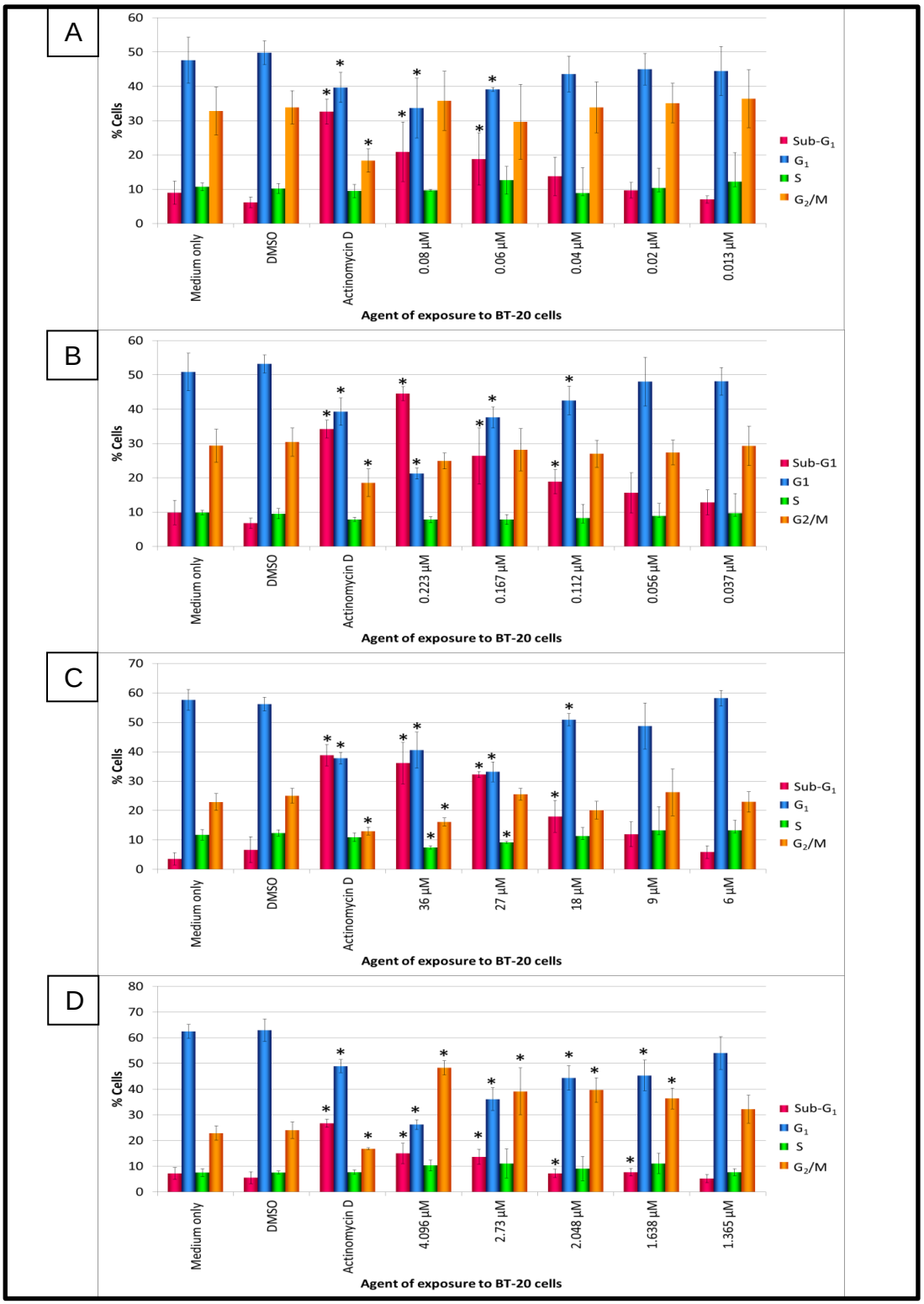

Figure 2F: Graphical representation of the cell cycle analysis of BT-20 cells exposed to compound dose-response curves. The lowest dose that significantly increased the sub-G_1 phase in BT-20 cells was 0.06 µM for ESE-15-one (A), 0.112 µM for ESE-16 (B), 18 µM for T4 (C) and 1.638 µM for LimPyr1 (D). Bars indicate the mean of three biological repeats, with standard deviations represented by T-bars. Statistical significant differences are indicated with * (*P*-value <0.05).

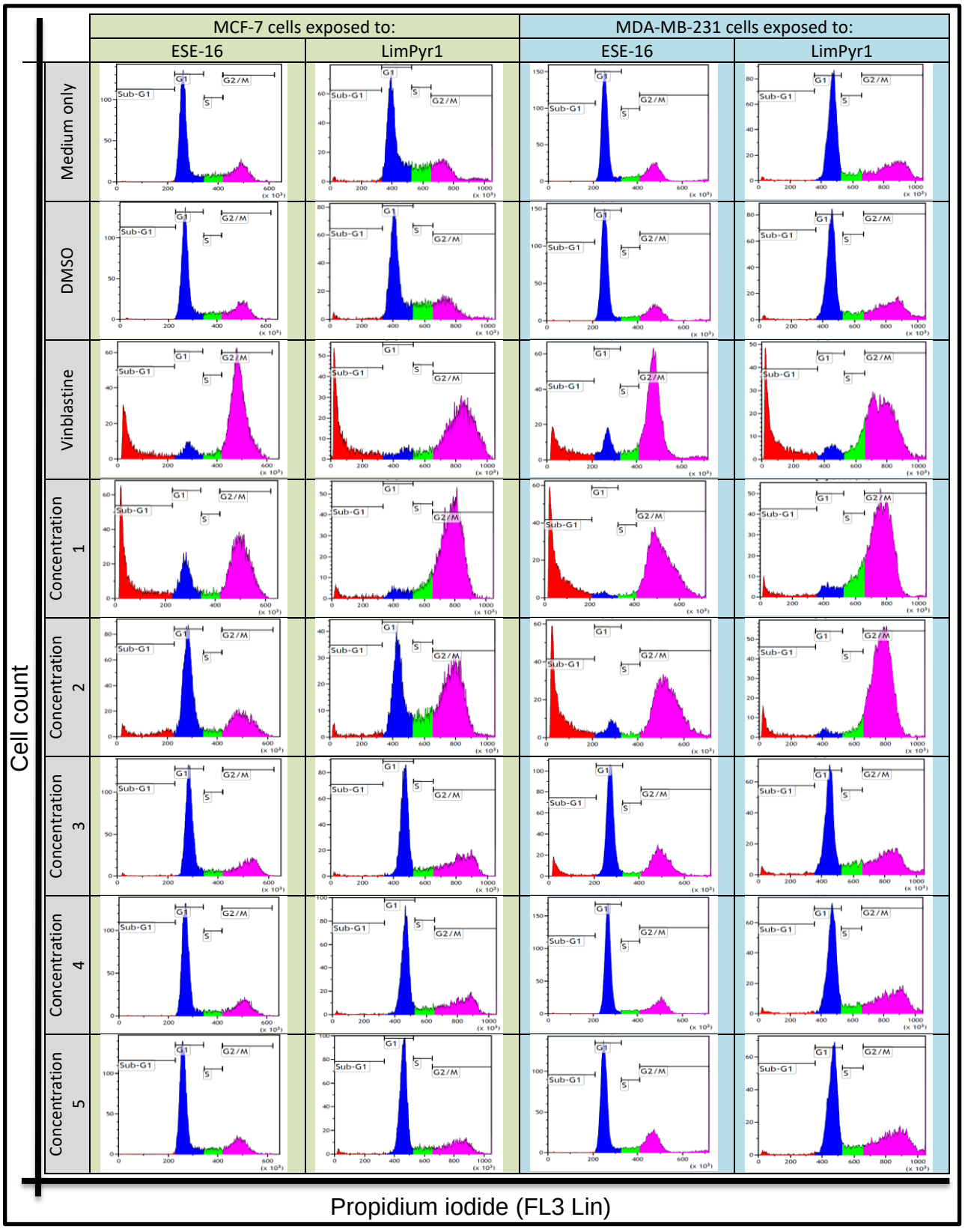

Figure 2G: Histograms representing the cell cycle distributions of MCF-7- and MDA-MB-231 cells exposed to compound dose-response curves. Cell numbers were plotted against propidium iodide (FL3 Lin). MCF-7- and MDA-MB-231 cells propagated in medium only served as

negative controls and cells exposed to DMSO as vehicle controls. Vinblastine exposure provided a positive method control. The lowest dose of each compound that significantly increased the sub-G_1 phase of MCF-7- and MDA-MB-231 cells were identified following exposure to an ESE-16 and a LimPyr1 dose-response curve (Table 2A).

Table 2E: Flow cytometric analysis of MCF-7- and MDA-MB-231 cells exposed to compound dose-response curves. Kaluza Analysis software version 1.5 (FL, USA) was used to acquire the data followed by analysis using an ANOVA-single factor model. A two-tailed Student's *t*-test was used to calculate statistical significance. The averaged percentage of three biological repeats (M%) and their standard deviations (SD) are displayed for each phase of the cell cycle. Statistically significant differences (*P*-value <0.05) were calculated using the DMSO samples as baselines.

							Drug concentrations				
				Medium only	DMSO	Vinblastine	0.313 µM	0.235 µM	0.157 µM	0.078 µM	0.052 µM
MCF-7	ESE-16	Sub-G_1	M%±SD	0.44±0.12	0.33±0.10	23.17±4.18	34.81±9.96	11.81±6.92	1.05±0.32	0.62±0.18	0.45±0.01
			P-value	0.26	-	**6.93E-04**	**3.90E-03**	**4.54E-02**	**0.02**	0.07	0.23
		G_1	M%±SD	66.25±9.57	65.28±9.39	9.43±4.08	14.32±4.61	52.97±13.71	65.47±10.22	66.54±10.05	71.07±6.92
			P-value	0.91	-	**7.00E-04**	**1.08E-03**	0.27	0.98	0.88	0.44
		S	M%±SD	8.86±4.67	8.59±4.69	4.72±0.92	3.61±0.59	4.70±0.42	8.07±4.23	7.47±3.93	6.14±1.25
			P-value	0.95	-	0.23	0.14	0.23	0.89	0.77	0.43
		G_2/M	M%±SD	24.44±5.12	25.79±4.73	62.65±5.36	47.23±11.49	30.46±6.66	25.35±7.02	25.33±6.41	21.25±4.44
			P-value	0.75	-	**8.67E-04**	**0.04**	0.38	0.93	0.93	0.29
							4.875 µM	**3.25 µM**	**2.437 µM**	**1.95 µM**	**1.625 µM**
	LimPyr1	Sub-G_1	M%±SD	1.81±0.44	1.59±0.49	36.28±6.37	3.28±0.64	2.95±0.50	3.67±1.35	2.23±1.05	1.80±0.51
			P-value	0.55	-	**7.38E-04**	**0.03**	**0.03**	**0.04**	0.18	0.16
		G_1	M%±SD	56.68±1.13	56.57±4.87	6.71±0.70	8.92±3.44	11.84±1.44	43.12±3.52	49.46±0.69	60.09±4.35
			P-value	0.15	-	**1.26E-05**	**7.23E-05**	**4.01E-04**	**0.01**	0.06	0.92
		S	M%±SD	14.58±3.66	9.43±5.87	5.92±0.71	6.93±2.05	9.61±1.35	4.70±1.74	6.72±0.93	4.92±1.36
			P-value	0.92	-	**0.02**	**4.54E-02**	0.12	0.95	0.07	0.79
		G_2/M	M%±SD	25.55±1.65	32.43±5.23	51.13±7.54	80.90±2.17	76.61±1.90	48.47±3.45	41.67±2.11	33.16±3.97
			P-value	0.26	-	**0.02**	**1.90E-04**	**2.33E-03**	**0.01**	0.11	0.72
							0.274 µM	**0.206 µM**	**0.137 µM**	**0.069 µM**	**0.046µM**
MDA-MB-231	ESE-16	Sub-G_1	M%±SD	0.48±0.42	0.62±0.32	20.82±5.52	34.22±6.75	31.18±5.35	7.83±0.08	0.83±0.67	0.87±0.92
			P-value	0.68	-	**3.20E-03**	**2.53E-03**	**1.70E-03**	**8.55E-05**	0.65	0.67
		G_1	M%±SD	66.82±8.96	65.57±4.75	11.38±2.35	3.60±1.17	8.41±2.23	49.33±4.15	67.81±7.31	65.46±9.00
			P-value	0.84	-	**5.98E-05**	**4.26E-04**	**6.06E-04**	**0.03**	0.68	0.99
		S	M%±SD	5.63±2.33	5.62±0.93	5.74±0.50	2.08±0.30	2.64±1.03	4.21±1.27	5.01±1.50	5.31±1.48
			P-value	0.99	-	0.86	**0.02**	**0.04**	0.24	0.58	0.77
		G_2/M	M%±SD	23.86±6.49	25.11±3.99	50.10±5.54	53.05±5.88	49.41±4.16	35.47±3.44	23.56±6.33	24.56±7.18
			P-value	0.79	-	**3.16E-03**	**0.01**	**0.01**	0.06	0.74	0.91
							4.875 µM	**3.25 µM**	**2.437 µM**	**1.95 µM**	**1.625 µM**
	LimPyr1	Sub-G_1	M%±SD	1.15±0.35	1.30±0.36	26.99±4.35	3.45±0.55	2.00±0.11	3.00±0.90	2.94±0.82	2.54±0.71
			P-value	0.57	-	**5.20E-04**	**3.14E-03**	**0.02**	**4.56E-02**	0.07	0.10
		G_1	M%±SD	41.87±1.64	49.99±7.12	5.90±0.54	8.17±3.07	7.02±3.42	35.61±5.48	39.95±5.43	37.31±7.33
			P-value	0.10	-	**5.32E-05**	**1.81E-04**	**1.37E-03**	**0.02**	0.09	0.07
		S	M%±SD	9.31±3.12	6.76±3.29	4.67±0.73	8.91±1.04	6.32±3.70	6.04±3.19	6.50±0.83	6.66±0.64
			P-value	0.30	-	**4.76E-02**	0.97	0.40	0.55	0.37	0.33
		G_2/M	M%±SD	27.04±2.77	32.85±7.74	48.37±5.03	66.63±5.65	69.62±4.67	60.49±2.60	50.62±5.45	53.52±7.25
			P-value	0.26	-	**1.69E-03**	**2.56E-04**	**4.48E-04**	**0.01**	0.07	0.06

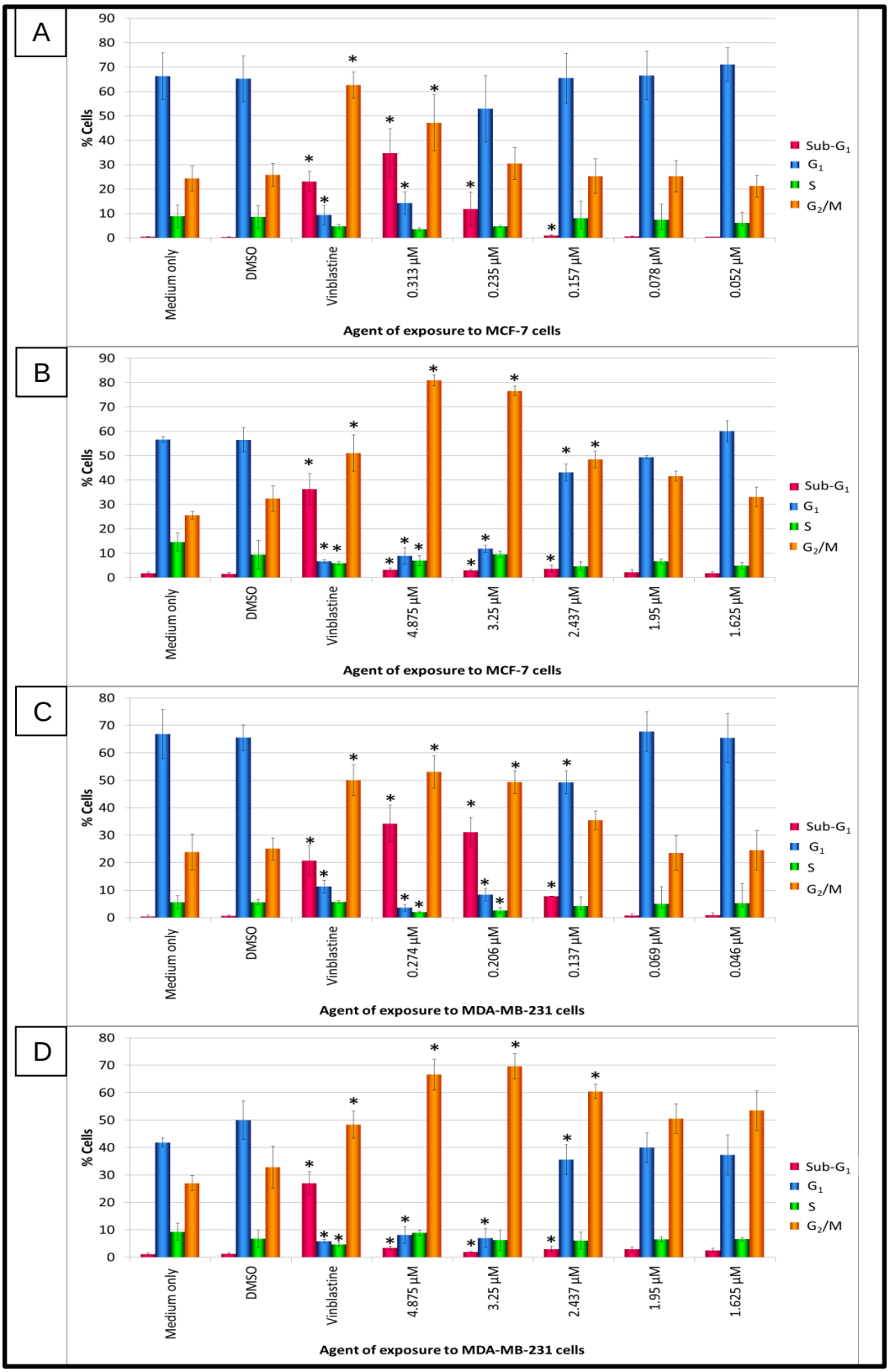

Figure 2H: Graphical representation of the cell cycle analysis of MCF-7- and MDA-MB-231 cells exposed to compound dose-response curves. The lowest doses that significantly increased the sub-G_1 phase in MCF-7 cells were calculated to be 0.157 µM for ESE-16 (A) and 2.437 µM for LimPyr1 (B). Apoptosis was significantly increased in MDA-MB-231 cells after exposure to 0.137

µM ESE-16 (C) and 2.437 µM LimPyr1 (D). The average of three biological repeats is displayed in the bar graphs with standard deviations represented by T-bars. Statistical significant differences are indicated with * (*P*-value <0.05).

11. Appendix A: Data analysis of Incucyte® experiments

Table A1: IncuCyte® Cytotox Green fluorescence in HeLa cells exposed to ESE-15-one and ESE-16, indicating cell death. The average of green fluorescence measured per mm^2 (mean) and standard error of the mean (SE) of two biological repeats are displayed in the table below. HeLa cells exposed to DMSO served as a baseline for the calculation of statistical significance (*P*-value <0.05).

Time (Hours)		DMSO	ESE-15-one	ESE-16
0	Mean±SE	2.29±0.31	2.80±0.34	2.03±0.32
	P-value	-	0.36	0.65
4	Mean±SE	2.68±0.40	3.73±0.48	3.07±0.33
	P-value	-	0.18	0.54
6	Mean±SE	2.70±0.39	4.02±0.46	3.46±0.33
	P-value	-	0.07	0.25
8	Mean±SE	2.68±0.40	4.13±0.49	3.51±0.30
	P-value	-	**4.51E-02**	0.15
10	Mean±SE	2.98±0.44	4.43±0.46	3.88±0.29
	P-value	-	**0.04**	0.16
12	Mean±SE	3.20±0.42	4.90±0.48	4.59±0.35
	P-value	-	**0.02**	**0.04**
14	Mean±SE	3.75±0.46	5.89±0.52	5.49±0.40
	P-value	-	**0.01**	**0.02**
16	Mean±SE	3.97±0.45	6.18±0.49	6.53±0.51
	P-value	-	**8.95E-03**	**2.21E-03**
18	Mean±SE	4.44±0.43	7.28±0.59	7.35±0.57
	P-value	-	**2.79E-03**	**1.28E-03**
20	Mean±SE	4.47±0.42	8.78±0.55	8.41±0.59
	P-value	-	**2.24E-05**	**3.42E-05**
22	Mean±SE	4.96±0.44	10.22±0.67	10.46±0.66
	P-value	-	**4.97E-05**	**4.56E-07**
24	Mean±SE	5.60±0.49	12.93±0.83	13.72±0.87
	P-value	-	**2.28E-06**	**1.91E-08**
26	Mean±SE	6.37±0.58	15.91±1.07	16.75±0.88
	P-value	-	**4.22E-06**	**1.29E-08**
28	Mean±SE	6.87±0.73	19.11±1.24	20.32±1.06
	P-value	-	**1.52E-06**	**4.74E-09**
30	Mean±SE	7.23±0.76	22.20±1.35	23.61±1.13
	P-value	-	**7.20E-07**	**4.68E-10**
32	Mean±SE	7.89±0.85	26.74±1.59	28.11±1.26
	P-value	-	**7.71E-07**	**1.17E-09**
34	Mean±SE	8.27±0.76	33.14±1.71	33.98±1.67
	P-value	-	**3.36E-08**	**9.88E-10**
36	Mean±SE	9.02±1.04	39.94±1.78	41.26±1.92
	P-value	-	**2.77E-09**	**1.02E-09**
38	Mean±SE	9.60±1.10	46.69±2.12	48.26±2.28

	P-value	-	**5.07E-09**	**8.33E-10**
40	Mean±SE	10.12±1.08	55.32±2.38	56.60±2.63
	P-value	-	**1.88E-09**	**3.37E-10**
42	Mean±SE	11.39±1.25	64.69±2.60	66.24±3.28
	P-value	-	**2.77E-10**	**5.82E-10**
44	Mean±SE	12.22±1.23	73.39±2.63	75.09±3.71
	P-value	-	**9.77E-11**	**4.49E-10**
46	Mean±SE	13.43±1.36	86.40±3.14	89.21±5.34
	P-value	-	**3.77E-11**	**2.65E-09**
48	Mean±SE	13.85±1.26	94.46±3.48	97.77±5.11
	P-value	-	**3.55E-11**	**7.09E-10**
50	Mean±SE	14.40±1.34	103.55±3.48	105.78±5.28
	P-value	-	**7.66E-12**	**1.96E-10**
52	Mean±SE	15.33±1.50	123.05±4.61	125.22±7.56
	P-value	-	**5.41E-12**	**1.77E-10**
56	Mean±SE	17.16±1.69	139.78±5.14	138.57±8.91
	P-value	-	**2.32E-12**	**5.21E-10**
58	Mean±SE	17.71±1.51	145.67±5.31	145.58±8.57
	P-value	-	**1.18E-12**	**3.62E-11**
60	Mean±SE	18.40±1.58	151.05±5.71	152.77±9.80
	P-value	-	**2.62E-12**	**1.29E-10**
62	Mean±SE	20.00±1.83	156.75±5.80	157.52±9.80
	P-value	-	**1.04E-12**	**8.59E-11**
64	Mean±SE	21.40±1.91	161.20±5.62	161.27±10.23
	P-value	-	**5.55E-13**	**9.13E-11**
66	Mean±SE	22.73±2.01	165.35±5.69	163.94±10.05
	P-value	-	**8.19E-13**	**7.69E-11**
68	Mean±SE	23.03±2.03	169.83±6.22	169.32±10.21
	P-value	-	**1.66E-12**	**2.82E-11**
70	Mean±SE	24.68±2.31	172.04±6.33	173.01±10.00
	P-value	-	**2.92E-12**	**2.28E-11**
72	Mean±SE	24.33±2.17	173.43±6.38	176.10±10.37
	P-value	-	**3.51E-12**	**1.81E-11**

Table A2: Wound healing in HeLa cells exposed to ESE-15-one and ESE-16, indicating cell migration. The mean wound width (µm) and standard error of the mean (SE) of two biological repeats are displayed in the table below. Statistical significance (*P*-value <0.05) was calculated using HeLa cells exposed to DMSO as a baseline.

Time (Hours)		DMSO	ESE-15-one (0.4 µM)	ESE-15-one (0.2 µM)	ESE-16 (0.4 µM)	ESE-16 (0.2 µM)
0	Mean±SE	678.58±5.21	705.55±14.04	698.04±13.94	680.10±8.06	676.63±15.38
	P-value	-	0.13	0.27	0.89	0.92
2	Mean±SE	654.15±5.11	689.66±20.53	668.77±13.29	648.93±7.39	632.39±18.91
	P-value	-	0.17	0.38	0.60	0.35
4	Mean±SE	637.76±8.90	665.45±15.42	649.39±13.41	628.70±7.44	606.98±19.37
	P-value	-	0.18	0.52	0.44	0.22
6	Mean±SE	608.94±4.83	654.78±20.28	631.32±13.16	608.91±7.16	581.66±18.48
	P-value	-	0.08	0.18	1.00	0.24
8	Mean±SE	580.92±5.44	643.90±18.32	621.85±13.06	594.26±6.73	547.44±22.62
	P-value	-	**0.01**	**2.11E-02**	0.16	0.23
10	Mean±SE	557.78±6.21	659.56±29.57	615.27±12.59	581.64±7.66	534.31±18.69
	P-value	-	**0.01**	**2.01E-03**	**0.04**	0.32
12	Mean±SE	535.54±6.82	650.68±27.23	617.73±13.75	579.13±8.56	510.73±18.32
	P-value	-	**2.62E-03**	**1.79E-04**	**1.61E-03**	0.28
14	Mean±SE	503.42±7.49	666.99±29.94	634.70±13.47	587.81±12.00	473.10±20.16
	P-value	-	**2.84E-04**	**6.48E-07**	**4.45E-05**	0.24
16	Mean±SE	473.74±9.60	741.75±39.97	652.84±13.51	594.75±10.74	449.16±19.17
	P-value	-	**3.24E-05**	**1.54E-08**	**3.44E-07**	0.32
18	Mean±SE	440.06±11.56	817.00±47.99	687.76±14.35	605.03±12.25	425.59±19.44
	P-value	-	**4.96E-06**	**4.42E-10**	**3.52E-08**	0.57
20	Mean±SE	415.79±11.33	937.22±63.12	732.42±19.79	634.72±18.48	394.82±21.01
	P-value	-	**2.42E-06**	**5.19E-10**	**5.30E-08**	0.44
22	Mean±SE	387.88±12.07	1095.86±73.94	807.52±32.78	669.51±30.24	362.48±19.17
	P-value	-	**3.37E-07**	**7.82E-09**	**7.58E-07**	0.32

12. Appendix B: Distribution of micronuclei in breast cancer cells exposed to various treatment conditions

Table B1: Micronuclei quantification in breast cancer cells pre-treated with ESE-16. MCF-7- and MDA-MB-231 cells propagated in DMEM, and BT-20 cells propagated in DMEM/F-12 were exposed to ESE-16, 8 Gy radiation and ESE-16 in combination with radiation. Micronuclei quantification followed 2 and 24 hours after radiation.

		Number of micronuclei	MCF-7		MDA-MB-231		BT-20	
			2h	24h	2h	24h	2h	24h
Cells presented with micronuclei	Medium only	0	481	486	474	471	442	434
		1	18	13	25	27	52	62
		2	1	1	1	1	5	4
		3	0	0	0	0	1	0
		4	0	0	0	0	0	0
		5	0	0	0	0	0	0
		>5	0	0	0	0	0	0
	DMSO	0	481	484	471	477	452	456
		1	16	15	29	22	43	40
		2	3	1	1	2	6	3
		3	0	0	0	0	0	0
		4	0	0	0	0	0	0
		5	0	0	0	0	0	0
		>5	0	0	0	0	0	0
	ESE-16	0	478	482	471	476	444	425
		1	19	14	28	23	53	66
		2	3	4	1	1	3	7
		3	0	0	0	0	0	1
		4	0	0	0	0	0	0
		5	0	0	0	0	0	0
		>5	0	0	0	0	0	0
	8 Gy radiation	0	219	220	299	303	273	280
		1	226	244	145	146	162	176
		2	45	35	34	45	49	39
		3	8	1	21	6	12	6
		4	2	0	1	0	3	1
		5	0	0	0	0	1	0
		>5	0	0	0	0	0	0
	ESE-16 + radiation	0	286	249	298	293	254	259
		1	102	188	144	137	160	164
		2	86	50	34	54	62	54
		3	18	11	24	15	16	17
		4	7	2	0	0	7	5
		5	1	0	0	0	1	1
		>5	0	0	0	0	0	1

Table B2: Micronuclei quantification in breast cancer cells pre-treated with LimPyr1. MCF-7-, MDA-MB-231- and BT-20 cells propagated in RPMI growth medium were exposed to LimPyr1, 8 Gy radiation and LimPyr1 24 hours prior to radiation. Micronuclei quantification followed 2 and 24 hours after radiation.

		Number of micronuclei	MCF-7		MDA-MB-231		BT-20	
			2h	24h	2h	24h	2h	24h
Cells presented with micronuclei	Medium only	0	488	487	477	477	449	443
		1	11	12	21	19	47	52
		2	1	1	2	4	4	5
		3	0	0	0	0	0	0
		4	0	0	0	0	0	0
		5	0	0	0	0	0	0
		>5	0	0	0	0	0	0
	DMSO	0	489	491	483	485	454	450
		1	10	7	16	14	42	47
		2	2	2	1	1	4	2
		3	0	0	0	0	0	1
		4	0	0	0	0	0	0
		5	0	0	0	0	0	0
		>5	0	0	0	0	0	0
	LimPyr1	0	488	485	481	467	426	426
		1	10	14	17	31	57	46
		2	2	1	2	2	12	19
		3	0	1	0	0	4	9
		4	0	0	0	0	0	0
		5	0	0	0	0	0	0
		>5	0	0	0	0	0	0
	8 Gy radiation	0	222	264	255	300	259	276
		1	206	185	154	118	174	167
		2	63	42	59	62	59	54
		3	7	8	30	20	9	3
		4	2	0	2	0	0	0
		5	0	0	0	0	0	0
		>5	0	0	0	0	0	0
	LimPyr1 + radiation	0	257	272	269	267	256	264
		1	137	107	132	115	127	126
		2	82	87	58	77	82	81
		3	18	32	38	40	19	25
		4	6	2	3	1	14	4
		5	0	0	0	0	2	0
		>5	0	0	0	0	0	0

13. Video's

Video 4.1, 4.2 and 4.3 are available at: http://tiny.cc/vdye4y

14. Ethics approval

The Research Ethics Committee, Faculty Health Sciences, University of Pretoria complies with ICH-GCP guidelines and has US Federal wide Assurance.
- FWA 00002567, Approved dd 22 May 2002 and Expires 03/20/2022.
- IRB 0000 2235 IORG0001762 Approved dd 22/04/2014 and Expires 03/14/2020.

UNIVERSITEIT VAN PRETORIA
UNIVERSITY OF PRETORIA
YUNIBESITHI YA PRETORIA

Faculty of Health Sciences Research Ethics Committee

27/07/2017

Approval Certificate
New Application

Ethics Reference No: 285/2017

Title: Pro-apoptotic and radiosensitizing potential of four candidate microtubule regulators in breast cancer cells

Dear Ms Elsie Nolte

The **New Application** as supported by documents specified in your cover letter dated 30/06/2017 for your research received on the 30/06/2017, was approved by the Faculty of Health Sciences Research Ethics Committee on its quorate meeting of 26/07/2017.

Please note the following about your ethics approval:
- Ethics Approval is valid for 2 years
- Please remember to use your protocol number (**285/2017**) on any documents or correspondence with the Research Ethics Committee regarding your research.
- Please note that the Research Ethics Committee may ask further questions, seek additional information, require further modification, or monitor the conduct of your research.

Ethics approval is subject to the following:
- The ethics approval is conditional on the receipt of **6 monthly written Progress Reports**, and
- The ethics approval is conditional on the research being conducted as stipulated by the details of all documents submitted to the Committee. In the event that a further need arises to change who the investigators are, the methods or any other aspect, such changes must be submitted as an Amendment for approval by the Committee.

We wish you the best with your research.

Yours sincerely

Dr R Sommers; MBChB; MMed (Int); MPharMed,PhD
Deputy Chairperson of the Faculty of Health Sciences Research Ethics Committee, University of Pretoria

The Faculty of Health Sciences Research Ethics Committee complies with the SA National Act 61 of 2003 as it pertains to health research and the United States Code of Federal Regulations Title 45 and 46. This committee abides by the ethical norms and principles for research, established by the Declaration of Helsinki, the South African Medical Research Council Guidelines as well as the Guidelines for Ethical Research: Principles Structures and Processes, Second Edition 2015 (Department of Health).

☎ 012 356 3084 deepeka.behari@up.ac.za / fhsethics@up.ac.za http://www.up.ac.za/healthethics
✉ Private Bag X323, Arcadia, 0007 - Tswelopele Building, Level 4, Room 60, Gezina, Pretoria

15. Declaration

DECLARATION OF ORIGINALITY

UNIVERSITY OF PRETORIA

The Department of ..... Physiology ..... places great emphasis upon integrity and ethical conduct in the preparation of all written work submitted for academic evaluation.

While academic staff teach you about referencing techniques and how to avoid plagiarism, you too have a responsibility in this regard. If you are at any stage uncertain as to what is required, you should speak to your lecturer before any written work is submitted.

You are guilty of plagiarism if you copy something from another author's work (eg a book, an article or a website) without acknowledging the source and pass it off as your own. In effect you are stealing something that belongs to someone else. This is not only the case when you copy work word-for-word (verbatim), but also when you submit someone else's work in a slightly altered form (paraphrase) or use a line of argument without acknowledging it. You are not allowed to use work previously produced by another student. You are also not allowed to let anybody copy your work with the intention of passing if off as his/her work.

Students who commit plagiarism will not be given any credit for plagiarised work. The matter may also be referred to the Disciplinary Committee (Students) for a ruling. Plagiarism is regarded as a serious contravention of the University's rules and can lead to expulsion from the University.

The declaration which follows must accompany all written work submitted while you are a student of the Department of ..... Physiology ..... No written work will be accepted unless the declaration has been completed and attached.

Full names of student: Elsie Magdalena Nolte

Student number: 10005022

Topic of work: Pro-apoptotic and radiosensitizing potential of four candidate microtubule regulators in breast cancer cells

Declaration

1. I understand what plagiarism is and am aware of the University's policy in this regard.

2. I declare that this ..... thesis ..... (eg essay, report, project, assignment, dissertation, thesis, etc) is my own original work. Where other people's work has been used (either from a printed source, Internet or any other source), this has been properly acknowledged and referenced in accordance with departmental requirements.

3. I have not used work previously produced by another student or any other person to hand in as my own.

4. I have not allowed, and will not allow, anyone to copy my work with the intention of passing it off as his or her own work.

SIGNATURE ..... Nolte .....

"Everything in this book may be wrong."

~Richard Bach~

RESUME

Les agents ciblant les microtubules sont des médicaments anticancéreux efficaces. Leur utilisation dans le cadre d'un traitement combiné avec des rayonnements ionisants est également une stratégie prometteuse. Cependant, l'apparition de résistances aux produits chimiques et aux radiations nécessite de rechercher d'autres types de traitements. Nos laboratoires ont récemment décrit plusieurs médicaments qui ciblent directement ou indirectement les microtubules. Plus particulièrement, d'une part un analogue du 2-méthoxyestradiol, un poison de fuseau se liant à des microtubules et provoquant la formation de fuseaux mitotiques anormaux: le 2-éthyl-3-*O*-sulphamoyle-estra-1,3,5 (10) 16-tétraène (ESE-16). D'autre part, le 9-benzoyloxy-5,11-diméthyl-2H, 6H-pyrido [4,3-b] carbazol-1-one (LimPyr1), un nouvel inhibiteur des LIM kinases induisant indirectement la stabilisation des microtubules. Il a été démontré récemment que LimPyr1 est actif sur les modèles de cancer du sein résistants au taxol. En tant que médicaments ciblant les microtubules, les deux agents, ESE-16 et LimPyr1, induisent des défauts mitotiques. Nous émettons donc l'hypothèse qu'ils pourraient sensibiliser les cellules aux radiations. Le but de ce projet de thèse était de vérifier cette hypothèse et, plus précisément, de déterminer si de faibles doses de ESE-16 et de LimPyr1 pourraient augmenter l'apoptose et retarder la réparation nucléaire induite par le rayonnement dans les cellules du cancer du sein *in vitro*.

Différentes lignées cellulaires cancéreuses, les cellules MCF-7, MDA-MB-231 et BT-20, ont été exposées à ESE-16 et à LimPyr1 pendant 24 heures avant un rayonnement de 8 Gy. Les effets de ces combinaisons thérapeutiques ont été comparés à ceux obtenus à partir de cellules exposées aux composés seuls ou aux seules radiations. L'activation des voies de survie et des voies apoptotiques intrinsèques a été étudiée. Les résultats ont révélé une augmentation de la signalisation de la survie et de la mort dans les cellules exposées aux traitements individuels. Les traitements combinés ont diminué la survie des cellules alors que la signalisation apoptotique augmentait, entraînant une apoptose accrue. En outre, les traitements combinés ont augmenté de manière significative la présence de micronoyaux dans les cellules BT-20, indiquant une augmentation des dommages à l'ADN. Les cellules MCF-7 et MDA-MB-231 présentent une formation de micronoyaux similaire lorsqu'elles sont exposées à la combinaison de traitements ou au rayonnement uniquement. La phosphorylation de H2AX (γH2AX) (normalement augmentée lors de dommages à l'ADN) et l'expression de Ku70 (nécessaire pour la réparation de l'ADN) étaient diminuées dans les cellules de cancer du sein prétraitées 2 heures après l'irradiation par rapport aux cellules exposées à l'irradiation uniquement. L'expression de H2AX et Ku70 est cependant significativement accrue 24 heures après irradiation des cellules prétraitées par rapport aux cellules exposées aux traitements individuels. Des expériences portant sur la réponse adaptative ont révélé que LimPyr1 diminuait le développement de la résistance aux radiations en augmentant la perméabilité transmembranaire mitochondriale et en générant des ROS, un mécanisme qui n'est pas observé dans cellules traitées par ESE-16. Nous avons également observé une communication intercellulaire entre les cellules exposées au rayonnement et les cellules non exposées via l'effet induit par le rayonnement.

En conclusion, le blocage mitotique partiel induit par ESE-16 et LimPyr1 rend les chromosomes plus exposés aux dommages dus aux radiations, comme l'indique l'augmentation de la présence de micronoyaux. De plus, les deux composés diminuent la signalisation et le trafic des protéines de protection et de dommages à l'ADN. En outre, LimPyr1 empêche le développement de résistances aux radiations dans les cellules exposées aux radiations.

MOTS CLES : Cancer, Radiosensibilisation, Dynamique des microtubules, Apoptose, Lésions de l'ADN

Summary

Microtubule targeting agents are effective anti-cancer drugs. Their use as part of a combined treatment modality with ionising radiation is also a promising strategy. However, the emergence of chemical and radiation resistance requires searching for alternative treatments. Our laboratories have recently described several drugs that directly or indirectly target the cellular microtubules. 2-Ethyl-3-*O*-sulphamoyl-estra-1,3,5(10)16-tetraene (ESE-16), an analogue of 2-methoxyestradiol, is a microtubule targeting agent that binds to microtubules causing the formation of abnormal mitotic spindles. 9-Benzoyloxy-5,11-dimethyl-2H,6H-pyrido[4,3-b]carbazol-1-one (LimPyr1) is a novel inhibitor of LIM kinases that indirectly induces microtubule stabilization. As microtubule-targeting drugs, both agents, ESE-16 and LimPyr1, induce mitotic defects. We thus hypothesized that they could sensitize cells to radiation as the G_2/M phase is the most radiosensitive phase of the cell cycle. The aim of this PhD project was to test that hypothesis and, more specifically, to investigate whether low-doses of ESE-16 and LimPyr1 could increase apoptosis and delay nuclear repair induced by radiation in breast cancer cells *in vitro.*

Breast cancer cell lines namely MCF-7-, MDA-MB-231- and BT-20 cells, were exposed to ESE-16 and LimPyr1 for 24-hours prior to 8 Gy radiation. The effects of these combination therapies were compared to those obtained from cells exposed to the compounds alone or only to radiation. The activation of the survival and intrinsic apoptotic pathways were investigated. Results revealed an increase in survival and death signaling in cells exposed to the individual treatments. The combination treatments decreased cell survival while apoptotic signaling was increased, resulting in increased cell death. Furthermore, the combination treatments significantly increased the presence of micronuclei in BT-20 cells, indicating an increase in deoxyribonucleic acid (DNA) damage. MCF-7- and MDA-MB-231 cells displayed similar micronuclei formation when exposed to the combination treatments or radiation only. Phosphorylation of H2AX (γH2AX) (normally increased upon DNA damage) and Ku70 expression (required for DNA repair) were decreased in pre-treated breast cancer cells 2 hours after irradiation compared to cells exposed to radiation only. The expression of γH2AX and Ku70, however, was significantly increased 24 hours after irradiation in the pre-treated cells relative to the cells exposed to the individual treatments. Investigation into the radiation-induced resistance by dose fractionation revealed that LimPyr1 decreased radiation resistance development by increasing the permeability of the mitochondrial transmembrane (flow cytometry measuring Mitocapture™). An increase in the generation of reactive oxygen species (ROS) (flow cytometry employing hydroethidine) was not observed in ESE-16 pre-treated cells exposed to fractionated radiotherapy. We also observed pro-apoptotic signaling between cells exposed to radiation and non-exposed cells via the radiation-induced bystander effect.

In conclusion, the anti-mitotic effect of ESE-16 and LimPyr1 renders the chromosomes more exposed to radiation damage as assessed by the increased occurrence of micronuclei. Moreover, both compounds decreased the signaling and trafficking of DNA damage and repair proteins. Additionally, LimPyr1 prevented the development of radiation resistance in cells exposed to fractionated radiation doses.

KEY WORDS: Cancer, Radiosensitization, Microtubule dynamics, Apoptosis, DNA damage